Knee Extension with less Hip Flexion:
Biomechanical and Evoked EMG Analysis during Selective Surface Stimulation of the Quadriceps

Kylie de Jager

A thesis submitted in partial fulfilment
of the requirements for the degree of
Doctor of Philosophy
of the
Department of Medical Physics and Bioengineering
University College London.

Supervisor: Prof. N. de N. Donaldson
Second Supervisor: Prof. D. Newham

November 23, 2012

We are at the very beginning of time for the human race. It is not unreasonable that we grapple with problems. But there are tens of thousands of years in the future.
Our responsibility is to do what we can, learn what we can, improve the solutions,
and pass them on.

- Richard Feynman

Official declaration

I, Kylie de Jager, confirm that the work presented in this thesis is my own. Where information has been derived from other sources, I confirm that this has been indicated in the thesis.

Abstract

During FES cycling when the Quadriceps muscles are activated both knee extension and hip flexion moments occur simultaneously, decreasing the total power output. Of the three superficial muscles, Rectus femoris is a biarticular muscle that produces both a knee extension and a hip flexion, while Vastus lateralis and Vastus medialis are only knee extensors. This thesis is an investigation whether, using surface stimulation, selective stimulation of the Vastii can produce knee extension moment with less hip flexion. A system was developed for measurement of the joint moments and evoked myoelectric response in these three muscles, while seated subjects were stimulated.

The dynamometer measures the magnitude and position of two forces that restrain the leg, from which joint moments are calculated. The design and construction of the hardware, electronics and software is presented. Validation of the dynamometer against known moments produced with a spring-loaded dummy leg showed good correlation. The influence of random and systematic errors on the estimated joint moments indicate that the dynamometer should be used for comparing the responses for different electrode configurations within single sessions.

The close proximity of the EMG recording electrodes to the stimulating electrodes causes artefact that obscures the M-wave. This was partly overcome by amplifying with a current conveyor circuit, and by a novel biphasic stimulator with pulse width ratio adjustment. The design and construction of both stimulator and amplifier are discussed, also the mechanisms causing the artefact (voltage gradient, skin-electrode interface and common mode voltage).

A study with ten able-bodied subjects was performed. EMG analysis showed that it is possible to selectively stimulate the Vastii and this does reduce hip flexion moment, however beside the inevitable reduction of knee extension moment, the reduction of the hip flexion is less than expected, perhaps due to stimulation of other muscles of the anterior thigh.

Opsomming

Tydens fietsry wat bewerkstellig word deur funksionele elektriese stimulasie, vind daar gelyktydig beide ’n knieguitrekking asook heupfleksie plaas as die verhoofdige dybeenspiere oftewel Musculus quadriceps femoris geaktiveer word. Dit verlaag die totale uitset drywing. Van die drie opervlakkige spiere is Rectus femoris ’n tweerigting artikulêre spier wat beide ’n knieguitrekking en ’n heupfleksie bewerkstellig terwyl Vastus lateralis en Vastus medialis slegs ’n knieguitrekking bewerkstellig. Hierdie tesis ondersoek of deur die gebruikmaking van oppervlaktestimulasie, die selektiewe stimulasie van die Vastii ’n knieguitrekking kan veroorsaak met verminderde heupfleksie. ’n Stelsel is ontwikkel vir die meet van die gewrigsbewegings en gepaardgaande mioelektriese respons in die drie spiere terwyl die sittende persoon gestimuleer word.

’n Dinamometer meet die grotte en posisie van die twee kragte wat die been vashou waarvandaan die gewrigsmomente bereken word. Die ontwerp en konstruksie van die apparaat, elektronika en programmatuur word aangebied. Die uitset van die dinamometer het goeie korrelasie getoon met die bekende momente van ’n veerbelaaide kunsbeen. Die invloed van lukrake- en sistematiese foute op die geskatte gewrigsmomente dui daarop dat die dinamometer gebruik moet word om die response van verskillende elektrodes te vergelyk tydens ’n enkele sessie.

Die nabyheid van die elektromiograaf se elektrodes en die stimulasie elektrodes veroorsaak effekte wat die M-golf versteur. Hierdie is gedeeltelik oorkom deur gebruik te maak van ’n eenheids-stroomversterker en ’n tweefase stimulator met dienssiklus verstelling. Die ontwerp en konstruksie van beide die stimulator en die versterker word bespreek asook die meganismes wat die versteuring veroorsaak (spanningsgradiënt, vel-elektrode voegvlak en die gemenemodus-spanning).

’n Studie met tien gesonde persone is uitgevoer. Elektromiograaf analise toon dat dit moontlik is om selektief die Vastii te stimuleer en dit veroorsaak wel ’n vermindering in die heupfleksiemoment. Hoewel die knieguitrekkingmoment ook verminder is, is die vermindering in heupfleksie minder as verwag. Moontlik as gevolg van ander spiere in die anterieure dy wat ook gestimuleer is.

Acknowledgements

There is a famous saying, “No man is an island”. I however, have a bad habit of not expressing my gratitude to the fellow inhabitants of my island. Therefore, I’m taking this opportunity to name all of those that played a part in helping me through the last four and a half years of my life, no matter how small, no matter when, no matter what aspect of life they contributed to. If I have by chance forgotten to include someone, please don’t think that your help was any less appreciated. We truly are the sum of our parts, and these are the people who make up the various parts of my life.

Firstly, I’d like to thank the *Implanted Devices Group* at UCL. My supervisor, Nick, for his patience, understanding and support. Under your guidance I have learnt so much during my time with the group, and gained both experience and confidence in my abilities as an engineer. Tim P, for your wealth of engineering experience, and willingness to share this through answering the hundreds of questions I bombarded you with. Anne, for your never ending help, ready advice when listening to the trials and tribulations of a PhD student, and for being a life-saver by taking me in as your flatmate during the last stages of writing up. Joe E, for your expertise and help with the building aspect of my project. I had a habit of springing things on you at the last minute and you were always ready to help. Runhan, for sharing the load, visits to the noodle bar, and being a true friend. Modupe, your patience and help with the chair was invaluable, especially during those early days when we were still learning. The rest of the IDG group, Nate, Antoine, Pablo, Andreas, Nooshin, all of whom have helped out in some small way.

Secondly, the people at KCL. My second supervisor, Di, for sharing your insight and expertise on the physiological aspects of my thesis. With my engineering background this was unknown territory, and in some ways the most trying part of my work. Lynsey, you were my guide when I first started this project. Thank you for being so forthcoming with your knowledge and experience, I learnt a lot from you. The support staff at KCL, Tony and Lindsey, for all your help with the necessary equipment and lab-related technicalities of carrying out a study.

I’d also like to thank the EIT group at UCL. Prof David Holder, for letting me take up valuable work space when I sat with your group for six months. The Siberians, Hwan, Brett, Tugba and James, for assisting me with my work and numerous visits to *Hare and Tortoise*.

A special thanks to all the subjects who took part in my study, all the members of the Medical Physics Department at UCL and the funding bodies of my scholarship (the *British Council* and the *Commonwealth Scholarship Commission*). Without all of you this would not have been possible.

Away from the university environment I need to make a special mention for the crew from *Barnfield Horse Riding School*, Suzanne, Wendy, Wiola, Dasha, Angela and Anja. You have been my PhD-support network, by giving me much needed respite from the PhD work. Your

unique brand of insanity helped to keep me sane! A special thanks to Suzanne and Dasha for giving me a place to stay during my nomadic existence.

Adrian F, Ali and Melinda, my fellow residents of 42 Mill Street. Sara, for sharing your PhD experiences. Sato, for train journeys and lunches.

My South African friends who I've seen North of the equator. Matthew, for building snowmen in Richmond park, swimming sessions in Hamstead Heath, weekend hikes along the Thames and a much needed break when visiting you in Toulouse. Charné and Bruce for trips to Cornwall and Wales, and, your on going support and understanding from South Africa. Tim F, Jaycee, Barry and Barbara, for London based adventures and for being the familiar faces from home in such a crowded city. Johan and Taryn, for your support and encouragement, and giving me somewhere to stay in Delft.

To my friends from across the puddle in Blacksburg, Virginia, all of whom I've seen on this side of the puddle too; Adrian B, on the speakers box in Hyde park, Joe G, during an Irish roadtrip, and Pankaj, in countless Skype chats. All of you were further along in the PhD process than me, and you all readily provided support and advice when needed.

My friends back home in South Africa, Michelle (aka Hutchy), Roderick, Cindy, Adelle, Shawn, Rubendran, Adrian C, Candice, and Dean deB. I've known all of you for more than a decade, some closer to three. Thank you for all the years of support and friendship and always being there. Special thanks as well to Ivan Hofsajer, my undergraduate lecturer, master's thesis supervisor and later friend. Thank you for your support and guidance in the early years which gave me the confidence I needed in my own abilities to complete this PhD.

To my family in South Africa, Daan, Rita, Geoffrey, Cynie, and Richard, who is sadly no longer with us. Thank you, for a lifetime of being there. My cousin, Dean deJ, for the UK visit and bumper cars in Leicester square. Thank you as well to my Australian family for meeting up with me in London after travelling all the way from down under; Norman and Vivienne, for sharing your PhD experiences with me and Suzie, for your enthusiasm for all things engineering, which gave me renewed motivation and perspective.

The Townies, Donna-Lee and Gary. Thank you for being supportive, inviting me into your home and being part of the UK South African contingent, a little piece of home.

Gill, my mom's long lost cousin in Broadstairs, that living in London gave me the opportunity to meet for the first time. Thank you for your support and help, giving me somewhere to stay, for long chats and cranberry salads.

The Bobs, Viv and Zane. You have been there from day one. Thank you for inviting me into your lives and home, for looking out for me and always being ready to help. Thank you for never saying no, the countless times I needed to sleep on your couch, and, for being my family in the UK.

My family back home in South Africa. My mom and dad, Mother and Mouse, my brother, Justin, and my grandparents, Ouma (gone, but not forgotten) and Oupa. For everything you've ever given me, your guidance and love. For being my rock and always believing in me, even when my own belief faltered. Your selfless, unflinching support. For helping me through the difficult times and never thinking less of me, even when confronted by a somewhat frayed about the edges, PhD student. For showing me what the truly valuable things in life are, for being yourselves and for being such an integral part of my life, even when separated by oceans.

And lastly, *the Creator*, for the privilege.

Contents

Official declaration iii

Abstract v

Opsomming vi

Acknowledgements vii

Contents x

List of Figures xvi

List of Tables xxii

List of Abbreviations xxv

I FES in context 1

1 Background and thesis outline 2

1.1 Muscle activation during recumbent cycling 3

1.2 Neuromuscular stimulation 6

1.2.1 Neuromuscular anatomy 6

1.2.2 The origin of the M-wave 7

1.3 Evoked EMG measurements 7

1.3.1 Typical M-wave measurements 7

1.3.2 Crosstalk 9

1.4 Hypotheses for the low PO and efficiency of FES cycling 12

1.5 Research question 14

1.5.1 Thesis outline 15

II Biomechanical analysis 19

2 Bi-moment chair for the measurement of hip and knee joint moments 20

2.1 Introduction . . . 20
2.2 Freebody analysis of a seated subject . . . 21
2.3 Construction of the Bi-moment chair . . . 24
2.3.1 Data acquisition card . . . 24
2.3.2 Sensors . . . 24
2.3.3 Stimulation equipment . . . 26
2.3.4 Sensor electronics box . . . 27
2.4 Calibration of the sensors . . . 27
2.4.1 Spring pot calibration . . . 27
2.4.2 Strain gauge transducer calibration . . . 29
2.5 Data analysis and moment calculation . . . 30
2.5.1 Timing interval identification using the pulse width recorder . . . 32
2.5.2 Spring pot string lengths . . . 33
2.5.3 Hip joint centre . . . 34
2.5.4 Knee joint centre . . . 35
2.5.5 Position of point $\boldsymbol{p_{ft}}$ . . . 35
2.5.6 Position of point $\boldsymbol{p_{fs}}$ . . . 37
2.5.7 Direction vectors . . . 37
2.5.8 Force vectors . . . 37
2.5.9 Moment vectors $\mathbf{M}_k$ and $\mathbf{M}_h$ . . . 40
2.6 Summary . . . 40

3 Error analysis and validation of Bi-moment chair measurements 41
3.1 Introduction . . . 41
3.2 Validation of measurements . . . 42
3.2.1 Construction of LiAM . . . 42
3.2.2 Calibration of LiAM . . . 43
3.2.3 Experimental results for LiAM . . . 45
3.3 Random errors . . . 49
3.3.1 Source of random errors . . . 49
3.3.2 Influence of random errors on calculated joint moments . . . 52
3.3.3 Discussion . . . 54
3.4 Systematic errors . . . 57
3.4.1 Source of systematic errors . . . 57
3.4.2 Influence of assumptions on calculated joint moments . . . 60
3.4.3 Discussion . . . 61
3.5 Overall measurement errors seen with the Bi-moment chair . . . 62
3.5.1 Combined influence of random and systematic errors . . . 62
3.5.2 Typical joint moment measurements . . . 64

3.6 Summary 68

4 Joint moments captured using the Bi-moment chair 69

4.1 Introduction 69
4.2 How the study was structured 69
4.2.1 Electrode positions 70
4.2.2 Recruitment curve protocol 71
4.2.3 Fatigue tests 73
4.2.4 Protocol followed during each session 74
4.2.5 Subject participation 75
4.3 Study outcome 76
4.3.1 Muscle fatigue 76
4.3.2 Moment curves 79
4.4 The way forward 86
4.5 Summary 89

III Capturing evoked EMG measurements 91

5 Constant current biphasic stimulator with pulse width ratio adjustment 92

5.1 Introduction 92
5.2 Circuit Design 92
5.2.1 Biphasic Output board 94
5.2.2 μC Header board 100
5.2.3 Power Supply board 101
5.2.4 Current Amplitude Display (CAD) board 103
5.2.5 Interconnection board 104
5.3 Construction and assembly 106
5.4 Programming the microcontroller 109
5.5 Stimulator development 113
5.5.1 Output waveforms 113
5.5.2 Calibrating the stimulator 115
5.6 Stimulator performance 116
5.6.1 Effect of PW_r on C_b voltage 116
5.6.2 Output impedance 121
5.7 Summary 122

6 Current conveyor based blanking EMG amplifier 124

6.1 Introduction 124
6.2 Circuit design 125
6.2.1 Power Supply board 127

6.2.2 Preamplifier board . . . 128
6.2.3 Signal Processing board . . . 132
6.3 Construction and assembly . . . 139
6.3.1 The power supply unit . . . 139
6.3.2 The preamplifier unit . . . 142
6.3.3 The amplifier box . . . 145
6.4 Amplifier development . . . 150
6.4.1 Common mode voltage range . . . 150
6.4.2 Interference reduction . . . 151
6.5 EMG amplifier performance . . . 154
6.5.1 Frequency response . . . 154
6.5.2 Blanking interval response . . . 156
6.5.3 Transient response . . . 159
6.5.4 Recording electrode orientation and M-wave polarity . . . 162
6.6 Summary . . . 162

7 Stimulation artefact: understanding the causes and reducing the effect 164
7.1 Introduction . . . 164
7.2 Voltage gradient . . . 167
7.2.1 Electrode orientation and stimulation artefact polarity . . . 168
7.2.2 Longitudinal versus transverse placement of recording electrodes . . . 170
7.3 Electrode-skin interface . . . 172
7.3.1 PSPICE model of the *Stimulator-Body-Amplifier* system . . . 175
7.3.2 Inter-electrode voltage . . . 178
7.3.3 Stimulation artefact and current density . . . 180
7.3.4 Stimulation artefact and electrode properties . . . 181
7.3.5 Pulse width ratio and stimulation parameters . . . 182
7.4 Common mode voltage . . . 186
7.4.1 Initial investigation . . . 187
7.4.2 Positioning of the reference electrode . . . 190
7.4.3 Limiting the common mode voltage at the EMG amplifier input . . . 193
7.5 Other causes of stimulation artefact . . . 197
7.6 The final verdict on stimulation artefact . . . 198
7.7 Summary . . . 201

IV Biomechanical and evoked EMG analysis 203

8 Simultaneous measurement of joint moments and M-waves 204
8.1 Introduction . . . 204

8.2 How the study was structured . . . 205
8.2.1 Equipment setup . . . 205
8.2.2 Electrode orientation . . . 205
8.2.3 Recruitment curve protocol . . . 207
8.2.4 Protocol followed during each session . . . 208
8.2.5 Subject participation . . . 209
8.3 Understanding the results . . . 209
8.3.1 Effectiveness of stimulation artefact elimination methods . . . 213
8.3.2 Effect of stimulation artefact elimination on data analysis . . . 218
8.3.3 Crosstalk . . . 219
8.4 Study outcome . . . 220
8.4.1 Muscle fatigue . . . 220
8.4.2 Moment curves . . . 223
8.4.3 Selectivity of stimulation . . . 226
8.4.4 Biomechanical and evoked EMG measurements . . . 233
8.4.5 Conclusion . . . 237
8.5 Summary . . . 237

9 Discussion and future work 239
9.1 Introduction . . . 239
9.2 Measuring joint moments with the Bi-moment chair . . . 240
9.2.1 The system developed to measure joint moments . . . 240
9.2.2 Critical evaluation of the Bi-moment chair . . . 242
9.2.3 Future work . . . 243
9.3 Evoked EMG measurements . . . 243
9.3.1 The system developed to measure evoked EMG . . . 244
9.3.2 Future work . . . 247
9.4 The research question . . . 249
9.4.1 Study results . . . 249
9.4.2 Discussion and conclusions . . . 250
9.4.3 Shortcomings of the Bi-moment chair study . . . 251
9.4.4 Implications for FES cycling . . . 252

V Appendices and References 253

A Bi-moment chair design and construction 254
A.1 Data acquisition card . . . 254
A.2 Stimulation equipment . . . 256
A.2.1 Optoisolator . . . 256

A.2.2 Pulse width recorder . . . 256
A.3 Sensor electronics box . . . 257
A.3.1 Spring pot circuitry . . . 257
A.3.2 Strain gauge amplifiers . . . 257
A.3.3 Power supply . . . 259
A.3.4 DAQ6024E connector block . . . 261
A.4 Simultaneous solution of distance equations . . . 261
A.4.1 Solution in two dimensions . . . 261
A.4.2 Solution in three-dimensions . . . 263

B Error analysis **265**
B.1 *Codamotion* investigation of Bi-moment chair assumptions . . . 266

C Biphasic stimulator design and construction **267**
C.1 Stanmore stimulator . . . 267
C.2 Biphasic stimulator user guide . . . 268

D Blanking amplifier design and construction **271**
D.1 Circuit description of the AD844 . . . 271
D.2 Isolation amplifier design . . . 272
D.3 Differential gain calibration . . . 273

E Stimulation artefact **275**
E.1 Estimation of time constants from measured data . . . 275
E.2 Derivation of $\boldsymbol{PW_r}$ equations, as used for the recruitment curve protocol . . . 275
E.3 Residual charge on recording electrodes . . . 276

F Bi-moment chair study **280**
F.1 Origin of the *major* positions . . . 280
F.2 Stanmore stimulator recruitment curve protocol settings . . . 282
F.3 T-test analysis of the *major* position moment curves . . . 282
F.4 M-wave scatter plots and EMG curves without crosstalk adjustments . . . 284

References **288**

List of Figures

1.1 Anatomy of the human leg, reproduced from [Cash, 2000], with permission. . . 4
1.2 Recumbent cycling polar plot, reprinted from Johnston et al. [2007], with permission. 5
1.3 The motor unit concept, after Jones et al. [2004], with permission. 6
1.4 A typical M-wave measurement and M-wave properties. 8
1.5 Detection systems for assessing crosstalk, reproduced from Koh and Grabiner [1993], with permission. 10
1.6 Power generated during FES cycling, reproduced from Szecsi et al. [2007], with permission. 13
1.7 Thesis layout. 15

2.1 Link-segment models used in the freebody analysis of a seated subject. 21
2.2 Schematic representation of the Bi-moment chair. 23
2.3 Wiring diagram of the hardware used to construct the chair. 25
2.4 The sensors. 26
2.5 Sensor electronics box assembly. 28
2.6 Fitted and adjusted calibration lines used for a spring pot. 29
2.7 Calibration of strain gauge transducers. 29
2.8 Definitions of dimensions, location of three-dimensional coordinates and orientation of vectors, as used during the Bi-moment chair analysis. 30
2.9 A subject in the Bi-moment chair showing the reference system used. 31
2.10 Flow diagrams of the Bi-moment chair data analysis. 32
2.11 Typical Stanmore stimulator and pulse width recorder signals. 32
2.12 Pulse width recorder calibration data extraction. 33
2.13 Calculation of spring pot string lengths. 33
2.14 Approximation of the position of the HJC, after Kirkwood et al. [1999], with permission. 34
2.15 Calculation of HJC position. 35
2.16 Calculation of KJC position. 36
2.17 Calculation of position p_{ft}. 36
2.18 Calculation of position p_{fs}. 37
2.19 Calculation of direction vectors. 38

2.20 Calculation of force vectors $\mathbf{F}_s$ and $\mathbf{F}_t$. 38
2.21 Strain gauge transducer force extraction. 39
2.22 Calculation of moment vectors $\mathbf{M}_k$ and $\mathbf{M}_h$. 40

3.1 Schematic representation of LiAM. 43
3.2 Calibration of LiAM, showing the pointer and demarcated scale. 44
3.3 Polynomial fitted to LiAM's calibration measurements. 44
3.4 LiAM positioned in the Bi-moment chair. 45
3.5 Scatter plots of moment error vs $\mathbf{M}_k$. 46
3.6 Sling used to replace the rigid support. 47
3.7 Schematic representation of the position of sp_1 in the Bi-moment chair. 48
3.8 Spring pot measurement error analysis. 50
3.9 Variation seen in strain gauge transducer calibration measurements. 51
3.10 Error propagation flow diagram. 52
3.11 Movement in the ASIS, KJC and point p_{ft}, (subject A). 59
3.12 Overall standard deviation of joint moments. 63
3.13 Comparison of moments calculated using Bi-moment chair and *Codamotion* analysis system data. 65

4.1 The three *major* electrode positions, reproduced from Duffell and Newham [2008], with permission. 71
4.2 Recruitment curve stimulation protocol, after Duffell and Newham [2008], with permission. 72
4.3 Moment curves depicting the recruitment of the muscles for the three *major* electrode positions. 72
4.4 Force-frequency relationship, after Jones et al. [2004], with permission. 74
4.5 Force measurements, $\mathbf{F}_s$, captured during a session. 78
4.6 Moment curves measured during all sessions. 80
4.7 Mean moment curves for subjects A, B, C and D. 83
4.8 Placement of recording electrodes between stimulating electrodes. 86
4.9 Typical voltage response of an electrode to a monophasic and biphasic current pulse. 88

5.1 Correlation between the Stanmore stimulator and the Biphasic stimulator. 93
5.2 Circuit schematic for the Biphasic Output board. 94
5.3 Interconnection of supply rails. 95
5.4 Full bridge output stage with gate signals. 96
5.5 Pulse width ratio adjustment principle. 97
5.6 Timing diagrams for current regulator, black traces represent digital signals, while grey traces are analog. 98

5.7 PCB layout for the Biphasic Output board. 100
5.8 Circuit schematic for the Biphasic stimulator Power Supply and μC Header boards. 102
5.9 Delays introduced into power-on signals. 103
5.10 Circuit schematic for the Biphasic stimulator Current Amplitude Display (CAD) board. 105
5.11 Circuit schematic for the Biphasic stimulator Interconnection board. 105
5.12 Timing diagram for the BIT signal. 106
5.13 Photographs of the individual boards. 107
5.14 Board assembly in metal case. 108
5.15 Stimulator wiring diagram, relative to earth. 109
5.16 Schematic of the LCD showing the various menus. 110
5.17 Flow chart of the *Main* routine. 111
5.18 Flow chart of the *Interrupt* routine. 112
5.19 Channel 1 output voltage, showing the oscillation. 113
5.20 Channel 1 output voltage, under full load, prior to adding the second 200V DC-DC converter. 114
5.21 Final output waveform across a 1kΩ resistive load. 115
5.22 Measured values of PW_p and PW_n versus the stimulation pulse width setting. 115
5.23 Voltage across C_b. 117
5.24 Effect of current and PW_r settings on the baseline voltage across C_b. 119
5.25 Average voltage across the blocking capacitor. 119
5.26 Calculation of V_{NT} over a range of N values. 120
5.27 Norton equivalent circuit, after Bobrow [1996], with permission. 121

6.1 Schematic diagram of the current conveyor at the input stage of the EMG amplifier, after Bruun and Haxthausen [1991] and Sedra and Smith [1970], with permission. 124
6.2 Blanking EMG amplifier board layout and shielded interconnections. 126
6.3 Schematic of Blanking amplifier power rails and isolation requirements. 126
6.4 Circuit schematic for the Power Supply board. 127
6.5 Circuit schematic for the Preamplifier board. 129
6.6 PCB layout for the Preamplifier board. 131
6.7 Circuit schematic for the Signal Processing board. 132
6.8 Timing diagram for the blanking interval. 133
6.9 Instrumentation amplifier input filter. 134
6.10 Isolation amplifier circuit, after Vishay [2004], with permission. 135
6.11 Unity-gain amplifier, low pass filter, after Bronzite [1970], with permission. . . 136
6.12 PCB layout for the Signal Processing board. 137

6.13 Edge connector wiring diagram. 139
6.14 Comparison of EMG output signal measured with onboard DC-DC converters and separate power supply unit. 140
6.15 The power supply unit. 141
6.16 Blanking interval switching spikes. 143
6.17 The assembled preamplifier unit. 144
6.18 Enlarged view of Signal Processing board PCB. 145
6.19 Photographs of the Signal Processing board. 147
6.20 Signal Processing board assembly in the amplifier box. 148
6.21 Stimulator and amplifier wiring diagram, relative to earth. 149
6.22 Measurement of the Blanking amplifier's common mode voltage range. 150
6.23 Positioning of the stimulating and recording electrodes on the Quadriceps. . . . 151
6.24 EMG measurements without filters. 152
6.25 Filter frequency response and measured M-waves. 153
6.26 Frequency response of the three EMG amplifiers. 155
6.27 CMRR of the three EMG amplifiers. 156
6.28 EMG output signal dependence on current conveyor biasing (R_CC-BIAS). . . 157
6.29 Origin of the Blanking interval response. 157
6.30 Origin of signal jitter. 158
6.31 Transient response of EMG amplifier 1, differential input voltage. 161
6.32 Transient response of EMG amplifier 1, common input voltage. 161
6.33 Influence of recording electrode orientation on polarity of the M-wave. 162

7.1 Influence of stimulation artefact on EMG measurements. 165
7.2 Schematic representation of current flow between stimulating electrodes. 167
7.3 Path of the discharge current in the *Stimulator-Body-Amplifier* system. 168
7.4 Influence of stimulating electrode orientation on artefact polarity. 169
7.5 Influence of recording electrode orientation on artefact polarity. 169
7.6 EMG measured with longitudinal and transverse recording electrodes. 171
7.7 Equivalent circuit for a surface electrode. 173
7.8 Electrode current and voltage waveforms for a biphasic stimulation pulse. . . . 173
7.9 The *Stimulator-Body-Amplifier* system. 174
7.10 PSPICE simulation of the electrode-skin interface. 175
7.11 PSPICE simulation results. 176
7.12 Inter-electrode voltage, V_{ac} and EMG measurements. 179
7.13 C_b voltage compared against EMG output waveform - current density. 181
7.14 C_b voltage compared with EMG output waveform - electrode properties. 182
7.15 Adjustment of PW_r setting as current intensity increases. 183
7.16 Theoretical and measured PW_r setting as a function of pulse width. 185

7.17 Proximity of recording electrodes to the stimulating electrodes. 186
7.18 EMG measurements, variable PW_r, *Standard* position, reference electrode knee. 187
7.19 Differential and common mode EMG measurements, *Rectus* position. 188
7.20 Differential and common mode EMG measurements, *Standard* position, reference electrode knee. 188
7.21 Voltage gradients for the *Rectus* and *Standard* electrode positions. 189
7.22 Reducing common mode voltage using the reference electrode position. 190
7.23 Differential and common mode EMG measurements *Standard* position, reference electrode posterior thigh. 192
7.24 EMG measurements, variable PW_r, *Standard* position, reference electrode posterior thigh. 192
7.25 Common mode voltage measured at the recording electrodes. 195
7.26 PW_r setting and M-wave measurement with clamping diodes. 196
7.27 Skin-electrode interface effect at the recording site. 196

8.1 Moment curves for the three *major* electrode positions. 204
8.2 The Bi-moment chair, Biphasic stimulator and Blanking amplifier setup. 206
8.3 Orientation of electrodes for the three *major* positions. 206
8.4 Recruitment curve stimulation protocol. 207
8.5 A typical set of results. 210
8.6 M-wave measurements, *Vastii* position, with clamping diodes. 213
8.7 Comparison of M-waves measured with different reference electrode positions, prior to the introduction of clamping diodes. 215
8.8 Comparison of M-waves measured with different reference electrode positions, after introduction of clamping diodes. 217
8.9 Force measurements, $\mathbf{F}_s$, captured during a session. 222
8.10 Moment curves captured for each of the 10 subjects. 224
8.11 Scatter plot of moment curves captured for all 10 subjects. 225
8.12 Normalised peak-to-peak M-wave amplitudes, plotted against the charge delivered with each stimulation pulse. 228
8.13 EMG curves for the three *major* electrode positions. 230
8.14 EMG curves captured for each of the 4 subjects with complete data sets. 231
8.15 Normalised peak-to-peak M-wave amplitudes, plotted against $\mathbf{M}_k$. 234
8.16 Normalised peak-to-peak M-wave amplitudes, plotted against $\mathbf{M}_h$. 235

9.1 Proposed changes to stimulator output stage. 247

A.1 Differential input connections for the DAQ6024E ground-referenced signals, reproduced from NI [2000], with permission. 255
A.2 Pinout of the NI DAQ6024E, reproduced from NI [2005], with permission. . . 255

A.3 Optoisolator circuit diagram. 256
A.4 Pulse width recorder circuit diagram. 256
A.5 Spring pot circuitry. 257
A.6 Strain gauge amplifier circuit diagram, after Shell [1990] and Yu [1999], with permission. 257
A.7 Power supply schematic. 259
A.8 Geometric setup used to define the distance equations. 262

B.1 Movement in the ASIS, KJC and point p_{ft}, (subject B). 266

C.1 Circuit schematic of the Stanmore stimulator Monophasic Output board, reproduced from Phillips et al. [2003], with permission. 267

D.1 Simplified schematic of the AD844, reproduced from AD [1989], with permission. 271
D.2 Isolation amplifier circuit, after Vishay [2004], with permission. 272
D.3 Amplifier gain calibration. 274

E.1 Points used to calculate the time constant of an exponential waveform. 275
E.2 Skin-electrode interface effect at the recording site. 277
E.3 PSPICE simulation of the electrode-skin interface (both stimulating and recording electrodes). 278
E.4 PSPICE simulation results (both stimulating and recording electrodes). 279

F.1 Normalised peak-to-peak M-wave amplitudes without crosstalk adjustments, plotted against the charge delivered with each stimulation pulse. 284
F.2 EMG curves without crosstalk adjustments, captured for each of the 4 subjects with complete data sets. 285
F.3 Normalised peak-to-peak M-wave amplitudes without crosstalk adjustments, plotted against $\mathbf{M}_k$. 286
F.4 Normalised peak-to-peak M-wave amplitudes without crosstalk adjustments, plotted against $\mathbf{M}_h$. 287

List of Tables

1.1 Muscle groups used for FES cycling; muscle functions reproduced from [Cash, 2000], with permission. . . . 3
1.2 Crosstalk in muscles of the Quadriceps. . . . 10
1.3 Crosstalk present in the muscles of the hind limb of the cat, reproduced from [Solomonow et al., 1994], with permission. . . . 11

2.1 Assumptions made by the Bi-moment chair. . . . 23
2.2 Spring pot specifications 25
2.3 Definitions of the spatial coordinates shown in figure 2.8(a). . . . 31
2.4 Definitions of the dimensions shown in figure 2.8(b). . . . 31
2.5 Definitions of the vectors shown in figure 2.8(c). . . . 31

3.1 Calibration measurements for LiAM. . . . 44
3.2 Scale measurements for LiAM. . . . 44
3.3 Standard deviation of spring pot measurements. . . . 50
3.4 Standard deviation of position and dimension measurements. . . . 51
3.5 Sensitivity of moment calculations to σ_{sp} and σ_{SG}. . . . 53
3.6 Sensitivity of moment calculations on position measurements. . . . 55
3.7 Sensitivity of moment calculations on dimension measurements. . . . 56
3.8 Standard deviation of movement seen in the ASIS, KJC and point p_{ft}. . . . 58
3.9 Sensitivity of moment calculations to assumptions. . . . 60
3.10 Overall measurement error, calculated for each stimulation burst. . . . 63
3.11 Maximum joint moment error due to different types of individual errors. . . . 68

4.1 Stimulation parameters for the recruitment curve protocol, reproduced from [Duffell and Newham, 2008], with permission. . . . 72
4.2 Stimulation parameters for the FF ratio, reproduced from [Duffell and Newham, 2008], with permission. . . . 74
4.3 Subject participation in the study. . . . 76
4.4 Results for the MVC and FF ratio tests. . . . 76
4.5 Percentage difference in $\mathbf{F}_s$ measurements during the 9^{th} stimulation burst. . . . 78
4.6 F-test results for standard deviation of *default* and *minor* sessions. . . . 82

4.7 Number of tests carried out with subjects A and B during *default* sessions. . . . 83
4.8 T-test results, difference between moments measured with *major* positions. . . 85
4.9 Percentage of significant differences found. 85

5.1 DC-DC converter characteristics. 95
5.2 Output impedance measurements for both stimulator channels. 122
5.3 Biphasic stimulator specifications. 123

6.1 Power supply design. 128
6.2 Front and back panel components associated with the edge connector. 138
6.3 Shielded cabling pairs. 142
6.4 Blanking amplifier specifications. 163

7.1 *Stimulator-Body-Amplifier* system time constants. 200

8.1 Stimulation parameters, recruitment curve protocol. 207
8.2 Subject participation in the study. 209
8.3 Settings used during sessions for each of the subjects. 211
8.4 M-wave recordings for the *Standard* electrode position. 217
8.5 M-wave recordings for all three *major* positions. 219
8.6 Crosstalk adjustments. 219
8.7 Example: M-wave amplitudes adjusted for crosstalk, *Rectus* position. 220
8.8 Fatigue measurements calculated using $\mathbf{F}_s$ measurements. 220
8.9 Percentage difference in $\mathbf{F}_s$ measurements during the 9^{th} stimulation burst. . . 222
8.10 Electrode positions and stimulation settings used for the complete data sets. . . 226
8.11 Influence of *major* position on relative size of M-waves. 229
8.12 EMG curve observations. 232
8.13 *Major* positions listed in descending order of joint moments. 233
8.14 Muscle functions, reproduced from [Cash, 2000], with permission. 236
8.15 Summary of observations made with the M-wave measurements. 238

A.1 Offset and gain resistor values. 258
A.2 Power supply specifications. 259
A.3 Transformer design. 260
A.4 Output capacitor design. 260
A.5 Data acquisition card and connector block pinouts. 260

E.1 PW_r setting dependence on PW_p. 276
E.2 Example PW_r calculation. 276

F.1 SENIAM recommendations for recording electrode placement on the superficial muscles of Quadriceps, reproduced from Hermens et al. [1999], with permission. 281
F.2 Settings used on the Stanmore Stimulator, reproduced from [Duffell and Newham, 2008], with permission. 282
F.3 Percentage of significant differences found. 282
F.4 T-test results, difference between moments measured with *major* positions. . . 283

List of Abbreviations

AB	Able Bodied
AD	Analog to Digital
AI	Analog Input
AP	Action Potential
ASIS	Anterior Superior Iliac Spine
BI	Blanking Interval
BIT	Blanking Interval Trigger
C1	Channel 1
C2	Channel 2
CAD	Current Amplitude Display
CC	Current Conveyor
CD	Calibration Data
CED	Cambridge Electronic Design
Ch1	Channel 1
Ch2	Channel 2
CM	Common Mode
CMRR	Common Mode Rejection Ratio
COM	Centre of Mass
DC	Direct Current
DD	Double Differential
DM	Differential Mode
EMG	Electromyograph
FES	Functional Electrical Stimulation
FF	Force-Frequency
GT	Greater Trochanter

HJC	Hip Joint Centre
KJC	Knee Joint Centre
IC	Integrated Circuit
LCD	Liquid Crystal Display
LDO	Low Drop Out
LG	Lateral gastrocnemius
LI	Linear Interpolation
LiAM	Limb for the Application of Moments
MAP	Muscle fibre Action Potential
MG	Medial gastrocnemius
MOSFET	Metal-Oxide-Semiconductor Field-Effect Transistor
MUAP	Motor Unit Action Potential
MVC	Maximum Voluntary Contraction
NMJ	Neuromuscular Junction
NR	Not Recorded
PCB	Printed Circuit Board
PO	Power Output
PS	Pubic Symphysis
PW	Pulse Width
PW_n	Negative phase Pulse Width
PW_p	Positive phase Pulse Width
PW_r	Pulse Width Ratio
pwr	Pulse Width Recorder
QPR	QUESTOR Precision Radiography
RE	Recording Electrodes
RF	Rectus femoris
RST	Reset
SA	Stimulation Artefact
SCI	Spinal Cord Injury
SD	Single Differential

SE	Stimulating Electrodes
SENIAM	Surface ElectroMyoGraphy for the Non-Invasive Assessment of Muscles
$SG_{1,2}$	Strain gauge transducers 1 and 2
$sp_{1,2,3,4}$	Spring pots 1 through 4
SSDE	Simultaneous Solution of Distance Equations
TA	Tibialis anterior
VCVS	Voltage Controlled Voltage Source
VL	Vastus lateralis
VM	Vastus medialis
μC	Microcontroller

Part I

FES in context

Chapter 1

Background and thesis outline

Functional Electrical Stimulation (FES) is defined as "the electrical stimulation of the intact lower motor neuron to initiate contraction of paralysed muscle to produce functional movement" [Reed and Low, 2000]. It has been used for many years in the treatment of people with Spinal Cord Injury (SCI), for applications such as standing [Chaplin, 1996], walking [Kralj and Bajd, 1989], and recumbent cycling [Perkins et al., 2001; Szecsi et al., 2007], both with implanted electrodes [Kern et al., 1985] and surface stimulation [Petrofsky et al., 1983].

FES cycling is known to have a number of health benefits, both physiological and psychological [Van Soest et al., 2005]. The physiological benefits have been well documented and include improved muscle strength, improved skin condition and increase in bone density [Mohr et al., 1997*b*]. However, the power output (PO) and metabolic efficiency of SCI cyclists, remains considerably lower than that of Able Bodied (AB) cyclists.

In studies carried out by Duffell et al. [2008] and Mohr et al. [1997*a*], SCI cyclists participated in year long training programs. At the end of the twelve month period Duffell et al. [2008] reported peak PO values ranging from 8.8W to 35.5W, while Mohr et al. [1997*a*] reported similar values ranging from 6W to 42W. Even though both training programs did show an increase in the PO values, when compared with those measured at the start of the year, the values themselves are still moderate. This is especially true when we consider that, in a study carried out by Reiser et al. [2002], AB cyclists were able to cycle at 250W, after just two weeks acclimatisation to recumbent cycling. Furthermore, the metabolic efficiency of SCI cyclists ranges from 2% up to 5% [Glaser et al., 1989; Petrofsky and Stacy, 1992], while for AB cyclists efficiencies around 20% have been recorded [Glaser et al., 1989; Hansen et al., 2002].

These low PO and efficiency values mean that the potential application of FES cycling for functional use is limited. However, as the reasons for the low PO and efficiencies are not understood, it is no simple matter to improve either the PO or the efficiency of SCI cyclists.

Before we can consider various hypotheses for the low values, it is beneficial to develop a better understanding of what actually happens during recumbent cycling and neuromuscular stimulation, at the physiological level. Typical electromyograph (EMG) measurements, recorded from stimulated muscle, as well as the phenomenon of crosstalk, are also discussed as this is relevant to discussions from Chapter 6 onwards.

1.1 Muscle activation during recumbent cycling

During FES cycling, the muscles of the lower limb are electrically stimulated. However, particularly in the case of surface stimulation, the number of muscles to be stimulated are limited by the number of channels available in the stimulator and the number of electrodes that can be placed on the thigh, and, with some stimulation setups, the shank as well [Duffell et al., 2008]. Previous studies have successfully created a cycling action by stimulating the Quadriceps, the Gluteals and the Hamstrings [Perkins et al., 2001; Szecsi et al., 2007].

A brief overview of the function of the muscles, used during FES cycling, is provided in table 1.1, [Cash, 2000]. Figure 1.1 shows the anatomy of the lower limb and the location of the muscles listed in the table.

The table also distinguishes the muscles as being either mono- or bi-articular, according to whether they cross one or two joints [Jarmey, 2004; Trew, 2005]. Mono-articular muscles therefore only have one main function while bi-articular muscles have two. For example the mono-articular muscle, Vastus lateralis, performs a knee extension, while a bi-articular muscle such as Rectus femoris, is responsible for both knee extension and hip flexion.

The exact sequence of muscle contraction and relaxation that produces the cycling action in AB cyclists is quite involved. Hakansson and Hull [2005] and Johnston et al. [2007] measured muscle activity during recumbent cycling. Figure 1.2 shows a polar plot of the regions of muscle activity (in the left leg) during a revolution of the crank arm, as measured by Johnston et al. [2007].

Table 1.1: Muscle groups used for FES cycling; muscle functions reproduced from [Cash, 2000], with permission.

	Muscle	Bi- or mono-articular	Action
Anterior leg muscles			
Quadriceps	Rectus femoris	Bi-	Hip flexion and knee extension
	Vastus lateralis Vastus intermedialis Vastus medialis	Mono-	Knee extension
Posterior leg muscles			
Gluteals	Gluteus maximus	Mono-	Extend and outwardly rotate hip, extend trunk *Proximal part*: slight abduction *Distal part*: Slight adduction
	Gluteus medius Gluteus minimus	Mono-	*Anterior*: Flex and inwardly rotate hip *Posterior*: Extend and outwardly rotate hip
Hamstrings	Biceps femoris	Bi-	Knee flexion and outward rotation when flexed, and hip extension
	Semimembranosus Semitendinosus	Bi-	Knee flexion and inward rotation when flexed, and hip extension

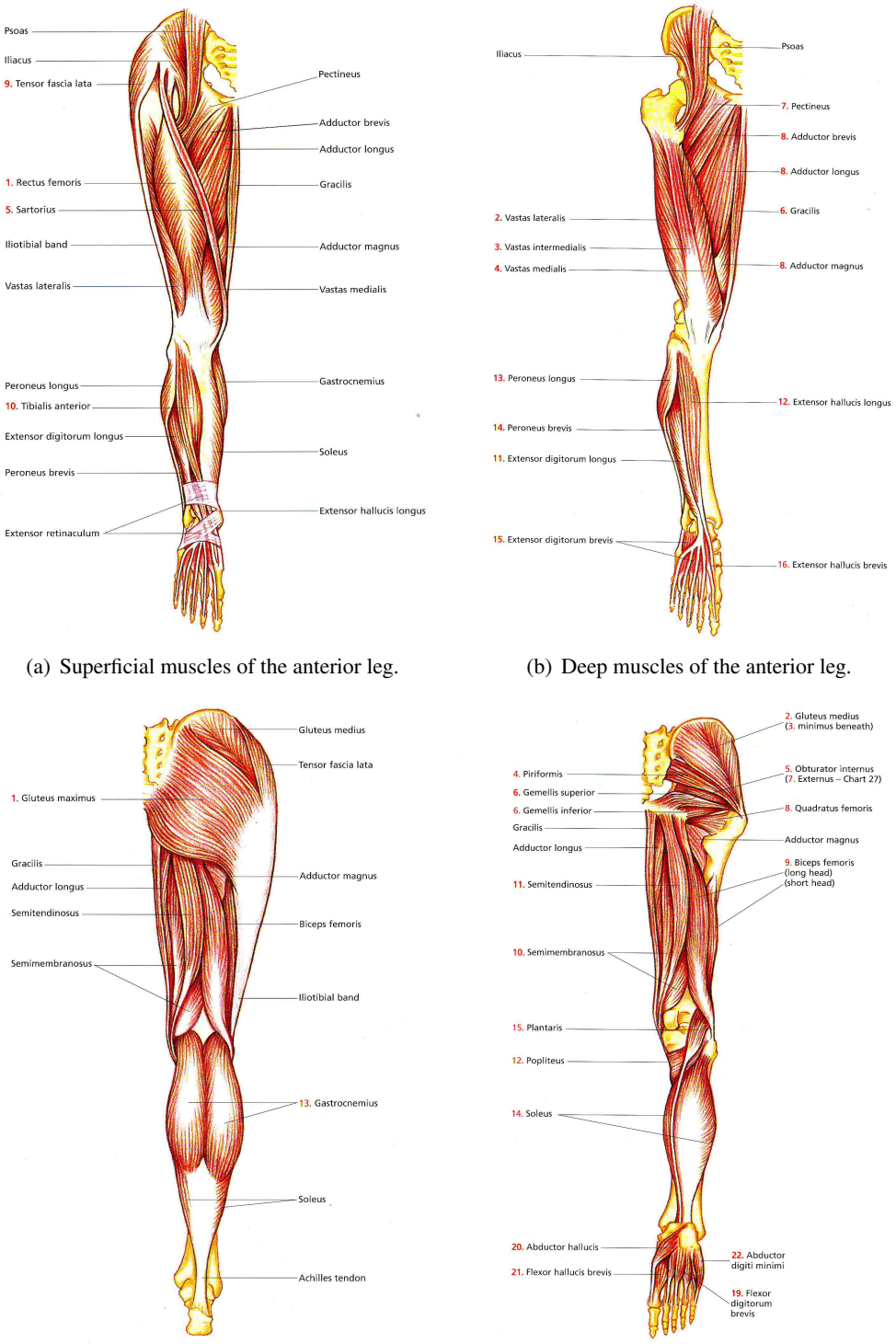

(a) Superficial muscles of the anterior leg.

(b) Deep muscles of the anterior leg.

(c) Superficial muscles of the posterior leg.

(d) Deep muscles of the posterior leg.

Figure 1.1: Anatomy of the human leg, reproduced from [Cash, 2000], with permission.

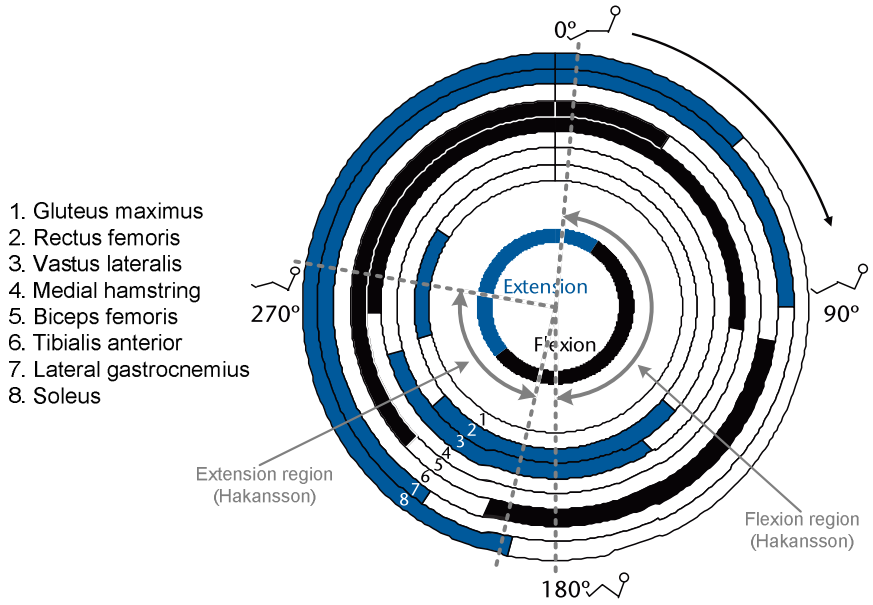

Figure 1.2: Polar plot showing the average regions of muscle activity during recumbent cycling, reprinted from Johnston et al. [2007], with permission of the American Physical Therapy Association. This material is copyrighted, and any further reproduction or distribution requires written permission from APTA.

Johnston et al. [2007] used the following guidelines in drawing the figure:

1. Zero degrees was taken to be when the the left crank arm was horizontal and farthest from the subject.

2. Muscles other than the Gluteus maximus were labeled as primary extensors and flexors based on their actions at the knee and at the ankle.

3. The innermost circle represents when hip flexion and extension occurred.

4. The stick figures show the approximate position of the lower extremities (left leg) at that point in the revolution, and the arrow indicates forward movement of the crank when viewed from the right side of the cycle.

The later discussion in Section 1.4 mentions the role of the Quadriceps during FES cycling. For this reason, it is important to note what the results of Hakansson and Hull [2005] and Johnston et al. [2007] reveal about Rectus femoris (RF), Vastus lateralis (VL) and Vastus medialis (VM).

Hakansson and Hull [2005] showed similar results to Johnston et al. [2007]. However, they also included the muscle activity of VM, which was found to be active simultaneously with VL, although a slight difference, about two degrees, in the onset and offset angles of the two muscles was seen. Furthermore, they also showed that changes in cycling cadence did not cause a change in the co-activation of RF, VM and VL, although a shift in the onset and offset angles did occur.

Hakansson and Hull [2005] split the cycling revolution into functional regions, also referred to as extension and flexion regions, as have been indicated in figure 1.2. According to them, during the extension region, the mono-articular muscles VL and VM (responsible for knee extension), would primarily have contributed towards power development. While the bi-articular muscle, RF, assists in propelling the leg through the transition between the flexion and extension regions. RF also contributes towards the knee extension moment generated by the Vastii muscles.

1.2 Neuromuscular stimulation

During FES cycling, a shaft encoder measures the crank angle. The crank angle is then used to determine which muscle group is stimulated at any given time [Perkins et al., 2001; Szecsi et al., 2007]. The level of muscle activity is dependent on the stimulation intensity, which is controlled by adjusting the various stimulation parameters, namely, pulse width, frequency and current amplitude. The mechanism behind how the stimulation pulse triggers an impulse in the nerve fibres has been well documented in the literature. A brief overview of the relevant neuromuscular anatomy and the mechanism itself is given here.

1.2.1 Neuromuscular anatomy

Figure 1.3 shows the anatomy behind the concept of a motor unit, which consists of a neuron and muscle fibres.

According to Tortora and Derrickson [2006], a neuron is a nerve cell. It consists of a cell body, dendrites and an axon. Motor neurons are responsible for carrying impulses from the brain and spinal cord to the muscles. At the end of the nerve cell we find the neuromuscular junction (NMJ), which was described by Jones et al. [2004] as a "synaptic connection at which the axon branch of the motor neuron meets the muscle fibre." Every axon has many terminal branches, each of which is connected to a muscle fibre [Basmajian and De Luca, 1985]. The muscle fibres supplied by all the branches from a single axon constitute the motor unit.

The number of muscle fibres present in a motor unit, and the number of motor units present in a muscle, depends on the intended function of that muscle. Muscles controlling fine movements and adjustments (e.g. the muscles of the ear, eye, hand and larynx) have from 3 to 300

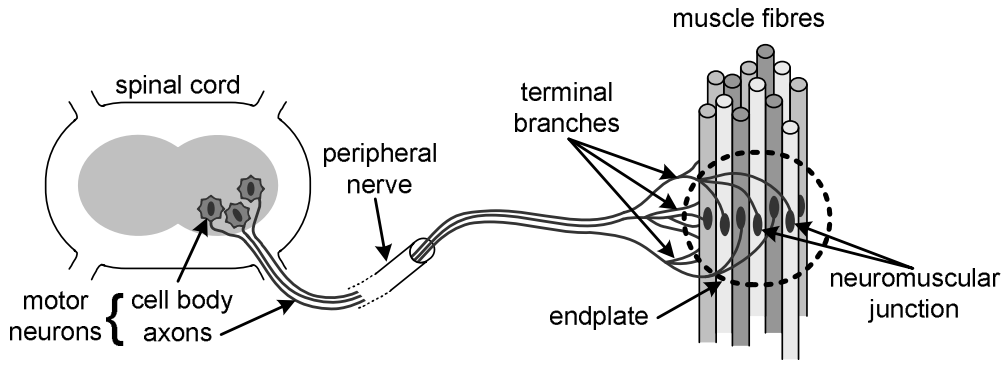

Figure 1.3: The motor unit concept, after Jones et al. [2004], with permission from Elsevier.

muscle fibres per unit, and, ∼120 motor units. In contrast, large coarse-acting muscles (e.g. those of the limbs) have ∼2000 muscle fibres per unit, and, ∼600 motor units [Basmajian and De Luca, 1985; Jones et al., 2004].

The neuromuscular junctions, are normally found near the middle of the muscle fibres, in a region known as the endplate [Basmajian and De Luca, 1985], although adjacent muscle fibres are not necessarily part of the same motor unit [Jones et al., 2004]. Generally there is only one motor endplate in a muscle, although it is possible, in some muscles, in some individuals, for there to be two endplates in a single muscle [Basmajian and De Luca, 1985].

1.2.2 The origin of the M-wave

According to Tortora and Derrickson [2006] the nerve fibres, in this case referring to the axon, have resting potentials determined by ion concentrations on either side of the cell membrane. Gated channels, found in the cell membrane, open and close in response to the membrane potential, thereby allowing ions, on either side of the membrane, to diffuse across it. The membrane also has an inherent threshold potential. If the membrane potential is depolarised to this threshold level, a flow of ions will occur through the gated channels, which results in a further change in the membrane potential, known as the action potential (AP).

Basmajian and De Luca [1985] discussed the activation of motor units during voluntary contractions. They said that the AP propagates along the nerve fibre till it reaches the the NMJ. From the NMJ, the AP continues to propagate in both directions along the muscle fibre, where it is now referred to as a muscle fibre action potential (MAP). An AP will trigger MAPs within all the muscle fibres in one motor unit, causing the fibres to contract almost simultaneously. The MAPs sum together to form what is known as a motor unit action potential (MUAP). Depending on the size of the detection area associated with EMG recording electrodes, and the location of the motor units under these electrodes, the final EMG waveform consists of the sum of a number of MUAPs.

Hodgkin et al. [1952] showed that by introducing a stimulation current to the nerve, the membrane potential is suddenly changed, causing the membrane to depolarise, which triggers an AP. The only difference in the ensuant AP propagation, as compared with that of a voluntary contraction, is that in the case of electrical stimulation, the MUAPs are triggered simultaneously by the stimulation pulse. The resultant EMG measurement, referred to as evoked EMG, is effectively a compound MUAP, termed the M-wave [Farina et al., 2004*a*; Merletti et al., 1992; Tucker et al., 2005]. A M-wave would be measured for each stimulation pulse in a burst of stimulation.

1.3 Evoked EMG measurements

The discussions presented in this section are relevant for later chapters.

1.3.1 Typical M-wave measurements

Figure 1.4 shows a typical M-wave measurement, as often encountered in the literature. The various properties of the M-wave have also been indicated in the figure.

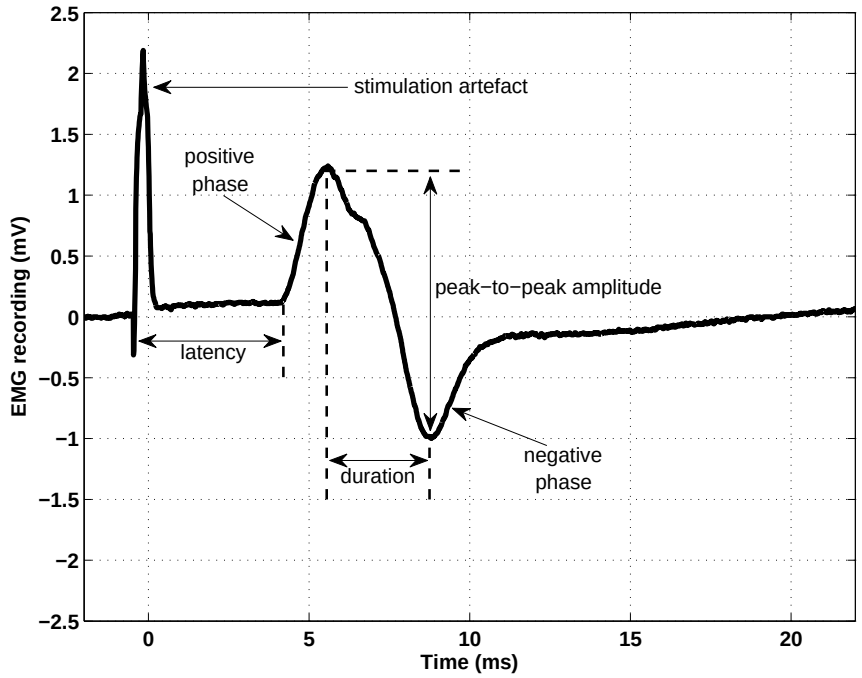

Figure 1.4: A typical M-wave measurement and M-wave properties.

Peak-to-peak amplitude M-wave amplitudes normally range from a few hundred μV to around 5mV [Basmajian and De Luca, 1985]. The M-wave amplitude increases with stimulation current amplitude [Farina et al., 2004*a*].

Duration "The time interval between the positive and negative peaks of the M-wave" [Merletti et al., 1992]. Generally the duration increases during sustained stimulation [Farina et al., 2004*a*].

Latency Latency identifies the period of time between the start of the stimulation pulse (corresponds with the start of the stimulation artefact shown in figure 1.4) and the onset of the M-wave. The length of this time period is dependent on the separation distance between the stimulating and recording electrodes, the shorter the distance, the shorter the latency. Such differences in measured latencies are commonly used to calculate the conduction velocity of nerve fibres [Basmajian and De Luca, 1985].

Shape The shape of the M-wave describes the number of phases present. The M-wave shown in figure 1.2 has two phases. The number of phases is dependent on the position of the muscle fibres relative to the recording electrodes [Basmajian and De Luca, 1985]. In the literature, it is convention that M-wave measurements are drawn so that the first phase is positive, for example, as in Merletti et al. [1992] and Farina et al. [2004*a*].

As mentioned earlier, the level of muscle activity is dependent on the stimulation intensity. By increasing the pulse width or the current amplitude, the amount of charge delivered with each pulse increases. This has the effect of enlarging the region in which nerves may be activated. If this region includes motor fibres, then the corresponding muscles will be stimulated. As

the strength of the muscle contraction is determined by the number of recruited muscle fibres, generally increasing the stimulation intensity in this way, results in a stronger contraction [Reed and Low, 2000].

However, adjusting the stimulation frequency does not alter the number of recruited muscle fibres. At low stimulation frequencies (<15Hz, [Kralj and Bajd, 1989]), the muscle will contract due to a stimulation pulse. It will then return to its relaxed state before the next stimulation pulse, resulting in a muscle twitch. By increasing the frequency, the muscle is unable to fully relax before the next stimulation pulse is delivered, which results in the contraction being superimposed "on the force remaining from the previous stimulus" [Jones et al., 2004]. In so doing the twitches fuse and eventually produce a smooth contraction of muscle.

1.3.2 Crosstalk

Crosstalk is defined in the literature [De Luca and Merletti, 1988; Knaflitz et al., 1988; Merletti et al., 1992] as the measurement of EMG in a given muscle, when the signal itself originates in a different muscle. This is problematic as it can lead to "an erroneous conclusion of coactivation among different muscles when only one muscle is active" [Merletti et al., 1992], particularly in the case of muscles that are close to each other [Farina et al., 2004*b*], such as the Quadriceps. The crosstalk phenomenon has even lead to the detection of muscle activity in totally inactive or denervated muscle, simply by intensely activating a neighbouring muscle [Denny-Brown, 1949].

According to De Luca and Merletti [1988] and Merletti et al. [1992], the type of electrode used to record the EMG greatly influences the amount of crosstalk present in the measurements. Muscle activity recorded using intramuscular electrodes is mostly unaffected by crosstalk. This is due to the small detection volume associated with these types of electrodes. On the other hand, surface electrodes have a much larger detection volume. This has the advantage that the measurements are more indicative of the activation of an entire muscle, but can lack selectivity and are more susceptible to crosstalk.

Anatomical conditions also affect the likelihood of crosstalk being present. The thicker the layer of subcutaneous fat covering the muscles below the recording electrodes, the more prevalent the presence of crosstalk in the measurements [Farina et al., 2004*b*; Solomonow et al., 1994].

One method that has been used to assess the presence of crosstalk is a multi-electrode detection system that captures two signals, a single differential (SD) signal and a double differential (DD) signal, as shown in figure 1.5. The DD detection system has a smaller pick-up volume than the SD detection system, which causes it to have greater selectivity [Koh and Grabiner, 1993]. According to Merletti et al. [1992] a signal generated below the detection electrodes (i.e. a true measurement of muscle activation), would produce a SD and a DD signal of roughly the same amplitude, while a signal generated far from the detection electrodes (i.e. a crosstalk signal), would produce a DD signal of much smaller amplitude than the SD signal. This was shown experimentally by Merletti et al. [1992] when stimulation of VL resulted in an

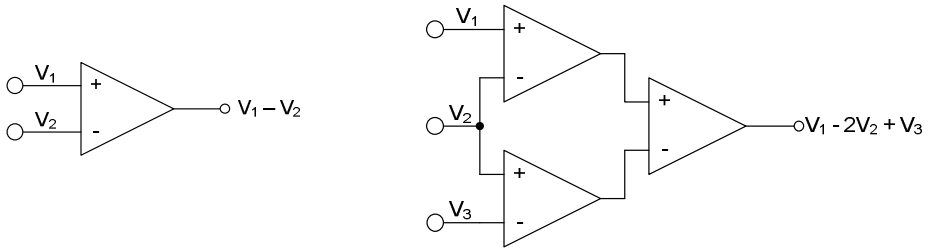

(a) Single differential. (b) Double differential.

Figure 1.5: Detection systems for assessing crosstalk, reproduced from Koh and Grabiner [1993], with permission from Elsevier.

M-wave being measured in VM using the SD detection system, but not with the DD detection system, even though both systems measured an M-wave of similar amplitude in VL.

Knaflitz et al. [1988] and Farina et al. [2002] both used similar SD and DD detection systems to characterise crosstalk in the thigh. Surface stimulating electrodes were placed on the motor point of one of the Quadriceps muscles, to achieve selective stimulation. The peak-to-peak amplitude of the M-waves were then used to calculate a percentage of the SD M-wave amplitude measured in the stimulated muscle that would appear as crosstalk in the adjacent non-stimulated muscle. The results are shown in table 1.2. Knaflitz et al. [1988] gave the maximum percentage crosstalk recorded from a study carried out with 8 subjects, while Farina et al. [2002] calculated the mean from a study carried out with 10 subjects, most of whom had both thighs tested, giving a total of 18 thighs.

Table 1.2: Crosstalk in muscles of the Quadriceps.

Stimulated muscle	**Percentage SD signal attributed to crosstalk**		
	VL	**RF**	**VM**
Maximum percentage, [Knaflitz et al., 1988][a]			
VL	-	18.2	7.7
VM	10.7	8.6	-
Mean $\pm$ Standard Error, [Farina et al., 2002][b]			
VL	-	24.1 ± 5.4	12.8 ± 3.5
RF	12.3 ± 1.6	-	17.8 ± 11.3
VM	19.3 ± 4.2	20.3 ± 4.7	-

[a] With permission from Elsevier. [b] With permission, copyright ©2002 Wiley Periodicals, Inc.

From these results it appears that, when using a SD detection system, the EMG recorded in the non-stimulated muscles of the Quadriceps will partially be attributed to crosstalk. As much as 7.7% up to 24.1% of the peak-to-peak amplitude of the M-wave recorded in the stimulated muscle may appear in the M-wave recorded in the non-stimulated muscle.

However, the studies carried out by Knaflitz et al. [1988] and Farina et al. [2002] selectively stimulated the muscles by placing surface stimulating electrodes on the motor point of the

muscle. Both parties took care in determining the position of the motor point and discuss this at length, but even then there was still an M-wave present in some of the DD signals of the non-stimulated muscle, although its amplitude was far less than that detected in the SD signals. Farina et al. [2002] even concluded that there was crosstalk present in the DD signals, ranging from 9.2% up to 22.7%. This still raises the question, was the selective stimulation used by Knaflitz et al. [1988] and Farina et al. [2002] truly selective, thereby giving rise to a true indication of the influence of crosstalk in the Quadriceps? The issue of crosstalk is complicated and Farina et al. [2002] say that "...controversies exist in the literature, because of confusion about the sources of signal that are mostly responsible for crosstalk."

Solomonow et al. [1994] used a different approach to evaluate crosstalk, although it was tested in the hind limb of a cat, as opposed to the Quadriceps muscles of a human thigh. Surface electrodes measured muscle activity in the medial gastrocnemius (MG), lateral gastrocnemius (LG) and tibialis anterior (TA) in response to supramaximal nerve stimulation. The nerves to LG and TA were then cut and the muscle activity measured again in response to stimulation of the nerve to MG. Any muscle activity measured after the nerves had been cut was solely attributed to crosstalk.

Their results (summarised in table 1.3), were found using the two methods listed below:

1. "Peak-to-peak M-wave recorded from LG and TA after their nerves were cut, normalized with respect to the corresponding values of MG (the only innervated muscle throughout the experiment). Assesses how much of the EMG from a maximally active muscle could be expected to contaminate a neighbouring muscle."

2. "Peak-to-peak of each M-wave recorded from each muscle before and after the nerves were cut calculated and normalized with respect to their corresponding values before the nerves were cut. Assesses how much of the EMG recorded from a muscle exerting its maximal force is due to crosstalk in terms of percentage peak-to-peak."

Table 1.3: Crosstalk present in the muscles of the hind limb of the cat, reproduced from [Solomonow et al., 1994], with permission from Elsevier.

Mean ± standard deviation of crosstalk in the LG and TA muscles, expressed as a percentage of MG activity			
	MG	**LG**	**TA**
Little fat	-	4.45 ± 1.93	1.99 ± 0.77
Mean ± standard deviation of crosstalk after cutting the nerves to the LG and TA muscles, expressed as a percentage of the activity that was present before their nerves were cut			
	MG	**LG**	**TA**
Little fat	97.96 ± 4.76	4.55 ± 2.39	3.99 ± 2.99
Excessive fat	91.60 ± 6.27	16.25 ± 12.15	5.04 ± 2.82

Unfortunately no quantification was given to distinguish between the *little fat* and *excessive fat* categories used in the table, other than to say that, in the case of the latter "an appreciable layer of subcutaneous fatty tissue was discovered in the post-experimental dissection...such that a layer of fat existed between the muscle and the electrodes".

They concluded the following:

1. For both evaluation methods the amount of crosstalk is less than 5% provided there is little subcutaneous fat below the recording electrodes.

2. Crosstalk values increased up to 16% when a substantial amount of subcutaneous fat covered the muscles.

To be able to extrapolate these results across to human thigh muscle Solomonow et al. [1994] made the argument that due to the closer proximity of the muscles in the cat's leg, the results shown here are more susceptible to crosstalk than in human muscle. However, the larger human muscles would generate more EMG interference, which would increase the amount of crosstalk. They proposed that "...the net effect is that the proportions are similar and therefore the crosstalk values found in the cat are expected to be valid for human studies as well."

From Knaflitz et al. [1988] and Farina et al. [2002] we see that at most 25% of the desired signal can appear as crosstalk in the non-stimulated muscle. Solomonow et al. [1994] showed far less crosstalk ($\sim$5%), although this value could increase to as much as 16$\pm$12%, giving a worst case scenario of 28%, if there is a substantial amount of subcutaneous fat present.

1.4 Hypotheses for the low PO and efficiency of FES cycling

Duffell et al. [2009] pointed out that it is important to understand the reasons for the low efficiency, as this may make it possible to improve the method used for FES cycling, which may in turn increase the PO. They went on to discuss a number of hypotheses, attempting to explain the reasons behind the low PO and efficiency, that can be grouped into three main categories:

1. Muscle activation.

2. Factors inherent to SCI.

3. Biomechanical causes.

Muscle activation

The recruitment of the muscles during FES cycling is grossly crude compared with normal motor control. The main focus of the work of Duffell et al. [2009] was to investigate the efficiency dependence on electrical activation of the muscles. This was accomplished by measuring metabolic efficiency during electrically stimulated concentric contractions of the Quadriceps in AB people. The results indicated the influence of only electrical stimulation on efficiency, without contributing factors due to SCI.

They found the efficiency to be slightly less than 30%, which they then compared against the data of Barclay et al. [1993] (single fibre experiments indicating that efficiency should be on the order of 22% to 30%, depending on the muscle fibre type). Duffell et al. [2009] concluded that although the efficiency during these electrically stimulated contractions was slightly less than that seen during voluntary contractions, it was still greater than the efficiency seen during FES cycling ($\sim 5\%$). Consequently a large part of the drop in efficiency must be attributed to factors inherent to SCI, or be biomechanical in nature.

Factors inherent to SCI

Kjær et al. [1994] performed a study on AB subjects, where their metabolic efficiency was measured during cycling. The cycling was carried out under voluntary muscle action and again using FES after complete epidural anaesthesia. Physiological responses, such as heart rate, ventilation and PO were recorded for both cases. Hunt et al. [2007] pointed out that the efficiency of the anaesthetised cyclists was similar to that measured for SCI cyclists ($\sim 7.6\%$). As the AB cyclists did not have any of the factors inherent to SCI, such as atrophied muscles, this result implied that the main cause for the low metabolic efficiency must be biomechanical.

Biomechanical causes

The difference in FES cycling performance due to forced smooth pedalling (with fixed gearing), as opposed to free pedalling (jerky with freewheeling) was investigated by Szecsi et al. [2007]. This study showed that the smooth pedalling had superior performance, in that greater distances were covered by the cyclists. Measurements of the joint moments, about the knee and hip, were taken during the cycling action, the results have been reproduced in figure 1.6.

It was seen that during a cycling revolution, a crank angle region existed in which an

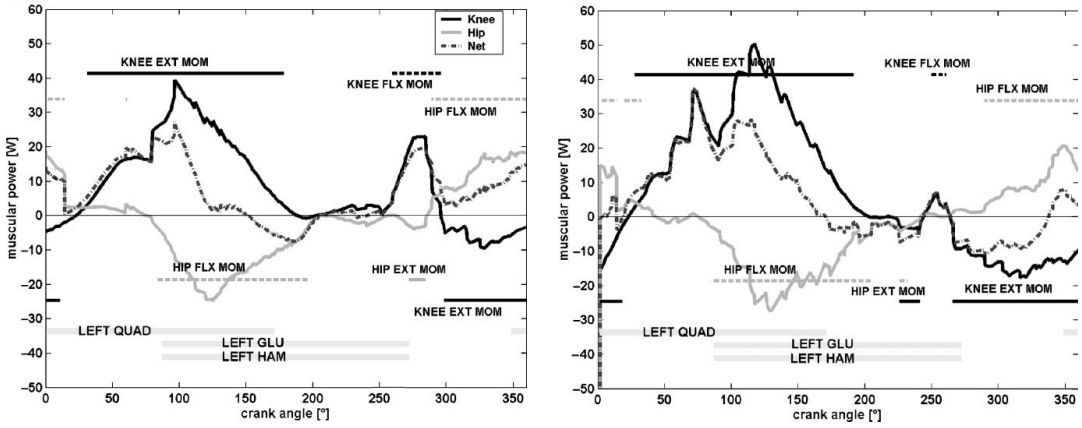

(a) Free pedalling.

(b) Forced smooth pedalling.

Figure 1.6: Reproduced from Szecsi et al. [2007], with permission. Power generated (concentric, positive) and absorbed (eccentric, negative) in the hip (solid gray) and knee (solid black) joints. Nett power is given as dashed-dotted curve. Crank angular regions with concentric- and eccentric-acting extensor or flexor moments are marked with corresponding (concentric as positive and eccentric as negative) straight lines and labels (e.g., KNEE EXT MOM). The stimulation intervals of muscles are indicated by gray bars and labels (e.g., LEFT QUAD).

extension moment was measured about the knee simultaneously with a flexion moment about the hip. The knee extension moment was responsible for the generation of concentric, positive power while the hip flexion moment generated eccentric, negative power, the difference of which gave the nett power in the region where the two moments occurred simultaneously.

In the figure the eccentric power is seen to be comparable for both free and forced smooth pedalling. However, the latter produced increased concentric power. This indicates that greater nett power was generated when producing a larger knee extension moment. If the hip flexion moment could be reduced, without influencing the knee extension moment, a further increase in the nett power would be seen.

These results show that the co-activation of the Quadriceps muscles, currently used in FES cycling, reduce the PO. This would also contribute to the poor efficiency, as metabolic energy is expended to produce both the knee extension and hip flexion moments.

1.5 Research question

Thus far we have seen that the low PO and efficiency values are most likely due to the simultaneous generation of both knee extension and hip flexion moments, during the cycling action. From table 1.1, RF stands out as the only component muscle of the Quadriceps group that has the dual function of both knee extension and hip flexion. The Vastii on the other hand, only perform knee extension actions. During FES cycling with surface stimulation electrodes, the typical electrode placement [Perkins et al., 2001; Szecsi et al., 2007] is such that all of the superficial muscles of the Quadriceps (RF, VM and VL) are activated simultaneously. This would produce the situation seen, where a knee extension and hip flexion moment are produced together. Even for AB cyclists the work of Hakansson and Hull [2005] and Johnston et al. [2007], showed that there should be a difference in the onset and offset angles of RF, VM and VL.

These observations imply that the method currently used to stimulate the Quadriceps, is one of the main factors influencing the biomechanics of the FES cycling action, which contribute towards the low efficiency. This gave rise to the research question of this thesis, namely:

> *Is it possible to maximise knee extension moments,* $\mathbf{M}_k$*, while minimising hip flexion moments,* $\mathbf{M}_h$*, using selective surface stimulation of the superficial muscles of the Quadriceps?*

If such selective stimulation is practicable, PO should be increased in FES cycling.

The approach taken to answer the research question was to design and construct an apparatus that directly measured moments generated about the knee and hip joints, in response to electrical stimulation of the Quadriceps with careful placement of the stimulating electrodes, intended to selectively stimulate target muscles. Even though the eventual application of this research was with SCI cyclists, the studies presented here were only carried out with AB subjects. The reason for this was to investigate the feasibility of the selective stimulation without contributing factors due to SCI.

During the course of this research, questions arose regarding the initial joint moment measurements. The scope of the study was, therefore, expanded to include EMG measurements of the stimulated muscles. Consequently, an additional contribution of this thesis, is the development of a system which is able to simultaneously measure joint moments and evoked EMG responses to electrical stimulation. Although the system itself is perhaps limited in the range of applications for which it can be used, the knowledge gained while working on this thesis can be carried across to other projects.

For this reason, a number of chapters are dedicated to discussing the design and development of the various pieces of electronic equipment. Furthermore, it was necessary to discuss the Biphasic stimulator (Chapter 5) and the Blanking EMG amplifier (Chapter 6) in great detail, because it is difficult to record the evoked EMG signals in the presence of stimulation artefact. Even with the appropriate apparatus, the recording of useful EMG signals proved to be complicated, as discussed in Chapter 7.

1.5.1 Thesis outline

Figure 1.7 shows how the thesis has been structured. The two main contributions, namely, the investigation of the research question and the development of the system, are represented on either axis. The Chapters discuss the consecutive steps taken to develop the system. The Parts outline the broader view of the thesis, in which the Chapters were grouped together according to various aspects of the research question. A brief outline of each Part and Chapter is provided.

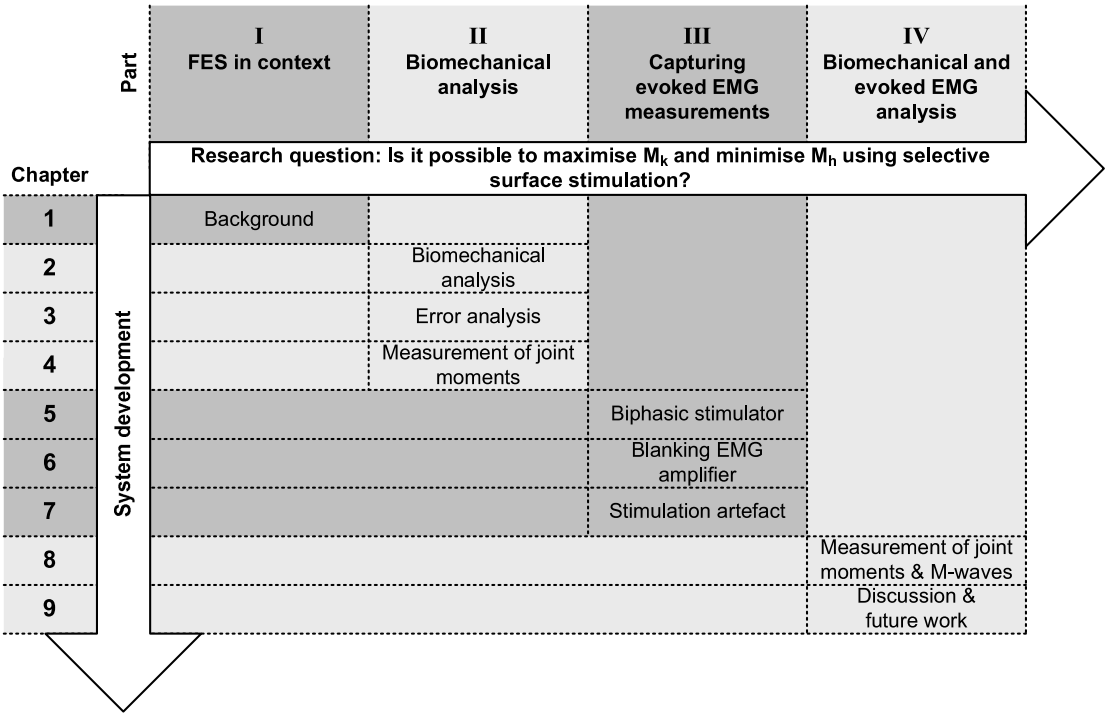

Figure 1.7: Thesis layout, showing the various steps taken to answer both the research question, as well as the development of the system.

Part I: FES in context

Chapter 1 - Background and thesis outline

The concept of FES cycling is introduced. Reasons for the low PO and efficiency of SCI cyclists are discussed. The most likely cause appears to be biomechanical in nature, specifically that the current placement of stimulating electrodes on the Quadriceps results in the simultaneous generation of both a knee extension and a hip flexion moment. This has the effect of reducing the nett PO during cycling. The research question is introduced, namely to investigate selective stimulation of the Quadriceps with the intention of reducing the hip flexion moment. This served as the starting point for both the investigation of the research question and the development of the system required to answer the question.

Part II: Biomechanical analysis

To answer the research question it was decided to directly measure the joint moments while selectively stimulating the Quadriceps muscles through careful placement of the electrodes.

Chapter 2 - Bi-moment chair for the measurement of hip and knee joint moments

A biomechanical analysis of a seated subject was performed, with the aim of determining the magnitude of the joint moments. This lead to the design and construction of the Bi-moment chair, a system capable of simultaneously measuring moments about the knee and hip joints in a seated subject.

Chapter 3 - Error analysis and validation of Bi-moment chair measurements

Measurement errors are inherent in all equipment. It was therefore necessary to perform an error analysis of the Bi-moment chair to determine the size of the errors associated with it. This also helped to highlight the type of analysis that the Bi-moment chair should be used for, namely, a comparative analysis of joint moments.

Chapter 4 - Joint moments captured using the Bi-moment chair

Three different stimulating electrode positions were investigated; *Standard* (non-selective stimulation of the Quadriceps), *Rectus* (selective stimulation of RF) and *Vastii* (selective stimulation of VM and VL). An initial study was carried out with the Bi-moment chair, in which knee and hip joint moments were measured while stimulating with each of the three electrode positions. It was expected to see a reduction in the hip flexion moment when stimulating with the *Vastii* position, as compared with that measured using the *Standard* position. However, analysis of the results showed that this was not the case and the reason behind these results was not understood. It was therefore deemed necessary to measure the evoked EMG response in the three superficial muscles of the Quadriceps (RF, VM and VL) during stimulation, to ascertain whether or not placement of the stimulating electrodes was selectively stimulating the muscles.

Part III: Capturing evoked EMG measurements

When recording evoked EMG responses it is possible to have stimulation artefact present in the measurements, in addition to the desired M-wave signal. The closer the EMG recording electrodes are placed to the stimulating electrodes, the more likely the M-wave measurement will be distorted, or even completely obscured, by the stimulation artefact. The presence of the stimulation artefact becomes especially problematic when trying to record evoked EMG responses in the stimulated muscle (i.e. placing the recording electrodes between the stimulating electrodes). It is therefore necessary to eliminate the stimulation artefact, which can be done through the choice of stimulator and EMG amplifier, and, by giving consideration to the interaction of all these apparatus while recording the EMG.

Chapter 5 - Constant current biphasic stimulator with pulse width ratio adjustment

The stimulator required to reduce stimulation artefact needs to produce a biphasic output pulse. Furthermore, the pulse width of one of the phases should be adjustable. In so doing, residual charge deposited on the stimulating electrodes during the stimulation pulse, which is a source of stimulation artefact, can be eliminated. Chapter 5 presents the design and construction of such a stimulator.

Chapter 6 - Current conveyor based blanking EMG amplifier

EMG amplifiers are susceptible to saturation, when large signals, such as a stimulation pulse, are applied across the input terminals. If the time required for the amplifier to recover from saturation is greater than the latency of the M-wave to be measured, the amplifier will fail to record the desired signal. To prevent such a scenario, a Blanking EMG amplifier was designed and developed. The Blanking amplifier is shut down during the stimulation pulse preventing saturation.

Chapter 7 - Stimulation artefact: understanding the causes and reducing the effect

There are several mechanisms that result in stimulation artefact. Exactly which of these mechanisms are at work, and the extent that each influences the final EMG measurement, is unique to the equipment used in the experimental setup, and how the pieces of equipment interact.

This chapter discusses the various mechanisms when using the Biphasic stimulator and Blanking amplifier. By identifying how the stimulation artefact arises in the first place it was then possible to present various methods for reduction.

Part IV: Biomechanical and evoked EMG analysis

Evoked EMG signals (M-waves) indicated whether, for particular placement of the stimulating electrodes, the targeted muscles were stimulated without the unintentional stimulation of adjacent muscles.

Chapter 8 - Simultaneous measurement of joint moments and M-waves

The Bi-moment chair was used in a study with 10 subjects, in which joint moments were measured, while simultaneously measuring the M-waves in the superficial muscles of the Quadriceps, during stimulation with the three electrode positions introduced in Chapter 4. The selectivity of the stimulation, as indicated by the M-wave measurements, is considered. The joint moments are revisited, in combination with the EMG measurements, to investigate how the muscles are activated by the stimulation to produce the measured moments. Finally the implication of these results, with regards to research question, is discussed.

Chapter 9 - Discussion and future work

A summary of the main outcomes from the thesis, both in terms of system development and the research question, are presented. Limitations of the system currently used are discussed and ways to improve the system are proposed for future work. The possibility of using selective stimulation to improve the PO in FES cycling is considered.

Part II

Biomechanical analysis

Chapter 2

Bi-moment chair for the measurement of hip and knee joint moments

2.1 Introduction

The main aim of this thesis is to investigate whether it is possible to selectively stimulate the superficial muscles of the Quadriceps, thereby generating a knee extension moment with as little hip flexion moment as possible. In Section 1.1 the function of the component muscles of the Quadriceps were presented. Here it was seen that Vastus medialis (VM) and Vastus lateralis (VL) produced knee extension, while Rectus femoris (RF) produced both hip flexion and knee extension. It was therefore decided to selectively stimulate the Vastii, so as to produce only a knee extension. To investigate the efficacy of this selective stimulation it was necessary to measure the resultant joint moments, about both the hip and knee joint centres simultaneously.

The eventual application of this research was intended for FES cycling, which is a dynamic action. According to Winter [2005], the determination of joint moments during cycling would involve performing a dynamic freebody analysis. For such an analysis a number of variables need to be known:

- Kinetic forces - Internal and external forces causing the movement.
- Kinematic variables - Variables describing the movement (such as displacements, velocities and accelerations)
- Anthropometric data - Information such as the mass, centre of mass, centre of rotation and moment of inertia for the various limb segments of the lower leg.

The measurement of all these variables is challenging, therefore, to avoid the complexities of such an analysis it was decided to focus on the central idea, namely the influence of selective surface stimulation on joint moments. Consequently it was decided to use a simpler approach, by measuring the joint moments in a seated subject, whose movement was restricted. This meant that a static freebody analysis could be performed, provided that the external restraining forces were known.

For a seated subject a dynamometer is normally used to measure knee extension moments. However standard dynamometers do not provide any facility to measure the hip joint moment.

For our purpose it was necessary to measure both. To this end a *Bi-moment* chair was developed that could measure both joint moments simultaneously. The focus of the rest of this chapter is the design, construction and implementation of the Bi-moment chair.

2.2 Freebody analysis of a seated subject

Figure 2.1 shows the link-segment models used in the freebody analysis of a seated subject. The analysis is done in two parts, firstly, only the shank (part of the leg below the knee joint) is considered as in figure 2.1(a), after which the entire leg below the hip joint is analysed (figure 2.1(b)). Three types of forces are shown in the figures, gravitational forces $m_s\mathbf{g}$ and $m_{st}\mathbf{g}$, joint reaction forces $\mathbf{R}_k$ and $\mathbf{R}_h$, and, the external restraining forces $\mathbf{F}_s$ and $\mathbf{F}_t$. The knee extension moment, $\mathbf{M}_k$, and the hip flexion moment, $\mathbf{M}_h$, are also shown.

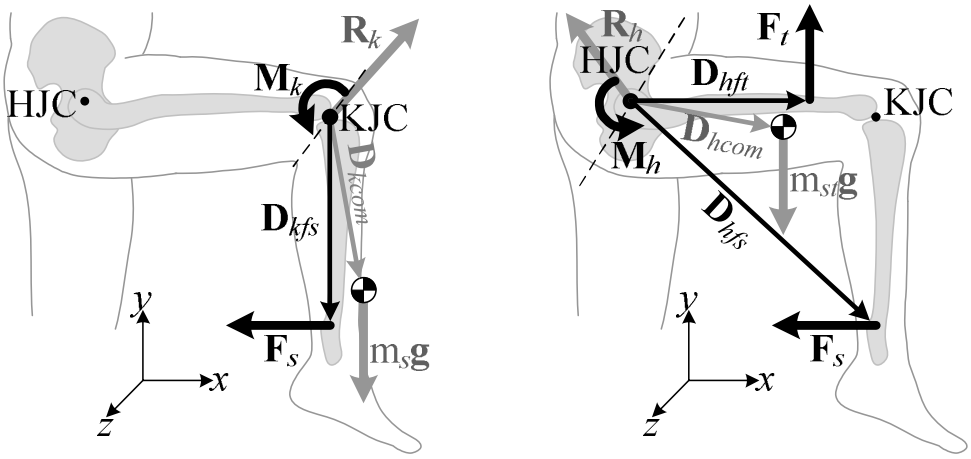

(a) Model for the shank.

(b) Model for the shank and thigh.

Figure 2.1: Link-segment models used in the freebody analysis of a seated subject. (Anatomical outline adapted from an image in *The Atlas of Musculo-skeletal Anatomy* by Chris Jarmey, published by Lotus Publishing and North Atlantic Books, copyright ©2004 by Chris Jarmey. Reprinted by permission of publisher.)

For a subject seated in the Bi-moment chair, two distinct situations occur. Initially there would be no stimulation and the subject would be *at rest*. The second situation occurs when the muscles of the Quadriceps are *stimulated* thereby causing changes in the moments about the knee joint centre (KJC) and hip joint centre (HJC). These joint moment changes are the moments of interest. Even though a change occurs in the joint moments, the movement of the subject is prevented, thereby ensuring that at all times, all of the forces and moments shown in figure 2.1, are in static equilibrium. Consequently the following condition is met:

$$\sum \mathbf{M} = 0 \tag{2.1}$$

By applying equation 2.1 about the KJC in figure 2.1(a), we can find two equations for $\mathbf{M}_k$; one for the subject *at rest* and one *during stimulation* (equations 2.2 and 2.3 respectively).

Because the subject is restrained, thereby preventing movement in the leg, the position of the centre of mass (COM) would remain unchanged for both situations. Consequently the same direction vectors, $\mathbf{D}_{kfs}$ and $\mathbf{D}_{kcom}$, can be used in both expressions. The joint reaction force is omitted from the analysis as it acts at the joint centre, thus not contributing towards the knee joint moment.

$$\mathbf{M}_{k\_rest} = \mathbf{D}_{kfs} \times \mathbf{F}_{s\_rest} + \mathbf{D}_{kcom} \times m_s\mathbf{g} \tag{2.2}$$

$$\mathbf{M}_{k\_stim} = \mathbf{D}_{kfs} \times \mathbf{F}_{s\_stim} + \mathbf{D}_{kcom} \times m_s\mathbf{g} \tag{2.3}$$

The change in joint moment can be found by taking the difference between equations 2.2 and 2.3, whereby the moments due to the gravitational forces are eliminated.

$$\Delta\mathbf{M}_k = \mathbf{M}_{k\_stim} - \mathbf{M}_{k\_rest} = \mathbf{D}_{kfs} \times \Delta\mathbf{F}_s \tag{2.4}$$

Using a similar approach (applying equation 2.1 about the HJC in figure 2.1(b)), the change in $\mathbf{M}_h$ can be found:

$$\mathbf{M}_{h\_rest} = \mathbf{D}_{hfs} \times \mathbf{F}_{s\_rest} - \mathbf{D}_{hft} \times \mathbf{F}_{t\_rest} + \mathbf{D}_{hcom} \times m_{st}\mathbf{g} \tag{2.5}$$

$$\mathbf{M}_{h\_stim} = \mathbf{D}_{hfs} \times \mathbf{F}_{s\_stim} - \mathbf{D}_{hft} \times \mathbf{F}_{t\_stim} + \mathbf{D}_{hcom} \times m_{st}\mathbf{g} \tag{2.6}$$

$$\Delta\mathbf{M}_h = \mathbf{M}_{h\_stim} - \mathbf{M}_{h\_rest} = \mathbf{D}_{hfs} \times \Delta\mathbf{F}_s - \mathbf{D}_{hft} \times \Delta\mathbf{F}_t \tag{2.7}$$

The changes in the joint moments, $\Delta\mathbf{M}_k$ and $\Delta\mathbf{M}_h$, can therefore be quantified by only considering the changes in the two external forces, $\Delta\mathbf{F}_t$ and $\Delta\mathbf{F}_s$. For simplicity the Δ signs are omitted throughout this thesis, as in equation 2.8.

$$\mathbf{M}_k = \mathbf{D}_{kfs} \times \mathbf{F}_s \qquad \mathbf{M}_h = \mathbf{D}_{hfs} \times \mathbf{F}_s - \mathbf{D}_{hft} \times \mathbf{F}_t \tag{2.8}$$

It should be noted that the vector moments have a $\hat{x}$, $\hat{y}$ and $\hat{z}$ component, the $\hat{z}$ component of which describes the knee extension and hip flexion moments.

This analysis showed that the Bi-moment chair was required to measure the magnitudes and directions of forces $\mathbf{F}_s$ and $\mathbf{F}_t$, relative to the KJC and HJC, so that the joint moments could be calculated. Figure 2.2 shows a schematic diagram of the Bi-moment chair. The magnitude of the forces, F_t and F_s, were measured using strain gauge transducers, labelled as SG_1 and SG_2 in the figure. The Bi-moment chair was intended to be a stand alone measurement apparatus without the need to use a motion analysis system to take position measurements. Therefore position sensors known as *spring pots*, labelled as sp_1 through sp_4, were used to determine the direction of the forces and to monitor the position of the KJC.

The cord attached between the shank and SG_2 was necessary to measure $\mathbf{F}_s$, however, it also restricted forward movement of the leg. The subject was further held in place through the use of a number of straps running across the shoulders and hips (not shown in the diagram[1]). In

[1]Figure 2.9 shows a photograph of a subject in the Bi-moment chair in which the restraining straps can be seen.

so doing the movement of the subject was constrained which was necessary to justify the use of the static freebody analysis presented, and the assumption that the position of the HJC was constant. This assumption, along with a number of other assumptions mentioned throughout this chapter, are summarised in Table 2.1.

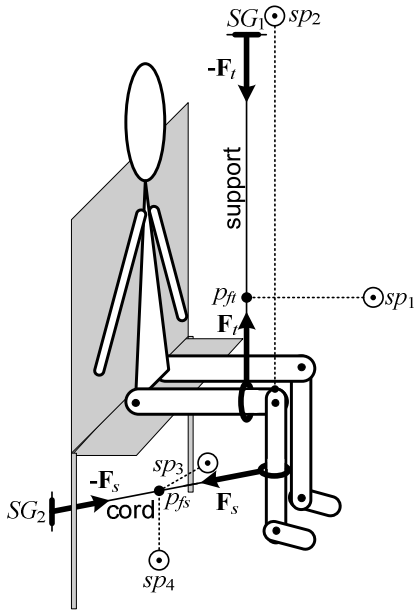

Figure 2.2: Schematic representation of the Bi-moment chair, showing a seated subject and the position of the strain gauge transducers and spring pots.

Table 2.1: Assumptions made by the Bi-moment chair.

	Assumptions regarding movement of the subject
1	The restraining straps were sufficient to ensure that stimulation of the Quadriceps caused no movement in the COM of the shank or thigh.
2	The position of the HJC was constant.
3	No lateral movement in the KJC.
4	No lateral movement in point p_{ft}.
	Assumptions regarding the set up procedure when first seating a subject in the chair
1	sp_2 positioned directly above the KJC.
2	String between sp_2 and the KJC lies parallel with the cord between the thigh and SG_1.
3	The subject was seated in the chair such that the position of the KJC and HJC had the same z-coordinate.
	Other assumptions used in the data analysis
1	The dimension measurement l_t, as defined in table 2.4, lies parallel to the sagittal plane. *Such an assumption implies that the $\hat{z}$ offset of the HJC from the GT[a] is the same as the $\hat{z}$ offset of the KJC from the lateral KJC[b]. When considering the anatomy of the human leg this is unlikely to be true. However, the length of l_t would be much greater than the size of the offsets. Consequently any error introduced through this assumption was considered to be negligible.*

[a] Greater trochanter. [b] The *knee joint space* between the femur and tibia on the lateral side of the leg, located through palpation.

The schematic diagram of the chair (figure 2.2) shows a very narrow seat. This was intentionally done so that the seat was only in contact with the subject's buttocks. This ensured that there was no reaction force between the thigh and the chair seat, as such a force had not been accounted for in the freebody analysis. It was therefore necessary to support the thigh to ensure that it was held in a horizontal position. One end of the support was attached to the thigh while the other end was attached to SG_1. Initially the support took the form of a rigid bar, however, later on the bar was replaced with a sling attached to a cord, as discussed in Section 3.2.3.

SG_1 and sp_2 could be moved forwards and backwards, to account for the different leg lengths of the subjects. It was also possible to move these two sensors to the left and right to ensure that sp_2 was always located directly above the KJC.

In the remainder of this chapter, the hardware design and calibration of the sensors used in the Bi-moment chair is presented in Sections 2.3 and 2.4 respectively. The analysis of the data collected from the chair is then discussed in Section 2.5, where the procedure used to calculate the moments is laid out.

2.3 Construction of the Bi-moment chair

The Bi-moment chair hardware can be grouped into four main categories:

1. Data acquisition card.
2. Sensors.
3. Stimulation equipment.
4. Sensor electronics box.

Figure 2.3 is the wiring diagram of the hardware. It shows the constituent parts of each group, as well as the electrical connections between each part.

2.3.1 Data acquisition card

The sensor data was recorded using a laptop with a NI DAQ6024E data acquisition card, running a real time *Simulink* program. The data was later processed and analysed using MATLAB. The specifications of the data acquisition card have been included in Section A.1 of Appendix A.

2.3.2 Sensors

The sensors consisted of the spring pots, sp_1 through sp_4, and the strain gauge transducers, SG_1 and SG_2. The sensor measurements were used in the calculation of the joint moments.

Spring pots

The spring pots serve as position sensors and are used to determine the position of the points, p_{ft} and p_{fs} (refer to figure 2.2), as well as the vertical position of the KJC. They are each constructed from a rotary potentiometer connected to a pulley and a spring motor, as shown in figure 2.4(a). Spring pots were originally used by Yu [1999].

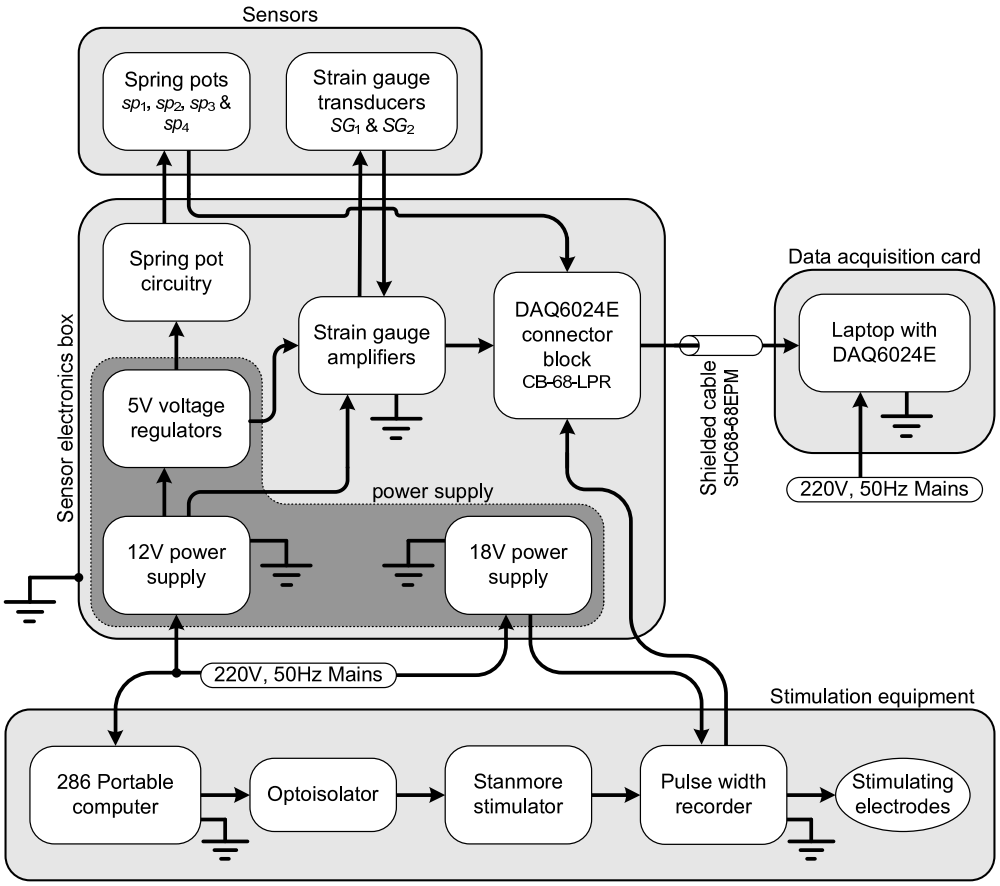

Figure 2.3: Wiring diagram of the hardware used to construct the chair, showing the categories into which each part was grouped.

The pulley was enclosed within a case to prevent the string from jumping off of the pulley, which would adversely affect the measurements. The radius of the pulley, r_p, is related to the number of revolutions of the potentiometer, n_r, and the measurement range of the spring pot, l_{sp}, as in equation 2.9.

$$l_{sp} = n_r 2\pi r_p \tag{2.9}$$

The spring pots were customised according to their application in the Bi-moment chair, and the expected range of movement that each would need to monitor. The specifications for each spring pot is given in table 2.2.

Table 2.2: Spring pot specifications

Spring pot	**Value (kΩ)**	**Linearity (%)**	n_r	l_{sp} **(mm)**	r_p **(mm)**
sp_1	$5 \pm 3\%$	0.5	1	35	6
sp_2	$5 \pm 3\%$	0.5	1	43	7
sp_3	$5 \pm 5\%$	0.25	3	275	14
sp_4	$5 \pm 5\%$	0.25	3	233	12

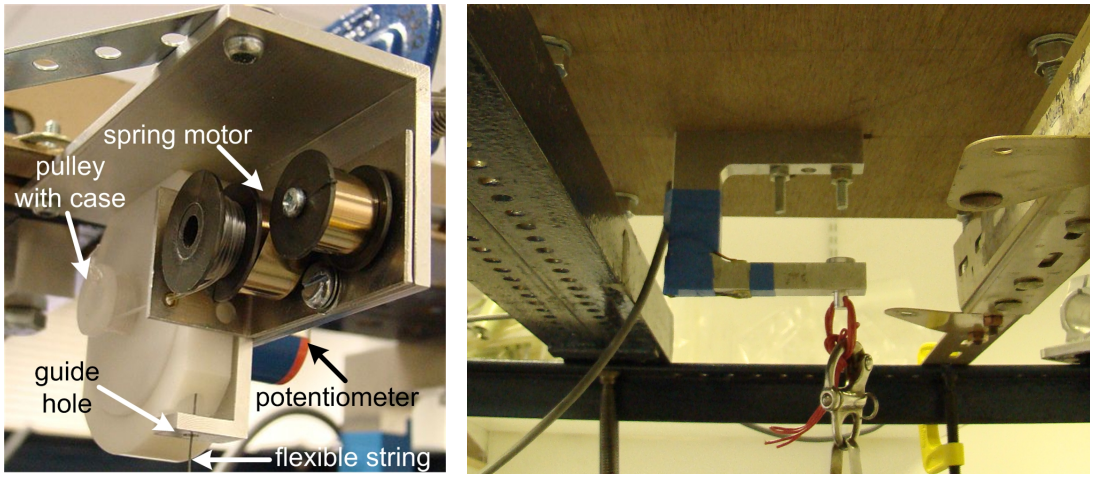

(a) A spring pot module.

(b) A strain gauge transducer.

Figure 2.4: The sensors.

Strain gauge transducers

The strain gauge transducers were were used to measure the magnitude of the forces $\mathbf{F}_s$ and $\mathbf{F}_t$. Each strain gauge transducer consisted of four 120Ω strain gauge foils attached to a U-shaped metal bar, as shown in figure 2.4(b).

2.3.3 Stimulation equipment

The equipment used for the stimulation of the muscles was developed jointly by the *Department of Medical Physics and Bionegineering* at UCL and the *Salisbury District Hospital*. It has been used for many years in FES clinical trials.

286 Portable computer

A 286 computer communicates with the Stanmore stimulator by means of a terminal program, *Telex*. The program is used to set the stimulation parameters. The 286 computer was included in figure 2.3 so as to present a complete picture of the ground paths present in the setup.

Optoisolator

The optoisolator provided electrical isolation between the 286 computer and the Stanmore stimulator. Refer to Section A.2.1 of the Appendix for the optoisolator circuit diagram.

Stanmore stimulator

The Stanmore stimulator is an eight channel, monophasic, constant-current stimulator [Phillips et al., 2003].

Pulse width recorder

The pulse width recorder generates a DC voltage that is proportional to the intensity of a burst of stimulation. This waveform was used to identify the timing of the stimulation bursts, which is further discussed in Section 2.5.1. The circuit diagram for the pulse width recorder can be found in Section A.2.2 of the Appendix.

Stimulating electrodes

The stimulating electrodes used are commercially available PALS Platinum Neurostimulation electrodes.

2.3.4 Sensor electronics box

A shielded box was constructed that facilitated the electrical connections to the DAQ6024E It also housed the required power supplies, the spring pot driving circuitry and the strain gauge amplifiers. Detailed specifications, design steps and circuit diagrams for each part have been included in Section A.3 of Appendix A.

The fully assembled chair electronics box is shown in figure 2.5. The box was powered directly from mains. The front and back panels, as well as the shield coating inside the box were connected to mains earth. On the front panel shown in figure 2.5(c), a 4mm socket can be seen. This was used to connect the cases of the Biphasic stimulator and Blanking amplifier to earth, as mentioned in Chapters 5 and 6.

In Chapter 8 it was mentioned that the DAQ6024E and the real time *Simulink* program were later replaced with the CED Micro1401 and *Signal* software, as the data acquisition system. The chair electronics box was modified so that the sensor output signals could be connected to the Micro1401 instead of the DAQ6024E. This involved adding op-amp unity gain buffers to the electronics (see figure 2.5(b)), the output of which went to BNC connectors on the front and back panels of the box (see figures 2.5(c) and 2.5(d)).

2.4 Calibration of the sensors

Calibration measurements were taken for the spring pots and the strain gauge transducers.

2.4.1 Spring pot calibration

The spring pots functioned as position measurement devices by producing a voltage signal proportional to the length of string extended from the spring pot. The supply rails between which the spring pots operated was ± 4.3V (refer to Section A.3.1).

Once a subject was seated in the Bi-moment chair, the spring pot strings were attached as in figure 2.2, in such a way that the potentiometer voltage was approximately in the middle of the ± 4.3V range. The measurement range of the spring pot, l_{sp} in table 2.2, was used to generate a *fitted calibration line*, as shown in figure 2.6. The actual length of the string extended from the spring pot was then measured using a tape measure to find the value l_{meas}. The corresponding voltage measurement, V_{meas}, was measured with the DAQ6024E.

Using these values it was possible to calculate the offset distance, l_{offset}, and the so-called *adjusted calibration line*. The latter was then used to convert any further spring pot voltage measurements to a corresponding length measurement. By adjusting the spring pot calibration data in this manner, the spring pots were used to measure variation around a known point as opposed to an absolute length measurement. The random measurement errors, inherent to the spring pots, are discussed in Section 3.3.

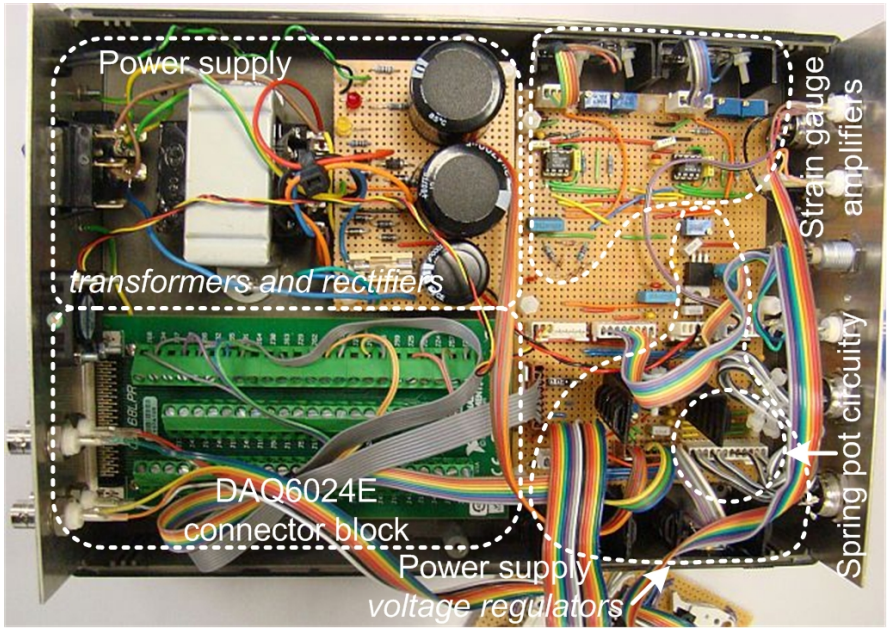

(a) Constituent parts of chair electronics box.

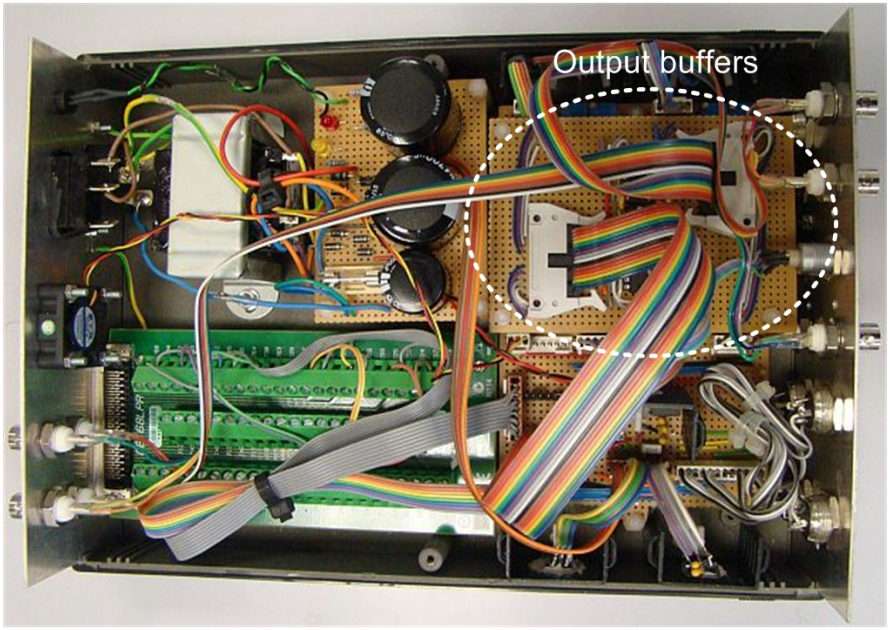

(b) Modifications made for Micro1401 data acquisition system.

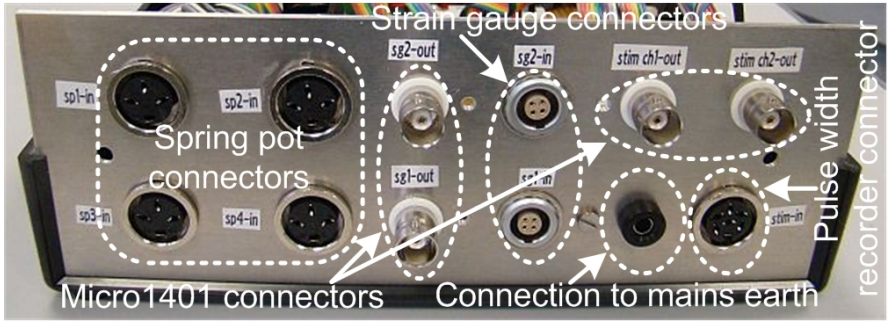

(c) Front panel.

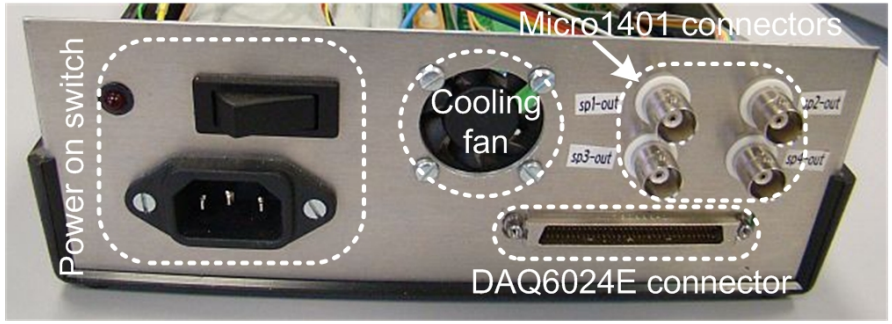

(d) Back panel.

Figure 2.5: Sensor electronics box assembly.

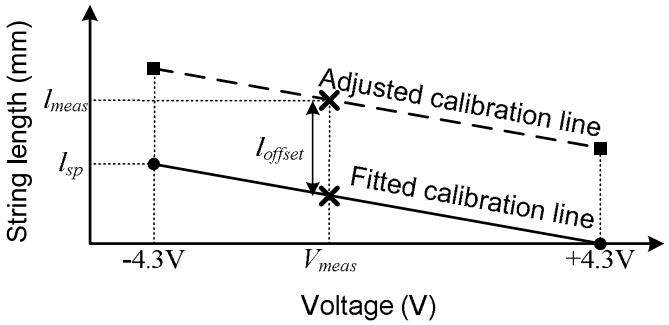

Figure 2.6: Fitted and adjusted calibration lines used for a spring pot.

2.4.2 Strain gauge transducer calibration

The strain gauge transducers were calibrated using weights of known mass suspended from the transducers, as shown in figure 2.7(a). The average voltage measured at the output of the amplifiers, over a period of 5s, was recorded using the DAQ6024E. The voltage difference between no load (no weights suspended) and with a load (weights suspended) was calculated for a series of weights ranging from 5kg up to 30kg. The results for both strain gauges have been plotted in figure 2.7(b) and a straight line fitted to the data. It was preferable to use a voltage difference as opposed to an absolute voltage measurement so that possible errors, due to drift present in the electronics, were eliminated. The random measurement errors, inherent to the strain gauge transducers, are discussed in Section 3.3.

The gradients of the two lines in figure 2.7(b) is notably different from each other. This is due to the fact that the two strain gauge amplifiers were designed with different gain resistor values to account for the difference in expected magnitude of the forces, $\mathbf{F}_s$ and $\mathbf{F}_t$ (discussed

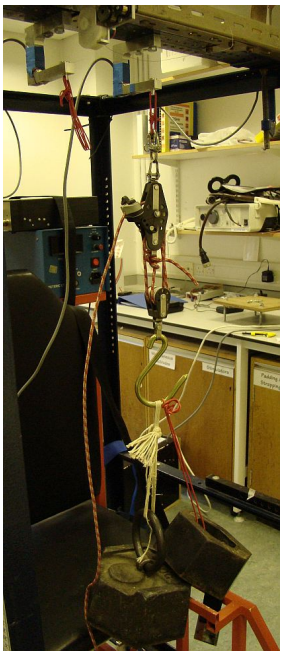

(a) Suspended weights.

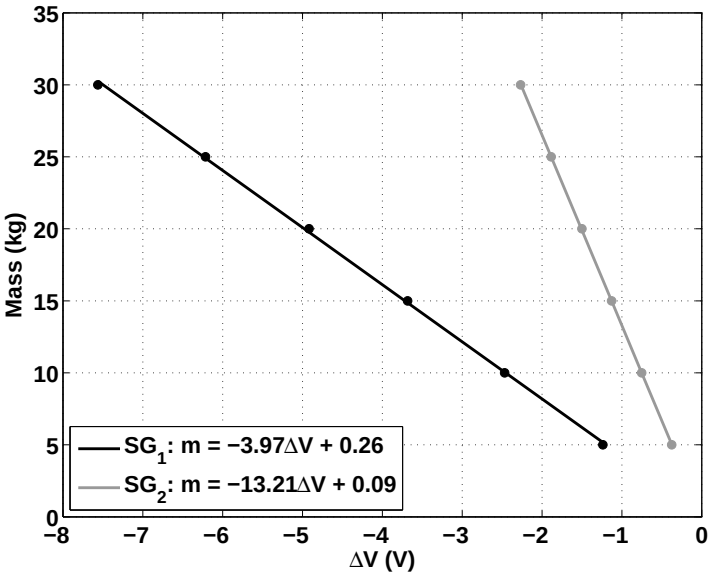

(b) Calibration measurements.

Figure 2.7: Calibration of strain gauge transducers.

in Section A.3.2). The gradient of the line for SG_2 is much steeper than that of SG_1 because $F_s > F_t$. The amplifiers output signal has a voltage range of $\pm$5V. Using the gradients of the two lines, we find that SG_1 has a force measurement range of just under 400N, while SG_2 has a force measurement range of approximately 1.3kN.

During the studies, discussed in Chapters 4 and 8, the strain gauges were calibrated at the start of each day. The data captured, during the sessions carried out on that day, were later analysed using the relevant day's calibration data.

2.5 Data analysis and moment calculation

So as to calculate the direction vectors, force vectors and final joint moments, position and dimension data also had to be captured, in addition to the sensor measurements. The definition of the positions, dimensions and vectors can be found in figure 2.8. Tables 2.4 through 2.5 give a brief description of each parameter.

To measure the spatial coordinates (figure 2.8(a) and table 2.3), it was necessary to define a coordinate system that the positions were measured with reference to. Such a system was realised by constructing the Bi-moment chair within a frame, as shown in figure 2.9. The orientation of the axes (figure 2.8(a)), corresponds with the convention used by Winter [2005] for freebody analysis. The axes were positioned so that the origin was located as shown in figure 2.9. Tape measures attached to the frame aided the position measurements in the $\hat{x}$ and $\hat{y}$ directions. Once the data had been gathered it was then possible to calculate all of the vectors and moments. Figure 2.10 is a flow diagram outlining the analysis process.

The data captured by the sensors were measurements taken over a period of time. To be able to use this data the time intervals during which the subject was stimulated, and a force was applied on the strain gauge transducers, had to be determined. To this end a preliminary analysis was performed on the pulse width recorder measurement.

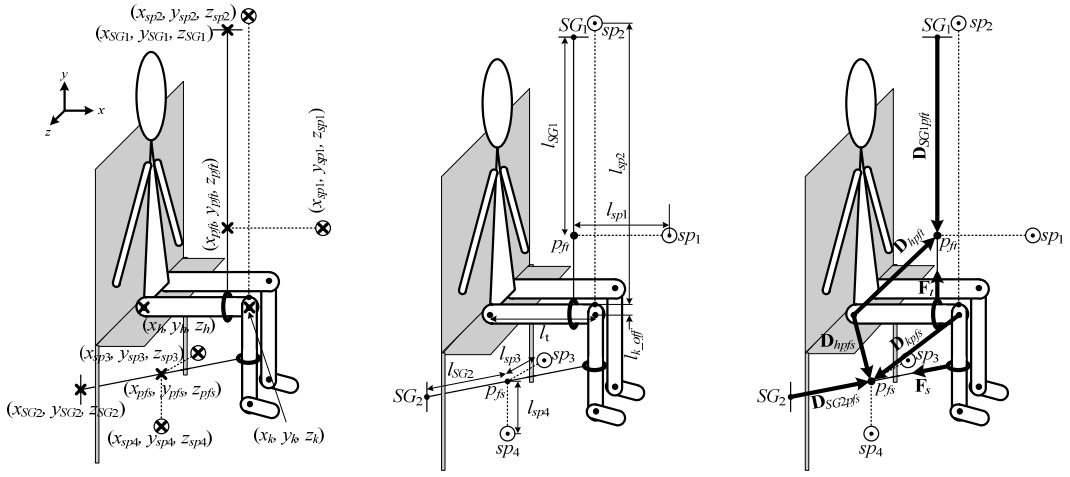

(a) Coordinate system. (b) Dimensions. (c) Vectors.

Figure 2.8: Definitions of dimensions, location of three-dimensional coordinates and orientation of vectors, as used during the Bi-moment chair analysis.

Table 2.3: Definitions of the spatial coordinates shown in figure 2.8(a).

Spatial coordinates		
p_{sp1}	$(x_{sp1}, y_{sp1}, z_{sp1})$	Position of spring pot sp_1
p_{sp2}	$(x_{sp2}, y_{sp2}, z_{sp2})$	Position of spring pot sp_2
p_{sp3}	$(x_{sp3}, y_{sp3}, z_{sp3})$	Position of spring pot sp_3
p_{sp4}	$(x_{sp4}, y_{sp4}, z_{sp4})$	Position of spring pot sp_4
p_{SG1}	$(x_{SG1}, y_{SG1}, z_{SG1})$	Position of strain gauge transducer SG_1
p_{SG2}	$(x_{SG2}, y_{SG2}, z_{SG2})$	Position of strain gauge transducer SG_2
HJC	(x_h, y_h, z_h)	Position of HJC
KJC	(x_k, y_k, z_k)	Position of KJC
p_{ft}	$(x_{pft}, y_{pft}, z_{pft})$	Position of p_{ft}, the point of intersection between the rigid support and the string of sp_1
p_{fs}	$(x_{pfs}, y_{pfs}, z_{pfs})$	Position of p_{fs}, the point of intersection between the cord and the strings of sp_3 and sp_4

Table 2.4: Definitions of the dimensions shown in figure 2.8(b).

Dimensions	
l_{sp1}	sp_1 string length measurement
l_{sp2}	sp_2 string length measurement
l_{sp3}	sp_3 string length measurement
l_{sp4}	sp_4 string length measurement
l_{SG1}	Distance between p_{f_t} and p_{SG_1}
l_{SG2}	Distance between p_{f_s} and p_{SG_2}
l_t	Distance between the GT[a] and the lateral KJC[b]
l_{k_off}	Offset distance between the KJC and the proximal edge of the patella

[a] Greater trochanter. [b] The *knee joint space* between the femur and tibia on the lateral side of the leg, located through palpation.

Table 2.5: Definitions of the vectors shown in figure 2.8(c).

Vectors	
$\mathbf{D}_{SG1pft}$	Direction vector from p_{SG1} to p_{ft}
$\mathbf{D}_{SG2pfs}$	Direction vector from p_{SG2} to p_{fs}
$\mathbf{D}_{hpft}$	Direction vector from HJC to p_{ft}
$\mathbf{D}_{hpfs}$	Direction vector from HJC to p_{fs}
$\mathbf{D}_{kpfs}$	Direction vector from KJC to p_{fs}
$\mathbf{F}_s$	Force vector applied at the shank
$\mathbf{F}_t$	Force vector applied at the thigh

Figure 2.9: A subject in the Bi-moment chair showing the reference system used.

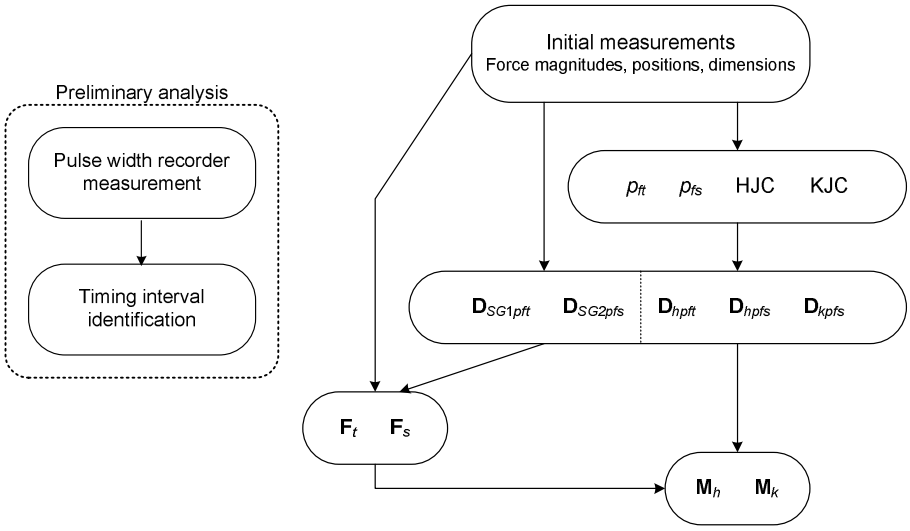

(a) Timing identification. (b) Moment calculation.

Figure 2.10: Flow diagrams of the Bi-moment chair data analysis.

These timing intervals were then used to find the set of initial measurements, consisting of the force magnitude, position and dimension data. This data was used to find the position of the HJC, KJC, p_{ft} and p_{fs}. The vectors could then be found using these calculated positions, which in turn were used to find the moments. A breakdown of each of the steps in this analysis process is presented in the following sections.

2.5.1 Timing interval identification using the pulse width recorder

The Stanmore stimulator is a constant-current, monophasic stimulator. The pulse width, PW, of each individual stimulation pulse can be adjusted. The amplitude of the stimulation current, I_{stim}, is also variable. The stimulation protocol to be used in the study involved bursts of stimulation, the intensity of which was controlled by the PW and I_{stim} settings (further discussed in Section 4.2.2). The function of the pulse width recorder is to generate a voltage signal, V_{pwr}, in response to a burst of stimulation, as shown in figure 2.11.

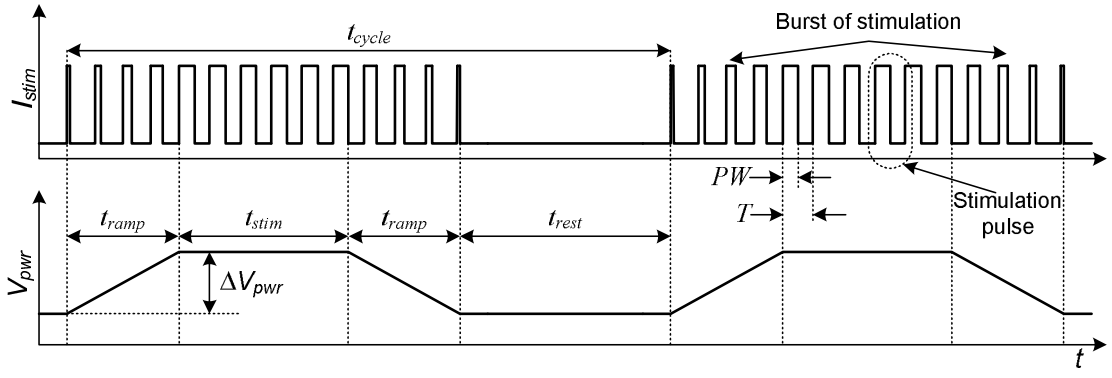

Figure 2.11: Typical Stanmore stimulator and pulse width recorder signals.

The amplitude of the generated voltage pulse, ΔV_{pwr} is dependent on the pulse width, current amplitude and period, T, of the stimulation signal. Therefore, it was decide to not use ΔV_{pwr} to identify the time intervals of interest, t_{rest} and t_{stim} (shown in figure 2.11). Instead a moving standard deviation of V_{pwr} was calculated and used to identify the timing intervals, refer to figure 2.12.

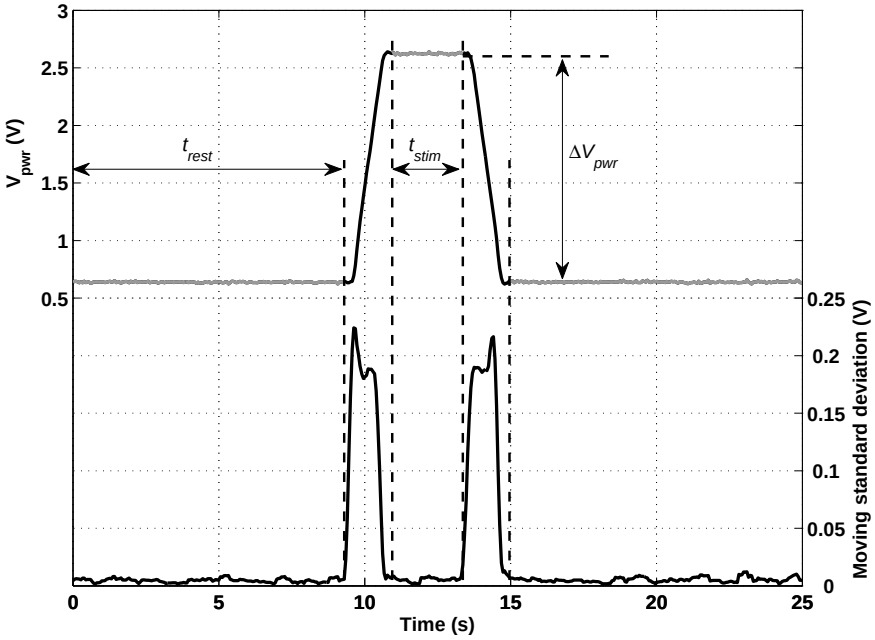

Figure 2.12: Pulse width recorder calibration data extraction.

2.5.2 Spring pot string lengths

Figure 2.13 outlines the calculation of the spring pot string lengths and how this step fits into the overall analysis procedure. As discussed in Section 2.4.1, the string lengths were initially measured with a tape measure, represented as $\tilde{l}_{sp_1}$ through $\tilde{l}_{sp_4}$ in the figure, which were used

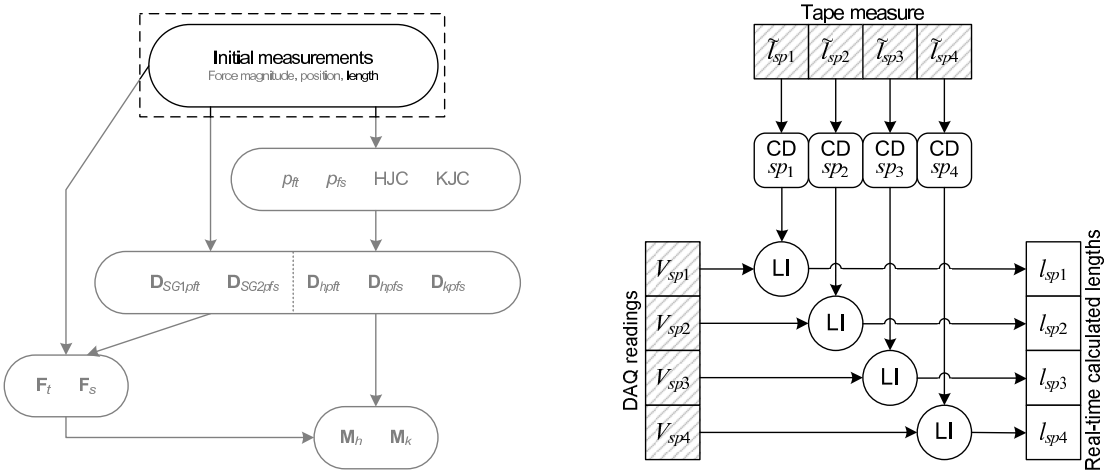

Figure 2.13: Calculation of spring pot string lengths from voltage measurements recorded by the DAQ6024E.

to adjust the *Calibration Data* (CD) of each spring pot. *Linear Interpolation* (LI) was then performed using the CD, as well as the voltage measurements, V_{sp_1} through V_{sp_4}, obtained from the DAQ6024E. This resulted in real-time string length measurements for each spring pot, l_{sp_1} through l_{sp_4}.

2.5.3 Hip joint centre

The position of the hip joint centre (HJC) had to be estimated using position measurements of anatomical landmarks taken once the subject was seated in the Bi-moment chair. The position of the landmark was measured using a dowel stick that pointed at its location. The dowel stick was held in a specially designed bracket that was attached to the frame of the chair.[2] Using the measuring tapes attached to the frame (refer to figure 2.9), and demarcated positions on the bracket, it was possible to express the location of the point of the dowel stick in three dimensional space within the coordinate system used for the chair.

Andriacchi et al. [1980] suggested a method for approximating the position of the HJC using the position of the greater trochanter (GT) and anterior superior iliac spine (ASIS):

> *Correct the position of GT in the frontal plane to a point, p_B, "1.5-2cm distal to the midpoint of a line between the right ASIS and the pubic symphysis (PS)"* (refer to figure 2.14(a)).

Bell et al. [1989] suggested a method using the position of only the ASIS:

> *"The HJC is located at 14% of l_{AA} medial to the right ASIS, 30% of l_{AA} distal to the right ASIS and 22% of l_{AA} posterior to the right ASIS", where l_{AA} is the distance between the left and right ASIS*, (refer to figure 2.14(b)).

(a) Andriacchi's method. (b) Bell's method.

Figure 2.14: Approximation of the position of the HJC, after Kirkwood et al. [1999], with permission from Elsevier.

In the initial study of Chapter 4 only the position of the GT had been recorded. The method used to find the HJC was an adaptation of that of Andriacchi et al. [1980] and Bell et al. [1989]. The one aspect that both methods had in common was a medial displacement of the initial starting position, in order to approximate the HJC. Following this principle the z-coordinate position of GT was corrected by an amount equal to 14% of l_{AA} plus the offset between the ASIS and GT, labelled as l_{GA} in the figure. However, it was difficult to accurately measure l_{GA}.

[2] Figure 3.4 shows a photograph of the Bi-moment chair when using LiAM (Limb for the Application of Moments) to validate the joint moment measurements. The dowel stick and bracket can also be seen in the picture.

This led to the method of Bell et al. [1989] being implemented in the later study discussed in Chapter 8, when the position of the ASIS was recorded.

The accuracy of the approximations of Andriacchi et al. [1980] and Bell et al. [1989], and the resultant error introduced into hip joint moment calculations was investigated and compared by Kirkwood et al. [1999]. This is further discussed in Section 3.4.3 (*Additional remarks on the position of the HJC*).

Figure 2.15 outlines the calculation of the HJC within the analysis procedure, showing both methods presented here.

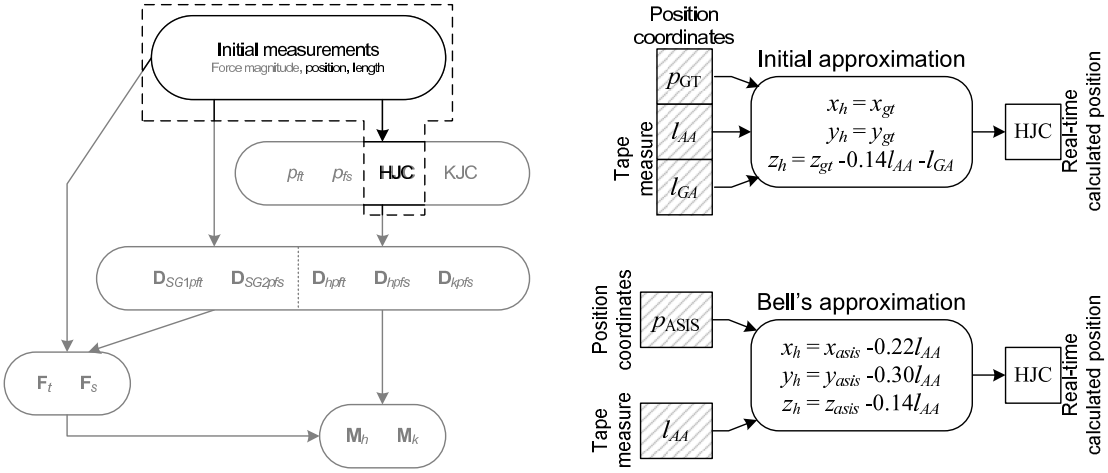

Figure 2.15: Calculation of HJC position.

2.5.4 Knee joint centre

The position of the knee joint centre (KJC) was calculated using the HJC position and known dimensions, the flow diagram of which is shown in figure 2.16.

Firstly, the lateral position of the knee was assumed to be in line with that of the hip (equation 2.10), the validity of this assumption is further discussed in Section 3.4. Next, the vertical position of the knee was determined relative to the position of sp_2 (equation 2.11). The function of sp_2 was to measure small variations in the vertical position of the KJC. Finally, using the value of y_k, the position of the HJC, and, the measured value of l_t, it was possible to calculate the value of x_k using a distance formula (equation 2.12).

$$z_k = z_h \tag{2.10}$$

$$y_k = y_{sp_2} - \left(l_{sp_2} + l_{k\_off}\right) \tag{2.11}$$

$$l_t^2 = (x_k - x_h)^2 + (y_k - y_h)^2 \tag{2.12}$$

2.5.5 Position of point p_{ft}

The flow diagram for point p_{ft} is shown in figure 2.17. The position of point p_{ft} was only determined in two dimensions, as it was assumed that there was no lateral movement (equation 2.13). This assumption, the validity of which is further discussed in Section 3.4, was made as the subjects were positioned in the chair in such a way as to minimise any lateral movement

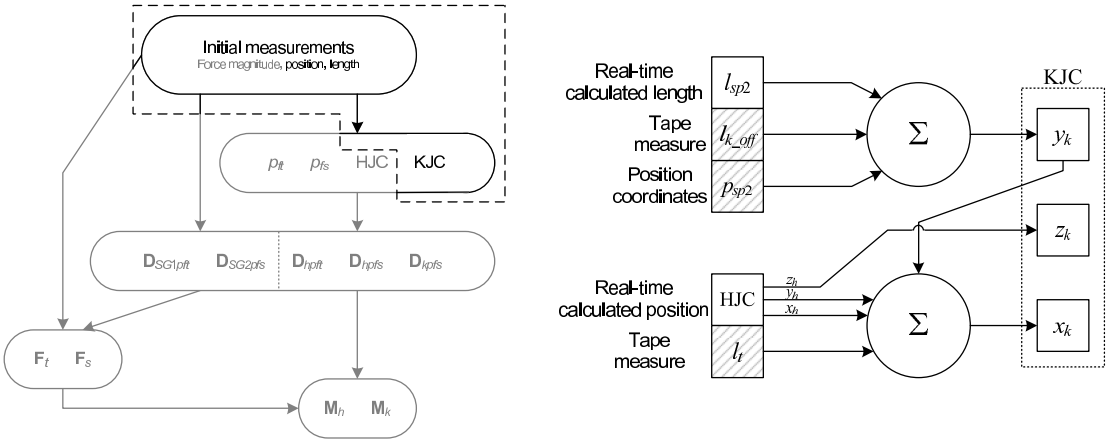

Figure 2.16: Calculation of KJC position.

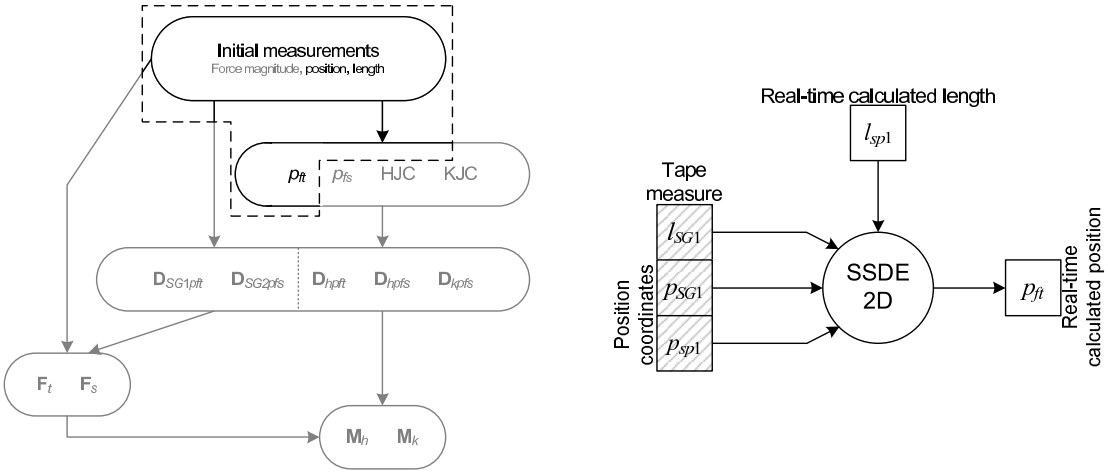

Figure 2.17: Calculation of position p_{f_t}.

of the leg during knee extension.

$$z_{pft} = z_{SG1} \tag{2.13}$$

From the geometry of the Bi-moment chair setup (refer to figure 2.8), it was possible to produce distance equations 2.14 and 2.15, for the two unknown coordinates, x_{pft} and y_{pft}.

$$l_{SG1}^2 = (x_{pft} - x_{SG1})^2 + (y_{pft} - y_{SG1})^2 \tag{2.14}$$

$$l_{sp1}^2 = (x_{pft} - x_{sp1})^2 + (y_{pft} - y_{sp1})^2 \tag{2.15}$$

An analytical solution for these two distance equations is included in Section A.4 of Appendix A. It is based on the *Simultaneous Solution of Distance Equations* (SSDE) for the three-dimensional case, given in Hsiao and Keyserling [1990] and Yu [1999].

The solution effectively reduces to that of a quadratic equation, which yields two final positions for p_{ft}. However, in the Bi-moment chair application, the positions of SG_1 and sp_1 were fixed at all times. As a result, the same quadratic equation solution was valid at all times, which was identified through application of this procedure to an actual data set.

2.5.6 Position of point p_{fs}

The position of point p_{fs} (flow diagram in figure 2.18), was determined by simultaneously solving the set of three distance equations 2.16 through 2.18. Once again this solution could be expressed as a quadratic equation (refer to Section A.4), which had one valid solution that was identified using an experimental data set.

$$l_{sp3}^2 = (x_{pfs} - x_{sp3})^2 + (y_{pfs} - y_{sp3})^2 + (z_{pfs} - z_{sp3})^2 \tag{2.16}$$

$$l_{sp4}^2 = (x_{pfs} - x_{sp4})^2 + (y_{pfs} - y_{sp4})^2 + (z_{pfs} - z_{sp4})^2 \tag{2.17}$$

$$l_{SG2}^2 = (x_{pfs} - x_{SG2})^2 + (y_{pfs} - y_{SG2})^2 + (z_{pfs} - z_{SG2})^2 \tag{2.18}$$

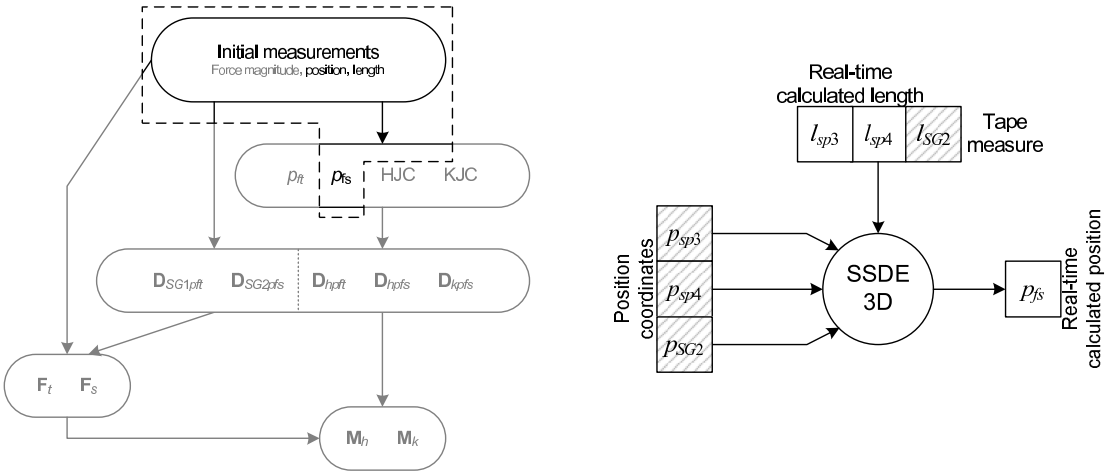

Figure 2.18: Calculation of position p_{fs}.

2.5.7 Direction vectors

The direction vectors were calculated using equation 2.19, which represents a direction vector pointing from an arbitrary point p_a, to an arbitrary point p_b, which have coordinates (x_a, y_a, z_a) and (x_b, y_b, z_b) respectively. This principle was used to calculate all of the directional vectors listed in table 2.5, using the coordinates found in table 2.3.

$$\mathbf{D}_{ab} = (x_b - x_a)\hat{x} + (y_b - y_a)\hat{y} + (z_b - z_a)\hat{z} \tag{2.19}$$

A flow diagram showing the direction vector calculations can be found in figure 2.19.

2.5.8 Force vectors

Figure 2.20 outlines the procedure used to find the force vectors.

The first step was to find the time intervals, t_{rest} and t_{stim}, (defined in Section 2.5.1). These time intervals were then used to find the so-called *plateau* stages, when the muscles were either fully contracted or fully relaxed. This was normally seen as a constant voltage in the strain gauge transducer output measurements V_{SG1} and V_{SG2}.

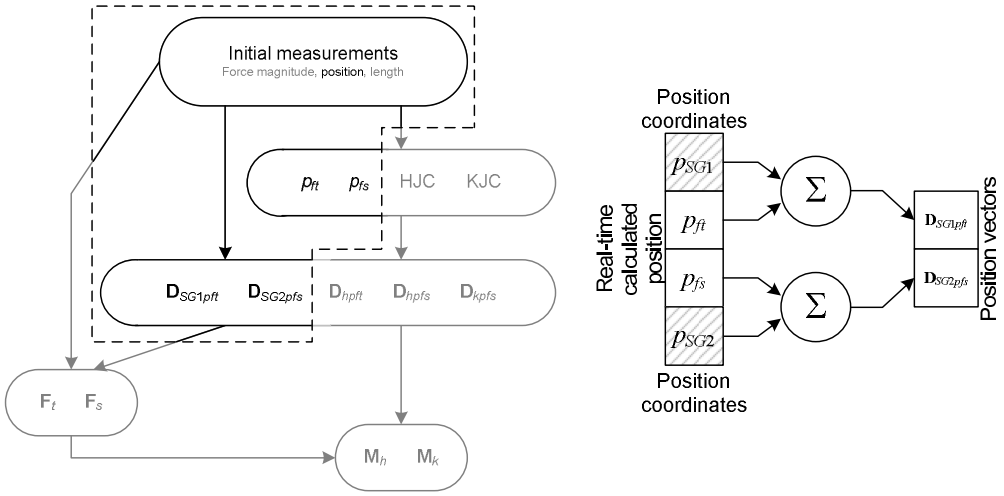

(a) $\mathbf{D}_{SG1pft}$ and $\mathbf{D}_{SG2pfs}$

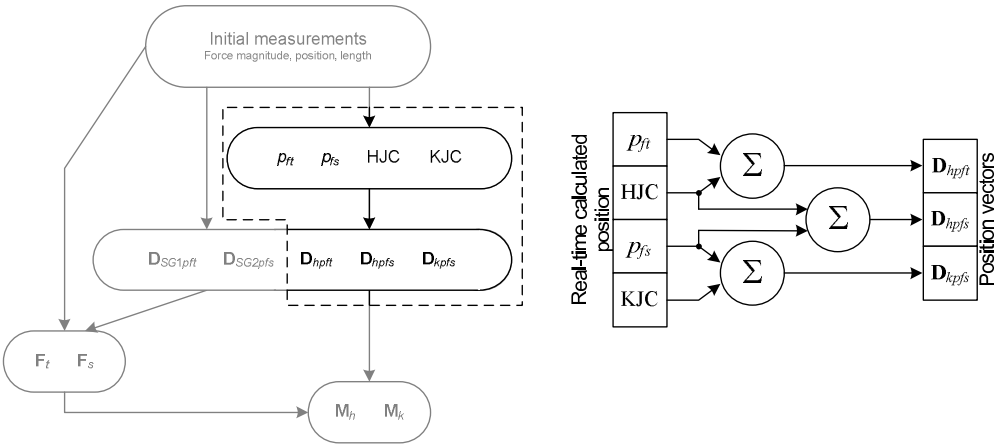

(b) $\mathbf{D}_{hpf}$, $\mathbf{D}_{hpfs}$ and $\mathbf{D}_{kpfs}$

Figure 2.19: Calculation of direction vectors.

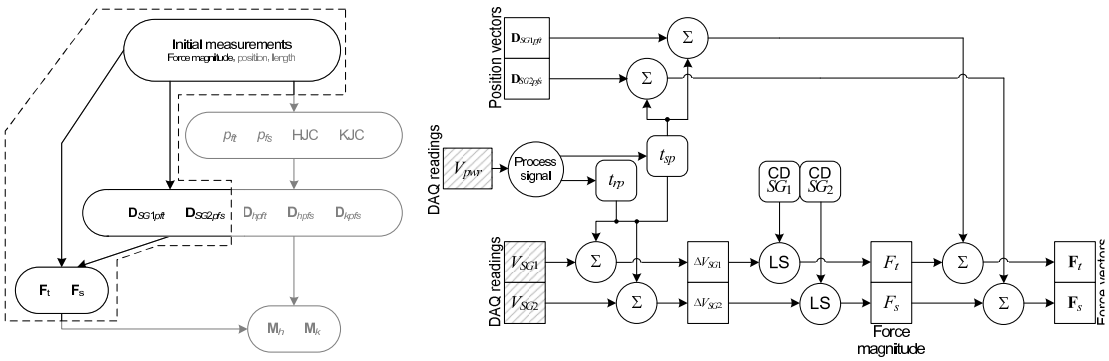

Figure 2.20: Calculation of force vectors $\mathbf{F}_s$ and $\mathbf{F}_t$.

Figure 2.21 shows a typical set of strain gauge transducer measurements with the accompanying V_{pwr} signal. The length of the plateau was identified through inspection of experimentally measured data. It was decided to use a plateau duration of 1s at the end of the t_{stim} and t_{rest} intervals. The plateau intervals are highlighted and labelled in the figure as t_{rp}, *rest plateau*, and t_{sp}, *stimulation plateau*.

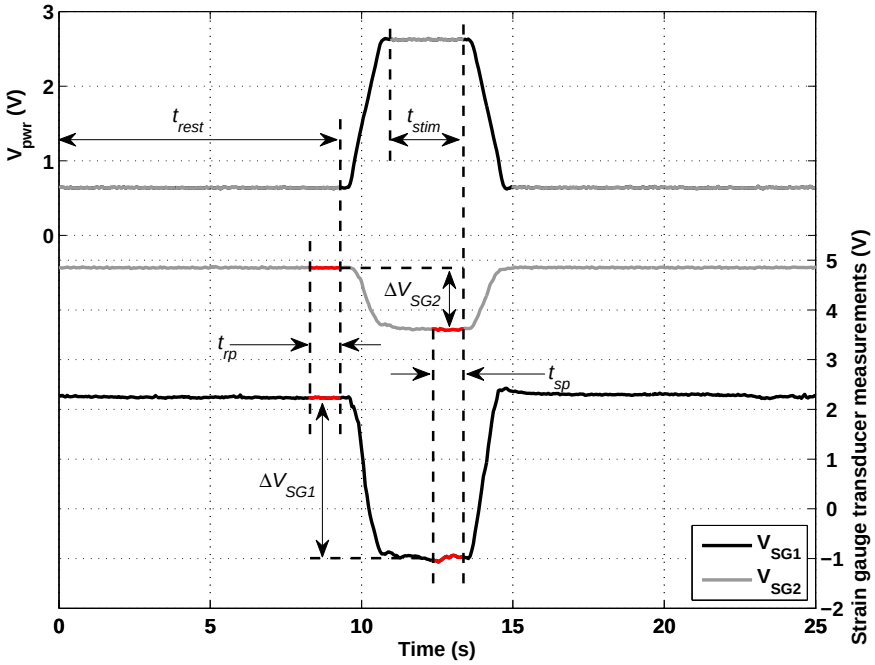

Figure 2.21: Strain gauge transducer force extraction.

Once the plateau time periods had been identified the second step was to extract the force magnitude data from the strain gauge transducer measurements. This was done by finding the average of the voltage measurement during t_{rp} and t_{sp}, from which the voltage difference was found, labelled as ΔV_{SG1} and ΔV_{SG2} in the figure. These values were then used with the strain gauge transducer calibration data (refer to Section 2.4.2), to find the magnitude of the forces, F_s and F_t.

Next, the force vectors, $\mathbf{F}_s$ and $\mathbf{F}_t$, were found using the direction vectors positioned on the lines of action of the forces, as in equation 2.20.

$$\mathbf{F}_t = -F_t \frac{-\mathbf{D}_{SG1pft}}{||\mathbf{D}_{SG1pft}||} \qquad \mathbf{F}_s = -F_s \frac{-\mathbf{D}_{SG2pfs}}{||\mathbf{D}_{SG2pfs}||} \tag{2.20}$$

The first negative sign accounts for the fact that the forces applied at the strain gauge transducers are equal and opposite to the forces applied on the limbs, refer to figure 2.2. While the second negative sign is needed as the direction of vectors $\mathbf{D}_{SG1pft}$ and $\mathbf{D}_{SG2pfs}$ are opposite to that of the force vectors, refer to figure 2.8(c).

2.5.9 Moment vectors M_k and M_h

Once the direction vectors and force vectors were known, it was possible to calculate the joint moments about the knee and the hip, using equation 2.8 (repeated as equation 2.21 in the Summary). The flow diagram is shown in figure 2.22.

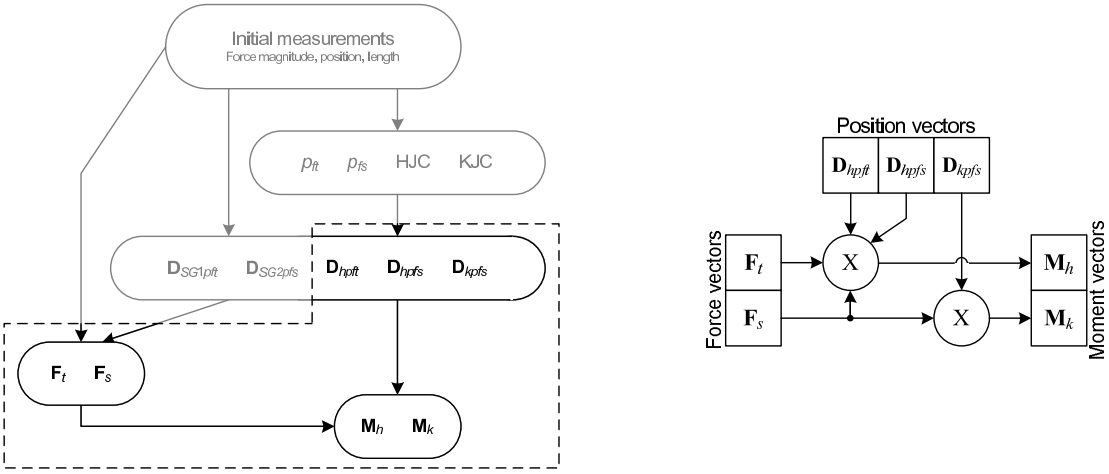

Figure 2.22: Calculation of moment vectors $\mathbf{M}_k$ and $\mathbf{M}_h$.

2.6 Summary

The influence of selective stimulation on moments about the hip and knee joints was to be experimentally measured. This lead to the biomechanical analysis of a seated subject, from which the kinetic variables needed to calculate the joint moments were identified. The two main variables were:

1. Force vectors, $\mathbf{F}_s$ and $\mathbf{F}_t$.
2. Direction vectors, $\mathbf{D}_{kpfs}$, $\mathbf{D}_{hpfs}$ and $\mathbf{D}_{hpft}$.

Using these variables the knee extension moment, $\mathbf{M}_k$, and hip flexion moment, $\mathbf{M}_h$, could be calculated as follows:

$$\mathbf{M}_k = \mathbf{D}_{kpfs} \times \mathbf{F}_s \qquad \mathbf{M}_h = \mathbf{D}_{hpfs} \times \mathbf{F}_s - \mathbf{D}_{hpft} \times \mathbf{F}_t \tag{2.21}$$

Based on this analysis, a Bi-moment chair was designed and constructed. The forces were measured using strain gauge transducers. The relevant positions, from which the direction vectors could be calculated, were measured with respect to the reference frame of the Bi-moment chair. For positions that were not expected to be stationary, position sensors in the form of spring pots, were used to monitor changes.

Chapter 3

Error analysis and validation of Bi-moment chair measurements

3.1 Introduction

Experimental data always has an inherent measurement error associated with it. If the data captured is to be of any use, then it is important to not only be aware of the presence of the measurement error, but also to know the size of the error, and, if possible, ways in which to reduce it. The size of the error depends on the experimental setup and the equipment used.

Taylor [1982] presents a conventional approach to the analysis of measurement errors, in which the errors can be classified as one of two types. The first type, random errors, appear as a statistical variation in a set of repeated measurements, which can lead to either over- or under-estimation in the final result. The second type are known as systematic errors. These errors cannot be revealed through repeated measurements and will tend to push a result in a certain direction, by either consistently overestimating or consistently underestimating a measurement. However, systematic errors are by their very nature difficult to detect and hard to evaluate. Taylor [1982] suggests that one should try to limit systematic errors by comparing measurement equipment against accepted standards.

The joint moment measurements captured with the Bi-moment chair were calculated from a large number of variables. Some of these variables were directly measured by the chair, while others comprised the initial measurements that were used as inputs to the data analysis procedure used by the chair. All of these variables were susceptible to measurement error, each acting as a possible source of error in the final joint moment calculations. Sometimes the initial error could be classified as a random error, however, it would then propagate through the data analysis procedure, so that the final effect of the error was then more akin to that of a systematic error. Other errors that were present at the start of a session with the chair were categorised as systematic errors. However the size of these errors were then seen to vary randomly while capturing measurements with the chair. This made it difficult to investigate the measurement error of the Bi-moment chair using just a conventional approach, instead several methods were used to investigate the error.

Firstly a means to validate the Bi-moment chair measurements was developed. This involved the construction of a spring-loaded dummy-leg that generated moments of known magnitude about pin joint models of the hip and knee joints. These moments were then compared against the moments measured by the chair. In so doing an indication of the size of the overall measurement error was obtained, without any of the additional complications that inherently arise when using a human subject.

Next, the conventional approach in which errors are classified as either random or systematic was considered. Random errors were identified through repeated measurements, after which the influence, that each of these errors had on the joint moments, was investigated. This helped to indicate the sensitivity of the joint moments to the various variables. Chapter 2 discussed a number of assumptions that were used in the joint moment calculations. If the assumptions did not hold true, they would serve as a source of systematic errors. The validity of these assumptions was investigated using a *Codamotion* analysis system.

Finally the overall measurement error was considered in two ways. Firstly, the combined effect of the random and systematic errors were investigated by using a theoretical approach presented by Taylor [1982], in which it was possible to obtain an estimation of the overall standard deviation. Lastly, typical joint moment measurements captured with human subjects in the Bi-moment chair are presented. These results help to show the shortcomings of the Bi-moment chair measurements as well as indicate how the chair should be used if the data gathered is to be of any use.

3.2 Validation of measurements

The purpose for building the Bi-moment chair was to simultaneously measure moments generated about the knee joint centre (KJC) and the hip joint centre (HJC). This was achieved by taking force magnitude, length and position measurements, which were then used to calculate the joint moments. Each of these measurements are inherently susceptible to errors, even before the additional complications that are introduced when we consider the human factor. For this reason it was decided to first validate the measurements captured with the Bi-moment chair, before placing a human subject in the chair, as a way to develop a better understanding of the instrument itself.

This was achieved by applying known moments about a point in space and using the Bi-moment chair to measure these moments. The moments were produced using a custom designed piece of apparatus called the *Limb for the Application of Moments* (LiAM).

3.2.1 Construction of LiAM

A schematic representation of LiAM is shown in figure 3.1(a). LiAM was built from 18mm ply-wood and consisted of two thigh sections and one shank section, the dimensions of which were approximately that of an actual limb, as given in figures 3.1(b) and 3.1(c). The two thigh sections, used to ensure symmetry of applied forces about the “knee joint”, were placed on either side of the shank.

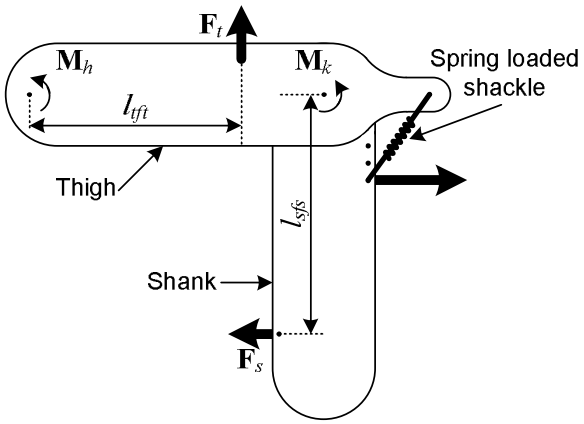

(a) Fully assembled schematic of LiAM showing forces and moments.

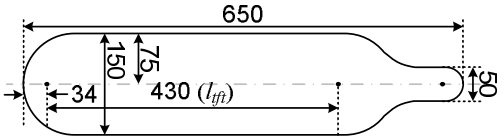

(b) Thigh section dimensions.

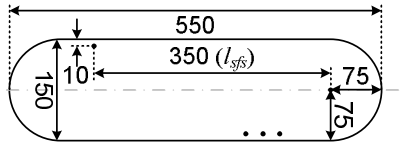

(c) Shank section dimensions.

Figure 3.1: Schematic representation of LiAM.

A spring loaded shackle was used to generate the moment about the knee joint. This allowed us to have a "knee moment" without any "hip moment." For all of the measurements taken with the aid of LiAM, the hip joint moment was fixed at 0Nm. Prior to placing LiAM in the Bi-moment chair, a series of calibration measurements were made so that the knee moment could be read off a scale.

3.2.2 Calibration of LiAM

LiAM was clamped so that the thigh was held vertically and the shank was free to move, as shown in figure 3.2. A pointer was attached to the thigh at the knee joint, after which a series of weights were suspended from the shank and the angle of deflection of the pointer, β, was measured. The magnitude of the knee moment for each mass was calculated using $M_k = mgl_{sfs}$. The value of l_{sfs} was taken to be 350mm, as in figure 3.1(c). The complete set of calibration measurements and calculations can be found in table 3.1.

Through trial and error it was decided to fit a fourth order polynomial to the measured data, using a least squares approach. The result of which is given in equation 3.1. Figure 3.3 shows the measured data and the fitted curve from the polynomial.

$$\beta = -0.0002M_k^4 + 0.0107M_k^3 - 0.1663M_k^2 + 0.0004M_k + 98.5021 \tag{3.1}$$

Using equation 3.1, it was possible to produce a demarcated scale for a range of knee moments, as shown in figure 3.2. Once the scale had been produced and attached to LiAM a series of measurements were taken to ensure that the scale gave the correct reading. The results are shown in table 3.2.

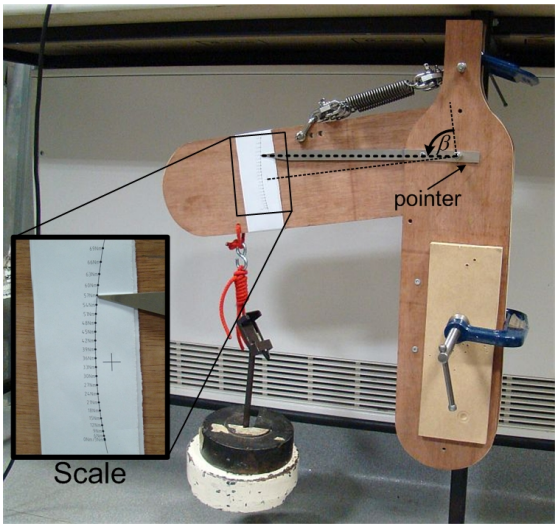

Figure 3.2: Calibration of LiAM, showing the pointer and demarcated scale.

Table 3.1: Calibration measurements for LiAM.

Calibration measurements											
Weight (kg)	0.0	1.4	4.6	4.9	6.4	8.1	9.6	11.5	13.1	15.0	16.5
β (°)	98.5	98.2	96.0	95.6	94.0	92.2	90.6	88.5	86.7	84.7	83.0
Moment (Nm)	0	4.8	15.8	16.8	22.0	27.8	33.0	39.5	45.0	51.5	56.7

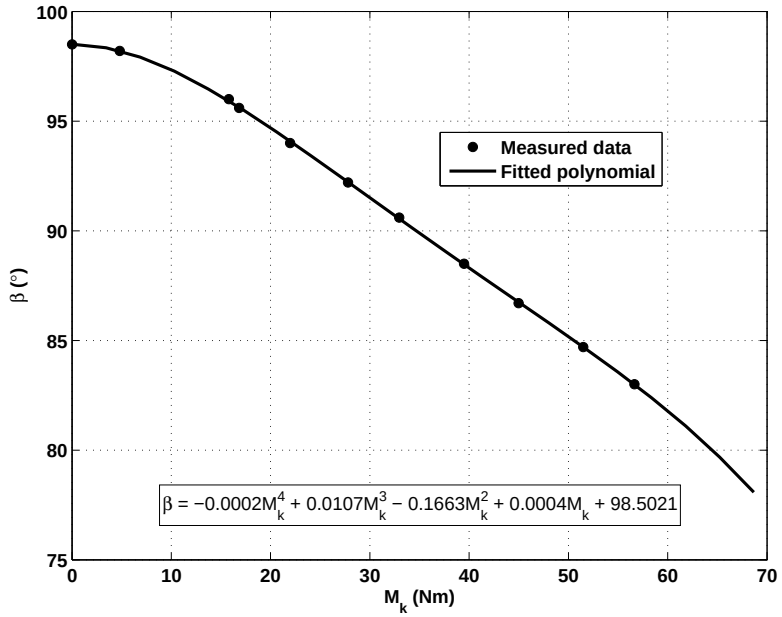

Figure 3.3: Polynomial fitted to LiAM's calibration measurements.

Table 3.2: Scale measurements for LiAM.

Weight (kg)	**1.4**	**3.5**	**6.4**	**9.9**	**11.5**	**14.9**	**15.0**	**16.5**	**18.2**	**20.0**
Moments (Nm)	4.8	12.0	22.0	34.0	39.5	51.2	51.5	56.7	62.5	68.7
Scale reading (Nm)	3	11	22	34	39.5	51	51.5	56.5	61.25	65

Errors were seen to be present in the scale readings for moments smaller than 22Nm. This was attributed to the non-linearity of the scale, as shown in figure 3.2, where the space between markings can initially be seen to be quite small and to progressively increase as the magnitude of the applied moment increased. Consequently it was difficult to obtain accurate readings from the scale at the lower moment magnitudes.

Magnitudes above 56Nm were also seen to be erroneous. This was due to the fact that the measured values in table 3.1 only went up to 56Nm. As a result the polynomial used to generate the scale could only be confidently used within the range of calibration measurements. Good correlation was seen in the range 22Nm - 56Nm.

3.2.3 Experimental results for LiAM

LiAM was placed in the Bi-moment chair, as shown in figure 3.4. In the figure a rigid support, connected to SG_1 is seen to support LiAM's thigh, while a cord connected to SG_2 was attached to LiAM's shank, exactly as would be the case for a human subject. The magnitude of $\mathbf{F}_s$, measured using SG_2, was determined by adjusting the tension in the cord connected to the shank. This would change the position of LiAM's shank, which in turn altered the tension in the spring loaded shackle and thereby produced a variable knee joint moment. The hip joint moment produced by LiAM, $\mathbf{M}_{hLiAM}$, was taken to consistently be 0Nm.

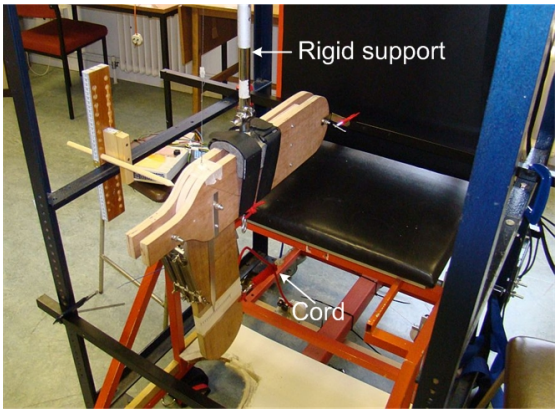

Figure 3.4: LiAM positioned in the Bi-moment chair.

Each knee joint moment produced by LiAM actually consisted of two parts, one where LiAM was "*at rest*" and one where LiAM was "*being stimulated*". The cord was tensioned in such a manner that the magnitude of the knee joint moment produced by LiAM *at rest* was always less than that of the moment produced by LiAM *being stimulated*, as read directly off of LiAM's calibration scale. The difference between these two moments was used to find the knee extension moment produced by LiAM, $\mathbf{M}_{kLiAM}$, as shown in equation 3.2. The magnitude of the knee joint moment, $\mathbf{M}_k$, measured with the Bi-moment chair, was compared against the magnitude of $\mathbf{M}_{kLiAM}$.

$$\mathbf{M}_{kLiAM} = \mathbf{M}_{kLiAM\_being\ stimulated} - \mathbf{M}_{kLiAM\_at\ rest} \tag{3.2}$$

It was necessary to produce two knee moments, LiAM *at rest* and LiAM *being stimulated*, so that the force magnitudes, $\mathbf{F}_s$ and $\mathbf{F}_t$, measured by the Bi-moment chair could be calculated from a change in voltage measured by the transducers, as discussed in Section 2.5.8.

LiAM was used to produce knee joint moments in a series of three tests. Each test consisted of a number of $\mathbf{M}_h$, $\mathbf{M}_k$, $\mathbf{M}_{hLiAM}$ and $\mathbf{M}_{kLiAM}$ measurements, taken over a range of $\mathbf{M}_{kLiAM}$ magnitudes. The percentage difference between the moments captured with the chair and those produced by LiAM were calculated as in equations 3.3 and 3.4. For both $\mathbf{M}_k$ and $\mathbf{M}_h$, the $\mathbf{M}_{range}$ value was calculated using the minimum and maximum $\mathbf{M}_{kLiAM}$ moments, measured within a test, as shown in equation 3.5.

$$\% \text{ difference in } \mathbf{M}_k = \frac{\mathbf{M}_k - \mathbf{M}_{kLiAM}}{\mathbf{M}_{range}} \times 100 \tag{3.3}$$

$$\% \text{ difference in } \mathbf{M}_h = \frac{\mathbf{M}_h - \mathbf{M}_{hLiAM}}{\mathbf{M}_{range}} \times 100 \tag{3.4}$$

$$\mathbf{M}_{range} = \begin{cases} \mathbf{M}_{k\_max}; & \mathbf{M}_{k\_min} \geq 0 \\ \mathbf{M}_{k\_max} - \mathbf{M}_{k\_min}; & \mathbf{M}_{k\_min} < 0 \end{cases} \tag{3.5}$$

The results for the three tests can be found in figure 3.5. Straight lines were fitted to the measured data of each test and have also been included in the figure so that trends in the measurements would be easier to identify.

The trends seen for the percentage difference in $\mathbf{M}_k$ was roughly the same for all three tests. The size of the percentage difference increased as the magnitude of the knee moment increased. Nonetheless the percentage difference was consistently less than 10%. The negative

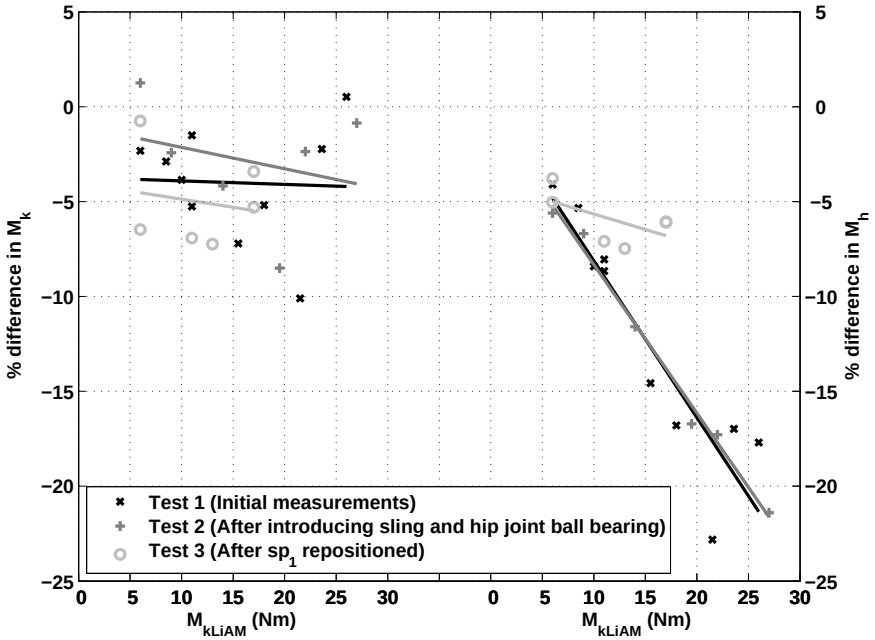

Figure 3.5: Scatter plots of moment error vs $\mathbf{M}_k$.

percentages indicated in the figure imply that the magnitude of the knee moment measured with the Bi-moment chair, $\mathbf{M}_k$, was up to 10% less than that produced by LiAM.

When considering the percentage difference in $\mathbf{M}_h$, the same trend was seen in that the size of the percentage difference increased as the magnitude of the knee moment increased. However, during the first test the percentage difference was larger than 20% at the higher $\mathbf{M}_{kLiAM}$ magnitudes. This indicated that there was a substantial error in the $\mathbf{M}_h$ measurement of the Bi-moment chair. Consequently it was set about to try and eliminate the source of this error.

A first attempt to eliminate the error involved introducing a ball bearing into the pin joint that served as LiAM's hip joint. Previously the pin joint had been realised with a steel rod pushed through a hole drilled in the ply-wood. It was possible that the friction around the steel rod was causing the hip joint moment to be something other than the expected 0Nm. In addition to this, the thigh was supported with a rigid support (refer to figure 3.4). A second possibility for erroneous $\mathbf{M}_h$ measurements was due to the rigid support allowing torsional moments to be applied on SG_1. To prevent this, the rigid support was replaced with a cord and a sling, as shown in figure 3.6. The sling was custom made with pulleys on the side to prevent the cord from being able to apply moment to the leg. After these modifications had been made to LiAM and the setup, the measurements were repeated (test 2 in figure 3.5). However, still no improvement was seen in the percentage difference of the hip joint moments.

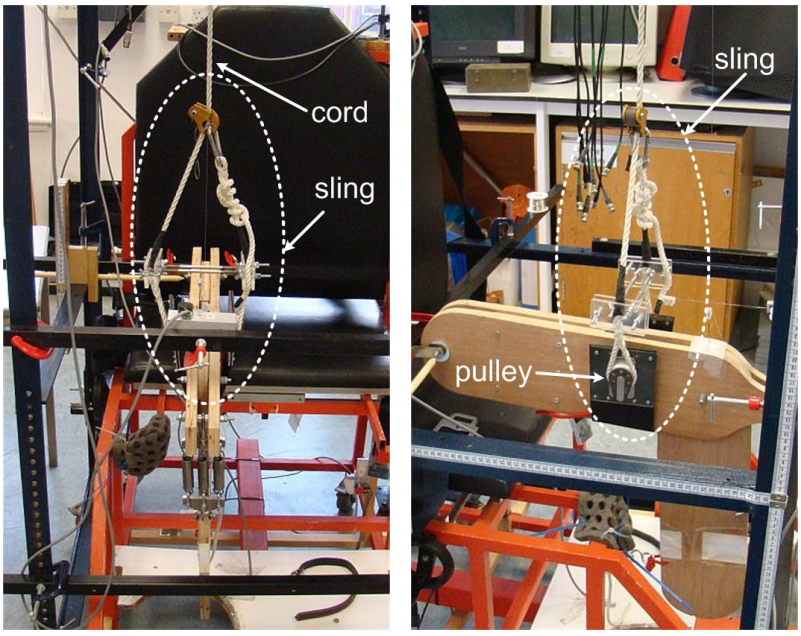

(a) Front view. (b) Side view.

Figure 3.6: Sling used to replace the rigid support.

Next the position of sp_1 was considered, as shown in figure 3.7. Initially sp_1 was located behind the subject. In Section 2.5.5 it was shown that the length measurement captured with sp_1 was ultimately used to find point p_{ft}, which in turn was used to determine the direction vector of force $\mathbf{F}_t$ (refer to Section 2.5.8), that was finally used to calculate $\mathbf{M}_h$. However, with

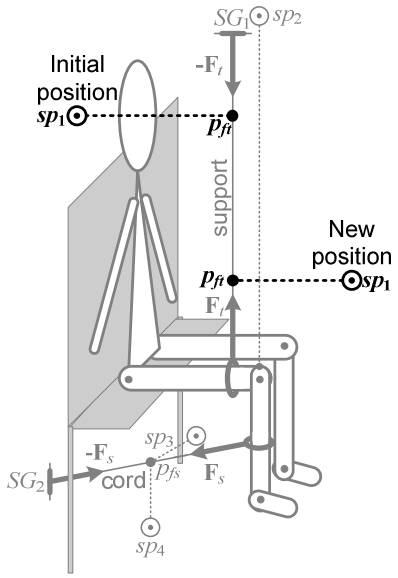

Figure 3.7: Schematic representation of the position of sp_1 in the Bi-moment chair.

sp_1 positioned behind the subject the calculation of point p_{ft} was very sensitive to errors in the length measurement of sp_1. Simply by changing the position of sp_1 to be in front of the subject, as shown in figure 3.7, it was possible to substantially decrease this sensitivity. This was reflected in the validation measurements captured with LiAM where the percentage difference in $\mathbf{M}_h$ was successfully reduced to less than 10% in the third test (refer to figure 3.5).

Discussion

From these results we were able to show that the moments measured with the Bi-moment chair were within 10% of the known moments produced by LiAM. The validation measurements captured with LiAM were also able to highlight important features of the Bi-moment chair:

1. The magnitude, of both moments measured with the Bi-moment chair, was less than the actual magnitude of the moments produced by LiAM. This indicates that the measurement errors inherent in the Bi-moment chair tend to result in an under-estimation of the moment magnitudes.[1]

2. Errors present in the initial measurements (force magnitudes, positions and dimensions) captured with the chair, propagate through the calculation of the moments and can result in substantial error in the final joint moments, as identified for the length measurement of sp_1.

The use of LiAM did help to develop a better understanding of the Bi-moment chair and its capabilities, however, LiAM was a simplified case compared to the situation when using a human subject. LiAM was perfectly stationary throughout all three tests, and the KJC and HJC of LiAM were well defined points in space. Neither of which are true for a human subject.

[1] In retrospect there was an error in the calibration of LiAM. The moment should have been calculated as $M_k = mgl_{sfs}\cos(90^\circ - \beta)$. This would have in part accounted for the under-estimation.

3.3 Random errors

One of the observations made, in the previous investigation with LiAM, was that any errors present in the initial measurements could influence the final joint moment measurements. The initial measurements are inherently susceptible to random errors. According to Taylor [1982] random errors can be quantified by repeating the same measurement a number of times and using the standard deviation, σ, to express the measurement error or uncertainty. This approach was used to estimate the random error present in each of the the initial measurements. The sensitivity of $\mathbf{M}_k$ and $\mathbf{M}_h$, on each of these random errors, was then investigated.

3.3.1 Source of random errors

Spring pots

Measurement errors in the spring pot can originate from the non-linearity of the potentiometers, stretching of the string and the change in pulley radius through the overlapping of turns as they wind onto the spring pot [Yu, 1999]. The combined effect of all of these factors was investigated by extending the string to positions marked on a tape measure around an arbitrarily chosen centre point. This approximated the type of measurements in the Bi-moment chair where the spring pots were used to monitor variation in position around a known point, as mentioned in Section 2.4.1. Figure 3.8(a) shows the measurement obtained for sp_1 during five sets of such measurements. The left axis gives the value of the measured voltage and the right axis gives the length measurement, obtained using the calibration method discussed in Section 2.4.1.

Figure 3.8(b) shows the difference between the spring pot measurements (right axis of figure 3.8(a)) and the actual distances demarcated on the tape measure, plotted against the actual distances. This gives an indication of the spread of the spring pot measurements around a point. These measurements were repeated for all four spring pots and the standard deviation of the difference was used to represent the measurement error associated with each spring pot. The results are given in table 3.3.

Strain gauge transducers

Figure 3.9 shows the fitted lines for 30 different calibration measurements, taken for both strain gauge transducers, that show the day to day variance. The lines do not exactly overlap, but instead some spread is present between the measurements. For both SG_1 and SG_2 the spread tends to become greater as the amount of force applied to the transducer increases. This has been indicated in the figure for SG_1 at $m = 5$kg and $m = 30$kg.

The strain gauge transducer amplifiers did allow an offset adjustment to be made (refer to Appendix A, Section A.3.2). However, as the force measurements were determined from the change in voltage, ΔV, measured by the strain gauge transducers, and not the absolute voltage, any offset that may have been present in the voltage measurements would not affect the resultant force magnitudes.

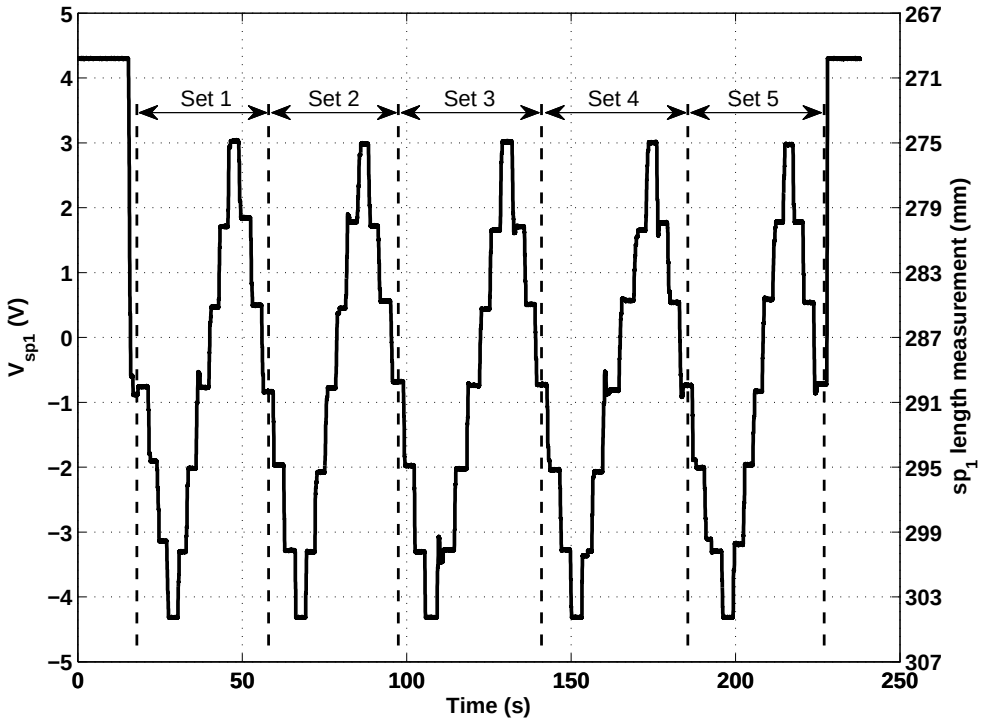

(a) Voltage and length measurements obtained for sp_1.

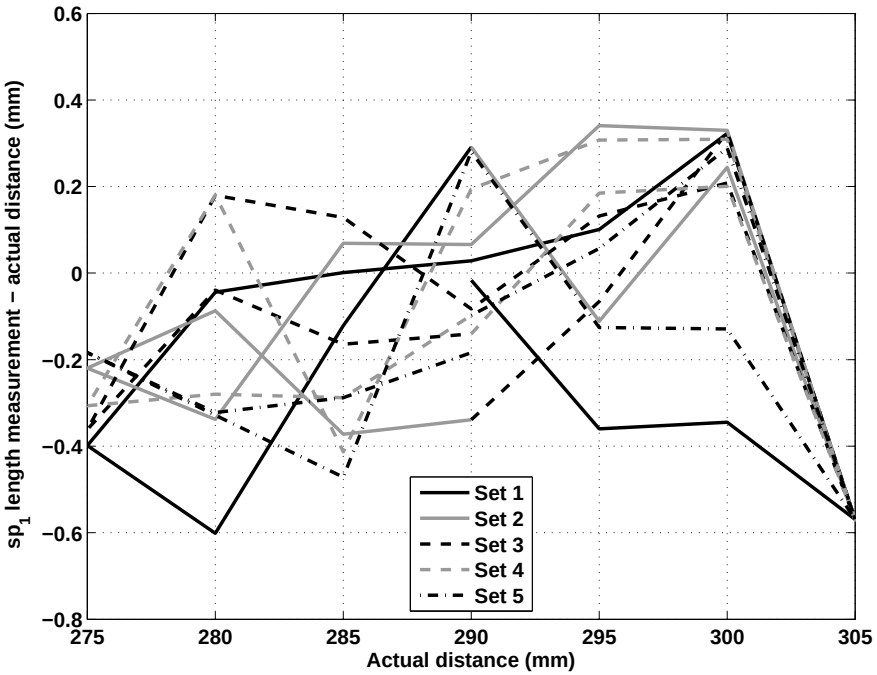

(b) Spread seen in sp_1 measurements.

Figure 3.8: Spring pot measurement error analysis.

Table 3.3: Standard deviation of spring pot measurements.

	sp_1	sp_2	sp_3	sp_4
σ_{sp_x} (mm)	0.28	0.51	0.53	1.38

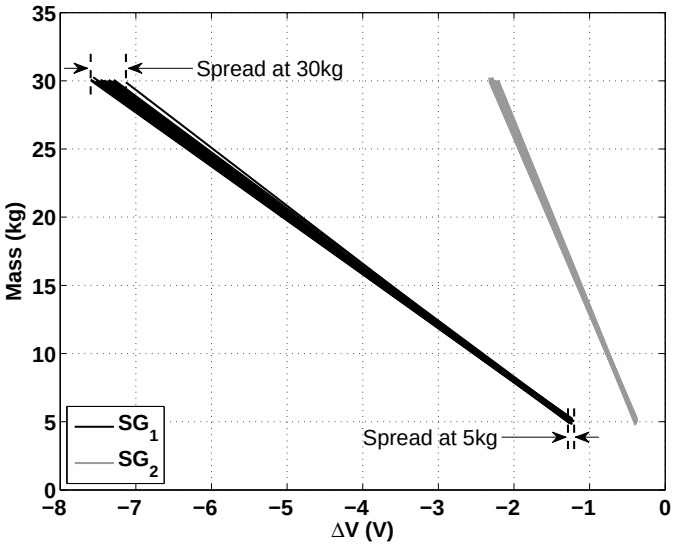

Figure 3.9: Variation seen in strain gauge transducer calibration measurements.

The standard deviation in the ΔV values was found at increments of 5kgs, corresponding to the series of weights used to take the calibration measurements. A mass-dependent expression for the standard deviation was then found, as given in equation 3.6.

$$\sigma_{SG_1} = 0.0037 \cdot m - 0.0040 \qquad \sigma_{SG_2} = 0.0011 \cdot m + 0.0015 \tag{3.6}$$

Position and dimension measurements

There is also an inherent uncertainty in the position and dimension measurements, listed in tables 2.3 and 2.4. These measurements were recorded at the start of a session using measuring tapes and the frame reference within which the chair was constructed. This meant that these measurements were particularly susceptible to mis-readings, parallax and stretchability of the measurement tapes used. Over a series of 10 days, the measurements were recorded for a fixed chair setup. The standard deviation was then calculated, as shown in table 3.4.

Table 3.4: Standard deviation of position and dimension measurements.

Position measurements							
	sp_1	sp_2	sp_3	sp_4	SG_1	SG_2	**Average**
σ_x (mm)	0.70	1.52	1.26	1.45	1.35	1.49	1.30
σ_y (mm)	1.55	0.92	0.88[a]	1.20[a]	0.84	3.25	1.44
σ_z (mm)	2.30	0.74	2.22	1.18	0.32	3.10	1.64

Dimension measurements									
	l_{sp1}	l_{sp2}	l_{sp3}	l_{sp4}	l_{SG1}	l_{SG2}	l_t	l_{k_off}	**Average**
σ_{l_x} (mm)	3.71	3.16	2.22	3.02	0.52	1.63	1.40	0.42	2.01

[a] As found from data sets recorded over 9 days, due to an outlier in the measurements.

The standard deviation of the position measurements are all on the order of a few mm. The y values for sp_3 and sp_4 were found to have an outlier in their data sets, attributed to a recording error. If the outlier was included, standard deviations of 19.80mm and 20.34mm, respectively, were found. This is a clear indication of the care that needs to be taken when recording the position and dimension measurements, as this would cause a large error in the final joint moment calculations.

3.3.2 Influence of random errors on calculated joint moments

Thus far the errors associated with individual measurements have been discussed. Each of these errors will propagate through the data analysis procedure (refer to Section 2.5) and have an influence on the final calculation of the moments. Figure 3.10 shows a flow diagram of these errors and their relationship with various parts of the procedure.

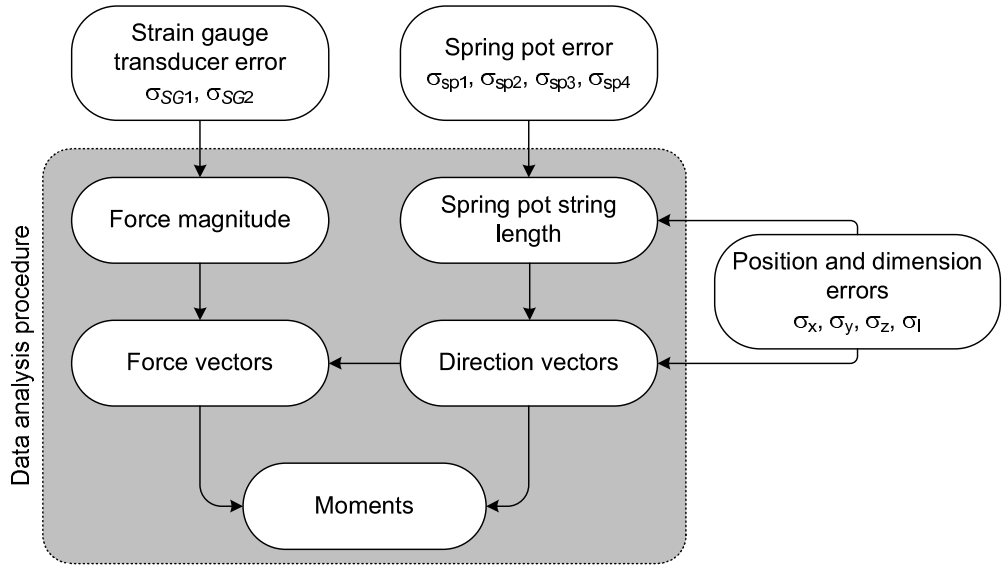

Figure 3.10: Error propagation flow diagram.

As mentioned earlier, the sensitivity of the calculation of the moments, on the measurement error associated with each initial measurement, was investigated individually. This was accomplished by taking an actual data set captured for a subject, introducing an error, equal to one standard deviation, into the raw data to create a modified data set. The now-modified data set was then used to calculate the joint moments, the result of which was compared with the joint moments calculated using the original unmodified data set. The results are presented in tables 3.5 through 3.7. The percentage error shown in the tables was calculated as in equation 3.7.

$$\%\text{ error in } \mathbf{M} = \frac{\mathbf{M}_{modified} - \mathbf{M}_{original}}{\mathbf{M}_{range}} \times 100 \tag{3.7}$$

The stimulation protocol used in the chair study is discussed in greater detail in Section 4.2.2. For the purposes of the tabulated data presented here, it is sufficient to know that the stimulation protocol consisted of 9 bursts of stimulation, the stimulation intensity increasing with each burst. The $\mathbf{M}_{range}$ value seen in equation 3.7 was found as in equation 3.8, using

the original data set's minimum and maximum moments over all nine stimulation bursts.

$$\mathbf{M}_{range} = \begin{cases} \mathbf{M}_{max}; & \mathbf{M}_{min} \geq 0 \\ \mathbf{M}_{max} - \mathbf{M}_{min}; & \mathbf{M}_{min} < 0 \end{cases} \tag{3.8}$$

In the tables, percentage errors less than 0.1% were considered to be negligible and have been omitted, while errors greater than 2% (an arbitrarily chosen limit), were highlighted.

Sensitivity of moment calculations on errors inherent to the spring pots and the strain gauge transducers

Table 3.5 lists the percentage error found in the moment calculations due to the spring pot errors (refer to table 3.3) and the the strain gauge transducer errors (described by equation 3.6). The mass required to produce a gravitational force equivalent to the maximum force magnitude measured in the original data set was used to calculate σ_{SG1} and σ_{SG2}, thereby giving an approximation of the expected error for the worst case scenario.

From table 3.5 it was seen that errors inherent to sp_2 and sp_4 propagated through to the knee moment, while sp_1, sp_3 and sp_4 were found to influence the calculation of the hip moment. Keeping in mind the fact that sp_1 helps to calculate the direction of $\mathbf{F}_t$, sp_2 is used to find the position of the KJC, and, sp_3 and sp_4 are used to find the direction of $\mathbf{F}_s$, one can easily see why the errors had an influence on either $\mathbf{M}_k$ or $\mathbf{M}_h$, or both. All of the errors were found to be less than 2%, for the expected measurement error inherent in the spring pots.

It was also seen that the error inherent in SG_1 produced a corresponding error in $\mathbf{M}_h$, but had no effect on $\mathbf{M}_k$. This was to be expected as $\mathbf{M}_k$ was solely dependent on $\mathbf{F}_s$ (measured by SG_2), while $\mathbf{M}_h$ is determined by $\mathbf{F}_s$ and $\mathbf{F}_t$ (the latter being measured by SG_1), refer to

Table 3.5: Sensitivity of moment calculations to σ_{sp} and σ_{SG}.

Stimulation burst	**1**	**2**	**3**	**4**	**5**	**6**	**7**	**8**	**9**
Error	**% error in $\mathbf{M}_k$**								
σ_{sp1}					-				
σ_{sp2}				-			-0.1	-0.2	-0.1
σ_{sp3}					-				
σ_{sp4}		-	-0.1	-0.1	-0.2	-0.2	-0.7	-0.9	-0.8
σ_{SG1}					-				
σ_{SG2}	-2.0	-2.0	-1.9	-1.9	-1.8	-1.8	-1.7	-1.6	-1.6
Error	**% error in $\mathbf{M}_h$**								
σ_{sp1}			-		0.1	0.1	0.2	0.2	0.2
σ_{sp2}					-				
σ_{sp3}		-		-0.1		-		-0.1	-
σ_{sp4}		-	-0.1	-0.2	-0.2	-0.2	-0.8	-1.1	-0.9
σ_{SG1}	2.0	2.0	2.0	2.0	2.0	2.0	1.9	1.9	1.9
σ_{SG2}	-4.4	-4.4	-4.3	-4.2	-4.1	-4.0	-3.9	-3.8	-3.8

equation 2.8. Even though an error was introduced into $\mathbf{M}_h$, the magnitude of the error was only 2% or less.

An error in SG_2 introduced an error into both $\mathbf{M}_k$ and $\mathbf{M}_h$. The error in $\mathbf{M}_k$ was approximately 2% for all nine stimulation bursts. However, the error in $\mathbf{M}_h$ was much larger, at around 4% for all nine stimulation bursts.

From these results we can see that the errors inherent to the the spring pots produce negligible errors in the joint moments. Although the errors introduced by the strain gauge transducers are larger than those of the spring pots, the errors are still less than 5%.

Sensitivity of moment calculations on position measurement errors

Table 3.6 shows the errors introduced into the joint moment calculations due to errors present in the position measurements, as listed in table 3.4. The errors present in the position of the HJC and KJC were taken as the average values of the standard deviations found for the position measurements shown in table 3.4. This gave an indication of the influence that measurement errors in the position of the ASIS or the GT would have on the joint moments. Errors inherent in the determination of the HJC and the KJC are further discussed in Section 3.4.

All of the errors shown in table 3.6, for both $\mathbf{M}_k$ and $\mathbf{M}_h$, are less than 2%.

Sensitivity of moment calculations on dimension measurement errors

Finally, the errors associated with the dimension measurements, listed in table 3.4, were used to calculate percentage errors in the joint moments, as shown in table 3.7. Table 3.7 also shows the error associated with dimension l_{AA}, which was used in the calculation of the HJC (refer to Section 2.5.3). The error in l_{AA} was taken as the average standard deviation from table 3.4.

In table 3.7, all of the errors shown for $\mathbf{M}_k$ were less than 2%, while $\mathbf{M}_h$ had errors larger than 2% due to random errors present in the measurements of l_{sp1} and l_{sp4}. The errors present due to the l_{sp1} dimension measurement, can be explained when we consider the fact that dimension l_{sp1} is used to calibrate sp_1, find the position of point p_{ft}, determine the orientation of $\mathbf{F}_t$, which is finally used in the calculation of $\mathbf{M}_h$. The error, however, was not particularly large, with a maximum percentage error of only 3.1%. The l_{sp4} measurement is used to calibrate sp_4 and find point p_{fs}, which is in turn used to determine the orientation of force $\mathbf{F}_s$. Finally $\mathbf{F}_s$ is used to calculate $\mathbf{M}_k$ and $\mathbf{M}_h$. Once again, even though the errors were greater than 2%, they were at most, only 2.3%.

3.3.3 Discussion

In the introduction it was mentioned that it was difficult to classify the measurement errors of the Bi-moment chair as either random or systematic. Although the results presented in this section were discussed under the topic of random errors, this was not always exactly true. In this section two main sources of error were identified:

1. Errors inherent to the sensors.

2. Errors present in the initial measurements.

Table 3.6: Sensitivity of moment calculations on position measurements.

Stimulation burst		**1**	**2**	**3**	**4**	**5**	**6**	**7**	**8**	**9**
Error		**% error in $\mathbf{M_k}$**								
p_{sp1}	x_{sp1}					-				
	y_{sp1}					-				
	z_{sp1}					-				
p_{sp2}	x_{sp2}					-				
	y_{sp2}			-		0.1	0.1	0.2	0.3	0.3
	z_{sp2}					-				
p_{sp3}	x_{sp3}					-				
	y_{sp3}					-				
	z_{sp3}			-			-0.1	-0.1	-0.2	-0.2
p_{sp4}	x_{sp4}				-			-0.1	-0.1	-0.1
	y_{sp4}		-	-0.1	-0.1	-0.2	-0.2	-0.6	-0.8	-0.7
	z_{sp4}				-			0.1	0.1	0.1
p_{SG1}	x_{SG1}					-				
	y_{SG1}					-				
	z_{SG1}					-				
p_{SG2}	x_{SG2}				-			0.1	0.1	0.1
	y_{SG2}		-	0.1	0.1	0.2	0.3	0.9	1.2	1.1
	z_{SG2}				-			0.1	0.1	0.1
HJC	x_h					-				
	y_h					-				
	z_h					-				
KJC	x_k					-				
	y_k		-		0.1	0.1	0.1	0.3	0.4	0.4
	z_k					-				
Error		**% error in $\mathbf{M_h}$**								
p_{sp1}	x_{sp1}		-	-0.1	-0.1	-0.1	-0.1	-0.5	-0.6	-0.4
	y_{sp1}					-				
	z_{sp1}		-		-0.1		-	-0.1	-0.1	-
p_{sp2}	x_{sp2}					-				
	y_{sp2}					-				
	z_{sp2}					-				
p_{sp3}	x_{sp3}					-				
	y_{sp3}				-				-0.1	-
	z_{sp3}		-		-0.1		-	-0.2	-0.3	-0.2
p_{sp4}	x_{sp4}		-		-0.1		-	-0.1	-0.1	-0.1
	y_{sp4}	-		-0.1	-0.2	-0.1	-0.2	-0.7	-0.9	-0.8
	z_{sp4}			-		0.1	0.1	0.1	0.1	0.1
p_{SG1}	x_{SG1}			-		0.1	0.1	0.3	0.4	0.3
	y_{SG1}					-				0.1
	z_{SG1}					-				0.1
p_{SG2}	x_{SG2}			-		0.1	0.1	0.1	0.1	0.1
	y_{SG2}			-		0.1	0.1	0.2	0.3	0.3
	z_{SG2}			-		0.1	0.1	0.1	0.2	0.2
HJC	x_h		-		0.1	0.3	0.3	0.7	0.7	0.6
	y_h	-		0.1	0.1	0.2	0.3	0.8	1.0	0.9
	z_h					-				
KJC	x_k					-				
	y_k					-				
	z_k					-				

Table 3.7: Sensitivity of moment calculations on dimension measurements.

Stimulation burst	**1**	**2**	**3**	**4**	**5**	**6**	**7**	**8**	**9**
Error	**% error in $\mathbf{M_k}$**								
l_{sp1}					-				
l_{sp2}		-	-0.1	-0.1	-0.2	-0.3	-0.8	-1.0	-0.9
l_{sp3}			-			-0.1	-0.2	-0.2	-0.2
l_{sp4}		-	-0.1	-0.3	-0.4	-0.5	-1.5	-2.0	-1.7
l_{SG1}					-				
l_{SG2}				-			0.1	0.1	0.1
l_t					-				
l_{k_off}				-			-0.1	-0.1	-0.1
l_{AA}					-				
Error	**% error in $\mathbf{M_h}$**								
l_{sp1}	-	0.1	0.2	0.5	0.9	1.0	2.7	3.1	2.3
l_{sp2}					-				
l_{sp3}		-		-0.1		-	-0.2	-0.3	-0.2
l_{sp4}	-	-0.1	-0.2	-0.3	-0.4	-0.6	-1.8	-2.3	-2.0
l_{SG1}					-				
l_{SG2}			-		0.1	0.1	0.1	0.1	0.2
l_t					-				
l_{k_off}					-				
l_{AA}		-	-0.1	-0.1	-0.1	-0.2	-0.5	-0.7	-0.5

The errors associated with the sensors (i.e. the spring pots and the strain gauge transducers) were true random errors. The size of the error varied randomly while capturing measurements with the Bi-moment chair. Although nothing could be done to reduce these errors, it was necessary to be aware of the size of the errors.

On the other hand, the errors present in the initial measurements were only random in the sense that when the measurements are initially recorded at the start of a session, the error would be random. However, after this, the same initial measurements are used throughout the session, which means that the errors are fixed and propagate through the data analysis procedure in such a way that they behave more like systematic errors. Nonetheless, the initial measurement errors were presented in this section, as it was possible to estimate the size of the errors by treating them as random errors. From this, it was possible to indicate the sensitivity of the final joint moments on the errors. Generally the results showed that care should be taken when recording all of the initial measurements to reduce the resultant error in the calculated joint moments. This was however, especially true for initial measurements l_{sp1} and l_{sp4}, which were found to produce the largest errors in the joint moments.

All of the errors presented here were calculated assuming random errors of one standard deviation. In practice these errors could be smaller, and in the odd exception, larger. The effect of the errors on the joint moments could also be reversed (i.e. negative values in the tables indicate a decrease in joint moment magnitude, while the opposite effect would be to increase the joint moment magnitude, positive values).

3.4 Systematic errors

In the conventional sense, systematic errors cause a measurement to be consistently over- or under-estimated [Taylor, 1982]. Aside from the initial measurement errors, that were ultimately seen to be systematic errors masquerading as random errors, it was inevitable that additional systematic errors were also present in the Bi-moment chair setup. Typically systematic errors are difficult to identify. However, by careful consideration of the Bi-moment chair setup, we were able to identify a few possible sources of systematic error.

3.4.1 Source of systematic errors

Spring pots and strain gauge transducers

The sensors, namely the spring pots and strain gauge transducers, captured voltage measurements which were converted to distance and force magnitude measurements, respectively. An offset present in these voltage measurements could act as a source of systematic error. To reduce the effect of such an offset, the sensors were used to monitor changes in distance or force, as opposed to absolute magnitudes.

In the case of the spring pots, during the calibration process at the start of each session, the voltage measurements were "zeroed", as discussed in Section 2.4.1 .

The force magnitudes were calculated from a change in voltage, ΔV, as measured with the strain gauge transducers. The ΔV measurement was captured during each stimulation burst (refer to Section 2.5.8), thereby preventing errors being introduced through drift in the offset, that might occur in the voltage measurements during the session.

Assumptions

In table 2.1 the assumption used in the Bi-moment chair were listed. Of these, three of the assumptions regarding the movement of the subject are now considered, namely:

1. The position of the HJC, and by relation the ASIS, was constant.
2. No lateral movement in the KJC.
3. No lateral movement in the position of point p_{ft}.

If these assumptions did not hold true, then they would act as a source of systematic error. The validity of these assumptions was investigated by using a *Codamotion* analysis system. This involved placing a subject in the chair. Markers from the *Codamotion* system were then placed on the ASIS, the KJC and point p_{ft}. In so doing it was possible to monitor these three positions, throughout an entire session, in real time.

The protocol carried out during the session is discussed in detail in Section 4.2. For now it is sufficient to know that the stimulating electrodes were placed in three different positions, referred to as the *major* positions, namely *Standard*, *Rectus* and *Vastii*. For each of these positions the Bi-moment chair captured measurements for a number of tests. Each test constituted one run of the stimulation protocol, where the stimulation protocol consisted of the nine stimulation bursts, consecutively increasing in intensity.

Two subjects took part in the investigation, each subject participating in a single session. The results for subject A are shown in figure 3.11. A similar figure for subject B has been included in the appendix, figure B.1.

Figure 3.11(a) shows the movement of the ASIS, in three dimensions, and the lateral movement (along the z-axis), of both the KJC and point p_{ft}, over time. The top trace in the figure shows the output of the pulse width recorder (refer to Section 2.5.1), which is used to indicate the timing of the stimulation bursts.

From the figure two types of positional changes were identified. The most evident is that which occurs during a contraction initiated by a stimulation burst. For subject A, the largest movement was seen in the vertical position (along the y-axis) of the ASIS. This was particularly true for the *Vastii* position. For the *Standard* and *Rectus* positions, the movement was considerably smaller. Figure 3.11(b) shows the change in position measured due to each stimulation burst. From the figure we can seen that the absolute magnitude of the change in position tends to increase as the stimulation intensity increases. For this reason it was decided to find the standard deviation of these changes in position, for each stimulation burst, as shown in table 3.8 for both subjects.

From the results in the table we can also see that subject B did not experience as large a change in position, along any of the directional axes, as experienced by subject A for the ASIS along the y-axis. This implies that, although it is possible for large movements to occur, it is not always necessarily the case that they do occur.

The second type of positional changes that occurred, arbitrary movements, refer to changes in position due to the natural tendency of the subjects to move. This is shown in figure 3.11(a) by the fact that the baselines of the traces (position measurements between stimulation bursts), for the different tests, do not overlap. The change in position of the baselines, as compared with the baseline of the very first test of the session, were used to calculate standard deviation values for the arbitrary movements. The results were included in table 3.8.

Table 3.8: Standard deviation of movement seen in the ASIS, KJC and point p_{ft}.

	Stimulation burst	**1**	**2**	**3**	**4**	**5**	**6**	**7**	**8**	**9**	**Arbitrary movement**
Subject A	σ_{x_asis}	1.34	2.10	3.75	3.40	3.80	3.48	3.30	3.17	3.40	4.50
	σ_{y_asis}	1.19	8.48	26.30	27.41	26.26	25.42	26.66	24.17	24.45	7.34
	σ_{z_asis}	1.12	1.53	2.37	2.91	3.05	2.91	2.75	2.98	2.57	10.36
	σ_{z_kjc}	0.80	1.12	2.85	2.85	3.11	3.75	2.93	2.74	2.12	10.65
	σ_{z_pft}	0.21	0.34	0.62	1.19	2.32	1.80	2.02	0.98	1.05	7.48
Subject B	σ_{x_asis}	0.73	0.48	0.37	0.78	0.72	1.16	1.61	1.77	2.10	1.71
	σ_{y_asis}	0.66	0.49	0.36	0.89	1.08	1.55	1.31	1.19	1.43	2.57
	σ_{z_asis}	0.59	0.43	0.34	1.02	0.81	1.15	1.83	2.34	2.78	2.55
	σ_{z_kjc}	0.72	0.70	1.32	1.82	1.81	2.45	2.80	2.89	3.47	3.72
	σ_{z_pft}	0.09	0.08	0.13	0.29	0.46	0.77	0.73	1.03	0.96	1.21

All standard deviations given in mm.

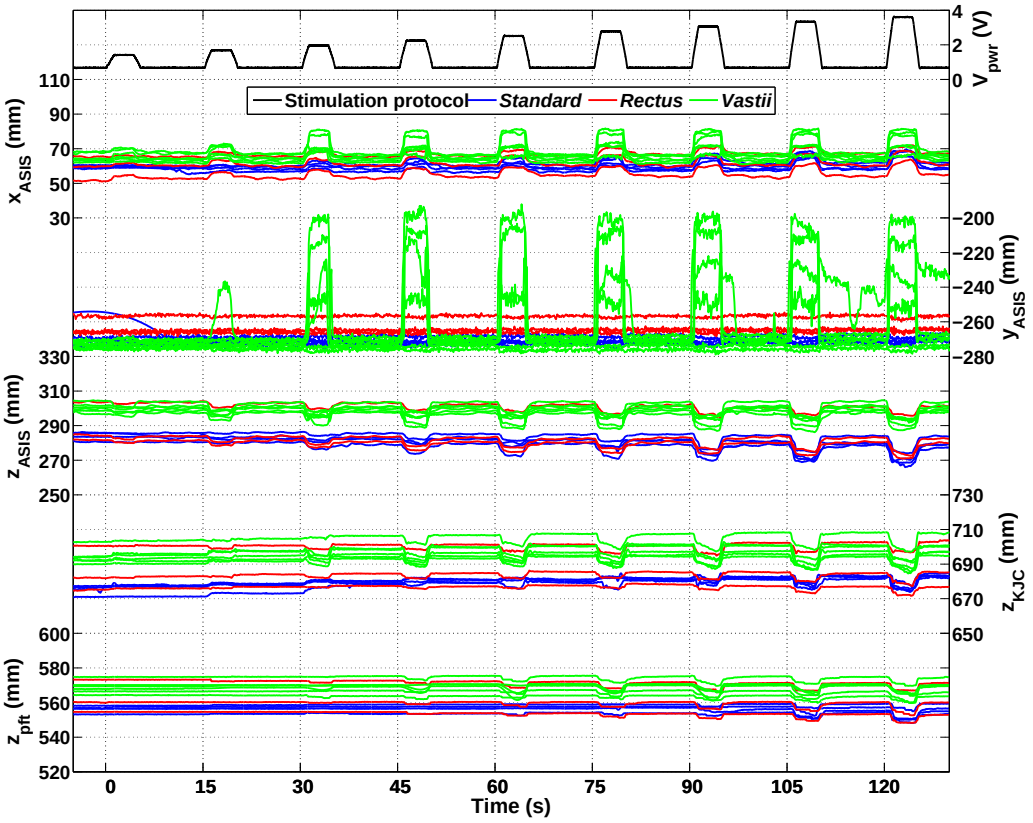

(a) Movement in the ASIS in three-dimensional space and lateral movement (along the z-axis), in the KJC and point p_{ft}.

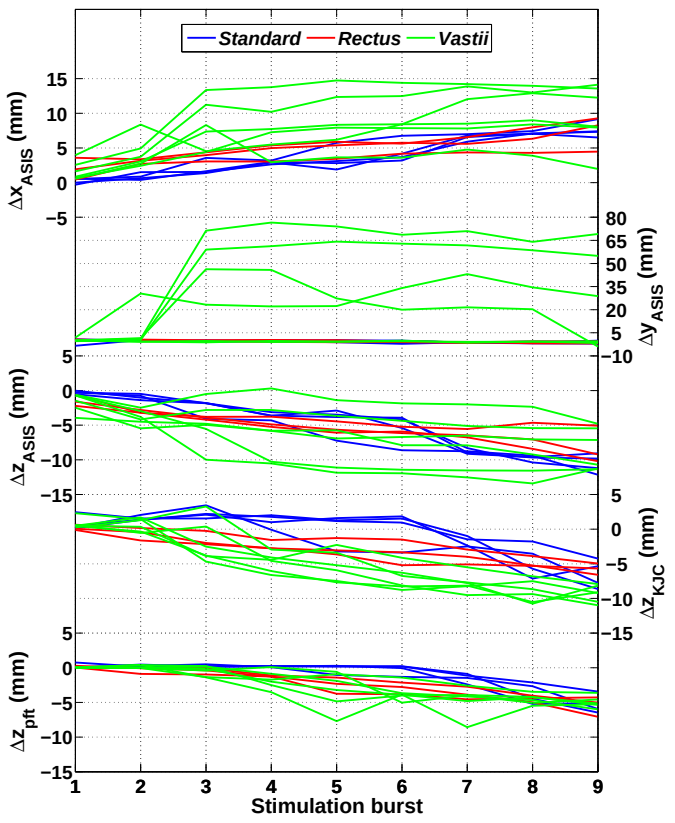

(b) Change in ASIS position in three-dimensional space and lateral change in position, in the KJC and point p_{ft}.

Figure 3.11: *Codamotion* analysis system measurements of movement in the ASIS, KJC and point p_{ft}, (subject A).

3.4.2 Influence of assumptions on calculated joint moments

The average standard deviations, from the results for subjects A and B shown in table 3.8, were found. After which the procedure outlined in Section 3.3.2 was used again, in which the average standard deviations were used to modify a data set, from which the percentage error in the calculated joint moments was found. The results are shown in table 3.9. It should be noted that for the movements occurring during the stimulation bursts, different standard deviation values were used for each burst, while the same standard deviation value was used for all nine bursts, for the arbitrary movements.

Table 3.9: Sensitivity of moment calculations to assumptions.

Stimulation burst			**1**	**2**	**3**	**4**	**5**	**6**	**7**	**8**	**9**
Error			**% error in $\mathbf{M_k}$**								
During stimulation	ASIS	x_{asis}					-				
		y_{asis}					-				
		z_{asis}					-				
	KJC	z_k					-				
	p_{ft}	z_{pft}					-				
Arbitrary movement	ASIS	x_{asis}					-				
		y_{asis}					-				
		z_{asis}					-				
	KJC	z_k					-				
	p_{ft}	z_{pft}					-				
Error			**% error in $\mathbf{M_h}$**								
During stimulation	ASIS	x_{asis}		-	0.1	0.2	0.4	0.4	1.2	1.4	1.2
		y_{asis}		-	0.7	1.3	2.0	2.5	7.6	8.8	8.0
		z_{asis}					-				
	KJC	z_k					-				
	p_{ft}	z_{pft}					-				
Arbitrary movement	ASIS	x_{asis}					-				
		y_{asis}	-	0.1	0.1	0.3	0.6	0.6	1.6	1.7	1.3
		z_{asis}	-	0.1	0.2	0.4	0.8	0.9	2.7	3.4	3.1
	KJC	z_k					-				
	p_{ft}	z_{pft}					-				

From the table we can see that typical movements, both during stimulation and arbitrary, in the position of the ASIS, KJC and point p_{ft} had no effect on the magnitude of the knee extension moment, $\mathbf{M}_k$. This implied that although the three assumptions were not technically true, the use of these assumptions showed no detrimental effect on the calculation of the knee joint moments.

The same can be said for the hip flexion moment, $\mathbf{M}_h$, when considering the assumptions regarding lateral movement in the KJC and point p_{ft}. However, this was not the case for $\mathbf{M}_h$ when considering movements in the position of the ASIS. ASIS movements in both the x and y directions during the stimulation bursts were seen to cause corresponding changes in the $\mathbf{M}_h$ magnitude. While arbitrary movements in the ASIS in the y and z directions were seen to also produce changes in the magnitude of $\mathbf{M}_h$. This shows that the calculation of the hip joint moment is sensitive to movements in the ASIS in any direction.

3.4.3 Discussion

Although the errors caused by the assumptions were discussed as systematic errors, this was once again not exactly true. By definition, systematic errors push results in one particular direction, so that the final outcome is consistently too large or too small. When we think about the assumptions, it appears logical to categorise them as systematic errors, as we would expect the error, provided that the assumptions were not true, to have this very particular influence on the results associated with systematic errors. However, after investigating the movement of the three positions assumed to be stationary, it was found that the change in the movements were random and that the standard deviation with which the size of these movements changed, also varied throughout the session. Consequently the resultant errors due to the assumptions were more akin to random errors than systematic errors. Nonetheless, by thinking of these errors as systematic errors it was possible to identify them in the first place. This then enabled an estimate of the size of the errors to be found, which in turn was used to investigate the sensitivity of the final joint moment calculations on these errors.

As already mentioned, the only assumption that could possibly introduce a large error, specifically into the final hip joint moment calculation, was that of the ASIS being stationary, when in fact it was not. However, the extent to which this assumption did not hold varied considerably. Large movements in the vertical direction of the ASIS were seen for subject A, when testing with the *Vastii* position. However, for the same subject the movements were considerably smaller for both the *Standard* and *Rectus* positions. This was also the finding for subject B for all three positions. This shows that although it is possible for a large movement in the ASIS to occur, it is not always the case; and even when these movements do occur and cause an error in the magnitude of $\mathbf{M}_h$, the size of the error due to the average movement in the ASIS, was still less than 10% (refer to table 3.9).

Additional remarks on the position of the HJC

Section 2.5.3 discussed the method presented by Bell et al. [1989], which was used to determine the position of the HJC from that of the ASIS. Any such method used to approximate the position of the HJC from an anatomical landmark such as the ASIS, would itself be susceptible to error.

Kirkwood et al. [1999] investigated the error present in moment calculations, using the method of Bell et al. [1989], as compared to those calculated with HJC positions found using the so-called golden standard of HJC location, namely the QUESTOR Precision Radiography

(QPR) system. A disadvantage of using the results of Kirkwood et al. [1999], is that Kirkwood et al. [1999] investigated the error during gait, and not in a seated subject as in the Bi-moment chair. However, the paper of Kirkwood et al. [1999] was the most relevant paper produced by a literature search. Therefore, even though the circumstance under which Kirkwood et al. [1999] collected his data was different from that of the Bi-moment chair application, it would at least give an indication of the size of the error to be expected.

Kirkwood et al. [1999] found that on average using the technique of Bell et al. [1989], an error of -0.05Nm/kg was introduced into the hip joint moments in the sagittal plane. The moments were normalised by body weight, which implies that for a subject weighing 75kg, the hip joint moment would on average be 3.75Nm less than its actual value.

3.5 Overall measurement errors seen with the Bi-moment chair

From the error investigations presented thus far, it is still difficult to say anything about the overall error present in the joint moment measurements. In this section two approaches are used to investigate both the size and the type of errors present. Firstly a theoretical approach is used to quantify the combined influence of both the random and systematic errors. Secondly, typical measurements captured with the Bi-moment chair were compared against joint moments calculated using position measurements captured with the *Codamotion* analysis system.

3.5.1 Combined influence of random and systematic errors

Taylor [1982] described a situation where a number of independent variables $(x, y, \ldots, z)$ are measured, each variable susceptible to random errors that can be described by standard deviations $(\sigma_x, \sigma_y, \ldots, \sigma_z)$, respectively. If the variables are used to calculate some quantity $q(x, y, \ldots, z)$, then the overall error associated with quantity q can be found as in equation 3.9.

$$\sigma_q = \sqrt{\left(\frac{\partial q}{\partial x}\sigma_x\right)^2 + \left(\frac{\partial q}{\partial y}\sigma_y\right)^2 + \ldots + \left(\frac{\partial q}{\partial z}\sigma_z\right)^2} \tag{3.9}$$

Consider the first term of equation 3.9. The partial derivative in this term indicates the change seen in quantity q, due to a change in variable x. This can be compared with the investigations carried out in Sections 3.3.2 and 3.4.2, in which the effect on the final joint moments were determined, due to small changes in individual measurements. This effect was mathematically described in the numerator of equation 3.7, as the difference in joint moment magnitudes. Recalling that this difference was obtained for a change of one standard deviation in each of the individual measurements, equation 3.9 can then be reduced to equation 3.10.

$$\sigma_{\mathbf{M}} = \sqrt{\sum_{\textit{random errors}} (\mathbf{M}_{modified} - \mathbf{M}_{original})^2 + \sum_{\textit{systematic errors}} (\mathbf{M}_{modified} - \mathbf{M}_{original})^2} \tag{3.10}$$

Using equation 3.10, and the difference in joint moments used to calculate the results shown in tables 3.5 through 3.7 and table 3.9, it was possible to calculate the overall standard deviation for $\mathbf{M}_k$ and $\mathbf{M}_h$. The results are provided in table 3.10.

Table 3.10: Overall measurement error, calculated for each stimulation burst.

Stimulation burst	**1**	**2**	**3**	**4**	**5**	**6**	**7**	**8**	**9**
$\sigma_{\mathrm{M}k}$	0.75	0.74	0.71	0.71	0.69	0.70	1.01	1.20	1.10
$\sigma_{\mathrm{M}h}$	0.76	0.75	0.75	0.78	0.81	0.85	1.58	1.81	1.63

Discussion

From table 3.10 we can see that both σ_{M_k} and σ_{M_h} tend to increase with consecutive stimulation bursts (i.e. increased stimulation intensity). The magnitudes of $\mathbf{M}_k$ and $\mathbf{M}_h$ would also increase as the stimulation intensity is increased. This is therefore a similar result to that seen with LiAM, in which the percentage difference increased as the magnitude of the knee joint moment increased. The results from table 3.10 were plotted against the measured joint moments, as shown in figure 3.12.

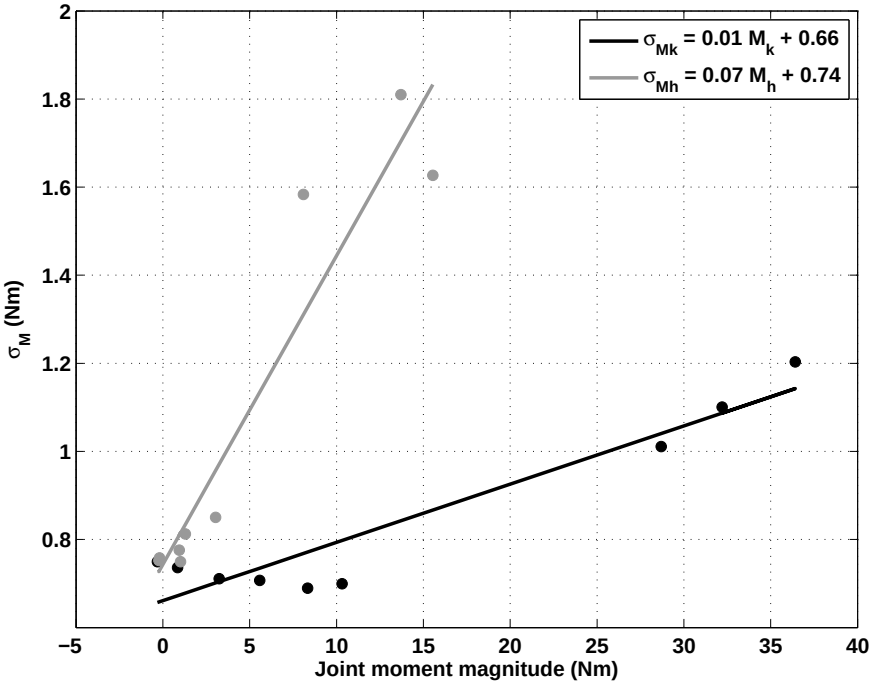

Figure 3.12: Overall standard deviation of joint moment measurements versus the magnitude of the joint moments.

A notable difference, when compared with the results of LiAM (refer to figure 3.5), is that in the case of LiAM, the percentage difference was negative, while the combined effect of all the individual measurement errors is positive. This is due to adding the individual difference in moment magnitude, in quadrature. However, by looking at tables 3.5 through 3.7 and table 3.9, we can see that many of the individual percentage errors were in fact negative.

In figure 3.12 straight lines were fitted to the data to give an indication of the relationship between the overall standard deviation and the joint moment magnitudes. However, it should be remembered that these results were obtained from a single data set captured with a single

subject. The investigation carried out here would have to be repeated for numerous data sets, captured with many subjects, before being able to present a final mathematical formula for the relationship, similar to those shown in the figure for $\sigma_{\mathbf{M}_k}$ and $\sigma_{\mathbf{M}_h}$. This would be a time consuming process and may not even yield a useful result.

Instead, typical measurements captured with the Bi-moment chair are presented next, that serve as a platform with which to discuss the presence of measurement errors and the effect they have on the type of analysis to be performed with the chair.

3.5.2 Typical joint moment measurements

In the previous sections a conventional approach to error analysis, in which the errors were categorised as either random or systematic, was used. However, the fact that the measurement errors present in the chair did not always fit the definition of random and systematic errors was also discussed. Clearly this meant that the conventional approach towards error analysis was not entirely sufficient for the chair application. For the joint moment measurements captured with the chair to be of any use, it was necessary to be aware of how much error was expected to occur during a session. This was achieved by comparing the a typical set of chair joint moment measurements against measurements captured using a widely accepted measurement apparatus, namely the *Codamotion* analysis system.

In Section 3.4.1, the use of a *Codamotion* analysis system, to monitor the movements of a subject seated in the Bi-moment chair, was first discussed. During the two sessions carried out with subjects A and B, the *Codamotion* system was used to not only monitor the position of the ASIS, the KJC and point p_{ft}, but all of the positions of the spatial coordinates listed in table 2.3. The *Codamotion* captured positions were then used in combination with the Bi-moment chair force measurements to calculate the joint moments in the same way that the moments would be calculated using the position measurements captured with the Bi-moment chair.

In Chapters 4 and 8, the joint moments measured with the chair are presented in figures referred to as moment curves. The reason for presenting the data in such a way is discussed in Section 4.2.2. For now, it is sufficient to know that the moment curves show a plot of the hip joint moment, $\mathbf{M}_h$, versus the knee joint moment, $\mathbf{M}_k$. Each trace in the plot corresponds with one test of the nine burst stimulation protocol. The colour scheme used for the individual traces is such that the three *major* stimulating electrode positions mentioned earlier, *Standard*, *Rectus* and *Vastii*, can easily be distinguished.

Figure 3.13 shows the moment curves captured with the Bi-moment chair (solid lines) and the *Codamotion* system (dashed lines). Furthermore, the equations given in figure 3.12 were used to find $\sigma_{\mathbf{M}k}$ and $\sigma_{\mathbf{M}h}$ for each test trace measured with the Bi-moment chair. These standard deviations gave an indication of the uncertainty associated with joint moments captured during each test, due to measurement error. In figure 3.13, the uncertainty has been indicated by a shaded area surrounding each Bi-moment chair test trace (solid lines).

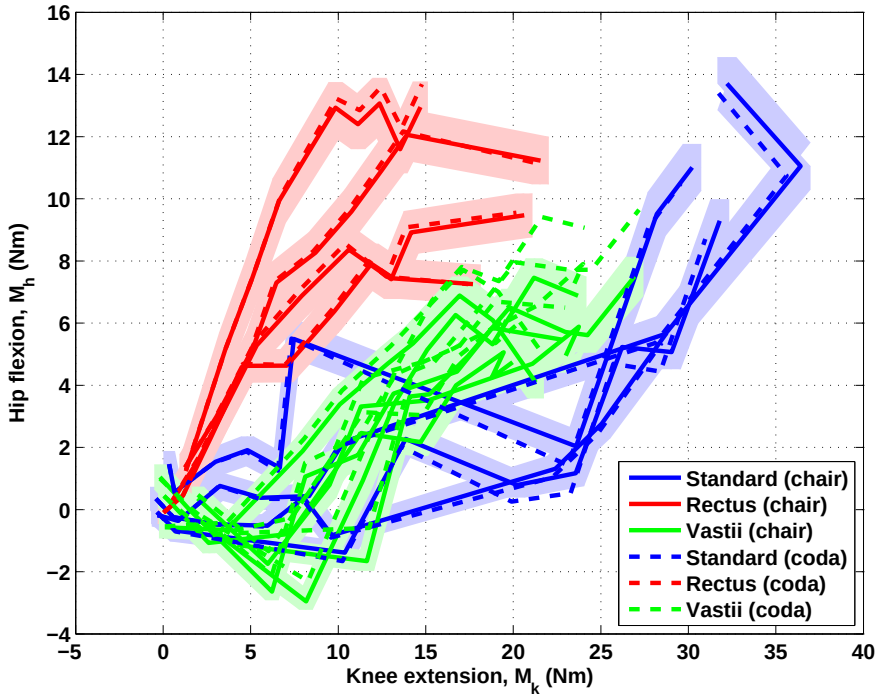

(a) Subject A.

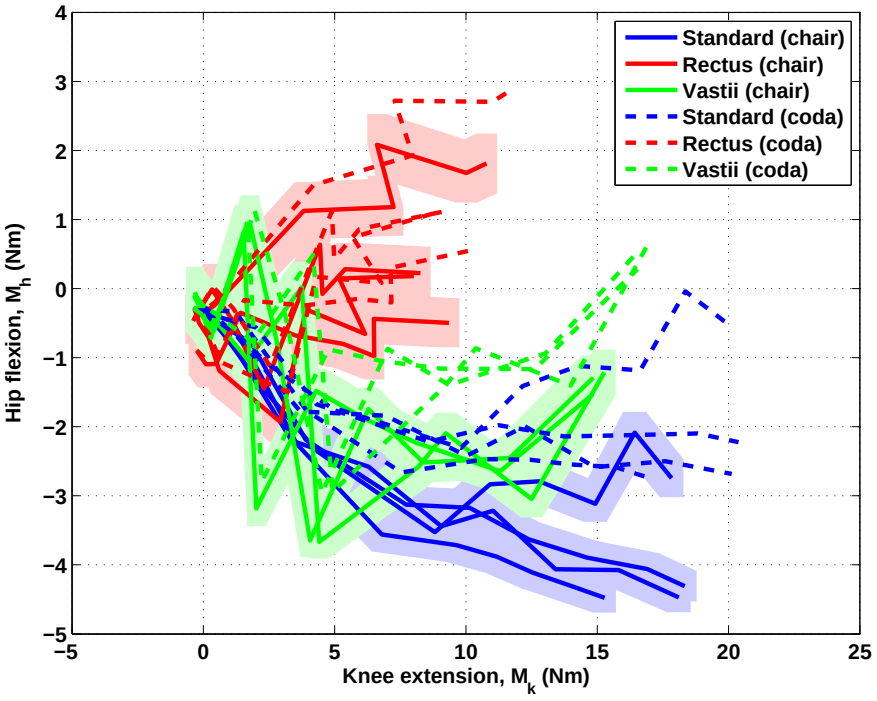

(b) Subject B.

Figure 3.13: Comparison of moments calculated using Bi-moment chair data (solid lines) and *Codamotion* analysis system data (dashed lines), as captured with two subjects.

Discussion

Even though the *Codamotion* system is also susceptible to measurement error, a similar region of uncertainty was not indicated in the figure, as it was difficult to quantify the size of this error. This was in part due to the fact that no indication of measurement error size was given in the *Codamotion* system manual [Charnwood Dynamics Ltd, 2008]. Furthermore, just by considering how the system works, two sources of error become evident. Firstly, the fact that the *Codamotion* markers are placed on the skin above the ASIS and the KJC. It is possible that the skin would move over these bony protrusions as the subject moves. Therefore the *Codamotion* system is actually monitoring the position of the markers on the skin, and not necessarily the anatomical landmark of interest. Secondly, errors could enter the *Codamotion* measurements due to a misalignment of the *Codamotion* coordinate frame with that of the Bi-moment chair.

Nonetheless, even though these errors were present in the *Codamotion* measurements, the system was still considered to be more sensitive than the chair. This was because the *Codamotion* system continually monitored the positions throughout the session, as opposed to initial measurements captured only at the start of the session. The positions were also monitored in three dimensional space, whereas with the Bi-moment chair some of the measurements were limited to two dimensions due to the number of spring pots used. Lastly, errors present in the *Codamotion* measurements, such as that caused by the movement of the skin over the bony landmarks, would also be present in the chair measurements.

The presence of errors in both the Bi-moment chair and the *Codamotion* system ultimately meant that some uncertainty existed in the absolute magnitude of the moments captured with either system. One of the required outcomes of the studies discussed later, was to determine if the hip flexion moments generated with each of the three *major* positions (*Standard*, *Rectus* and *Vastii*) were different from one another, ideally with similar knee extension moments. This means that the final analysis would be comparative in nature. Consequently, even though an error could exist in the absolute magnitudes of the moments, provided that differences in the trends seen with the three positions was still evident, the error would be considered acceptable. Seeing the same trends in both the chair and *Codamotion* results, served as an indication that the Bi-moment chair measurements would be sensitive enough for our application.

A couple of conclusions can be drawn from figure 3.13.

Firstly, the traces for each of the three *major* positions are grouped together, whether captured with the Bi-moment chair (solid lines), or the *Codamotion* system (dashed lines). This grouping was still evident when the uncertainty, due to measurement error, was taken into account (shaded areas). This indicates that although the measurement error is present, the size of the error was not large enough to prevent different trends from being discernible between the three *major* positions. This finding shows that measurements captured with the Bi-moment chair would be sufficient for the intended application and analysis (studies discussed in Chapters 4 and 8).

Secondly, when comparing the chair results (solid lines) against the *Codamotion* results (dashed lines), in the case of subject A (figure 3.13(a)), excellent correlation was seen between the two sets of results. However, for subject B (figure 3.13(b)), this was not the case. The results of subject B, captured with the chair, appear to be rotated clockwise when compared with those captured by the *Codamotion* system, which gave rise to the term *rotational error*.

Even though the chair results were rotated, the same groupings were seen, for each of the *major* positions, as those found with the *Codamotion* results. The uniformity with which the results were shifted implies that the rotational error was most likely caused by the presence of a systematic error. There is a strong possibility that the error was a random error introduced at the start of the session when recording the initial measurements, which then acted as a systematic error for the rest of the session.

Nonetheless, even though the rotational error has a large impact on the absolute magnitudes of the moments, the presence of the rotational error would not cause any misinterpretations of the findings, by performing a comparative analysis on the chair results. In this thesis a comparative analysis means that the joint moments measured for each of the three *major* positions, for a single subject, are compared against one another. The results from this comparison can then be used to analyse data from different subjects. The comparative analysis is however limited to the case where all of the tests were carried out in a single session, as with the results shown in figure 3.13 for each of the subjects. For results captured during multiple sessions, it would be unknown as to whether a rotational error was present in some or all of the sessions. There would also be no guarantee that rotational errors in different sessions would have the same influence on the results.

From these observations we can list a few guidelines that should be adhered to when using the Bi-moment chair:

1. Great care should be taken when recording initial measurements, to reduce the uncertainty inherent in $\mathbf{M}_k$ and $\mathbf{M}_h$, due to the presence of random and systematic errors.

2. The assumptions used in the moment calculations can be a source of large errors, particularly the assumption that the position of the ASIS is constant. The subjects are therefore required to sit as still as possible during a session, to prevent excessive arbitrary movements. If the subject does happen to move between tests, the position of the ASIS should be remeasured.

3. If possible, all tests should be carried out during a single session to prevent misinterpretations due to rotational errors.

4. Joint moment measurements should be used in a comparative analysis, as the uncertainty in the absolute magnitudes is relatively unknown. The comparative outcome from each session can be used to compare results from different subjects.

3.6 Summary

The force magnitude, position and dimension measurements captured by the Bi-moment chair, are all susceptible to measurement error. By treating the errors as random errors, it was possible to estimate the size of the errors, and to determine the influence that each error had on the final joint moment calculations. The validity of the assumptions used in these calculations, as well as the error attributed to the assumptions was also investigated. Table 3.11 summarises the maximum errors found in $\mathbf{M}_k$ and $\mathbf{M}_h$ by the various investigations. These results indicate that in order to help minimise the resultant joint moment errors, great care should be taken when recording the initial measurements.

Table 3.11: Maximum joint moment error due to different types of individual errors.

Source of errors		**% error in**	
		$\boldsymbol{M_k}$	$\boldsymbol{M_h}$
Errors inherent to sensors			
Strain gauge transducers	SG_1	-	2.0
	SG_2	-2.0	-4.4
Spring pots	sp_1	-	0.2
	sp_2	-0.2	-
	sp_3	-	-0.1
	sp_4	-0.9	-1.1
Initial measurements			
Position measurements	x	$\pm$0.1	0.7
	y	1.2	1.0
	z	-0.2	-0.3
Dimension measurements	l	-2.0	3.1
Assumptions			
ASIS (stationary)		-	8.0
KJC (no lateral movement)		-	-
p_{ft} *(no lateral movement)*		-	-

The combined influence of these individual errors were used to find an approximation for the overall uncertainty in the joint moments, as shown in equation 3.11.

$$\sigma_{\mathbf{M}k} \approx 0.01 \cdot \mathbf{M}_k + 0.66 \qquad \sigma_{\mathbf{M}h} \approx 0.07 \cdot \mathbf{M}_h + 0.74 \tag{3.11}$$

An analysis of typical measurements captured with the Bi-moment chair highlighted two important aspects about the measurements:

1. The overall uncertainty due to random and systematic errors was not large enough to obscure differences in the results captured for the three stimulating electrode positions, *Standard*, *Rectus* and *Vastii*.
2. The absolute magnitude of the joint moments could be shifted due to the presence of a rotational error.

Ultimately this meant that the Bi-moment chair was limited to a comparative analysis of results captured within a single session.

Chapter 4

Joint moments captured using the Bi-moment chair

4.1 Introduction

Chapter 2 presented the main objective of the Bi-moment chair, namely to investigate the possibility of selectively stimulating the Vastii in order to generate a knee extension moment with as little hip flexion moment as possible. This chapter discusses the initial study in which various electrode positions were tested on able bodied (AB) subjects, and the resultant joint moments measured.

The way in which the study was structured, namely the electrode positions and the stimulation protocols used, are presented. The measured results were then analysed with consideration given to muscle fatigue and small deliberate movements in the electrode positions, as well as a direct comparison of the hip and knee joint moments.

4.2 How the study was structured

The title of the study, initially setup by Dr. Lynsey Duffell, was "*Improving the efficiency of electrically stimulated cycling*", (Kings College Research Ethics Committee approval, Reference no. CREC/07/07-179).

The following definitions were used:

Study Investigation into the selective stimulation of the Quadriceps by measuring hip and knee joint moments in response to placing the surface stimulation electrodes in three different positions, as discussed in Section 4.2.1. The final study (discussed in Chapter 8) aimed to have 10 able bodied subjects.

Recruitment curve protocol The stimulation protocol used in the study, consisting of 9 bursts of stimulation, each burst increasing in stimulation intensity (refer to Section 4.2.2).

Session Each subject took part in 3-6 sessions. During each session the subject was seated in the Bi-moment chair and the joint moments measured in response to a number of tests of the recruitment curve protocol. The position of the stimulating electrodes was either one of the three possible *major* electrode positions, or, one of the three *major* electrode

positions and *minor* variances. The *major* and *minor* positions are further defined in Section 4.2.1.

Test Each iteration of the recruitment curve protocol carried out within a session was referred to as a test.

The rest of this section individually discusses the main four parts of the study, namely, the different electrode positions investigated, the recruitment curve protocol, muscle fatigue tests that were carried out and the overall procedure followed during each session. The sessions in which each of the subjects participated is also summarised.

4.2.1 Electrode positions

The stimulating electrodes were placed in such a way as to try and selectively stimulate certain muscles. To this end, three *major* electrode positions were defined. Figure 4.1 shows the placement of the electrodes on the thigh with respect to anatomical landmarks: the ASIS, the medial and lateral KJC[1], the patella and the GT. A protocol was also devised for each of the *major* positions, as described below. The origin of this protocol is discussed in Section F.1 of the Appendix.

Standard Typical electrode position used in previous electrical stimulation studies [Perkins et al., 2001; Szecsi et al., 2007], wherein both Rectus femoris and the Vastii are stimulated simultaneously.

Placement of electrodes: Proximal electrode (proximal-medial corner) 30% along the line between ASIS and medial KJC; Distal electrode (mid-point) 80% on the line between ASIS and medial KJC.

Rectus Electrodes are positioned with the intention that only Rectus femoris is stimulated.

Placement of electrodes: Proximal electrode (proximal edge) 25% on the line between ASIS and the proximal border of the patella; Distal electrode (distal edge) 75% on the line between ASIS and the proximal border of the patella.

Vastii Vastus lateralis and Vastus medialis only.

Placement of electrodes: Medialis - Distal electrode (mid-point) 80% along the line between ASIS and medial KJC; Proximal electrode above distal electrode (mid-point) by 23% of the line between ASIS and medial KJC. Lateralis - Distal electrode 66% along the line between GT and lateral KJC, mid-point of electrode positioned, 9% of leg circumference, medial to this line; Proximal electrode 17% along the line between GT and lateral KJC, centre of electrode positioned, 9% of leg circumference, medial of this line.

[1]The *knee joint space* between the femur and tibia on the medial and lateral side of the leg, that can be located through palpation.

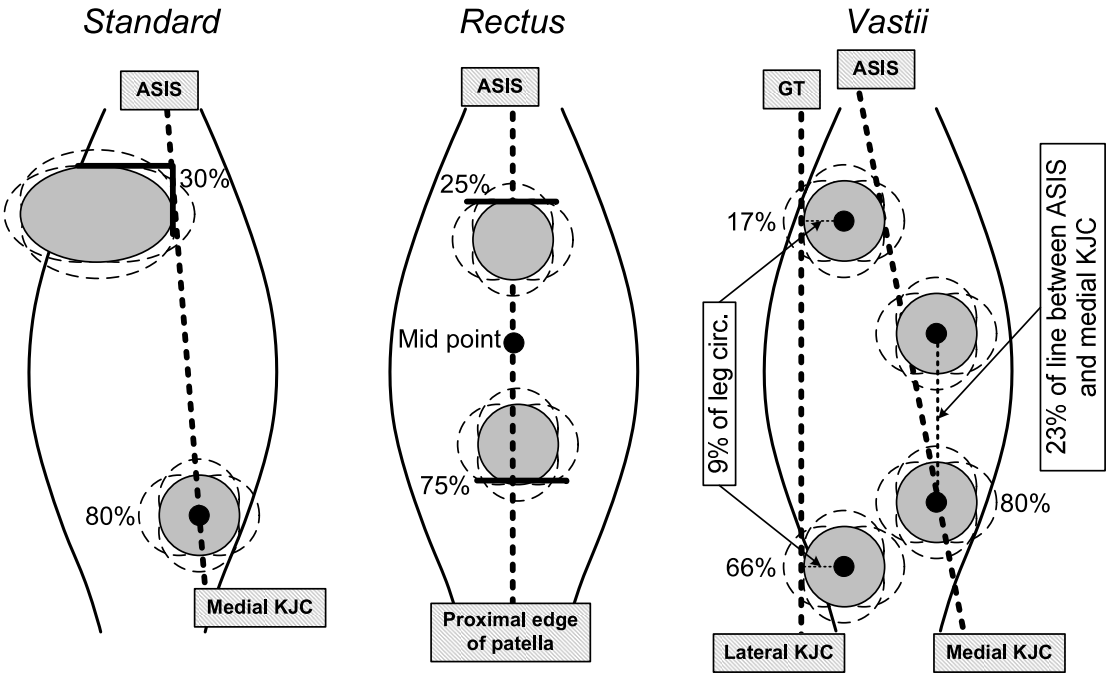

Figure 4.1: The three *major* electrode positions, reproduced from Duffell and Newham [2008], with permission.

In figure 4.1 the *default major* electrode positions are shown in grey. A number of dashed lines can be seen around these positions. These represent a movement of 1cm in the electrode position, called the *minor* positions.

Most SCI cyclists do not follow a precise protocol for placing the electrodes, as presented here. Instead the electrodes are randomly placed on the leg, to realise the *Standard* position. Consequently there will be small variations in the electrode positions. The *minor* positions, with an arbitrarily chosen movement of 1cm, were used to investigate the influence of these small changes.

The stimulating electrodes used in the study were the same as those previously used in FES cycling studies [Duffell, 2007; Perkins et al., 2001], namely commercially available PALS Platinum Neurostimulation Electrodes:

- Model 896350, with multistick gel, $3'' \times 5''$ (7.5cm $\times$ 13cm), oval.
- Model 879200, Part no. 0477, 50mm, round.

4.2.2 Recruitment curve protocol

Stimulation intensity is determined by the frequency, pulse width and current amplitude of the stimulation pulses. The stimulation settings that were used, for each of these parameters are shown in table 4.1, which realised the stimulation protocol shown in figure 4.2.

The protocol consisted of nine stimulation bursts sequentially increasing in intensity, which was achieved by varying the pulse width, from 80μs (20% of the maximum intensity) up till 400μs (100%), in 40μs (10%) increments. Throughout all nine bursts, the frequency and

Table 4.1: Stimulation parameters for the recruitment curve protocol, reproduced from [Duffell and Newham, 2008], with permission.

Parameter	**Setting**
Frequency	33 Hz
Pulse width	80μs up to 400μs, in steps of 40μs
Current amplitude	Highest that is tolerable by the subject at a pulse width of 400μs OR where the force attains a plateau, whichever occurs first. For *Vastii*, different currents can be used medially and laterally.

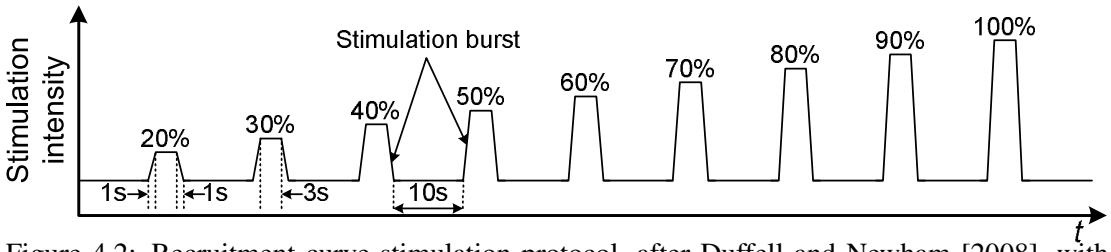

Figure 4.2: Recruitment curve stimulation protocol, after Duffell and Newham [2008], with permission.

current were held constant. The stimulation frequency was set to 33 Hz, so that a tetanic contraction was achieved. The current amplitude was adjusted for each subject, to the maximum tolerable current at the maximum pulse width of 400μs. Each burst was also set to ramp on for 1s, hold for 3s and ramp off for 1s, with a 10s rest interval between.

The reason for using a series of stimulation bursts can be explained if we consider the relationship between the knee moment and the hip moment, as shown in figure 4.3. As the stimulation intensity increases, the number of recruited motor units increases, which in turn increases the magnitude of the contraction force and the resultant joint moments. Consequently, tracing a path along the moment curves is equivalent to traversing the recruitment curve. We know that a maximum stimulation intensity level exists, whereafter, any further increase in stimulation intensity produces no corresponding increase in the contraction force, as all of the available motor units have been recruited [Jones et al., 2004]. Bearing this in mind, it is expected that at this unknown maximum level of stimulation intensity, the three moment curves will tend to converge, as shown in the figure. As the stimulation intensity level at which this happens was

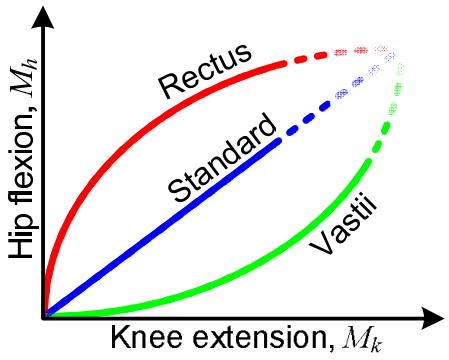

Figure 4.3: Moment curves depicting the recruitment of the muscles for the three *major* electrode positions.

unknown and would vary from subject to subject, it would not be possible to have confidence in any conclusions drawn from a comparison of the measurements taken for the *major* electrode positions, if only a single burst of stimulation was used. However, by using a series of stimulation bursts, the entire recruitment curve was effectively measured, which prevented the aforementioned uncertainty from being introduced.

Figure 4.3 also shows the results that were expected, before the study was carried out. The *Rectus* electrode position was expected to produce the most hip flexion per unit knee extension, while *Vastii* was expected to produce the least hip flexion per unit knee extension. These expectations were due to the fact that Rectus femoris is a bi-articular muscle, responsible for hip flexion and knee extension, while Vastas lateralis and Vastas medialis are mono-articular muscles, responsible for knee extension only [Cash, 2000] (refer to Section 1.1).

4.2.3 Fatigue tests

On the physiological level fatigue can be complicated to understand as there is a chain of events that cause a muscle contraction [Vøllestad, 1997]. The literature discusses various ways of measuring fatigue, each method testing a different segment of the activation chain, where the mechanisms for fatigue are located. In our study it was necessary to monitor the amount of fatigue the subjects would experience during a session, thereby indicating whether or not the joint moments measured at the beginning of a session could be compared with those measured at the end.

Vøllestad [1997] provides a definition for fatigue as "any exercise-induced reduction in the maximal capacity to generate force or power output" and says that the force or power output measured during a maximal voluntary contraction (MVC) can be used to identify whether fatigue occurs or not. A MVC, carried out at the beginning and end of each session, served as one of the ways to monitor the fatigue experienced by the subject.

However, during the tests, the joint moments were being measured in response to an electrically stimulated contraction as opposed to a voluntary contraction. This meant, that although the MVC did give an indication of overall fatigue, the electrically induced fatigue could be better monitored by making use of the force-frequency (FF) ratio [Binder-Macleod and McDermond, 1992].

The FF ratio describes the relationship between the contraction force and stimulation frequency, while keeping the stimulation pulse width and current amplitude constant [Jones et al., 2004]. As the frequency increases the contraction changes from a twitch to a tetanic contraction, normally between 15Hz and 20Hz, although the exact frequency depends on muscle fibre properties [Kralj and Bajd, 1989]. Initially, an increase in frequency corresponds with an increase in the generated force, but eventually the force reaches a plateau. This is due to an inherent property of the muscle and due to the time available for calcium re-uptake between stimuli. In the case of electrically stimulated contractions, muscle fatigue will result in a decrease in the maximum contraction force, as well as a shift in the FF response [Jones et al., 2004], as shown in figure 4.4.

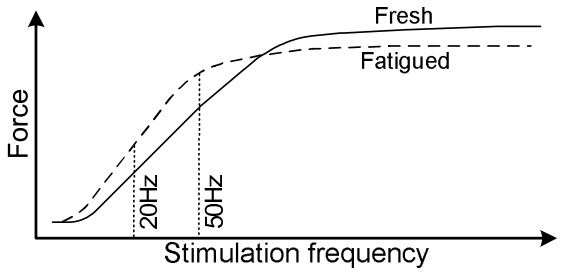

Figure 4.4: Force-frequency relationship, after Jones et al. [2004], with permission from Elsevier.

Common practice is to calculate the 20Hz:50Hz ratio in non-fatigued muscle and compare that to the ratio measured with fatigued muscle [Binder-Macleod and McDermond, 1992]. Force measurements were taken using a single burst of stimulation at frequencies of 20Hz and 50Hz, at the beginning and end of each session, from which the ratio could be calculated. The stimulation parameter settings, used for the FF stimulation bursts are given in table 4.2.

Table 4.2: Stimulation parameters for the FF ratio, reproduced from [Duffell and Newham, 2008], with permission.

Parameter	**Setting**
Frequency	20 Hz & 50 Hz
Pulse width	400μs
Current amplitude	20mA less than the current setting used for the recruitment curve stimulation protocol.

4.2.4 Protocol followed during each session

Initial setup phase

At the start of each session, the current amplitude to be used in the recruitment curve protocol was found. This was done by using a constant 33Hz, 400μs, and incrementally increasing the current amplitude till the subject stated that they had reached the limit they were able to tolerate. The final current was used subsequently during the recruitment curve protocol ($PW \leq 400\mu$s). After this initial setup phase, the remainder of the session was used to capture the joint moments in response to a number of tests of the recruitment curve protocol. Depending on the procedure followed, the session was classified as one of two types, either a *minor* session or a *default* session.

Minor session

Each *minor* session was performed as follows [Duffell and Newham, 2008]:

1. One session was carried out for each *major* electrode position.
2. At the beginning and end of each session, MVC and FF tests were performed.
3. Within each session, 11 tests of the recruitment curve stimulation protocol were completed.

- For the first (*default*) *major* position, two stimulation tests were initially carried out.
- For the *Standard* and *Rectus* positions, the proximal electrode were moved to the four *minor* positions; one stimulation test was carried out in each new position. Once completed, the proximal electrode was returned to its *default* position and the distal electrode was moved to the four *minor* positions, with one stimulation test carried out in each position.
- For the *Vastii* position, the two proximal electrodes were moved simultaneously to each of the *minor* positions, before being returned to the *default* positions. The two distal electrodes were then moved simultaneously to each *minor* position.
- After performing tests for each of the *minor* positions a final stimulation test was carried out with the electrodes once again in the *default* positions.

4. The subject was allowed a 5 minute rest between tests.

5. The order in which the *major* position sessions were carried out, the choice of proximal or distal electrode to be placed in the *minor* positions first, and the order of *minor* positions, were all randomly selected.

In point 3 we see that a total of three tests were carried out with the electrodes in the *default major* position, namely, the first, second and last tests of each session. These tests were helped to monitor the fatigue experienced by the subject during the session, and are further discussed in Section 4.3.1.

Default session

The *default* session was identical to the *minor* session, except that the movement of the electrodes to the *minor* positions was omitted. Instead, the electrodes were placed in the *default* position, where they remained during all 11 tests. The results from the *default* sessions were used to help determine the influence of the *minor* electrode movements.

Only one session was carried out on a day. Subjects were required to return on as many days as sessions in which they took part. The same current amplitude was used during both *minor* and *default* sessions, for a particular *major* position.

In Section 3.5.2 (*Discussion*), it was concluded that all tests with the Bi-moment chair should be carried out in a single session. However, due to the number of tests required for the *minor* positions it was impractical to investigate all three *major* positions in one session, as the fatigue experienced by the subjects would be to great.

4.2.5 Subject participation

Three subjects took part in the initial study. The profiles of each subject as well as the sessions in which they participated are listed in table 4.3. Eleven tests were carried out in each session.

Table 4.3: Subject participation in the study.

Subject	Profile				Session participation						Total no. sessions
	Gender	Age (years)	Height (m)	Weight (kg)	*Minor*			*Default*			
					S	R	V	S	R	V	
A	M	56	1.79	79	✓	✓	✓	-	-	-	3
C	F	27	1.75	74	✓	✓	✓	✓	✓	✓	6
D	F	21	1.70	53	✓	✓	✓	✓	✓	✓	6

M - Male, F - Female.
S - *Standard* position, **R** - *Rectus* position, **V** - *Vastii* position.

4.3 Study outcome

4.3.1 Muscle fatigue

Results: MVC and FF tests

As previously mentioned, the muscle fatigue experienced during a session was investigated by means of maximum voluntary contraction (MVC) and force-frequency (FF) tests performed at the beginning and end of each session. Table 4.4 shows the results of these tests for each of the sessions that the 3 subjects took part in. The shank force, $\mathbf{F}_s$, was used to calculate the percentage values shown in the table. The force measured before the session was taken to be 100%. For the FF tests, the 20Hz to 50Hz ratio was calculated before and after each session.

Table 4.4: Results for the MVC and FF ratio tests.

Subject	Session	*Major* position	MVC %	FF ratio	
				before	after
A	*Minor*	*Standard*	81.0	0.71	0.34
		Rectus	102.8	0.67	0.50
		Vastii	102.6	0.60	0.55
C	*Minor*	*Standard*	96.1	0.67	0.11
		Rectus	82.8	0.66	0.53
		Vastii	101.0	0.80	- [a]
	Default	*Standard*	92.5	0.74	0.62
		Rectus	99.9	0.76	0.56
		Vastii	101.0	0.61	0.17
D	*Minor*	*Standard*	91.9	0.77	0.71
		Rectus	86.0	0.80	0.69
		Vastii	94.1	0.73	0.56
	Default	*Standard*	98.4	0.75	0.69
		Rectus	90.9	0.77	0.67
		Vastii	87.0	0.75	0.53

[a] An error occurred while recording the FF measurements.

Discussion: MVC and FF tests

Generally a drop was seen in the MVC measured after the sessions. The size of the MVC decrease varied from subject to subject and session to session. In some cases the percentage drop was negligible (less than 5%), while in other cases a drop of almost 20% was seen, which is indicative of fatigue.

Similar observations were made with the FF ratios, in which the change in ratio value before and after the sessions varied from subject to subject and session to session. Once again the magnitude of the change in before and after ratios also varied. In Binder-Macleod and McDermond [1992] a decrease of about 0.2 in the ratio values was indicative of electrically induced fatigue.

For some subjects the two tests showed contradictory results, for instance subject C, *minor* session, *Standard* position, where a negligible drop was seen in the MVC measurements, while a large drop was measured in the FF ratio. The MVC and FF ratio, test different fatigue mechanisms. The former test includes the voluntary drive to the muscle, as well as the activation of the muscle from the nerve, which is the only part tested with the latter. Consequently, contradictory results like those seen for subject C, indicate that the subject did not provide a true MVC at the start of the session.

The main observation made from these results was that it is necessary to evaluate muscle fatigue for each session individually.

Results: Comparison of force measurements

A third approach was also used to evaluate fatigue. This involved comparing the $\mathbf{F}_s$ measurements recorded during each session. Figure 4.5 shows a typical set of force measurements, captured with subject C during the *minor* session, *Vastii* position. The first, second and last tests have been highlighted, as these were the three tests in which the electrodes were placed in the *default major* positions. Inspection of the figure shows that the first test tended to produce the largest force measurements, while the forces measured during the remaining 10 tests were generally grouped together.

Table 4.5 shows the percentage difference in $\mathbf{F}_s$ magnitude, for the ninth stimulation burst, as measured for all of the sessions. Differences in $\mathbf{F}_s$ magnitude measured during the first and second tests, which exceeds twice the mean difference between consecutive tests, have been highlighted. These highlighted values correspond with large differences in the force measurements between the first and second tests, similar to that seen in figure 4.5.

Discussion: Comparison of force measurements

When we consider the difference between the second and last tests (last column of table 4.5), we see that for all of the sessions, it is comparable to the expected drop as determined using the mean difference (i.e. for subject A, *minor* session, *Standard* position $-0.38 \times 9 = -3.42$). This large drop between the first two tests and a more gradual, consistent drop in force magnitude between the remaining 10 tests indicates that the subjects experienced a significant amount of

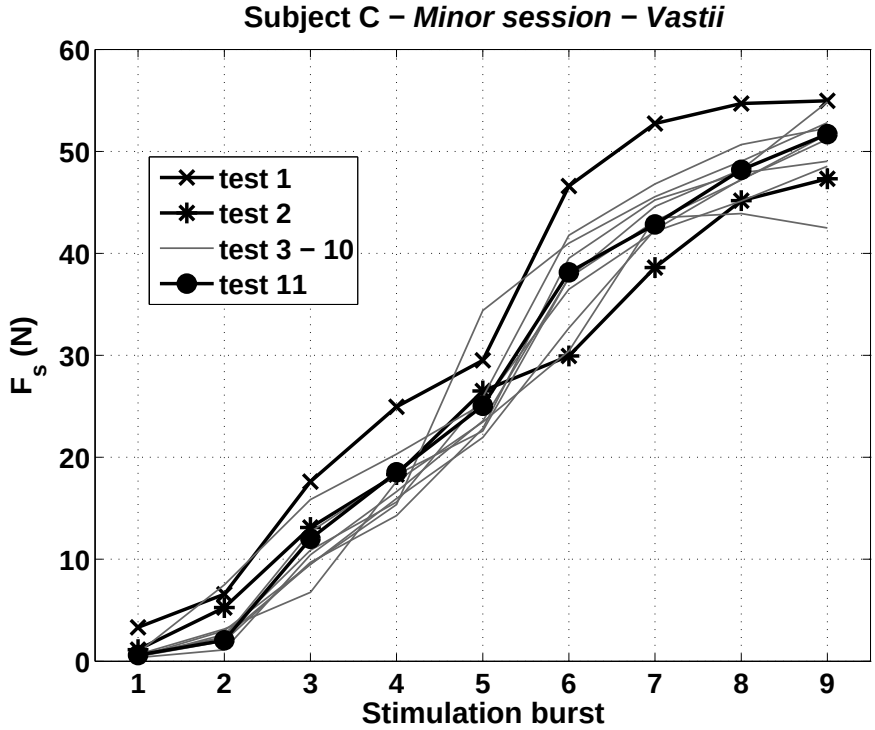

Figure 4.5: Force measurements, $\mathbf{F}_s$, captured during a session for all 11 tests. Measurements captured during the first, second and last tests, *default* electrode positions, have been highlighted.

Table 4.5: Percentage difference in $\mathbf{F}_s$ measurements during the 9th stimulation burst.

Subject	Session	*Major* position	Difference between tests 1 and 2 (%)	Mean difference between consecutive tests from test 2 onwards (%)	Difference between 2nd and last tests (%)
A	*Minor*	*Standard*	-0.03	-0.38	-3.42
		Rectus	-9.01	-1.48	-13.36
		Vastii	-12.10	-1.85	-16.65
C	*Minor*	*Standard*	-1.99	-0.74	-6.64
		Rectus	1.41	-1.72	-15.49
		Vastii	-13.91	0.88	7.95
	Default	*Standard*	16.75	-2.96	-26.67
		Rectus	8.75	-1.45	-13.06
		Vastii	-12.87	-2.22	-19.97
D	*Minor*	*Standard* [a]	2.14	-0.41	-3.25
		Rectus	-1.43	-0.93	-8.39
		Vastii	-1.47	-1.31	-11.83
	Default	*Standard*	1.59	-0.88	-7.91
		Rectus	-	-	-
		Vastii	-4.29	-1.53	-13.74

Negative percentages indicate a drop and positive percentages indicate an increase in force magnitude.
[a] Only 10 tests performed in the session.

fatigue during the first few minutes of the session. This agrees with the results of Duffell et al. [2008] in which AB subjects subjected to intermittent stimulation show a large drop in torque measurements during the first three minutes of stimulation, after which any decrease in torque occurs much more gradually.

From the various methods used to measure fatigue, it was concluded, that although some fatigue seems to be present during the sessions, the extent of the fatigue is not great, and did not seem to adversely affect the results (as shown by the close grouping of tests 2 through 11 in figure 4.5). Consequently, the only adjustment made to the results to account for fatigue, was to omit test 1 from further analysis, for all of the sessions.

4.3.2 Moment curves

The joint moments measured by the Bi-moment chair were used to produce a moment curve, in which the hip joint moment was plotted against the knee joint moment. Figure 4.6 shows the moment curves captured for both the *minor* and *default* sessions, for all three subjects. Each session consisted of 11 tests, each test corresponding with a single trace on the moment curve. In the figures, each session is represented by 10 like-coloured traces, as the first test was always omitted, as discussed earlier.

Note, in figure 4.6(c) the results for the *default* session, *Rectus* position have been omitted, due to a recording error that occurred during the session which yielded the results unusable.

Results: Minor electrode positions

For subjects C and D, the results for both the *minor* and *default* sessions were plotted on the same axes (refer to figures 4.6(b) and 4.6(c)). By inspection of the figures, a few observations can be made:

1. The individual test traces for any single session are grouped together (e.g. green dashed lines are grouped together).

2. The results from the *minor* and *default* sessions for a particular *major* electrode position tend to overlap (e.g. green dashed lines tend to overlap green solid lines).

3. Even when the traces from different sessions do not overlap, trends are still evident. For example, the *minor* session, *Standard* position traces do not overlap the *default* session, *Standard* position traces in figure 4.6(c). Nonetheless the *Standard* results are still below the *Vastii* and *Rectus* results for all sessions.

Discussion: Minor electrode positions

From points 1 and 2, it seemed that the *minor* movements did not play a significant role in the moment curves. This was further investigated through a statistical analysis. Typically a T-test, perhaps in combination with an F-test, would be used. However, in this case, the T-test was not considered to be a useful way of analysing the data.

In point 3, it was mentioned that the *Standard* moment curves, captured with subject D, did not overlap exactly. Such a result could have been obtained if there was a rotational error

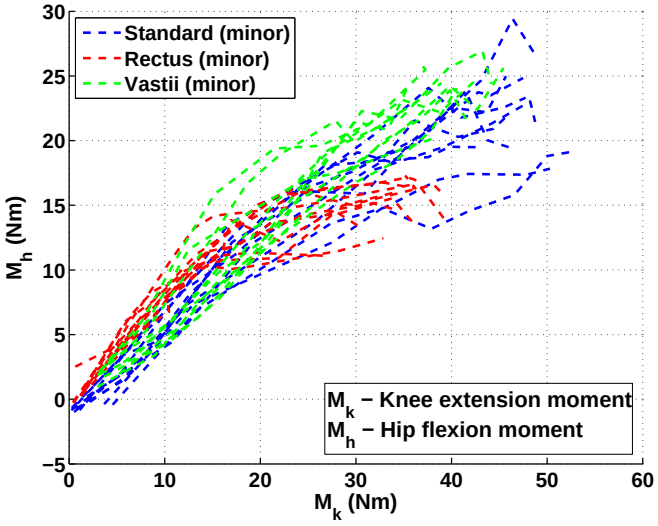

(a) Subject A.

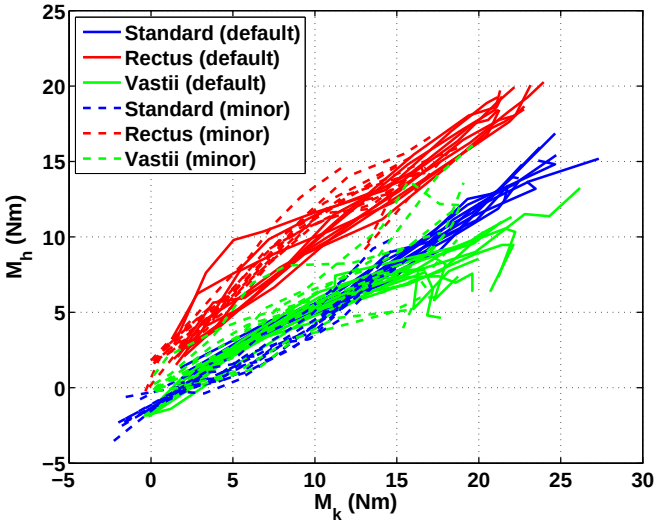

(b) Subject C.

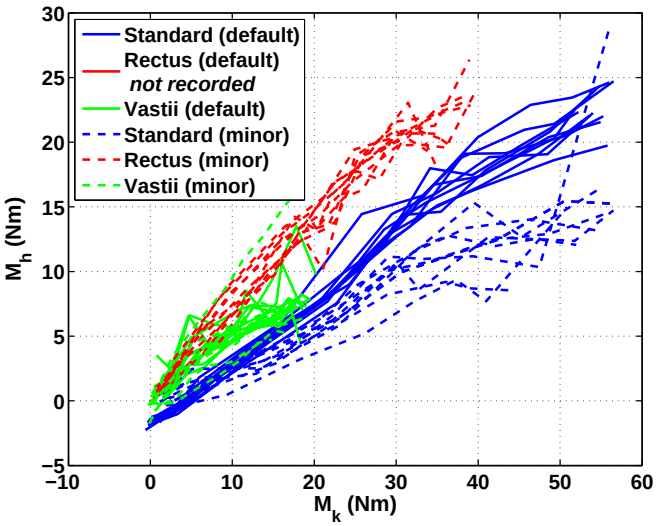

(c) Subject D.

Figure 4.6: Moment curves measured during all sessions.

present in the moment curves, similar to that discussed in Section 3.5.2. The possibility of such a rotational error being present made it impractical to compare the means between the sessions (for a particular *major* position), as is done during a T-test.

Further motivation for not using the T-test was found upon inspection of figure 4.6(b). In the figure we saw that although the *minor* and *default* traces for the *Rectus* sessions did overlap, the magnitude of the moments measured in the *minor* session were less than those seen in the *default* session, even though the stimulation intensity settings were identical in both sessions. The reason for the difference could have been due to different fatigue experienced by subject C during the two sessions. In a T-test these results would show a large difference between the mean moments at individual stimulation bursts, even though the trend seen in the figure by the overlapping traces was the same.

It was therefore decided to compare the standard deviation, of the *minor* and *default* session results, to determine the influence of the *minor* movements on the moment curves. To this end the standard deviations seen in the moments measured during the *minor* and *default* sessions (σ_{min} and σ_{def} respectively), were calculated for subjects C and D, as shown in table 4.6.

The standard deviations were calculated from the 10 test traces shown in figure 4.6, at each burst of stimulation, for $\mathbf{M}_k$ and $\mathbf{M}_h$ separately. This resulted in the table of standard deviations shown. Nine standard deviation values for each *major* position for both the *minor* and *default* sessions.

An F-test was used to determine if the difference between σ_{min} and σ_{def} was significant or not. P-values of 0.05 or less indicated that the difference was indeed significant, and have been highlighted in the table. Most of the p-values in the table are not highlighted, which implies that the standard deviations are generally not significantly different. Of the p-values in the table, 63 of 90 p-values are not highlighted. This means that 70% of the measured values show that there is no statistical difference between the *minor* and *default* session results. It was therefore concluded that the *minor* positions have little effect on the results obtained from the *major* positions.

Results: Major electrode positions

The mean moments, shown in figure 4.7, were found for each of the three subjects (A, C, D) by calculating the mean of the 10 traces captured in each session.

In Chapter 3 moment curves were presented that were captured with subjects A and B (refer to figure 3.13). Each subject participated in a single session in which all three *major* positions were tested using the *default* electrode positions. The results from these sessions were included in the current analysis of the *major* positions, so that all of the results captured to date could be considered. Table 4.7 shows the number of tests performed for each *major* position; the first test was discarded, the mean moments calculated, and the resultant mean moment curves included in figure 4.7.

Table 4.6: F-test results for standard deviation of *default* and *minor* sessions, for subject C and D. Standard deviations, σ_{min} and σ_{def}, calculated from 10 tests, for each stimulation burst. Highlighted p-values indicate a significant difference.

Stimulation burst		**1**	**2**	**3**	**4**	**5**	**6**	**7**	**8**	**9**
Subject C - $\mathbf{M_k}$										
Standard	σ_{min}	1.12	0.74	0.73	0.75	0.84	0.96	1.36	1.30	1.05
	σ_{def}	0.46	0.41	0.55	0.53	0.36	0.64	0.77	1.26	1.65
	p-value	0.01	0.09	0.40	0.32	0.02	0.24	0.11	0.91	0.19
Rectus	σ_{min}	0.47	0.92	0.55	0.89	0.87	1.52	1.83	2.22	1.94
	σ_{def}	0.34	0.68	0.80	1.37	2.05	1.73	1.17	0.82	1.00
	p-value	0.37	0.38	0.28	0.22	0.02	0.70	0.20	0.01	0.06
Vastii	σ_{min}	0.09	0.73	0.93	0.67	1.28	1.50	0.82	0.74	1.28
	σ_{def}	0.17	0.61	0.95	1.12	1.56	1.62	2.18	2.34	2.29
	p-value	0.06	0.59	0.95	0.14	0.56	0.82	0.01	<0.01	0.10
Subject C - $\mathbf{M_h}$										
Standard	σ_{min}	1.11	0.55	0.75	0.82	0.76	0.71	1.21	1.22	1.05
	σ_{def}	0.22	0.25	0.21	0.52	0.54	0.56	0.62	0.66	1.30
	p-value	<0.01	0.03	<0.01	0.19	0.32	0.49	0.06	0.08	0.55
Rectus	σ_{min}	0.98	0.84	0.67	1.14	0.83	0.80	0.70	1.76	0.92
	σ_{def}	0.51	1.32	1.33	1.18	1.10	1.32	0.91	0.77	0.72
	p-value	0.07	0.19	0.05	0.92	0.41	0.16	0.44	0.02	0.48
Vastii	σ_{min}	0.30	0.69	1.20	1.74	1.49	1.78	2.69	2.78	3.88
	σ_{def}	0.13	0.80	0.72	0.75	0.72	0.85	1.91	2.13	2.72
	p-value	0.02	0.64	0.14	0.02	0.04	0.04	0.32	0.44	0.31
Subject D - $\mathbf{M_k}$										
Standard	σ_{min}	0.83	1.00	2.35	2.76	2.70	2.09	2.12	4.03	3.76
	σ_{def}	0.87	1.00	2.83	1.59	1.64	2.13	2.66	1.69	1.55
	p-value	0.88	1.00	0.59	0.11	0.15	0.95	0.51	0.02	0.01
Rectus	σ_{min}	0.73	1.38	2.20	1.35	1.05	1.17	2.33	2.67	2.77
Vastii	σ_{min}	0.16	0.30	0.38	0.49	1.05	0.94	0.99	0.98	1.42
	σ_{def}	0.10	0.21	0.17	0.51	0.42	0.55	0.40	0.96	0.92
	p-value	0.15	0.30	0.02	0.92	0.01	0.13	0.01	0.95	0.21
Subject D - $\mathbf{M_h}$										
Standard	σ_{min}	0.68	1.03	0.91	1.46	2.45	2.35	2.39	3.55	5.67
	σ_{def}	0.31	0.91	1.67	2.08	1.22	2.05	2.09	1.40	1.55
	p-value	0.03	0.72	0.08	0.31	0.05	0.69	0.69	0.01	<0.01
Rectus	σ_{min}	0.85	0.97	0.66	0.68	1.99	1.32	1.61	1.73	2.64
Vastii	σ_{min}	0.66	0.57	1.03	1.47	1.87	2.25	2.38	2.91	3.28
	σ_{def}	1.11	0.84	1.60	1.09	0.76	1.07	1.05	2.39	1.33
	p-value	0.14	0.27	0.20	0.39	0.01	0.04	0.02	0.57	0.01

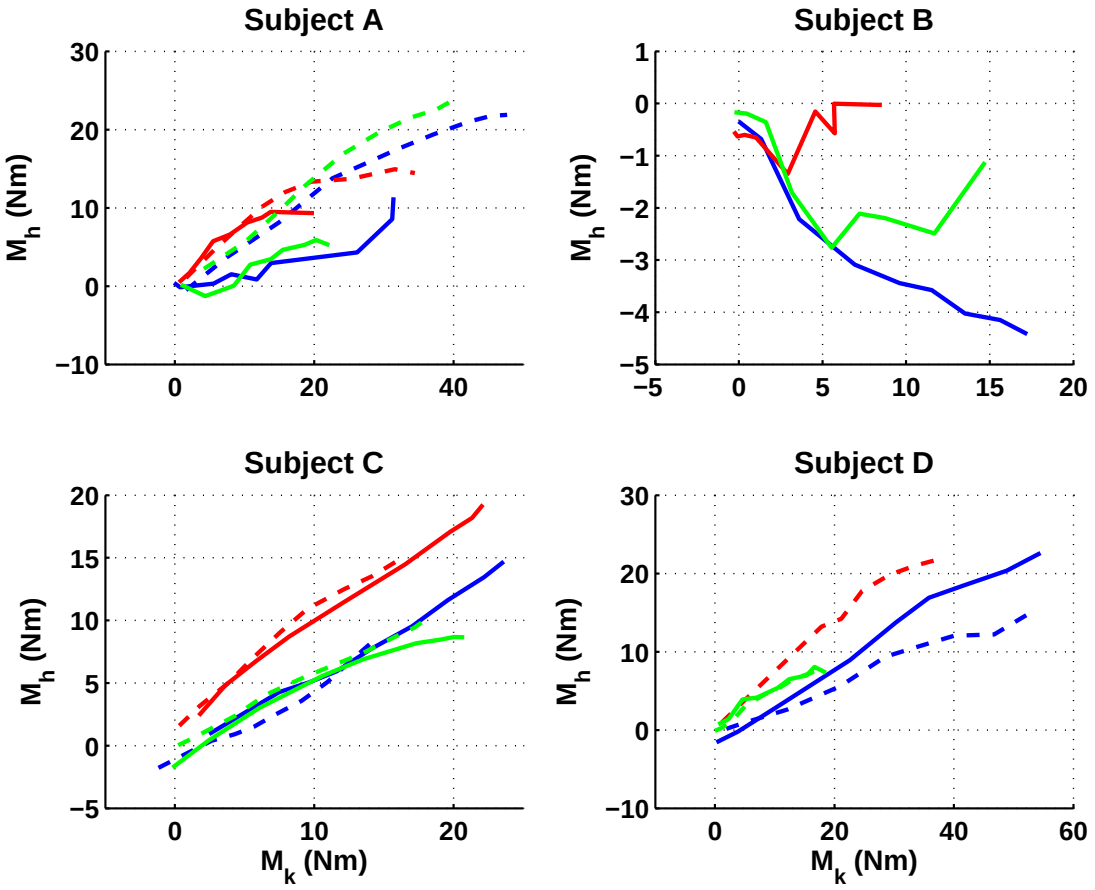

Figure 4.7: Mean moment curves for subjects A, B, C and D, for all three *major* electrode positions (blue - *Standard*, red - *Rectus*, green - *Vastii*), *default* positions only (solid lines) and with *minor* movements (dashed lines).

Table 4.7: Number of tests carried out with subjects A and B during *default* sessions.

Subject	***default* session**		
	Standard	***Rectus***	***Vastii***
A	4	4	6
B[a]	4	4	5

[a] Profile: female, 27 years (age), 1.76m (height), 62kg (weight).

Discussion: Major electrode positions

All four subjects show the same trend in that the moment curve for the *Rectus* electrode position normally lies above that of both the *Standard* and *Vastii* electrode positions. This agrees with the expected results shown in figure 4.3. However, contrary to expectations, the *Vastii* moment curve is seen to either overlap the *Standard* (subjects A and C), or lie above it (subjects B and D), instead of beneath it.

An exception shown to these trends was in the *minor* electrode position sessions of subject A, where the results for all three *major* positions were seen to overlap (dashed lines in figure 4.7). This is possibly due to current spread, as subject A used a stimulation current of

70mA for these sessions, as opposed to 50mA used for the *default* session (solid lines), where once again the *Rectus* curve lay above the overlapping *Standard* and *Vastii* curves.

A T-test was performed on the results from each of the four subjects. The null hypothesis was such that the mean moments measured in the *Rectus* and *Vastii* sessions were the same as those measured in the *Standard* session. The calculated p-values are shown in table 4.8, where p-values less than 0.05 (i.e. where the measured moments are significantly different) have been highlighted. The percentage of significant differences found is shown in table 4.9, where the results for the *minor* and *default* sessions were grouped together. In general the differences between the mean moments were significantly different, although the significant difference between the *Standard* and *Rectus* moments occurred with a higher percentage than between the *Standard* and *Vastii* moments. This agrees with the fact that the *Standard* and *Vastii* moments did tend to overlap at times.

The *Rectus major* position was merely used as a control, to show that stimulating Rectus femoris did indeed, generate larger hip flexion moments. However, the hoped for result, in which the *Vastii major* position produced knee extension moments with less hip flexion than the *Standard major* position, was not seen.

One possible explanation for these results was the fact that measurement error inherent in the Bi-moment chair could cause a rotation in the moment curves (Section 3.5.2), which would influence the conclusions drawn by comparing measurements taken during different sessions. By being able to measure all three *major* positions in a single session, this problem would be avoided. However, with the *minor* positions as part of the study, it was not possible to to do this, as the fatigue experienced by the subjects would be too great.

The analysis of the *minor* position results, discussed earlier, showed that they had little influence on the moment curves. This meant that the *minor* curves could be eliminated from subsequent measurements, thereby making it possible to test all three *major* positions in a single session, without excessive fatigue, as the total number of tests would be reduced. This was the approach used during the study discussed in Chapter 8.

Even though the possible presence of this measurement error cast doubt on the conclusion that could be drawn from the results, it was not likely that the error was always present during all of the sessions in which the subjects took part. The fact that similar trends for the three *major* positions were seen in the results for all four subjects, especially the *default* sessions of subjects A and B where all three *major* positions were tested in a single session, implied that even if the error did influence the measurement of the absolute magnitudes of the moments, there was most likely another reason for the negative results.

A possible explanation involved the anatomy of the leg, namely the positions of the motor axons in the thigh, and the placement of the stimulating electrodes. Were the superficial muscles of the Quadriceps group being selectively stimulated as we intended them to be? To answer this question it was necessary to measure the EMG response of the three superficial muscles during stimulation.

Table 4.8: T-test results investigating the difference between mean moments measured with the *major* positions for all four subjects. P-values were calculated for each stimulation burst. Highlighted p-values indicate a significant difference.

Stimulation burst			**1**	**2**	**3**	**4**	**5**	**6**	**7**	**8**	**9**
						***minor* session**					
						$\mathbf{M_k}$					
Standard	*- Rectus*	Subject A	0.96	0.03	0.01	<0.01	<0.01	<0.01	<0.01	<0.01	<0.01
		Subject B	-	-	-	-	-	-	-	-	-
		Subject C	<0.01	<0.01	0.02	0.58	0.10	0.31	0.01	0.01	<0.01
		Subject D	<0.01	0.17	0.57	0.02	<0.01	<0.01	<0.01	<0.01	<0.01
Standard	*- Vastii*	Subject A	<0.01	<0.01	0.89	<0.01	<0.01	<0.01	<0.01	<0.01	<0.01
		Subject B	-	-	-	-	-	-	-	-	-
		Subject C	<0.01	<0.01	0.99	0.05	<0.01	<0.01	<0.01	<0.01	<0.01
		Subject D	<0.01	<0.01	<0.01	<0.01	<0.01	<0.01	<0.01	<0.01	<0.01
						$\mathbf{M_h}$					
Standard	*- Rectus*	Subject A	<0.01	0.12	0.44	<0.01	<0.01	<0.01	<0.01	<0.01	<0.01
		Subject B	-	-	-	-	-	-	-	-	-
		Subject C	<0.01	<0.01	<0.01	<0.01	<0.01	<0.01	<0.01	<0.01	<0.01
		Subject D	0.03	<0.01	<0.01	<0.01	<0.01	<0.01	<0.01	<0.01	0.01
Standard	*- Vastii*	Subject A	<0.01	0.01	0.19	0.37	0.63	0.83	0.75	0.62	0.18
		Subject B	-	-	-	-	-	-	-	-	-
		Subject C	<0.01	0.61	0.02	0.01	<0.01	<0.01	0.01	0.05	0.18
		Subject D	0.21	0.02	0.01	<0.01	<0.01	<0.01	<0.01	<0.01	<0.01
						***default* session**					
						$\mathbf{M_k}$					
Standard	*- Rectus*	Subject A	0.34	0.13	0.42	0.39	0.42	0.55	0.01	0.02	<0.01
		Subject B	0.04	0.01	<0.01	<0.01	<0.01	<0.01	<0.01	<0.01	0.01
		Subject C	<0.01	<0.01	<0.01	<0.01	0.01	0.37	0.70	0.02	<0.01
		Subject D	-	-	-	-	-	-	-	-	-
Standard	*- Vastii*	Subject A	0.41	0.08	0.27	0.41	0.59	0.71	0.10	0.10	<0.01
		Subject B	0.08	0.10	0.02	<0.01	0.13	0.02	0.02	0.08	0.19
		Subject C	<0.01	<0.01	<0.01	<0.01	0.24	0.56	0.43	0.01	<0.01
		Subject D	0.26	<0.01	<0.01	<0.01	<0.01	<0.01	<0.01	<0.01	<0.01
						$\mathbf{M_h}$					
Standard	*- Rectus*	Subject A	0.92	0.23	0.20	0.03	0.05	0.15	0.08	0.79	0.42
		Subject B	0.39	0.81	0.04	0.04	0.02	0.02	0.01	<0.01	<0.01
		Subject C	<0.01	0.24	<0.01	<0.01	<0.01	<0.01	<0.01	<0.01	<0.01
		Subject D	-	-	-	-	-	-	-	-	-
Standard	*- Vastii*	Subject A	0.52	0.12	0.83	0.18	0.12	0.43	0.35	0.25	0.05
		Subject B	0.07	0.40	0.25	0.19	0.54	<0.01	0.01	0.03	<0.01
		Subject C	<0.01	<0.01	<0.01	0.14	0.01	<0.01	<0.01	<0.01	<0.01
		Subject D	<0.01	<0.01	0.01	<0.01	<0.01	<0.01	<0.01	<0.01	<0.01

Table 4.9: Percentage of significant differences found.

	Standard - Rectus	***Standard - Vastii***
$\mathbf{M}_k$	74.1% (40/54)	69.8% (44/63)
$\mathbf{M}_h$	77.8% (42/54)	60.3% (38/63)

4.4 The way forward

If the stimulation was truly selective, the EMG response would show the presence of M-waves only in the targeted muscles. For example, measuring with the *Vastii* electrode positions, M-waves would only be recorded in Vastus lateralis and Vastus medialis, with no response seen in Rectus femoris. However, with surface stimulation, current spread can cause a contraction in the muscles adjacent to the targeted muscles. By measuring the M-waves it would then be possible to investigate the extent of current spread for the three *major* electrode positions, to see if this was the reason for the negative results.

To this end it would be necessary to place the recording electrodes between the stimulating electrodes, as shown in figure 4.8. Although in principle the recording of the M-waves appears to be simple, in practice there are known problems when using the setup shown in the figure.

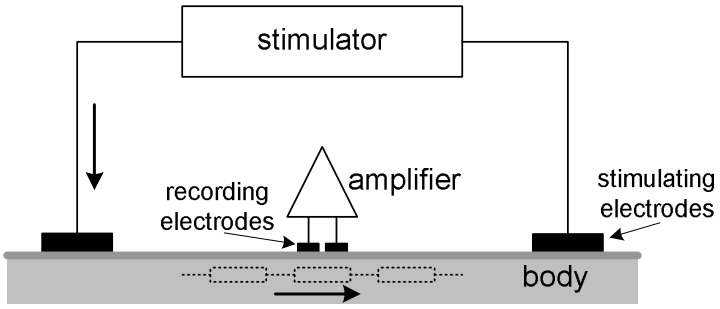

Figure 4.8: Placement of recording electrodes between stimulating electrodes.

The first problem that arises is that of amplifier saturation. During a stimulation pulse, current will flow between the stimulating electrodes, through the volume resistance of the tissue within the body. This volume resistance can be thought of as a potential divider, as shown. The input to the amplifier corresponds with the potential difference across the resistance below the recording electrodes. If the amplifier had infinite voltage range and infinite bandwidth, the output would always look like the input. However, in practice the amplifier only behaves linearly for a limited range of input and output voltages. The maximum and minimum values of the output voltage are determined by the supply rails between which the amplifier operates. If the input voltage is sufficiently large to drive the amplifier output outside of this range, the amplifier is said to be saturated [Sedra and Smith, 1998]. After removing the input overdrive it takes a finite amount of time for the output to return from saturation to linear operation.

For biopotential amplifiers, recovery times of around 5 to 10 milliseconds have been observed [McGill et al., 1982; Walker and Kimura, 1978]. This is not a problem if the latency of the M-wave is long enough so that the start of the M-wave occurs after the amplifier has recovered. However, the latency is dependent on the separation distance between the stimulating and recording electrodes [Basmajian and De Luca, 1985], the shorter the distance, the shorter the latency. For the situation shown in figure 4.8, Bruun and Haxthausen [1991] measured an M-wave with a latency of less than 5ms. In such a case, the M-wave would be distorted or possibly completely obscured by stimulation artefact due to amplifier saturation [Bruun and Haxthausen,

1991; Harding, 1991; Reichel et al., 2001; Walker and Kimura, 1978], unless steps are taken to prevent the amplifier from saturating in the first place.

Various hardware solutions have been proposed in the literature. Babb et al. [1978] and Thorsen [1999] prevented saturation by using fast-recovery amplifiers. In addition to this Babb et al. [1978] used a sample and hold circuit at the output to blank any residual stimulus artefact. Another approach was to use switching to control which signal was seen by the amplifier during the stimulation pulse. Sennels et al. [1997] included a switching circuit between the preamplifier and the gain stage of the amplifier. This prevented the gain stage from saturating, but this was not always the case for the preamplifier. However, Sennels et al. [1997] were only interested in measuring the volitional EMG occurring after the M-wave. Knaflitz and Merletti [1988] and Chesler and Durfee [1997] used similar amplifiers, but also included a slew rate limiting circuit at the input stage to prevent the preamplifier from saturating. Chesler and Durfee [1997] went one step further and also shorted the stimulating electrodes between stimulation pulses. A simpler switching scheme was presented by Minzly et al. [1993] in which the switching was performed at the amplifier input stage. An extension of this was developed by Muraoka [2002] in which the same pair of electrodes were used both for stimulating and recording. Switches were used to disconnect the stimulator from the electrodes immediately after a stimulation pulse. The electrodes were then discharged by shorting them to ground, before connecting the electrodes to the input of the amplifier. The method used in this thesis was that of Bruun and Haxthausen [1991], as not only did their method prevent the amplifier from saturating but their application was precisely the same as the one here, where the intention was to measure M-waves from recording electrodes placed between the stimulating electrodes.

Bruun and Haxthausen [1991] used a technique in which the amplifier was effectively shut down during the stimulation pulse, thereby preventing it from being saturated. A current conveyor configuration was used for the differential input stage which allowed the switching to occur on a low impedance node, a marked difference from the other switching schemes. This had the advantage that the low impedance node is significantly less susceptible to switching transients from the shutdown control. This method is further discussed in Chapter 6.

Solving the issue of amplifier saturation was only half the problem. Consideration also had to be given to the type of stimulator used, as well as the shape of the stimulation pulse.

There are two main types of stimulators, constant-current and constant-voltage. Constant-current stimulators are normally used for FES as the muscle activation response tends to be more repeatable and reliable when using this type of stimulator [Chesler and Durfee, 1997; Knaflitz and Merletti, 1988]. For this reason only the constant-current stimulator type will be discussed further.

The Stanmore stimulator, used in the Bi-moment chair study, is a constant-current monophasic stimulator. Figure 4.9 shows the current waveform for such a stimulator, and the voltage response of a typical electrode [Webster et al., 2009]. At the onset of the stimulation pulse, the voltage increases quickly, due to a voltage drop across the resistive components of

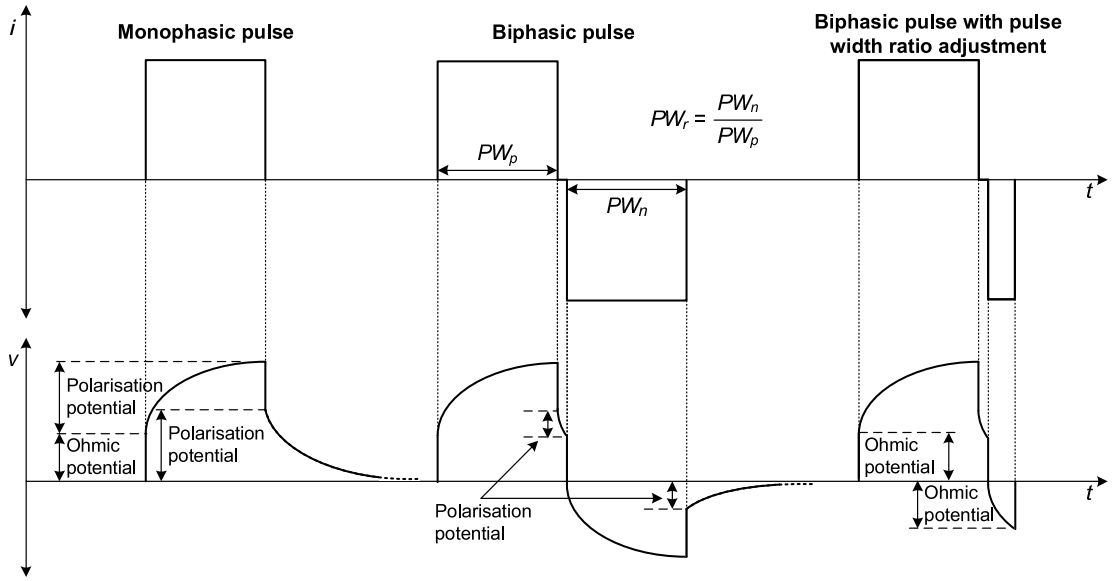

Figure 4.9: Typical voltage response of an electrode to a monophasic and biphasic current pulse. (Monophasic pulse reproduced from Webster et al. [2009], with permission.)

the electrode-skin interface (labelled as the *ohmic potential*). After this initial increase in potential, the voltage continues to increase as long as the current is held constant, (labelled as the *polarisation potential*). This is due to polarisation that occurs at the capacitive electrode-skin interface. At the end of the stimulation pulse, the voltage decreases by an amount equal to the ohmic potential, after which the voltage can be seen to be non-zero. This non-zero voltage is attributed to residual charge that still remains on the electrodes due to the polarisation of the electrode-skin interface.

This voltage will gradually decay towards zero as the interface capacitance discharges. If the stimulator presents an infinite output impedance between stimulation pulses, the discharge current would be confined to the electrode-skin interface. However, if the electrical topology of the stimulator be such that a current path is present around which the discharge current can flow then a potential difference would occur across the recording electrodes. Although the potential difference setup by the discharge current is not normally sufficient to saturate the amplifier, it can result in a stimulation artefact at the amplifier output that may obscure the M-wave measurement.

Spencer [1981], Nilsson et al. [1988] and Reichel et al. [2001] all discussed the use of a biphasic stimulation pulse as a means to reduce the residual polarisation charge. Figure 4.9 also shows the voltage response of an electrode to a biphasic constant-current pulse. The polarisation potential present at the end of the stimulation pulse is considerably smaller than in the monophasic case. The amount of residual charge can be even further reduced by changing the pulse width of the negative phase [Reichel et al., 2001]. This principle is referred to as pulse width ratio adjustment, where the pulse width ratio, PW_r, describes the ratio between the pulse width of the positive phase PW_p and the pulse width of the negative phase, PW_n.

To be able to measure the M-waves during stimulation in the Bi-moment chair it was therefore necessary to use a biphasic stimulator with pulse width ratio adjustment capability in combination with an EMG amplifier that avoids saturation by using a switching scheme at the input stage. The focus of Chapters 5 and 6 cover the design and construction of such a stimulator and amplifier.

Chapter 7 investigates how the entire system works as a whole, looking at the various causes of stimulation artefact and ways to remove it. Finally, Chapter 8 presents a second study, in which joint moments and EMG measurements were simultaneously recorded.

4.5 Summary

Through careful placement of surface electrodes, it was hoped to selectively stimulate the superficial muscles of the Quadriceps group, so that a knee extension moment could be produced with as little hip flexion moment as possible. Three different electrode positions were investigated, referred to as the *major* positions:

1. *Standard*, previously used in FES cycling to simultaneously stimulate RF, VM and VL.
2. *Rectus*, intended to selectively stimulate RF.
3. *Vastii*, intended to selectively stimulate VM and VL.

Three subjects participated in a study in which the Bi-moment chair was used to measure hip and knee joint moments produced in response to stimulation using the three different *major* positions. In addition to this, the influence on the joint moments of *minor* movements in the stimulating electrode positions, like those typically seen in practice, were investigated. This involved introducing small changes in the placement of the electrodes for the *major* positions (1cm laterally, medially, proximally or distally). The stimulation protocol consisted of nine bursts of stimulation, consecutively increasing in intensity.

The various outcomes of the study were as follows:

1. Fatigue experienced by the subjects was assessed using MVC, FF ratio and force comparison tests, however no substantial fatigue was seen.
2. An F-test revealed that the *minor* positions had no significant influence on the joint moments. Consequently these movements were eliminated from future studies (as in Chapter 8).
3. The joint moments produced by the three *major* positions, and measured with the Bi-moment chair, were used to generate moment curves ($\mathbf{M}_h$ plotted against $\mathbf{M}_k$). The two main observations made from the moment curves, were:
   (a) The *Rectus* moment curve *lay above* those of the *Standard* and *Vastii* positions, as *Rectus* produced the largest hip flexion moment. This agreed with expectations.

(b) The *Standard* and *Vastii* moment curves overlapped. This meant that the *Vastii* did not produce a reduction in hip flexion, as compared against that produced with the *Standard* position. This was contrary to expectations.

There was no obvious explanation for the negative results seen with the *Standard* and *Vastii* moment curves. It was hypothesised that the *major* positions did not selectively stimulate the superficial Quadriceps muscles, as intended. This hypothesis was to be investigated by measuring the EMG in these muscles during stimulation. However, such measurements are difficult to capture due to amplifier saturation and residual charge at the electrode-skin interface giving rise to stimulation artefact. To help overcome these problems two items of equipment were required:

1. A biphasic stimulator with pulse width ratio adjustment capability.
2. An EMG amplifier that employs a switching scheme at the input stage.

Part III

Capturing evoked EMG measurements

Chapter 5

Constant current biphasic stimulator with pulse width ratio adjustment

5.1 Introduction

As discussed at the end of the previous chapter, the Stanmore stimulator is a constant-current monophasic stimulator [Phillips et al., 2003]. In order to measure the M-waves of interest, a constant-current biphasic stimulator, with pulse width ratio adjustment capability, was needed. Stimulator design and construction is a well known field and a number of topologies exist that would realise such a stimulator. As the circuit schematics of the Stanmore stimulator were readily available, it was decided to use this as the starting point for the design of the new Biphasic stimulator. The two main modification that were made, were:

1. The output stage was modified to produce a biphasic output pulse.

2. The microcontroller based operating system used to control the stimulator was rewritten to allow for pulse width ratio adjustment.

5.2 Circuit Design

The Stanmore stimulator comprised of two PCB's, namely the Output board, which consisted of the electronics to produce the monophasic output pulse, and the Control board, which used a microcontroller (μC) to generate the signals that were used to drive the output board. Figure 5.1 shows the correlation between the Stanmore stimulator and the Biphasic stimulator.

The Output board of the Biphasic stimulator was realised by modifying that of the Stanmore stimulator.

The Control board was completely replaced with a new microcontroller based design. For construction purposes the Control board was broken into four separate boards: the Power Supply board, the μC Header board, the Interconnect board and the Current Amplitude Display (CAD) board. The electrical connections between these boards, shown in the figure, are discussed in greater detail in the following sections. An LCD and push buttons were also incorporated as part of the user interface.

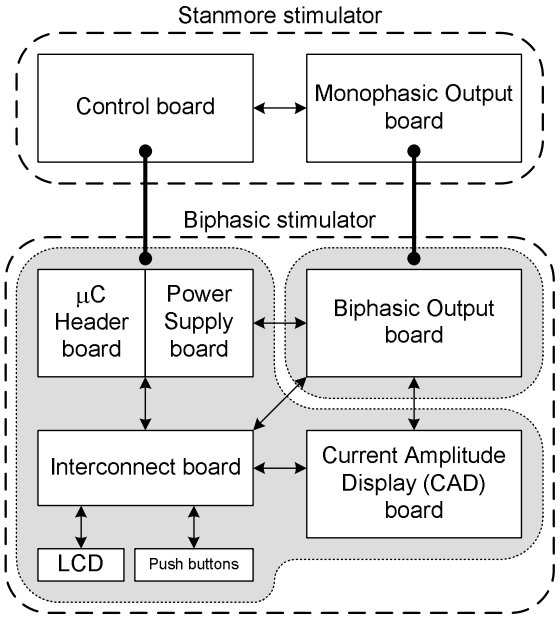

Figure 5.1: Correlation between the Stanmore stimulator and the Biphasic stimulator.

The design specifications that the Biphasic stimulator had to meet were as follows:

1. Constant-current stimulator.
2. Battery powered (for electrical safety).
3. Isolation of output signals from mains earth (for electrical safety).
4. Biphasic output pulse.
5. Two output channels (maximum required for the *Vastii* electrode position).
6. Variable current amplitude (0mA to 120mA), set using potentiometers.
7. Variable stimulation period (20ms to 5s, the slower periods in excess of 1s were used to investigate M-wave responses to individual stimulation pulses).
8. Variable pulse width (20μs to 400μs, so that constant stimulation tests could be carried out over a range of pulse widths up to the maximum pulse width of 400μs used in the recruitment curve stimulation protocol, refer to Section 4.2.2).
9. Adjustable pulse width ratio.
10. Generation of blanking interval trigger (BIT) signals (ensures that the blanking interval of the Blanking amplifier is timed to the stimulation pulse).
11. Continuous stimulation protocol.
12. Recruitment curve stimulation protocol (refer to Section 4.2.2).

Specifications 1 to 3 were inherent in the electronic design of the Stanmore stimulator and consequently carried across to the Biphasic stimulator. Points 4 to 6 required modifying the electronics of the Stanmore stimulator, while points 7 through 12 were realised in the micro-controller based software.

5.2.1 Biphasic Output board

Figure 5.2 shows the schematic of the final Biphasic Output board. The schematic of the Monophasic Output board, upon which it was based, has been included in Appendix C, Section C.1, for reference.

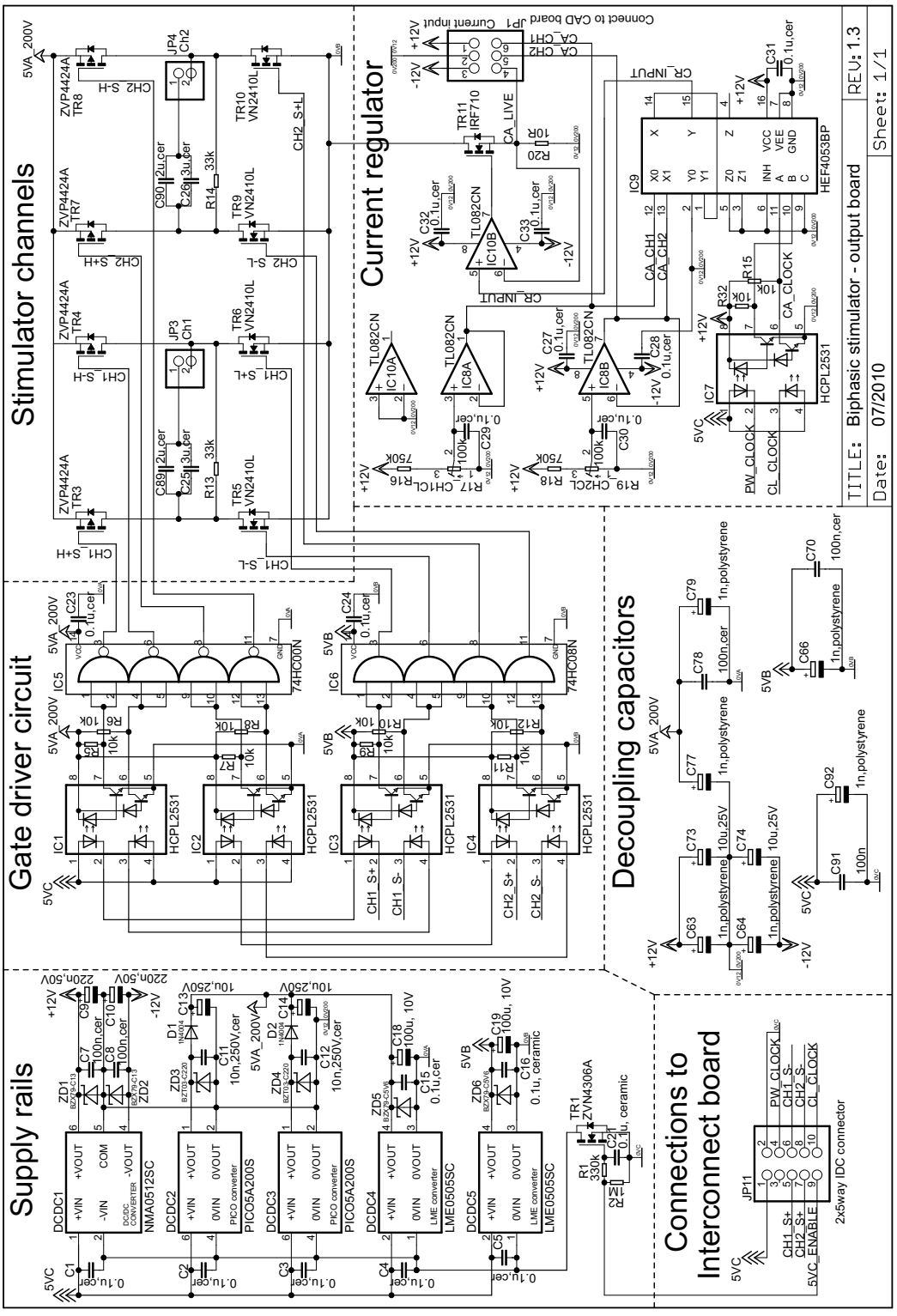

Figure 5.2: Circuit schematic for the Biphasic Output board.

Supply rails

As in the case of the Stanmore stimulator, the Biphasic stimulator has five different supply rails, labelled 5VA, 5VB, 5VC, $\pm$12V and 200V. 5VC was taken from the Power Supply board (discussed later) and used as the input voltage for the DC-DC converters. Two LME0505SC converters were used to produce 5VA and 5VB, an NMA0512SC converter produced the $\pm$12V rail and two PICO5A200S converters, connected in parallel, were used for the 200V rail.

The three converters were selected due to their DC isolation between the input and output voltages. This was a necessity as the supply rails had to be connected as depicted in figure 5.3 to facilitate the functioning of the stimulator. The 200V rail served as the high voltage rail of the output channels. 5VA was used to generate the gate signals for the high-side MOSFETs and 5VB was used to drive the low-side MOSFETs. When no stimulation is present the potential of 5VB is floating relative to the 200V rail, however, during stimulation the potential is determined according to the amplitude of the stimulation current. The $\pm$12V rail was used to drive the current regulator. The isolation characteristic of the converters also served as a safety feature, in which the output of the stimulator (to be connected to a subject), was isolated from mains earth, the batteries powering the stimulator, and the electronics used to control the stimulator.

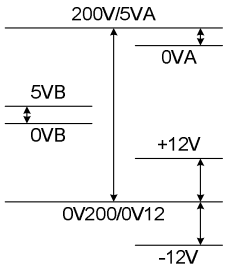

Figure 5.3: Interconnection of supply rails.

Table 5.1 lists the characteristics of each of the converters. A disadvantage of using this stimulator topology was the low efficiency of the converters. The converters also do not have a regulated output, hence the need for the zener diodes at the output stages as well as ensuring that the input voltage, 5VC, was regulated.

Table 5.1: DC-DC converter characteristics.

DC-DC converter	Supply rail	Power rating (W)	Efficiency (%)	DC isolation (V)
LME0505SC	5VA/B	0.25	70	1000
NMA0512SC	$\pm$12V	1	77	1000
PICO5A200S	200V	1.25	75	500

The PICO5A200S converters were expected to deliver the entire stimulation current. The expected voltage drop, at maximum load (PW = 400μs per phase, I_{stim} = 120mA and T = 20ms), with the 10μF output capacitors (C13 and C14 in the circuit schematic) was calculated as 9.6V (refer to equation 5.1), which is only a 4.8% drop in the 200V rail.

$$\Delta V = \frac{I_{stim}\Delta t}{C} = \frac{120\text{mA} \cdot 2 \cdot 400\mu\text{s}}{10\mu\text{F}} = 9.6\text{V} \tag{5.1}$$

The average power consumption for the maximum load was found to be 0.96W, which is within the power rating of the converter.

$$P_{avg} = \frac{2 \cdot PW \cdot V_o \cdot I_{stim}}{T} = \frac{2 \cdot 400\mu\text{s} \cdot 200\text{V} \cdot 120\text{mA}}{20\text{ms}} = 0.96\text{W} \tag{5.2}$$

However, when both stimulation channels operate together, the average power consumption is doubled. This corresponded with a measured voltage drop to around 160V, in the 200V rail. To compensate for this, a second 200V converter was introduced into the circuit and connected in parallel.

Stimulator channels

The Stanmore stimulator has 8 output channels. Each channel consists of a half bridge, used to generate the monophasic pulse, and an active charge balancing circuit. This was changed to two channels, each consisting of a full bridge, so as to generate a biphasic pulse, with passive charge balancing.

Figure 5.4 shows the full bridge circuit used for each channel. A timing diagram showing the gate signals for both the high and the low side switches is also included. By using this switching scheme, a constant-current biphasic pulse, I_{stim}, is realised which flows from the "anode-first" electrode (labelled as *anode* in the figure) to the "cathode-first" electrode (labelled as *cathode*) during the positive phase of the pulse. The current direction is reversed between the two electrodes during the negative phase.

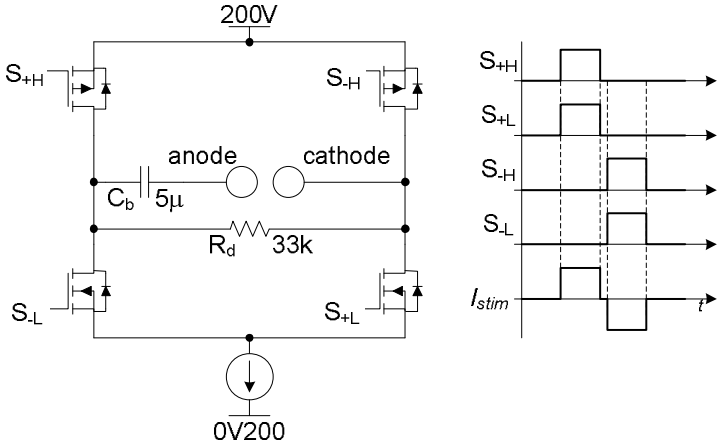

Figure 5.4: Full bridge output stage with gate signals.

The charge balancing is achieved with the blocking capacitor C_b and the discharge resistance, R_d. C_b performs a safety function whereby it prevents large DC currents from flowing if the stimulator were to fail short circuit. It also prevents DC from normally passing through the electrodes, which in turn prevents electrolysis occurring at the electrodes, with consequent pH changes. However, this function may not be of great importance as the electrodes are presumably at the surface of the stainless steel wire in the hydrogel, and not in direct contact with the

skin. It was necessary to include R_d as a passive discharge path for any residual charge on C_b after a stimulation pulse.

The blocking capacitor would also help to prevent the stimulation pulse from dropping below 200V, during stimulation. In the most unbalanced case, the biphasic pulse would appear as a monophasic pulse, with the maximum pulse width of 400μs and the maximum current amplitude of 120mA. The capacitance value needed to only allow a 5% drop in the 200V rail was calculated as:

$$C_b = \frac{\Delta t}{\Delta V} I_{stim} = \frac{400\mu\text{s}}{0.05 \cdot 200\text{V}} 120\text{mA} = 4.8\mu\text{F} \tag{5.3}$$

It was decided to use ceramic capacitors for C_b as relatively small surface mount capacitors are available that have voltage ratings well above 200V. Other types of capacitors with similar voltage ratings are generally large and bulky. However, as the surface mount capacitors used were only 1μF in value, five of these capacitors were stacked in parallel, realising a total C_b value of 5μF as shown in figure 5.4.

The average resistance between the anode and cathode, R_{ac}, due to the presence of the stimulating electrodes and biological tissue, was measured by Perkins [2004] as 1.5kΩ for a surface electrode with a 5cm diameter, similar to those used in this thesis. This would result in a time constant, during the stimulation pulse, of $\tau_{on} = R_{ac}C_b = 7.5$ms, which is in excess of ten times greater than the maximum pulse width (400μs per phase). This should prevent any significant decay in current amplitude during stimulation.

To ensure that most of the stimulation current flows through R_{ac} and not R_d, we require that $R_d \gg R_{ac}$. The value of R_d was chosen to be 33kΩ. This resulted in a time constant of $\tau_{off} = R_d C_b = 165$ms between stimulation pulses, which is greater than the stimulation period (30ms as used in the recruitment curve protocol), and therefore should not affect the actual stimulation pulse.

By controlling the length of the gate signals for the high and low side switches, the pulse width ratio adjustment capability of the stimulator was realised. As discussed at the end of Chapter 4, the pulse width ratio, PW_r, of the biphasic pulse is defined as the ratio between the pulse widths of the positive and negative phases, refer to figure 5.5 and equation 5.4. The pulse width of the positive phase was always equal to the pulse width setting, PW, defined by the user, while the pulse width of the negative phase was then calculated using the PW_r setting. In this thesis, whenever referring to a biphasic pulse PW is used interchangeably with PW_p.

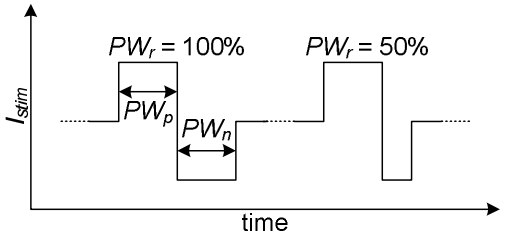

$$PW_r = \frac{PW_n}{PW_p} \tag{5.4}$$

Figure 5.5: Pulse width ratio adjustment principle.

Gate driver circuit

The gate drive signals are generated using the microcontroller. A series of optocouplers, HCPL2531, are used to transfer the signal from the microcontroller (5VC voltage rail) to both the high side switches (5VA voltage rail) and the low side switches (5VB voltage rail). As the high side switches are P-channel FETs, the gate signal is inverted using a quad 2-input NAND gate, 74HC00N. The low side switches are buffered using a quad 2-input AND gate, 74HC08N, so as to keep the timing of the switching pairs as identical as possible. For this same reason, the gate signal for a high and low side switching pair are taken from a single output port of the microcontroller, as opposed to using two ports to do the required signal inversion.

Current regulator

A single current regulator was used to set the current amplitude during the stimulation pulse for both output channels even though the respective amplitudes for each channel could be different. This was achieved by using an analog multiplexer, HEF4053BP, to switch between the amplitude settings of each channel depending on which channel was active. For this purpose another two control signals, CA_CLOCK and PW_CLOCK, were generated by the microcontroller and connected to the output board via an optocoupler. Figure 5.6 shows the timing diagram for the various signals, compared with the gate drive signals of both channels ($S_{+H/L}$ and $S_{-H/L}$).

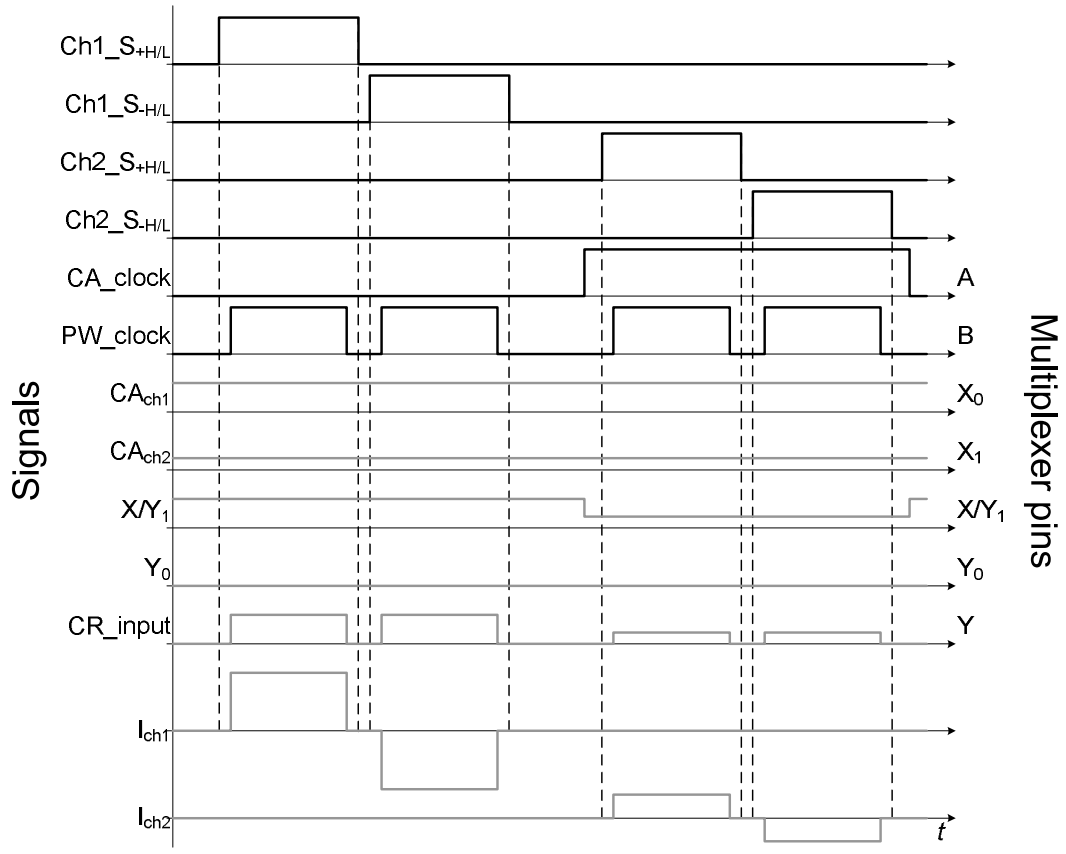

Figure 5.6: Timing diagrams for current regulator, black traces represent digital signals, while grey traces are analog.

The current amplitude for each channel, CA_{ch1} and CA_{ch2}, is set by means of potentiometers (circuit schematic, figure 5.2, R17 and R19) and op-amp voltage buffers (circuit schematic IC8). The op-amps are operated between $\pm$12V to ensure an output voltage swing around 0V, thereby allowing a minimum current setting of 0mA.

The voltage levels defined by the potentiometers are then used as inputs to the multiplexer, on pins X_0 and X_1. CA_CLOCK, which is high when channel 2 is active and low the rest of the time, is used as a control signal for the multiplexer (pin A). This produces an analog signal (pin X) that has two distinct levels determined by the current amplitude settings of each channel. This signal is fed back into the multiplexer (pin Y_1) and along with signal ground input at pin Y_0 and PW_CLOCK control signal at pin B, produces the current regulator input voltage, CR_INPUT (pin Y). When comparing CR_INPUT with the gate drive signals, we can see that the MOSFETs of the full bridges are soft switched, i.e. the gates are turned on or off only when the current flowing through the MOSFETs is 0A. The soft switching delay was 3μs long and was necessary to help reduce ringing on the output voltage measured across a 1kΩ load resistor (discussed in Section 5.5.1).

The final constant current, biphasic output pulses, I_{ch1} and I_{ch2}, have pulse widths, corresponding to the pulse width of the PW_CLOCK signal, and amplitudes determined by CA_{ch1} and CA_{ch2}.

Decoupling capacitors

Eleven capacitors of varying size and type (namely, polystyrene, ceramic and electrolytic), were placed across the board to provide damping for ringing over a range of frequencies.

Connections to Interconnect board

The control signals were carried to the Interconnect board by means of an IDC connector. The supply rail (5VC) was brought across directly from the Power Supply board using cable suitable to carry the maximum supply current required if all *five* DC-DC converters (2$\times$LME0505SC, 1$\times$NMA0512SC, 2$\times$PICO5A200S), were operating at full load. The maximum supply current, I_{max}, was calculated using the values for power, P_{rated}, and efficiency, η, given in table 5.1 for an input voltage, V_i, of 5V.

$$I_{max} = \sum_{\text{DC-DC converter}} \frac{P_{rated}}{\eta V_i} = 1.1\text{A} \tag{5.5}$$

PCB layout

The PCB, as shown in figure 5.7(a), for the Biphasic Output board was designed using *Cadsoft* EAGLE. It was decided to use a four-layer PCB, so that ground planes and power planes could be used for each of the supply rails. This ensured that the supply rails had low resistance and could carry the higher currents with a low ripple in the supply voltage. Figure 5.7(b) and 5.7(c) show the inner two PCB layers, route 2 and route 15, on which the power planes and ground planes, respectively, were placed. The +12V and 200V supply rails shared a ground plane, while 200V and 5VA shared a power plane. This corresponds with the way in which the supply

rails were interconnected, refer to figure 5.3.

Isolation barriers, in the form of 2mm gaps, were placed between the planes on the copper layers. All the components that served an isolating function (DC-DC converters and optocouplers) were positioned across the barrier. All other tracks, other than essential connections between components connected to different supply rails, were kept away from the barriers.

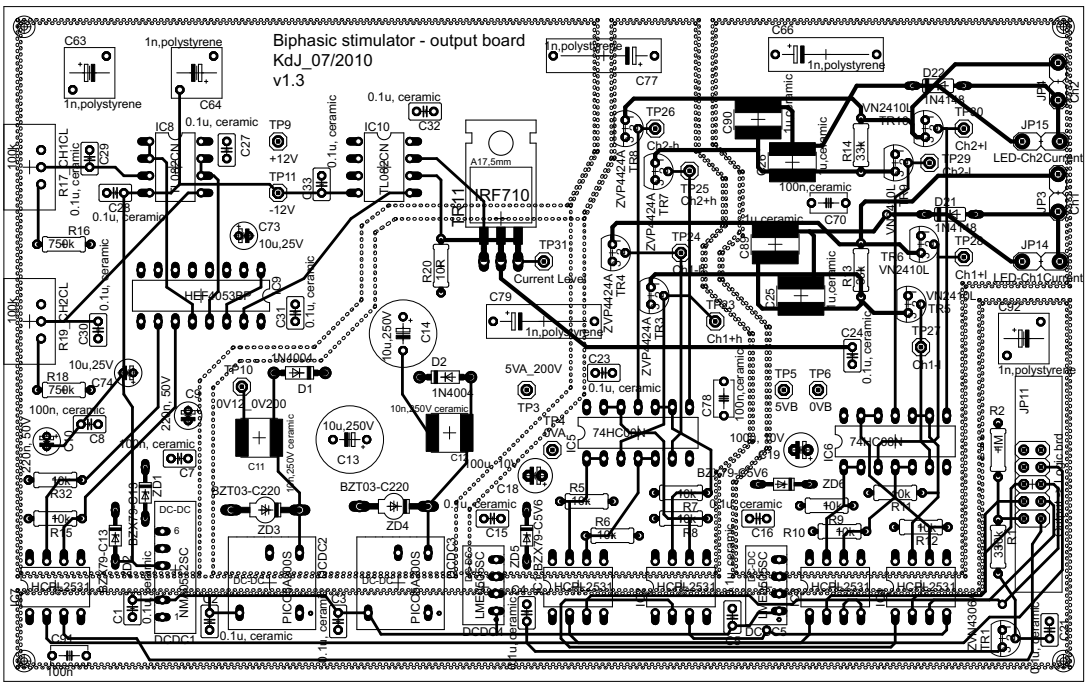

(a) Four-layer PCB.

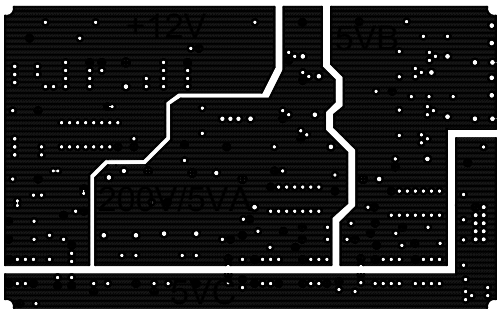

(b) Route 2 - power planes.

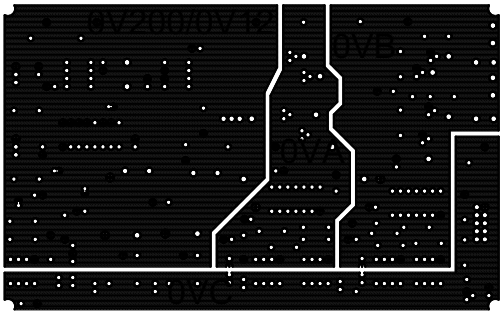

(c) Route 15 - ground planes.

Figure 5.7: PCB layout for the Biphasic Output board.

5.2.2 μC Header board

The microcontroller used in the Stanmore stimulator was a *Motorola* MC68HC11G5FN1. As this stimulator was originally designed and built during the 90's the *Motorola* chip was considered to be very outdated. Newer microcontrollers currently available are vastly superior. Consequently a new control circuit based around a different microcontroller was designed from scratch.

The specifications used to help select the new microcontroller were as follows:

1. Six digital output pins to produce the digital signals shown in figure 5.6.
2. Two digital output pins for the BIT signals used to trigger the blanking intervals in the EMG amplifier, one for each channel.
3. Digital output pins needed to control the LCD (12 for the LCD used).
4. Two digital output pins to control a sample and hold circuit.
5. Six digital input pins for the push buttons in the user interface.
6. Three analog input pins to monitor current amplitude settings for both channels, both during stimulation and when the stimulator is inactive.
7. An onboard analog to digital converter, used to monitor and display the stimulation current intensity on the LCD.

Texas Instruments produces the MSP430 range of microcontrollers. It was decided to use the MSP430F149 microcontroller, as it met all the specifications and has 60KB+256B Flash Memory, as well as 2KB of RAM, which was found to be adequate memory for the application. This meant that there was no need for EEPROM devices as used in the Stanmore stimulator. The MSP430F149 can be bought from OLIMEX Inc, ready mounted on a Header board, the circuit schematic of which is shown in figure 5.8. Component Q2 in the schematic was replaced with an 8MHz crystal oscillator, the highest frequency at which the MSP430F149 can operate. This was necessary to be able to control the pulse width of the stimulation pulses with a resolution of 1μs.

5.2.3 Power Supply board

The circuit schematic for the Power Supply board can be found in figure 5.8.

Supply rails

The Biphasic stimulator is powered by a battery, to ensure that it is isolated from mains earth. It was decided to use a Li-ion rechargeable battery pack, (7.5V, 2200mAh) as Li-ion batteries are readily available, have high open-circuit voltages and little memory effect, as well as excellent charge density. Large capacitors were connected across the batteries to smooth out voltage ripple.

Two Low Drop Out (LDO), adjustable output, voltage regulators, TPS7A4501, were used to produce the regulated 5VC supply rail and a 3.3V supply rail, needed to power the microcontroller. An LDO regulator was necessary to ensure that 5V was generated for the entire battery supply voltage range from fully charged (7.5V) to its cut-off voltage of 6V. The TPS7A4501 has a dropout voltage of 300mV and an output current of 1.5A, which would allow the regulator to operate throughout the battery's voltage range, as well as meet the maximum current requirement of 1.1A (as calculated in equation 5.5).

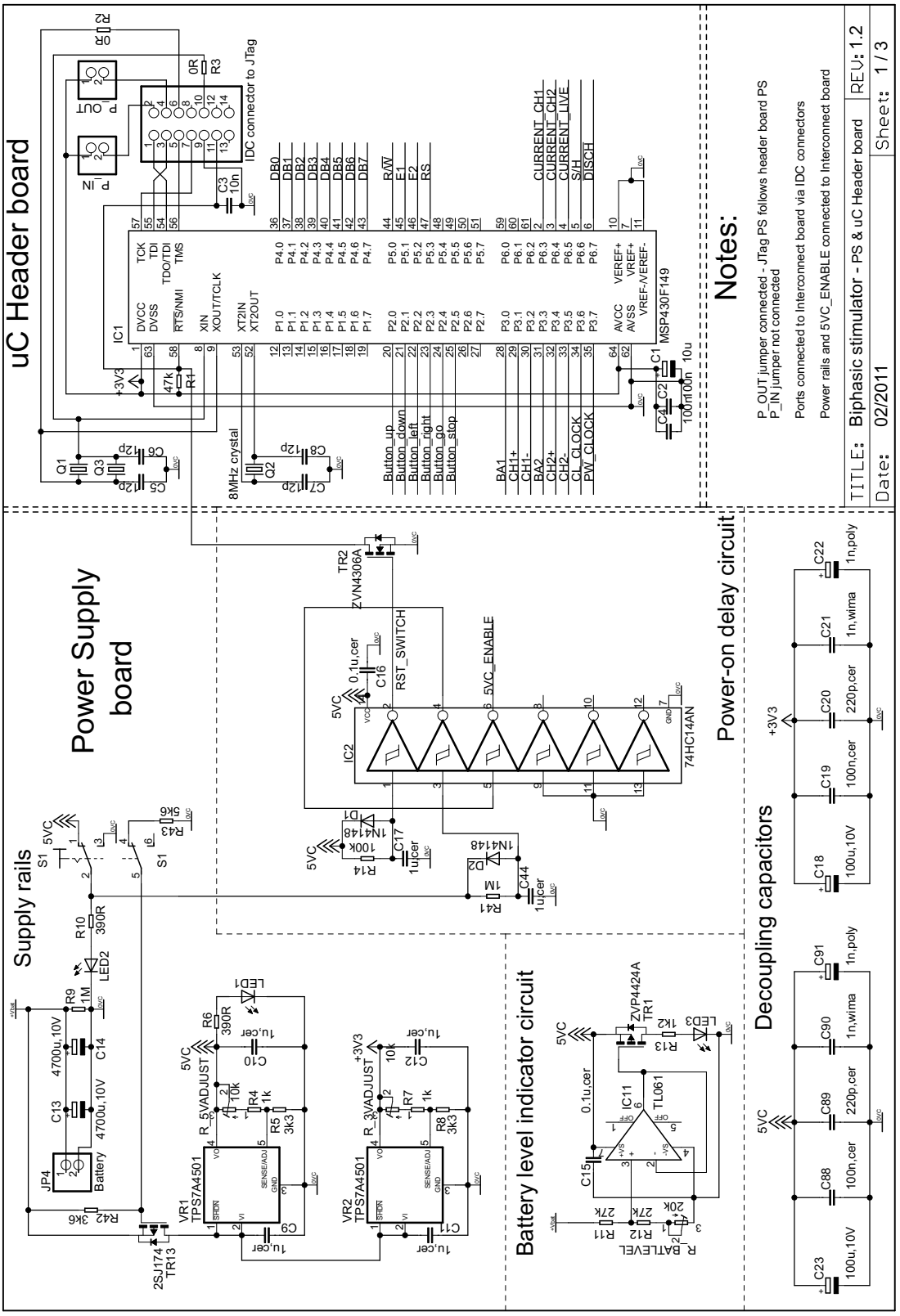

Figure 5.8: Circuit schematic for the Biphasic stimulator Power Supply and μC Header boards. (μC Header board schematic after OLIMEX [2002], with permission.)

Battery level indicator

The battery level indicator is used to monitor the battery output voltage. When this voltage reaches the cut-off voltage of 6V, a warning LED is turned on. At this point the battery in use should be exchanged for a fully charged battery.

Power-on delay circuit

Two delays were used in the circuit, at power-on. The first was a 100ms delay, introduced at the reset input (RST - pin 58) of the microcontroller via a MOSFET with the gate signal RST_SWITCH. This was to ensure that the supply rails had time to rise to their respective values, before turning on the microcontroller, which was in addition to a 470μs delay already present in the hardware of the μC Header board. The second delay was to create a 1s interval between turning the stimulator on and powering up the Biphasic Output board (5VC_ENABLE signal). This ensured that the microcontroller was fully operational before turning on the output stage, thereby preventing the occurrence of erroneous stimulation pulses. Figure 5.9 shows the two signals RST_SWITCH and 5VC_ENABLE relative to 5VC at power-on. Slight differences in the measured delay times, from those expected are due to mismatches in the resistors and capacitors used in the delay circuit.

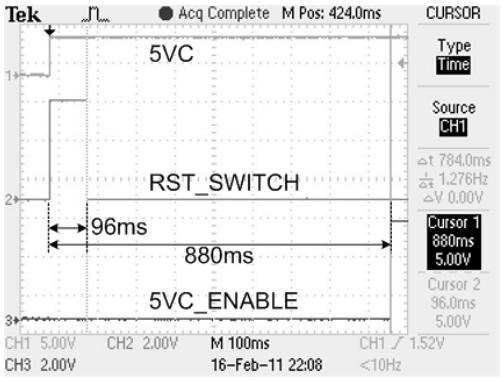

Figure 5.9: Delays introduced into power-on signals.

5.2.4 Current Amplitude Display (CAD) board

Figure 5.10 shows the circuit schematic for the CAD board.

Isolation amplifiers

It was desirable to know what the current amplitudes settings were for each channel. This was achieved by using the microcontroller's onboard AD converter. When the stimulator was turned on, but inactive (i.e. not currently stimulating), the voltage output of the two potentiometers used to set CA_{ch1} and CA_{ch2}, of the current regulator circuit, were monitored. During stimulation, the live current amplitude (CA_LIVE), was measured as the voltage across the 10Ω resistor (R20 in figure 5.2) connected to the source of the MOSFET in the current regulator. Isolation amplifiers were used to carry these signals from the Biphasic Output board, to the microcontroller, thereby not compromising the electrical safety of the stimulator. ISO124P precision isolation amplifiers, with a rated AC isolation voltage of 1.5kV, were used. As the CAD

board was made using strip board, an isolation barrier was introduced by removing a section of track, at the back of the board, underneath the isolation amplifiers. The voltages measured at the output of the amplifiers were calibrated and the current amplitudes displayed on the LCD.

Sample and Hold circuit

The current amplitude measurements, when the stimulator is inactive, are DC signals that can easily be monitored. However, the live current amplitude can only be measured during a stimulation pulse, the duration of which varies according to the pulse width setting. Furthermore, the AD conversion process takes a number of clock cycles to execute. Initial measurements showed that the conversion took longer to complete than the length of the maximum pulse width. This problem was overcome by introducing a sample and hold circuit. The operation of the circuit is controlled by the microcontroller, to ensure that the sample function is executed during a stimulation pulse. The AD conversion is then carried out after the stimulation pulse has come to an end, before discharging the sample and hold capacitor.

5.2.5 Interconnection board

Due to the large number of input and output signals (32 in total), going to and from the microcontroller, it was necessary to build an interconnection board, that merely facilitated the connections between the Power Supply, Header, Isolation and Biphasic Output boards. The Interconnection board also contained a small amount of circuitry needed to drive the peripherals, namely the LCD and the push buttons. Figure 5.11 shows the circuit schematic for the Interconnection board.

Push button circuit

Six push buttons were used to navigate the stimulator menus displayed on the LCD performing the functions *Up*, *Down*, *Left*, *Right*, *Go/Select* and *Stop/Backup*. Between each push button and the microcontroller is an RC debouncing circuit.[1] The debouncing of the buttons is further aided through software delays.

Output board optocoupler driver circuit

As mentioned earlier, the control signals generated by the microcontroller are connected to the Biphasic Output board through HCPL2531 optocouplers. However, while the output signals from the microcontroller are voltage signals, the optocouplers are current driven. Consequently MOSFETs were used to ensure that the current sourcing capabilities of the microcontroller were not exceeded.

In addition to the control signals taken to the Biphasic Output board, two other control signals, BIT_{Ch1} and BIT_{Ch2} can also be seen in figure 5.11. These signals are connected to the Blanking amplifier via an optocoupler, the driver circuit of which was included on the Interconnection board. The blanking interval trigger (BIT) signals are 20μs pulses generated by the microcontroller prior to the gate drive signals for each channel, as shown in figure 5.12.

[1] Courtesy Pablo Aqueveque

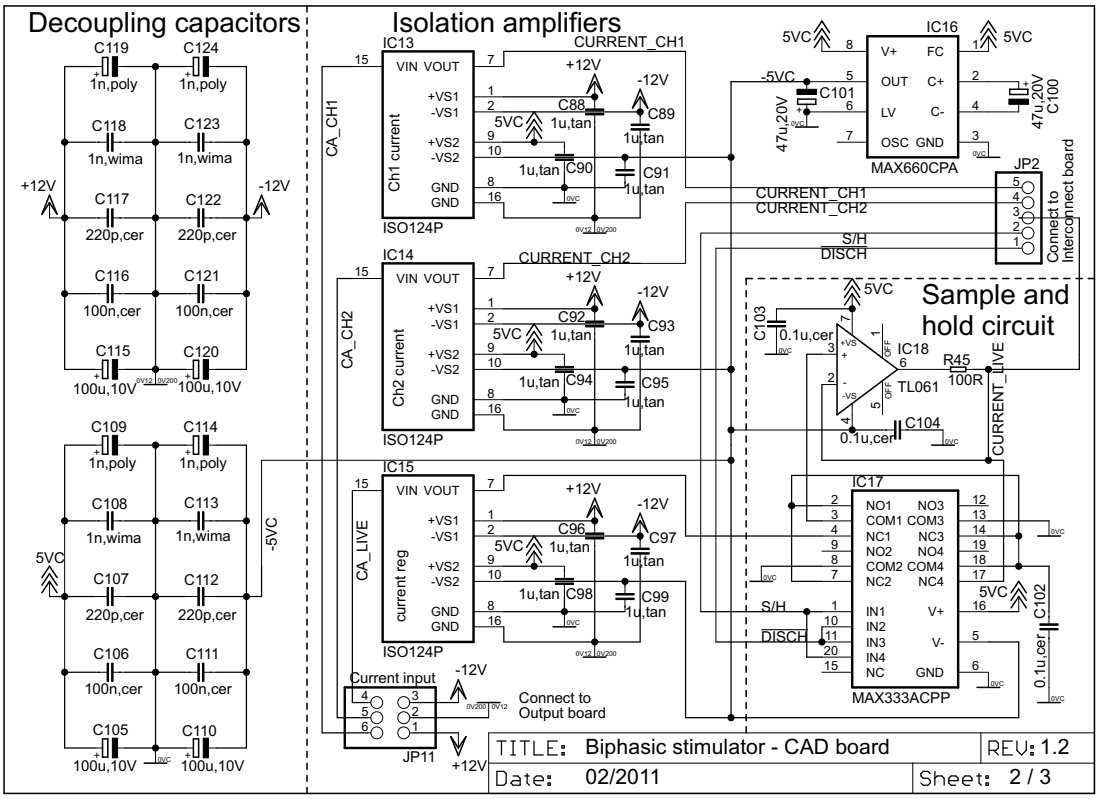

Figure 5.10: Circuit schematic for the Biphasic stimulator Current Amplitude Display (CAD) board.

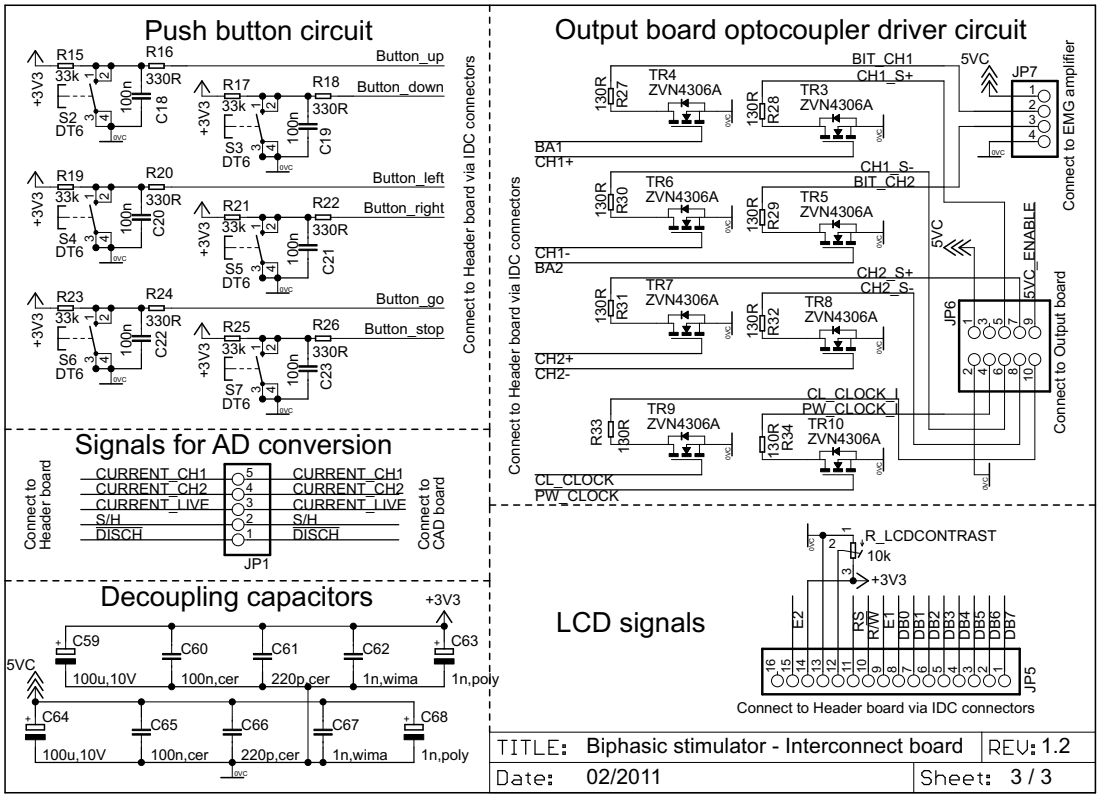

Figure 5.11: Circuit schematic for the Biphasic stimulator Interconnection board.

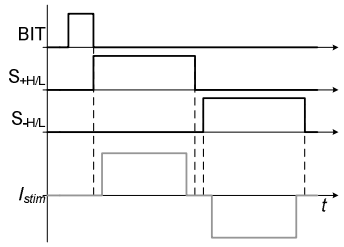

Figure 5.12: Timing diagram for the BIT signal, black traces represent digital signals, while grey traces are analog.

LCD signals

An alphanumeric, 40×4 LCD, model no. CFAH4004A-TFH-JP, was used. Eight data bits were used to specify a character, while four control signals determined when and where the character was to be displayed. All 12 signals were generated with the microcontroller and connected to the LCD via the Interconnect board.

5.3 Construction and assembly

As discussed earlier, a PCB was designed for the Biphasic Output board, while the μC Header board was commercially available. The remaining three boards were made using strip board. Figure 5.13 shows photographs of the boards, with the various sections of each board labelled. The location of the isolation barrier at the back of the CAD board has been highlighted.

The boards were then placed in a metal case as shown in figure 5.14. The front and back panels of the stimulator box were custom made using a milling machine.

The front panel made up the user interface, consisting of the push buttons, LCD, current amplitude potentiometers for channels one and two, and the output leads that were to be connected to the stimulating electrodes.

The power switch for turning the stimulator on and off was found on the back panel, as well as three different connectors. A battery lead, seen coming out of the back panel, needed to be connected to the battery connector. Without this connection, the battery would be electrically isolated from the stimulator's circuitry. Two battery leads can be seen in figure 5.14(d), one for each of the two batteries. Having two batteries enabled one battery to be recharged, possibly while using the second battery, without compromising the electrical isolation of the stimulator from mains earth. The EMG amplifier connector carried the blanking interval trigger signals (see figure 6.8), to the Blanking amplifier. The mains earth connector allowed the metal case to be earthed. This ensured that the potential of the case, relative to mains earth, was always well defined and not some arbitrary value determined by parasitic capacitive coupling to the surroundings as well as the internal circuitry. In so doing, the experimental setup was consistent for all the subjects participating in the final study (discussed in Chapter 8).

Within the box, the boards were placed on nylon spacers, so that there was a spatial isolation barrier between all the boards and the earthed casing.

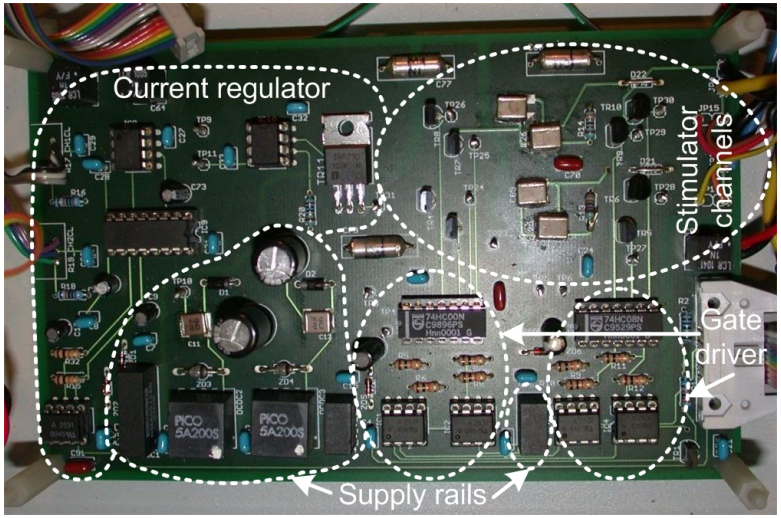

(a) Biphasic Output board.

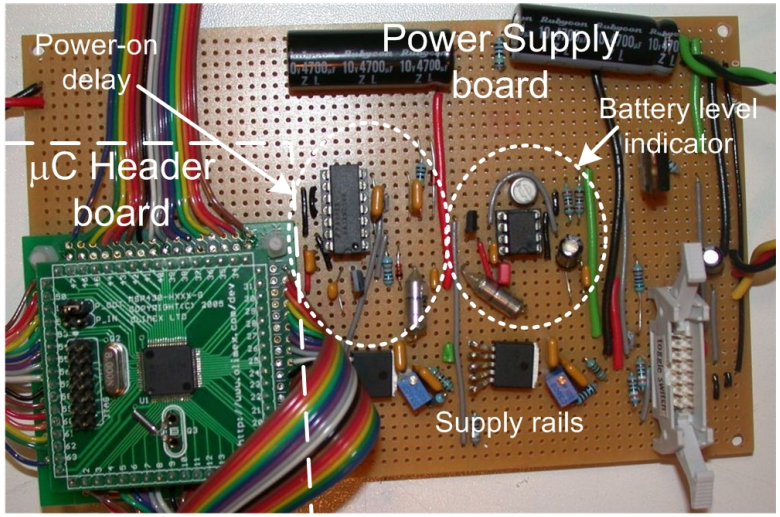

(b) Power Supply and μC Header boards.

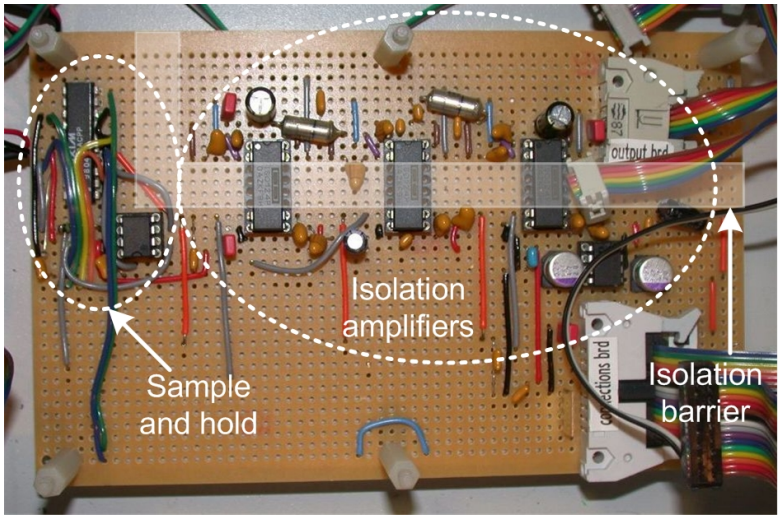

(c) Current Amplitude Display (CAD) board.

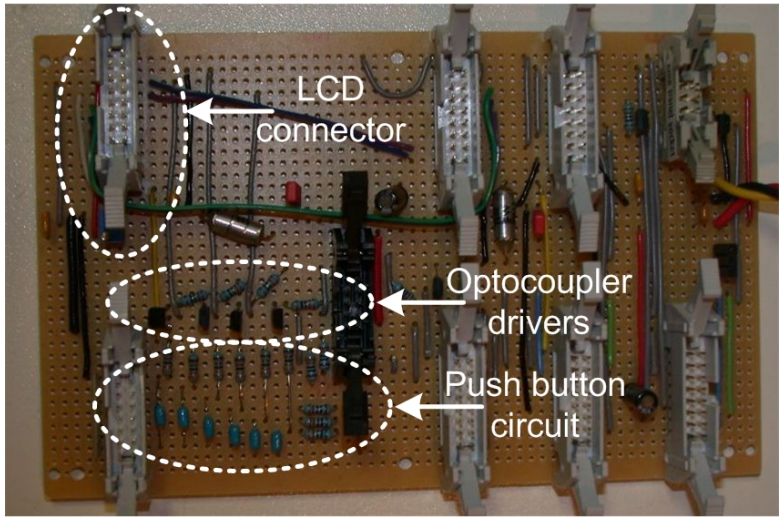

(d) Interconnection board.

Figure 5.13: Photographs of the individual boards.

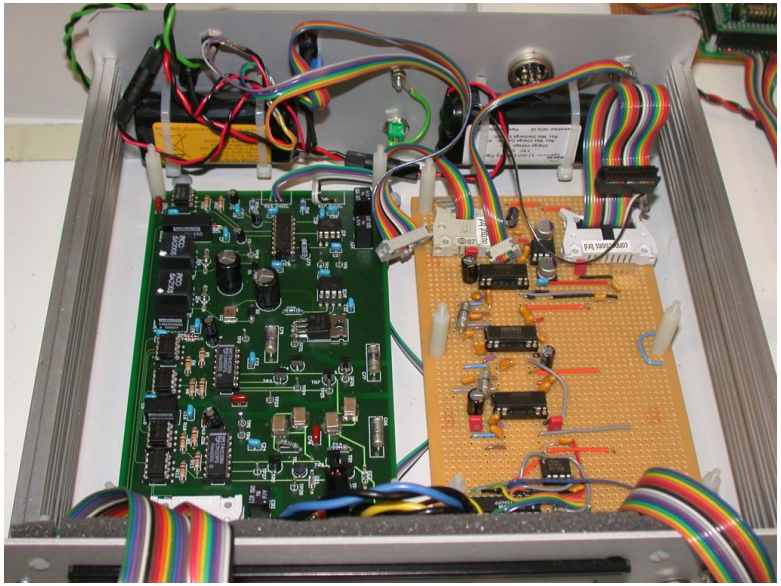

(a) Lower level placement of Biphasic Output and CAD boards.

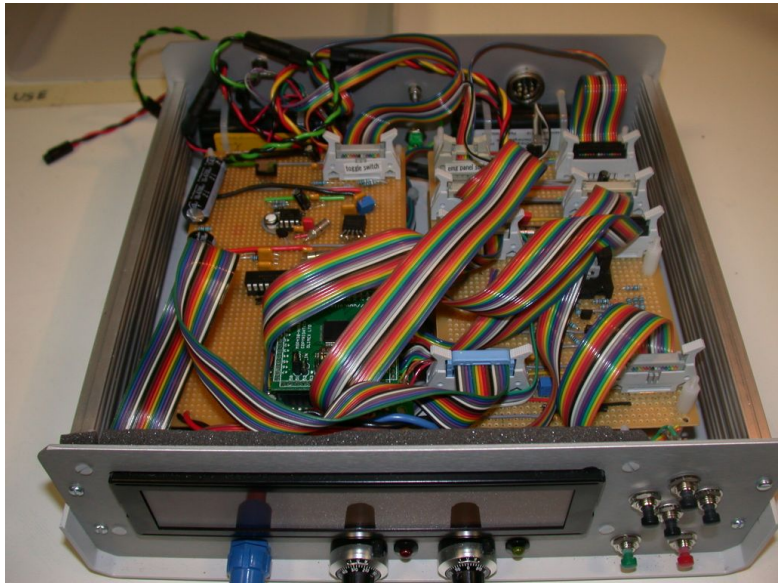

(b) Upper level placement of Power Supply, Header and Interconnection boards.

(c) Front panel.

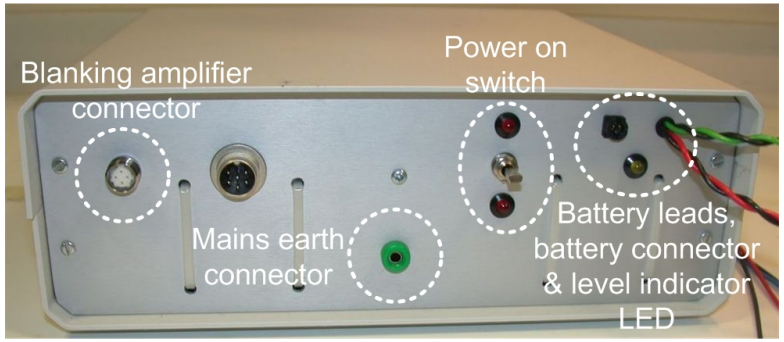

(d) Back panel.

Figure 5.14: Board assembly in metal case.

Figure 5.15 shows a wiring diagram of the fully assembled stimulator, relative to mains earth. The connection of the stimulator to a subject via the stimulating electrodes is also shown. There exists a direct electrical connection between the subject and the Biphasic output board. Isolation barriers in the form of optocouplers, isolation amplifiers and physical separation prevent the subject from being exposed to either the batteries or to mains earth.

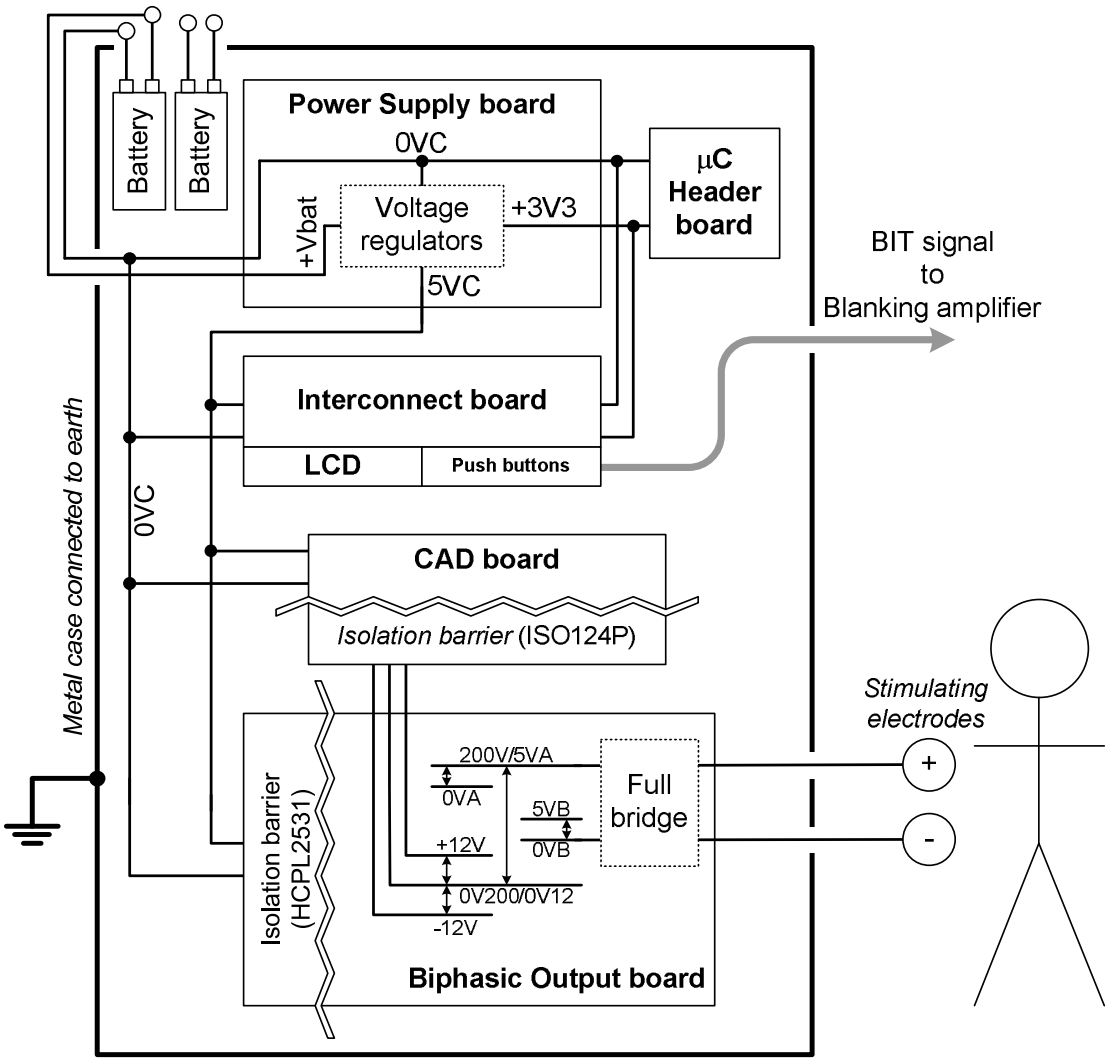

Figure 5.15: Wiring diagram showing the circuit boards, supply rails and isolation barriers, relative to earth.

5.4 Programming the microcontroller

The microcontroller was programmed using the C-compiler in the MSP430 IAR *Embedded Workbench*®, which is an Integrated Development Environment software package. The microcontroller performed two main functions:

1. Display of user interface menus on LCD for parameter selection.

2. Generation of various control signals using the parameters specified by the user.

Figure 5.16 shows the three menu options, namely, the Start menu, the Constant stimulation menu and the Recruitment curve menu. The Start menu is the first menu to appear on the LCD when the stimulator is turned on. The pointer, seen in the top left hand corner of the Start menu, can be positioned using the black push buttons (*Up*, *Down*, *Left*, *Right*) to point at any features within a menu that the user can select/change using the green, *Run/Select*, or red, *Stop/Backup*, push buttons.

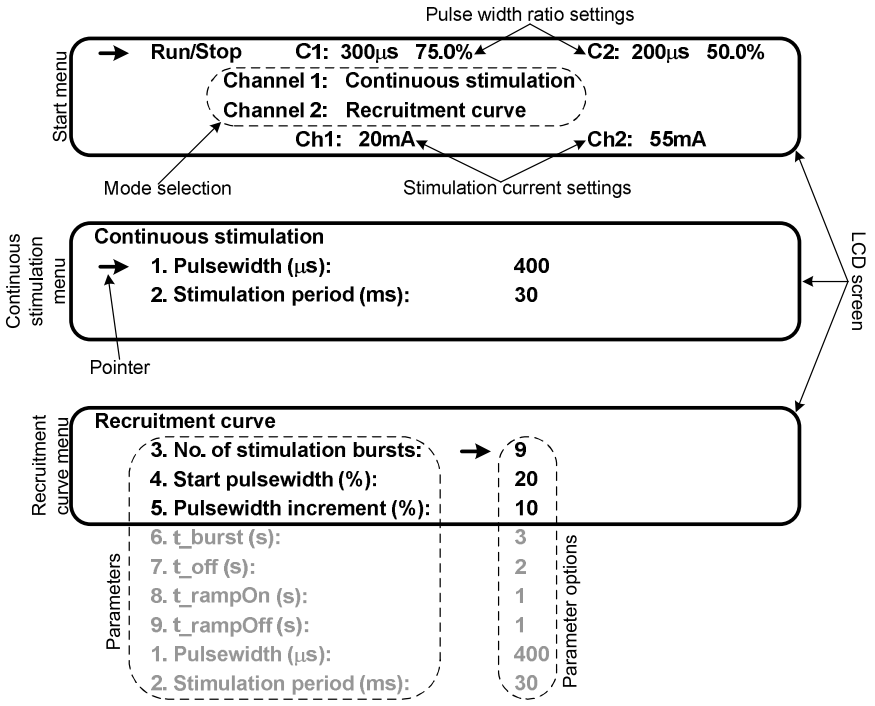

Figure 5.16: Schematic of the LCD showing the various menus.

The Start menu displays the state of the stimulator (stimulation running or stopped) and the pulse width ratio setting (PW_n and PW_r), the selected stimulation mode and the current amplitude setting for each channel.

The Continuous stimulation menu has two parameters that the user can set, namely the stimulation pulse width and period. Stimulation in this mode has to be stopped by the user.

The Recruitment curve menu has nine parameters, as shown in the figure, that must be defined for a recruitment curve protocol to be carried out. However, due to the size of the LCD only three parameters can be displayed at a time. Stimulation in this mode is automatically stopped after the stimulation protocol has been completed.

The features and parameters for each menu are discussed in more detail in Appendix C, Section C.2.

The microcontroller program has a *Main* routine, that runs continuously in a loop. Within this routine, the appropriate menus and parameter options are displayed on the LCD, and the push buttons are monitored so as to detect when one of them is pressed. As soon as a press is detected, various flags are set which are then used to update the display and/or to enable or disable the *Interrupt* routine. A flow chart depicting the *Main* routine can be found in figure 5.17.

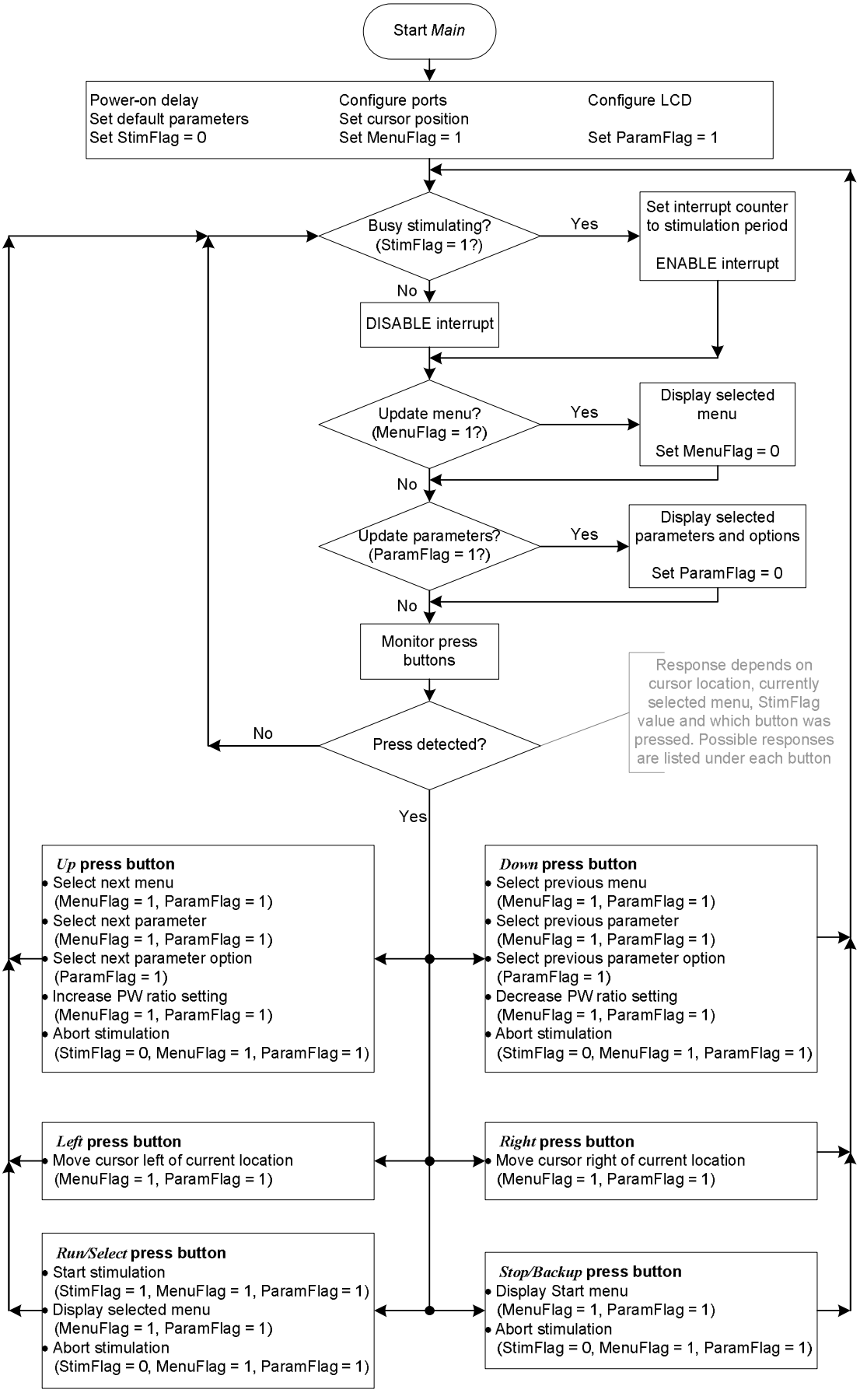

Figure 5.17: Flow chart of the *Main* routine.

Figure 5.18 shows a flow chart, outlining the *Interrupt* routine, which is used to generate the control signals that produce the stimulation pulses. This routine works in such a way that, once the interrupt is enabled and the interrupt counter has been set, every time the counter overflows, the *Main* routine will be stopped so that the interrupt counter can be reset and the code within the *Interrupt* routine executed. Once complete, the program returns to the same position in the *Main* routine as it was before the interrupt occurred and continues to execute this code until another interrupt is called. This process continues until the interrupt is disabled. By placing the code to generate the control signals within the *Interrupt* routine, it ensures that

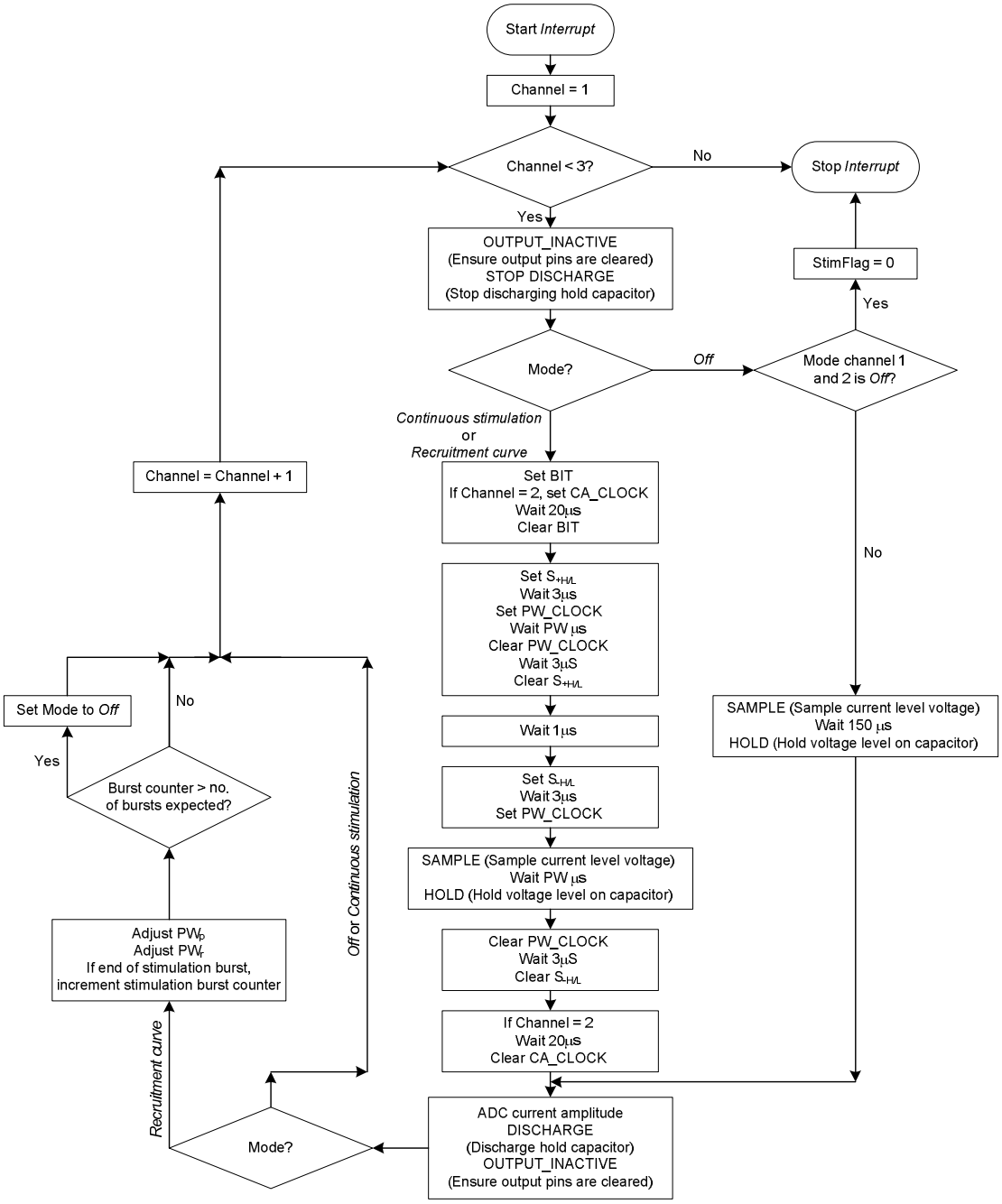

Figure 5.18: Flow chart of the *Interrupt* routine.

the stimulation period is accurately timed. The stimulation period is varied by using the user defined value for this parameter to set the interrupt counter, thereby adjusting the time period between overflow events.

5.5 Stimulator development

In the previous sections the final version of the Biphasic stimulator was presented. However, during development of the stimulator, a few modifications were made to the original design in response to problems that arose. The following section discusses these modifications to highlight some of the challenges encountered in building a working system, and to provide insight to others who wish to build FES stimulators in the future.

For reasons discussed in Chapter 7, it was necessary to accurately know the pulse width of the output waveforms compared with the pulse settings defined by the user. To this end the stimulator was calibrated, the results of which are also presented in this section.

All of the measurements discussed in this section were taken with a 1kΩ resistive load connected to the stimulator output, serving as a rough estimate of the average resistance, R_{ac}, seen between the anode and cathode. The voltage across the resistive load was then measured using an oscilloscope (either a Tektronix TDS2004B or an Agilent 54622D).

5.5.1 Output waveforms

Figure 5.19 shows the voltage measured across the load resistor, with the settings shown in the table above the figure.

	T (ms)	PW (μs)	PW_r (%)	I_{stim} (mA)
Ch1	50	176	100	178

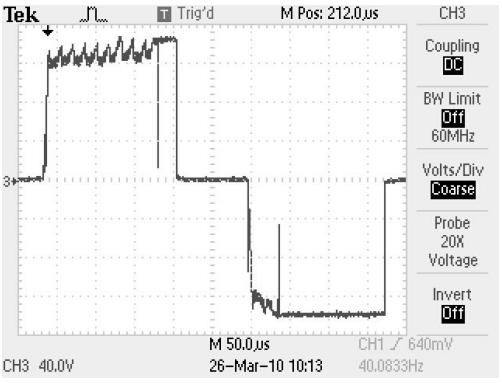

Figure 5.19: Channel 1 output voltage, showing the oscillation.

The oscillation seen during the positive phase of the pulse, and partly during the negative phase, was of the order of a few MHz. Although figure 5.19 does not show oscillation at such a high frequency, when taking the measurements the oscilloscope was used to look at a magnified view of the oscillations, which showed the MHz response. The oscillations would only occur at the higher current amplitude settings. The introduction of the polystyrene decoupling capacitors (C63, C64, C70, C77, C79 and C92 in figure 5.2), which are radio frequency capacitors

that operate to the order of hundreds of MHz, helped to reduce the oscillation, but not completely eliminate it. This measurement was however taken, prior to the introduction of the soft switching scheme using the PW_CLOCK signal. When the signals shown in figure 5.19 were measured, the current regulator was always on and the output voltage across the 10Ω resistor (R20 in figure 5.2, CA_LIVE), merely adjusted according to which channel was currently active. (i.e. CR_INPUT was taken from pin X of the multiplexer, refer to figure 5.6.) Switching the MOSFETs, in the output stage of the stimulator channels while the current was still flowing, caused the op-amp (IC10B in figure 5.2) in the current regulator circuit to oscillate. The introduction of the soft switching scheme eliminated the oscillations.

Figure 5.20 shows the voltage measured across the load resistor connected to channel 1, with the stimulator settings as shown.

	T (ms)	PW (μs)	PW_r (%)	I_{stim} (mA)
Ch1	20	400	100	132
Ch2	20	400	100	122

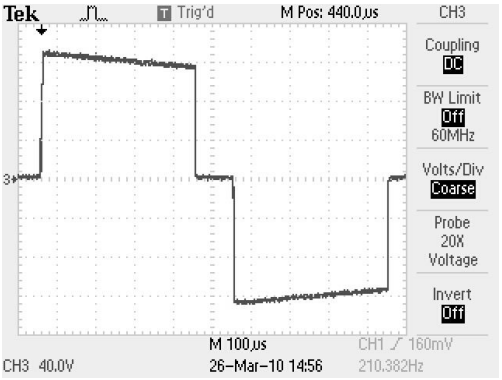

Figure 5.20: Channel 1 output voltage, under full load, prior to adding the second 200V DC-DC converter.

This measurement was taken before a second 200V DC-DC converter was introduced onto the Biphasic Output board, while driving the stimulator at maximum load. The drop in voltage amplitude of the two phases, measured across the resistive load, indicates a similar drop occurred in the output current. The measurement shown here corresponds with the voltage drop seen in the 200V rail, that was mentioned in Section 5.2.1 (*Supply rails*). This problem was solved by including a second DC-DC converter to increase the available output power of the stimulator.

Figure 5.21 shows the final output waveform measured on channel 1, using the stimulation settings indicated in the table (channel 1 and channel 2 driven at maximum load). As can be seen in the figure, the oscillations were successfully eliminated and the amplitudes of both phases of the biphasic pulse were now constant; the oscillations were still absent. Channel 2 of the Biphasic stimulator produced a virtually identical output waveform.

	T (ms)	PW (μs)	PW_r (%)	I_{stim} (mA)
Ch1	20	400	100.8	116
Ch2	20	400	100.0	116

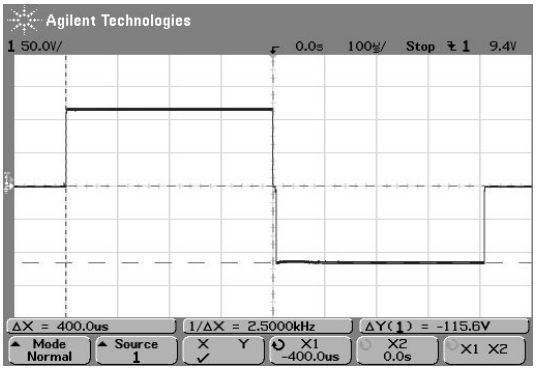

Figure 5.21: Final output waveform across a 1kΩ resistive load.

5.5.2 Calibrating the stimulator

When the stimulator was used on a subject with the recruitment curve protocol, it was found that the PW_r setting had to be adjusted according to the instantaneous PW value, as discussed in Section 7.3.5 (*Influence of pulse width on the PW_r setting required to eliminate stimulation artefact*). Because of this fact, the stimulator had to be calibrated so that the exact positive phase and negative phase pulse widths (PW_p and PW_n respectively), for a given PW setting, were known. To this end the output voltage over the 1kΩ resistive load, was measured for a range of current amplitudes and PW settings for both channels. The PW_r value was held fixed at the maximum possible setting. Figure 5.22 shows the results measured for a stimulation current of 50mA.

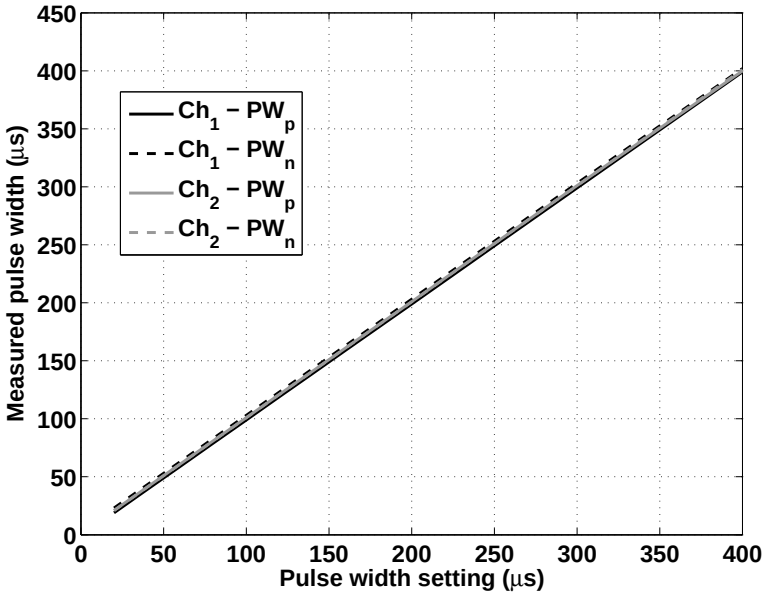

Figure 5.22: Measured values of PW_p and PW_n versus the stimulation pulse width setting.

There were small deviations in the actual pulse width values measured, from those expected. For channel 1 it was found that the positive phase pulse width, PW_p was always 1μs less than the PW setting, while the negative phase pulse width, PW_n, was 3μs greater. For channel 2 both positive and negative phase pulse widths were 1μs greater than the PW setting. These offset values did change slightly for stimulation currents below 30mA but were consistent for stimulation currents of 30mA and greater. As it was expected that the subjects would generally be able to tolerate a current intensity of 30mA or more, therefore the calibration values presented here were considered to be sufficient.

It should be noted that due to the way in which the high and low side gate signals were generated with the microcontroller, the stimulator was not able to generate a true monophasic pulse, even with a PW_r setting of 0%. The minimum PW_n value for channel 1 was 3μs, while for channel 2 it was 2μs.

5.6 Stimulator performance

In this section the voltage across the blocking capacitor was investigated to develop a better understanding of how the stimulator functions. The output impedance of the stimulator was also measured.

5.6.1 Effect of PW_r on C_b voltage

The 1kΩ resistor was connected between the anode and the cathode to represent the average resistance, R_{ac}. The voltage across the blocking capacitor, V_{Cb}, was measured, as shown in figure 5.23. The measurements were taken using the stimulation settings given in the table above the figures.

In figure 5.23(a), the complete voltage waveform is shown for a PW_r setting of 102%. The expected biphasic output pulse was added to the figure to clearly indicate when each phase of the stimulation pulse starts and stops. During the positive phase, charge is placed on the capacitor, resulting in a linear increase in the voltage across it. During the negative phase the capacitor is discharged, causing the voltage to linearly decrease. Figure 5.23(b) shows a magnified view of the baselines (highlighted section of Fig 5.23(a)). In this figure, we can clearly see that the baselines, before and after the stimulation pulse, are not equal, but instead there is a 43.8mV difference between the two, which corresponds to approximately 220nC of charge.

$$Q = C_b V_{Cb} = 5\mu\text{F} \cdot 43.8\text{mV} \approx 220\text{nC} \tag{5.6}$$

This charge imbalance can be accounted for by the slight difference in the pulse widths of the positive and negative phases, as found when the stimulator was calibrated. For a PW setting of 200μs, the stimulator would produce a biphasic pulse with $PW_p = 199\mu$s and $PW_n = 203\mu$s. For the stimulation current of 50mA, a mismatch of 4μs would result in a charge difference of 200nC.

$$\Delta Q = I_{stim}\Delta t = 50\text{mA} \cdot 4\mu\text{s} = 200\text{nC} \tag{5.7}$$

	T (ms)	PW (μs)	PW_r (%)	I_{stim} (mA)
Ch1	30	200	Varied	50

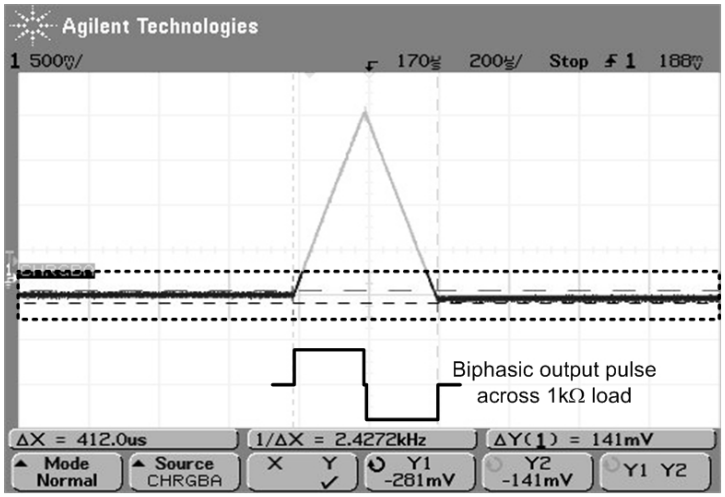

(a) PW_r = 102%, PW_p = 199μs, PW_n = 203μs.

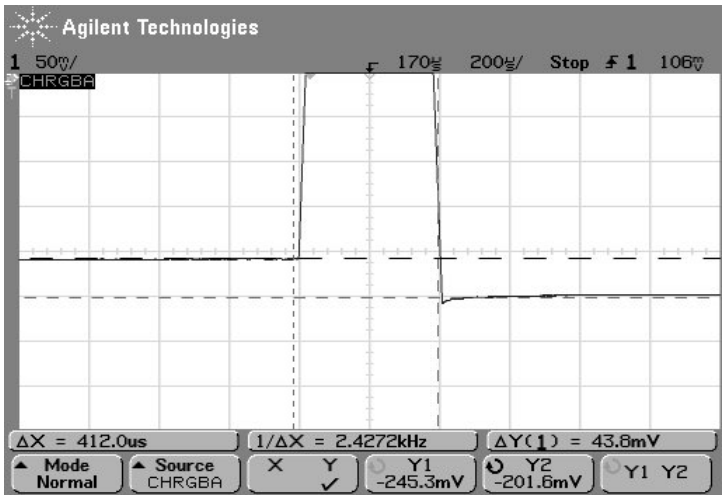

(b) Magnified baseline: PW_r = 102%, PW_p = 199μs, PW_n = 203μs.

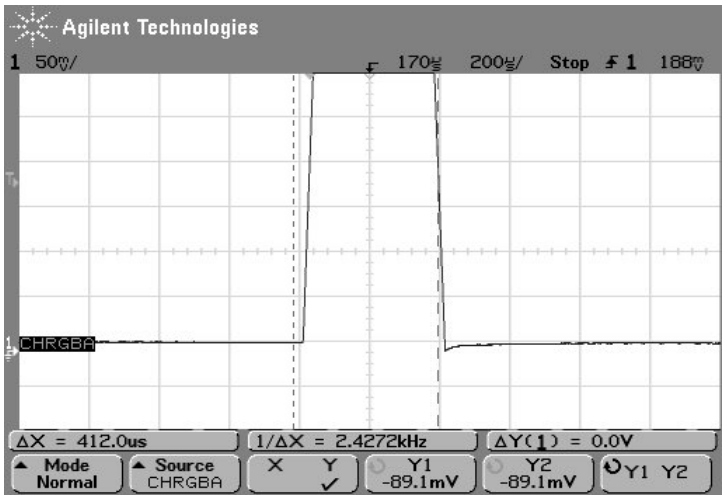

(c) Magnified baseline: PW_r = 100%, PW_p = 199μs, PW_n = 199μs.

Figure 5.23: Voltage across C_b.

The remaining 20nC is within the measurement error of the various voltage, current and pulse width values used in the calculations. By adjusting the PW_r setting and thereby correcting the charge imbalance, the voltage difference in the baseline can be removed, as shown in figure 5.23(c).

Figure 5.24(a) shows the magnified baseline measurements over a range of current amplitudes. At each current setting, a PW_r of 100% ensured that the difference in the baseline before and after the stimulation pulse, was minimised. However, each waveform also had a DC offset, which increased with current intensity ($\sim$0V at 10mA, increasing up to $\sim$60mV at 120mA).

Figure 5.24(b) shows the baseline images for $I_{stim} = 120$mA, at three different PW_r settings, over a larger time base, so that the entire stimulation period can be seen. For each trace, the DC offset is different. Furthermore, the voltage varies with time between the stimulation pulses, as is clearly evident in the top and bottom traces.

This can be explained by considering the output stage of the stimulator (refer to figure 5.4), which can be drawn as in figure 5.25(a) with a 1kΩ resistor connected between the stimulating electrodes. During the stimulation pulse, the stimulation current flows through C_b and R_{ac}. If the pulse widths of the positive and negative phases are not exactly equal, there will be a residual charge on C_b after the stimulation pulse. The capacitor will then discharge through R_d between the stimulation pulses. This will give rise to the voltage waveforms shown in figure 5.25(b). If the capacitor does not discharge fully before the start of the next stimulation pulse, each consecutive pulse will add yet more charge to the capacitor, in turn causing an increase in the voltage across the capacitor, directly after the stimulation pulse ($V_{1P} < V_{2P} < V_{3P}$). After some time V_{Cb} will reach an equilibrium position with a non-zero DC offset value. An expression for this value can be found.

Equation 5.8 gives the residual charge on the capacitor after a stimulation pulse.

$$Q_{res} = I_{stim}\Delta t = I_{stim}\left(PW_p - PW_n\right) \tag{5.8}$$

Which can be used to find the residual voltage.

$$V_{res} = \frac{Q_{res}}{C_b} = \frac{I_{stim}\left(PW_p - PW_n\right)}{C_b} \tag{5.9}$$

After the first stimulation pulse the voltage across the capacitor is equal to the residual voltage.

$$V_{1P} = V_{res} \tag{5.10}$$

After T seconds the capacitor has partially discharged so that the voltage can now be expressed as in equation 5.11. The variable R_{acd} is the series combination of R_{ac} and R_d.

$$V_{1T} = V_{1P}e^{-A} = V_{res}e^{-A}; \qquad A = \frac{T - (PW_p + PW_n)}{R_{acd}C_b} \tag{5.11}$$

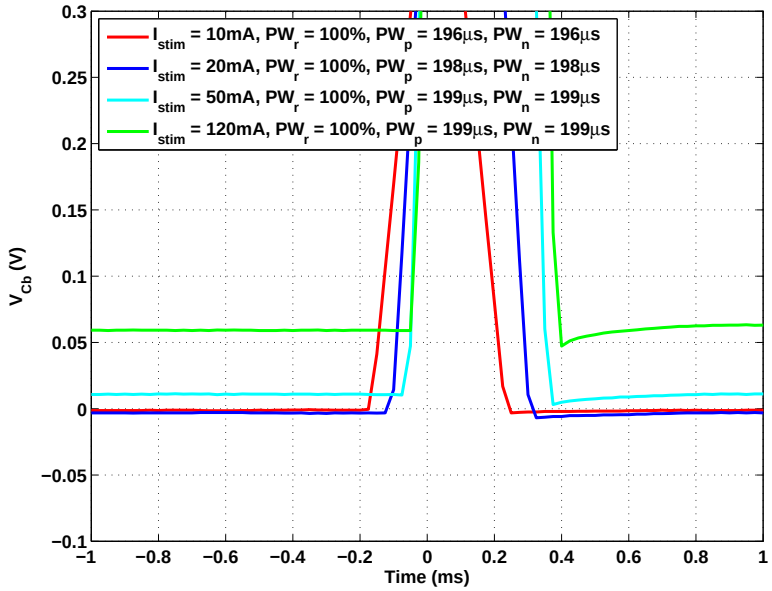

(a) Different current settings.

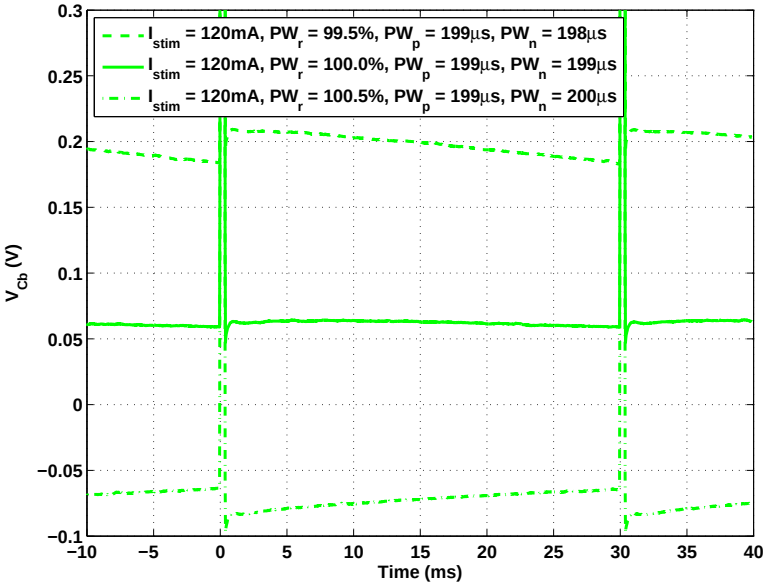

(b) Different PW_r settings for $I = 120$mA.

Figure 5.24: Effect of current and PW_r settings on the baseline voltage across C_b.

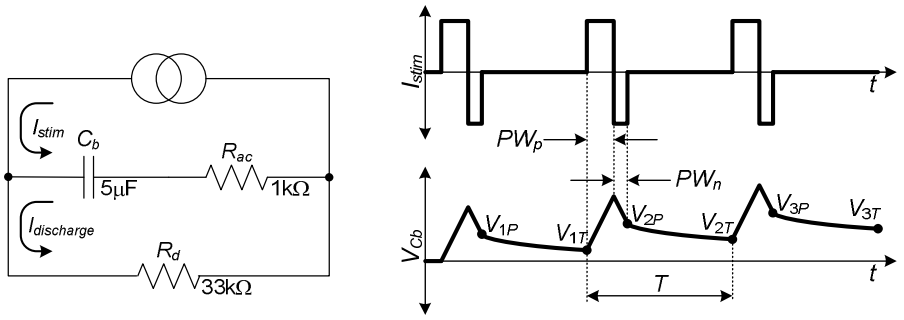

(a) Stimulator output stage.

(b) C_b current and voltage waveforms.

Figure 5.25: Average voltage across the blocking capacitor.

Using the same approach, the voltages after n stimulation pulses and n intervals of T seconds, can be expressed as in equation 5.12.

$$V_{nP} = V_{res} + V_{(n-1)T}; \qquad V_{nT} = V_{nP}e^{-A} \tag{5.12}$$

Using these expressions we can write out the voltages for a few values of n.

$$\begin{aligned} V_{2P} &= V_{res}\left(1 + e^{-A}\right) & V_{2T} &= V_{res}\left(e^{-A} + e^{-2A}\right) \\ V_{3P} &= V_{res}\left(1 + e^{-A} + e^{-2A}\right) & V_{3T} &= V_{res}\left(e^{-A} + e^{-2A} + e^{-3A}\right) \\ &\vdots & &\vdots \\ V_{NP} &= V_{res}\left(1 + e^{-A} + \ldots + e^{-(N-1)A}\right) & V_{NT} &= V_{res}\left(e^{-A} + \ldots + e^{-NA}\right) \end{aligned}$$

From this we can find a series expression for the voltage across C_b after N intervals of T seconds.

$$V_{NT} = V_{res}\sum_{n=1}^{N} e^{-nA} \tag{5.13}$$

The series is convergent, which means that as N approaches infinity, V_{NT} approaches a limit, or, in practical terms a constant DC offset voltage can be seen in the baseline of V_{Cb}. The rate of convergence is dependent on the value of A.

The stimulation settings used to capture the measurements shown in figures 5.23 and 5.24, and the component values of figure 5.25, were used to plot V_{NT} over a range of N values. The PW_n values were adjusted so that the limit approached by V_{NT} was close to the DC offset values measured in figure 5.24. The results are shown in figure 5.26.

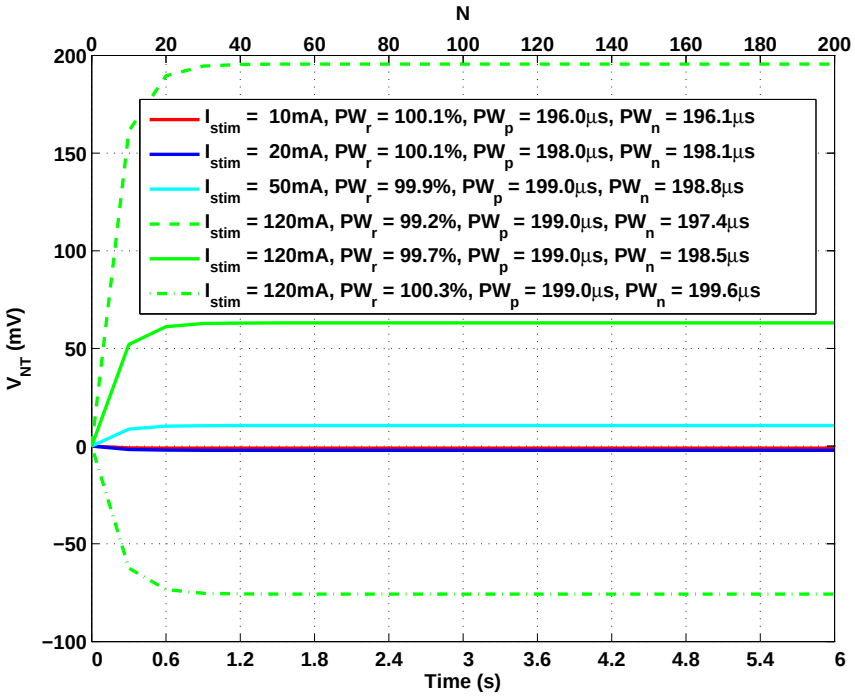

Figure 5.26: Calculation of V_{NT} over a range of N values.

The figure shows that the series converged for $N > 40$ (upper horizontal axis). This was converted into a value of time (lower horizontal axis) using the stimulation period of 30ms, which shows that the voltage across C_b has settled at its average value after ~1.2s of stimulation.

In figure 5.24, for $I_{stim} = 120$mA and $PW_r = 100\%$, A DC offset of ~60mV was measured. According to equation 5.13, if the PW_r value was truly 100%, the DC offset would have been zero. Compare this with figure 5.26, where a V_{NT} value of ~60mV was found for $PW_r = 99.7\%$ (equivalent to a difference in PW_p and PW_n of 0.5μs). A similar observation can be made for all of the I_{stim} settings of figure 5.24(a), where differences between PW_p and $PW_n < 1\mu$s were used in figure 5.26.

This indicates a limitation of the microcontroller, in which the negative phase pulse width can only be varied in steps of 1μs. Consequently, mismatches in PW_p and PW_n less than 1μs in length, cannot be adjusted for.

5.6.2 Output impedance

To fully characterise the stimulator, its output impedance was experimentally measured, using the Norton equivalent circuit [Bobrow, 1996] shown in figure 5.27. The stimulator can be approximated as an ideal current source, I_s, with an inherent shunt output impedance, Z_o. The load impedance, Z_l, represents the load connected between the terminals of one of the stimulator's output channels.

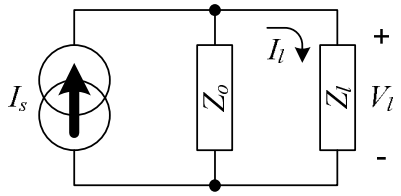

Figure 5.27: Norton equivalent circuit, after Bobrow [1996], with permission.

Assume that the stimulation current is set to some value, I_s, and two load impedances of different magnitude, Z_{l1} and Z_{l2}, are connected to an output channel, one after the other. The current flowing through each load impedance, I_{l1} and I_{l2} respectively, can be measured. Using basic circuit analysis an expression for Z_o can be found:

$$Z_o = \frac{Z_{l1}I_{l1} - Z_{l2}I_{l2}}{I_{l2} - I_{l1}} \tag{5.14}$$

This principle was used to calculate the output impedance of the Biphasic stimulator, for both channels, the results of which are shown in table 5.2. The maximum I_{stim} setting was used for each channel, so as to produce the largest possible values for I_{l1} and I_{l2}. Z_{l1} and Z_{l2} were arbitrarily chosen to have nominal values of 100Ω and 1kΩ. An output impedance was found both during the positive and negative phase of the biphasic pulse, as each phase involved the turning on or off of a different set of switches in the full bridge output stage (see figure 5.4).

The output impedances shown in the table are those of the stimulator during a stimulation pulse, when at least one pair of the switches in the full bridge is turned on. We expect that the

Table 5.2: Output impedance measurements for both stimulator channels.

	I_{stim} (mA)[a]	Stimulation pulse phase	Z_l (Ω)[b]	V_l (V)	I_l (mA)[c]	Z_o (kΩ)
Channel 1	124	positive	99.1	12.50	126.1	63.7
			992	123.4	124.4	
		negative	99.1	12.66	127.7	33.0
			992	123.4	124.4	
Channel 2	123	positive	99.1	12.50	126.1	33.6
			992	121.9	122.9	
		negative	99.1	12.50	126.1	33.6
			992	121.9	122.9	

[a] Biphasic stimulator current setting. [b] Nominal load resistances 100Ω and 1kΩ. [c] $I_l = \frac{V_l}{Z_l}$

output impedance would be close to 33kΩ, due to the presence of the discharge resistor, R_d. This was indeed the case for 3 of the 4 calculated Z_o values. The value of 63.7kΩ measured during the positive phase of channel 1 is most likely due to measurement error when capturing the V_l magnitudes (for the 99.1Ω load impedance there was only a difference of 0.16V in the V_l measurements during the positive and negative phases).

Between stimulation pulses, when all of the switches are turned off, the output impedance of the stimulator would also be predominantly determined by the 33kΩ discharge resistor, R_d.

5.7 Summary

A biphasic constant-current stimulator, with pulse width ratio adjustment capability, as needed for stimulation artefact elimination during evoked EMG measurements, was designed and constructed.

- The Biphasic stimulator was based on the existing Stanmore stimulator, a monophasic constant-current stimulator. The principle of using floating supply rails, as produced from DC-DC converters was carried across directly from the Stanmore stimulator. The output board was modified from a half bridge to a full bridge, so as to generate a biphasic pulse.

- The various functions of the stimulator were implemented by means of a microcontroller. This included the incorporation of a user interface into the stimulator design, a marked improvement over the Stanmore stimulator that requires a computer connection to adjust the stimulation parameters.

- The layout design, component selection and assembly of the Biphasic stimulator all took into consideration the need for electrical safety, namely that the stimulator output, which is connected to a subject, be isolated from earth.

The specifications of the Biphasic stimulator are summarised in table 5.3.

Table 5.3: Biphasic stimulator specifications.

Pulse	Shape	Biphasic	
	Type	Constant-current	
	Period (ms)	20, 30, 40, 50, 100, 500, 1000, 2000, 3000, 4000, 5000	
	Pulse width (μs) (per phase)	20, 40, 60, 80, 100, 120, 140, 160, 180, 200, 225, 240, 250, 280, 300, 320, 360, 400	
Supply	Battery	Li-ion, 7.5V, 2200mAh, rechargeable, internal battery pack	
Protocols	Continuous stimulation Recruitment curve stimulation		
Output	Channels:	1	2
	Current (mA)	0-125	0-128
	Impedance, positive phase (kΩ)	$\sim 33^a$	33.6
	Impedance, negative phase (kΩ)	33.0	33.6
Current consumption (full load)		1.1A	
Compliance voltage[b]		200V	
Blocking capacitance (C_b)		5μF	
Discharge resistance (R_d)		33kΩ	

[a] Measurement error prevented the experimental validation of this value, however it is expected to be similar in value to the discharge resistor R_d.
[b] Maximum amount of voltage that a constant current stimulator can provide. Once the compliance voltage has been reached, further increases in tissue resistance will cause a drop in delivered current.

A couple of design problems that arose during development of the stimulator were addressed:

1. The original current regulator design caused oscillations to occur in the biphasic pulse. Using a soft-switching scheme in the full bridge output stage eliminated the oscillations.

2. A drop in the 200V rail when stimulating at maximum load was prevented by using two 200V converters for the output stage.

Two limitations of the stimulator were also identified:

1. The stimulator was calibrated for pulse width and current amplitude. The pulse width calibration was later used to determine PW_r settings necessary to remove the stimulation artefact. The first limitation of the stimulator was shown to be its inability to produce a true monophasic pulse, even when the PW_r setting was reduced to 0%.

2. The presence of a residual voltage across the blocking capacitor resulted in a current flowing through the discharge resistor, between stimulation pulses. This could be corrected by adjusting the PW_r setting. However, the negative phase pulse width can only be adjusted in 1μs increments, consequently it was not always possible to eliminate the residual charge entirely.

Chapter 6

Current conveyor based blanking EMG amplifier

6.1 Introduction

Measuring the EMG response from the stimulated muscle, required that the recording electrodes be placed between the stimulating electrodes. However, as discussed at the end of Chapter 4, such an arrangement can easily result in the amplifier becoming saturated. It takes a finite amount of time for the amplifier to recover from this state. If this time period is longer than the latency of the M-wave, the amplifier will be unable to measure said M-wave.

Bruun and Haxthausen [1991] overcame this problem by effectively shutting down the amplifier during the stimulation pulse, thereby preventing it from being saturated and enabling the amplifier to record EMG signals directly after the stimulation pulse. This was accomplished by using two second generation positive current conveyors (CC) at the input stage of the amplifier, as shown in figure 6.1.

A current conveyor was first introduced by Smith and Sedra [1968] as a circuit building block in which "current is conveyed between two ports at different impedance levels". The terminal voltages and currents of the current conveyor are given in equation 6.1. Of the two input terminals, terminal y is a high impedance node, while terminal x is a low impedance node.

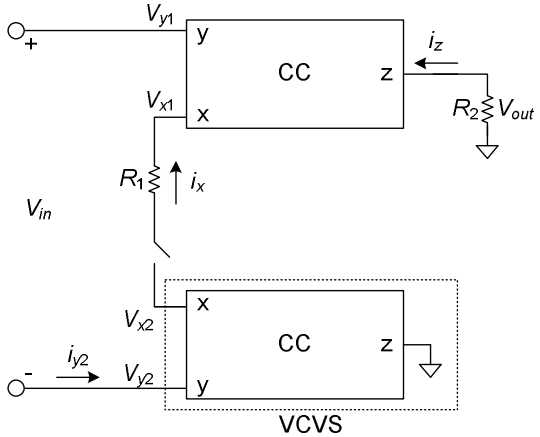

Figure 6.1: Schematic diagram of the current conveyor at the input stage of the EMG amplifier, after Bruun and Haxthausen [1991] (©The Institution of Engineering and Technology), with permission, and Sedra and Smith [1970] (©IEEE), with permission.

The voltages at the two nodes are held constant, $V_x = V_y$, while the current in i_x is reflected at the output, i_z. In the figure the lower current conveyor is connected as a voltage controlled voltage source (VCVS) [Sedra and Smith, 1970] that ensures $V_{y2} = V_{x2}$ while $i_{y2} = 0$.

$$\begin{bmatrix} i_y \\ v_x \\ i_z \end{bmatrix} = \begin{bmatrix} 0 & 0 & 0 \\ 1 & 0 & 0 \\ 0 & 1 & 0 \end{bmatrix} \begin{bmatrix} v_y \\ i_x \\ v_z \end{bmatrix} \tag{6.1}$$

The amplifier is shutdown by opening the switch between the low impedance nodes. By switching on a low impedance node as opposed to a high impedance node the switching spikes are kept small and thus prevented from saturating the amplifier [Bruun and Haxthausen, 1991]. The current, i_x, is determined by the voltages V_{x1} and V_{x2}, which is in turn reflected at the output i_z.

The small signal gain of the circuit, when the amplifier is active, is given by equation 6.2. When the amplifier is shutdown, the gain is effectively changed to zero by switching out the R_1 resistor. The output during this time is effectively *blanked*, therefore giving rise to the term *Blanking amplifier*.

$$A_v = \frac{V_{out}}{V_{in}} = \frac{R_2}{R_1} \tag{6.2}$$

The amplifier described in this Chapter is based on the design of Bruun and Haxthausen [1991].

6.2 Circuit design

Figure 6.2 shows a schematic of the constituent parts of the Blanking amplifier. It was required of the amplifier to record three EMG signals simultaneously, using a bipolar electrode configuration. The recordings were to be made from each of the three Quadriceps muscles of interest, namely, Rectus femoris (RF), Vastus lateralis (VL) and Vastus medialis (VM). This corresponds with the three EMG amplifiers shown in the figure. Each EMG amplifier consisted of a Preamplifier board and a Signal Processing board. The Preamplifier board was connected directly to the recording electrodes and was where the current conveyor circuit was used as the initial input stage of the amplifier. The Signal Processing board performed a number of functions, namely:

1. Generation of the blanking interval (BI) signal.
2. Providing additional gain stages for the measured EMG signals.
3. Providing an isolation barrier for the EMG measurements.

For electrical safety reasons it was required that the subject be isolated from mains earth at all times. However, the Blanking amplifier only provided the means to measure an EMG signal, not to record it. The recording of the signal had to be carried out using separate recording apparatus. In the study discussed in Chapter 8, a Micro1401 data acquisition system, by *Cambridge Electronic Design* (CED), was used for recording. As it is common practice for electronic equipment to be connected to mains earth it was necessary for the EMG amplifiers to

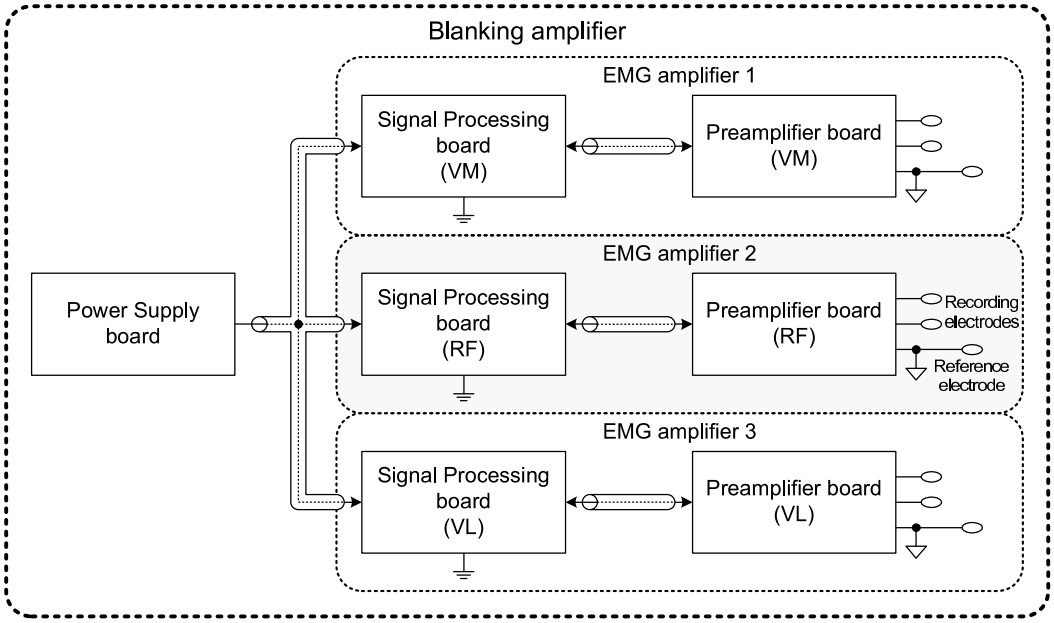

Figure 6.2: Blanking EMG amplifier board layout and shielded interconnections.

be isolated from the recording apparatus. This meant that the Power Supply board was required to produce two isolated supply rails, labelled as ±15VD and ±5VE as shown in figure 6.3.

The supply rail, labelled as 5VC in the figure, is the supply rail used for the microcontroller in the Biphasic stimulator, which generates the blanking interval trigger (BIT) signals. These signals were used by the Signal Processing board to generate the BI signal. The isolation barriers shown in the figure were necessary to ensure that the Biphasic stimulator remained isolated from mains earth and from the Blanking amplifier.

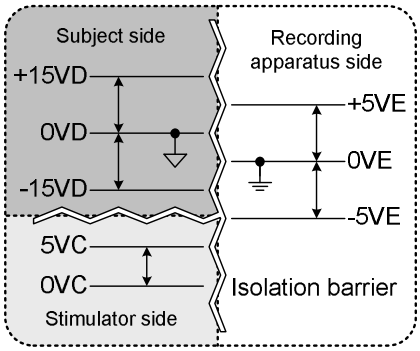

Figure 6.3: Schematic of Blanking amplifier power rails and isolation requirements.

Another consideration of the Blanking amplifier was its required bandwidth. For EMG signals recorded using surface electrodes, the bandwidth of the EMG signal itself is commonly accepted to be in the range 20-500Hz [Basmajian and De Luca, 1985; Bilodeau et al., 1993; Kwatny et al., 1970]. Consequently a cut-off frequency of 1kHz for the amplifier would be more than adequate.

The circuit design of the three boards, shown in figure 6.2, are further discussed in the following sections.

6.2.1 Power Supply board

The circuit schematic for the Power Supply board is shown in figure 6.4.

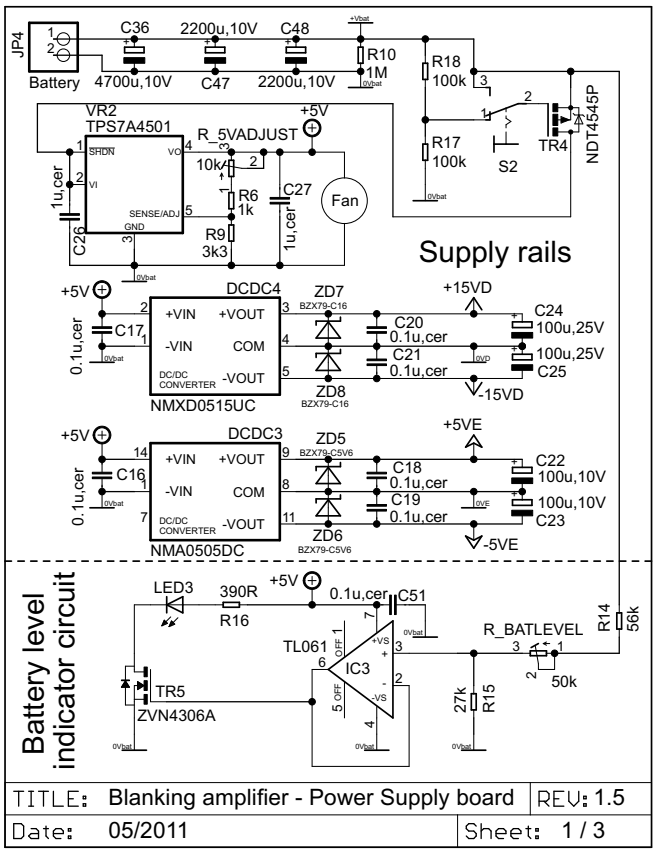

Figure 6.4: Circuit schematic for the Power Supply board.

Supply rails

It was decided to use a $\pm$15V supply for the subject side of the amplifier, and a $\pm$5V supply for the recording apparatus side of the amplifier, as shown in figure 6.3 (labelled as $\pm$15VD and $\pm$5VE in the circuit schematic). The $\pm$15V supply was to maximise the common mode voltage range of the current conveyors in the Preamplifier board (further discussed in Section 6.4.1). On the recording apparatus side of the isolation barrier, the supply voltage was determined by the input range capability of the recording apparatus. For the Micro1401 this was 10V which led to the choice of a $\pm$5V supply.

The Blanking amplifier was to be battery powered. This had the advantage over using a mains supply that 50Hz interference would not be introduced into the amplifier supply rails. This precaution was taken because 50Hz falls within the frequency range of EMG signals, and any such interference could distort the measurements. The switching DC-DC converters used in the Biphasic stimulator had switching frequencies in the order of tens of kilo Hertz, well above the EMG frequency range, which made them ideal candidates for the amplifier's power supply.

During development of the Blanking amplifier, the Preamplifier and Signal Processing boards were built first. It was therefore possible to measure the current consumption of each

EMG amplifier using an ammeter while powering the boards from bench power supplies. This gave supply current requirements of 60mA (180mA total) for the $\pm$15VD supply and 5mA (15mA total) for the $\pm$5VE supply.

The NMX0515UC and NMA0505DC isolated DC-DC converters by *Murata* were selected to produce the two supply rails. The specifications for both converters are given in table 6.1. The required battery current rating was calculated, as laid out in the table. The rechargeable Li-ion batteries and the Low Drop Out (LDO) voltage regulator, used for the Biphasic stimulator, had current ratings of 2200mAh and 1.5A respectively. As both of these ratings were greater than the required battery current it was decided to use the same components in the amplifier's Power Supply board. Large supply capacitors were connected across the battery terminals to reduce ripple.

Table 6.1: Power supply design.

Design parameter	**$\pm$15VD**	**$\pm$5VE**
Measured supply current per amplifier, I_m	60mA	5mA
Total supply current, I_s[a]	180mA	15mA
DC-DC converter	NMXD0515UC	NMA0505DC
DC isolation	1kV	1kV
Nominal input voltage, V_i	5V	5V
Nominal output voltage, V_o	$\pm$15V	$\pm$5V
Maximum output current	333mA	200mA
Rated output power	5W	1W
Efficiency, η	75%	69%
Required output power, P_o[b]	2.7W	75mW
Required input power, P_i[c]	3.6W	109mW
Required input current, I_i[d]	720mA	22mA
Minimum current rating of battery[e]	742mA	

[a] $3I_m$ [b] $|V_o|I_s$ [c] $\frac{100P_o}{\eta}$ [d] $\frac{P_i}{V_i}$ [e] Sum I_i for both supply rails

Battery level indicator

A battery level indicator was used to monitor the battery output voltage. When the battery voltage dropped to 6V the LED would be turned off, indicating that the battery needed to be recharged.

6.2.2 Preamplifier board

Figure 6.5 shows the circuit schematic for the Preamplifier board. By building a preamplifier unit, separate from the rest of the EMG amplifier, the first stage of amplification can be located physically close to the recording electrodes. This allows the electrode leads to be kept as short as possible to minimise motion artefact [Basmajian and De Luca, 1985].

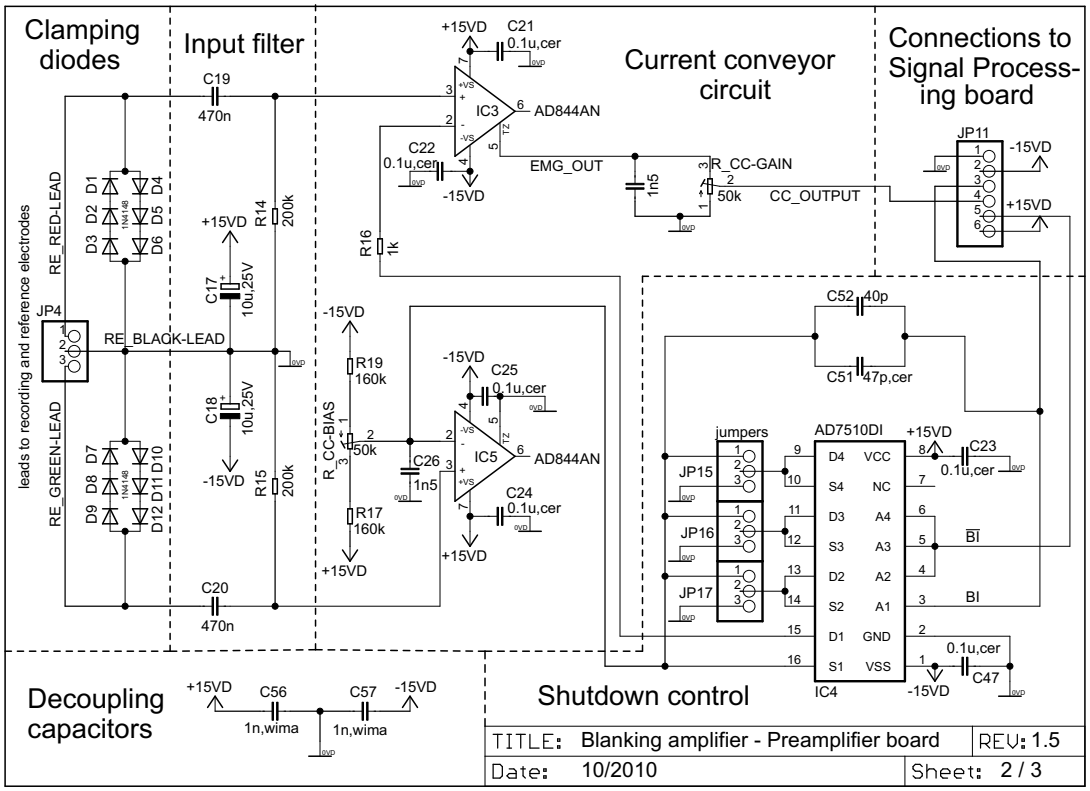

Figure 6.5: Circuit schematic for the Preamplifier board.

Clamping diodes

On the far left of figure 6.5 can be found the connection for the two recording electrodes (REs) and the reference electrode, as necessary for a bipolar electrode arrangement. The three leads, coming from the connector were colour coded:

- Black for the reference electrode, connected to signal ground (0VD) on the Preamplifier board.
- Red for the recording electrode connected to the top current conveyor.
- Green for the recording electrode connected to the bottom (VCVS) current conveyor (refer to figure 6.1).

Voltage clamping diodes were placed between each of the recording electrode leads and the reference electrode. Each voltage clamp consisted of two sets of three 1N4148 signal diodes in series, connected back to back, thereby allowing a voltage swing of no more than 2.1V either side of the reference electrode potential. This was necessary to ensure that any common mode voltage seen at the input of the amplifier did not appear as stimulation artefact at the amplifier output. In the next chapter, Section 7.4.3, discusses a situation where this happened, until the clamping diodes were introduced into the circuit.

Input filter

A simple RC high pass filter just after the clamping diodes, with a cutoff frequency of 1.7Hz, ensured that the EMG signal of interest was centred around signal ground, removing any possi-

ble DC offset that may be present. The RC values used were the same as those found in Bruun and Haxthausen [1991].

Current conveyor circuit

Bruun and Haxthausen [1991] used the AD844, a transimpedance amplifier from *Analog Devices*, to realise the current conveyors. The circuit description and schematic of the datasheet have been included in Section D.1 of the Appendix, for reference.

The gain resistors (R_1 and R_2 in figure 6.1), can be seen in the circuit schematic (figure 6.5), as the 1kΩ resistor (R16) and the 50kΩ potentiometer (R_CC-GAIN), respectively. Bruun and Haxthausen [1991] provides a gain calculation taking into account the resistance of the analog switch ($\sim$75Ω) and the input impedances of the two AD844 ICs ($\sim$50Ω), as shown in equation 6.3.

$$A_v = \frac{R_2}{R_1 + 75\Omega + 50\Omega + 50\Omega} \approx 43 \tag{6.3}$$

This gives a gain of at most 32dB, which is variable due to the potentiometer. However, this is only part of the total gain of the Blanking amplifier, as additional gain stages are included in the Signal Processing board.

Upon inspection of the VCVS current conveyor in figure 6.5, it can be seen that a potentiometer (R_CC-BIAS) is connected to the low impedance node (pin 2 of the AD844), which was absent in figure 6.1 (terminal x of the bottom, VCVS, current conveyor). The purpose of the potentiometer was to provide a variable bias current to one of the AD844 low impedance nodes, thereby ensuring that the same output voltage could be obtained both during and between blanking intervals, in the absence of an input signal. The two voltages are not inherently the same, due to the input bias and offset errors of the AD844 producing a nonzero output voltage, the value of which is different when the amplifier is shut on or off [Bruun and Haxthausen, 1991].

The AD844 datasheet specifies the bandwidth of the AD844 to be around 60MHz for a gain of 1, and 33MHz for a gain of 10. This indicates that the AD844 generally had a bandwidth on the order of a few MHz, which far exceeds the bandwidth requirement of the Blanking amplifier.

Shutdown control

The switching on the low impedance node was realised with an AD7510 analog switch, as used by Bruun and Haxthausen [1991]. The BI signal was used as the control signal for the switch. The remaining three switches of the AD7510 were controlled by $\overline{\text{BI}}$ and connected to either one side of the analog switch or to signal ground, via a jumper. This was a feature included in the circuit of Bruun and Haxthausen [1991], in which switching transients were limited by introducing switching spikes of opposite polarity by means of a *dummy switch*. The jumpers allowed each Preamplifier board to be customised as to how many of the dummy switches were used. However, the dummy switches did not show significant reduction in the switching spikes.

Instead, two capacitors (C51 and C52) were introduced between the BI signal line and the low impedance node of the VCVS current conveyor. The capacitors served a similar function as

the intended purpose of the dummy switches by producing voltage spikes of opposite polarity to those seen at the output of the current conveyor. During initial testing of the amplifier circuit, the inclusion of these capacitors showed promising results, however, this was no longer the case after the PCB had been designed and assembled. It was then found that the switching spikes seen at the output of the amplifier were due to layout issues on the PCB. A more detailed discussion can be found in Section 6.3.3.

Connections to Signal Processing board

The digital control signals, BI and $\overline{\text{BI}}$, as well as the supply rails, ± 15VD and 0VD, originate from the Signal Processing and Power Supply boards, and were connected to the Preamplifier board via a cable. The same cable was used to carry the analog output signal of the current conveyor, CC_OUTPUT, back to the Signal Processing board.

PCB layout

Once again, *Cadsoft* EAGLE was used to design the four-layer PCB, as shown in figure 6.6(a). The board has two power planes and a ground plane, as shown in figure 6.6(b) through 6.6(d), which were placed on the two inner layers and the bottom layer of the PCB. The size and shape of the PCB was customised to fit into a plastic container, small enough to serve as the preamplifier unit of the Blanking amplifier.

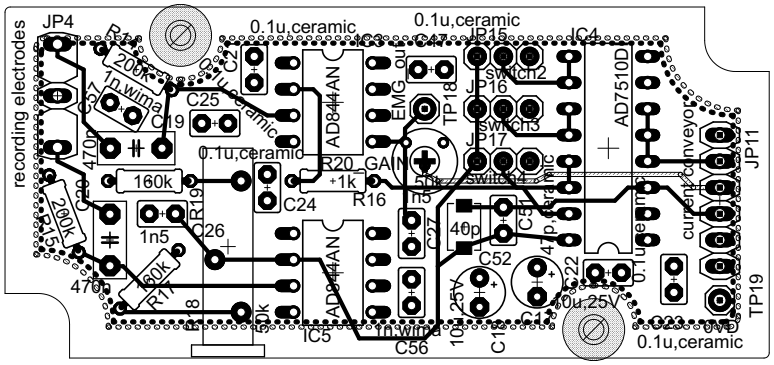

(a) Four-layer PCB.

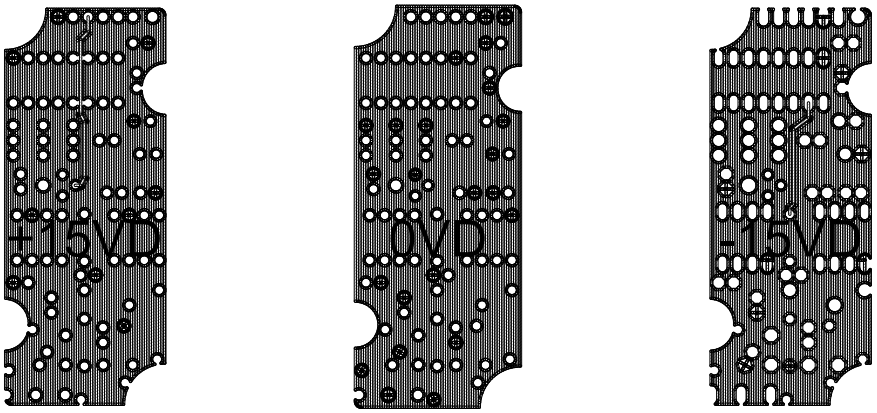

(b) Route 2 - positive power plane. (c) Route 15 - ground plane. (d) Bottom - negative power plane.

Figure 6.6: PCB layout for the Preamplifier board.

6.2.3 Signal Processing board

The circuit schematic for the Signal Processing board is shown in figure 6.7.

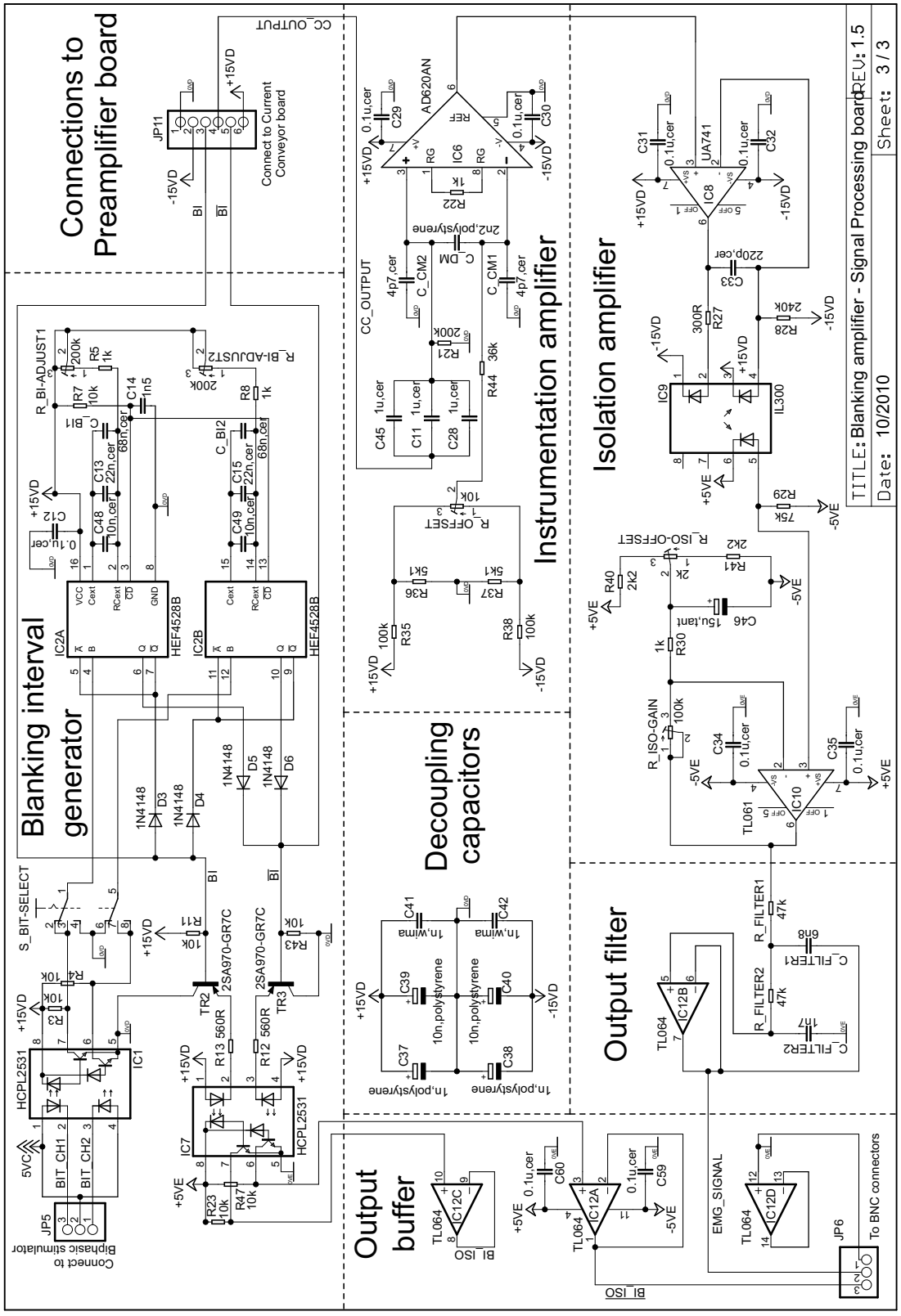

Figure 6.7: Circuit schematic for the Signal Processing board.

Blanking interval generator

The blanking interval generator is responsible for producing the BI and $\overline{\text{BI}}$ control signals which are triggered by the BIT signals, produced by the Biphasic stimulator (refer to Section 5.2.5, *Output board optocoupler driver circuit*).

The BIT signals for both channels, as well as their timing with respect to a stimulation pulse, are shown in figure 6.8. The rising edge of each BIT signal occurs around 23μs (BIT pulse width of 20μs + soft switching delay of 3μs) before the start of a stimulation pulse. The BIT signals are connected to the Signal Processing board via an HCPL2531 optocoupler, which provides isolation between the stimulator and the amplifier, as shown in figure 6.3. A selector switch allows the user to specify whether BIT_{ch1} or BIT_{ch2} or both trigger signals, are used as the inputs to the HEF4528 dual monostable.

The monostable was configured to be rising edge triggered, producing two output pulses, one for each BIT signal. The duration of the output pulses (t_{BIch1} and t_{BIch2}) is variable, ranging from $\sim$40μs up to $\sim$6.5ms, as determined by the 200kΩ potentiometers (R_BI_ADJUST 1 and 2). The two complementary output pulses ($\overline{\text{Q}}$) are combined using a diode logic AND gate to produce the BI signal shown in figure 6.8. Similarly, $\overline{\text{BI}}$ is obtained using the two output pulses (Q) and a diode logic OR gate. By combining the the blanking intervals from channel 1 and channel 2 to form the overall BI signal, the maximum pulse width of the blanking interval would be slightly more than 6.5ms plus the duration of the stimulation pulse. This would give a maximum blanking interval of roughly 8ms for a 400μs biphasic pulse.

These two control signals are connected to the Preamplifier board, and, through an opto-coupler, to the output buffer.

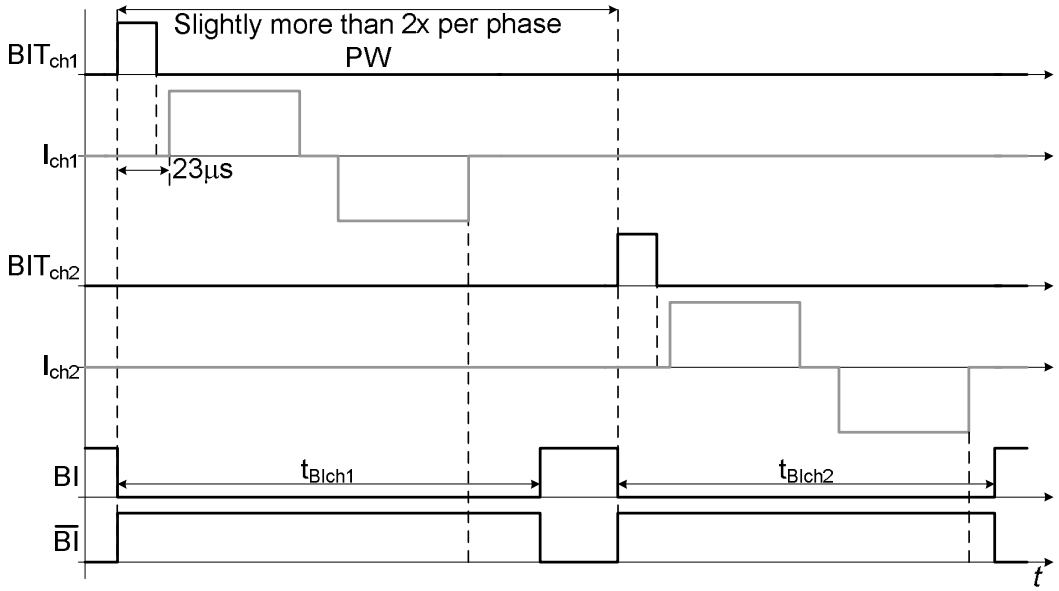

Figure 6.8: Timing diagram for the blanking interval, black traces represent digital signals, while grey traces are analog.

Instrumentation amplifier

The AD620 instrumentation amplifier was used to provide additional gain to the output signal of the Preamplifier board. The CC_OUTPUT signal is AC coupled to the AD620 input, to remove any possible DC offset attributed to the input offset errors of the AD844 [Bruun and Haxthausen, 1991].

According to its datasheet [AD, 2004], the gain of the AD620 can be calculated as in equation 6.4. The gain resistor, R_G, is located between pins 1 and 8, corresponding to the 1kΩ resistor (R22) in the circuit schematic. From this we can calculate that the gain of the amplifier is just over 34dB (or $50\times$).

$$A_v = \frac{49.4\text{k}\Omega}{R_G} + 1 \tag{6.4}$$

In figure 6.7, it can be seen that a resistive network is connected to the inverting input of the AD620 via resistor R44. The purpose of the potentiometer in the network (R_OFFSET), is to allow the user to adjust for any offset in the amplifier output, due to input offset voltages and bias currents. By connecting the potentiometer to the resistive network it ensures that the zero potential (0VD) is roughly in the centre of the potentiometer wiper range, thus allowing the offset to be adjusted for, either side of 0VD.

In the datasheet a bandwidth of 120kHz is specified for a gain of 100. For a gain of 50, the bandwidth could potentially be even greater, which once again, is well above the amplifier's bandwidth requirement of 1kHz. When testing the amplifier, there was initially high frequency switching interference present at the output of the Blanking amplifier. The source of this interference was found to be the DC-DC converters of the Biphasic stimulator (refer to Section 6.4.2). By reducing the excess bandwidth of the AD620, the interference problem was partially solved. A method for filtering high frequencies was suggested in the datasheet, by including the capacitors, C_{CM} and C_{DM}, as shown on the left of figure 6.9. The differential mode cut-off frequency of the AD620 would then be given by equation 6.5.

$$f_{DM} = \frac{1}{2\pi R(2C_{DM} + C_{CM})} \tag{6.5}$$

The circuit on the right hand side of figure 6.9 shows an equivalent circuit of the AD620 as it was realised on the Signal Processing board. The input resistance seen at the non-inverting

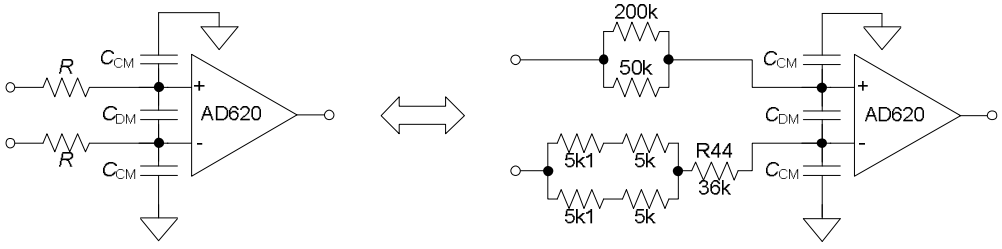

Figure 6.9: Instrumentation amplifier circuit as compared with the suggested filter circuit (reproduced from AD [2004], with permission from Analog Devices).

input terminal can be thought of as the parallel combination of the 50kΩ potentiometer (R_CC-GAIN), at the output of the current conveyor, and the 200kΩ bias resistor (R21), which yields a total of 40kΩ. At the non-inverting input terminal, the resistive network used for the offset adjustment, can be approximated by the parallel resistors shown in the figure, in series with R44, which gives an input resistance close to 40kΩ.

As the AD620 was connected single-endedly, only the differential mode cut-off frequency was of interest. By choosing C_{CM} to be at least one order of magnitude smaller than C_{DM} and designing for a cut-off frequency of 1kHz, the necessary capacitor values were found to be $C_{DM} = 2.2$nF and $C_{CM} = 4.7$pF.

Isolation amplifier

The isolation amplifier, which has been redrawn in figure 6.10, served two purposes. Firstly, it provided the necessary electrical isolation between the subject side and the apparatus side of the amplifier for the measured EMG signal. Secondly, it provided a gain adjustment for the user.

An IL300, linear optocoupler, was used for the isolation amplifier. This optocoupler provides 5.3kV$_{\text{rms}}$ isolation and a high bandwidth, typically greater than 200kHz. The configuration shown ensured that the isolation amplifier could accept bipolar signals, referenced to ground. The choice of resistor values is discussed in Section D.2 of the Appendix.

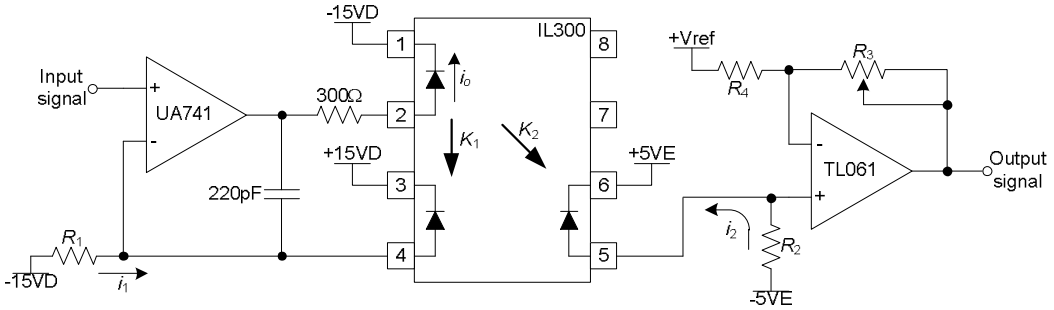

Figure 6.10: Isolation amplifier circuit, after Vishay [2004], with permission from Vishay Intertechnology, Inc.

The gain adjustment is realised with the feedback resistors of the TL061. Choosing $R_3 = 100$kΩ and $R_4 = 1$kΩ, noting that the TL061 is being used as a non-inverting amplifier and accounting for the factor of 3 difference between the supply rails on either side of the isolation, the gain of the isolation amplifier is given by:

$$A_v = \frac{1}{3}\left[1 + \frac{R_3}{R_4}\right] \tag{6.6}$$

By using a potentiometer for R_3 (R_ISO-GAIN in the circuit schematic) the range of the isolation amplifier gain is found to be -9.5dB to 30.5dB (or $0.33\times$ to $33.67\times$). The potential, $+V_{ref}$, to which resistor R_4 is connected is realised with a preset, (R_ISO-OFFSET in figure 6.7).

The total gain of the Blanking amplifier is a combination of the gains due to the current conveyor, instrumentation and isolation amplifiers. Provided the current conveyor gain is set to

its maximum level, the gain range of the Blanking amplifier is 56.5dB to 96.5dB (or 7717× to 72383×). Calibration measurements for the total gain are presented in Section D.3.

Output buffer

Unity-gain op-amps were used to buffer the output signals on the recording apparatus side of the amplifier. The two signals of interest were the complementary blanking interval ($\overline{\text{BI\_ISO}}$) and the EMG signal. While developing the amplifier, the blanking interval signal (BI_ISO) was also used, but later became redundant. As it was originally necessary to buffer three signals, a quad op-amp TL064 IC was used. The input of the fourth, unused op-amp, was connected to signal ground (0VE). Due to the use of ground planes, as discussed in the PCB layout, it was not possible to modify this fourth op-amp for other purposes, as seen in the output filter discussion next. The buffered output signals were wired to BNC connectors, that could in turn readily be connected to the data acquisition system.

Output filter

After including the high frequency filter at the instrumentation amplifier input, the high frequency interference that had been initially seen in measurements, although somewhat reduced, was still present. It was therefore decided to include a second stage of filtration in the form of an output filter. Measurements of the interference and the frequency response of each filtration stage are presented in Section 6.4.2, however, the electronic design of the output filter is discussed here.

Bronzite [1970] presents a design procedure for higher order active filters using unity-gain amplifiers. As an output buffer utilising unity-gain amplifiers was already included in the amplifier design, it was decided to modify the buffer to function as a low pass filter, at the output of the Blanking amplifier.

According to Bronzite [1970], a third order, Butterworth filter, can be realised using the two op-amp units shown in figure 6.11. Furthermore, Bronzite [1970] goes on to say that it is possible to separate the two units with intervening linear circuitry, without influencing the performance of the filter, due to the isolation provided by the unity-gain amplifiers. The passive filter at the input of the instrumentation amplifier, acts as a first order filter. It was therefore possible to exclude the second unit of the Bronzite [1970] filter, while still maintaining an overall third order filter performance (in Section 6.5.1 the frequency response of the EMG amplifiers is shown to have a roll-off close to 60dB per decade). This was a necessary step as only one

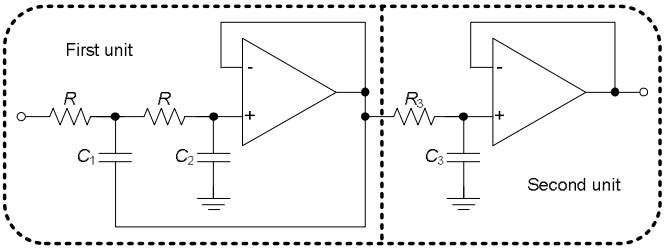

Figure 6.11: Unity-gain amplifier, low pass filter, after Bronzite [1970], with permission.

op-amp was available in the output buffer that could be used as part of the filter.

Bronzite [1970] goes on to provide the following design equations for the capacitor values.

$$C_1 = \frac{1}{\pi f_{3\text{dB}} R} \qquad C_2 = \frac{1}{4\pi f_{3\text{dB}} R} \tag{6.7}$$

For a 3dB cut-off frequency of 1kHz, we can use $R = 47\text{k}\Omega$, $C_1 = 6.8\text{nF}$ and $C_2 = 1.7\text{nF}$.

PCB layout

Figure 6.12(a) shows the PCB layout for the Signal Processing board. As with the Preamplifier PCB, a four-layer PCB design was used in which the middle two layers (route 2 and route 15), and the bottom layer, were used to realise the power planes and ground planes, for the supply

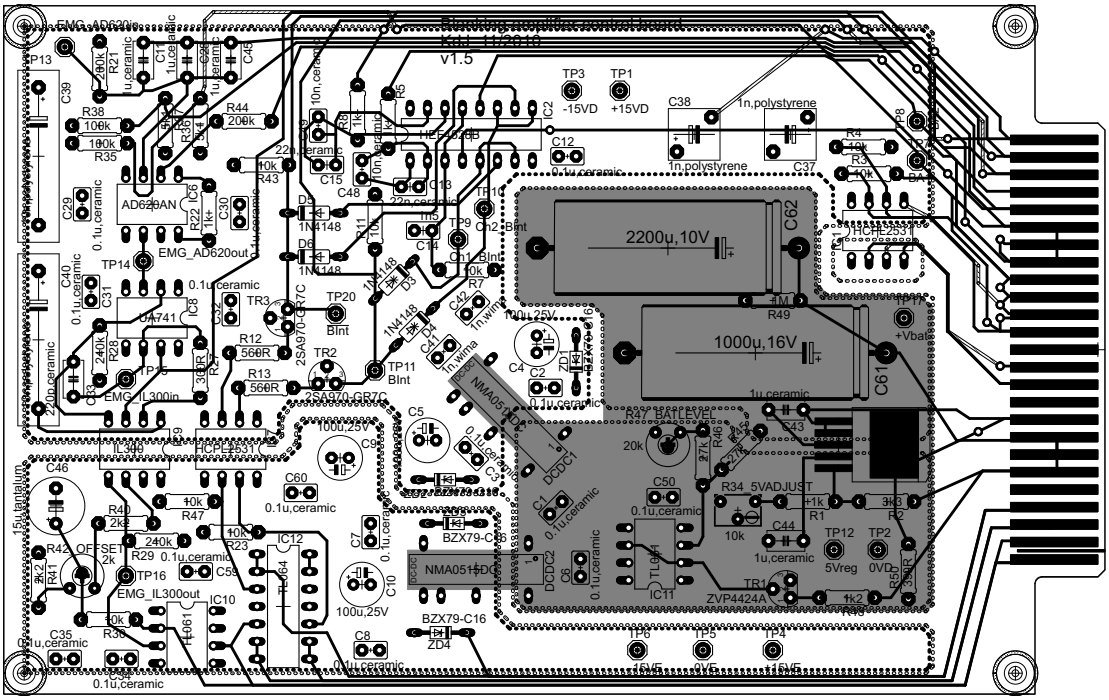

(a) Four-layer PCB.

(b) Route 2 - positive power planes.

(c) Route 15 - ground planes.

(d) Bottom - negative power planes.

Figure 6.12: PCB layout for the Signal Processing board.

rails, shown in figures 6.12(b) through 6.12(d). Isolation between the 5VC, $\pm$15VD and $\pm$5VE supply rails was ensured by introducing isolation barriers in the form of 2mm gaps, between the planes on each layer. The isolating components (HCPL2531 and IL300) were placed across the barriers, while all the other components and the copper tracks were not allowed to cross the barriers.

Originally the PCB was designed for a single EMG amplifier. This meant that the supply capacitors, voltage regulator, DC-DC converters and battery level indicator circuit of the power supply were included on the board. These components fall in the grey section shown in figure 6.12(a), and were the reason for the design of the power planes, 5V_REG and VBAT, as shown in figure 6.12(b). However, in a step to eliminate the high frequency interference caused by the DC-DC converters (refer to Section 6.3.1), it was decided to remove the power supply from the PCB and build the Power Supply board as a separate unit. This meant that all of the components in the grey section were now redundant. Consequently the DC-DC converters were physically removed from the board, and the 5V_REG plane was shorted to 0VD to ensure that the potentials on all the pins of the remaining redundant components were set to a defined value.

Not all of the components in the Signal Processing board were placed on the PCB. Instead, they were located on the front and back panel of the amplifier case. Table 6.2 lists these components and their functions. An edge connector was included in the PCB design to facilitate the connections to these panel components, a wiring diagram of which is shown in figure 6.13.

The edge connector used was a 50$\times$ connector, with 25 pads situated on the top layer (pins CT*n* in the figure) and 25 pads on the bottom layer (CB*n*). The pad connections were grouped

Table 6.2: Front and back panel components associated with the edge connector.

Component	Function
Front panel	
Power LED	Indicator light to show there is power on the Signal Processing board.
S_BIT-SELECT1	Selector switch to determine which channel's BIT signals are used to generate the BI signal.
Cable connector to preamplifier	Power supply for Preamplifier board, control signals BI and $\overline{\text{BI}}$ and CC_OUTPUT signal.
BNC connectors	Output signals (blanking interval and EMG signal) produced by the Blanking amplifier. Facilitates connection to recording apparatus.
R_BI-ADJUST 1 & 2	Potentiometers used to set the BI pulse width for channels 1 and 2.
R_ISO-GAIN	Gain adjustment of EMG signal.
R_OFFSET	Offset adjustment of EMG signal.
Back panel	
Cable connector to Biphasic stimulator	BIT signals produced by the Biphasic stimulator that are used to trigger the BI pulse.

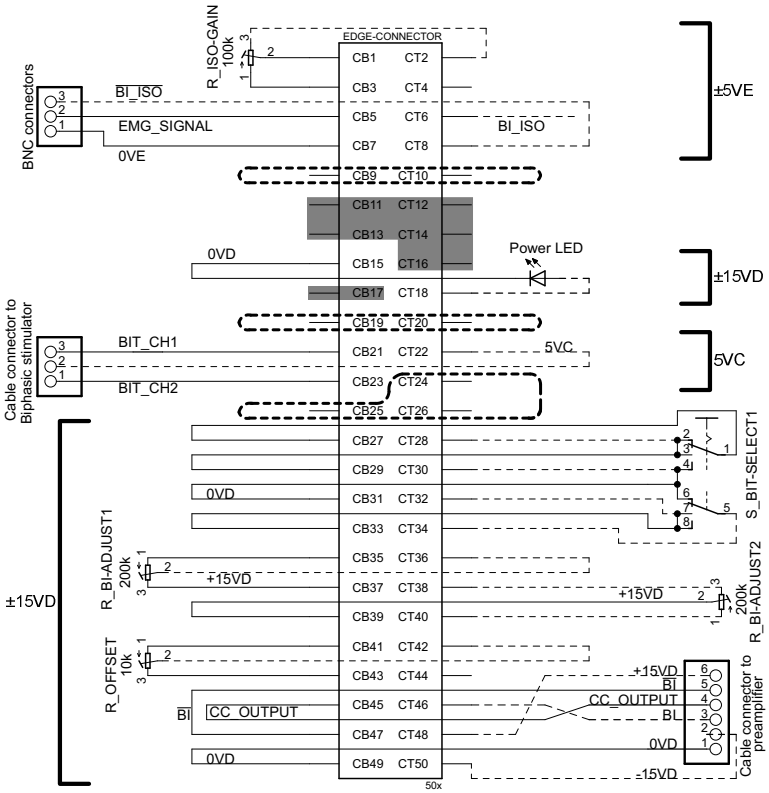

Figure 6.13: Edge connector wiring diagram.

according to the supply rails of the components. Between each of these groups at least one top and bottom pad was left unconnected, thereby serving as an isolation barrier (note the outlined pins in the figure, e.g. CB9 and CT10).

The pins in the grey sections were originally used for connections to and from the redundant components in the PCB and no longer served any purpose.

6.3 Construction and assembly

The Blanking amplifier was assembled as three main parts, namely, the power supply unit, the main amplifier box (in which the three Signal Processing boards were placed) and three preamplifier units. During the construction and assembly phase, a number of interference issues were encountered that it was possible to eliminate through careful consideration of the physical layout of the amplifier.

6.3.1 The power supply unit

As mentioned earlier, the Signal Processing board was originally designed so that the power supply was included as part of the board. This meant that after the main amplifier box had been assembled, with all three Signal Processing boards, there was a total of six DC-DC converters to be found inside the box. Figures 6.14(a) and 6.14(b) show initial measurements taken at the output of the Blanking amplifier. The input to the amplifier was a 10V sine wave as provided by a function generator, connected to the preamplifier through a 1000× resistive attenuator circuit. The output waveform was quite noisy (figure 6.14(a)) and upon closer inspection a 240kHz,

500mV$_{p\text{-}p}$ interference signal was found superimposed on the waveform (figure 6.14(b)).
As the DC-DC converters were the only possible source of this interference it was decided to:

1. Remove the converters from the Signal Processing boards.
2. Build a single power supply to provide power to all three EMG amplifiers.
3. House the power supply in a separate box, thereby reducing high frequency emitted radiation - a likely contributor to the interference when the DC-DC converters were placed within the amplifier box.

After the power supply unit had been constructed, the sine wave measurements were repeated using the same amplifier gain settings, the results are shown in figures 6.14(c) and 6.14(d). The high frequency interference was virtually eliminated.

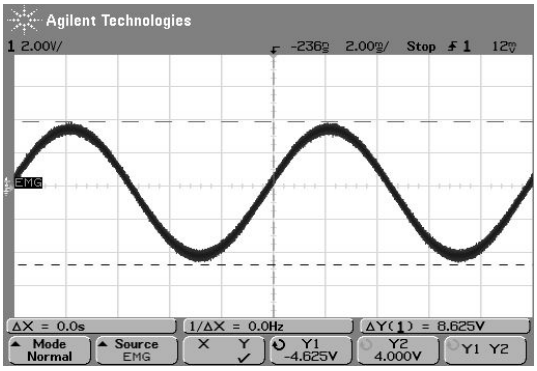

(a) EMG output signal, onboard DC-DC converters.

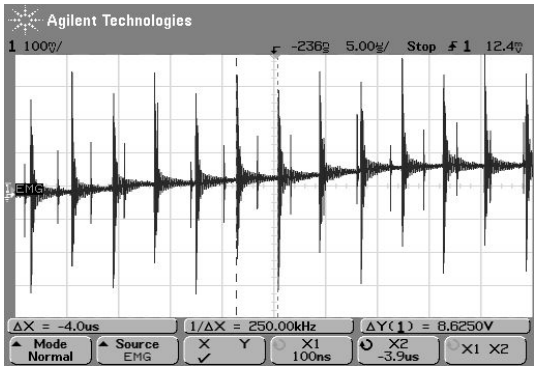

(b) Switching interference due to onboard DC-DC converters.

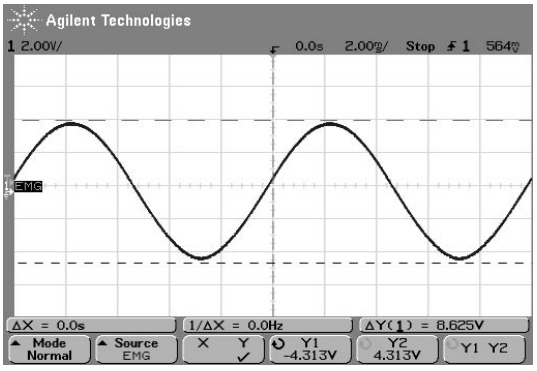

(c) EMG output signal, separate power supply.

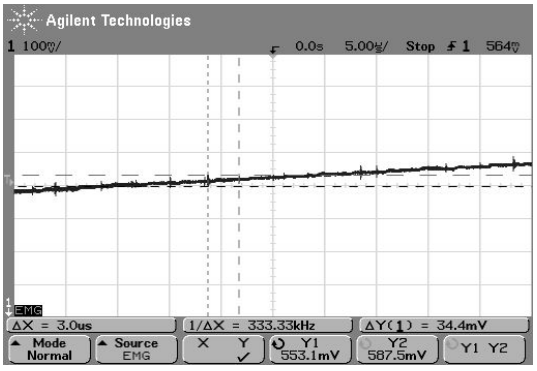

(d) Reduced switching interference with separate power supply unit.

Figure 6.14: Comparison of EMG output signal measured with onboard DC-DC converters and separate power supply unit.

Figure 6.15 shows the assembled power supply unit. The batteries were fastened to the base of the box. The approach used for the Biphasic stimulator was also used here, namely, two batteries were placed in the box, both of which were isolated from the Power Supply board unless the battery lead was plugged into the battery connector. Once again it would be possible to recharge one of the batteries while using the other to power the Blanking amplifier, without compromising the amplifier's isolation from mains earth.

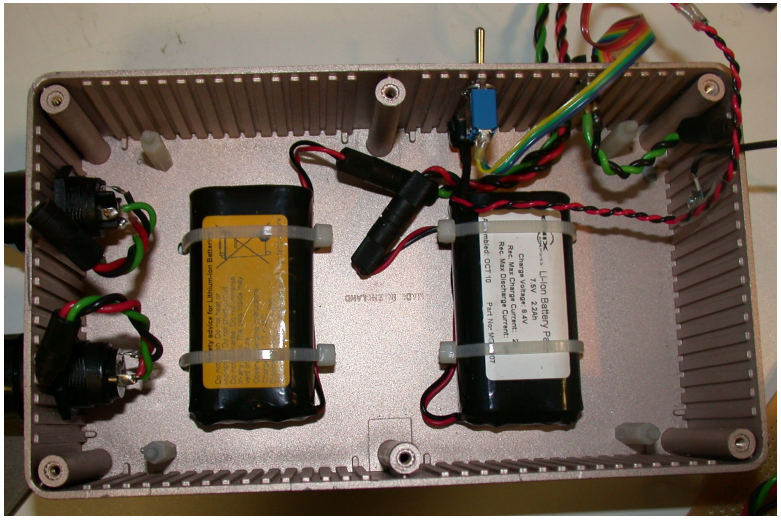

(a) Placement of batteries in the power supply box.

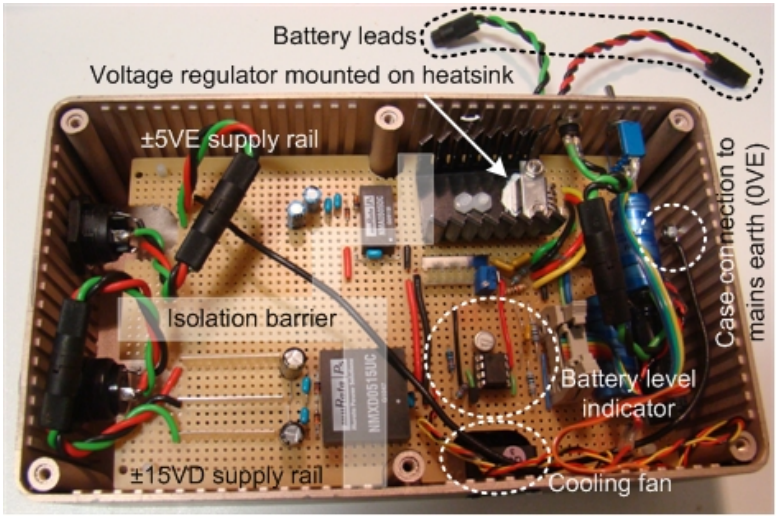

(b) Power Supply board, placed on top of the batteries.

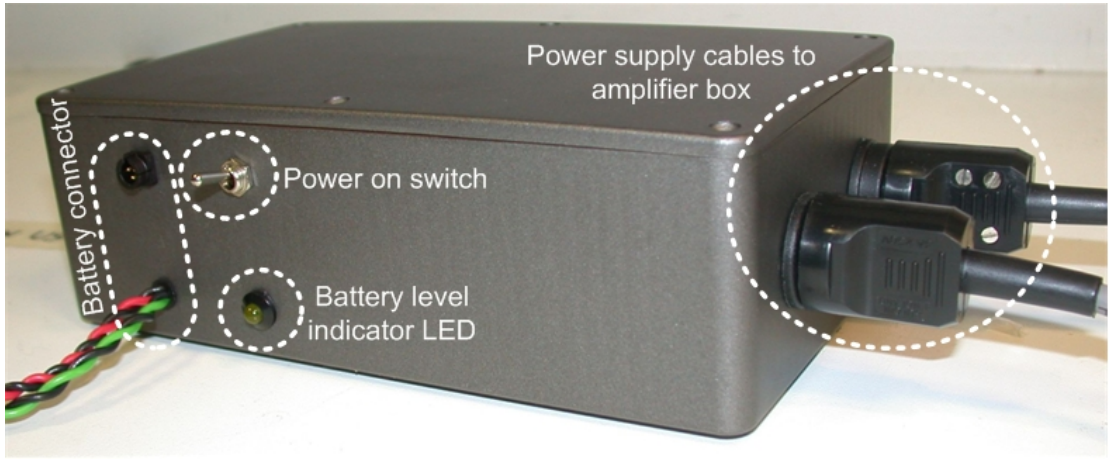

(c) The power supply user interface.

Figure 6.15: The power supply unit.

The Power Supply board was constructed using strip board and placed above the batteries, using nylon spacers. An isolation barrier was introduced between the two supply rails and the rest of the board by removing the copper strips on the back of the board. The location of the barrier has been indicated in figure 6.15(b). Even though the current required by the Blanking amplifier was within the power ratings of the DC-DC converters and the voltage regulator, the components still tended to get quite hot. This led to the voltage regulator being mounted on a heatsink and the introduction of a 5V DC cooling fan.

The box used to house the power supply was shielded. A connection was introduced between the metallic lining of the box and 0VE. In the amplifier box 0VE was connected to mains earth. The cables used to connect the power supply to the amplifier box were also shielded to help reduce any radiated emissions.

6.3.2 The preamplifier unit

The Preamplifier board was placed in a box, separate from the rest of the amplifier, so that the recording electrode leads could be kept as short as possible to reduce motion artefact. However, this meant that the cable between the Preamplifier and the Signal Processing boards was quite long, and therefore susceptible to capacitive coupling between the wires of the cable.

The input terminals of the Blanking amplifier were shorted together, and the outputs of the various amplification stages measured. Figure 6.16 shows the waveform for each stage, current conveyor, instrumentation amplifier and isolation amplifier, (figures 6.16(a), 6.16(b) and 6.16(c), respectively), captured during a blanking interval (top trace of each figure).

Initially, all six of the power and signal lines (as mentioned in Section 6.2.2, *Connections to Signal Processing board*), were bundled together by using a six core, shielded cable. At every stage of amplification a switching spike was present that corresponded with the rising and falling edges of the blanking interval (second trace in figures 6.16(a) through 6.16(c)). The presence of the spike became more evident with each additional gain stage.

It was found that the cause of the spike was mainly due to capacitive coupling between the digital control signal and analog output signals, carried by the cable. Within the six core cable two digital control signals were present (BI and $\overline{\text{BI}}$), as well as the analog output signal of the current conveyor (CC_OUTPUT). The six core cable was then replaced with a three pair, individually shielded cable. The signal lines were grouped, as shown in table 6.3, so that the digital control signals were in a different shielded pair as the analog output signal. In so doing, the switching spike was almost completely removed at the output of the current conveyor and significantly reduced at the instrumentation and isolation amplifier outputs, (see third trace

Table 6.3: Shielded cabling pairs.

Pair 1 (power)	**Pair 2 (digital)**	**Pair 3 (analog)**
+15VD	BI	CC_OUTPUT
-15VD	$\overline{\text{BI}}$	0VD

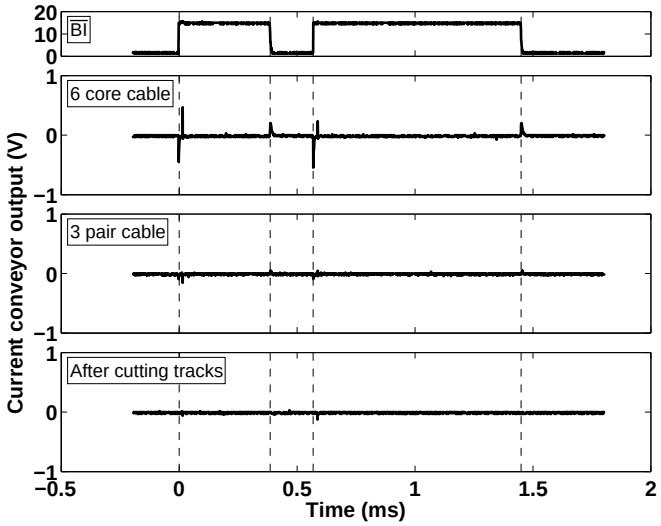

(a) Switching spikes seen at the output of the current conveyor.

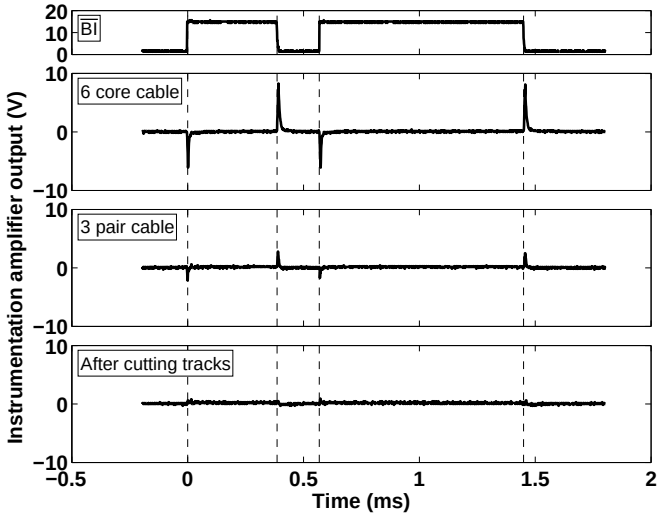

(b) Switching spikes seen at the output of the instrumentation amplifier.

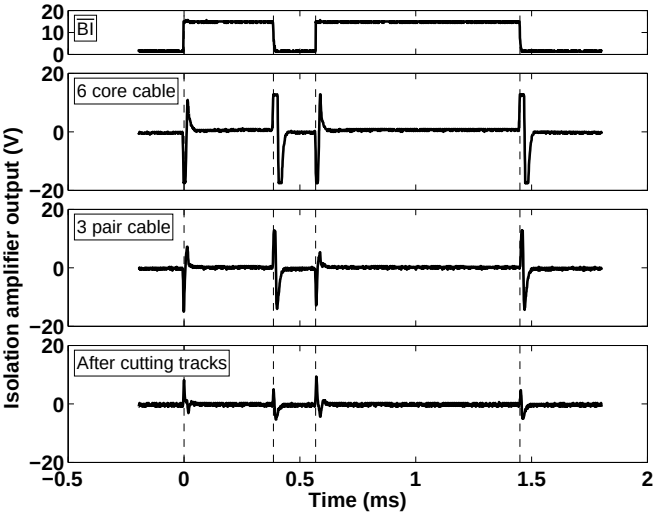

(c) Switching spikes seen at the output of the isolation amplifier.

Figure 6.16: Blanking interval switching spikes.

in figures 6.16(a) through 6.16(c)). Further reduction to the switching spike amplitude was achieved through modifications made to the Signal Processing board (see Section 6.3.3).

Figure 6.17 shows the populated Preamplifier board and the box within which it was housed. The clamping diodes, included at the input of the current conveyor circuit, were not part of the original Preamplifier board design but were a modification made to the PCBs, as shown in figure 6.17(b). The additional wires soldered to the 50k potentiometer (R_CC-GAIN), were necessary as the solder pads on the PCB were mistakenly designed too small. Consequently the contact between the solder pads and the legs of the potentiometer components was not reliable until the wire connections were soldered in place.

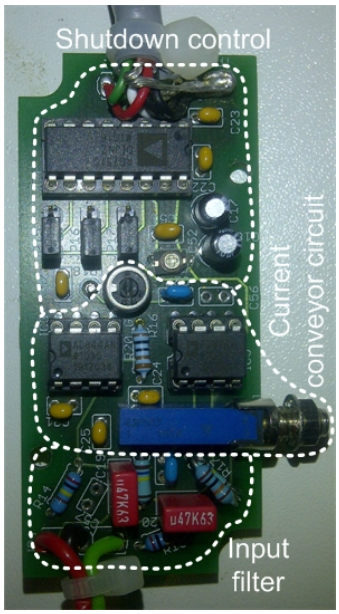

(a) Preamplifier board, front view.

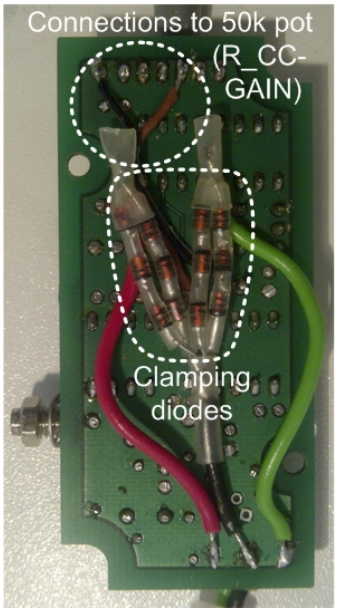

(b) Preamplifier board, back view.

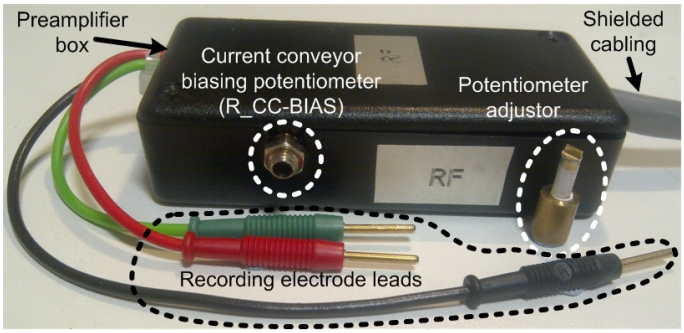

(c) The preamplifier box.

Figure 6.17: The assembled preamplifier unit.

The output voltage during the blanking interval is controlled by the biasing potentiometer (R_CC-BIAS). It was necessary for the user to adjust this level, for each subject individually, using the multi-turn, side adjustment potentiometer. For this purpose a custom made fitting was made[1], labelled in figure 6.17(c) as the *potentiometer adjustor*.

[1] Courtesy Mr Joe Evans

The recording electrodes to be used were the *Ambu Neuroline 720*, self-adhesive surface EMG electrodes. The electrodes come with a 10cm lead wire and a 1.5mm female pin connector. The male pin connectors on the recording electrode leads of the preamplifier were fashioned from a 2mm pin connector, using a lathe.

6.3.3 The amplifier box

It has already been discussed how the switching spikes, seen at the rising and falling edge of the blanking interval, were partly caused by capacitive coupling between digital and analog signal lines in the cable connecting the preamplifier to the amplifier box. Upon closer inspection of the Signal Processing board, a similar situation was seen to occur where a number of digital signal tracks had been routed close to the analog signal tracks. Figure 6.18 shows an enlarged section of the Signal Processing board PCB where the analog tracks are drawn in grey. The signal carried by each track has been labelled, as well as the corresponding edge connector pin number (refer to figure 6.13), that the track is connected to.

The four analog signal tracks shown (CC_OUTPUT and the three R_OFFSET lines) are all connected to the input of the instrumentation amplifier. Four digital signal tracks (BI, $\overline{\text{BI}}$ and the two BIT signals) can be seen to be in close proximity to the analog tracks. To prevent any capacitive coupling occurring, the digital signal tracks were cut and replaced by a shielded cable soldered directly to the board on one end, and, to the corresponding front panel component on the other. This meant that the routed tracks, the edge connector and the ribbon cable used to connect the components to the edge connector, were bypassed, all of which are possible locations for capacitive coupling to occur.

Once again, the output waveform at each amplification stage was measured, while shorting the amplifier's input terminals together. The measurements are shown as the bottom trace in each of the figures 6.16(a) through 6.16(c). Clearly the amplitude of the switching spikes was even further reduced, with the spikes now only evident at the output of the isolation amplifier.

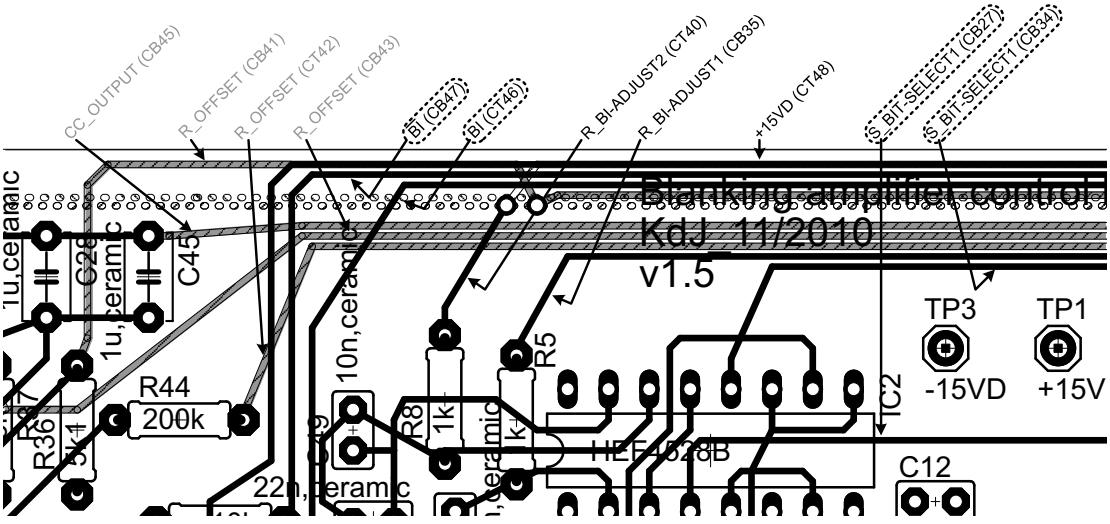

Figure 6.18: Enlarged view of Signal Processing board PCB.

The high overall gain of the Blanking amplifier makes it difficult to further reduce the switching spikes. However, the time constant of the remaining spikes is on the order of a few micro-seconds, which is much faster than the expected M-wave response and hence are unlikely to adversely affect the measurements.

Figure 6.19 shows the front and back views of the populated Signal Processing PCB. In the front view, three modifications that were made to the PCB can be seen. The first is the shielded cables that were used to replace the digital signal tracks. Next, a shunt connection between the 5V-REG and 0VD power planes can be seen, as mentioned in Section 6.2.3 (*PCB layout*). Lastly, a current limiting resistor was included on the board that was connected to the power LED (pin CT18 of the edge connector).

Further modifications made to the back of the Signal Processing board are shown in figure 6.19(b). The 1kHz output filter and the capacitive filter at the input of the instrumentation amplifier were not part of the original Signal Processing board design, and are therefore highlighted as two of the modifications. However, the origin of the interference that these circuits were filtering, was not due to a layout issue within the Blanking amplifier and is therefore not discussed here, but rather in Section 6.4.2. Another modification involved increasing the value of the timing capacitance of the HEF4528 monostable used in the blanking interval generator. This was merely to increase the pulse width of the blanking interval. Lastly, the shielded cables used to connect the Signal Processing board to the power supply are shown.

The three Signal Processing boards were placed in a metal case known as the amplifier box, as shown in figure 6.20(a). The power supply was connected to the amplifier box via the shielded cables shown in figure 6.15(c). However, it was still necessary, within the box, to connect each of the Signal Processing boards to the supply rails, as well as to the BIT signals produced by the Biphasic stimulator. This was achieved by building a Distribution board, shown in figure 6.20(b), from strip board and mounting it in the box. The cables connected to the Distribution board were shielded to reduce any possible emitted radiation originating from the supply rails or the digital BIT signals. The 0VE rail was also connected to the earthed amplifier box via the Distribution board.

For each of the three EMG amplifiers, the components listed in table 6.2 were mounted on the front panel of the amplifier box, as shown in figure 6.20(c). The shafts of the four potentiometers had dials fitted, so that the exact setting of the potentiometer could be monitored. This was necessary for the EMG signal gain adjustment potentiometer (R_ISO-GAIN).

A few additional connectors were to be found on the back panel (refer to figure 6.20(d)). This included the connector for the BIT signal cable from the Biphasic stimulator, connectors for the power supply cables and a mains earth connector, that allowed the amplifier box to be earthed via a connection to the chair electronics box.

Figure 6.21 shows the wiring diagram for the fully assembled amplifier, as well as that of the stimulator discussed in the previous chapter. The subject-side of the amplifier electronics is isolated from mains earth and from the stimulator. As in the case of the stimulator the

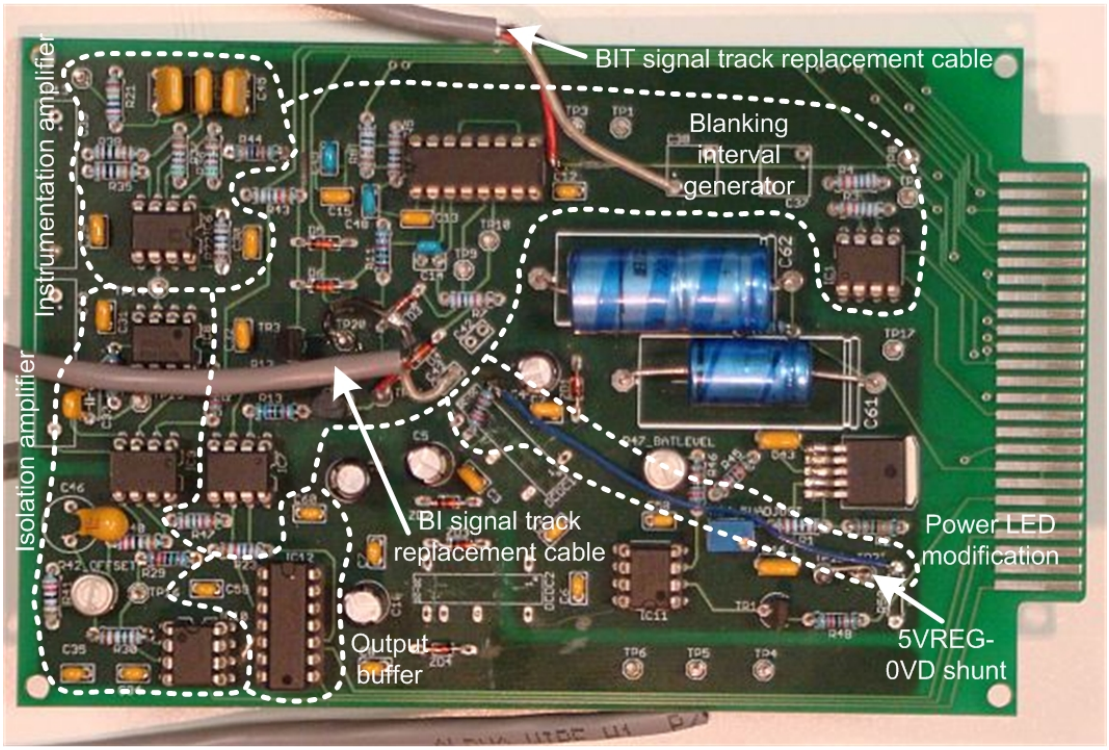

(a) Front view.

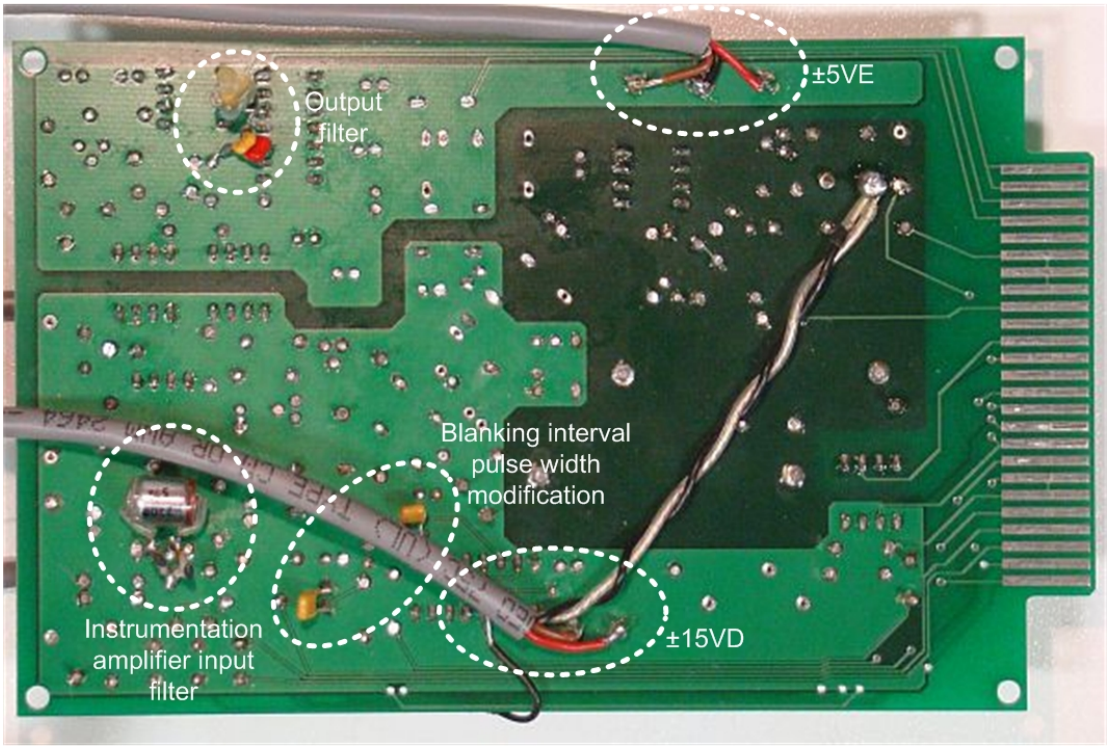

(b) Back view.

Figure 6.19: Photographs of the Signal Processing board.

optocouplers, isolation amplifiers and physical separation were used to realise the isolation barriers. This ensured that there was no direct connection between the subject and either the batteries or mains earth.

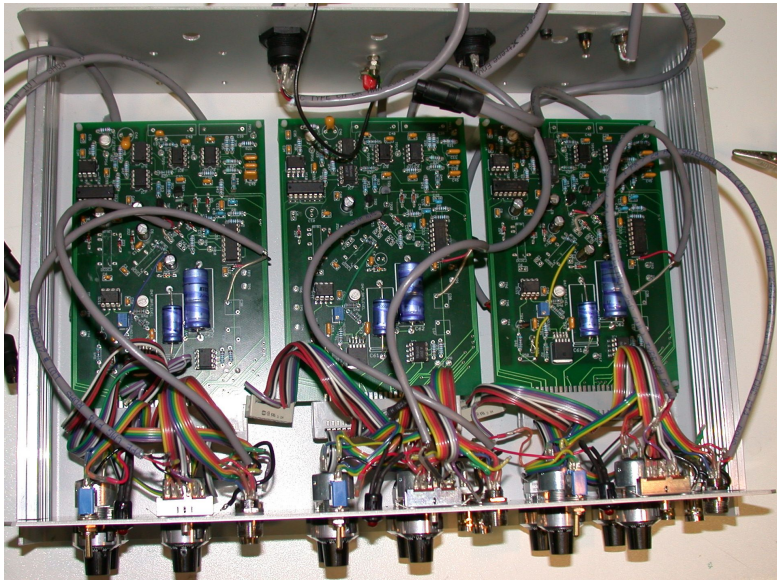

(a) Placement of Signal Processing boards in the amplifier box.

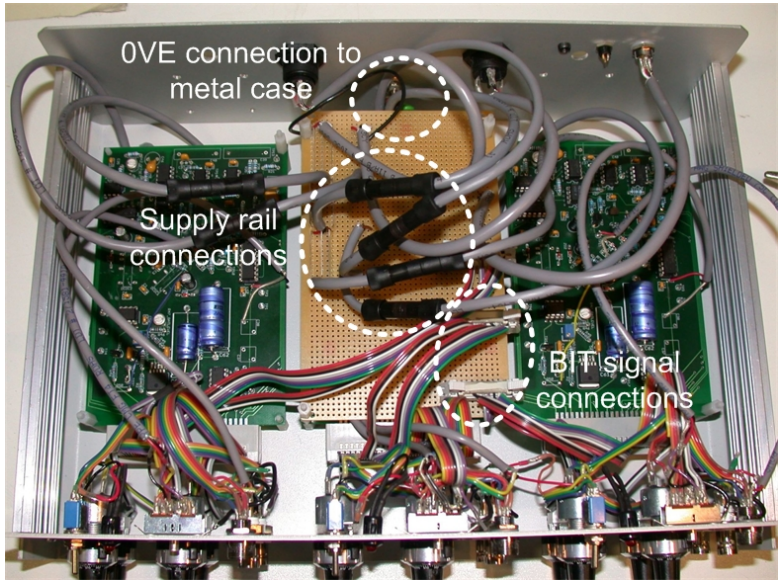

(b) Placement of Distribution board.

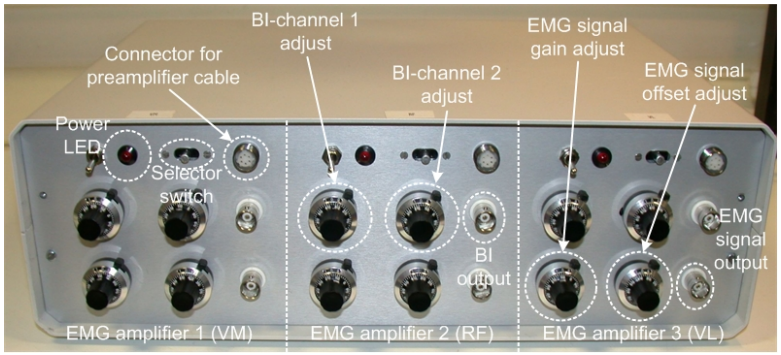

(c) Front panel.

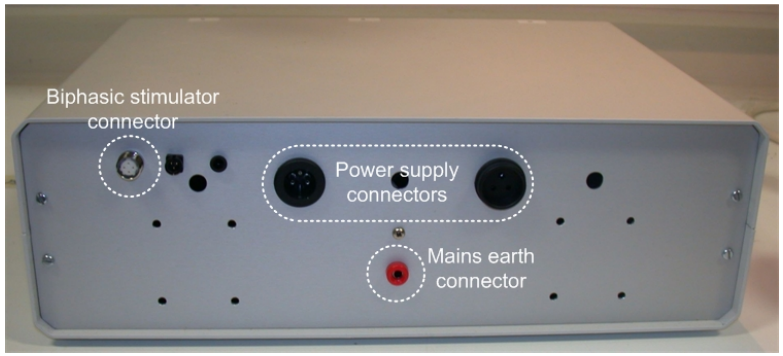

(d) Back panel.

Figure 6.20: Signal Processing board assembly in the amplifier box.

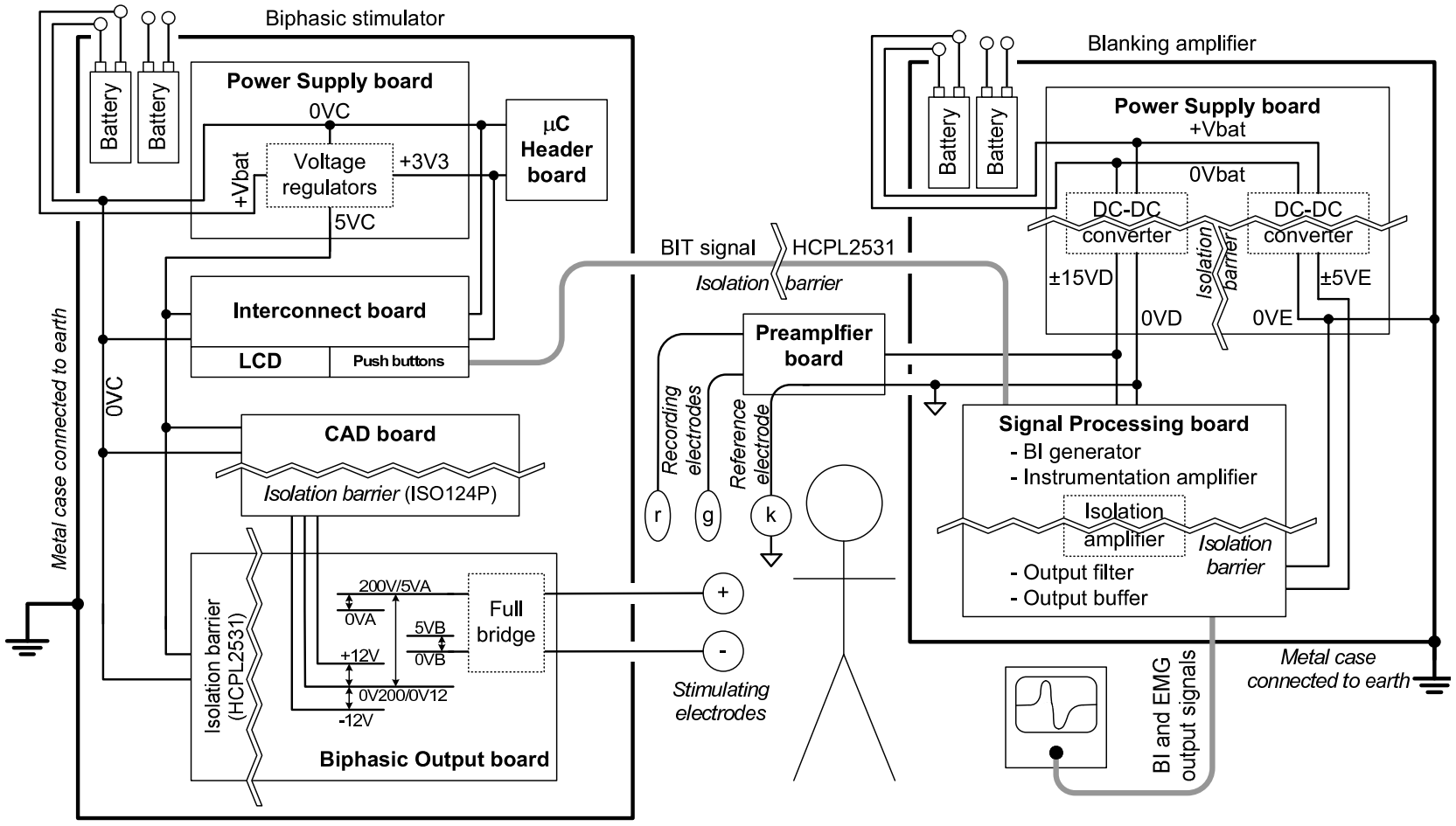

Figure 6.21: Wiring diagram showing the circuit boards, supply rails and isolation barriers, relative to earth, for both the Biphasic stimulator and the Blanking amplifier.

6.4 Amplifier development

The Blanking amplifier discussed thus far is the final version. However, during development some design decisions were influenced by the amplifier's measured performance. In this section the common mode voltage range of the amplifier, as well as interference issues encountered are discussed. Once again the aim of this section is to highlight the practical challenges in electronic design and by extension, those of building a working system.

6.4.1 Common mode voltage range

The common mode voltage range of a differential amplifier is defined as "...the range of the input voltage v_{CM} over which the differential pair behaves as a linear amplifier for differential input signals" [Sedra and Smith, 1998]. According to the AD844 datasheet, the common mode range is equivalent to the supply rails.

This was tested by connecting both input terminals of the preamplifier to a function generator. The amplitude of the input waveform at which the output waveform started to distort, signifying that the amplifier was no longer behaving linearly, was then found. Originally the subject side of the isolation barrier was powered by a $\pm$5VD rail. In figure 6.22(a) the current conveyor and instrumentation amplifier output waveforms (CC_OUTPUT and AD620_OUTPUT respectively) show the start of distortion when the input voltage was measured at 3.2$V_{p\text{-}p}$. This is considerably less than the 10V range of the supply rail.

By increasing the supply rail to $\pm$15VD, a common mode input waveform of 14.8$V_{p\text{-}p}$, still showed no distortion in the output signals (see figure 6.22(b)). This indicated a much larger common mode voltage range, which was preferable as the amplitude of the common mode voltage that the recording electrodes would be subjected to during stimulation, was at this stage, relatively unknown. The greater the common mode range of the current conveyor, the less likely the amplifier would behave non-linearly. Consequently it was decided to use the maximum possible supply rail for the AD844, namely $\pm$15V. In later experiments, discussed in Section 7.4.3 the largest common mode voltage measured was 5.68V, well below the common mode range of the current conveyor.

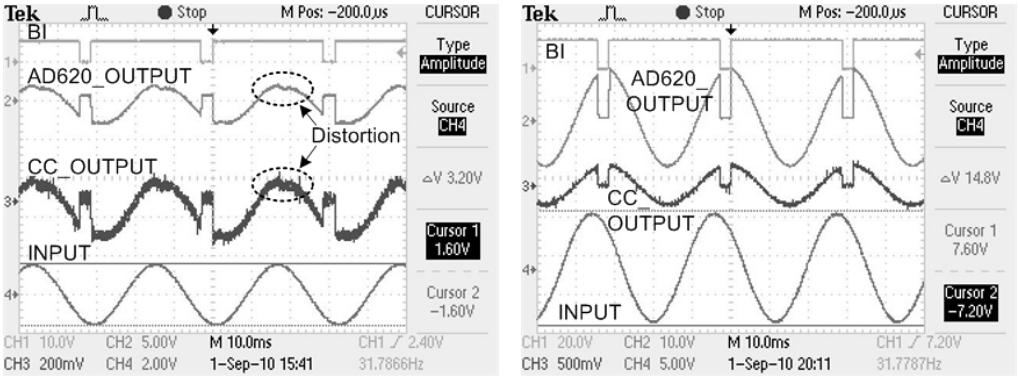

(a) $\pm$5VD supply rail. (b) $\pm$15VD supply rail.

Figure 6.22: Measurement of the Blanking amplifier's common mode voltage range.

6.4.2 Interference reduction

Previously, the interference issues inherent to the Blanking amplifier design, and the steps taken to reduce this interference, were discussed. However, further interference issues were found when the Blanking amplifier was used in a practical setup. Figure 6.23(a) shows the placement of the recording electrodes and the stimulating electrodes on the Quadriceps muscles of a subject's leg. The reference electrode was placed on the knee. Next to it is shown a schematic representation of the setup, that will be used throughout the rest of this thesis to describe the positioning of the electrodes for the various experiments discussed.

In the schematic, the position of the anode-first (+) and cathode-first (-) stimulating electrodes is indicated, as well as the position of the recording electrodes connected to the red (r) and green (g) amplifier input leads. The reference electrode, indicated with a ground symbol, is connected to the black (k) amplifier input lead (internally connected to 0VD). All three EMG amplifiers use the same reference electrode. The orientation of the recording electrodes is also shown, in this case the electrodes were placed longitudinally.

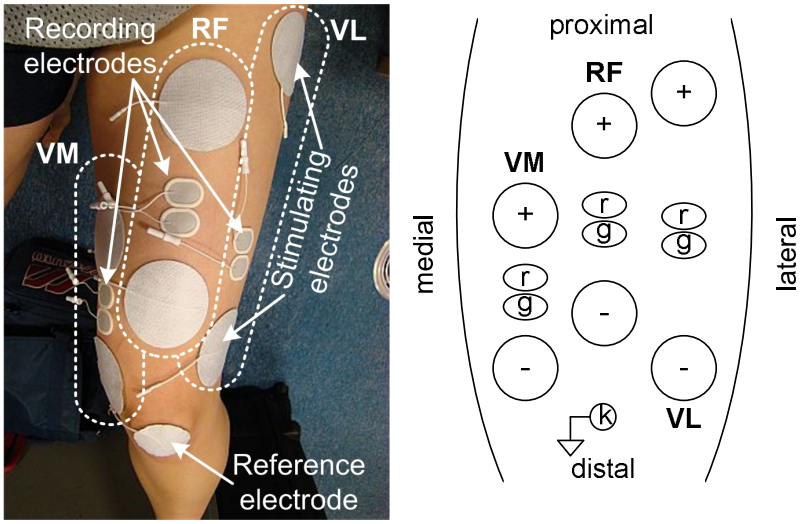

(a) Practical setup. (b) Schematic representation.

Figure 6.23: Positioning of the stimulating and recording electrodes on the Quadriceps.

Using this setup, the EMG in Rectus femoris (RF) and Vastus medialis (VM) with the subject at rest and the stimulator not connected to the stimulating electrodes, was recorded as shown in figure 6.24(a). The stimulator was then introduced into the setup using the stimulation settings shown in the table above figure 6.24.

Figure 6.24(b) shows the same measurement as in 6.24(a), after the stimulator was turned on with current amplitude settings of 0mA. The output EMG waveforms now appear very noisy, due to high frequency interference (on the order of 30kHz) superimposed on top of the EMG signal. The source of this high frequency interference was attributed to the DC-DC converters in the stimulator. During a stimulation pulse, even though there was no stimulation current flowing, the high and low side switches in the output stage of the amplifier were operational,

thereby creating an electrical connection between the subject and the 200V rail of the stimulator (refer to figure 6.21.

The stimulator settings for channel 1 were then changed to $I = 38$mA and $PW_r = 70\%$, for which the RF EMG recording is shown in figure 6.24(c). The inverted M-wave shape can be seen but the signal is still exceptionally noisy. The reason for the inversion of the M-wave, from the conventional M-wave shape discussed in Section 1.2, is to do with the orientation of the recording electrodes, further discussed in Section 6.5.4.

The presence of this high frequency switching interference was the reason for the inclusion of the capacitive filter at the input of the instrumentation amplifier and the output filter (refer to figure 6.7).

Figure 6.25(a) shows the frequency response of the instrumentation amplifier before and after the capacitive filter was added. Before the filter, the bandwidth of the AD620 was around 100kHz. After adding the filter the bandwidth was reduced to 1kHz, and had a roll-off of 20dB per decade (equivalent to a first order low pass filter). Figure 6.25(c) shows an M-wave measured in RF using a similar setup. Clearly most of the high frequency interference was eliminated.

	Quads	T (ms)	PW (μs)	PW_r (%)	I_{stim} (mA)
Ch1	RF	30	200	100	0
Ch2	VM	30	200	100	0

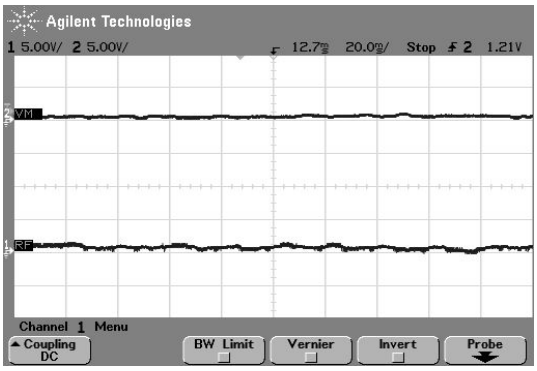

(a) At rest, before connecting stimulator to subject.

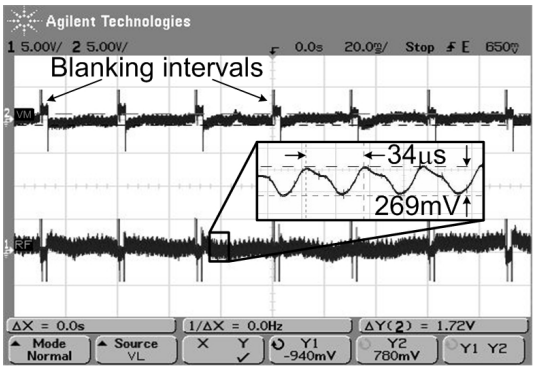

(b) At rest, after connecting stimulator to subject.

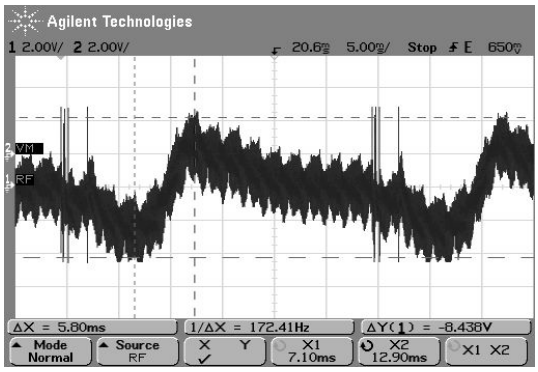

(c) M-wave measured in VM.

Figure 6.24: EMG measurements without filters.

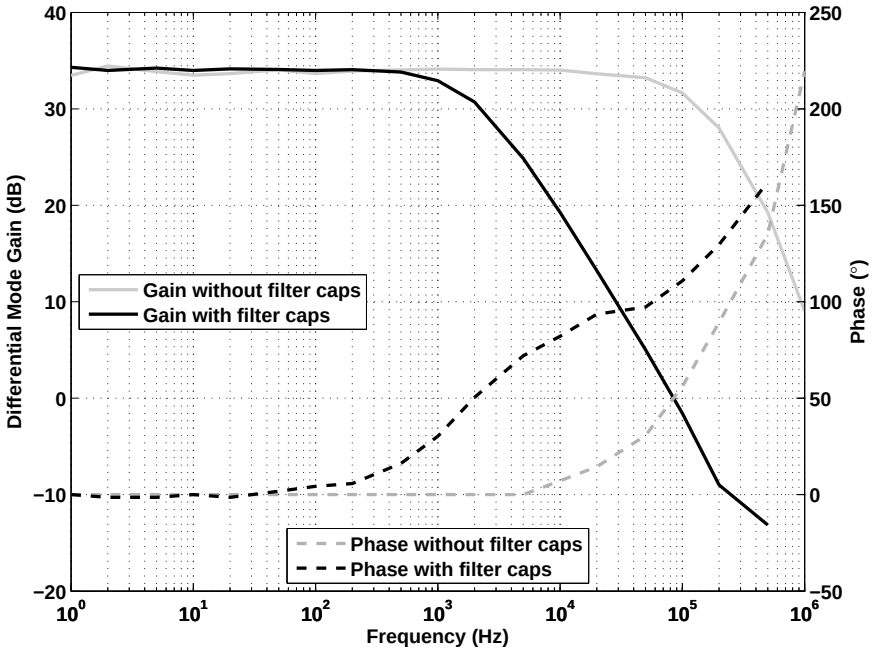

(a) Instrumentation amplifier frequency response.

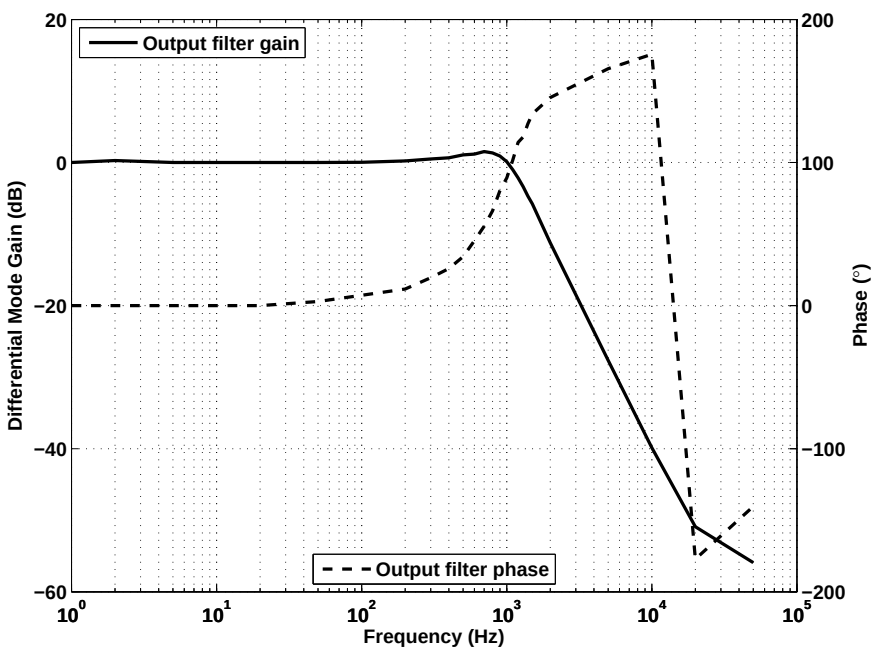

(b) Output filter frequency response.

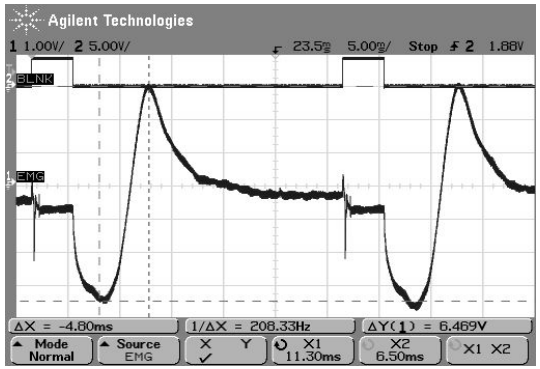

(c) M-wave, after introducing the capacitive filter.

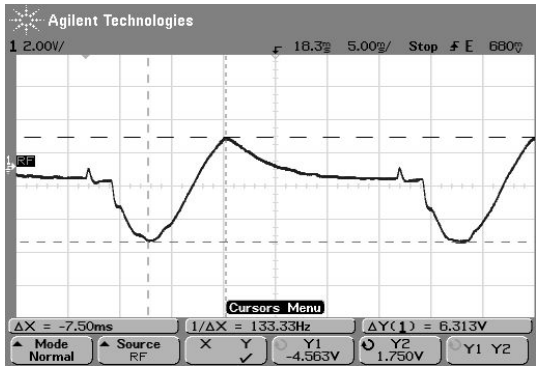

(d) M-wave, after introducing the output filter.

Figure 6.25: Filter frequency response and measured M-waves.

In order to further reduce the interference it was necessary to increase the order of the low pass filter. The output filter on the Signal Processing board served this purpose, the frequency response of which is shown in figure 6.25(b). It has a cut-off frequency of 1kHz and a roll-off of 40dB per decade, indicating that it is a second order filter. This implies that the overall filtering response of the Blanking amplifier would be similar to that of a third order filter with a cut-off frequency of 1kHz (further discussed in Section 6.5.1). Once again the M-wave measurement was repeated with the addition of the output filter. The result is shown in figure 6.25(d). The high frequency interference was no longer evident. The apparent difference in amplitude between the two M-waves shown in 6.25(c) and 6.25(d) is due to different display settings used on the oscilloscope (1V/div for the former and 2V/div for the latter).

6.5 EMG amplifier performance

The performance of the amplifier was characterised by looking at the overall frequency response, the so-called blanking interval response and the transient response. The influence of the orientation of the recording electrodes, on the polarity of the measured M-wave, was also considered.

6.5.1 Frequency response

The differential mode gain of the Blanking amplifier is determined by the potentiometer, R_ISO-GAIN which is found on the front panel of the amplifier box (refer to figure 6.20(c)). The dial, fitted over the potentiometer has numbers ranging from 0 to 84, represented by the variable d_n.

The differential mode frequency response of each EMG amplifier was measured, for a dial setting of $d_n = 6$. Such a low dial setting was chosen so that the output waveform did not clip for the passband frequencies, while the input voltage was still large enough to measure with the oscilloscope. The input was a $10V_{p\text{-}p}$ sine wave, attached through a $1000\times$ resistive attenuator, giving a nominal input voltage of $10mV_{p\text{-}p}$. A choice of $d_n = 6$ gave a good indication of the amplifier performance as, during the study discussed in Chapter 8, the gain settings used for all the subjects ranged from 5 to 12.

The gain and phase plots are shown in figure 6.26(a). All three amplifiers had a flat response over the expected EMG bandwidth of 20-500Hz, with a cut-off frequency around 1kHz. The roll-off is close to 60dB per decade, corresponding with the expected third order filter behaviour mentioned previously. The gain curves of EMG amplifiers 2 and 3 overlap, while the gain curve of EMG amplifier 1 is slightly less than the other two. The gains of each stage of amplification (current conveyor, instrumentation amplifier and isolation amplifier) are determined by resistors. A slight mismatch in the value of these resistors would explain the difference between the curves.

The same dial setting was used to measure the common mode gain of each EMG amplifier, as shown in figure 6.26(b). (Note that these measurements were taken before the clamping diodes were introduced into the preamplifier.) EMG amplifiers 1 and 3 showed similar common mode gain responses, while the response of EMG amplifier 2 was considerably different.

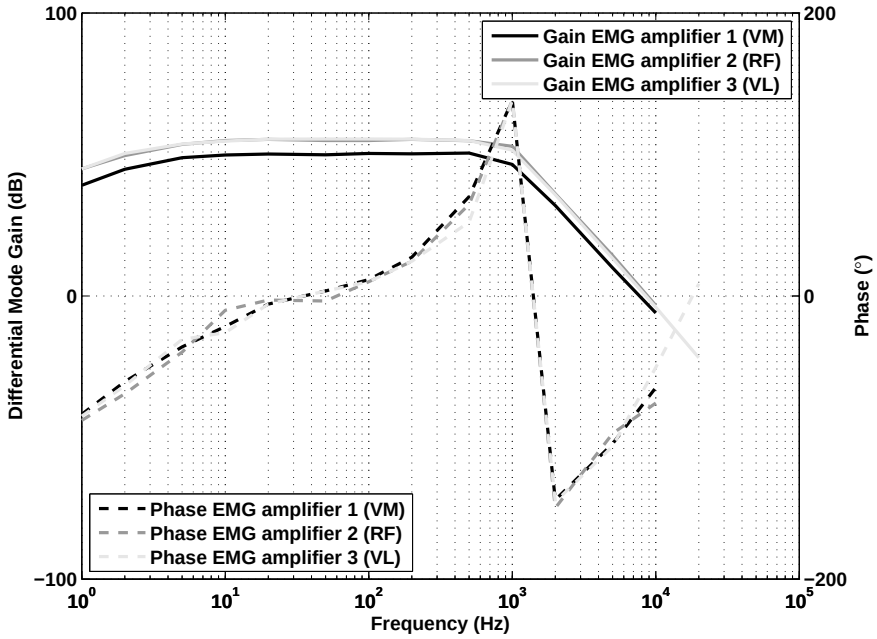

(a) DM frequency response.

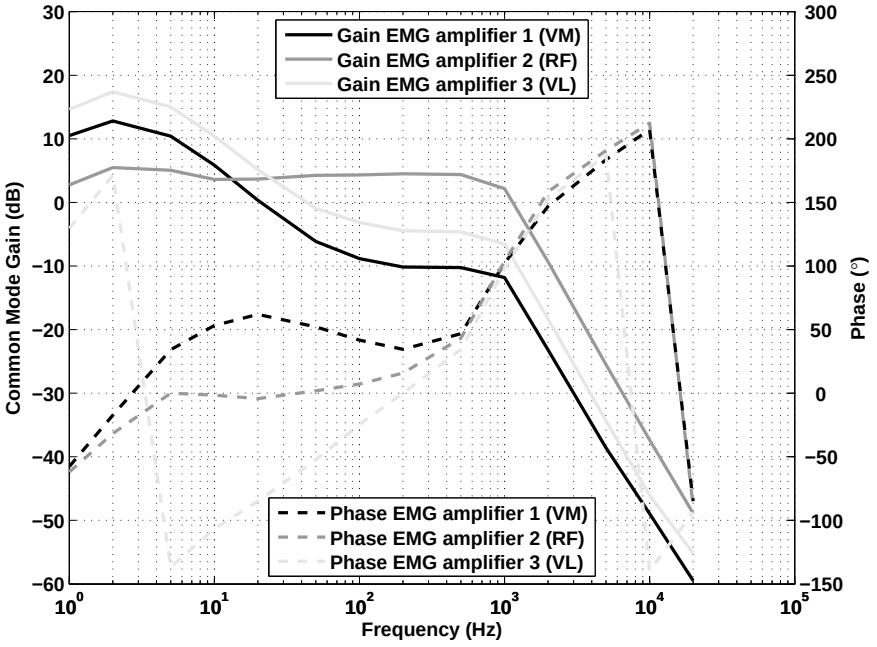

(b) CM frequency response.

Figure 6.26: Frequency response of the three EMG amplifiers.

It should be noted that only the current conveyor circuit was used as a differential amplifier. This means that the common mode gain of the EMG amplifiers is mainly determined by the performance of this circuit.

The difference in the common mode frequency response of EMG amplifier 2 can be explained by mismatches in component values. In particular, if we consider the input filter shown in figure 6.5, any mismatches in capacitors C19 and C20 and resistors R14 and R15 would cause a common mode voltage to appear as a differential mode voltage at the inputs of the cur-

rent conveyor circuit. The capacitors used had a tolerance of only 10%, while the resistors had a tolerance of 1%.

The differential and common mode gains were then used to calculate the Common Mode Rejection Ratio (CMRR), shown in figure 6.27.

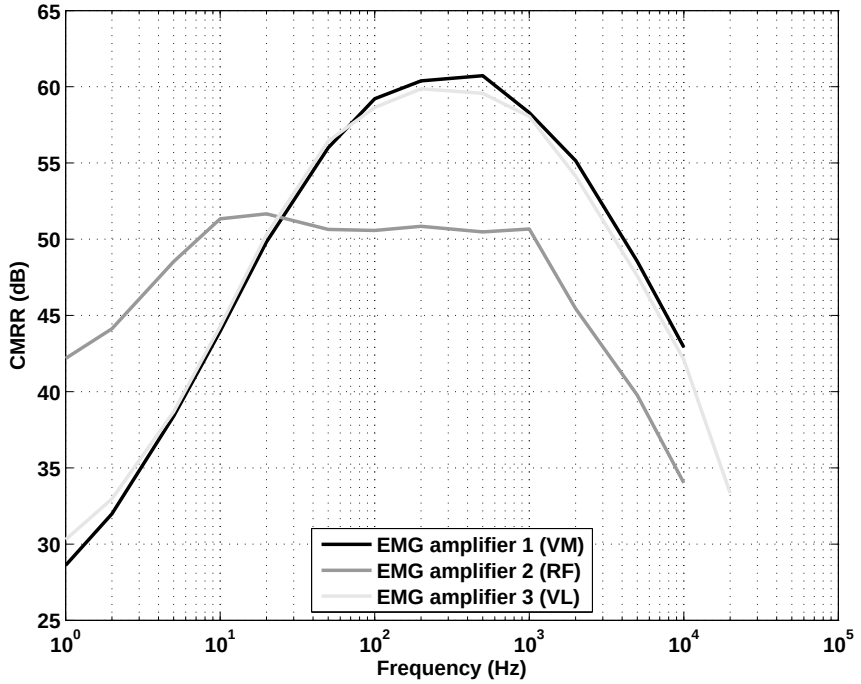

Figure 6.27: CMRR of the three EMG amplifiers.

6.5.2 Blanking interval response

The Blanking amplifier was connected to the Biphasic stimulator, so that a blanking interval (BI) could be triggered. The three input leads of each EMG amplifier were connected together, thereby effectively shorting the two input terminals to 0VD (the reference electrode potential). The output voltage of the three amplifiers was then measured; the gain settings used for each amplifier are indicated in the table above figure 6.28. This setup ensured that, other than the BI trigger connection, there was no connection between the stimulator and the amplifier. Therefore, no stimulation pulse would be present at the input terminals of the amplifier, hence, no stimulation artefact should be present in the output signal.

This was indeed the case in figure 6.28(a). The voltage level during the blanking interval was set to the same level as that measured between blanking intervals by adjusting the potentiometer R_CC-BIAS (discussed in Section 6.2.2, *Current conveyor circuit*). This was referred to as the bias position of the preamplifier being *centred*. However, if the bias position was changed, using R_CC-BIAS, so that the blanking interval voltage level swung to either side of the *centred* level, a transient response was seen, as shown in figure 6.28(b). This transient was not a stimulation artefact, although it has a similar appearance as the stimulation artefacts discussed in Chapter 7. The occurrence of this transient response was termed the *blanking interval response*.

EMG amplifier:	1 (VM)	2 (RF)	3 (VL)
Gain	80.8dB (10968×)	72.6dB (4254×)	78.3dB (8258×)

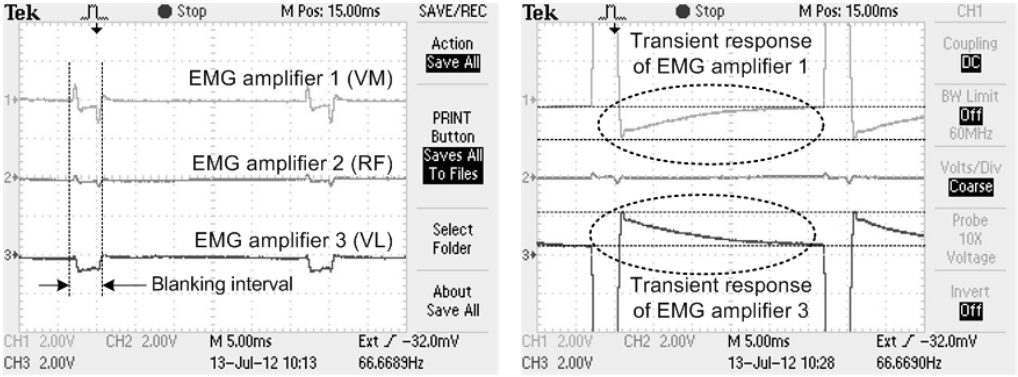

(a) Blanking interval voltage centred. (b) Blanking interval voltage not centred.

Figure 6.28: EMG output signal dependence on current conveyor biasing (R_CC-BIAS).

The magnitude of the BI response was dependent on how far beyond the *centred* position the bias position of the amplifier was adjusted. The transient responses shown in figure 6.28(b) were the worst case scenarios, where the bias position had been adjusted to the limits of R_CC-BIAS.

The origin of the BI response was investigated by measuring the response of the Blanking amplifier at each consecutive stage of amplification. In this manner the BI response was traced to the 1kHz output filter. Figure 6.29 shows the Blanking amplifier response measured at the output of the isolation amplifier, the input of the 1kHz output filter and finally the signal measured at the output of EMG amplifier 3. The pin numbers of the IC's where each measurement was captured have been indicated, and correspond with the circuit schematic shown in figure 6.7.

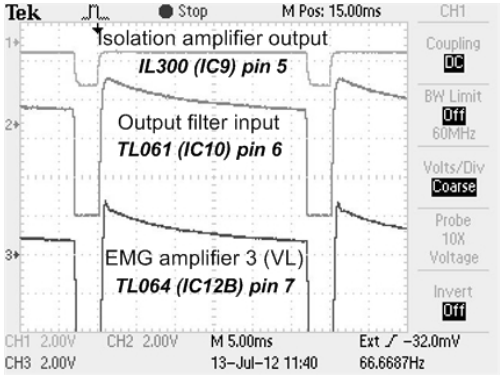

Figure 6.29: Origin of the Blanking interval response.

Up till the output of the isolation amplifier, there is no BI response present. It only appears at the input of the output filter, which is seen to have capacitive feedback from the filter output signal. This implies that the BI response is caused by the inherent transient response

of the output filter. The transient response of the Blanking amplifier is further considered in Section 6.5.3.

The implication of the BI response was that, when taking EMG measurements, it was necessary to ensure that the bias positions of the preamplifiers were *centred*, lest the BI response interfered with the measurement of the M-wave.

Spontaneous changes in BI voltage level

Centering the BI voltage level was not always straight forward as it was found that the voltage level did not stay constant. Figure 6.30(a) shows just such a situation. The top trace was captured at the output of the current conveyor (refer to figure 6.5) while the bottom trace was captured at the input of the instrumentation amplifier (refer to figure 6.7). Each of the traces show two overlapping measurements (dark and light traces), captured shortly after one another, without any changes being made to the experimental setup. In the lower trace the BI voltage level suddenly changed, when the scope probe was connected to the Preamplifier PCB. The voltage level was also seen to spontaneously change if:

1. The reference electrode was moved.

2. The reference potential of the subject was changed, for instance when the subject touched a metal case that was earthed.

3. The stimulation intensity changed, either by changing the amplitude of the stimulation current or by changing the pulse width (as happens during the ramp on and ramp off intervals of the recruitment curve stimulation protocol - refer to Section 4.2.2).

Jitter in EMG measurements

Another difficulty encountered when trying to *centre* the BI voltage level was the presence of jitter in the EMG measurements. Figure 6.30(b) shows how the voltage level of the entire signal, as measured at the input of the instrumentation amplifier, changed with time. This was seen as jitter in the final output of the Blanking amplifier.

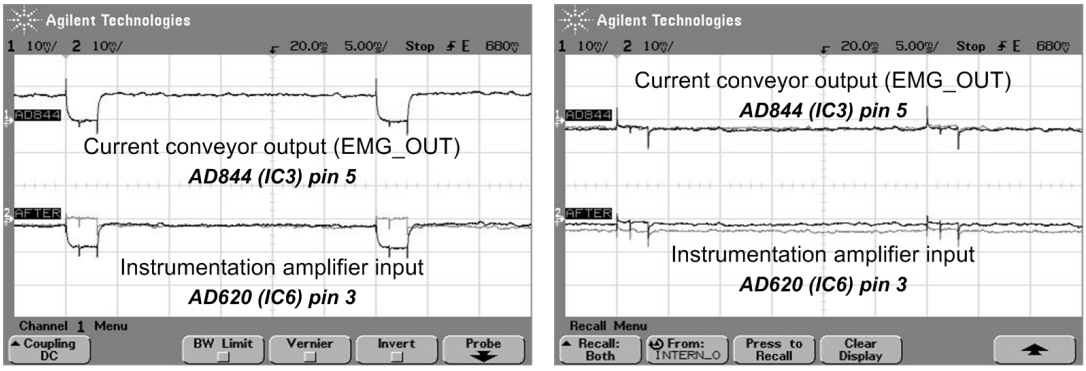

(a) Spontaneous change in BI voltage level. (b) Jitter seen in EMG amplifier output signal.

Figure 6.30: Origin of signal jitter.

Discussion

Between the two measurement points used in figure 6.30, capacitors were included to provide AC coupling (refer to figure 6.7). This was to ensure that the input to the instrumentation amplifier is centred around 0VD. From figures 6.30(a) and 6.30(b), it would appear that the AC coupling is the source of both the spontaneous change in the BI level and the jitter. In both cases the changes were only evident at the input to the instrumentation amplifier and not at the output of the current conveyor.

Consider the Preamplifier circuit, refer to figure 6.5. The presence of the input filter, before the AD844 ICs, ensures that the mean value seen at the current conveyor input is zero. However, by adjusting the BI voltage level (whether intentionally using R_CC-BIAS or spontaneously through changes in capacitive coupling) the mean value of the output of the current conveyor is no longer zero. The second AC coupling stage, between the current conveyor and the instrumentation amplifier, would cause the entire waveform to move up and down, appearing as jitter in the EMG amplifier output.

Recall that the BI voltage level change seen in figure 6.30(a) occurred when a scope probe was connected to the Preamplifier PCB. This had the effect of changing the capacitive coupling between the PCB and earth, when the ground terminal of the probe was connected to 0VD on the PCB. Prior to the scope probe connection directly to the PCB, the connection to earth had been through the shielded cabling connecting the Preamplifier unit to the amplifier box, where another scope prove had created a connection between 0VD and earth on the Signal Processing PCB. When we consider the fact that the reference electrode is directly connected to 0VD, it can be seen that the three situations listed as causing spontaneous changes in the BI voltage level, would all have the same effect of changing the capacitive coupling between the Preamplifier unit and earth, and as a consequence introduce jitter into the measurement.

By removing the coupling capacitors, both problems should be avoided, however, the likelihood that the output signal of the instrumentation amplifier would clip one of the supply rails, would be increased. At present, it is necessary for the user to adjust the biasing potentiometer, while taking measurements, to prevent the occurrence of the BI response, as triggered by a spontaneous change in the BI voltage level. Fortunately even though the BI voltage level did tend to jump around during the recruitment curve stimulation protocol, and although some jitter was present in the entire signal, provided that the BI voltage level was *centred* at the start of the protocol, it was seen to be possible to capture EMG measurements without being hindered by the BI response. For this reason no further steps were taken to eliminate either the spontaneous BI voltage level change or the jitter.

6.5.3 Transient response

The transient response of the amplifier was investigated by using a signal generator to produce a pulse waveform; 10V amplitude, 1ms pulse width, 30ms period. The signal generator was connected to the amplifier through a variable (2× - 1000×) resistive attenuator. All three EMG amplifiers showed similar transient responses, consequently the results from only one ampli-

fier are presented. There was no connection between the stimulator and the amplifier while capturing these measurements, therefore no blanking intervals were present in any of the measurements. It should be noted that all the transient response measurements were captured with the clamping diodes present in the Preamplifier circuit (refer to figure 6.5).

Differential input voltage

Figure 6.31 shows the transient response due to a differential input pulse at the input terminals of the amplifier.

In figure 6.31(a) we can see that the amplifier output at the falling edge of the pulse overshoots the baseline measured just before the start of the pulse. Figure 6.31(b) shows an enlarged view of the pulse waveform and the amplifier response. The pulse measured at the amplifier output is slightly delayed with respect to the input waveform. The shape of the waveform has also been more rounded, as expected due to the 1kHz cut-off frequency of the EMG amplifier.

The amplitude of the falling edge overshoot increased as the amplitude of the input pulse increased, eventually causing the EMG amplifier to saturate. This however seemed to be related to the current present at the input terminals, as opposed to the voltage amplitude, as even when the attenuator was set to $2\times$ and the amplifier was completely saturated, the input voltage was measured at only 53.1mV, due to the presence of the clamping diodes.

Figures 6.31(c) and 6.31(d) show the waveforms measured at the output of the isolation amplifier and the input of the output filter, respectively, (refer to figure 6.7). The transient response is already evident at the output of the isolation amplifier. However, considering the fact that this is after the current conveyor, instrumentation amplifier and part of the isolation amplifier gain stages, the amplitude of the transient response at this point was negligible. However, the response has become far more evident at the input of the output filter. As in the case of the BI response, the output filter transient response is mostly responsible for the EMG amplifier transient response, due to a differential input voltage.

Common input voltage

Similar measurements were taken to investigate the transient response of the EMG amplifiers due to a common input voltage. The results are shown in figure 6.32.

Figure 6.32(a) shows the input and output voltage waveforms, in which the transient response of the EMG amplifier is clearly evident. As with the case of a differential input voltage, increasing the amplitude of the common input voltage also increased the amplitude of the transient response. The measurement shown was captured with an input voltage of 2.313V.

The origin of this transient response was traced to the output of the current conveyor (refer to figure 6.32(b)). This implies that it is due to any mismatch present in the input filters as well as the inherent response of the AD844 ICs. The transient response then remained unchanged throughout all of the amplification stages, including that of the isolation amplifier (see figure 6.32(c)). However, at the input of the output filter, the transient response became more evident, as shown in figure 6.32(d).

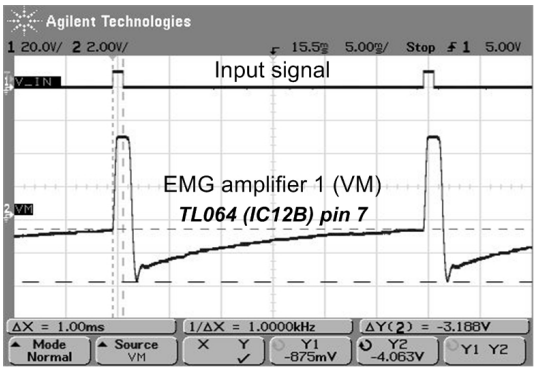

(a) Input and output waveforms, time scale 5ms/div.

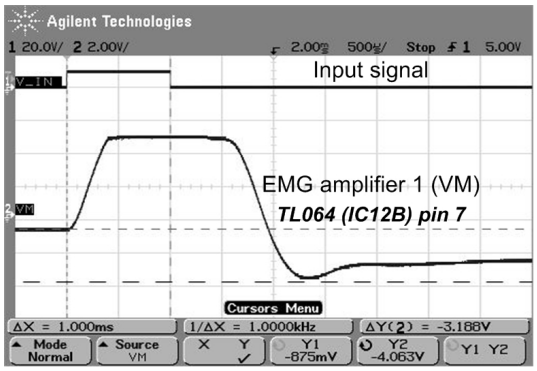

(b) Input and output waveforms, time scale 500μs/div.

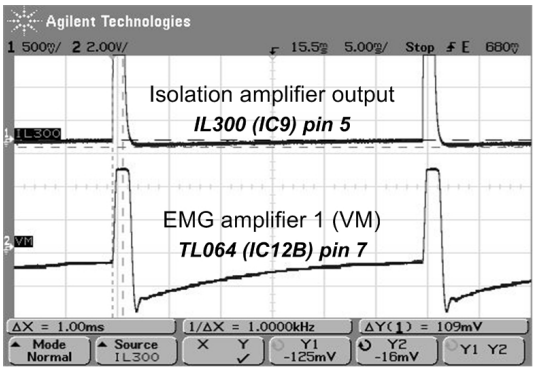

(c) Waveform at the isolation amplifier output.

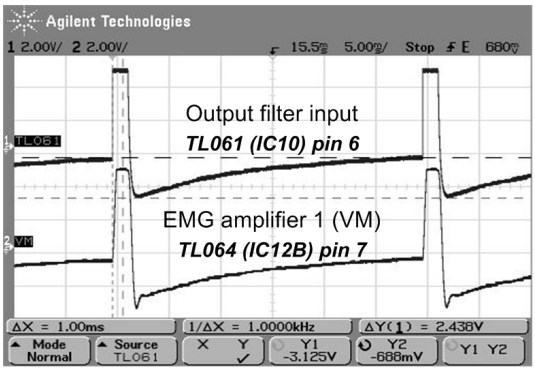

(d) Waveform at the output filter input.

Figure 6.31: Transient response of EMG amplifier 1, differential input voltage.

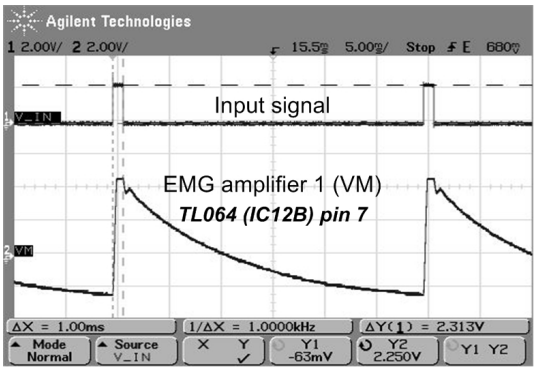

(a) Input and output waveforms, time scale 5ms/div.

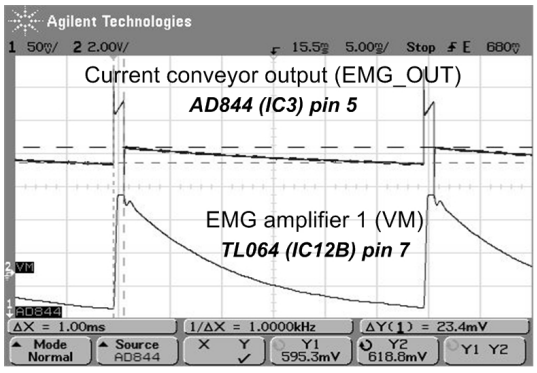

(b) Waveform at the current conveyor output.

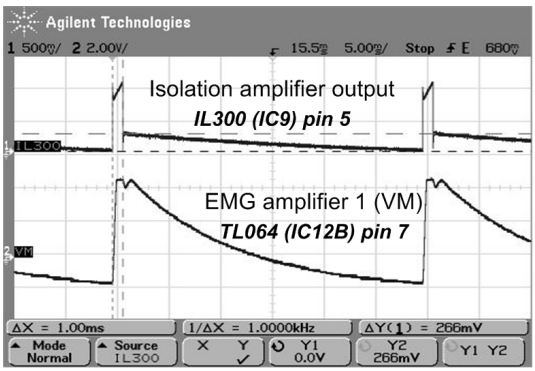

(c) Waveform at the isolation amplifier output.

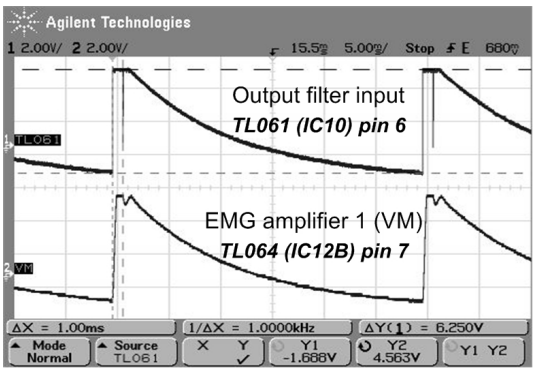

(d) Waveform at the output filter input.

Figure 6.32: Transient response of EMG amplifier 1, common input voltage.

In Section 7.4 a common input voltage was found to be a source of stimulation artefact. While the inherent transient response of the EMG amplifiers played a part in shaping the stimulation artefact, as discussed in Section 7.6.

6.5.4 Recording electrode orientation and M-wave polarity

The orientation of the recording electrodes was found to influence the polarity of the measured M-wave. Figure 6.33(b) shows two M-waves measured in the Biceps brachii muscle of the arm, with the electrode positions shown in figures 6.33(a) and 6.33(c). For both measurements the reference electrode was placed on the elbow, the same stimulation settings were used (as indicated in the table above the figure) and the same EMG amplifier gain setting were used.

The only differences between the two measurements was a reversal in the orientation of the recording electrodes and a slight difference in the stimulation current settings (16mA for position 1 and 12mA for position 2). By reversing the electrode orientation, a corresponding reversal in the polarity of the M-wave was seen. The slight difference in current amplitudes accounts for the difference in M-wave peak to peak amplitudes.

The stimulation artefact was removed by means of suitable adjustments to the pulse width ratio (further discussed in Chapter 7), although the exact setting was not recorded (NR). Furthermore, high frequency interference is seen to be present in the M-waves due to the fact that these measurements were taken prior to the introduction of the 1kHz filter at the amplifier output.

	T (ms)	PW (μs)	PW_r (%)	I_{stim} (mA)
Ch1	2000	200	NR	Varied

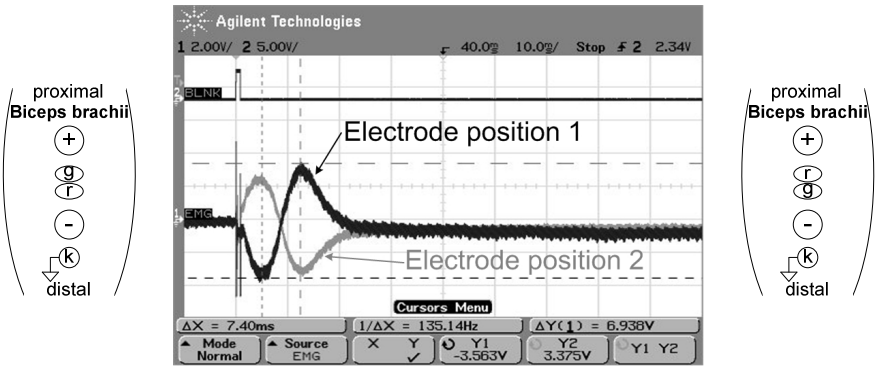

(a) Position 1. (b) Blanking interval (upper trace) and EMG signal (lower trace). (c) Position 2.

Figure 6.33: Influence of recording electrode orientation on polarity of the M-wave.

6.6 Summary

A Blanking amplifier, was designed and constructed that used a current conveyor circuit [Bruun and Haxthausen, 1991] at the input stage to shut down the amplifier during a stimulation pulse, thereby enabling the measurement of the EMG directly after the pulse. The time period during which the amplifier was shut down was referred to as the blanking interval.

The amplifier had three such input stages, so that EMG measurements in each of the three superficial muscles of the Quadriceps, could be measured simultaneously. The design of the amplifier incorporated isolation barriers, for electrical safety purposes.
Two performance issues that arose during the design process were addressed:

1. Switching spikes arose due to capacitive coupling between analog and digital signal lines that were in close proximity to one another. The spikes were reduced by changing the layout of cables and PCB tracks.

2. High frequency interference caused by the DC-DC switching converters was eliminated by building a separate power supply unit, to reduce emitted radiation, and by introducing low pass filters into the amplifier design.

The three EMG amplifiers were characterised, the specifications are provided in table 6.4.

Table 6.4: Blanking amplifier specifications.

	EMG amplifier 1 (VM)	EMG amplifier 2 (RF)	EMG amplifier 3 (VL)
Bandwidth (Hz)	3-1000	3-1000	3-1000
Gain (dB)	51-92	56-96	56-96
CMRR (dB)	60	50	60
Noise (μV)[a]	20	14	16
Supply	Battery	Li-ion, 7.5V, 2200mAh, rechargeable, internal battery pack	
Input impedance[b]	Differential Mode (kΩ)[c]		410
	Common Mode - 1 input terminal (kΩ)[d]		200
	Common Mode - 2 input terminals (kΩ)[e]		100
Output	Voltage range	$\pm$5V	
Assembly	3$\times$ preamplifier units 1$\times$ amplifier box 1$\times$ power supply unit		

[a] Output voltage referred back to input when $I_{stim} = 0$mA.
[b] Calculated by inspection of figure 6.5 at 50 Hz (middle of passband shown in figure 6.26(a)).
[c] $Z_{dm} = \frac{2}{X_C} + 2R = \frac{2}{100\pi \cdot 470\text{nF}} + 2 \cdot 200\text{k}\Omega \approx 410\text{k}\Omega$
[d] $Z_{cm1} = \frac{1}{X_C} + R = \frac{1}{100\pi \cdot 470\text{nF}} + 200\text{k}\Omega \approx 200\text{k}\Omega$
[e] $Z_{cm2} = 0.5\left(\frac{1}{X_C} + R\right) = 0.5\left(\frac{1}{100\pi \cdot 470\text{nF}} + 200\text{k}\Omega\right) \approx 100\text{k}\Omega$

The amplifiers showed a *blanking interval response*, namely the presence of a transient response similar in appearance to a stimulation artefact. This response was present if the voltage level, during the blanking interval, was not adjusted (using a biassing potentiometer) to the same level as that measured between blanking intervals.

The transient response of the amplifiers were measured and found to be a bandpass characteristic of the output filter. The role this played in the measured stimulation artefacts is further discussed in Chapter 7.

Chapter 7

Stimulation artefact: understanding the causes and reducing the effect

7.1 Introduction

To recapitulate, the difficulty with measuring EMG signals, when the recording electrodes are placed between the stimulating electrodes is the fact that the stimulation pulse can cause the amplifier to saturate. Often, the period of time required for the amplifier to recover is so long that the EMG signal of interest cannot be measured. The Blanking amplifier, discussed in the previous chapter, prevented the saturation of the EMG amplifiers, thereby enabling the EMG signal to be measured directly after the stimulation pulse. However, even with the aid of the blanking, it is not unusual for there to be a residual stimulation artefact present in the EMG signal [Parsa et al., 1998].

The stimulation artefact typically appears as a spike, followed by an exponential decay [McGill et al., 1982], the amplitude and time constant(s) of which, depend on several factors [O'Keeffe et al., 2001], including the "stimulator output characteristics, the interelectrode impedance, and the relative geometry of stimulation and detection electrodes" [Knaflitz and Merletti, 1988].

The presence of the stimulation artefact is also more prevalent when using surface electrodes for stimulation. When wire or needle electrodes, or nerve cuffs, are used, the "current field is limited to a relatively small tissue volume and does not extend to the region of space that contributes to the voltage sensed by the detection electrodes" [Knaflitz and Merletti, 1988]. However, these methods are invasive and not relevant to this thesis.

According to Scott et al. [1997], the "effective duration of the stimulus artefact depends upon the stimulator and stimulating electrodes chosen and on the impulse response of the preamplifier". If the latency of the M-wave is sufficiently long, the M-wave itself will not overlap with the artefact [Harding, 1991], however, the closer the recording electrodes are to the stimulating electrodes, the shorter the latency. In the case where the recording electrodes are placed between the stimulating electrodes, the M-wave usually starts directly after the stimulation pulse. This can result in the two responses overlapping [Harding, 1991].

Figure 7.1 shows a set of measurements that were recorded using the Biphasic stimulator and Blanking amplifier. Experimental results have been included in the introduction to illustrate the various facts discussed in the literature.

In figure 7.1(a) the amplitude of the stimulation current was set below threshold value for a muscle contraction, so as not to generate an M-wave. Initially, directly after the blanking interval, a stimulation artefact can be seen that fits the description given by Knaflitz and Merletti [1988] and McGill et al. [1982]. By adjusting the pulse width ratio, PW_r, setting it was possible to eliminate the stimulation artefact.

Figure 7.1(b) shows a similar set of measurements where the amplitude of the stimulation current was above the threshold value. Initially the stimulation artefact and the M-wave overlap, as predicted by [Harding, 1991]. As a result, the M-wave is so distorted that it is impossible to accurately measure the peak-to-peak amplitude or duration. In some cases the stimulation artefact was so severe that the presence of the M-wave was completely obscured. After adjusting the PW_r setting, the stimulation artefact was removed and the M-wave was easily discernible.

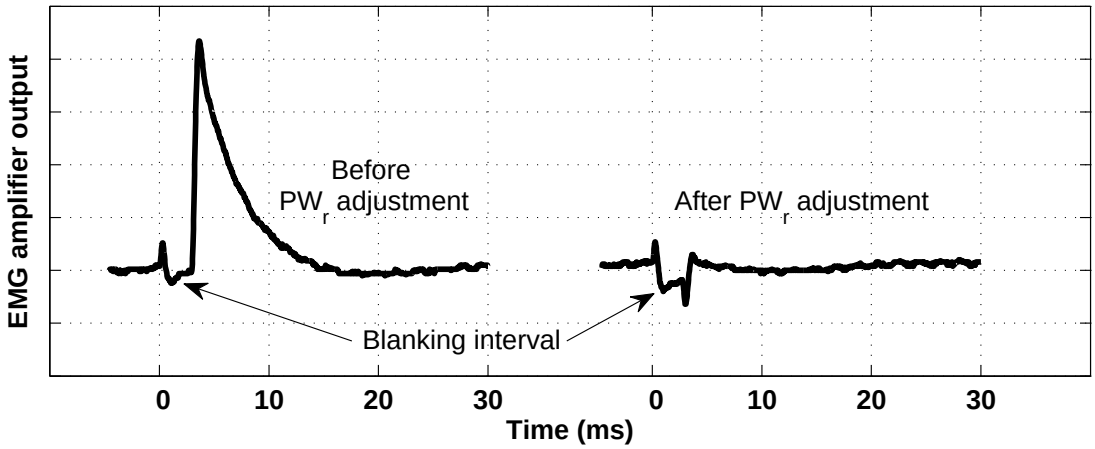

(a) Stimulation intensity below threshold.

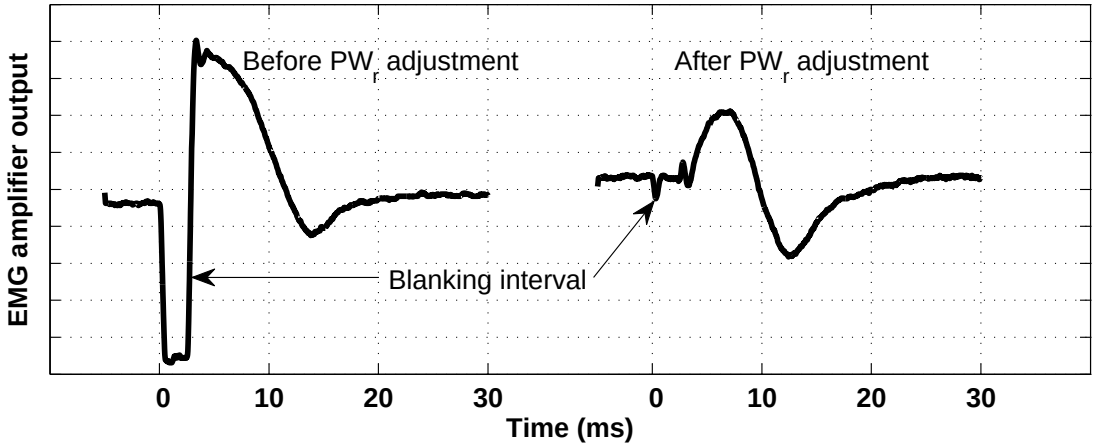

(b) Stimulation intensity above threshold.

Figure 7.1: Influence of stimulation artefact on EMG measurements.

McGill et al. [1982] and McLean et al. [1996] both discussed the cause of the stimulation artefact as a product of several factors, namely:

1. The stimulation current, travelling through the limb of the subject, sets up a voltage gradient, that appears across the recording electrodes [McGill et al., 1982; McLean et al., 1996].
2. Common mode voltage present at the recording electrodes [McGill et al., 1982].
3. Shaping by the recording amplifier - the passage of the spike through the recording amplifier's high-pass filter introduces a slow exponential tail into the signal [McGill et al., 1982].
4. Displacement current travelling through the body tissue and via stray capacitance to ground [McLean et al., 1996].
5. Electromagnetic or capacitive coupling between the stimulating and recording leads [McLean et al., 1996].

McGill et al. [1982] also proposed an electrical model that had to be considered when investigating the various causes. The constituent parts of the model were:

1. Stimulator type.
2. Electrode/skin interface
3. Subcutaneous tissue of the limb.
4. The recording amplifier.

Scott et al. [1997] went on to say that the relative importance of each of these factors depended on "a number of parameters specific to the measurement system." He also showed that the individual causes could be investigated separately, as the total stimulation artefact could be considered to be the linear sum of the individual causes.

In this chapter, the various factors responsible for the stimulation artefact, specific to the *Stimulator-Body-Amplifier* system, realised with the Biphasic stimulator and the Blanking amplifier, are looked at. Of the five main causes listed above, only two were identified as being relevant, namely the voltage gradient and the common mode voltage. These causes were discussed by taking into account the relevant parts of the model, the most important being the electrode skin-interface. The resistance of the tissue of the limb being stimulated and the input impedance of the amplifier, were also touched on.

By developing a better understanding for the mechanisms causing the stimulation artefact it was possible to reduce, or, in some cases completely eliminate the artefact (refer to figure 7.1(b)). This, in turn, had a large influence on the experimental setup and protocols followed during the study discussed in Chapter 8.

7.2 Voltage gradient

During a stimulation pulse, current flows between the two stimulating electrodes, from the anode through the tissue, to the cathode, as shown in figure 7.2. The current density will be greatest closest to the stimulating electrodes, while midway between the two electrodes the current density will be much smaller [McLean et al., 1996]. Kornfield et al. [1985], McGill et al. [1982] and McLean et al. [1996] pointed out that a voltage gradient is set up in the tissue by the flow of the stimulation current, with equipotential lines occurring perpendicular to the direction of current flow.

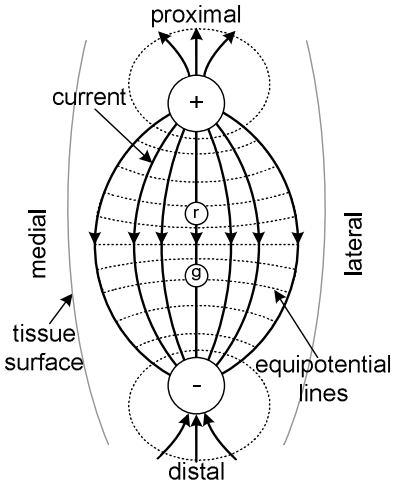

Figure 7.2: Schematic representation of current flow between stimulating electrodes.

This voltage gradient would cause a potential difference between the recording electrodes (shown in the figure), which is seen as a stimulation artefact at the output of the amplifier. They went on to say that, by increasing the distance between the stimulating and recording electrodes (i.e. by moving the stimulating electrodes further apart while keeping the recording dipole length fixed), the effect is greatly reduced. This is caused by the voltage gradient decreasing due to the rapid attenuation of the stimulation current density, as one moves away from the stimulation site.

However, this was not the case for our study, where the recording electrodes would always be placed in close proximity to the stimulating electrodes. Kornfield et al. [1985] also investigated the cancellation of the stimulation artefact by positioning the stimulating electrodes in such a way so that the recording electrodes lay on equipotential lines. Although this method is effective, it is not always practical, as tissue is a non-homogeneous medium, implying that the current flow lines would not be uniformly distributed as in the figure.

It stands to reason that the voltage gradient would be present only when a current was flowing through the tissue. In an ideal case this would be restricted to the duration of the stimulation pulse. Between pulses, there would be no current flowing, and the blanking capability of the amplifier would prevent the appearance of stimulation artefact, caused by the stimulation current. Figure 7.1(a) shows this was not the case. To understand the origin of this stimulation artefact we had to consider the *Stimulator-Body-Amplifier* system unique to our setup.

In Chapter 5 the output stage of the Biphasic stimulator was shown to include a blocking capacitor, C_b and a discharge resistor, R_d (refer to figure 5.4). Figure 7.3 shows the *Stimulator-Body-Amplifier* system, with the location of C_b and R_d explicitly shown.

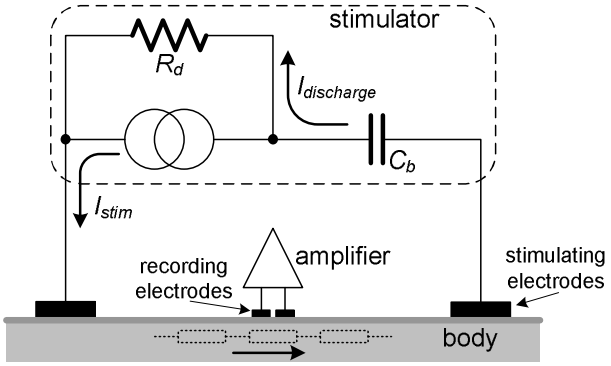

Figure 7.3: Path of the discharge current in the *Stimulator-Body-Amplifier* system.

The purpose for including C_b was to ensure that under fault conditions a DC current would not be passed through the subject. The resistor, R_d, was included as a discharge pathway for the blocking capacitor, as in practice the Biphasic stimulator would not have exactly equal charge in the two phases. In Section 5.6.1, it was shown that a non-zero voltage was measured across the blocking capacitor, between stimulation pulses. This would in turn cause a non-zero average discharge current to flow through R_d between pulses, thereby setting up a voltage gradient in the tissue.

A number of experiments were carried out to show the voltage gradient principle and its influence on stimulation artefact.

7.2.1 Electrode orientation and stimulation artefact polarity

Method

The stimulating and recording electrodes were placed on Rectus femoris (RF), with the reference electrode on the knee. The stimulation artefact was then recorded for different orientations of both types of electrodes, without any changes to the stimulation intensity. The results are shown in figures 7.4 and 7.5; the stimulation settings used are indicated in the table between the two figures.

Results

Reversing the position of the anodal and cathodal stimulating electrodes showed a corresponding reversal in the polarity of the stimulation artefact (refer to figure 7.4). A similar reversal result was seen when the positions of the stimulating electrodes were kept constant, but the positions of the recording electrodes were reversed (refer to figure 7.5).

Discussion

This agrees with the voltage gradient hypothesis, as the voltage would be greatest close to the anode, and smallest close to the cathode. By switching the positions of the stimulating electrodes, while keeping the positions of the recording electrodes the same, the direction of

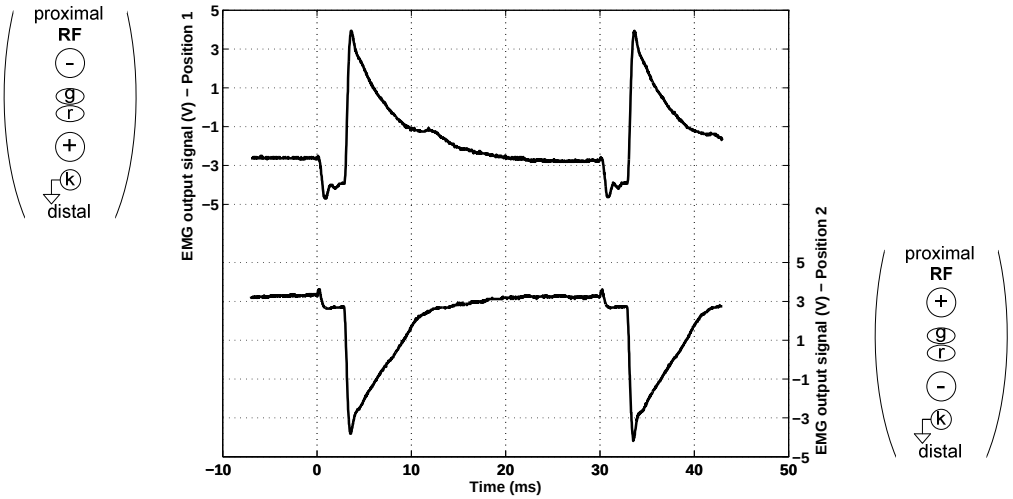

(a) Position 1. (b) Measured EMG signal. (c) Position 2.

Figure 7.4: Influence of stimulating electrode orientation on polarity of the stimulation artefact.

	T (ms)	PW (μs)	PW_r (%)	I_{stim} (mA)
Ch1	30	200	100	16
EMG amplifier:		1	2 (RF)	3
Gain		-	77dB ($7049\times$)	-

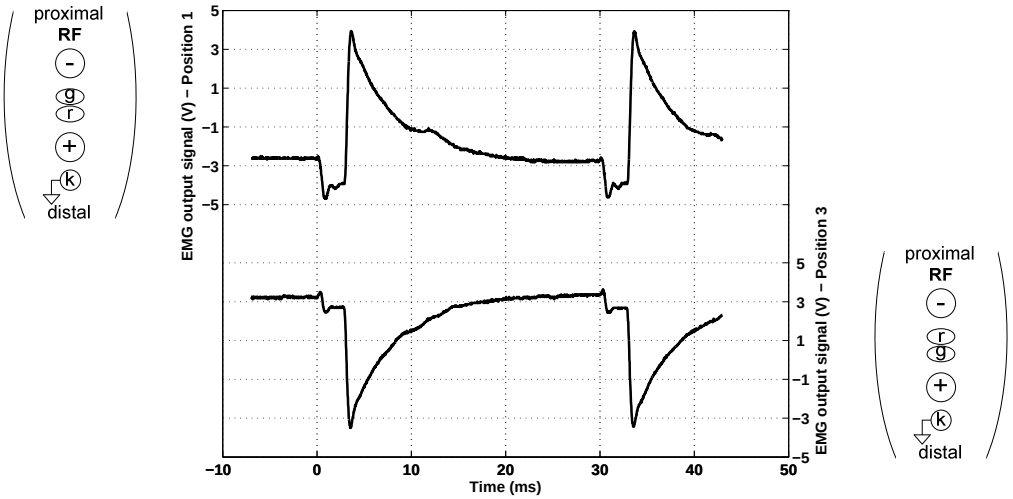

(a) Position 1. (b) Measured EMG signal. (c) Position 3.

Figure 7.5: Influence of recording electrode orientation on polarity of the stimulation artefact.

the voltage gradient would be reversed, resulting in the reversal of stimulation artefact polarity. Similarly, when reversing the positions of the recording electrodes, the potential difference between the electrodes was reversed, as the direction of the voltage gradient in the tissue had remained unchanged.

7.2.2 Longitudinal versus transverse placement of recording electrodes

Method

The effect on the stimulation artefact, of placing the recording electrodes in either a transverse or longitudinal orientation, was then investigated. For this experiment the reference electrode was always placed on the knee. Figure 7.6(a) shows the initial electrode positions used, in which recording electrodes were placed longitudinally on both RF and Vastus medialis (VM). On RF, there were two sets of recording electrodes, placed adjacent to one another.

Results

Figure 7.6(b) shows the voluntary EMG signals measured, with the two RF signals overlapping. Although the two signals are not identical, they are highly correlated when the detecting dipoles are so close together.

The muscle was then stimulated, using the stimulation settings given in the table above the figures; initially the PW_r setting was 102%. The signals measured at the output of the EMG amplifiers are shown in figure 7.6(c). Stimulation artefact was seen to be present on all three traces. The amplitude of the artefact spike can be read from the figure, to be approximately 3V, 5V and 6V for the VM longitudinal, RF longitudinal 1 and RF longitudinal 2 recording electrodes respectively.

The PW_r setting was then adjusted to 69.3% (figure 7.6(d)). At this setting the stimulation artefact was virtually eliminated from all three EMG signals. The mechanism behind this is further discussed in Section 7.3.

Method

The orientation of one of the RF electrode sets and the VM electrode set was then changed from being longitudinal to transverse, as indicated in figure 7.6(e). The position of the reference electrode, the stimulation settings and the gain settings of the EMG amplifiers were all kept the same as before.

Results

The voluntary EMG was again measured, with the measurement from the two RF recording electrode sets overlapping. The results are shown in figure 7.6(f). The two EMG signals are no longer as highly correlated as seen previously. This is most likely due to the change in the pickup area beneath the RF transverse recording electrodes. Nonetheless, the two signals are not entirely dissimilar.

	T (ms)	PW (μs)	PW_r (%)	I_{stim} (mA)
Ch1	30	200	Varied	18

EMG amplifier:	1 (VM$_{long\ \&\ trans}$)	2 (RF$_{long1}$)	3 (RF$_{long2\ \&\ trans}$)
Gain	84dB (15061×)	78dB (7868×)	77dB (7072×)

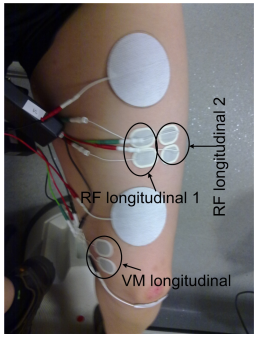

(a) Electrode positions.

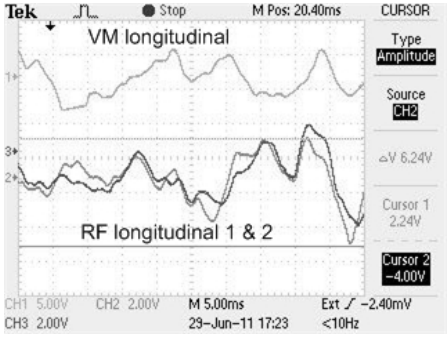

(b) Voluntary EMG.

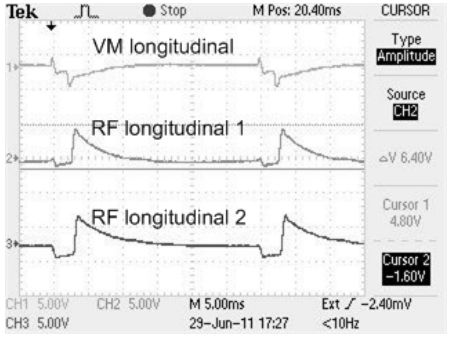

(c) PW_r = 102%.

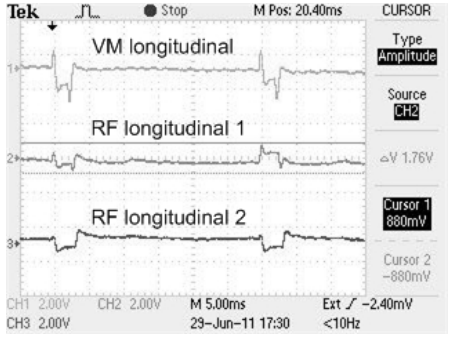

(d) PW_r = 69.3%.

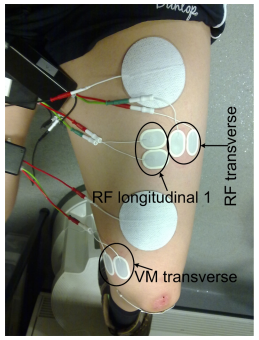

(e) Electrode positions.

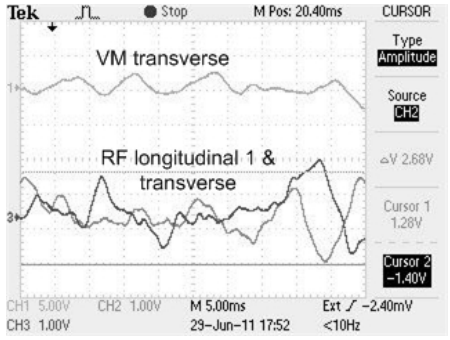

(f) Voluntary EMG.

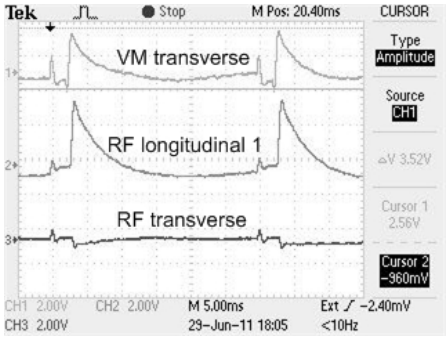

(g) PW_r = 102%.

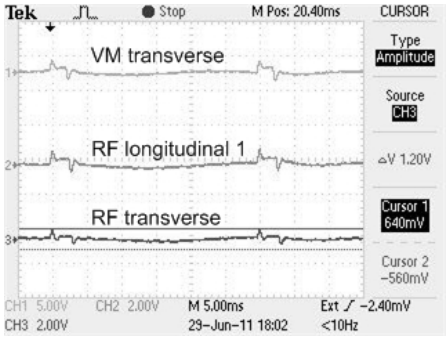

(h) PW_r = 68.3%.

Figure 7.6: Comparison of EMG measurements with longitudinal and transverse placement of recording electrodes.

Figure 7.6(g) shows the EMG signals measured when the stimulator was turned on with a PW_r setting of 102%. The amplitude of the stimulation artefact on the VM transverse signal was roughly the same as before, at around 3V, although the polarity was reversed. The RF longitudinal 1 electrode set also showed a similar stimulation artefact. However, the stimulation artefact was completely eliminated from the RF transverse electrode set. A further change in the PW_r setting to 68.3% eliminated the stimulation artefact in the VM transverse and RF longitudinal electrode sets, but had no effect on the RF transverse measurement (refer to figure 7.6(h)).

Discussion

Consider the difference seen in the amplitude of the stimulation artefact, as measured with the three different recording electrode sets (refer to figure 7.6(c)). Even after taking the gain settings of the individual amplifiers into account (refer to the table above the figures) the potential difference at the amplifier input of the VM longitudinal recording electrodes is much smaller than that seen by the RF longitudinal electrode sets.

Scott et al. [1997] and Kornfield et al. [1985] both showed that placing the recording electrodes on equipotential lines would help to reduce the stimulation artefact. Inspection of figure 7.2 shows that the VM longitudinal electrode set is more closely aligned with an equipotential line than the two RF longitudinal electrode sets. This would result in a smaller stimulation artefact.

From all the results shown in figure 7.6, it can be seen that the presence of the stimulation artefact is dependent on the orientation of the recording electrodes with respect to the voltage gradients set up by the currents flowing through the tissue. If the electrodes can be placed on the same equipotential line it is possible to completely eliminate the stimulation artefact, however, the positions of the equipotential lines are unpredictable. As mentioned previously, the tissue is a non-homogenous medium, which does not result in the uniform distribution of the current flow and equipotential lines of figure 7.2. This is further confounded by the fact that the shape of the electric field in the tissue is frequency dependent and tends to shift slightly during a stimulation pulse [McGill et al., 1982; McLean et al., 1996]. Lastly, the electrode orientation is normally determined by other factors. In this study the orientation of the recording electrodes followed the recommendations of the SENIAM project (Surface Electromyography for the Non-Invasive Assessment of Muscles) [Hermens et al., 1999], namely that the electrodes are placed parallel to the muscle fibres, i.e. longitudinally.

7.3 Electrode-skin interface

Thus far, the current path created by including the blocking capacitor and the discharge resistor in the stimulator output stage, was considered. However, this is not the entire picture. The interface between the stimulating electrodes and the skin surface also needs to be considered. Figure 7.7 shows a three component model that has been extensively used in the literature to represent biopotential electrodes [Dorgan and Reilly, 1999; McGill et al., 1982; Neumann, 2000; Reichel et al., 2001; Rosell et al., 1988; Webster et al., 2009].

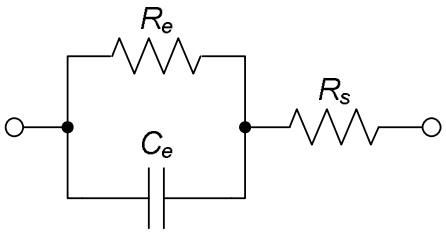

Figure 7.7: Equivalent circuit for a surface electrode.

According to Neumann [2000]:

- The parallel resistor and capacitor (R_e and C_e) represent the "impedance associated with the electrode-skin interface and the polarization at this interface."
- The series resistance, R_s, represents the "resistance associated with the interfacial effects and the resistance of the electrode materials themselves."

Figure 7.8 shows the typical response of an electrode to a constant-current biphasic stimulation pulse [Webster et al., 2009]. If the electrode-skin interface was purely capacitive and the stimulator were an ideal biphasic current source, with equal charge in the two phases, then the voltage across the electrode would be zero at the end of the stimulation pulse. However, the presence of the shunt resistors, R_e, causes some of the charge to be lost during the pulse. This results in a residual charge and a voltage across the electrodes, at the end of the stimulation pulse. By adjusting the pulse width ratio of the stimulation pulse, the charge in the second phase is reduced. It is theoretically possible to find a PW_r setting such that the voltage across the electrodes at the end of the stimulation pulse will be zero [Reichel et al., 2001].

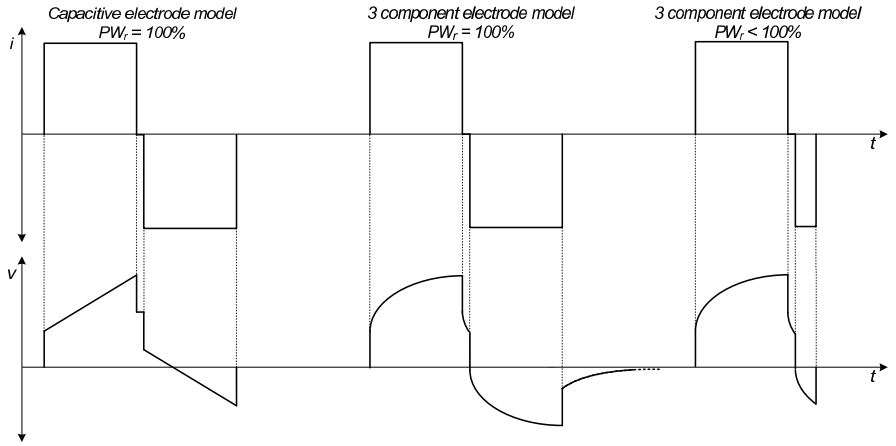

Figure 7.8: Electrode current and voltage waveforms for a biphasic stimulation pulse.

The system used by Reichel et al. [2001] was analysed by means of the linear component surface electrode model of figure 7.7, to represent both the anode and the cathode together. No other components were included in the model. In so doing they were able to express the relationship between the pulse width, PW_p, and the pulse width ratio, PW_r, as in equation 7.1. The time constant, τ, resulted from the three-component model.

$$PW_r = \frac{\tau}{PW_p} \ln\left(2 - \exp^{\frac{PW_p}{\tau}}\right) \tag{7.1}$$

If we now include the model for the stimulating electrodes in the *Stimulator-Body-Amplifier* system (refer to figure 7.3), we obtain the equivalent circuit diagram of figure 7.9.

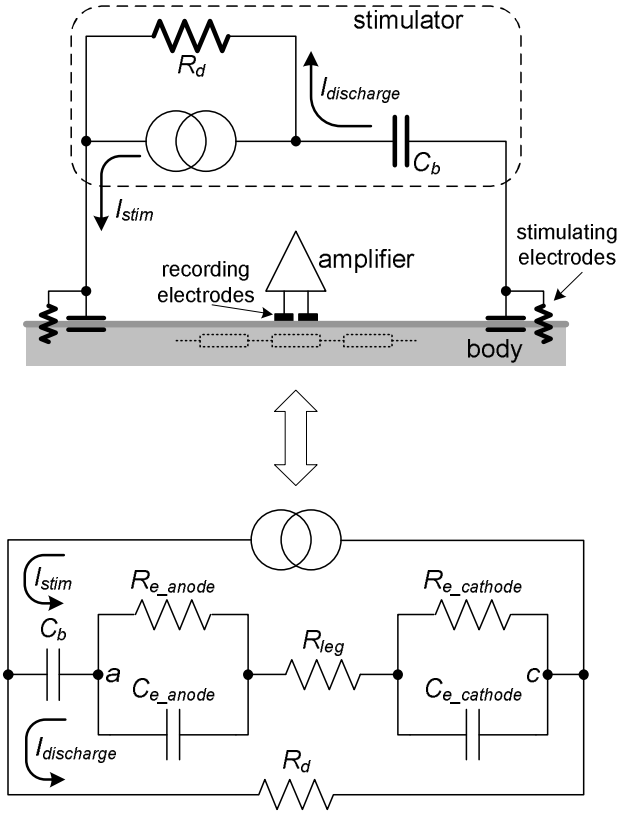

Figure 7.9: The *Stimulator-Body-Amplifier* system.

Neumann [2000] discussed the effect of the electrode properties (surface area, polarisation, surface roughness, radius of curvature and surface contamination) on the electrode impedance. As it is unlikely for all of these properties to be identical for both the anode and the cathode, the two electrodes were modelled separately. According to McGill et al. [1982] the tissue of the limb can be modelled as a resistive volume conductor. The series resistance R_{leg} represents the combination of the volume conductor resistance and the series resistance of the two electrodes.

During a stimulation pulse, the stimulation current flows through the blocking capacitor, the electrodes and the tissue. At the end of the stimulation pulse, the residual voltage across all three capacitors, will discharge through R_d, which in turn causes a current to flow through R_{leg}. This discharge current causes a potential difference across the recording electrodes, which is seen as a stimulation artefact at the amplifier output that consists of three superimposed time constants.

The stimulation artefact seen thus far (refer to figures 7.4 and 7.5), had a time constant of around 10ms. A PSPICE model was used to investigate whether the electrode-skin interface caused the observed time constant. The simulation model and results are discussed next. In

the rest of this section various experiments are presented. Firstly, the inter-electrode voltage and the influence of the PW_r setting thereupon, was measured. Secondly, the influence of the current density and the electrode properties on the stimulation artefact was investigated. Lastly, the relationship between the PW_r setting and the stimulation intensity was characterised.

7.3.1 PSPICE model of the *Stimulator-Body-Amplifier* system

Method

A PSPICE simulation of the *Stimulator-Body-Amplifier* system was produced. The component values of the electrode-skin interface were approximated using the results of Perkins [2004] where the R_e and C_e values, of surface electrodes placed on the Gastrocnemius muscle of ten subjects, were experimentally measured. It was found that the values were dependent on the size of the electrodes used. For 5cm, 7cm and 8×13cm electrodes the values ranged from 1.3kΩ to 1.7kΩ for R_e and 64nF to 334nF for C_e. The value of R_{leg} was taken as 1kΩ, as used previously in Chapter 5, which was also based on the measurements of Perkins [2004]. The values of R_d and C_b were set to be the same as those used in the Biphasic stimulator, 33kΩ and 5μF respectively. The circuit schematic, used in the simulation, is shown in figure 7.10.

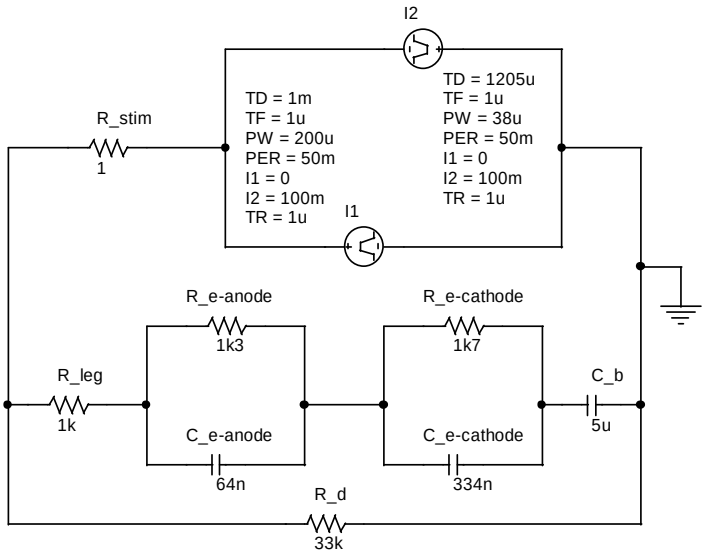

Figure 7.10: PSPICE simulation of the electrode-skin interface.

Results

The voltage across the anode-first electrode (parallel combination of R_{e_anode} and C_{e_anode}), the cathode-first electrode (parallel combination of $R_{e\_cathode}$ and $C_{e\_cathode}$) and the blocking capacitor, C_b, were found immediately after a stimulation pulse, over a range of pulse width ratio, PW_r, settings. The results are shown in figure 7.11(a). The residual voltage, V_{res}, was calculated as in equation 7.2.

$$V_{res} = V_{anode} + V_{cathode} + V_{Cb} \tag{7.2}$$

Figure 7.11(a), was used to find the PW_r settings at which each of the four voltages crossed the 0V line. For each of these PW_r settings, the discharge current, immediately after the negative phase of the stimulation pulse came to an end, was found. The current waveforms are shown in figure 7.11(b).

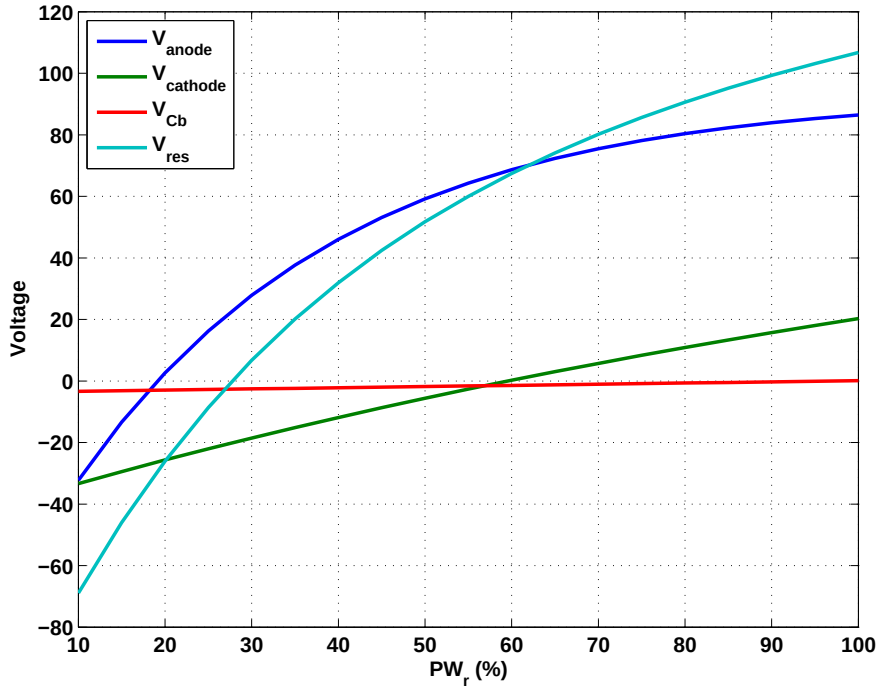

(a) Voltage across model components, immediately after a stimulation pulse, as a function of PW_r.

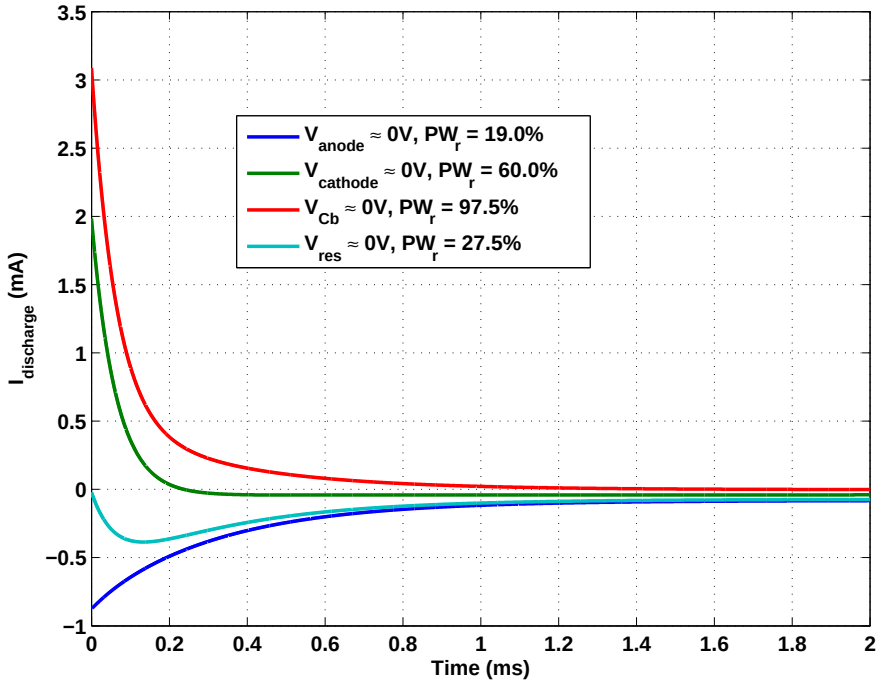

(b) Discharge current waveforms immediately after a stimulation pulse.

Figure 7.11: PSPICE simulation of the residual charge present at the electrode-skin interface.

Discussion

For the residual voltage to be zero, we require that $PW_r < 100\%$, and therefore $PW_n < PW_p$. This agrees with our expectations, as the presence of the shunt resistors, R_e, causes some of the charge to be lost during the positive phase of the stimulation pulse. Consequently, less charge is required during the negative phase of the pulse, to ensure that there is no residual charge left at the electrode-skin interface after the stimulation pulse.

However, it is improbable that the R_e and C_e values of both the anode and the cathode would be identical. This can be explained by remembering that the electrode impedance was dependent on the various properties of the electrodes [Neumann, 2000]. Such a mismatch in component values would cause V_{anode} and $V_{cathode}$ to be different for a given PW_r setting. Figure 7.11(a) showed this to be exactly the case. Altering the PW_r does not change both electrode voltages to zero volts together. Instead, a PW_r setting must be found such that the sum of the voltages, V_{res}, is zero.

The discharge current, when $V_{res} = 0$V, is seen to produce a wave (refer to figure 7.11(b)). This wave can potentially be mistaken for an action potential (AP). However, with the *Stimulator-Body-Amplifier* system discussed here, the wave lasts $\sim$ 2ms, due to the short time constants of the electrodes. Typically the blanking interval was around 3ms (refer to figure 7.1), which means that the wave-like response of the discharge current would have died away by the time the blanking interval comes to an end, thereby ensuring that the wave would not be mistaken for an M-wave.

The short time constants associated with the discharge current (less than 1ms as seen in figure 7.11(b)) do not explain the much longer time constant associated with the stimulation artefact ($\sim$ 10ms, refer to figure 7.1). Nonetheless, the residual voltage does play a part in generating a stimulation artefact, which can be eliminated by adjusting the PW_r setting to influence the discharge current.

The simulation model can be expanded to include the recording electrodes, which can also be represented with the three-component model of figure 7.7. In so doing, the only difference found with the simulation was that the PW_r setting, required for V_{res} to be zero, was slightly less. Details of this PSPICE simulation have been included in Section E.3 of the Appendix.

A limitation of the PSPICE simulations is that a simplified electrode model was used, in which all of the components were linear. In practice the situation is far more complicated as an electrode-electrolyte interface is actually a nonlinear system [Dymond, 1976]. Neumann [2000] suggested that the electrode impedance is frequency dependent, while Dorgan and Reilly [1999] successfully modelled the electrode response by using a nonlinear, time dependent resistor for R_e. Dymond [1976] and McGill et al. [1982] discussed the dependence of the nonlinearity of R_e on the current density conducted by the electrodes. These nonlinearities would result in artefacts with quite complicated shapes.

At the time that the *Stimulator-Body-Amplifier* system was being tested, the various causes of the stimulation artefact were not understood. Consequently a number of experiments were

carried out to investigate the influence of the PW_r setting, stimulation parameters and electrode properties on both the stimulation artefact and EMG measurements. The remainder of this section presents these experiments as they either explicitly show the influence the PW_r setting has on stimulation artefact, or, can be related to one of the component voltages (V_{anode}, $V_{cathode}$ and V_{Cb}), that comprise the residual voltage, V_{res}. The results of these experiments lead to the conclusion that the electrode-skin interface was one of the causes for the observed stimulation artefact.

7.3.2 Inter-electrode voltage

Aim

It is not possible to measure V_{anode} and $V_{cathode}$ directly, as part of the electrode-skin interface comprises the tissue of the leg. However, the so-called *inter-electrode* voltage, V_{ac} (voltage between nodes a and c in figure 7.9), can be measured by connecting an oscilloscope probe across both stimulating electrodes and the tissue resistance (R_{leg}). Changes in this voltage measurement corresponding with different PW_r settings, and the influence the latter had on stimulation artefact and M-wave measurements, were considered.

Methods

The electrodes were placed on the Quadriceps, as in position 1 of figure 7.4(a). The stimulator and amplifier settings used are shown in the table above figure 7.12.

During stimulation, an oscilloscope probe was connected to measure V_{ac}. No difference was seen in the measurements when using either a single-ended oscilloscope probe (thereby earthing the subject) or when using a differential probe (thereby retaining isolation from earth).

Results

Figure 7.12(a) shows V_{ac} at different PW_r settings. The timing with a stimulation pulse is explicitly shown. For a PW_r setting of 100%, V_{ac} has a voltage well below 0V at the end of the pulse. By reducing the PW_r setting to 64.5%, V_{ac} returned to 0V immediately after the pulse. Close inspection of the figure shows that further reduction of the PW_r setting to 56% caused V_{ac} to increase above 0V immediately after the pulse. A further decrease in the PW_r setting would have shown a further increase in V_{ac}.

Figure 7.12(b) shows the corresponding EMG measurements captured with the Blanking amplifier. Initially, with a PW_r setting of 100%, the M-wave was completely obscured by the stimulation artefact. By decreasing the PW_r setting to 64.5%, the stimulation artefact was completely removed and the M-wave was clearly visible. Further reducing the PW_r to 56%, resulted in the stimulation artefact reappearing, however its polarity was now reversed.

Discussion

Initially the stimulation current placed charge on the various capacitors of the *Stimulator-Body-Amplifier* system. At the end of the stimulation pulse, a residual amount of charge remained. This charge slowly dissipates, causing the discharge current to flow through R_{leg}, resulting in the amplifier measuring a potential difference that is seen as the stimulation artefact. By

	T (ms)	PW (μs)	PW_r (%)	I_{stim} (mA)
Ch1	30	200	Varied	30
EMG amplifier:		1	2 (RF)	3
Gain		-	73dB (4250×)	-

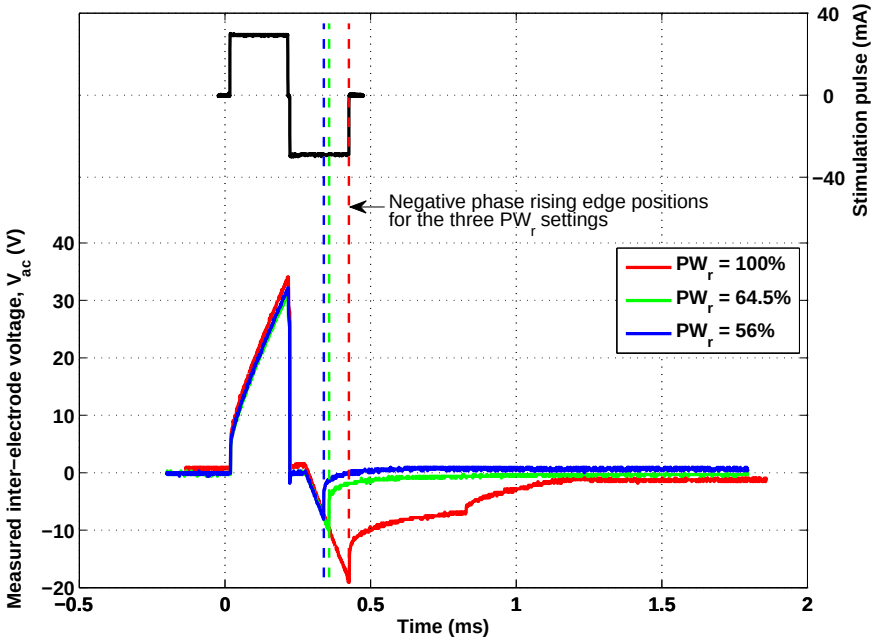

(a) Influence of the PW_r setting on the inter-electrode voltage.

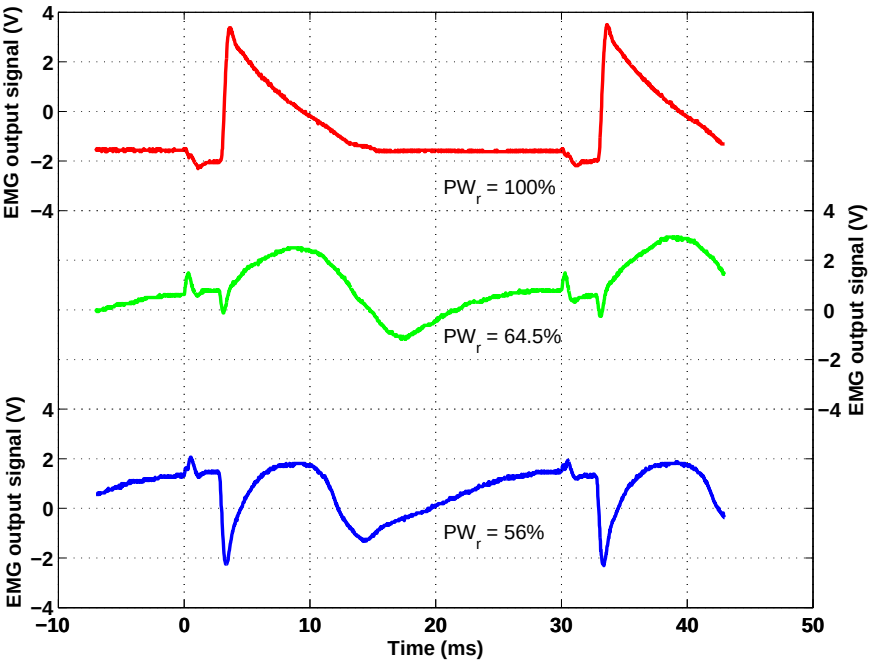

(b) Influence of the PW_r setting on the polarity of the stimulation artefact.

Figure 7.12: Inter-electrode voltage, V_{ac} and EMG measurements.

adjusting the pulse width ratio, and thereby changing the amount of charge injected into the capacitors, we were able to find a setting at which there was no residual charge at the end of the stimulation pulse. Consequently no discharge current flowed which meant that no stimulation artefact was measured.

By further decreasing the pulse width ratio, an imbalance was introduced into the system. However, this time, instead of negative phase removing more charge from the system than what was introduced during the positive phase, the reverse was true in which less charge was removed during the negative phase than what was introduced during the positive phase. This resulted in the direction of the discharge current being reversed, which in turn would reverse the polarity of the potential difference seen by the amplifier and hence reverse the polarity of the stimulation artefact. There was however no reversal in the polarity of the M-wave as the direction in which the stimulation current flowed, remained the same.

7.3.3 Stimulation artefact and current density

Aim

Unlike V_{anode} and $V_{cathode}$, it was possible to measure the last component of the residual voltage, V_{Cb}, directly, using an oscilloscope. This voltage was measured simultaneously with the amplifier output to investigate if V_{Cb} was related to the stimulation artefact.

Method

A set of stimulating and recording electrodes were placed on Biceps brachii; reference electrode placed on the elbow. The voltage across the blocking capacitor, C_b, was measured for a range of stimulation current amplitude settings (0mA, 0.7mA, 2.5mA, 5mA, 7.5mA, 10mA, 12.5mA and 15mA). The EMG amplifier output waveform was also captured. The electrode positions used, and the stimulator and amplifier settings, have been included with figure 7.13.

Results

The top trace of Fig 7.13(b) shows the baseline of the voltage measured across the blocking capacitor, C_b. The bottom trace shows the EMG amplifier output waveform. The maximum and minimum stimulation current amplitude settings used have been indicated on the figure.

Immediately after the stimulation pulse, the C_b voltage overshoots the baseline voltage with a spike, followed by an exponential decay. The amplitude of the spike is dependent on the current setting, and is seen to increase as the current amplitude increases. The time constant of the exponential decays were calculated (refer to Section E.1) and found to be 3.2ms. This value remained constant regardless of current amplitude. The same trend is seen in the stimulation artefact present in the EMG signal (lower trace). The time constant of the stimulation artefacts, measured at 3.6ms, also stayed the same regardless of current amplitude.

Discussion

The overshoot past the baseline, seen in the C_b voltage, is a measurement of the residual charge present on the charge balancing capacitor at the end of a stimulation pulse. The greater the residual charge, the greater the C_b voltage, the larger the amplitude of the stimulation artefact.

	T (ms)	PW (μs)	PW_r (%)	I_{stim} (mA)
Ch1	5000	200	100	Varied

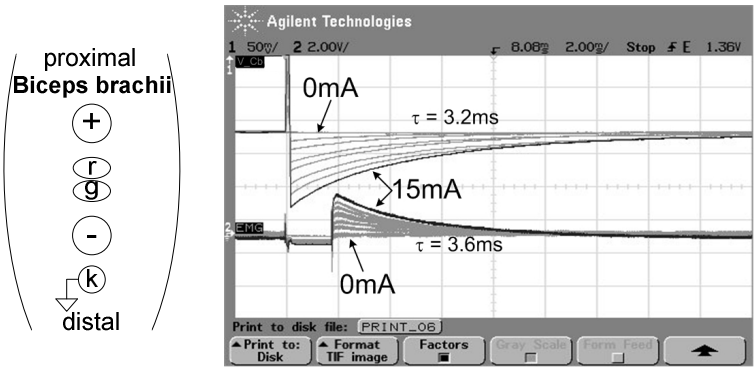

(a) Electrode positions. (b) Stimulation current amplitude influence on stimulation artefact.

Figure 7.13: C_b voltage (top trace) compared against EMG output waveform (lower trace) - current density.

However, opposite to the observations of Dymond [1976] and McGill et al. [1982], in which the value of R_e in the electrode model was considered to have a nonlinear dependence on the current density, these results showed a linear relation between the stimulation artefact and current density. The greater the current amplitude, the higher the current density and the greater the amplitude of the stimulation artefact.

7.3.4 Stimulation artefact and electrode properties

Aim

As a correlation had been seen between V_{Cb} and the stimulation artefact when increasing the stimulation intensity, it was then investigated whether the electrode properties not only influenced the shape of the stimulation artefact, but whether corresponding changes would be seen in V_{Cb}.

Method

Once again the blocking capacitor voltage and the EMG amplifier output were measured, this time in response to changes in the properties of the stimulating electrodes. An initial set of measurements were captured. The electrode properties were then altered by abrading the skin under the electrodes with sandpaper and cleaning with alcohol. The electrodes were replaced and the measurements repeated. The electrode positions used, and the stimulator and amplifier settings, have been included with figure 7.14.

Results

As before, the top trace in figure 7.14(b) shows the voltage measured across C_b, while the bottom trace shows the EMG amplifier output waveform. A change was seen in the amplitude and time constant of both traces, before and after the skin preparation used to alter the electrode properties. (The change in amplitude of the stimulation artefact would have been more evident

	T (ms)	PW (μs)	PW_r (%)	I_{stim} (mA)
Ch1	30	200	100	20

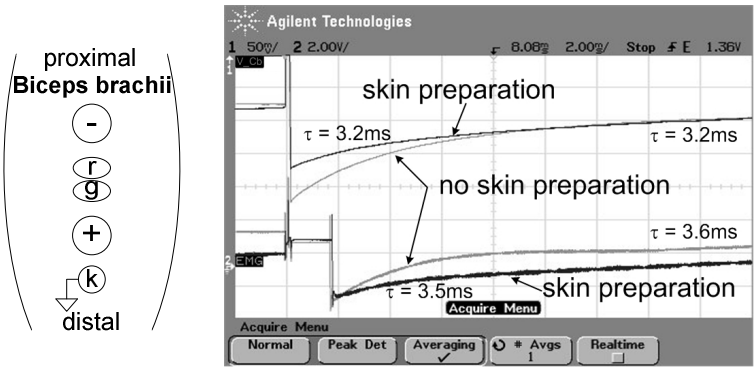

(a) Electrode positions. (b) Influence of changes in electrode properties, through skin preparation, on stimulation artefact.

Figure 7.14: C_b voltage (top trace) compared with EMG output waveform (lower trace) - electrode properties.

if the two traces had been aligned so that the baseline voltages, prior to the stimulation pulse, had overlapped, as opposed to the blanking interval voltage levels overlapping as shown in the figure.) The time constants for both traces were calculated and have been indicated in the figure.

Discussion

By preparing the skin, the electrode properties and hence the values of the capacitance and resistance of the skin-electrode interface would have changed. However, the difference in time constants, before and after skin preparation, did not appear to be significant (No change in C_b voltage; EMG amplifier output 3.6ms prior to skin preparation, and 3.5ms after). This can be attributed to the fact that the exponential decay of the stimulation artefact consists of a number of superimposed time constants [Scott et al., 1997]. Furthermore, the time constants associated with the skin-electrode interface are inherently short, which makes it particularly difficult to measure changes in their values.

Nonetheless, there is a very evident change in the stimulation artefact after preparing the skin and thereby slightly altering the electrode properties, that corresponded with a change seen in the voltage measured across C_b.

7.3.5 Pulse width ratio and stimulation parameters

The muscle response is dependent on three stimulation parameters, namely, the period, the current amplitude and the pulse width. During the various measurements discussed in this chapter, no dependence was ever seen between the stimulation artefact and the stimulation period. However, the current amplitude and the pulse width were both seen to influence the amplitude of the stimulation artefact. As a result, the pulse width ratio setting required to eliminate the stimulation artefact was dependent on the current and pulse width settings. These two dependencies were independently investigated.

Influence of current amplitude on the PW_r setting required to eliminate stimulation artefact

The stimulating and recording electrodes were placed on Vastus medialis (VM), using the same setup shown in figure 7.15(a). The current amplitude was increased in 5mA intervals from 10mA up to 35mA; the other relevant stimulator and amplifier settings are summarised in the table next to the electrode position figure.

Figure 7.15(b) shows the M-waves measured in VM, over the range of current values, along with the corresponding PW_r settings. As the current amplitude increased, more of the muscle fibres in VM would have been recruited, causing a stronger contraction, as indicated by the increasing peak-to-peak amplitude of the M-waves. The peaks of the M-wave, recorded at 25mA, were clipped. This was rectified for the higher current amplitudes by changing the gain of the amplifier from 78dB to 65dB (as indicated in the stimulation setting table).

As the current amplitude increased, it was necessary to decrease the PW_r setting, to ensure that the stimulation artefact was eliminated. Earlier it was seen that an increase in the current

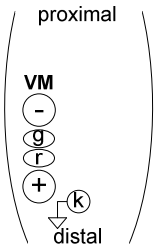

	T (ms)	PW (μs)	PW_r (%)	I_{stim} (mA)
Ch1	1000	200	Varied	Varied
EMG amplifier:	1 (VM)		2	3
Gain	65dB (1863×)	78dB (8188×)	-	-

(a) Electrode positions.

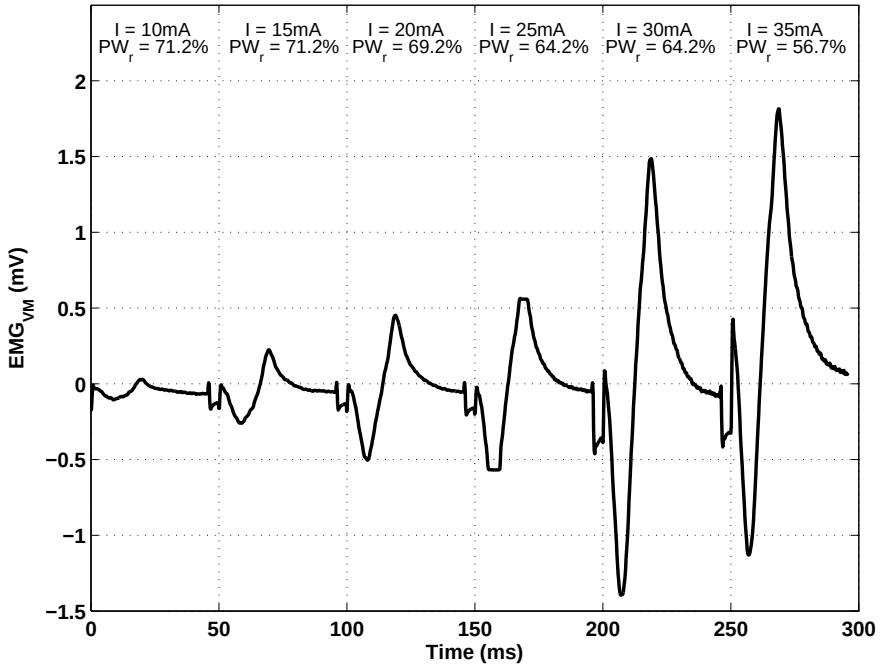

(b) EMG measured in Vastus medialis.

Figure 7.15: Adjustment of PW_r setting as current intensity increases.

amplitude caused a corresponding increase in the amplitude of the stimulation artefact (refer to figure 7.13(b)). As the current amplitude increases, the residual charge distributed across the interface capacitance and the blocking capacitor at the end of the stimulation pulse, becomes greater. This in turn results in a larger discharge current flowing between stimulation pulses, which in turn causes a larger potential difference across the recording electrodes and hence an increase in the amplitude of the stimulation artefact.

Influence of pulse width on the PW_r setting required to eliminate stimulation artefact

Recall that during the Bi-moment chair study, the stimulation intensity was determined by the recruitment curve protocol, refer to Section 4.2.2. As a brief reminder, the protocol consisted of nine bursts of stimulation, each burst increasing in stimulation intensity. This was achieved by holding the current amplitude constant and varying the pulse width.

It was decided to experimentally investigate the relationship predicted by Reichel et al. [2001] at the various pulse width increments defined by the recruitment curve protocol. To this end a set of stimulating and recording electrodes were placed on Rectus femoris (RF), using the same electrode setup shown in figure 7.4(a), with the reference electrode placed on the knee. The stimulation settings used are shown in the table above figure 7.16.

Measurements were carried out for two different values of the maximum possible pulse width, $PW_{p\text{-}max}$ (i.e. the PW_p setting used for the ninth stimulation burst of the recruitment curve stimulation protocol). Two values were investigated as both were used in the study discussed in Chapter 8. This meant that measurements were taken for pulse widths ranging from 40μs up till 200μs (in 20μs increments) and again from 80μs up till 400μs (in 40μs increments). At each of these pulse widths, the PW_r setting was adjusted so that the stimulation artefact was eliminated.

Figure 7.16 shows the measured results (solid lines) compared with the theoretical results (dashed lines) found using Reichel's equation 7.1. For a $PW_{p\text{-}max}$ value of 200μs, the measurements were repeated over a range of current amplitudes. These measurements were taken over a number of days. One set of measurements was taken for a $PW_{p\text{-}max}$ value of 400μs.

Clearly the experimental and theoretical curves do not correlate well. However this is not unexpected if we consider the fact that the model used by Reichel et al. [2001] consisted of only linear components, while the practical system is known to exhibit non-linear behaviour [Dorgan and Reilly, 1999; Dymond, 1976; McGill et al., 1982; Neumann, 2000]. Consequently the time constant appears to change for the experimental curves, presumably as the voltage across the electrode-skin interface changes.

What was evident from the results was the fact that the PW_r setting would need to be adjusted during the recruitment curve stimulation protocol, if we hoped to eliminate stimulation artefact in all nine bursts of stimulation. During the study it was not practical to measure the required PW_r setting for each stimulation burst, as this would be time consuming and would cause a lot of fatigue in a subject's Quadriceps even before starting the actual test. Instead, when

	T (ms)	$PW_{p\text{-}max}$ (μs)	PW_r (%)	I_{stim} (mA)
Ch1	30	200 or 400	Varied	Varied

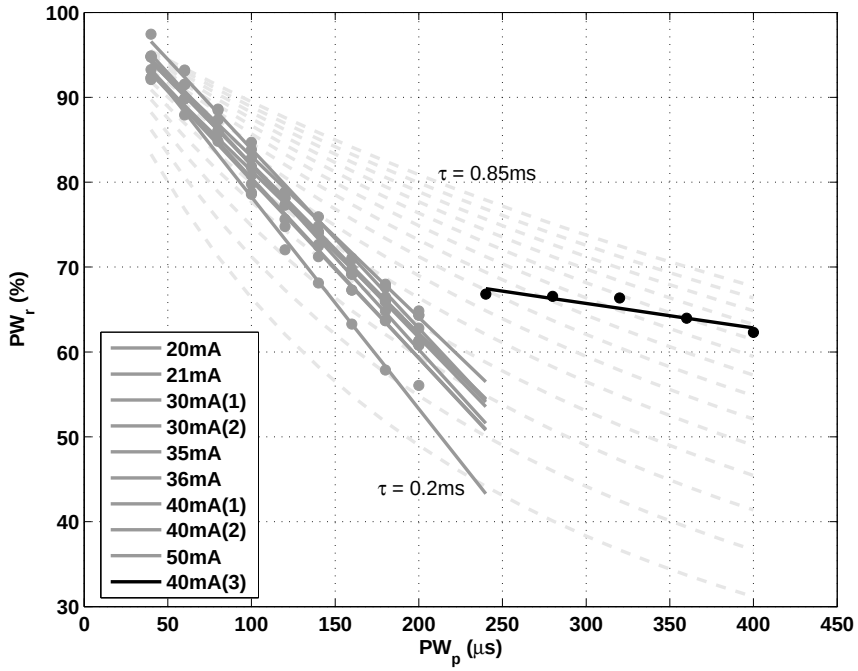

Figure 7.16: Theoretical and measured PW_r setting as a function of pulse width.

a subject was to be stimulated using the recruitment curve protocol, their maximum tolerable current was first found during continuous stimulation at $PW_{p\text{-}max}$. The PW_r setting required to eliminate the stimulation artefact under these conditions was then found, and noted down as $PW_{r\text{-}min}$. These two values were then used to calculate the PW_r setting required at the lower pulse width settings.

This lead to the use of a simple approximation to describe the relationship between PW_p and PW_r, by fitting straight lines to the measured data, as shown in figure 7.16. The derivation of equations 7.3 and 7.4 has been included in Appendix E, Section E.2. For a $PW_{p\text{-}max} \leq 200\mu$s, the following relationship was found:

$$PW_r = PW_{r\text{-}min} + 0.2\,(PW_{p\text{-}max} - PW_p) \tag{7.3}$$

For a $PW_{p\text{-}max} > 200\mu$s two curves were fit to the data, as described by equation 7.4.

$$PW_r = \begin{cases} PW_{r\text{-}240} + 0.2\,(240 - PW_p)\,; & PW_p < 240 \\ PW_{r\text{-}min} + 0.03\,(PW_{p\text{-}max} - PW_p)\,; & PW_p \geq 240 \end{cases}$$
$$PW_{r\text{-}240} = PW_{r\text{-}min} + 0.03\,(PW_{p\text{-}max} - 240) \tag{7.4}$$

Equations 7.3 and 7.4 were written into the microcontroller code of the Biphasic stimulator. Consequently the same relationship was used to calculate the PW_r settings for all subjects.

7.4 Common mode voltage

Figure 7.17 shows a schematic representation of the superimposed layout of the three *major* electrode positions (introduced in Section 4.2.1), *Standard*, *Rectus* and *Vastii*, as well as the positions of the recording electrodes. The orientation of the electrodes shown in the figure was that used for all of the experiments discussed in this section.

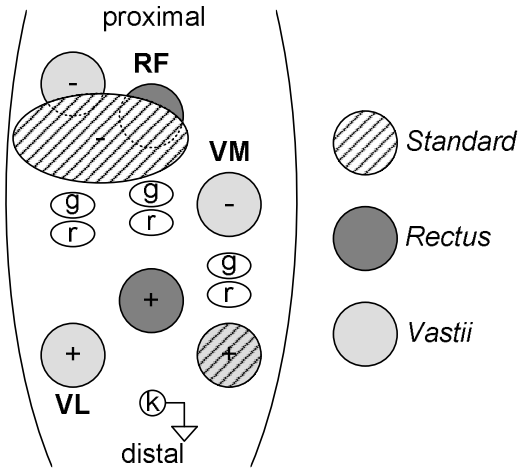

Figure 7.17: Proximity of recording electrodes to the stimulating electrodes, for the three *major* electrode positions.

The recording electrodes were placed on the belly of the muscle, generally found to be the midpoint between the stimulating electrodes used for the *Rectus* and *Vastii* positions. As the recording electrode placement was kept the same for all three *major* positions it resulted in the situation shown in the figure, where the Rectus femoris (RF) and Vatus lateralis (VL) recording electrodes were positioned exceptionally close to the cathode-first electrode for the *Standard* position.

While stimulating with the *Rectus* and *Vastii* positions, it was generally possible to eliminate the stimulation artefact using pulse width ratio adjustment. However, this was not the case when using the *Standard* position. Figure 7.18 shows the EMG measurements obtained for all three superficial muscles of the Quadriceps, using the *Standard* position and the stimulation settings indicated in the table above the figure. The PW_r setting was varied from 102% down to 1.5%. This had an influence on the stimulation artefact present in the EMG signal measured in Vastus medialis (VM), but had no effect on the stimulation artefact present in the EMG signals measured in RF or VL. This implied that when stimulating with the *Standard* position there was another cause behind the stimulation artefact, other than the flow of a discharge current, as discussed previously.

Initial experiments were performed, as discussed next, which indicated that in this case the stimulation artefact was being caused by the common mode input voltage of the EMG amplifiers being exceeded.

	T (ms)	PW (μs)	PW_r (%)	I_{stim} (mA)
Ch1	1000	200	Varied	50
Stimulating electrode position:			*Standard*	
EMG amplifier:		1 (VM)	2 (RF)	3 (VL)
Gain		78dB (8188×)	65dB (1832×)	69dB (2676×)
Reference electrode position:			Knee	

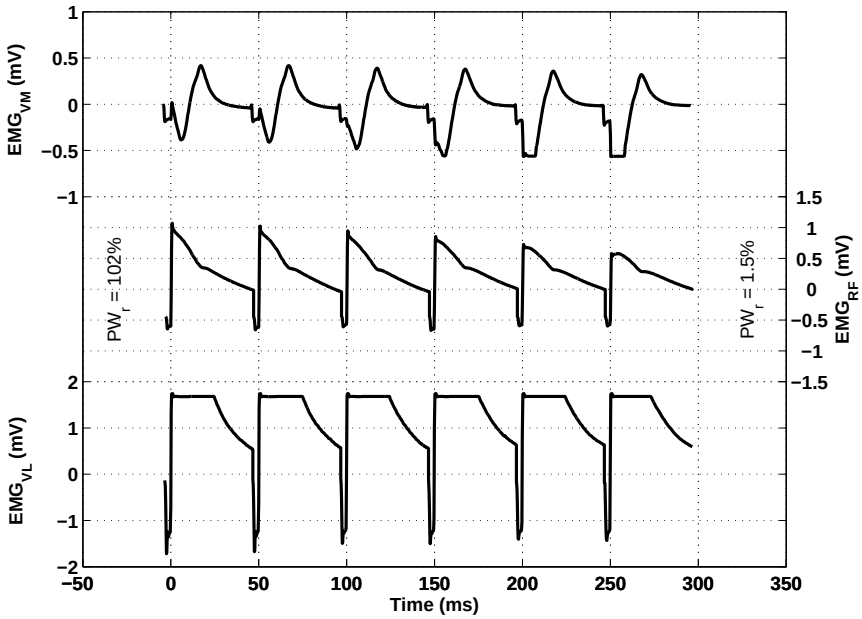

Figure 7.18: EMG measurements in the Quadriceps using the *Standard* electrode setup, for a range of PW_r settings, reference electrode knee.

7.4.1 Initial investigation

Method

For the *Rectus* position, one EMG amplifier was connected differentially to the recording electrodes on RF. From this the amplifier output could be measured in response to a differential mode input. Both inputs of a second EMG amplifier were connected to a single recording electrode on RF to obtain the amplifier output in response to a common mode input.

Results

Figure 7.19 shows the output signals measured by the two EMG amplifiers, for the stimulation settings indicated in the table above the figure. The differential mode measurement shows a stimulation artefact, which it was possible to eliminate using pulse width ratio adjustment. However, no stimulation artefact was detected on the common mode input measurement, regardless of the PW_r setting.

Method

The same measurements were repeated with the *Standard* position, as shown in figure 7.20. The stimulator and amplifier settings used have been included in the table above the figure.

	T (ms)	PW (μs)	PW_r (%)	I_{stim} (mA)
Ch1	30	200	100	33
Stimulating electrode position:			*Rectus*	
EMG amplifier:		1	2 (RF$_{dm}$)	3 (RF$_{cm}$)
Gain		-	82dB (12687×)	69dB (2676×)
Reference electrode position:			Knee	

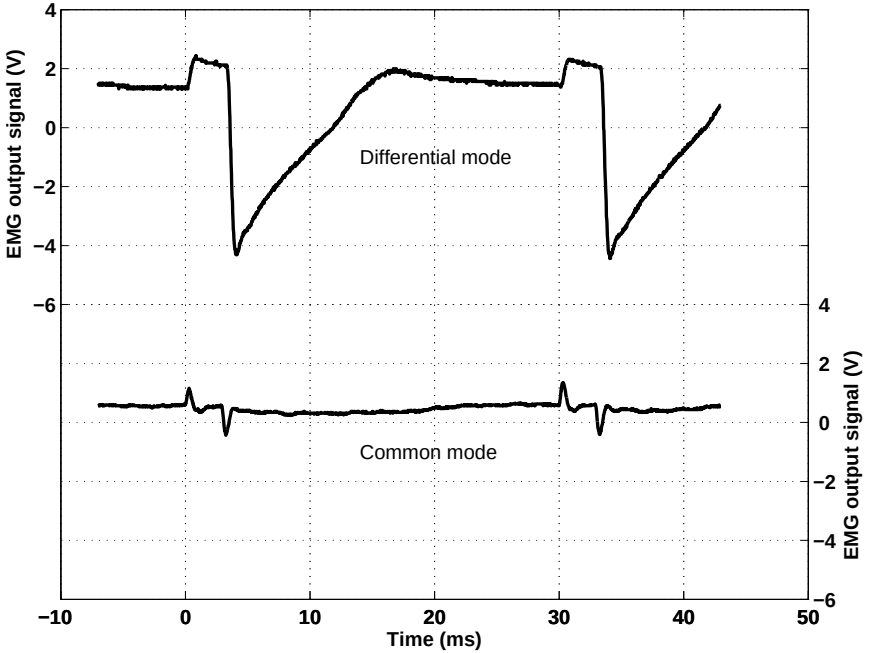

Figure 7.19: Differential and common mode EMG measurements for RF, with the *Rectus* setup, reference electrode knee.

	T (ms)	PW (μs)	PW_r (%)	I_{stim} (mA)
Ch1	30	200	15.1	-
Stimulating electrode position:			*Standard*	
EMG amplifier:		1	2 (RF$_{dm\&cm}$)	3
Gain		-	65dB (1832×)	-
Reference electrode position:			Knee	

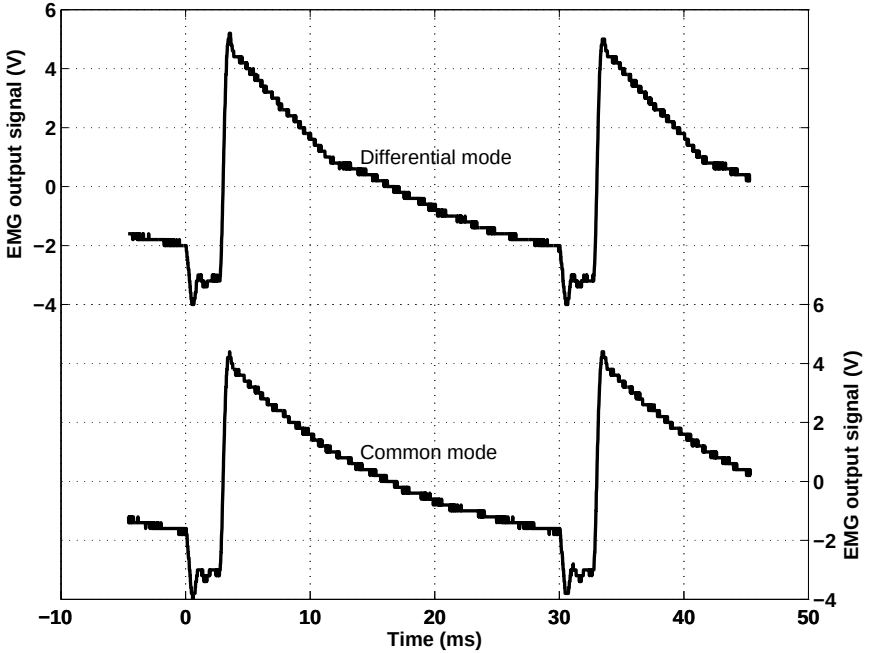

Figure 7.20: Differential and common mode EMG measurements for RF, with the *Standard* setup, reference electrode knee.

Results

A stimulation artefact was now present in both the differential mode and the common mode measurements, which any changes in the PW_r setting had no effect upon. This indicated that the cause for the stimulation artefact was due to the common mode response of the amplifiers.

Discussion

The common mode voltage, V_{cm}, seen by the recording electrodes is defined as the voltage difference between these two electrodes and the reference electrode. Consider the fact that the two stimulating electrodes form a dipole, a simplified two-dimensional interpretation is shown in figure 7.21, for both the *Rectus* and *Standard* positions. The voltage gradient between the anode and the cathode depends on the voltage difference, and, the separation distance, between the stimulating electrodes. A second voltage gradient exists between the distal stimulating electrode and the reference electrode, due to the strength of the electric field diminishing as one moves away from the dipole.

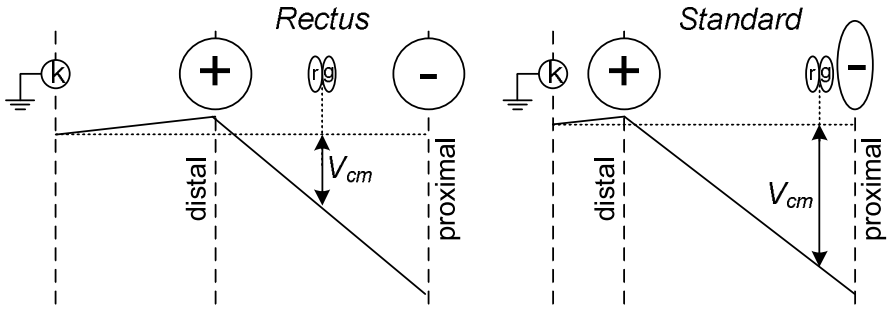

Figure 7.21: Voltage gradients for the *Rectus* and *Standard* electrode positions.

The figure was drawn using the following guidelines:

- The position of the reference electrode and recording electrodes was fixed. Consequently the separation distance between these electrodes was the same for both the *Rectus* and *Standard* positions.

- The position of the stimulating electrodes was varied. Consequently, the separation distance between the stimulating electrodes was less with the *Rectus* position than with the *Standard* position.

- For the *Rectus* position the recording electrodes were roughly in the middle of the two stimulating electrodes.

- For the *Standard* position the recording electrodes were positioned closer to the proximal stimulating electrode.

- The voltage difference between the stimulating electrodes was the same, regardless of which *major* position was used. (*Note: This implies a constant voltage stimulator, while the Bi-phasic stimulator is constant current. However, for the same current to flow, the*

difference in separation distance between the stimulating electrodes for the Rectus *and* Standard *positions would result in a larger voltage for the latter. This would further exaggerate the effect seen here.*)

All of these factors resulted in a larger common mode voltage seen by the recording electrodes for the *Standard* position, as compared with that seen by the recording electrodes for the *Rectus* position.

In Section 6.5.3 (*Common input voltage*), the transient response of the amplifier, due to a common input voltage was measured. Figure 6.32(a) shows the EMG amplifier output waveform, in response to an input voltage of 2.313V, which looks remarkably similar to the stimulation artefact seen in figure 7.20. In Section 7.4.3 it is shown how the common input voltage with the *Standard* setup can be greater than 5V, which is well above the 2.313V that was known to produce a transient response in the amplifier.

The rest of this section discusses two methods that were investigated as a means to eliminate the stimulation artefact due to excessive common mode voltage.

7.4.2 Positioning of the reference electrode

So far, the common mode voltage, V_{cm}, has been considered when placing the reference electrode on the knee, which is effectively placing it at one end of the dipole. Instead, by placing the reference electrode in the centre of the dipole, V_{cm} would be reduced, see figure 7.22(a).

It is generally accepted when recording EMG, that the reference electrode be placed on electrically inactive tissue. Basmajian and De Luca [1985] explicitly said that a reference electrode should be "...located in an environment which is either electrically quiet or contains electrical signals which are unrelated to those being detected..." where the term *unrelated* was defined as "...the two signals having minimal physiological and anatomical association..."

It was decided to place the reference electrode on the posterior thigh, as shown in figure 7.22(b), based on the assumption that the Gluteals and Hamstrings of the posterior leg would be inert during stimulation of the Quadriceps.

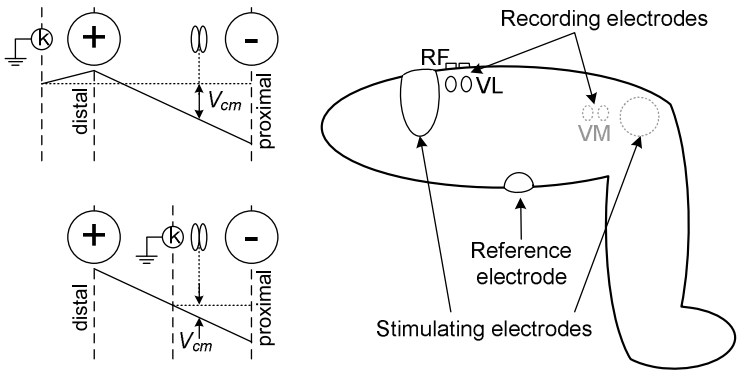

(a) Influence on CM voltage. (b) Positioning of reference electrode.

Figure 7.22: Using the reference electrode position to reduce common mode voltage for the *Standard* electrode setup.

Method

The common mode and differential mode measurements, discussed in Section 7.4.1, were repeated for the *Standard* position, with the reference electrode now placed on the posterior thigh.

Results

Figure 7.23 shows the EMG amplifier outputs captured with the recording electrodes on VL. Previously, with the reference electrode placed on the knee, the EMG amplifier output had shown stimulation artefacts for both the common mode and differential mode (similar to that shown in figure 7.20). Simply by moving the position of the reference electrode, not only was the stimulation artefact in the common mode signal eliminated, but an M-wave was detected in the differential mode signal.

Method

Keeping the reference electrode on the posterior thigh, the EMG measurements in all three Quadriceps muscles, were again measured over a range of PW_r settings.

Results

By comparing figure 7.24, reference electrode on the posterior thigh, against figure 7.18, reference electrode on the knee, we see that for the former case, the PW_r setting influences the presence of the stimulation artefact, not only in the EMG signal from VM, but also those captured for RF and VL.

Roughly in the middle of the PW_r range (60ms in figure 7.24), the stimulation artefact was completely removed for both RF and VL. Adjusting the PW_r setting above and below this point caused the polarity of the stimulation artefact to reverse, exactly as shown in Section 7.3.2 when the presence of the stimulation artefact was attributable to residual charge.

Discussion

The shape of the M-wave detected in VM was virtually identical for both positions of the reference electrode (compare figures 7.18 and 7.24). The difference in M-wave amplitude is attributed to the use of a 50mA stimulation current for the former, while only 30mA was used for the latter. This helped to justify the use of the posterior thigh as a reference electrode, even though it is not conventional to do this. Further support for this method is presented in Section 8.3.1 (*Position of the reference electrode*), where the results of the study are used to look at the influence, that the position of the reference electrode has, on M-wave measurements.

A shortcoming of the posterior thigh reference electrode placement, was the inability to always remove the stimulation artefact from all three Quadriceps muscles simultaneously. Careful inspection of the EMG signals shown in figure 7.24, for a PW_r setting close to 100% (0ms in the figure), shows that the stimulation artefact is completely absent from the EMG signal captured for VM, while there is still significant stimulation artefact present in the EMG signals of the other two Quadriceps muscles. For the PW_r setting at which the stimulation artefact in RF and VL (60ms in the figure) was eliminated, the M-wave detected in VM is starting to distort due to stimulation artefact.

	T (ms)	PW (μs)	PW_r (%)	I_{stim} (mA)
Ch1	30	200	15.1	-
Stimulating electrode position:			*Standard*	
EMG amplifier:	1	2	3 (VL$_{dm\&cm}$)	
Gain	-	-	78dB (8220×)	54dB (522×)
Reference electrode position:			Posterior thigh	

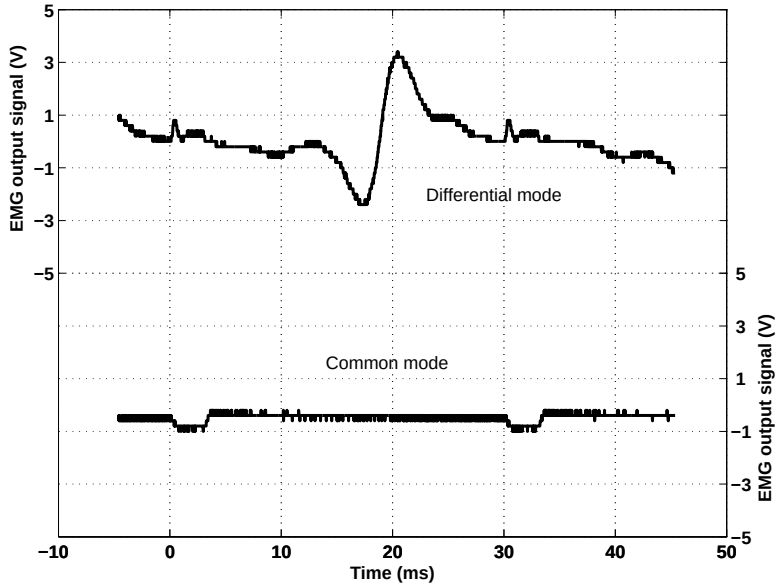

Figure 7.23: Differential and common mode EMG measurements for VL, with the *Standard* setup, reference electrode posterior thigh.

	T (ms)	PW (μs)	PW_r (%)	I_{stim} (mA)
Ch1	30	200	Varied	30
Stimulating electrode position:			*Standard*	
EMG amplifier:		1 (VM)	2 (RF)	3 (VL)
Gain		78dB (8188×)	65dB (1832×)	69dB (2676×)
Reference electrode position:			Posterior thigh	

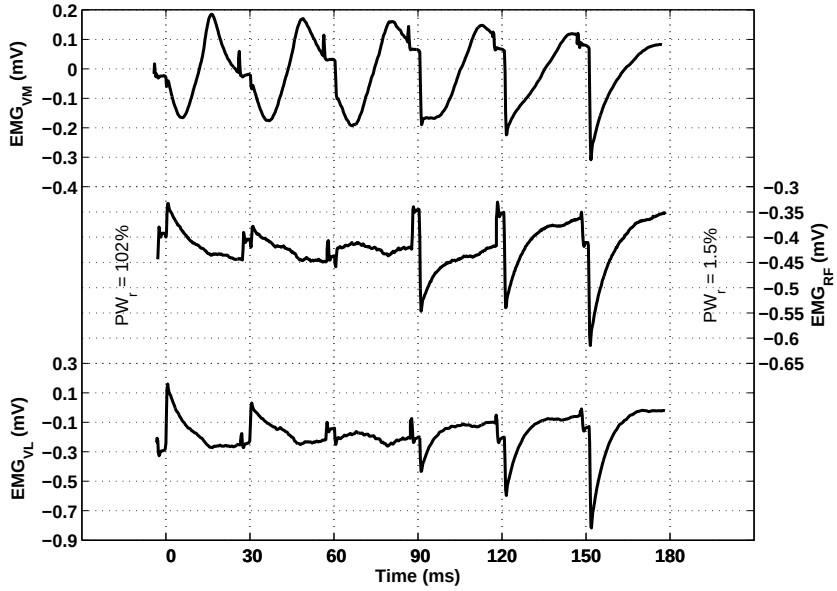

Figure 7.24: EMG measurements in the Quadriceps using the *Standard* electrode setup, for a range of PW_r settings, reference electrode on the posterior thigh.

The reason for this can be understood with reference to figure 7.22. By placing the reference electrode in the centre of the dipole, although V_{cm} was drastically reduced, it was not completely eliminated. If however, the reference electrode had been placed directly beneath the recording electrodes, a common mode voltage of 0V would have been achieved.

The dipole analogy is two dimensional, while the electric field setup in a subject's leg is three dimensional. Furthermore, the recording electrodes for RF and VL are situated on the lateral side of the leg, while those for VM are on the medial side. Consequently, to reduce the common mode voltage to near zero, as seen by the lateral side recording electrodes, the reference electrode would need to be placed on the medial side of the posterior thigh. Conversely, the reference electrode would need to be on the lateral side of the posterior thigh to reduce the common mode voltage seen by the medial recording electrodes to near zero. In both cases this means that the placement of the reference electrode would force the common mode voltage of one set of recording electrodes to near zero, but not for the other set, even though the common mode voltage would be reduced from that seen with the reference electrode on the knee.

This could potentially result in stimulation artefact due to two possible mechanisms. Firstly, if the common mode voltage was not sufficiently reduced, a stimulation artefact due to common mode voltage would still be present at the output of the amplifier. Secondly, any imbalance in the input impedance of the recording electrodes, in the presence of a common mode voltage, could result in a differential mode signal at the amplifier input, which would be seen as stimulation artefact in the output signal (as mentioned in Section 7.4.3, *Discussion*).

In practice the situation is further complicated by the inhomogeneity of the tissue resulting in an electric field with field lines that are not uniformly distributed. This makes it difficult to determine the required position for the reference electrode, to eliminate the common mode voltage stimulation artefact in either the medial or lateral side recording electrodes, let alone both simultaneously.

7.4.3 Limiting the common mode voltage at the EMG amplifier input

As placing the reference electrode on the posterior thigh was not an entirely satisfactory means to eliminate stimulation artefact, it was decided to rather limit the common mode voltage at the amplifier input, regardless of the reference electrode position. This was achieved through the introduction of the clamping diodes at the input terminals of the current conveyor circuit (refer to Section 6.2.2, *Clamping diodes*). Before the clamping diodes could be introduced it was necessary to know the size of the common mode voltage, present at the amplifier input terminals, that was causing the stimulation artefact. This was done by directly measuring V_{cm}.

Method

As before, the differential mode and common mode response of the amplifiers were measured, while stimulating with the *Standard* position. In addition to these measurements, an oscilloscope probe was connected between one of the recording electrodes and the reference electrode, thereby measuring V_{cm}.

These measurements were captured for three different setups:

1. Reference electrode on knee, without clamping diodes.
2. Reference electrode on posterior thigh, without clamping diodes.
3. Reference electrode on knee after introduction of clamping diodes.

The stimulator and amplifier settings used are indicated in the table with figure 7.25.

Results

Figures 7.25(a) through 7.25(c) show the waveforms captured for each of the three experimental setups. For each setup, three measurements were taken, namely:

1. EMG amplifier common mode (CM) response.
2. Potential difference between recording electrode and reference electrode (V_{cm}).
3. EMG amplifier differential mode (DM) response.

Figure 7.25(d) shows a magnified view of the V_{cm} measurements captured for each of the three setups.

Figures 7.25(a) and 7.25(b) show similar CM and DM amplifier responses to those discussed previously (refer to figures 7.20 and 7.23). Stimulation artefact was seen in both the DM and CM response, when the reference electrode was placed on the knee. Moving the reference electrode to the posterior thigh, eliminated the CM response stimulation artefact. In addition to this, we now see that with the reference electrode on the knee V_{cm} was measured at 5.68V. By repositioning the reference electrode V_{cm} was reduced to 3.36V.

This lead to the conclusion that, if the common mode voltage is limited to at most 3V, the common mode voltage induced stimulation artefact should be eliminated regardless of the reference electrode position. The clamping diodes were therefore introduced, as discussed in Section 6.2.2 (*Clamping diodes*), with a nominal limiting voltage of 2.1V.

The last trace in figure 7.25(d) shows the V_{cm} measurement after the inclusion of the clamping diodes. The amplitude of V_{cm} was now measured at 2.96V, even with the reference electrode moved back to the knee. Figure 7.25(c) shows that the CM response stimulation artefact had also been eliminated. The increase in the amplitude of the DM response stimulation artefact is attributed to the PW_r setting of 100.8%, as opposed to the PW_r setting of 61.4% that was used for the measurements shown in figures 7.25(a) and 7.25(b).

Method

The stimulation current setting of 20mA, used in the previous experiment, was below threshold voltage. Consequently no M-wave was present in the measurements. To investigate whether the addition of the clamping diodes influenced the M-wave measurements, the amplitude of the stimulation current was increased, the rest of the setup remained unchanged.

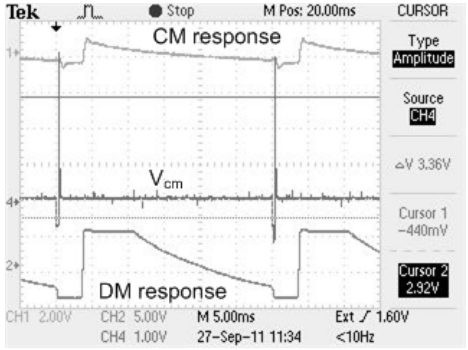

(a) Reference electrode on knee, $PW_r = 61.4\%$.

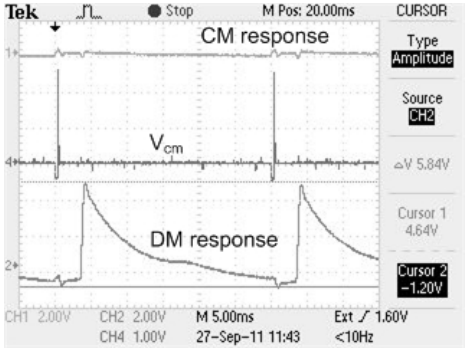

(b) Reference electrode on posterior thigh, $PW_r = 61.4\%$.

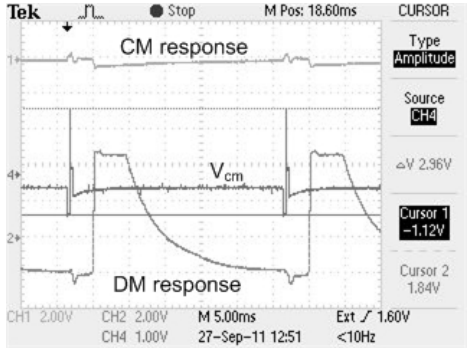

(c) Reference electrode on knee, with clamping diodes, $PW_r = 100.8\%$.

	T (ms)	PW (μs)	PW_r (%)	I_{stim} (mA)
Ch1	30	400	Varied	20
Stimulating electrode position:			*Standard*	
EMG amplifier:		1 (RF$_{cm}$)	2 (RF$_{dm}$)	3
Gain		63dB (1443×)	73dB (4250×)	-
Reference electrode position:			Knee or Posterior thigh	

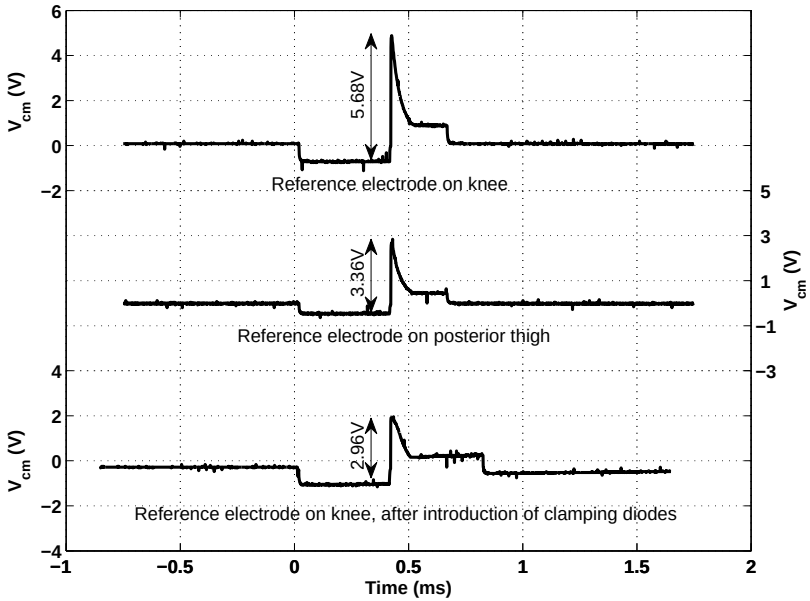

(d) Magnified view of common mode voltage measured at recording electrodes.

Figure 7.25: Influence of reference electrode position and clamping diodes on common mode voltage at the recording electrodes.

Results

For the top two traces in figure 7.26, the stimulation current was below threshold and no M-wave could be detected. For a PW_r setting of 42.9%, the stimulation artefact was present, although the amplitude thereof was quite small. Further decreasing the PW_r setting to 38.6% reduced the initial spike of the stimulation artefact, but also introduced a wave-like response in the EMG signal. The last trace in the figure shows the M-wave measured, after increasing the stimulation current to 40mA. The peak-to-peak amplitude of the M-wave is somewhat distorted by the presence of the wave-like response.

Discussion

Figure 7.27 shows the input stage of the preamplifiers, explicitly showing the clamping diodes and the input filter (refer to figure 6.5). From this figure we can see that presence of the diodes would have created a new discharge path for the residual charge present on the interface capacitance of the recording electrodes, (refer to Section E.3), which could lead to complicated

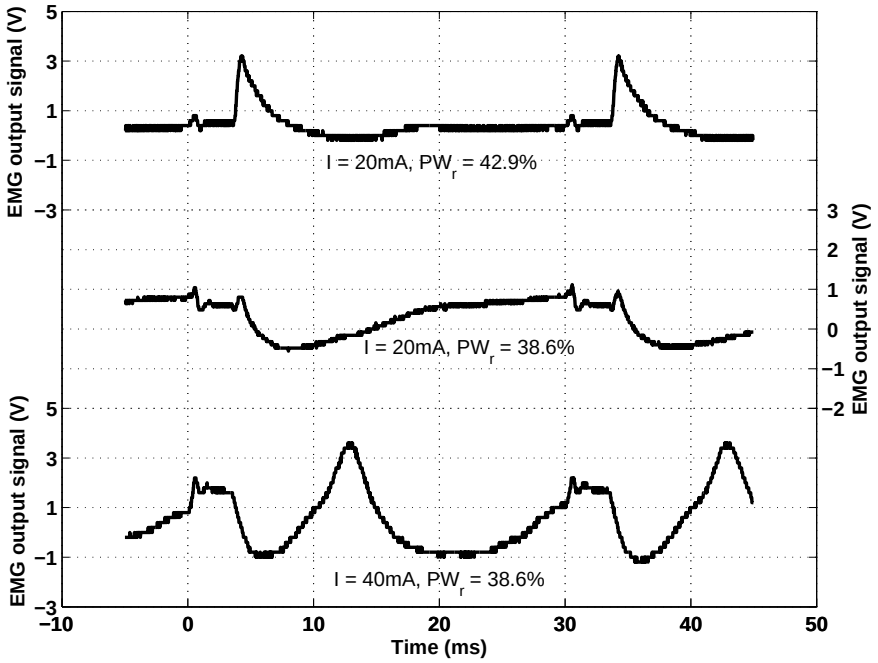

Figure 7.26: PW_r setting and M-wave measurement with clamping diodes.

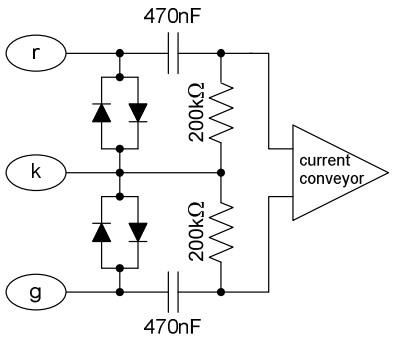

Figure 7.27: Skin-electrode interface effect at the recording site.

stimulation artefact shapes, a possible explanation for the wave-like response. However, no adverse effects on the M-waves, captured during the Bi-moment chair study discussed in Chapter 8, were seen due to this response. Consequently it was not given any further consideration.

Another shortcoming of the clamping diodes that should be pointed out, regards the input impedance of the EMG amplifiers, which is determined by the resistors and capacitors of the input filter. Any mismatch in these components would cause a mismatch in the input impedances. The presence of the clamping diodes could worsen this mismatch, which also serves as a source of stimulation artefact due to common mode voltage. This was discussed by McGill et al. [1982] who pointed out that the "common mode voltage present at the recording site is converted to an artefact signal proportional in amplitude to the imbalance between the recording electrode impedances."

7.5 Other causes of stimulation artefact

The main causes of stimulation artefact in the *Stimulator-Body-Amplifier* system used have already been presented. In this section, the blanking interval response is revisited and the relevance of other causes of stimulation artefact, as discussed by McGill et al. [1982] and McLean et al. [1996], are considered.

1. **Blanking interval response**

   In Section 6.5.2, the blanking interval (BI) response was introduced. Referring back to figure 6.28(b), we can see that the BI response could easily be mistaken for stimulation artefact. However, as this response was also present in the absence of a stimulation pulse, it was not classified as stimulation artefact. Section 6.5.2 discussed the need to keep the BI voltage level *centred*, by adjusting the biasing potentiometer, to prevent the BI response from occurring.

2. **Shaping by the recording amplifier**

   McGill et al. [1982] said that the passage of the spike through the recording amplifier's high pass filter introduces a slow exponential tail into the signal. This was not considered to be a main cause of stimulation artefact for the Blanking amplifier, although the high pass input filter would possibly influence the time constant of the exponential decay of the stimulation artefact. Possibly by changing the values of the components in the input filter or by completely removing the filter, it might be possible to reduce the time constant. The amplifier's role in shaping of the stimulation artefact is further discussed in Section 7.6.

3. **Displacement current travelling through the body tissue and via stray capacitance to ground**

   According to McLean et al. [1996] the entire body will be capacitively coupled to ground through a distributed capacitance over the entire length of the body through which some of the stimulation current will flow (referred to as the displacement current). This mech-

anism gave rise to stimulation artefact even when the recording electrodes were far removed from the stimulation site. The effect was reduced by placing a ground electrode between the recording and stimulating electrodes. For the setup considered here, where the recording electrodes were placed between the stimulating electrodes, it was not possible to differentiate between the stimulation artefact arising from voltage gradients, caused by the stimulation and discharge currents, from that due to the presence of displacement currents.

4. **Electromagnetic or capacitive coupling between the stimulating and recording leads**

   McLean et al. [1996] said that the coupling between the stimulating and recording leads could cause stimulation artefact, especially if very high impedance recording electrodes are used. The effect however is reduced by keeping the stimulating leads and recording leads separate, as short as possible and using shielding. In the system presented in this chapter, no thought was given to the placement of the leads while recording measurements. However, during construction of the Blanking amplifier the preamplifier design ensured that the recording electrode leads were as short as possible and that the cable between the preamplifier unit and the amplifier box was shielded.

7.6 The final verdict on stimulation artefact

For the system consisting of the Biphasic stimulator, the Blanking amplifier and the limb being stimulated, three main causes of stimulation artefact were identified, namely, voltage gradient, electrode-skin interface and common mode voltage.

Current flowing through tissue from an anode to a cathode sets up a voltage gradient in the tissue. This in turn causes a potential difference between the recording electrodes which is seen as stimulation artefact at the amplifier output. Ideally the current will only flow during a stimulation pulse. As soon as the current stops flowing between the stimulation pulses, there would be no voltage gradient and hence no stimulation artefact. By introducing the blanking capability into the EMG amplifiers, the amplifier would not be subjected to the voltage gradient caused by the stimulation current. However, a stimulation artefact was still present in the measurements taken with the Blanking amplifier. This implies that there is still current flowing between the stimulation pulses, that would produce a voltage gradient that affects the output of the amplifier. The source of this current was attributed to the presence of the blocking capacitor and the discharge resistor, found in the output stage of the Biphasic stimulator.

Any difference in charge during the positive and negative phases of the biphasic stimulation pulse, causes a residual charge to be present across the blocking capacitor at the end of a stimulation pulse. Between stimulation pulses, this residual charge would dissipate through the discharge resistor, causing a current to flow through the tissue, consequently setting up a voltage gradient and causing the stimulation artefact. However, the choice of components for the blocking capacitor and discharge resistor gives a time constant far longer than the stimulation period and far longer than that measured for the stimulation artefact. This indicated that,

although the presence of the blocking capacitor and discharge resistor created a path for the discharge current to flow between stimulation pulses, the blocking capacitor could not have been the only source of residual charge causing the discharge current to flow.

The electrode-skin interface, is actually an extension of the voltage gradient concept. The interface between the stimulating electrodes and the skin can be modelled as the parallel combination of a resistor and capacitor. This would further the charge imbalance between the positive and negative phases, as the interface resistance causes the interface capacitance to act as a leaky capacitor. At the end of a stimulation pulse there would be a residual charge distributed across the interface capacitance of both stimulating electrodes, as well as the blocking capacitor, which would give rise to the discharge current between pulses. The time constants of the electrode-skin interface would be much shorter than the stimulation period. By using the pulse width ratio adjustment capability of the Biphasic stimulator, it was possible to force the residual voltage to zero at the end of a stimulation pulse, thereby preventing a discharge current from flowing and eliminating the stimulation artefact.

The common mode voltage seen by the recording electrodes gave rise to the stimulation artefact through two mechanisms. Firstly, if the amplitude of the common mode voltage exceeded the common mode rejection capability of the amplifier, a response was measured at the output of the amplifier in the form of a stimulation artefact. This was combatted by reducing the amplitude of the common mode voltage either by careful placement of the reference electrode, or by using clamping diodes to limit the common mode voltage seen at the amplifier input. Secondly, any mismatch in impedance of the amplifier inputs, including the electrode-skin interface of the recording electrodes, results in a differential mode voltage at the amplifier input due to the presence of a common mode voltage.

A fourth cause of what appeared as stimulation artefact, although not considered to be one of the main three causes, was the blanking interval response of the amplifier. This response was inherent to the Blanking amplifier as it was present even in the absence of stimulation (i.e. no stimulation current, discharge current or common mode voltage). In the event that the bias position of the preamplifier was not *centred* (i.e. the blanking interval voltage was not matched to the baseline voltage prior to the stimulation pulse), then what appeared to be stimulation artefact would be present on the output of the amplifier. This was not rectified with the methods used for the previous three causes of artefact. Instead, this apparent stimulation artefact was eliminated by ensuring that the biasing level was *centred*.

Shaping of the stimulation artefact

Even though the causes behind the stimulation artefact were very different (voltage gradients set up by discharge currents, and, common mode voltage at the amplifier input), and each cause was eliminated by different methods (adjusting the PW_r setting, and, careful placement of the reference electrode or limiting V_{cm} at the amplifier input, respectively), the time constant of the stimulation artefact itself always appeared to be very similar.

For a number of the figures presented in this chapter, the time constant was estimated from the measurements and are listed in table 7.1. What immediately becomes evident is that there was a small difference in the stimulation artefact time constants. The artefact caused by voltage gradients had a time constant of around ∼10ms, while those caused by common mode voltage were around ∼20ms. The difference is particularly evident if we look at figures 7.19 and 7.20, where the two results are shown next to each other. Even though there was a difference between the two artefacts, it still raises the question, what is actually causing these time constants? To answer this, we first looked at observations that were made with regard to the discharge current and common mode voltages.

In Section 7.3.1 the PSPICE model indicated that the time constant associated with the discharge current varied according to the PW_r setting (refer to figure 7.11(b)). Nonetheless, the time constant itself was always less than 1ms. These values could be slightly out due to poor choices of the component values used in the electrode-skin interface model. However, it was unlikely that even with a more accurate model we would see time constants around 10ms, like those seen in the artefact.

Table 7.1: *Stimulator-Body-Amplifier* system time constants.

τ	**Artefact attributed to...**	**Refer to**	
		Section	**Figure**
∼8ms	Voltage gradient (discharge current)[a]	7.2	7.4(b)
∼10ms	Voltage gradient (discharge current)[a]	7.3	7.12(b)
∼10ms	Voltage gradient (discharge current)[a]	7.4	7.19
∼10ms	Voltage gradient (discharge current)[a]	7.4	7.25(b)
∼10ms	Voltage gradient (discharge current)[a]	7.4	7.25(c)
∼18ms	Common mode voltage (DM response)[b]	7.4	7.20
∼20ms	Common mode voltage (CM response)[b]	7.4	7.20
∼20ms	Common mode voltage (DM response)[b]	7.4	7.25(a)
∼15ms	Common mode voltage (CM response)[b]	7.4	7.25(a)
τ	**Observations**	**Refer to**	
		Section	**Figure**
<1ms	PSPICE model discharge current	7.3	7.11(b)
∼100μs	V_{cm} spike, same time constant for all three setups	7.4	7.25(d)
τ	**Stimulator and amplifier characteristics**	**Refer to**	
		Section	**Figure**
165ms	Stimulator output stage (R_d and C_b)	5.2.1[y]	-
∼10ms	BI response of amplifier	6.5.2	6.28(b)
∼10ms	DM transient response of amplifier	6.5.3	6.31(a)
∼15ms	CM transient response of amplifier	6.5.3	6.32(a)

[a] Adjusting PW_r eliminated stimulation artefact. [b] Adjusting PW_r had no effect on stimulation artefact.

In Section 7.4.3 the common mode voltage was measured. From figure 7.25(d) we can see that a spike in V_{cm}, which exceeded the common mode voltage capability of the amplifiers, resulted in stimulation artefact. However, the time constant of the spike was only $\sim$100μs.

From these observations we see that even though the discharge current and common mode voltage caused the stimulation artefacts, they were not responsible for the shape of the artefact.

McGill et al. [1982] proposed that the recording amplifier could be responsible for the shaping of the stimulation artefact. Taking this approach we next considered time constants inherent to the Biphasic stimulator and the Blanking amplifier, also listed in table 7.1. From this we can see that the Biphasic stimulator was not the cause, however, the transient response of the Blanking amplifier seemed to hold the answer.

In Section 6.5.3 the transient response of the Blanking amplifier, to both a differential mode (DM) and a common mode (CM) input voltage, was measured. The observed time constant of these two responses were $\sim$10ms and $\sim$15ms respectively. Remarkably similar to the two stimulation artefact time constants.

It was concluded that the stimulation artefact due to the voltage gradients, was being shaped by the output filter of the amplifier, just like the DM transient response, giving a time constant of $\sim$10ms. The stimulation artefact due to common mode voltage was being shaped by the CM response inherent to the current conveyor and the bandpass characteristic of the output filter, giving a time constant ranging from $15\text{ms} - 20\text{ms}$, just like the CM transient response.

7.7 Summary

Stimulation artefact is a known problem when recording M-waves in response to a stimulation pulse. If the stimulation artefact and the M-wave overlap, the M-wave measurement can be distorted, or even worse, its presence totally obscured. The artefact is typically seen as a voltage spike directly after the stimulation pulse, followed by an exponential decay. As the separation distance between the stimulating electrodes and the recording electrodes is reduced, the latency of the M-wave also decreases, thereby increasing the likelihood of the artefact and the M-wave overlapping.

The literature discusses a number of possible reasons for stimulation artefact. However, there is no global recipe, but rather the system consisting of the stimulator, amplifier and tissue being stimulated needs to be considered for each individual system, and the relevant causes of stimulation artefact identified.

For the system consisting of the Biphasic stimulator and the Blanking amplifier and the limb being stimulated the three main causes of stimulation artefact were identified as:

1. Voltage gradient.

2. Electrode-skin interface.

3. Common mode voltage.

Although, the electrode-skin interface is not actually a cause on its own. Rather it is a mechanism that sets up a voltage gradient in the tissue, which results in stimulation artefact.

A PSPICE model showed that the discharge current associated with the electrode-skin interface produces a wave-like response. This was attributed to different amounts of residual charge remaining on each stimulating electrode, after a stimulation pulse, due to differing electrode properties. However, the interface time constants were sufficiently short ($<$1ms) to ensure that there was little chance of the wave-like response being mistaken for an M-wave.

A number of experiments were discussed to highlight the effects of the various causes:

1. Electrode orientation was found to affect the polarity of the stimulation artefact. Reversing the orientation of the stimulating electrodes reverses the direction in which the discharge current flows and hence the direction of the voltage gradient. Reversing the orientation of the recording electrodes changes the polarity of the potential difference seen by the recording electrodes.

2. Placing the recording electrodes on equipotential lines removed the stimulation artefact.

3. By directly measuring the inter-electrode voltage, it was seen that pulse width ratio adjustment could be used to reduce the voltage to zero directly after a stimulation pulse, which corresponded with the elimination of the stimulation artefact at the amplifier output. Further decreasing the pulse width ratio setting beyond this point, reintroduced the stimulation artefact at the amplifier output, however the polarity had been reversed. This was due to the residual voltage being introduced into the system again, however the distribution of the charge had now been reversed, which resulted in the discharge current flowing in the opposite direction.

4. The amplitude of the stimulation current was directly proportional to the amplitude of the stimulation artefact. By increasing the amplitude of the current, the amount of residual charge present at the end of a stimulation pulse would also have increased. This in turn results in an increase in the amplitude of the discharge current, thereby increasing the amplitude of the stimulation artefact.

5. The values of the electrode interface components is dependent on various electrode properties. By using abrasive techniques and alcohol to prepare the skin under the electrodes the values of these components were changed, which showed a corresponding change in the amplitude and time constant of the stimulation artefact.

6. The PW_r setting required to eliminate stimulation artefact decreased as the stimulation current increased.

7. The PW_r setting also showed a dependency on the PW_p setting of the stimulation pulse. The higher the value of PW_p, the lower the required PW_r setting. The relationship between the two variables was exponential in nature, but due to the non-linearities inherent in the electrode-skin interface an exact model is difficult to obtain.

Part IV

Biomechanical and evoked EMG analysis

Chapter 8

Simultaneous measurement of joint moments and M-waves

8.1 Introduction

In an earlier study, discussed in Chapter 4, the Bi-moment chair was used to measure hip and knee joint moments, while using the three *major* electrode positions, *Standard*, *Rectus* and *Vastii*, to stimulate the Quadriceps. To briefly recapitulate, using the *Standard* position all three superficial muscles of Quadriceps, Rectus femoris (RF), Vastus lateralis (VL) and Vastus medialis (VM) were stimulated simultaneously. By using the *Rectus* position it was intended to only stimulate Rectus femoris, while the *Vastii* position targeted only Vastus lateralis and medialis. Due to the functionality of the three component muscles, we were expecting to see joint moment curves, for the three *major* positions, similar to those shown in figure 4.3 (repeated as figure 8.1 for ease of reference).

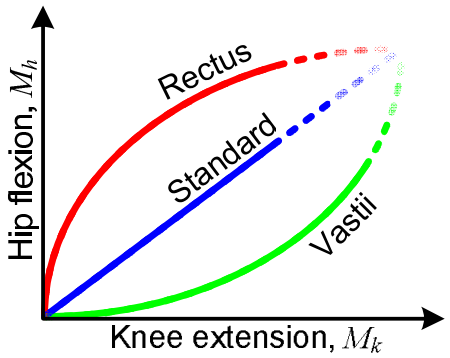

Figure 8.1: Moment curves for the three *major* electrode positions.

The *Rectus* position was expected to generate the largest hip flexion moment while the *Vastii* position would generate the smallest. However, the initial results did not show this outcome. Although the *Rectus* position did tend to produce the largest hip flexion moments, there was generally no reduction in the magnitude of the hip flexion moments measured with the *Vastii* position as compared with the *Standard* position (refer to the results discussed in Section 4.3.2).

It was shown that the reason for the negative results was not due to measurement error. Instead, it was thought that the explanation for the results was physiological. Were the three *major* electrode positions selectively stimulating the component muscles of Quadriceps as intended? To answer this question it was necessary to measure the evoked EMG response in the three muscles, during stimulation, for which the Biphasic stimulator and Blanking amplifier were designed and built. They were used during a second study with ten subjects, in which both joint moments and M-waves were simultaneously captured. The remainder of this chapter discusses this second study.

8.2 How the study was structured

The study was similar to that discussed in Section 4.2, although there were a few notable differences. The same terminology laid out at the start of Section 4.2 is used throughout this chapter.

8.2.1 Equipment setup

Figure 8.2(a) shows the wiring diagram of the various apparatus used in the setup. The interconnections between the apparatus are indicated, as well as the fact that the metal cases housing each piece of equipment were earthed.

Differences between this setup and that used previously were:

1. The Stanmore stimulator was replaced with the Biphasic stimulator. Consequently the 286 portable computer was also removed from the setup.

2. The Blanking amplifier was introduced into the setup.

3. The previously used real time *Simulink* program was replaced with the CED Micro1401 data acquisition system and *Signal* software. This was necessary as a sampling rate faster than that possible using the *Simulink* program, was required to capture the EMG data. The sensor electronics were also modified to facilitate a connection to the Micro1401, thereby using a single data acquisition system to capture all of the necessary signals simultaneously.

Photographs of the fully assembled system have been included in figures 8.2(b) and 8.2(c).

8.2.2 Electrode orientation

Figure 8.3 shows the positioning of both the recording and stimulating electrodes for all three *major* positions. One of the most prominent differences between this study and the study discussed in Chapter 4, is that each subject only took part in one session, because the *minor* positions were eliminated from the study and all three *major* positions were tested within a single session. The recording electrodes were therefore placed so that the stimulating electrodes could be repositioned (to realise each of the *major* positions), without having to move the recording electrodes. The electrode orientation was kept the same for all of the subjects.

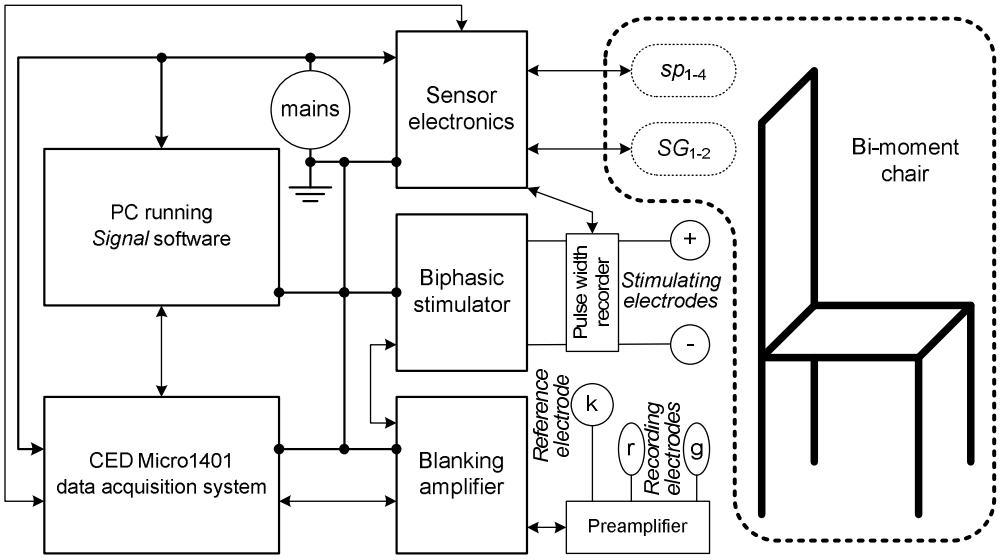

(a) Wiring diagram.

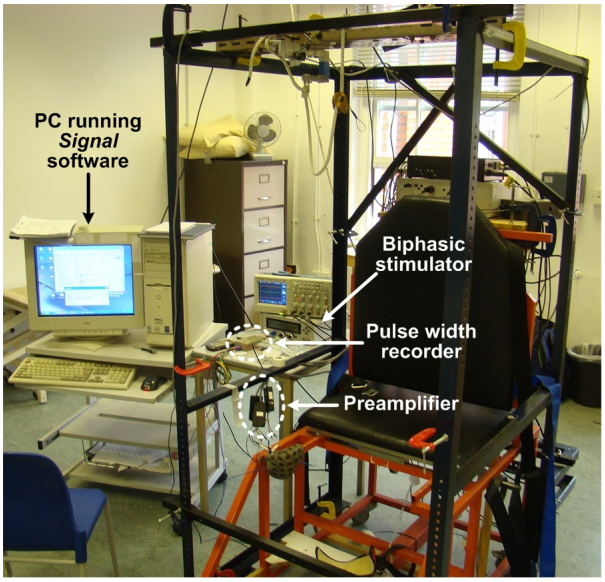

(b) Front view.

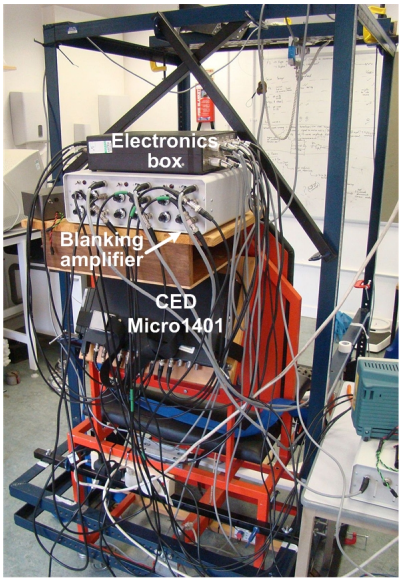

(c) Back view.

Figure 8.2: The Bi-moment chair, Biphasic stimulator and Blanking amplifier setup.

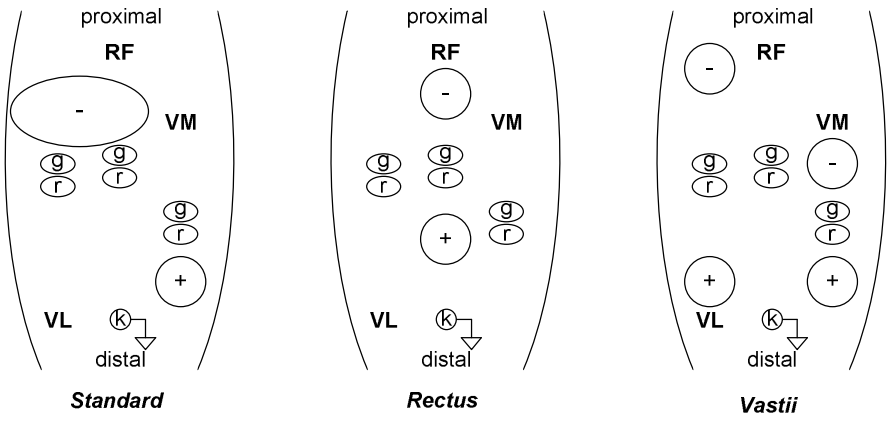

Figure 8.3: Orientation of stimulating and recording electrodes for the three *major* positions.

8.2.3 Recruitment curve protocol

The recruitment curve protocol used was similar to that discussed in Chapter 4; nine bursts of stimulation, each burst increasing in intensity by increasing the pulse width. The only difference was that the 10s rest interval between pulses was reduced to 3s. This was due to the manner in which the data was captured with the Micro1401 data acquisition system, which was limited to a recording frame seven seconds long when sampling data at 4.5kHz on 14 channels. The M-waves discussed in this chapter were captured during the last second of each stimulation burst, as highlighted in figure 8.4.

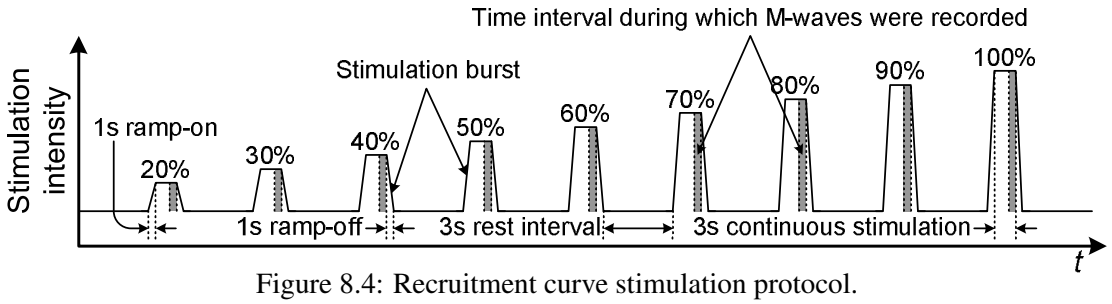

Figure 8.4: Recruitment curve stimulation protocol.

The stimulation parameters used are given in table 8.1. The maximum positive phase pulse width, PW_p, was set at either 200μs or 400μs. The choice of which maximum PW_p setting was used for each subject, is discussed in Section 8.3.

In Section 7.3.5 (*Influence of pulse width on the PW_r setting required to eliminate stimulation artefact*), the relationship between the PW_r setting and the pulse width of a biphasic stimulation pulse is discussed. Bearing in mind that biphasic stimulation pulses were used to produce the stimulation protocol shown in figure 8.4 and that the stimulation intensity of the protocol was varied by changing the PW_p setting of the individual stimulation pulses, it was therefore also necessary to adjust the PW_r setting during the protocol. The Biphasic stimulator was designed to automatically calculate the necessary adjustment, using equations 7.3 and 7.4, given that the PW_r setting required to cancel stimulation artefact at the maximum PW_p setting was known (as experimentally determined in the *initial setup phase*, discussed next).

Table 8.1: Stimulation parameters, recruitment curve protocol.

Parameter	**Setting**
Frequency	33 Hz
Positive phase pulse width	40μs up to 200μs, in steps of 20μs OR 80μs up to 400μs, in steps of 40μs
Current amplitude	Highest that is tolerable by the subject at the maximum positive phase pulse width OR where the force attains a plateau, whichever occurs first. For *Vastii*, different currents can be used medially and laterally.

8.2.4 Protocol followed during each session

After eliminating the *minor* positions, so that all three *major* positions were tested in a single session, the session itself was split up into two parts.

Initial setup phase

In the initial setup phase the stimulating and recording electrodes were placed on the subject. The skin beneath the recording electrodes was prepared using abrasive paper and alcohol. The current intensities that the subject was willing to withstand during constant stimulation (33Hz, maximum PW_p setting used in the recruitment curve protocol), for each of the three *major* positions, was then found. At the same time the PW_r setting required to eliminate stimulation artefact was found, at the highest stimulation intensity that the subject was able to tolerate. The Biphasic stimulator automatically calculated the PW_r settings required during each burst of stimulation of the recruitment curve protocol, using this PW_r setting.

As this phase was quite lengthy, upon completion the subject was allowed a half hour rest before being strapped into the Bi-moment chair for the second part of the session.

Measurement of joint moments and EMG

During this part of the session the joint moments and EMG measurements were captured in response to a number of tests of the recruitment curve protocol. The following procedure was used:

1. At the beginning and end of each session, MVC and FF tests were performed, similar to those discussed in Section 4.2.3.

2. One test of the recruitment curve stimulation protocol was completed for each of the *major* positions while placing the reference electrode on the knee.

3. A second test was performed for the *Standard* position with the reference electrode placed on the posterior thigh.

4. An additional two tests were performed on some of the subjects for the *Rectus* and *Vastii* positions with the reference electrode also placed on the posterior thigh. This helped to investigate the influence of moving the reference electrode on the M-wave measurements.

5. The order in which the *major* positions were tested was different for each of the 10 subjects, so as not to introduce a bias.

6. The subject was allowed a 5 minute rest between tests.

7. The first position tested was repeated again in the last test of the session to help monitor fatigue. It was ensured that the position of the reference electrode in the last test was the same as that used in the first test.

8.2.5 Subject participation

Ten subjects took part in the study (four female, six male; age: 33.4 ± 14.5 years; height: 1.75 ± 0.11 m; weight: 72.37 ± 12.51 kg). The number of tests that were carried out for each subject, the *major* electrode position tested and the position of the reference electrode during the test, are listed in table 8.2.

Table 8.2: Subject participation in the study.

Subject	No. of tests	Stimulating and reference electrode positions for each test
A	7	S(p), R(p), R(k), V(k), V(p), S(k), S(p)
B	6	V(p), V(k), R(k), S(p), S(k), V(p)
E	8	V(k), V(k), S(k), S(k), S(p), R(p), R(k), V(k)
F	6	R(k), V(k), S(k), S(p), R(p), R(k)
G	5	S(k), V(k), S(p), R(k), S(k)
H	6	R(k), S(p), V(p), V(k), S(k), R(k)
I	6	S(k), S(p), V(p), V(k), R(k), S(k)
J	5	S(k), V(k), R(k), S(p), S(k)
K	5	S(p), S(k), V(k), R(k), S(p)
L	5	R(k), S(k), V(k), S(p), R(k)

S - *Standard* position, R - *Rectus* position, V - *Vastii* position.
(k) - reference electrode knee, (p) - reference electrode posterior thigh.

8.3 Understanding the results

Figure 8.5 shows a typical set of measurements captured for one of the 10 subjects. The moment curves, figure 8.5(a), showed the knee joint and hip joint moments plotted against each other. Each trace corresponds to a test of the stimulation recruitment curve protocol.

In addition to the joint moment measurements, the M-waves were measured in RF, VL and VM during each test. Figure 8.5(b) shows the M-waves captured during the test where the electrodes were placed in the *Rectus* position (red line in figure 8.5(a)). A similar M-wave plot exists for each of the other moment curve traces (green and blue lines).

If we consider the top row of M-waves, namely the EMG measurements taken for VM, we see that there are nine M-waves, consecutively increasing in amplitude. Recalling that the recruitment curve protocol consisted of nine bursts of stimulation, each increasing in intensity we can see that each of these nine M-waves corresponds with a stimulation burst. It should also be noted that each of these nine M-waves actually consist of 33 M-wave traces plotted on top of one another. This can be explained by referring to figure 8.4 in which the time interval during each stimulation burst, in which the M-waves were captured, was highlighted. The M-waves were recorded during a 1s period, at the end of each stimulation burst. As the stimulation frequency was set at 33Hz, a total of 33 M-waves were captured during each 1s period. For each burst of stimulation, the average peak-to-peak amplitude found for the 33 overlapping M-wave traces was found, and has been displayed on the figure below each M-wave. Markers

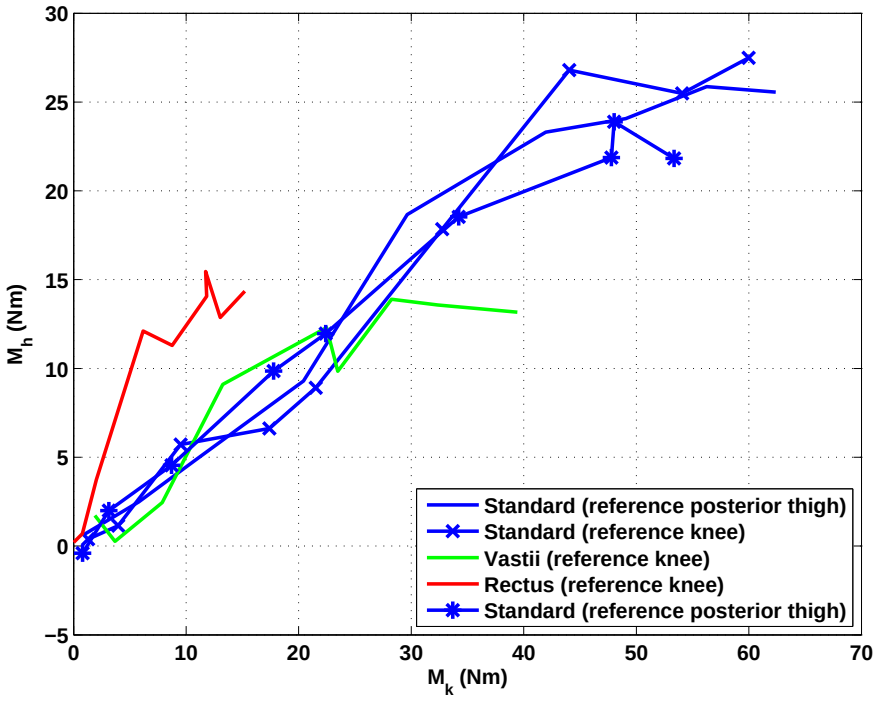

(a) The moment curves captured during the entire session. The red trace corresponds with the M-wave measurements.

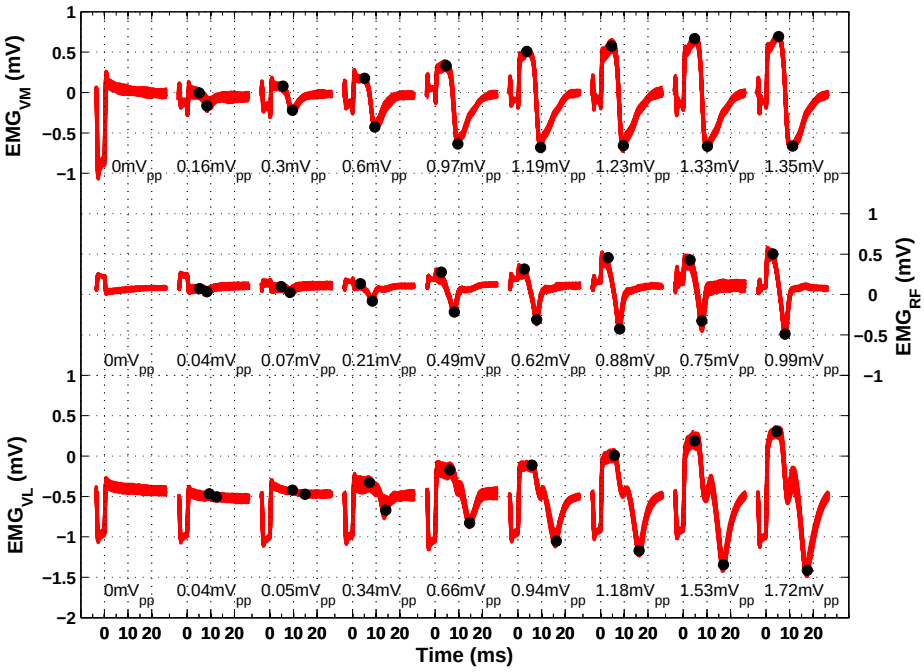

(b) M-waves measured in three component muscles of Quadriceps, when stimulating with the *Rectus major* position.

Figure 8.5: A typical set of results, captured for subject K.

were drawn on the peaks of each M-wave that were used to calculate the amplitude measurements. Similar results can be seen in the second and third rows of figure 8.5(b) for the EMG measurements of RF and VL respectively.

As mentioned in Section 8.2.2, the same electrode orientation was used for all of the subjects. However, the polarity of the recorded M-waves was not always the same. In the previous chapter the M-wave polarity was presented exactly as it was measured so that the influence of the electrode orientation on polarity and stimulation artefact could be discussed. In this chapter the results presented were sometimes plotted with opposite polarity to that actually measured so that the M-waves were always shown to have conventional polarity (refer to Section 1.2), thereby making visual comparisons easier, but not interfering with the relevant data, namely the peak-to-peak amplitudes.

From hereon, the term **data set** is used to refer to the moment curves and the corresponding M-wave measurements captured for the three superficial muscles of Quadriceps, for each subject.

The M-wave measurements shown in figure 8.5(b) are an ideal set of measurements in which the M-wave amplitude could easily be measured in all three Quadriceps muscles, for all nine stimulation bursts. This, however, was not always the case.

It was sometimes difficult and occasionally impossible to eliminate the stimulation artefact from all three muscles simultaneously. As a result the EMG measurements were sometimes saturated with stimulation artefact making it impossible to obtain a reliable M-wave amplitude measurement. As a consequence of this, the methods used to eliminate the stimulation artefact were modified during the study, after problems became evident from the data sets captured for the first few subjects and as more was learnt about the cause of the stimulation artefact and ways to eliminate it.

Table 8.3 gives a list of the 10 subjects and the various settings and methods used to eliminate stimulation artefact.

Table 8.3: Settings used during sessions for each of the subjects.

Subject	**Maximum PW_p (μs)**	**SA elimination methods**		
		PW_r equation	**Reference thigh**	**Clamping diodes**
A	200	(7.3)	✓	×
B	200	(7.3)	✓	×
E	200	(7.3)	✓	×
F	200	(7.3)	✓	×
G	200	(7.3)	✓	×
H	200	(7.3)	✓	×
I	400	(7.3)	✓	×
J	400	(7.4)	✓	✓
K	400	(7.4)	✓	✓
L	400	(7.4)	✓	✓

Maximum PW_p

In Section 8.2.3 it was mentioned that the maximum positive phase pulse width, PW_p, setting was either 200μs or 400μs. Table 8.3 explicitly shows the maximum PW_p setting used for each subject. Initially the maximum PW_p was set at 200μs. This was based on the assumption that a biphasic stimulation pulse with a pulse width of 200μs per phase would be equivalent to a monophasic stimulation pulse of 400μs (as used in the study discussed in Chapter 4).

However, a few of the subjects who had participated in the earlier study commented that the evoked contraction no longer felt as strong. Furthermore, the magnitude of the moments generated was also less, as can be seen when comparing the moment curves captured for subject A in the first study (refer to figure 4.7) with those captured for subject A in the second study (refer to figure 8.10). It was realised that the lower pulse width of 200μs accounted for the low moment magnitudes. Consequently, for subjects I through L, the per phase pulse width was increased to a maximum of 400μs.

An explanation for the 200μs PW_p producing weaker contractions than a monophasic pulse of 400μs was provided by Nilsson et al. [1988], who stated that the evoked response is only influenced by the first phase of the biphasic pulse. During the second phase the nerve is refractory, which means that the second phase only plays a part in helping to eliminate stimulation artefact.

Preventing discharge currents from flowing

The table also lists three different methods used to eliminate the stimulation artefact (SA). The first method shown, "PW_r *equation*", was used to eliminate stimulation artefact caused by the flow of discharge currents. The numbers given in the table refer to equations, presented in Section 7.3.5 (*Influence of pulse width on the PW_r setting required to eliminate stimulation artefact*), that describe the relationship between the PW_r setting and the pulse width. The Biphasic stimulator used these equations to automatically adjust the PW_r setting during the recruitment curve protocol.

The first equation used, equation 7.3, was limited to a maximum PW_p of 200μs, while the second equation used, equation 7.4, described the relationship up till 400μs.

Generally equation 7.3 was used for the subjects with a maximum PW_p of 200μs. While equation 7.4 was used for the subjects with a maximum PW_p of 400μs. The only exception to this rule was with subject I, where equation 7.3 was used even though the PW_p setting was 400μs. Subject I was the first subject to be stimulated with the higher PW_p setting. During this session it was found to be necessary to modify the equation describing the relationship between the PW_r and PW_p settings, as the stimulation artefact was no longer eliminated though out all nine stimulation bursts.

Limiting the common mode voltage

The last two methods listed in the table were both used to eliminate stimulation artefact caused by excessive common mode voltage.

The "*Reference thigh*" method, refers to the placement of the reference electrode on the posterior thigh, as discussed in Section 7.4.2. This method was used for all 10 subjects when stimulating with the *Standard* position.

The "*Clamping diodes*" method referred to the introduction of common mode voltage limiting diodes at the input stages of the Blanking amplifier (refer to Section 7.4.3). This modification was only made to the equipment setup prior to the sessions carried out with the last three subjects.

8.3.1 Effectiveness of stimulation artefact elimination methods

The effectiveness of each of these stimulation artefact elimination methods is now discussed with reference to M-wave measurements captured during the study.

Results: PW_r setting

Figure 8.6 shows the EMG measurements captured in RF, VM and VL for subject J, when stimulating with the *Vastii* position and the reference electrode placed on the knee. The table above the figure lists the maximum PW_p value used and the corresponding PW_r values, for the given stimulation current. These were the stimulator settings used during the recruitment curve protocol. The PW_r setting was adjusted during the nine bursts of stimulation using equation 7.4.

Inspection of the EMG measurements shows that M-waves were captured for all nine stim-

	PW_p (μs)	PW_r (%)	I_{stim} (mA)
VM	400	56.1	22
VL	400	67.1	40
Reference electrode position:			Knee

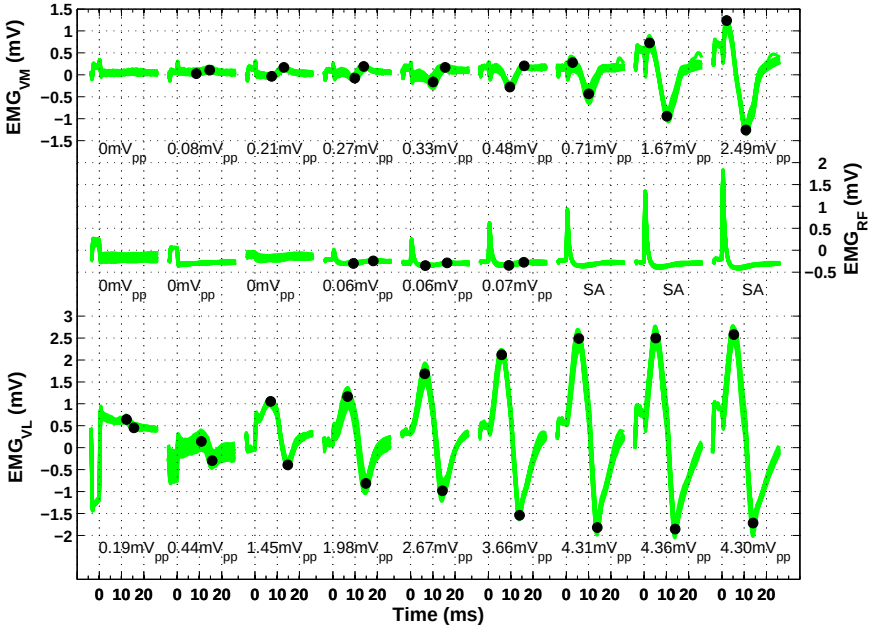

Figure 8.6: M-wave measurements for subject J, *Vastii* position, with clamping diodes.

ulation bursts for VM and VL. However, this was not the case for RF, where the stimulation artefact saturated some of the measurements.

Discussion: PW_r setting

This was one of the problems that arose during the study, namely that it was not always possible to find a PW_r setting that cancelled the stimulation artefact in all three muscles simultaneously. This problem seemed to be particularly prevalent when stimulating with the *Vastii* position, for which two stimulating channels were used simultaneously, where the PW_r setting for each channel was independently set.

In Section 7.3.1, the PSPICE model of the electrode-skin interface showed that a PW_r setting could be found such that the sum of the residual voltages, across the stimulating electrodes and the blocking capacitor, was zero. This was a simplified approximation where the electrode-skin interface was considered to behave linearly and the influence of the recording electrodes and the reference electrode were omitted. In practice, when stimulating with the *Vastii* position, there are a total of six stimulating electrodes, six recording electrodes, one reference electrode and two blocking capacitors. The component values, associated with each of the skin-electrode interfaces, would vary with time, and exhibit non-linear behaviour.

Clearly the situation is far more complicated than that considered earlier. It was therefore possible that, even after adjusting the PW_r setting, that residual charge present on some of the electrode interfaces would cause a discharge current to flow, between the electrodes, through the tissue, potentially causing a stimulation artefact.

The reason as to why it was possible to eliminate the stimulation artefact, while stimulating with the *Vastii* position, for some of the subjects, but not others, is not understood.

Results: Position of the reference electrode

Figure 8.7 shows similar M-wave measurements that were captured for each of the three *major* positions. All three plots show the results from more than one test. The black traces represent tests that were carried out with the reference electrode placed on the knee, while the coloured traces were captured during tests with the reference electrode placed on the posterior thigh. Other than the position of the reference electrode, no changes were made in stimulating and recording electrode positions, nor in the stimulation intensity settings.

Discussion: Position of the reference electrode

Figure 8.7(a) shows measurements captured with subject F, when stimulating with the *Standard* position. In this case it was impossible to eliminate the stimulation artefact from all three of the Quadriceps muscles, simply by adjusting the PW_r setting, as long as the reference electrode was placed on the knee (black traces captured for RF and VL). This was typical of results captured when stimulating with the *Standard* position, prior to using the clamping diodes. However, even without the aid of the clamping diodes, simply by moving the position of the reference electrode to the posterior thigh, the stimulation artefacts, in the RF and VL measurements, were eliminated and M-waves became discernible (blue traces).

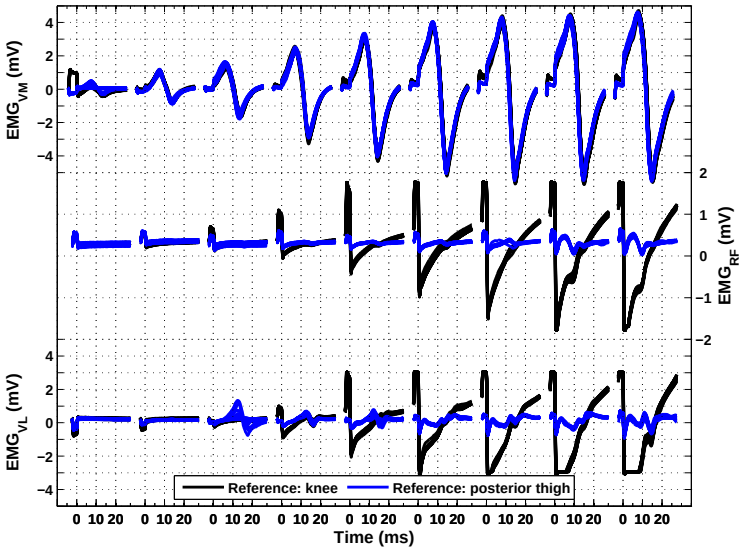

(a) Subject F, *Standard* position.

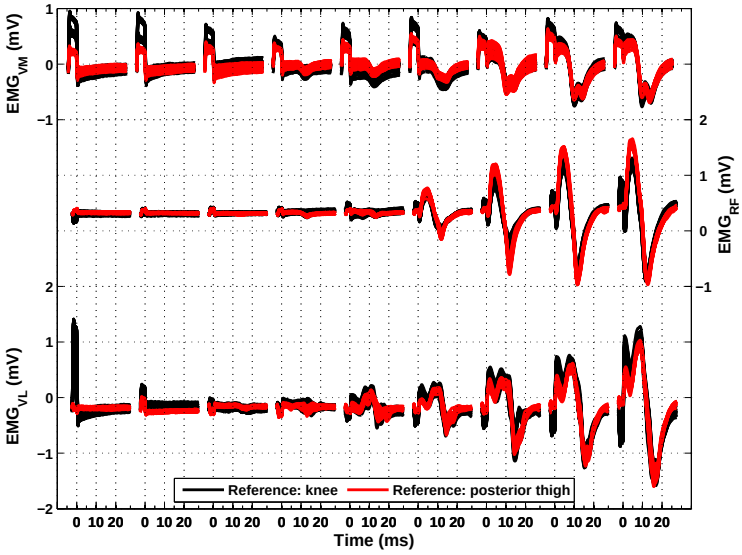

(b) Subject F, *Rectus* position.

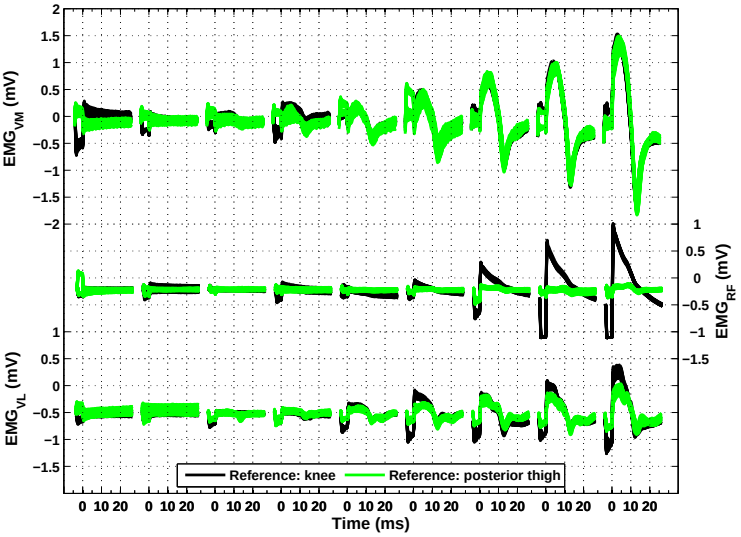

(c) Subject B, *Vastii* position.

Figure 8.7: Comparison of M-waves measured with the reference electrode placed either on the knee or on the posterior thigh, prior to the introduction of clamping diodes.

The stimulation artefact seen here was caused by the common mode voltage range of the amplifier being exceeded. By moving the reference electrode to the posterior thigh (i.e. the centre of the stimulation dipole), the common mode voltage was reduced, thereby eliminating the stimulation artefact (refer to Section 7.4).

In practice the reference electrode is normally placed on electrically inactive tissue, often making use of a bony protuberance such as the patella. Consequently, even though placing the reference electrode on the posterior thigh did remove the stimulation artefact, it still raised questions about the quality of the M-waves captured as the muscles in the posterior thigh can be electrically active. However, in our application it was expected that these muscles would be relaxed during the stimulation protocol, thus not influencing the M-wave measurements.

This was investigated by recording M-waves when stimulating with the *Rectus* position, for both positions of the reference electrode, as shown in figure 8.7(b). For the majority of tests carried out with the *Rectus* position, the common mode voltage of the amplifier was not exceeded when the reference electrode was placed on the knee. Consequently it was possible to eliminate stimulation artefact in all three muscles just by adjusting the PW_r setting (black trace in figure 8.7(b)). Moving the reference electrode to the posterior thigh showed no changes in the shape or timing of the measured M-waves, as indicated by the overlapping black and red traces. This was used to justify the placement of the reference electrode on the posterior thigh.

M-waves captured when using the *Vastii* position produced results somewhere between those captured for the *Standard* and *Rectus* positions:

- At times, it was possible to eliminate stimulation artefact from all three muscles with the reference electrode placed on the knee, just with careful selection of the PW_r settings.
- With some of the subjects it was not possible to eliminate all of the stimulation artefact. However, provided the stimulation artefact was caused by common mode voltage, it could be eliminated by placing the reference electrode on the posterior thigh (refer to figure 8.7(c)), or through the use of clamping diodes.
- In a few of the cases, no matter what method was used to try and reduce the artefact, it was not possible to eliminate it completely (refer to figure 8.6).

Results: Introduction of clamping diodes at amplifier input

Figure 8.8 shows the M-wave measurements captured for subject K, when stimulating with the *Standard* position. The clamping diodes were present at the amplifier input for these measurements.

As before, the black traces in the figure show M-wave measurements captured during a test with the reference electrode on the knee, while blue traces show measurements captured with the reference electrode on the posterior thigh. By introducing the clamping diodes the stimulation artefact that had previously been present, when the reference electrode was on the knee, was no longer evident. There was now virtually no difference between the two tests, regardless of the position of the reference electrode.

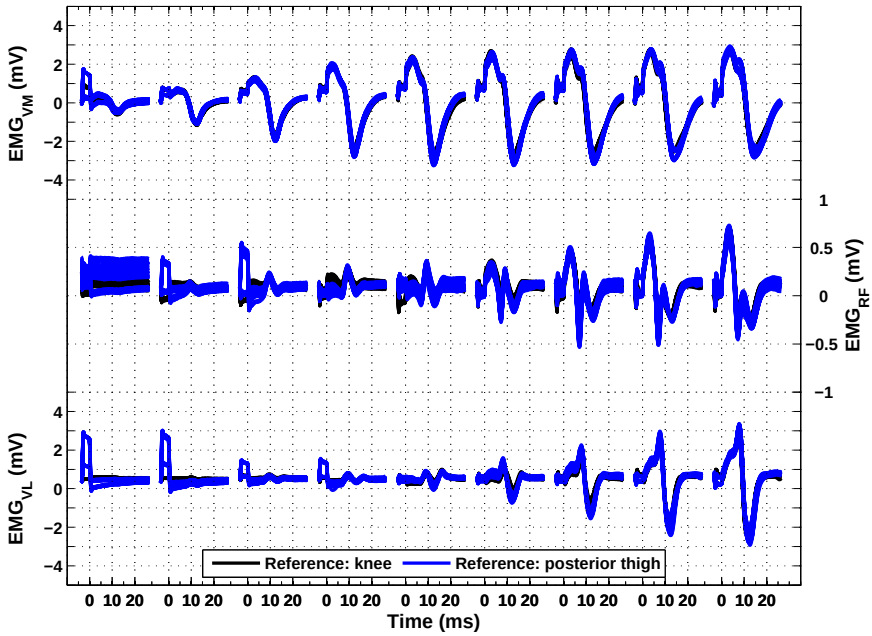

Figure 8.8: Comparison of M-waves measured with the reference electrode placed either on the knee or on the posterior thigh, after introduction of clamping diodes (Subject K, *Standard* position).

Discussion: Introduction of clamping diodes at amplifier input

The introduction of the clamping diodes to the input stage of the Blanking amplifier had a similar effect to that achieved by repositioning the reference electrode, namely ensuring that the common mode input voltage of the amplifier was not exceeded. The diodes did however work slightly differently by actually limiting the common mode voltage that could occur at the amplifier input (discussed in Section 7.4).

The M-waves captured using the *Standard* position have been summarised in table 8.4.

Table 8.4: M-wave recordings for the *Standard* electrode position.

Subject	Reference knee			Reference thigh		
	VM	RF	VL	VM	RF	VL
A	✓	SA	SA	✓	✓	✓
B	✓	SA	SA	✓	✓	✓
E	✓	SA	SA	✓	SA	SA
F	✓	SA	SA	✓	✓	✓
G	✓	SA	SA	✓	✓	SA
H	✓	SA	SA	SA	✓	✓
I	✓	SA	SA	SA	SA	SA
J	✓	✓	✓	✓	✓	✓
K	✓	✓	✓	✓	✓	✓
L	✓	✓	✓	✓	✓	✓

✓- Possible to measure M-wave peak-to-peak amplitude for all 9 stimulation bursts.
SA - Stimulation artefact present in at least one of the 9 stimulation bursts.

Clearly for the first 7 subjects the position of the reference electrode greatly influenced the presence of stimulation artefact. However, for the last 3 subjects, after the clamping diodes had been introduced, this was no longer the case. This is a clear indication that when stimulating with the *Standard* position, the stimulation artefact could be attributed to common mode voltages.

The only exception was seen in the results measured for subject I. This can be explained with reference to table 8.3 where it was shown that the equation used to calculate the required PW_r setting during the stimulation protocol was not intended for a PW_p value of 400μs. This meant that the stimulation artefact present in the results of subject I were due to discharge currents caused by the presence of residual voltage at the electrode-skin interface, and not common mode voltage. Consequently the methods used to eliminate stimulation artefact caused by common mode voltage did not work. However, by correcting the method used to calculate PW_r for the last three subjects, the stimulation artefact due to both discharge currents and common mode voltage were eliminated.

8.3.2 Effect of stimulation artefact elimination on data analysis

From the results presented thus far, it is evident that the effectiveness of the stimulation artefact elimination varied from subject to subject. Furthermore, for any one subject, the effectiveness of the stimulation artefact elimination also varied for the three different *major* positions. To be able to use these results to investigate the selectivity of the three *major* positions, it was necessary to have complete data sets. A **complete data set** was defined as a data set that had:

1. At least one moment curve captured for each of the three *major* positions.
2. For each of these three moment curves, the corresponding M-waves had to be captured, for each stimulation burst in all three superficial muscles RF, VL and VM. (i.e. Peak-to-peak amplitudes could be measured for all of the M-waves, no information was lost due to the presence of stimulation artefact.)

For all 10 subjects, the first requirement was met. However, due to the presence of stimulation artefact in some of the M-wave measurements, not all of the 10 subjects met the second requirement. The M-waves captured, for each of the *major* positions, have been summarised in table 8.5. For the *Standard* position results shown, the reference electrode was placed on the posterior thigh, while for the *Rectus* and *Vastii* positions it was placed on the knee, unless otherwise noted.

The subjects who met all of the criteria for a complete data set have been highlighted. Of the 10 subjects, a complete data set was only captured for 4 subjects. This indicates the difficulty of eliminating stimulation artefact from multiple muscles simultaneously, during a stimulation protocol in which the stimulating intensity is varied.

So as to prevent introducing a bias into the results, when investigating the selectivity of the *major* positions, only the four subjects with complete data sets were used in the group analysis discussed in Sections 8.4.3 and 8.4.4.

Table 8.5: M-wave recordings for all three *major* positions.

Subject	*Standard*			*Rectus*			*Vastii*		
	VM	**RF**	**VL**	**VM**	**RF**	**VL**	**VM**	**RF**	**VL**
A	✓	✓	✓	✓	✓	✓	✓	SA	✓
B	✓	✓	✓	✓	✓	✓	✓[a]	✓[a]	✓[a]
E	✓	SA	SA	✓	✓	✓	✓	SA	SA
F	✓	✓	✓	✓	✓	✓	✓	✓	✓
G	✓	✓	SA	✓	✓	✓	✓	SA	✓
H	SA	✓[b]	✓[b]	✓	✓	✓	✓[a]	✓[a]	✓[a]
I	SA	SA	SA	✓	SA	SA	SA	SA	SA
J	✓	✓	✓	✓	✓	✓	✓	SA	✓
K	✓	✓	✓	✓	✓	✓	✓	✓	✓
L	✓	✓	✓	✓	✓	✓	✓	✓	✓

✓- Possible to measure M-wave peak-to-peak amplitude for all 9 stimulation bursts.
SA - Stimulation artefact present in at least one of the 9 stimulation bursts.
[a] Reference electrode posterior thigh.
[b] No stimulation artefact to obscure results, but also no M-waves detected.

8.3.3 Crosstalk

In Section 1.3.2 the phenomenon of crosstalk was introduced. From the discussion it was evident that using a single differential (SD) detection system, which the input stage of the Blanking amplifier can be likened to, the EMG recorded in the non-stimulated muscles of the Quadriceps will partially be attributed to crosstalk. In Chapter 1 the results of Knaflitz et al. [1988], Farina et al. [2002] and Solomonow et al. [1994] were used to show that at most 25% to 28% of the EMG signal in the stimulated Quadriceps muscle can appear as crosstalk in the non-stimulated muscles.

It was therefore decided to adjust the M-wave measurements from the complete data sets, to account for crosstalk, prior to the group analysis discussed in Sections 8.4.3 and 8.4.4. The adjustment involved calculating 25% of the peak-to-peak amplitude from the M-wave measured in the stimulated muscle and subtracting this amount from the M-wave amplitudes measured in the non-stimulated muscle. Table 8.6 lists the adjustments made for each of the three *major* positions.

Table 8.6: Crosstalk adjustments.

***major* position**	**Adjustment made**
Standard	No adjustment for crosstalk as all three muscles (RF, VM and VL) are stimulated.
Rectus	25% of M-wave amplitude measured in RF subtracted from amplitude of M-waves measured in VM and VL.
Vastii	25% of M-wave amplitude measured in either VM or VL, whichever is larger, subtracted from amplitude of M-wave measured in RF.

As an example of the adjustments made, consider the M-waves shown in figure 8.5(b). Table 8.7 lists the M-wave amplitudes shown in the figure that were directly measured with the Blanking amplifier, as well as the M-wave amplitudes after being adjusted to account for the possibility of crosstalk.

Table 8.7: Example: M-wave amplitudes adjusted for crosstalk, *Rectus* position.

Stimulation burst	Peak-to-peak amplitude (mV)					
	Measured			Adjusted		
	RF	VM	VL	RF	VM	VL
1	0.00	0.00	0.00	0.00	0.00	0.00
2	0.04	0.16	0.04	0.04	0.15	0.03
3	0.07	0.30	0.05	0.07	0.28	0.03
4	0.21	0.60	0.34	0.21	0.55	0.29
5	0.49	0.97	0.66	0.49	0.85	0.53
6	0.62	1.19	0.94	0.62	1.03	0.79
7	0.88	1.23	1.18	0.88	1.01	0.96
8	0.75	1.33	1.53	0.75	1.14	1.35
9	0.99	1.35	1.72	0.99	1.11	1.47

8.4 Study outcome

8.4.1 Muscle fatigue

Results: MVC and FF tests

The results found for the MVC and FF fatigue tests are shown in table 8.8. The force measurements captured for the shank, $\mathbf{F}_s$, during the two tests were used to calculate:

1. The MVC force after the session, normalised to baseline values.
2. The 20Hz to 50Hz ratio before and after each session.

Table 8.8: Fatigue measurements calculated using $\mathbf{F}_s$ measurements.

Subject	MVC %	FF ratios	
		before	after
A	88.5	0.47	0.45
B	123.2	1.25	0.73
E	112.6	0.67	0.72
F	111.6	0.51	0.50
G	101.5	0.75	0.55
H	- [a]	0.11	0.26
I	120.9	0.60	0.07
J	77.0	0.77	0.72
K	102.7	0.56	0.40
L	96.4	0.87	0.65

[a] An error occurred while recording the MVC measurements.

Discussion: MVC and FF tests

Subject A and J show a sizable drop in the MVC, indicative of fatigue. Subjects G, K and L, show little change in the MVC at the end of the session, indicating minimal fatigue. However, subjects B, E, F and I, all show a stronger MVC at the end of the session. These results may indicate that they did not perform a true MVC at the start. Also, slippage sometimes occurred in the cord connecting the strain gauge transducer, SG_2, to the shank. This was the reason for no MVC measurements being captured for subject H. Even though the slippage affected the MVC measurements, it was not seen to be a problem when capturing force measurements in response to stimulation, as the magnitude of the forces generated (3N-160N), was substantially less than that measured during a voluntary contraction (196N-510N). Therefore it was not possible to draw any conclusions about the fatigue experienced, from the MVC results.

The FF test results were analysed as in Section 4.3.1, where a drop of 0.2 or greater was indicative of fatigue. For most of the subjects there was some fatigue (a drop of 0.2 or greater), or minimal fatigue (a drop of less than 0.2). However, once again, there were a few exceptions. Firstly as seen for subject B, where a ratio of greater than one was calculated and secondly for subjects E and H, where the FF ratio after the session was greater than that measured at the start of the session.

Further inspection of measurements for subjects B, E and H, show that they only generated forces of 5N or less during the FF tests. This meant that the difference between the forces, measured at 20Hz and 50Hz, was often less than 1N (force magnitudes of $\sim$10N, with differences of $\sim$5N, were often measured for the other seven subjects).

Using the strain gauge transducer calibration equations shown in figure 2.7(b) and the standard deviation equation (refer to equation 3.6), it was possible to convert the force difference in newton into the equivalent millivolt measurement captured by the strain gauge transducers. For subjects B, E and H, average millivolt measurements of $\sim 6.01 \pm 1.71$mV, were captured, as compared with measurements of $\sim 61.50 \pm 2.61$mV, for the other seven subjects. This indicates that the FF force magnitudes captured for subjects B, E and H were far more susceptible to measurement error, due to the small force magnitudes.

Part of the reason for the low force magnitudes can be seen by referring back to table 8.3. Subjects A through H used a recruitment curve protocol with a maximum PW_p of 200μs, while subjects I though L used a maximum PW_p of 400μs. In general the forces generated with the 400μs pulse were greater than those generated with the 200μs pulse.

Results: Comparison of force measurements

The results from the MVC and FF tests were not satisfactory, consequently, a third approach was used to investigate fatigue. This involved comparing the $\mathbf{F}_s$ values captured throughout a session, as shown in figure 8.9, for subject B. In the figure we can see that the forces measured using the same *major* position were grouped together. The force measurements for all 10 subjects showed similar groupings. Table 8.9 shows percentage differences between force measurements, captured during the ninth stimulation burst of the recruitment curve protocol.

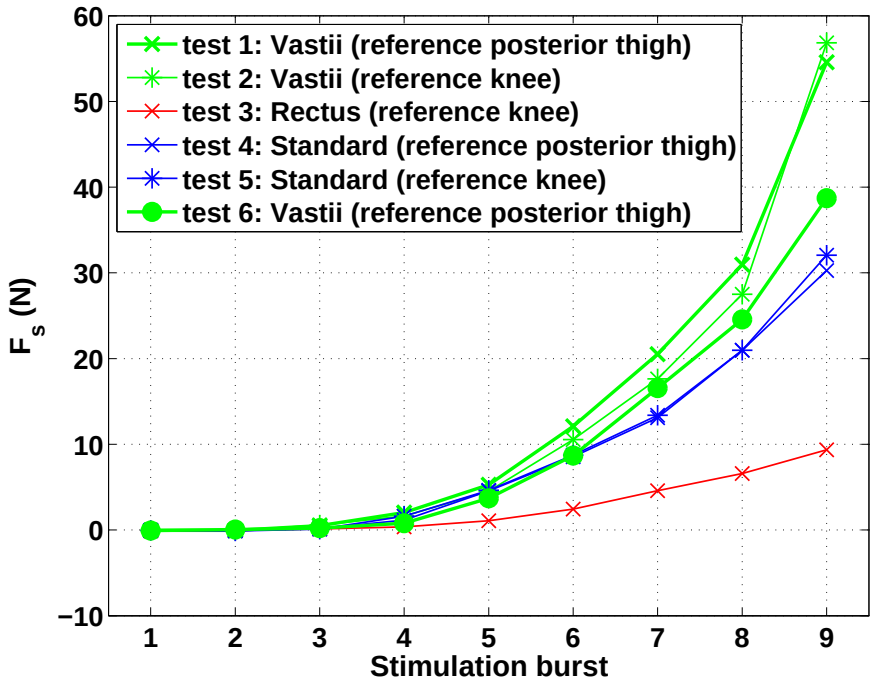

Figure 8.9: Force measurements, $\mathbf{F}_s$, captured during a session, for subject B.

Table 8.9: Percentage difference in $\mathbf{F}_s$ measurements during the 9$^{\text{th}}$ stimulation burst.

Subject	**Difference between tests 1 and 2 if the same *major* position tested (%)**	**Mean difference between all tests using the same *major* position (%)**	**Difference between first and last tests (%)**	**Number of tests performed**
A	-	-4.1	-12.3	7
B	4.1	-5.6	-29.1	6
E	1.3	-3.2	-10.3	8
F	-	-2.4	-5.8	6
G	-	7.4	14.8	5
H	-	0.5	9.6	6
I	-3.1	-19.2	-49.1	6
J	-	-1.9	-3.9	5
K	-4.7	-7.5	-14.9	5
L	-	9.9	16.9	5
Mean:	-0.6	-2.6	-8.4	-

Negative percentages indicate a drop and positive percentages indicate an increase in force magnitude.

Discussion: Comparison of force measurements

In Chapter 4 the first test was discarded due to a large drop (often $> 10\%$) between forces measured during the first and second test of a session. However, in the study presented in this chapter, the difference was always less than 5%, provided that the same *major* position was tested. These differences were comparable with the "*mean difference between all tests using the same major position*". As a result, the first test was not discarded from further analysis.

Previously, the reason for the difference in forces measured between the first and second test was attributed to the subjects experiencing substantial fatigue during the first three minutes of stimulation, after which the fatigue becomes much more gradual, as documented by Duffell et al. [2008]. In the study of Chapter 4 the initial setup phase involved finding the tolerable current amplitude for one of the *major* positions during constant stimulation. This often took just a couple of minutes or less. In contrast, during the initial setup phase of the study discussed in this chapter, it was necessary to find both the tolerable current amplitude and PW_r settings for all three *major* positions. This often took in excess of 10 minutes and consequently the subjects would have been more fatigued. The three minute period during which the substantial fatigue occurred would already have passed, and the muscles would have experienced gradual fatigue during the second part of the session.

Table 8.9 also shows the percentage "*difference between the first and last tests*". As mentioned earlier, the stimulating electrodes were placed in the same positions for these two tests. Subject B shows a large difference of 29.1%. However, if we compare this with the force measurements for subject B, shown in figure 8.9, we can see that a large difference between the first and last test occurred during the ninth stimulation burst, although the difference was far less for stimulation bursts 1 through 8. Furthermore, even though such a drop in force magnitude did imply that some fatigue had occurred, it was still possible to differentiate three distinct groups of force measurements according to the *major* position tested (namely that, like-coloured traces were grouped together). The same result was seen for the force of the other nine subjects, namely that although the force did tend to decrease during the session, the drop was not sufficient to prevent the like-coloured traces from being grouped together.

As the aim of the study was to determine if it was possible to selectively stimulate the muscles using the *major* positions, it was concluded that the fatigue experienced by the subjects would not adversely affect the results. Consequently no further issues relating to fatigue were considered when analysing the results.

8.4.2 Moment curves

Results: Major electrode positions

Figure 8.10 shows the moment curves, for each subject, from which we can observe that:

- For 9 of the 10 subjects the *Rectus* curves lie above the *Standard* and *Vastii* curves (i.e. by stimulating with the *Rectus* position the greatest hip flexion moments, $\mathbf{M}_h$, were measured). The only exception to this was seen in the results for subject L, where the *Vastii* curve was above the *Standard* and *Rectus* curves.

- Only two of the subjects (H and I) have results that agree with the expected moment curves shown in figure 8.1 (namely, *Rectus* curve above *Standard* and *Vastii* curve below *Standard*). Although, for both of these subjects the magnitude of the moments measured with the *Standard* position were much smaller, as compared with the magnitude of the moments measured with the other two *major* positions.

- No trends are readily visible for the *Standard* and *Vastii* curves.

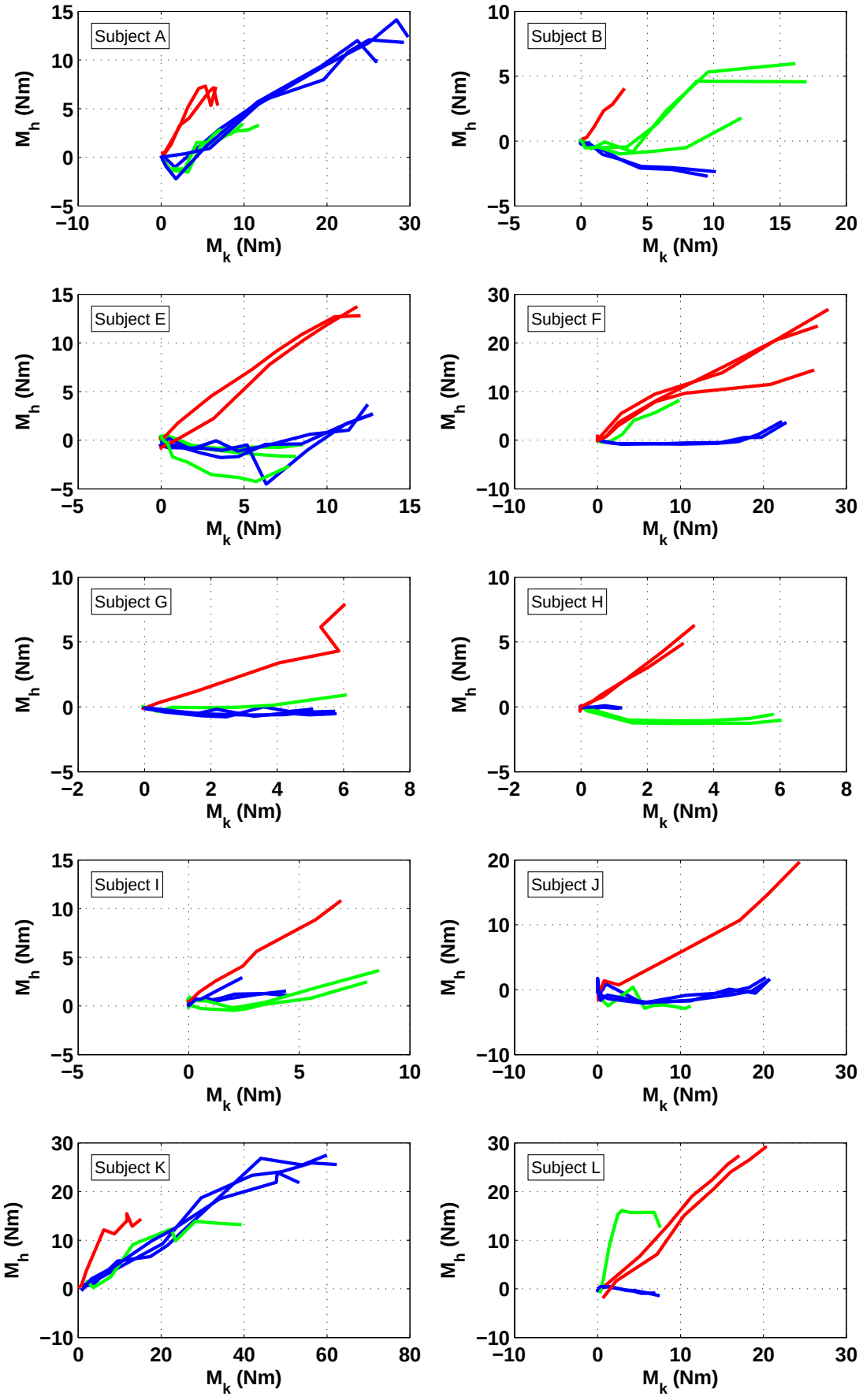

Figure 8.10: Moment curves captured for all three *major* electrode positions (blue - *Standard*, red - *Rectus*, green - *Vastii*), for each of the 10 subjects.

The moment curves for all 10 subjects were combined as a scatter plot, shown in figure 8.11. It is possible that a rotational error was present in some of the sessions (refer to Section 3.5.2). Nonetheless, the scatter plot allowed the data from all 10 subjects to be presented in a single figure.

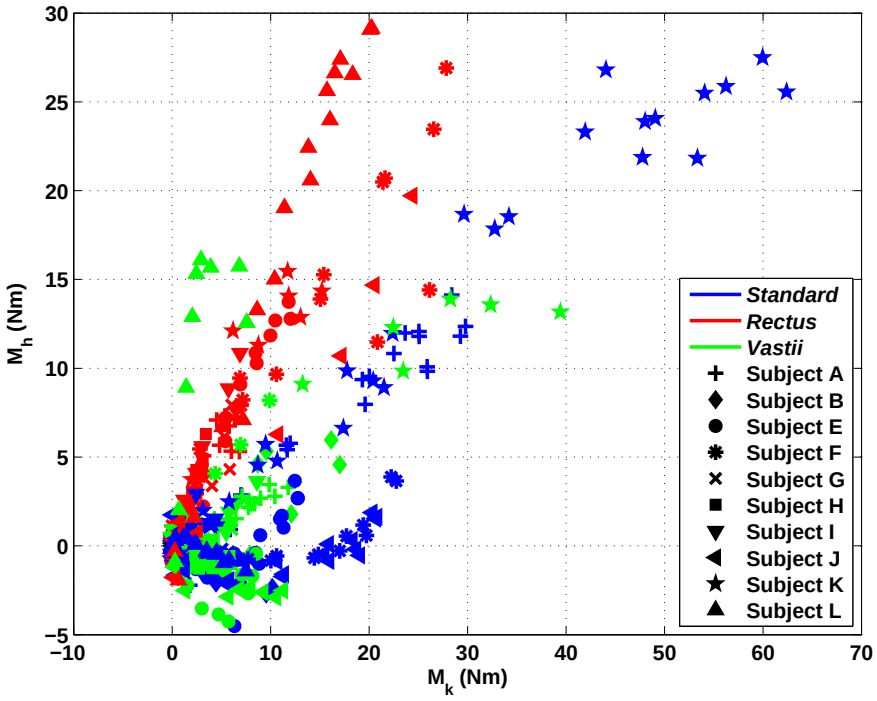

Figure 8.11: Scatter plot of moment curves captured for all 10 subjects.

A few observations were made from the figure:

- When directly stimulating RF with the *Rectus* position, it was possible to simultaneously generate hip flexion moments, $\mathbf{M}_h$, and knee extension moments, $\mathbf{M}_k$, of roughly the same magnitude.
- When stimulating with the *Standard* position smaller $\mathbf{M}_h$ moments were measured while the $\mathbf{M}_k$ moments were of the same magnitude or more, than those attained with the *Rectus* position.
- For the *Vastii* position, the moments varied greatly between subjects.
- No trends were evident when comparing the *Vastii* moments against those captured with the *Standard* and *Rectus* positions.

Discussion: Major electrode positions

Nothing new was learnt from the moment curves presented in figures 8.10 or 8.11, that was not already known from the moment curves discussed in Chapter 4. An additional T-test analysis, was however, carried out in Section 4.3.2. For the sake of completeness, the same T-test analysis

was performed on the moment curves captured with all 10 subjects, the results of which have been included in Section F.3.

In Chapter 4, 11 tests were performed for each *major* positions, which gave 22 data points (for each stimulation burst), to be used in the T-test analysis. In the current study the number of tests performed for each *major* position, varied from 1 to 3, giving only 2 to 6 data points for each stimulation burst. This was not enough points to perform a meaningful statistical analysis. Nonetheless, from the T-test analysis included in Appendix F, it was shown that the difference between the mean moments (when comparing either the *Rectus* and *Standard* results, or, the *Vastii* and *Standard* results), was significant for 70%-80% of the measured moments. This agrees with the observations made by inspection of figure 8.10.

8.4.3 Selectivity of stimulation

In Section 8.3.2, the concept of a complete data set was presented. The subjects who met the criteria for a complete data set were highlighted in table 8.5. The data sets captured for these four subjects (B, F, K and L) were used in a group analysis. The other six subjects were omitted from the analysis as it was possible that their *incomplete* data sets could skew the group analysis.

Table 8.10 lists the tests that were performed on each of the four subjects during their respective sessions. The tests that comprised the complete data sets, and were consequently used in the scatter plots shown in figures 8.12, 8.15 and 8.16, have been indicated. The table also shows the stimulation pulse width and current amplitude settings used for each subject.

The data was analysed using the peak-to-peak amplitude of the M-waves. However, it is known that these can be misleading. Merletti et al. [1992] discussed the fact that a given

Table 8.10: Electrode positions and stimulation settings used for the complete data sets.

Subject	**Stimulating and reference electrode positions for each test performed** *M-waves captured during tests typeset in bold, were used in the scatter plots*
B	**V(p)**, *V(k)*, **R(k)**, **S(p)**, *S(k)*, **V(p)**
F	**R(k)**, **V(k)**, *S(k)*, **S(p)**, **R(p)**, **R(k)**
K	**S(p)**, **S(k)**, **V(k)**, **R(k)**, **S(p)**
L	**R(k)**, **S(k)**, **V(k)**, **S(p)**, **R(k)**

Stimulation settings

Subject	**Maximum PW_p (μs)**	**Current amplitude (mA)**			
		Standard	***Rectus***	***Vastii***	
				VM	**VL**
B	200	30	38	30	34
F	200	50	50	30	40
K	400	65	50	50	60
L	400	25	40	20	30

S - *Standard* position, R - *Rectus* position, V - *Vastii* position.
(k) - reference electrode knee, (p) - reference electrode posterior thigh.

amplitude value may correspond to very different force levels, especially when comparing results from multiple subjects, while Zhang et al. [2011] pointed out that the relationship between evoked EMG and muscle force or torque is not constant but in fact time varying.

Consider the original research question:

> *Is it possible to maximise knee extension moments, $\mathbf{M}_k$, while minimising hip flexion moments, $\mathbf{M}_h$, using selective surface stimulation of the superficial muscles of the Quadriceps?*

The main focus of this analysis was to determine if the *major* positions were indeed exclusively stimulating the superficial muscles of the Quadriceps, targeted by each of the *major* positions. The purpose of the EMG measurements was, therefore, to indicate whether or not the muscles were being activated. Consequently the absolute amplitude of the M-waves was not important, but rather the amplitudes, recorded with each of the three *major* positions, relative to one another. For this reason, and to make it easier to compare results captured with different subjects, the M-wave amplitudes were processed in the following way:

- Firstly, the peak-to-peak amplitudes of the M-waves were adjusted for crosstalk as outlined in table 8.6.

- Secondly the M-wave amplitudes were normalised. For each subject, the largest M-wave amplitude measured in the complete data set, irrespective of *major* position or component muscle, was found. The M-wave amplitudes, for all 3 muscles, were then normalised with respect to this maximum value.

Results: M-wave amplitude and stimulation intensity

Figure 8.12 shows a scatter plot of the normalised M-wave amplitudes against stimulation intensity. From table 8.10 we can see that the stimulation settings (pulse width and current amplitude), were quite different for the four subjects. To account for these differences the stimulation intensity used in the figure was expressed as charge, Q, delivered per stimulation pulse; as calculated in equation 8.1. For the *Vastii* position, I_{stim} was taken as the mean of I_{stim_VM} and I_{stim_VL}.

$$Q = PW_p \times I_{stim} \tag{8.1}$$

Discussion: M-wave amplitude and stimulation intensity

As the stimulation intensity increases, the amplitude of the M-wave will also increase, due to the recruitment of more motor units [Merletti et al., 1992], up to the point of supramaximal stimulation. This effect was already seen when stimulating with the *Rectus* position (refer to figure 8.5(b)), where the M-waves were grouped according to consecutive stimulation bursts of the recruitment curve protocol. In figure 8.12 the same trend is seen to be true for all three *major* positions.

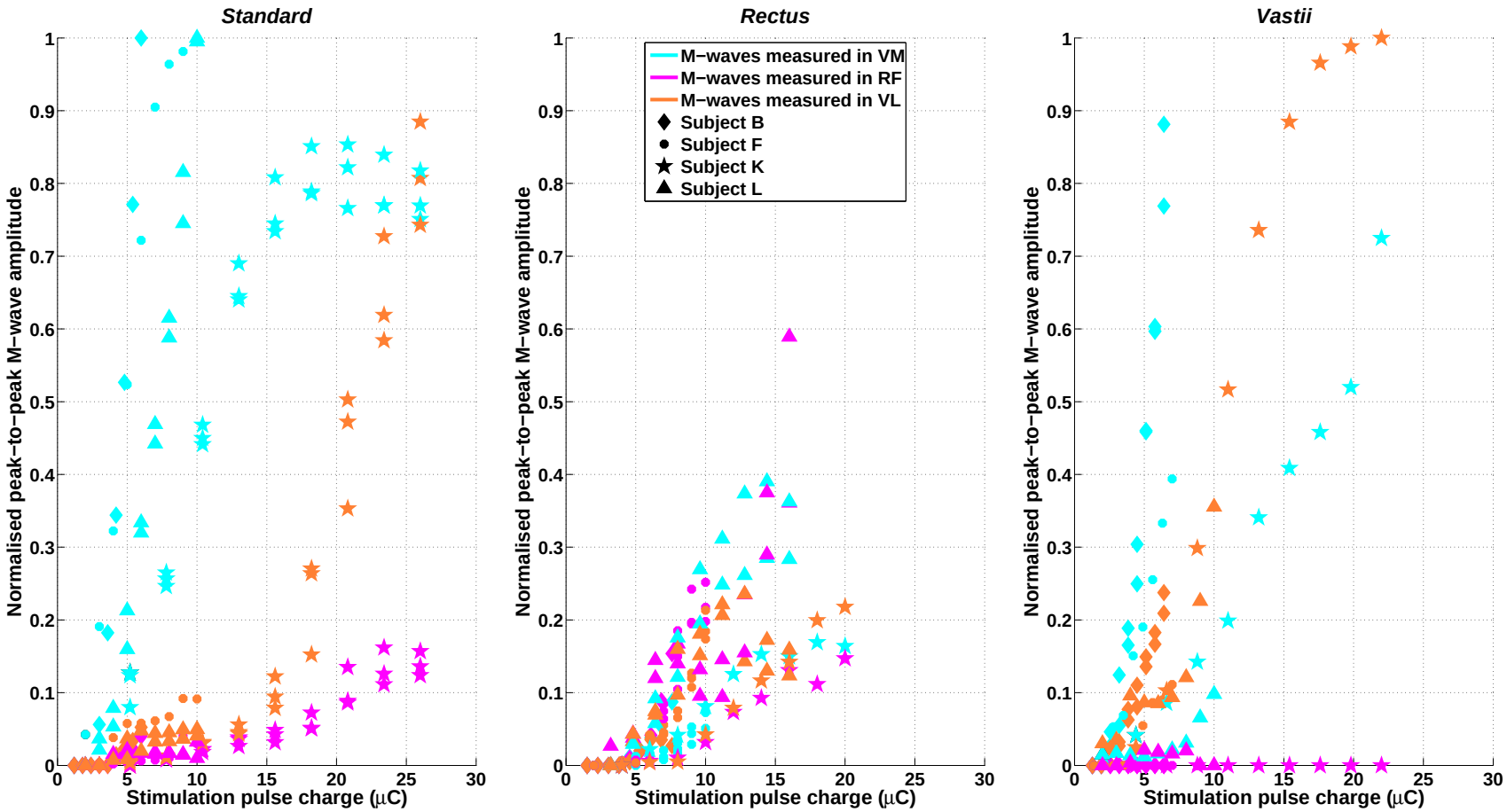

(a) (b) (c)

Figure 8.12: Normalised peak-to-peak M-wave amplitudes, measured in the Quadriceps muscles, plotted against the charge delivered with each stimulation pulse, for the three *major* positions.

By looking at the scatter plots for the three superficial muscles, we see that certain *major* positions result in a larger M-wave, in a given muscle, than another *major* position. Table 8.11 lists the *major* positions, for each of the muscles VM, RF and VL, in descending order of M-wave amplitude. As the recording electrodes were fixed in a certain position throughout the entire session, it stands to reason that the amplitude of the M-waves measured with each of the three *major* positions can be used as an indication of how much the position activated a particular muscle. In other words, the *major* position that generated the largest M-wave in a muscle indicates the position that produced the largest contraction in that muscle.

Table 8.11: Influence of *major* position on relative size of M-waves, in each superficial muscle of the Quadriceps group.

Quadriceps muscle	**Relative M-wave amplitude**		
	Largest	**Medium**	**Smallest**
VM	*Standard*	*Vastii*	*Rectus*
RF	*Rectus*	*Standard*	*Vastii*
VL	*Vastii*	*Standard*	*Rectus*

The expectations behind the three *major* positions were:

1. The *Rectus* position selectively stimulated RF.
2. The *Vastii* position selectively stimulated VM and VL.
3. The *Standard* position stimulated all three muscles equally, possibly generating as strong a contraction in each muscle as would be obtained by selectively stimulating the muscles.

Table 8.11 therefore shows that the *Rectus* position produced the largest contraction in RF, which agrees with what we would expect to see if *Rectus* selectively stimulated RF. However, from figure 8.12 we can see that, for the *Rectus* position, the normalised M-wave amplitudes were comparable in VM, VL and RF. Furthermore, the amplitudes for VM and VL were $\sim$40% of that seen in both muscles, with either the *Standard* or *Vastii* positions. These observations indicate that the *Rectus* position did not exclusively stimulate RF, nor did RF respond relatively more than VM or VL. Nonetheless, using this position did produce the largest contraction in RF, as well as smaller contractions in VM and VL, compared to those obtained with the other two *major* positions.

The *Vastii* position produced the largest contraction in VL, which once again agrees with what we would expect to see if VL was selectively stimulated. Even though the *Standard* position actually produced the largest contraction in VM, the M-wave amplitudes measured with the *Vastii* position were only around 10% less than the *Standard* case. What stands out for the *Vastii* position, is that the M-wave amplitudes in RF were virtually zero.[1] These observations

[1]The zero amplitude measurements were found after adjusting for crosstalk. For the interested reader the same scatter plots (figures 8.12, 8.15 and 8.16), as well as the EMG curves (figure 8.14), without any crosstalk adjustments, have been included in Section F.4 of the Appendix. Although the M-wave amplitudes did vary, no differences were seen in the conclusions that could be drawn.

imply that the *Vastii* position did selectively stimulate VM and VL.

With the *Standard* position, the largest contraction in VM was measured. At a first glance it seems that the contraction in VL was around 90% of that seen in the *Vastii* case. However, upon closer inspection we see that this result was only measured for subject K. For subject F, the VL M-wave amplitudes (*Standard* and *Vastii*) were comparable, while for subjects B and L, the *Standard* position contraction was less than 50% of that achieved with the *Vastii* position. Furthermore, the RF amplitudes in the *Standard* case are less than 25% of that measured with the *Rectus* position (except for subject K, where the amplitudes for *Standard* and *Rectus* were comparable).

Our expectation was that the *Standard* position stimulated all three muscles simultaneously. These observations indicate that all three muscles are active, however, the size of the contraction in RF and VL varied between subjects, and in some cases was less than expected.

Results: EMG curves

The selectivity of the stimulation was further investigate using so-called EMG curves. This involved plotting M-wave amplitude measured in RF against that measured in either VM or VL, for each of the *major* positions. Figure 8.13 shows the ideal EMG curves, where the stimulation is truly selective with only the targeted muscles being activated.

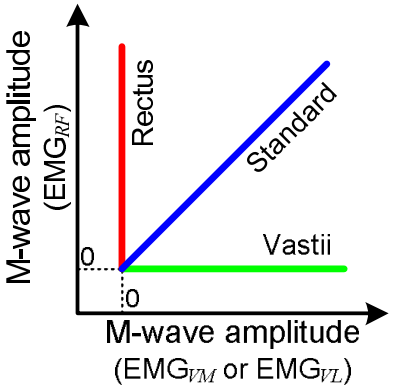

Figure 8.13: EMG curves for the three *major* electrode positions.

For the *Rectus* position, M-waves would be measured in RF, without any measurements (zero amplitude), captured in VM or VL. The opposite would hold true for the *Vastii* position. For the *Standard* position, provided that all three superficial muscles were activated, the EMG curve would lie between that of *Rectus* and *Vastii*.

The EMG curves were found for each of the four subjects (see figure 8.14), using the normalised peak-to-peak M-wave amplitudes, after crosstalk adjustments. *Good* selective stimulation was taken to imply that the targeted muscle was exclusively stimulated, with minimal activation of the adjacent muscles. *Moderate* selective stimulation was when the targeted muscle responded relatively more than the adjacent muscles.

Consider the very first graph of the figure (EMG_{RF} against EMG_{VM}, subject B). The *Rectus* position, although not ideal, is considered to show *good* selective stimulation of RF. The *Vastii* position did selectively stimulate VM, while the *Standard* position seems to have

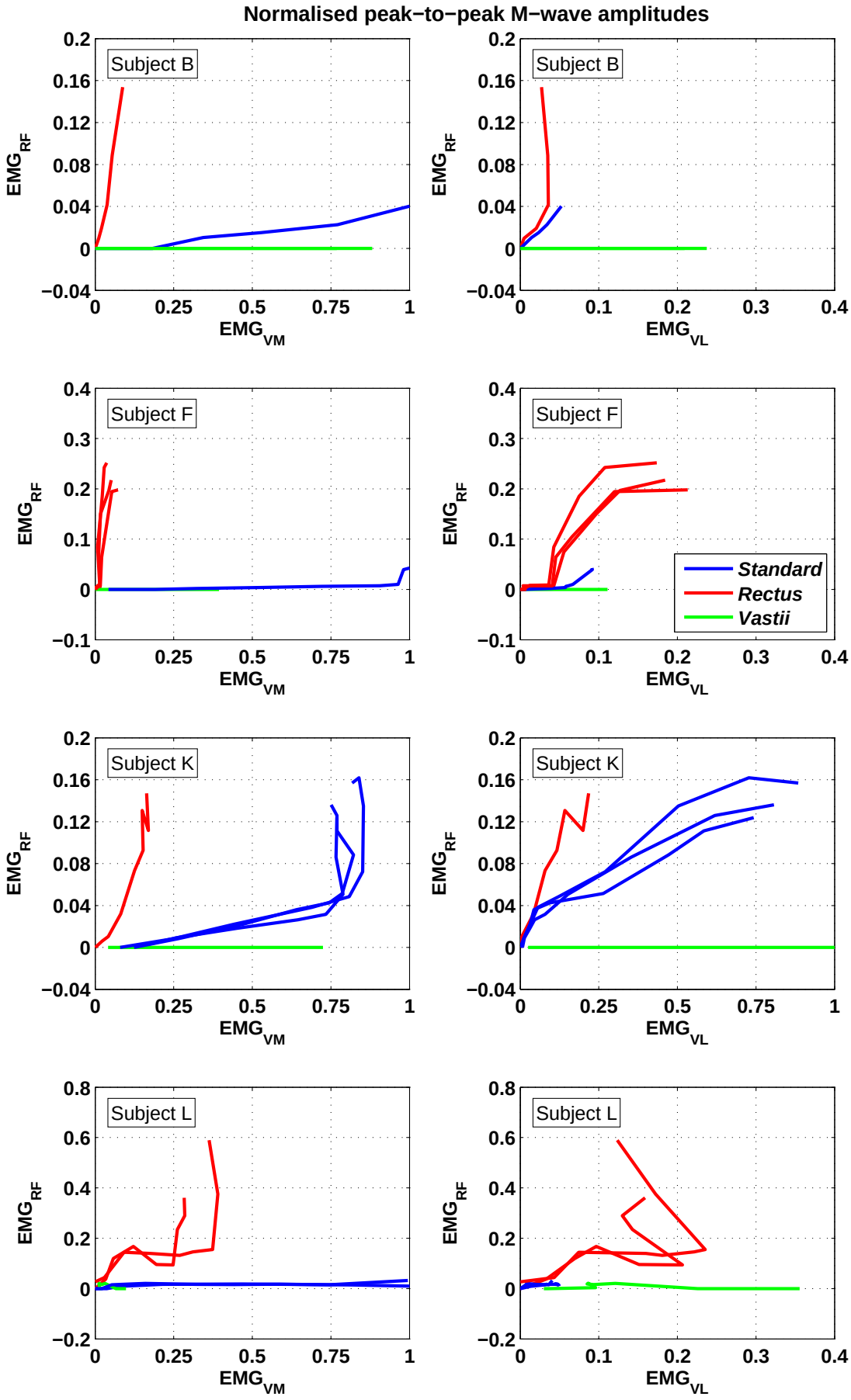

Figure 8.14: EMG curves captured for all three *major* electrode positions, for each of the 4 subjects with complete data sets.

produced a result closer to *moderate* selectivity of VM than the expected non-selective result. Similar conclusions can be drawn by looking at the second graph (EMG_{RF} against EMG_{VL}, subject B), with the only exception being that the *Standard* position produced a non-selective result. Table 8.12 lists these observations, along with similar observations made for the other three subjects.

Table 8.12: EMG curve observations.

***Major* position**	**Selective**		**Non-selective**
	Good	**Moderate**	
Standard	F, L	B[a]	B[b], K
Rectus	B, F[a]	K	F[b], L
Vastii	B, F, K, L	-	-

[a] EMG_{RF} against EMG_{VM}. [b] EMG_{RF} against EMG_{VL}.
No differentiation between EMG_{VM} and EMG_{VL} made, if the same conclusions drawn about selectivity.

Discussion: EMG curves

From the earlier discussion on the scatter plots (figure 8.12), the following points were made:

1. The *Rectus* position did not appear to selectively stimulate RF.

2. The *Vastii* position did selectively stimulate VM and VL.

3. The *Standard* position did stimulate all three muscles, although the size of the contraction in RF and VL was far less than that expected.

Point 1 agrees with the observations of table 8.12, as the selectivity achieved with the *Rectus* position varied from subject to subject. Consequently, on the whole it could not be concluded that this position was truly selective. Nonetheless, as observed from figure 8.12, the *Rectus* position did produce the strongest contraction in RF.

Point 2 agree with the observations listed in the table.

The assumption, throughout this thesis, was that the *Standard* position stimulated all three superficial muscles of the Quadriceps simultaneously. From the table, we see that the muscle activation obtained with the *Standard* position was not as expected. Depending on the subject the *Standard* position showed either good or moderate selectivity of VM or VL; completely against expectations. Although, for subject K, the expected non-selective result was seen.

If we consider these observations in conjunction with point 3, we can conclude that the *Standard* position caused a strong contraction in VM. The size of the contraction in RF and VL varied between subjects. Therefore, the assumption that all three superficial muscles were simultaneously stimulated, did not always hold true and was therefore misleading when interpreting the moment curves.

8.4.4 Biomechanical and evoked EMG measurements

Results

The normalised M-waves were plotted against the knee extension moments, $\mathbf{M}_k$, (figure 8.15) and against the hip flexion moments, $\mathbf{M}_h$, (figure 8.16).

Discussion

Using figures 8.15 and 8.16 it was possible to list the *major* positions in descending order of joint moments, as in table 8.13.

Table 8.13: *Major* positions listed in descending order of joint moments.

Joint moment	Largest	Medium	Smallest
$\mathbf{M}_k$	*Standard* ($\sim$ 65Nm)	*Vastii* ($\sim$ 40Nm)	*Rectus* ($\sim$ 30Nm)
$\mathbf{M}_h$	*Rectus* ($\sim$ 30Nm)	*Standard* ($\sim$ 28Nm)	*Vastii* ($\sim$ 16Nm)

From the table we see that the *Standard* position produced the greatest knee extension moments, while *Rectus* produced the least. From figure 8.15, we make the following observations:

- The large knee extensions, measured with the *Standard* and *Vastii* positions, coincided with large M-waves in VM and VL that were also similar in amplitude.
- The *Standard* position also showed a strong contraction in RF, when large $\mathbf{M}_k$ moments were measured.
- The *Vastii* position showed no contraction in RF.
- The *Rectus* position showed the largest contraction in RF, and the smallest contractions in VM and VL (as compared against *Vastii* and *Standard*).

From these observations we can conclude that the largest knee extension moments occurred due to the activation of RF, in addition to VM and VL. This agrees with what we would expect based on our knowledge of the function of the three muscles.

With regards to hip flexion moments, table 8.13 indicates that the *Rectus* position produced the largest moment, although only slightly larger than those measured with the *Standard* position. Furthermore, the *Vastii* position produced the smallest moments. The first impression of these observations is that this is exactly what was hoped for. However, upon closer inspection of the hip flexion moments in figure 8.16, we can see that:

- For subject K, the $\mathbf{M}_h$ (*Standard*) values are comparable with those measured with *Rectus* (for all four subjects).
- For subjects B, F and L, the $\mathbf{M}_h$ (*Standard*) values are much smaller than those achieved with either the *Rectus* or *Vastii* positions, (different from the overall result shown in table 8.13).

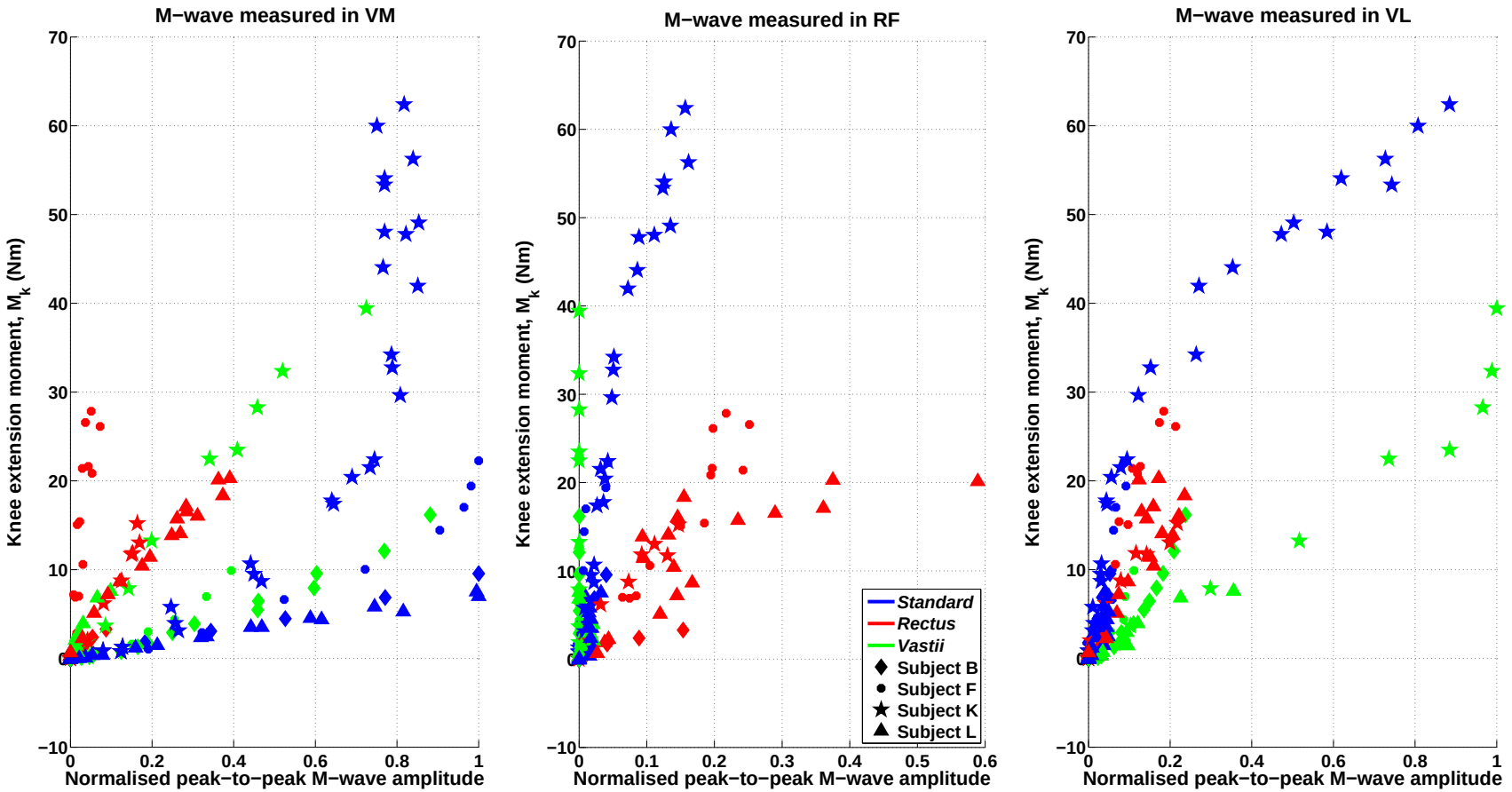

(a) (b) (c)

Figure 8.15: Normalised peak-to-peak M-wave amplitudes, plotted against the knee extension moment, for the three superficial muscles of the Quadriceps.

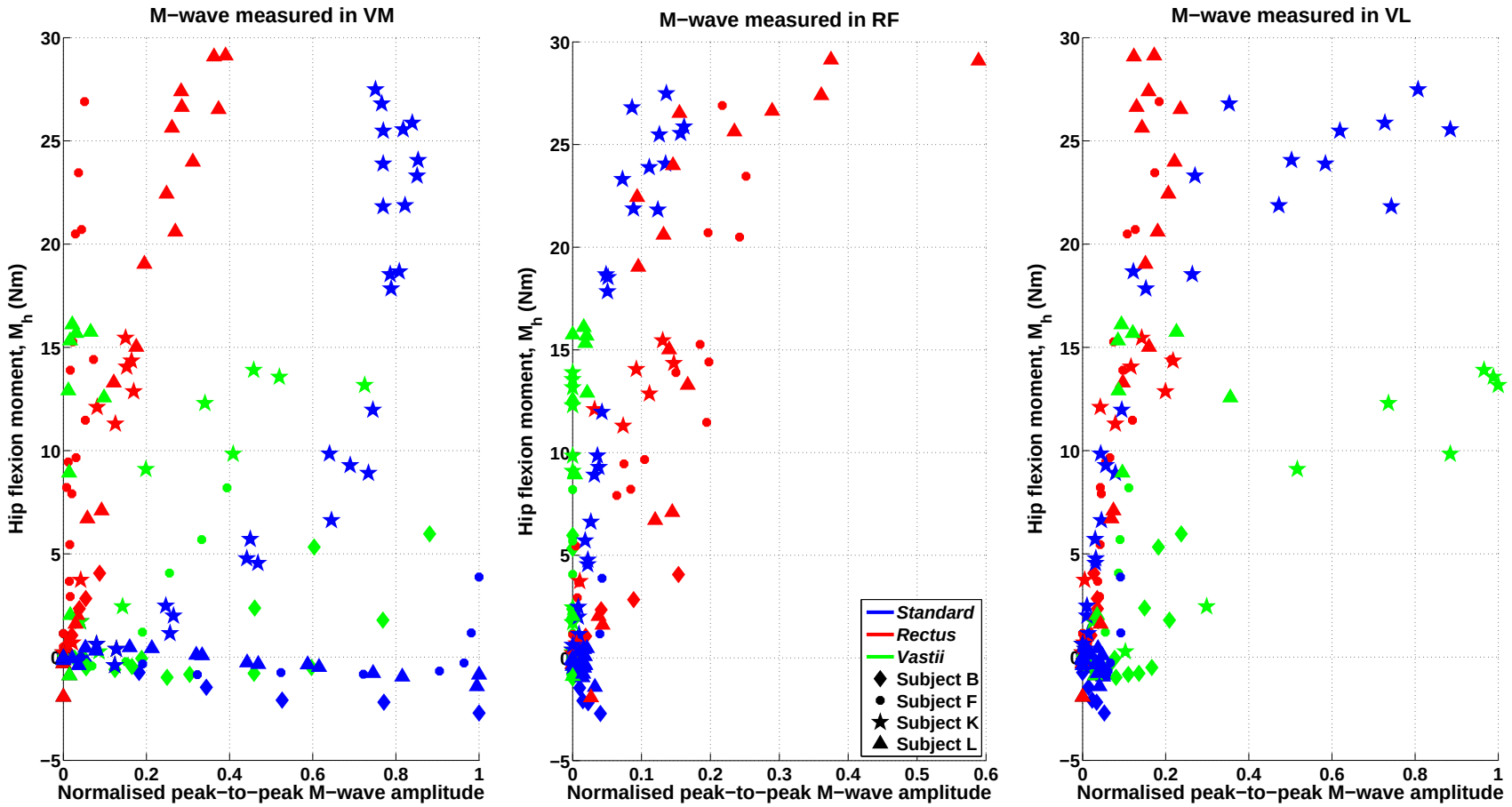

(a) (b) (c)

Figure 8.16: Normalised peak-to-peak M-wave amplitudes plotted against the hip flexion moment, for the three superficial muscles of the Quadriceps.

Referring back to figure 8.14 and table 8.12, subjects B, F and L tended to show poor activation of RF with the *Standard* position. Taking note of this fact, in conjunction with the $\mathbf{M}_h$ observations just made, we can deduce that when the *Standard* position does stimulate RF, VM and VL, then using the *Vastii* position will produce a smaller $\mathbf{M}_h$ value. However, it was already shown that the assumption that the *Standard* position always stimulates all three muscles was incorrect. With some subjects it did not stimulate RF; in these cases $\mathbf{M}_h$ (*Standard*) was less than that measured for subjects where RF was stimulated. Thus, if the *Standard* position was not causing a hip flexion moment by making RF contract, the *Vastii* position, by intentionally preventing the stimulation of RF, would not reduce hip flexion moments in comparison to the *Standard* position.

This erroneous assumption for the *Standard* position led to the expected moment curves for the three *major* positions (figure 8.1). Based on these expectations it was concluded that the measured moment curves (figure 8.10) showed negative results, when the *Standard* and *Vastii* curves tended to overlap, or if the *Standard* curve lay beneath the *Vastii* curve. In retrospect, these results could be explained by RF not being activated by the *Standard* position.

Finally, figure 8.16 and table 8.13 show that, even though the *Vastii* position repeatedly produced smaller hip flexion moments than *Rectus* and did not stimulate RF (as the stimulation was found to be selective), there was still some hip flexion present. In fact, in some cases this hip flexion was so large that $\mathbf{M}_h$ (*Standard*) $<$ $\mathbf{M}_h$ (*Vastii*), as already mentioned. Two possible explanations for this, are:

1. The crosstalk adjustment used (25% as in table 8.6), was based on a worst case scenario. Consequently the adjustment may have been too large, resulting in an RF M-wave amplitude of zero when in fact it may have been non-zero, thereby disguising the fact that RF was partially active (although much less so than in the *Rectus* case). A partial contraction in RF could account for the hip flexion seen with *Vastii*.

2. Consider the anatomy of the leg (figure 1.1). It is possible that the placement of the stimulating electrodes for the *Vastii* position also stimulated the Sartorius and Tensor fasciae latae muscles of the anterior leg. Table 8.14 lists the functions of these two muscles [Cash, 2000], both of which do perform a hip flexion.

Table 8.14: Muscle functions, reproduced from [Cash, 2000], with permission.

Muscle	Action
Anterior leg muscles	
Sartorius	Flex hip and knee, outwardly rotate and abduct hip, inwardly rotate knee.
Tensor fasciae latae	Abduct hip and slight flexion and inward rotation.

8.4.5 Conclusion

The research question states:

> *Is it possible to maximise knee extension moments, $\mathbf{M}_k$, while minimising hip flexion moments, $\mathbf{M}_h$, using selective surface stimulation of the superficial muscles of the Quadriceps?*

From the discussions presented in Sections 8.4.3 and 8.4.4, we can make the following statements in response to the research question:

1. Selective stimulation of VM and VL was possible with the *Vastii* position.
2. Selective stimulation of RF was not achieved with the *Rectus* position, although it did produce a strong contraction in RF and weak contractions in VM and VL.
3. Hip flexion moments were reduced if VM and VL were stimulated and RF was not.
4. In such a situation, knee extension moments were also reduced, as compared against the $\mathbf{M}_k$ values measured during simultaneous stimulation of VM, VL and RF.

We can then conclude that, it is possible to minimise the hip flexion moments, using selective surface stimulation, although it comes at the expense of reduced knee extension moments. The implication, with regards to FES cycling, is discussed in Chapter 9.

8.5 Summary

A study was carried out with 10 subjects; evoked EMG was measured while capturing joint moments with the Bi-moment chair. The resultant moment curves generally showed that the *Rectus* position produced the largest hip flexion moments. However, the joint moments measured for the *Standard* and *Vastii* positions varied greatly between subjects, hence no trends could be identified. The EMG measurements were analysed for only 4 subjects, as the measurements for the other subjects were rendered unusable due to the presence of stimulation artefact.

For each of the 4 subjects the peak-to-peak M-wave amplitudes were extracted, adjusted for crosstalk and normalised with respect to the largest M-wave amplitude measured. The relative amplitude of the M-waves was used to indicate the extent of the contraction present in the three superficial muscles of the Quadriceps (i.e. the larger the M-wave amplitude, the stronger the contraction). Table 8.15 lists the main observations that were made from inspection of the M-wave data.

Prior to the study, the expectations behind the three *major* positions were:

1. The *Rectus* position selectively stimulated RF.
2. The *Vastii* position selectively stimulated VM and VL.
3. The *Standard* position stimulated all three muscles equally, possibly generating as strong a contraction in each muscle as would be obtained by selectively stimulating the muscles.

Table 8.15: Summary of observations made with the M-wave measurements.

***Major* position influence on M-wave amplitude**	
Superficial muscle	**Amplitude in descending order**
VM	*Standard* > *Vastii* > *Rectus*
RF	*Rectus* > *Standard* > *Vastii*
VL	*Vastii* > *Standard* > *Rectus*
***Major* position influence on magnitude of joint moments**	
$\mathbf{M}_k$ (*Standard*) > $\mathbf{M}_k$ (*Vastii*) > $\mathbf{M}_k$ (*Rectus*)	
$\mathbf{M}_h$ (*Rectus*) > [$\mathbf{M}_h$ (*Standard*) and $\mathbf{M}_h$ (*Vastii*)]	

After the analysis, the following conclusions were drawn regarding selective stimulation:

1. The *Rectus* position did not exclusively stimulate RF, nonetheless, it did produce the strongest contraction in RF.
2. The *Vastii* position did selectively stimulate VM and VL.
3. The *Standard* position did not always activate all three muscles. For some subjects the contraction in RF and VL was so much smaller than that seen in VM, that it was more akin to selective stimulation of VM. (This contradicted the original assumption, and could have lead to misinterpretation of the moment curves.)

The main conclusions drawn for the joint moments, were as follows:

1. The largest knee extension moments occurred due to the activation of VM, VL and RF (as seen with the *Standard* position for some subjects).
2. If only VM and VL (*Vastii* and *Standard* positions) were activated, or only RF (*Rectus* position), then the knee extension moments were comparable.
3. $\mathbf{M}_h$ (*Standard*) > $\mathbf{M}_h$ (*Vastii*), when RF was activated by the *Standard* position.
4. $\mathbf{M}_h$ (*Standard*) < $\mathbf{M}_h$ (*Vastii*), when RF was not activated by the *Standard* position.

Even though the *Vastii* position did selectively stimulate VM and VL, a hip flexion moment did still occur. Possible explanations for the presence of this moment are:

1. The crosstalk adjustment was too large, disguising the presence of a contraction in RF which would produce a hip flexion moment.
2. The placement of the stimulating electrodes in the *Vastii* position could have also stimulated the Sartorius and Tensor fasciae latae muscles, both of which perform a hip flexion.

The implication of these findings for the research question was that *it is possible to minimise hip flexion moments, using selective surface stimulation, although it comes at the expense of reduced knee extension.*

Chapter 9

Discussion and future work

9.1 Introduction

In Chapter 1 the low power output (PO) and efficiency of SCI cyclists, during FES cycling, was discussed (PO values of 6W-42W [Duffell et al., 2008; Mohr et al., 1997*a*] and efficiencies from 2%-5% [Glaser et al., 1989; Petrofsky and Stacy, 1992], compared against 250W [Reiser et al., 2002] and 20% [Glaser et al., 1989; Hansen et al., 2002] for AB cyclists). However, the reason for the poor results is not well understood.

Three hypotheses for these results were discussed, namely muscle activation during stimulation, factors inherent to SCI, and, biomechanical causes, as presented by Duffell et al. [2009]. They went on to disprove the first hypothesis, while using the results of Kjær et al. [1994] and the analysis of Hunt et al. [2007] it was possible to eliminate the second hypothesis from further consideration. However, the third hypothesis was supported by a study carried out by Szecsi et al. [2007], in which a biomechanical analysis of FES cycling was presented. Joint moments were measured during FES cycling, from which it was shown that, during a cycling revolution, a knee extension moment (concentric positive power) was measured simultaneously with a hip flexion moment (eccentric negative power), which resulted in a decrease in the nett PO.

By looking at the anatomical functions of the component muscle of the Quadriceps group, it was seen that Vastus medialis (VM) and Vastus lateralis(VL) performed knee extensions, while Rectus femoris (RF) has the dual function of both knee extension and hip flexion. This gave rise to the research question:

> *Is it possible to maximise knee extension moments,* $\mathbf{M}_k$*, while minimising hip flexion moments,* $\mathbf{M}_h$*, using selective surface stimulation of the superficial muscles of the Quadriceps?*

If such selective stimulation was practicable, it could potentially be used to increase the PO and efficiency achieved during FES cycling. The approach used in this thesis was to simultaneously measure joint moments and evoked EMG, in the superficial muscles of the Quadriceps, during stimulation with careful placement of the stimulating electrodes, intended to selectively stimulate target muscles.

From the resultant body of work there were two main contributions:

1. Development of a system capable of simultaneously measuring joint moments and evoked EMG signals. The system itself comprised two main parts:
   (a) The Bi-moment chair, used to measure joint moments.
   (b) The Biphasic stimulator and Blanking amplifier, necessary for capturing evoked EMG measurements in stimulated muscle.
2. Using the evoked EMG measurements to investigate the selective stimulation of the Quadriceps muscles, and using these results to answer the research question.

The remainder of this chapter summarises the results and discussions from the earlier chapters, under the three points listed above. The shortcomings of the system are considered, as well as possible ways to improve it in the future. The outcome of the research question, and the implications this has for FES cycling are also discussed.

9.2 Measuring joint moments with the Bi-moment chair

The aim of the selective surface stimulation was to place the stimulating electrodes in such a manner, that certain muscles were targeted. To this end, three different placements of the electrode were used, referred to as the *major* positions (figure 4.1):

1. *Standard*, intended to simultaneously stimulate RF, VM and VL (typical electrode placement used in FES cycling).
2. *Rectus*, intended to selectively stimulate RF.
3. *Vastii*, intended to selectively stimulate VM and VL.

Vastii was the position of interest, as by stimulating VM and VL without RF, it was hoped to produce a knee extension moment with a hip flexion moment smaller than that generated by the *Standard* and *Rectus* positions, in which RF was stimulated. It was therefore necessary to measure the joint moments, during stimulation with each of the *major* positions.

It was decided to measure the joint moments in a seated subject, as opposed to during FES cycling, as the biomechanical analysis of a static action (seated subject) only requires the kinetic variables to be measured, while a dynamic action (cycling) also requires kinematic and anthropometric data. Furthermore, the aim of the investigation was to determine the influence of the *major* positions on the joint moments, for which the static analysis would be sufficient.

9.2.1 The system developed to measure joint moments

The Bi-moment chair

The Bi-moment chair was designed to simultaneously measure moments about the hip joint centre (HJC) and knee joint centre (KJC) of a seated subject. This was accomplished by using

strain gauge transducers to measure a shank force, $\mathbf{F}_s$, and a thigh force, $\mathbf{F}_t$. Direction vectors ($\mathbf{D}_{kpfs}$, $\mathbf{D}_{hpfs}$, $\mathbf{D}_{hpft}$), describing the orientation of the force vectors relative to the joint centres, were calculated from position measurements relative to the chair's reference frame. Changes in positions were monitored using custom built position sensors known as spring pots. The knee extension moment, $\mathbf{M}_k$, and the hip flexion moment, $\mathbf{M}_h$, could then be calculated:

$$\mathbf{M}_k = \mathbf{D}_{kpfs} \times \mathbf{F}_s \qquad \mathbf{M}_h = \mathbf{D}_{hpfs} \times \mathbf{F}_s - \mathbf{D}_{hpft} \times \mathbf{F}_t \tag{9.1}$$

The biomechanical analysis used in the Bi-moment chair made the following assumptions:

1. The restraining straps were sufficient to ensure that stimulation of the Quadriceps caused no movement in the COM of the shank or thigh, thereby allowing gravitational forces to be omitted from the static freebody analysis.

2. The position of the ASIS (an anatomical landmark, the position of which was used to determine the position of the HJC), was constant, based on the fact that the subject was held in place by a number of straps, thereby minimising movement of the HJC during stimulation.

3. No lateral movement in the KJC, as the subjects were positioned in the chair in such a way as to minimise lateral movement of the leg during knee extension.

4. No lateral movement the position of point p_{ft}, (used to find $\mathbf{D}_{hpft}$).

5. sp_2 positioned directly above the KJC.

6. String between sp_2 and the KJC lies parallel with the cord between the thigh and SG_1.

7. The subject was seated in the chair such that the position of the KJC and HJC had the same z-coordinate.

8. The dimension measurement l_t, lies parallel to the sagittal plane thereby implying that the $\hat{z}$ offset of the HJC from the GT is the same as the $\hat{z}$ offset of the KJC from the lateral KJC.

Measurement errors

The measurement errors, inherent to the Bi-moment chair, were investigated. This involved identifying the random and systematic errors associated with the strain gauge transducers, the spring pots, other position and dimension measurements taken with respect to the chair's reference frame, and the 3 assumptions used in the biomechanical analysis. The individual influence that each of these errors have on the joint moment calculations was found, by introducing the errors into an actual data set and finding the percentage difference in the final result.

From these results it was possible to find an expression for the overall uncertainty in the joint moments, shown in equation 9.2.

$$\sigma_{\mathbf{M}k} \approx 0.01 \cdot \mathbf{M}_k + 0.66 \qquad \sigma_{\mathbf{M}h} \approx 0.07 \cdot \mathbf{M}_h + 0.74 \tag{9.2}$$

By using these expressions to estimate the uncertainty of a typical set of joint moment measurements captured with the Bi-moment chair, the following conclusions were drawn:

1. The overall uncertainty due to random and systematic errors was not large enough to obscure differences in the results captured for the three *major* positions (figure 3.13).

2. The absolute magnitude of the joint moments could be shifted due to the presence of a rotational error (the clockwise or counter-clockwise rotation of the moment curves, refer to figure 3.13(b)). Consequently, it was recommended that the measurements captured with the Bi-moment chair be used for a comparative analysis, with all three *major* positions tested during a single session.

9.2.2 Critical evaluation of the Bi-moment chair

Rotational error

The error analysis carried out on the chair showed that it was possible for a rotational error to be present in the final joint moment measurements. However, by ensuring that all three *major* positions were tested in a single session, with one subject, the presence of such an error would not lead to erroneous conclusions being drawn in a comparison of the *major* positions.

However, this was not necessarily true when comparing the moments captured from different subjects. Consequently this did cast doubt on inter-subject analyses. Whenever possible, trends seen in the results between different subjects were used to draw conclusions, as opposed to using absolute measurements of the moments.

Force measurements

During calibration of the strain gauge transducers, weights were suspended from the transducers (see figure 2.7(a)). This meant that the forces were applied at right angles to the U-bar, to which the foils were attached. During the experiments with the Bi-moment chair, it was possible that the forces were actually applied at oblique angles. The influence that this would have on the force measurements was not known.

To improve the accuracy of the force measurements it would therefore be necessary to calibrate the transducers over a range of oblique angles. This data could then be used, in conjunction with the orientation of the directional force vectors (equation 2.20), to adjust the measurement of the force magnitude accordingly.

SCI subjects

When building the Bi-moment chair, it was originally intended for use with both AB and SCI subjects. However, after performing the studies with the AB subjects, it was found impractical for the chair to be used with SCI subjects.

- The reference frame within which the chair was constructed, which was necessary for the position measurements, also made it cumbersome to physically get in and out of the chair. This would be even more problematic for SCI subjects.

- The stimulation experienced by the subjects during the initial setup phase (constant stimulation carried out at the start of each session during which I_{stim} and PW_r settings were found), would severely fatigue SCI subjects.

- During the course of the session the subject was required to sit in the chair without moving. The session lengths were very long, as it included the measurement of the initial position and length measurements, the MVC and FF tests, and, the recruitment curve protocol tests. As SCI subjects need to shift their weight every few minutes, to prevent the occurrence of pressure sores, it was not practical for them to sit in the chair for the required time period.

9.2.3 Future work

For the Bi-moment chair study to be carried out with SCI subjects, it is suggested to only use the chair to capture force measurements, and to rather use the *Codamotion* analysis system to capture the position measurements. Unfortunately this would mean that the Bi-moment chair was no longer a stand alone apparatus, however, it would have two advantages:

1. The initial position and length measurements, taken at the start of each session, which was a lengthy procedure, would be eliminated. However, just how much this would shorten the session would depend on how long it takes to set up the *Codamotion* system and to place the relevant markers. Nonetheless, it is expected that once the setup procedure with the *Codamotion* system has been investigated, it would be possible to place the majority of markers prior to the session, with only a few markers to be placed on the subject at the start of each session.

2. Using the *Codamotion* system to continually monitor the subjects position during the session would eliminate the need for them to hold still, thereby allowing the SCI subjects to move as required.

9.3 Evoked EMG measurements

It was necessary to measure evoked EMG signals in the superficial muscles of the Quadriceps (RF, VM and VL) during stimulation. This required that the recording electrodes be placed between the stimulating electrodes, a configuration that is known for its difficulty in capturing the desired EMG signals.

Immediately after a constant-current stimulation pulse, a residual charge remains on the electrodes due to the polarisation of the electrode-skin interface. The interface can be modelled as the parallel combination of a resistor and capacitor, in series with a second resistor (figure 7.7). The electrode polarisation is equivalent to charge accumulating on the capacitor.

As the interface capacitance discharges, it is possible for a discharge current to flow through the tissue and the stimulator (depending on the stimulator design), creating a potential difference across the recording electrodes, which will appear as a stimulation artefact at the amplifier output. This situation can be avoided by using a biphasic stimulation pulse, with pulse width ratio adjustment, to reduce the residual charge on the electrodes at the end of a stimulation pulse [Nilsson et al., 1988; Reichel et al., 2001; Spencer, 1981].

It is also possible for the EMG amplifier to saturate, due to the large voltage seen at its input stage [Sedra and Smith, 1998], caused by the stimulation pulse. The latency of evoked M-waves, when placing the recording electrodes between the stimulating electrodes, has been measured at $\sim$5ms [Bruun and Haxthausen, 1991]. It is therefore likely that the amplifier would not recover from saturation fast enough to be able to measure the M-wave. To avoid this problem, it is necessary to use a switching scheme at the amplifier input stage.

9.3.1 The system developed to measure evoked EMG

The Biphasic stimulator

A 2-channel, biphasic, constant-current stimulator, with pulse width ratio (PW_r) adjustment capability, as needed for stimulation artefact elimination, was designed and constructed.

The user was able to vary the stimulation current amplitude, period, pulse width and PW_r settings. The stimulator was capable of producing continuous stimulation, or the recruitment curve protocol required by the Bi-moment chair study (see Section 4.2.2 or 8.2.3). Care was taken during the design of the electronics, as well as the component and PCB layout, to ensure that the stimulator did not create a connection between the subject and earth, thereby meeting electrical safety requirements.

During development of the stimulator, two problems arose, both of which were addressed (Section 5.5.1):

1. A soft-switching scheme was introduced in the full bridge output stage to eliminate oscillations seen in the stimulation pulse.

2. A drop in the 200V rail was prevented by using two 200V converters for the output stage.

Two limitations of the stimulator were also identified:

1. The stimulator was unable to produce a true monophasic pulse, even when the PW_r setting was reduced to 0% (Section 5.5.2).[1]

2. The presence of a residual voltage across the blocking capacitor resulted in a current flowing through the discharge resistor, between stimulation pulses (Section 5.6.1).

[1] For the Bi-moment chair study in which the stimulator was used, this limitation was inconsequential. However, it was mentioned here for the benefit of others who may wish to use the stimulator design for other applications.

The Blanking amplifier

To prevent the amplifier from saturating, a current conveyor circuit [Bruun and Haxthausen, 1991] was used at the input stage, which temporarily shut the amplifier down, prior to a stimulation pulse. For a period of time, longer than the duration of the pulse, the amplifier was unable to measure any signals present at the input terminals, which was referred to as the *blanking interval*.

The amplifier consisted of three such input stages, as well as an additional amplification and isolation stage, for each input. The combination of an input stage, an amplification stage and an isolation stage were referred to as EMG amplifiers, while all three EMG amplifiers together were referred to as the *Blanking amplifier* (see figure 6.2).

The EMG amplifiers were used to simultaneously measure EMG signals in each of the three superficial muscles of the Quadriceps. The three amplifiers had a bandwidth of 3Hz-1kHz, variable gain of 51-96dB and a CMRR of 50-60dB. As with the stimulator, design of the electronics, and, component and PCB layout was such that the subject remained isolated from earth at all times.

During development a few performance issues were found, and, where possible addressed:

1. Switching spikes, attributed to capacitive coupling between analog and digital signal lines, were reduced by introducing shielded cables and changing the layout of the PCB tracks (Sections 6.3.2 and 6.3.3).

2. High frequency interference, caused by the DC-DC switching converters, was eliminated by removing the converters from the main amplifier box and placing them in a separate power supply unit (Section 6.3.1). The noise was further reduced by introducing low pass filters into the amplifier design (Section 6.4.2).

3. The transient response of the amplifiers, for both DM and CM input voltages, were measured (Section 6.5.3). The responses were found to be a bandpass characteristic of the output filter, which was also responsible for the occurrence of the blanking interval response (a transient response seen to be present when the blanking interval voltage level was not adjusted to the same level as that measured immediately before and after the blanking interval, Section 6.5.2).

The Stimulator-Body-Amplifier system

A number of mechanisms cause stimulation artefact. However, exactly which mechanisms are at work depends on the system consisting of the stimulator, amplifier and tissue being stimulated. Such systems need to be evaluated individually, and the relevant causes of stimulation artefact identified.

For the system including the Biphasic stimulator and the Blanking amplifier, there were three main causes of stimulation artefact:

1. Voltage gradient (Section 7.2).

2. Electrode-skin interface (Section 7.3).

3. Common mode voltage (Section 7.4).

The first two causes are related. A voltage gradient is set up in tissue when current flows from an anode, through the tissue, to a cathode. In the application discussed here, where the recording electrodes are placed between the stimulating electrodes, the voltage gradient would create a potential difference between the recording electrodes. If there is a path for current to flow between stimulation pulses, such a potential difference at the amplifier input would appear as stimulation artefact at the amplifier output. In the case of the Biphasic stimulator, the blocking capacitor and discharge resistor found in the output stage, created just such a path. The discharge current arose due to residual charge, at the end of a stimulation pulse, remaining across the blocking capacitor and the capacitance of the electrode-skin interface of the two stimulating electrodes.

By adjusting the pulse width ratio, the total residual voltage was forced to zero, thereby preventing a discharge current from flowing and eliminating the stimulation artefact. A PSPICE model revealed that such a PW_r setting actually caused a wave-like response in the discharge current, due to different amounts of residual charge remaining on each stimulating electrode and the blocking capacitor, even though the overall residual voltage was zero. However, the short time constants inherent to the electrode interface prevented the transient response of the discharge current from being mistaken for an M-wave (figure 7.11(b)).

The common mode voltage referred to the potential difference between the recording electrode and the reference electrode. If the amplitude of this voltage exceeded the common mode rejection range of the amplifier, the inherent transient response of the amplifier resulted, which appeared as stimulation artefact at the amplifier output. In such a case, changing the PW_r setting had no effect on the stimulation artefact. Instead, it was eliminated by reducing the amplitude of the common mode voltage, either by careful placement of the reference electrode, or, by using clamping diodes to limit the common mode voltage at the amplifier input.

A second way in which common mode voltage could produce stimulation artefact was if there was a mismatch in impedance at the amplifier input terminals, which would result in a differential mode voltage seen by the amplifier.

Even though the discharge current and common mode voltage were the route causes of stimulation artefact with the *Stimulator-Body-Amplifier* system used, they were not responsible for the shape of the artefact. The shape of stimulation artefact due to discharge currents and voltage gradients were similar to the DM transient response of the amplifier. The measured time constant of $\sim$10ms was caused by the bandpass characteristic of the output filter. The shape of the common mode voltage stimulation artefact was similar to the CM transient response of the amplifier. The measured time constant, ranging from 15ms-20ms, was caused by the CM response inherent to the current conveyor, as well as the bandpass characteristic of the output filter.

9.3.2 Future work

Artefact free Stimulator-Body-Amplifier system

The blocking capacitor, C_b, and the discharge resistor, R_d, were originally included as part of the stimulator's output stage to provide charge balancing between the two phases. The capacitor served an additional safety function by preventing large DC currents from flowing if the stimulator were to fail short circuit. However, the inclusion of both these components also created a path for the discharge current to flow, thereby causing the stimulation artefact. In retrospect this was a flaw in the design of the stimulator, as at the time we had not realised that the residual charge on C_b and the electrode-skin interface, would spoil the system performance. A few suggestions are made to improve the system:

1. By removing R_d from the output stage, there would be no path around the stimulator circuit for the discharge current to flow. The blocking capacitor, C_b, should remain, as it performs an important safety function. However, this would mean that charge would accumulate on C_b. To prevent this, the voltage across C_b, between stimulation pulses, would need to be measured, as shown in figure 9.1. This could then be used to alter the charge in the next pulse pair to drive the residual voltage to zero.

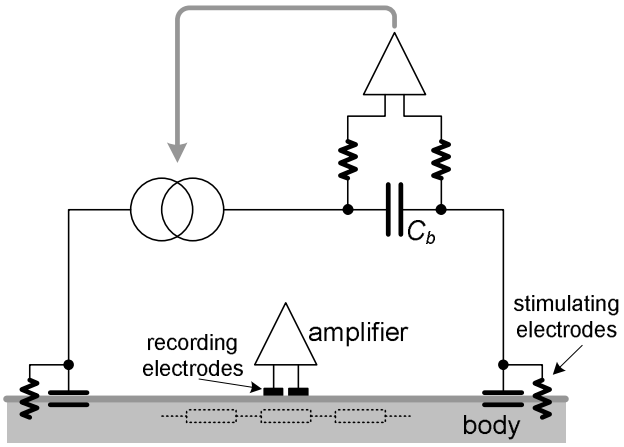

Figure 9.1: Proposed changes to stimulator output stage.

   A danger in this method is that one input to the new amplifier, is connected to the patient-side of the blocking capacitor, which risks allowing DC through that pathway. In the figure resistors have been placed in series with the amplifier inputs. These are intended to have a high impedance, so as to limit the fault current.

2. The voltage gradient that is present during the stimulation pulse will cause current to flow through the recording electrode circuit and this will later discharge causing an artefact. One possibility would be to have electronic switches immediately after the electrodes which are opened throughout the blanking period.

3. The stimulation artefact due to common mode voltage, was in part attributed to mismatches in the component values used for the input filter (figure 6.5). At present the

200kΩ resistors had a tolerance of $\pm 1\%$, and the 470nF capacitors had a tolerance of only $\pm 10\%$.

One option would be the use of precision components for the input filter, thereby reducing the mismatch. Alternatively the input filter could be entirely removed from the amplifier circuit. However, that would have the effect of increasing the input impedance of the amplifier, as it would now be determined by the input impedances of the AD844 ICs. Such a change could make the system more susceptible to stimulation artefact due to magnetic coupling between the stimulating and recording leads [McLean et al., 1996; Scott et al., 1997], consequently a reduction in the stimulation artefact may not be achieved.

In either case, improving the mismatch in the input filter would have no influence on the mismatch inherent to the recording electrodes. However, it could improve the CMRR of the EMG amplifier (measured at 50-60dB, refer to figure 6.27).

4. To further combat the stimulation artefact, caused by common mode voltage, the amplifier specification should have a CM range as large as possible. For the Blanking amplifier, the CM range was determined by the current conveyor circuits and the AD844 ICs. In Section 6.4.1 it was discussed how the CM range of these ICs, which is determined by their supply rails, was increased to the maximum possible of ± 15V. For a further increase in CM range it would be necessary to investigate using a different switching scheme at the amplifier input.

5. The bandpass characteristic of the output filter (figure 6.5) was responsible for shaping the stimulation artefact. By removing this filter the time constant of the artefact could be drastically reduced, however, the EMG signal would contain more high frequency interference caused by the DC-DC converters. Nonetheless, it would still be possible to identify M-waves measure peak-to-peak amplitudes (figure 6.25(c)).

Preventing crosstalk

In Chapter 8, the final M-wave measurements were adjusted for crosstalk, as the input stage of the Blanking amplifier, a single differential (SD) stage, is known to be susceptible to crosstalk. In the literature a double differential (DD) input stage was often used to reduce this susceptibility [De Luca and Merletti, 1988; Koh and Grabiner, 1993; Merletti et al., 1992]. The feasibility of converting the current conveyor circuit into a DD input stage would need to be investigated. However, it might be necessary to replace the current conveyors with a different input stage altogether.

Regardless of the switching scheme, using a DD stage increases the number of recording electrodes from 2 to 3 (refer to figure 1.5(b)). It is likely that this would make the system more susceptible to stimulation artefact, as the additional electrode would have residual charge after the stimulation pulse, contributing further towards the discharge current. Furthermore, three electrodes physically occupy more space than two, this means that the potential difference

between the outer two electrodes would be greater than a setup with just two electrodes, in the presence of the same voltage gradient. This could also increase the system's susceptibility to stimulation artefact.

9.4 The research question

The research question was investigated by measuring joint moments produced with each of the three *major* positions. The expectations behind the *major* positions were:

1. The *Rectus* position selectively stimulated RF, producing both a knee extension and a hip flexion moment, due to the bi-articular nature of RF.

2. The *Vastii* position selectively stimulated VM and VL, producing a knee extension moment, due to the mono-articular nature of VM and VL.

3. The *Standard* position stimulated VM, VL and RF equally, producing both a knee extension and a hip flexion moment. The hip flexion moment was expected to be smaller than in the case of *Rectus*, but greater than that measured with *Vastii*.

The relative amplitude of the M-wave measurements, in the three superficial Quadriceps muscles during stimulation with each of the *major* positions, was to indicate just how selective each of the positions actually were. However, from the work of Knaflitz et al. [1988], Farina et al. [2002] and Solomonow et al. [1994] it was found that at most 25% to 28% of the EMG signal in the stimulated Quadriceps muscle can appear as crosstalk in the non-stimulated muscles. The presence of such crosstalk in the measurements could lead to erroneous conclusions being drawn about the co-activation of the muscles. To prevent such a scenario it was decided to adjust the M-wave peak-to-peak amplitudes to account for crosstalk:

- *Standard* - No adjustment for crosstalk as all three muscles (RF, VM and VL) are stimulated.

- *Rectus* - 25% of M-wave amplitude measured in RF subtracted from amplitude of M-waves measured in VM and VL.

- *Vastii* - 25% of M-wave amplitude measured in either VM or VL, whichever is larger, subtracted from amplitude of M-wave measured in RF.

The M-wave amplitudes were also normalised with respect to the largest M-wave measured during a session, irrespective of *major* position or component muscle.

9.4.1 Study results

The results were used to produce moment curves ($\mathbf{M}_h$ plotted against $\mathbf{M}_k$, as in figures 4.6 and 8.10). The main observations made from these plots were:

1. The *Rectus* moment curve *lay above* those of the *Standard* and *Vastii* positions, as *Rectus* produced the largest hip flexion moment. This agreed with expectations.

2. The *Standard* and *Vastii* moment curves tended to overlap. *Vastii* did not produce a reduction in hip flexion moment, as compared against that produced with the *Standard* position. This was contrary to expectations.

The results were also used to produce EMG curves (M-wave amplitude measured in RF plotted against that measured in either VM or VL, see figure 8.14). The main observations seen here were:

1. For the *Standard* position the results varied greatly between subjects. Some subjects showed co-activation of VM, RF and VL, while other subjects tended to show activation predominantly of VM.

2. The results also varied between subjects for the *Rectus* position. Co-activation of all three muscles was seen, or, activation was predominantly seen in RF.

3. The *Vastii* position showed activation of VM and VL only.

9.4.2 Discussion and conclusions

The following conclusions were drawn from the EMG curves, regarding selective stimulation (Section 8.4.3):

1. The *Rectus* position did not selectively stimulate RF, nonetheless, it did produce the strongest contraction in RF.

2. The *Vastii* position did selectively stimulate VM and VL.

3. The *Standard* position did not always activate all three muscles. For some subjects the contraction in RF and VL was so much smaller than that seen in VM, that it was more akin to selective stimulation of VM. (This contradicted the original assumption, and could have lead to misinterpretation of the moment curves.)

By considering what had been learnt from the M-wave measurements, in combination with the joint moments, $\mathbf{M}_k$ and $\mathbf{M}_h$, the following conclusions were reached (Section 8.4.4):

1. The largest knee extension moments occurred when VM, VL and RF were simultaneously activated.

2. Activation of only VM and VL (*Vastii* and *Standard* positions), or only RF (*Rectus* position), produced knee extension moments comparable in magnitude.

3. When RF was activated by the *Standard* position, a larger $\mathbf{M}_h$ was measured with the *Standard* position than with the *Vastii*.

4. When RF was not activated by the *Standard* position, a smaller $\mathbf{M}_h$ was measured with the *Standard* position than with the *Vastii*.

If the stimulation with the *Vastii* position exclusively activated VM and VL, there should have been no hip flexion moment measured. However, this was not the case. Two possible explanations are:

1. The crosstalk adjustment was too large, thereby reducing the RF M-wave amplitudes to zero, when in actual fact a non-zero amplitude would have indicated a slight activation of RF.

2. The *Vastii* position could have also stimulated the Sartorius and Tensor fasciae latae muscles, both of which perform a hip flexion.

Finally, these results were used to make a few points regarding the research question:

> *Is it possible to maximise knee extension moments,* $\mathbf{M}_k$*, while minimising hip flexion moments,* $\mathbf{M}_h$*, using selective surface stimulation of the superficial muscles of the Quadriceps?*

The last part of the research question enquires about using surface stimulation to selectively activate target muscles. From the work presented it was seen that selective stimulation of VM and VL was possible with the *Vastii* position. However, the *Rectus* position did not selectively stimulate RF, although it did produce a strong contraction in RF and weak contractions in VM and VL.

Regarding the joint moments, it was found that hip flexion moments were reduced if VM and VL were selectively stimulated with the *Vastii* position. However, this did coincide with a reduction in the knee joint moments.

9.4.3 Shortcomings of the Bi-moment chair study

One of the shortcomings of the study was that the causes of the artefact and the various methods used to eliminate it, were being learnt about while the study was being executed, often due to unanticipated problems requiring modifications. Consequently the methods used to eliminate the stimulation artefact, and the effectiveness of this artefact elimination was not consistent for all 10 subjects. This meant that there was inconsistencies in the protocol used during the study. Furthermore, of the 10 subjects who participated in the final study, a complete data set (as used in the M-wave analysis) was only captured for 4 subjects.

A second shortcoming, is that the study was only carried out with AB subjects, who are unable to withstand the same stimulation current amplitudes typically used by SCI cyclists (40-110mA for SCI cyclists [Perkins et al., 2001], as compared against 20-65mA with AB subjects A-L). As the current intensity increases, the region in which nerve fibres are stimulated also increases, thereby recruiting more muscle fibres, including those from adjacent muscles. It is therefore uncertain if similar results for selective stimulation would be seen at the higher current amplitudes of the SCI cyclists.

9.4.4 Implications for FES cycling

Recall that in the results of Szecsi et al. [2007] a knee extension moment was measured simultaneously with a hip flexion moment, during FES cycling. The knee extension moments produced concentric positive power, while the hip flexion moment produced eccentric negative power. The nett effect, or power output (PO), would therefore be increased if the hip flexion moment could be reduced. Furthermore, metabolic energy is expended to produce both the knee extension and hip flexion moments. Therefore, by reducing the hip flexion moment, an improvement in the cycling efficiency should also be seen.

When the research question was phrased, the original intent was to use the *Vastii* position, during FES cycling, to reduce $\mathbf{M}_h$. The outcome of the study showed that it was possible to selectively stimulate VM and VL. However, whether this would result in an improvement in the PO and efficiency is still unclear, because:

1. In the studies of Perkins et al. [2001] and Szecsi et al. [2007] the *Standard* position was used during FES cycling to simultaneously stimulate the component muscles of Quadriceps. In this thesis, it was shown that the *Standard* position did not always activate VL and RF for a seated subject, as expected. As the aforementioned studies did not include evoked EMG measurements during cycling, we do not know if the hip flexion moment measured by Szecsi et al. [2007] was due to the activation of RF, or some other muscle such as Sartorius.

   Consequently, the effectiveness of using the *Vastii* position during cycling to reduce $\mathbf{M}_h$, would probably vary between cyclists. If the *Standard* position did activate RF, then a reduction in $\mathbf{M}_h$ would be seen when using the *Vastii* position. In cases where RF was not activated, this would not necessarily hold true.

2. The knee extension moments produced by the *Vastii* position were much smaller than those measured with the *Standard* positions (when RF was activated). This could result in a decrease in concentric positive power, as well as the eccentric negative power, hence producing no improvement in the PO.

Originally, the *Rectus* position was only intended as a control, the results of which could be used to compare against those of the *Standard* and *Vastii* positions. However, it may be feasible to use both the *Rectus* and *Vastii* positions to stimulate the Quadriceps during FES cycling. If we consider the results of Hakansson and Hull [2005] and Johnston et al. [2007], we see that during recumbent cycling with AB subjects there is a period during the cycling revolution in which both VM and VL, as well as RF, are activated (refer to figure 1.2). For FES cycling, it would be possible to better control when RF is activated relative to VM and VL, by using both *major* positions. This could potentially produce the desired reduction in $\mathbf{M}_h$, without losing any $\mathbf{M}_k$.

Part V

Appendices and References

Appendix A

Bi-moment chair design and construction

A.1 Data acquisition card

A DAQ6024E from *National Instruments* was used as the data acquisition card. The sampling rate of the card was set to 111Hz. The sampling rate was chosen so as not to be a multiple of 50Hz mains or one of the stimulation frequencies (20Hz, 33Hz or 50Hz) thereby preventing aliasing noise appearing in the measured data.

According to the user manual the DAQ6024E has an analog-to-digital converter resolution of 12-bits and can support 16 Analog Input (AI) channels with single-ended connections, or 8 AI channels with differential connections. The specifications also state that differential input connections should be used for any channel that meets any one of the following four conditions:

1. "The input signal is considered to be *low level* (less than 1V)."
2. "The leads connecting the signals to the device are greater than 3m."
3. "The input signal requires a separate ground-reference point or return signal."
4. "The signal leads travel through noisy environments."

As the connections to the sensors in the dynamometer were required to be of considerable length, and the range of measurements could easily drop below 1V it was decided to use differential input connections. This gave a total of eight available input channels, 4 that were assigned to the spring pots, 2 to the strain gauge transducers and 2 to the pulse width recorder. According to the manual, differential input connections had the added benefits of "reducing picked up noise and increasing common-mode noise rejection".

It was also decided to use *ground-referenced signal sources*, which means that the signals have the same ground reference as the computer in which the DAQ6024E is installed. A diagram of the ground-referenced signal source connection is shown in figure A.1.

The input range of the DAQ6024E can be selected by changing its gain setting. The drivers used in the *Simulink* program did not allow the gain setting of each channel to be individually selected. As a consequence the same gain setting had to be used for the spring pots, strain gauge transducers and the pulse width recorder. A gain setting of 1.0 was selected, which resulted in an input range of ± 5V, and a measurement precision of 2.44mV.

The pinouts of the DAQ6024E are shown in figure A.2.

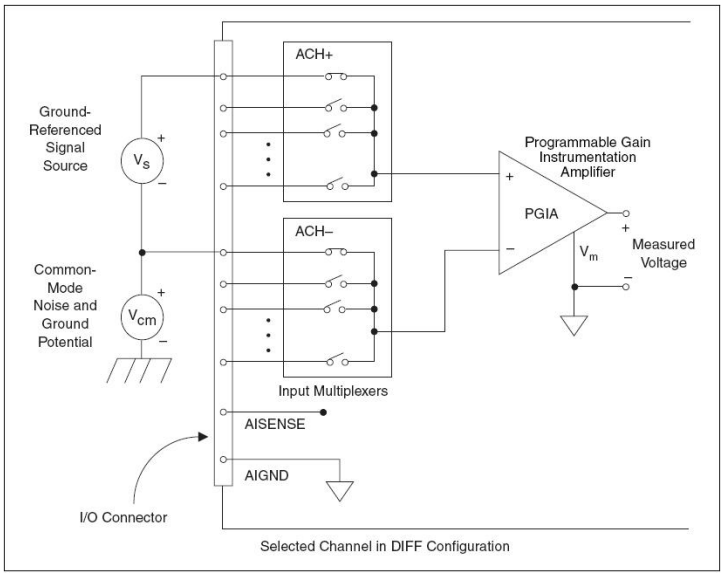

Figure A.1: Differential input connections for the DAQ6024E ground-referenced signals, reproduced from NI [2000], with permission.

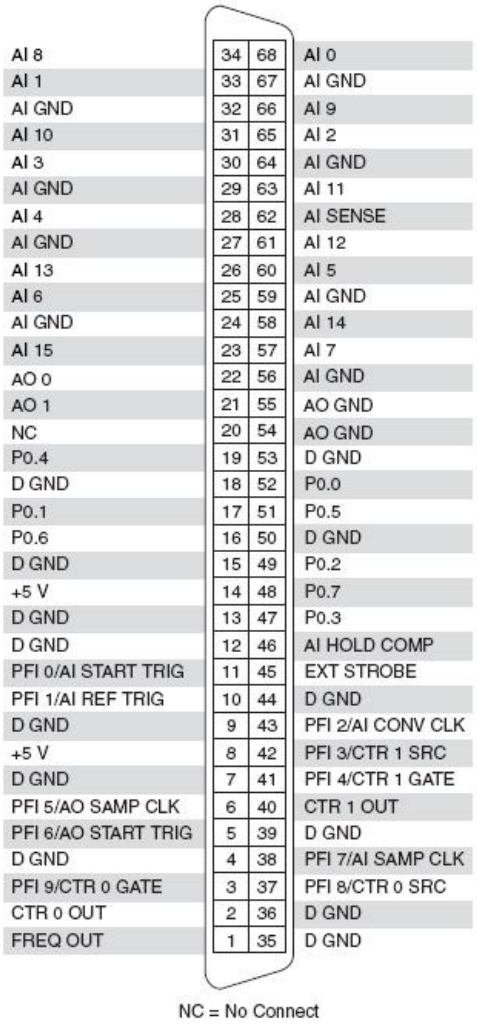

Figure A.2: Pinout of the NI DAQ6024E, reproduced from NI [2005], with permission.

A.2 Stimulation equipment

A.2.1 Optoisolator

Initially a fully integrated optoisolator, was used. However, this optoisolator was seen to introduce an offset into the strain gauge amplifier outputs whenever the stimulator was switched on. This was possibly due to the propagation of noise along the ground paths via the optoisolator, which implies that the integrated component did not provide proper isolation. This problem was overcome by using another optoisolator, the circuit diagram of which is given in figure A.3.[1]

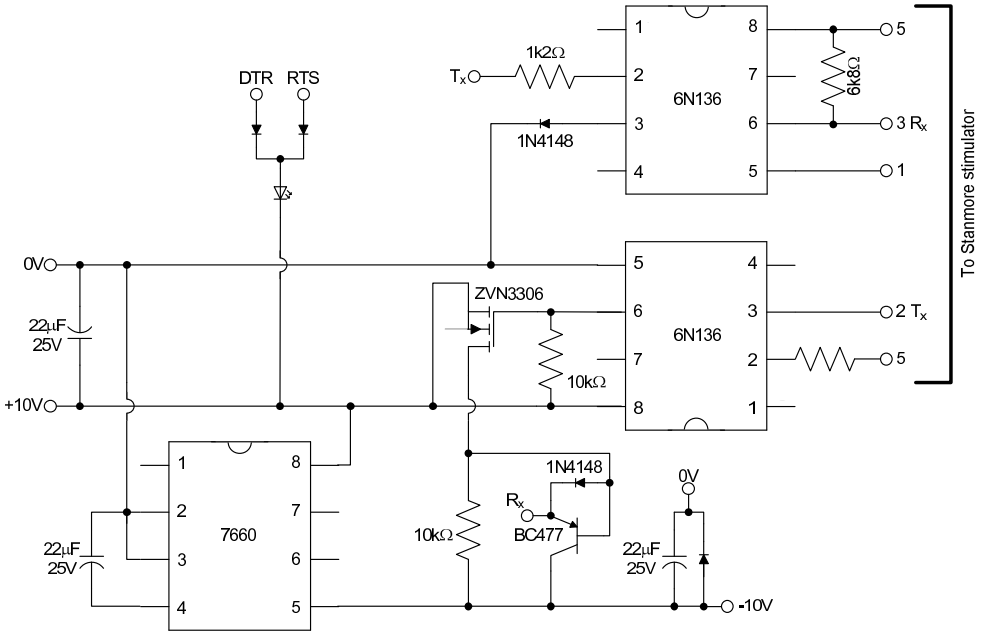

Figure A.3: Optoisolator circuit diagram.

A.2.2 Pulse width recorder

Figure A.4 shows the circuit diagram of the pulse width recorder, designed by Mr Tim Perkins. The 4N25 optoisolator ensures that the stimulator remains isolated from the sensor electronics box. The complete pulse width recorder consisted of two of these circuits, one for each of the required stimulation channels.

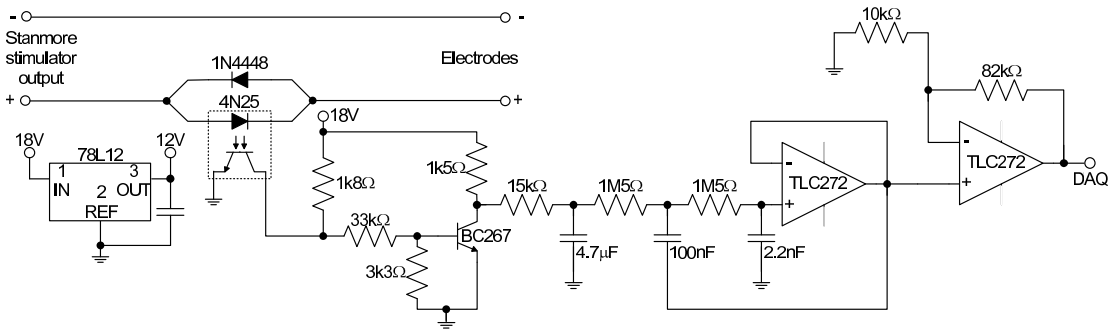

Figure A.4: Pulse width recorder circuit diagram.

[1] I'd like to acknowledge Mr Tim Perkins for the design of the replacement optoisolator.

A.3 Sensor electronics box

A.3.1 Spring pot circuitry

The four spring pots (each constructed using a 5kΩ potentiometer) were connected between the ±5V rails, as shown in figure A.5. The 100Ω resistors were used to drop the voltage rails between which the spring pots operate to ±4.3V. This was necessary as the DAQ6024E could potentially be damaged if an input voltage exceeded its selected input range. It was also found, that voltage measurements close to the limits of the input range (i.e. measurements close to ±5V) tended to be clipped. The introduction of the 100Ω resistors in series with the spring pots prevented this from happening, thereby avoiding inaccuracies being introduced into the spring pot measurements through the clipping.

The pinouts of the DAQ6024E, and the connector block, (refer to Section A.3.4), to which each of the spring pots was connected, are shown in the circuit diagram.

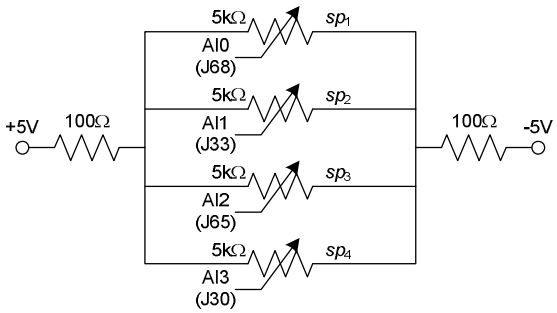

Figure A.5: Spring pot circuitry.

A.3.2 Strain gauge amplifiers

Shell [1990] presented a high-accuracy bridge amplifier, that cancels common-mode error, which was in turn used by Yu [1999] to amplify strain gauge signals. The same circuit, shown in figure A.6, was used for the strain gauge transducer signals in the Bi-moment chair.

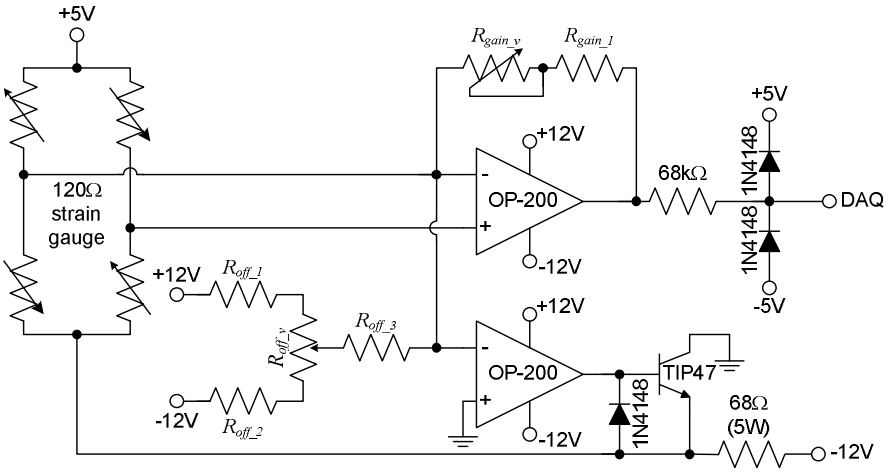

Figure A.6: Strain gauge amplifier circuit diagram, after Shell [1990], with permission, and Yu [1999], with permission.

The TIP47 NPN transistor supplied the current required by the strain gauge. The emitter resistance of 68Ω was selected so that the the strain gauge would operate between approximately ± 5V. This resistor was realised with a planar resistor that had a high power rating, which was mounted to a heat sink to compensate for the current requirements of the strain gauge.

The amplifier output was connected to the DAQ6024E through a 68kΩ current limiting resistor. The output was also passed through a simple voltage clamp to ensure that the amplifier output did not exceed the ± 5V input range of the DAQ6024E, as the amplifier itself operated between ± 12V rails.

The offset and gain resistor values of the amplifier were individually selected for each strain gauge transducer to accommodate for the large difference in expected magnitude of the forces, $\mathbf{F}_t$ and $\mathbf{F}_s$.

In figure 2.2, SG_1 is connected to the thigh by means of a rigid support. While, the subject is at rest, SG_1 would thus need to support the entire weight of the rigid support and the mass of the lower limb. Any force, $\mathbf{F}_t$, exerted on SG_1 during a contraction would either add to or subtract from this initial weight, depending on the direction of the applied force. According to Winter [2005], the weight of the lower limb can be approximated as $0.161m_{total}$, where m_{total} is the subject's total body mass. The weight of the rigid support is approximately 1kg. Taking these factors into account, for an average m_{total} of 80kg, and roughly estimating the magnitude of $\mathbf{F}_t$ to be 100N, the measurement range of the SG_1 amplifier would therefore need to be approximately 250N.

In the case of SG_2, it would only be measuring the magnitude of $\mathbf{F}_s$, as it does not support any weight initially. In Duffell et al. [2009], the knee extension moment measured for two AB subjects, during electrical stimulation, was approximately 145Nm. This was at a stimulation intensity such that the force realised was 40% of the measured MVC force for each of the subjects. Assuming the subjects had an average total height, h_{total}, of 1.7m, the distance between their KJC and ankle joint can be approximated as $0.246h_{total}$ [Winter, 2005]. This implies that, if force $\mathbf{F}_s$ is applied 5cm above the ankle joint, the magnitude of $\mathbf{F}_s$ needed to generate a knee extension moment of 145Nm, would be 394N. It was therefore necessary for the SG_2 amplifier to measure over a range of roughly 400N.

The offset and gain resistor values selected to meet these requirements were experimentally

Table A.1: Offset and gain resistor values.

Resistance	$\boldsymbol{SG_1}$ **(kΩ)**	$\boldsymbol{SG_2}$ **(kΩ)**
R_{gain_1}	56	20
R_{gain_v}	10	10
R_{off_1}	7.5	7.5
R_{off_2}	-	-
R_{off_3}	47	47
R_{off_v}	10	10

determined by suspending a 15kg weight from the transducers, measuring the amplifier output and adjusting the resistor values accordingly. The selected values are shown in table A.1. It should be noted that for both amplifiers, resistor R_{off_2} was replaced with a short circuit.

The actual force range that could be measured over ± 5V, for each of the strain gauges was later measured to be approximately 400N for SG_1 and 1.3kN for SG_2.

A.3.3 Power supply

A simple, transformer based, power supply was designed for the spring pots, the strain gauge transducers and the pulse width recorder of the Stanmore stimulator. It was decided to build a single power supply for all of these parts in order to limit the switching noise that would have been introduced into the system if each part utilised its own switch-mode power supply, as was originally the case. The circuit diagram of the power supply can be found in figure A.7. The voltage rails and current specifications required of the power supply, for each part, are given in table A.2. The current requirements were obtained through measurement of the current supplied to each part during operation.

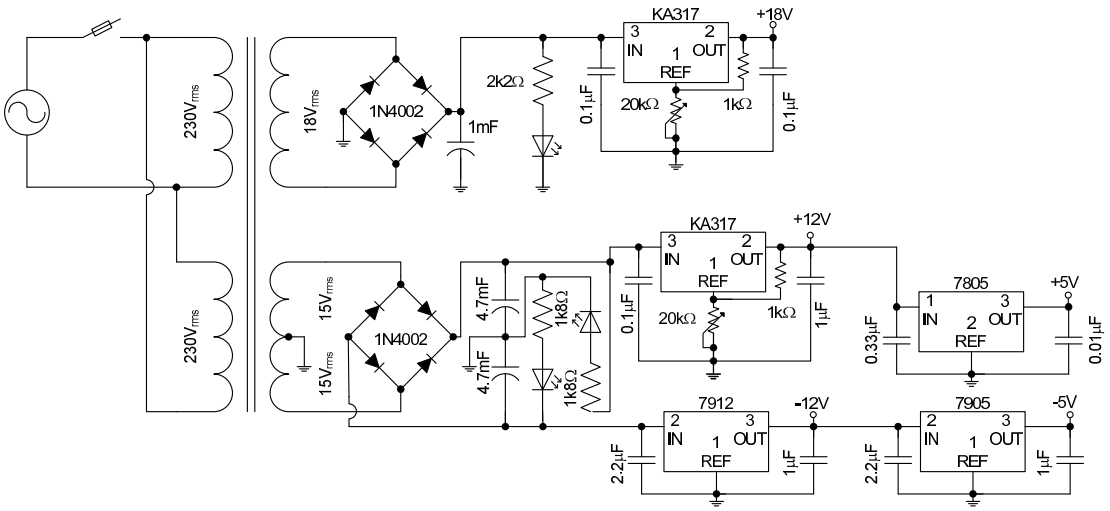

Figure A.7: Power supply schematic.

Table A.2: Power supply specifications.

Part	Voltage rails	Current rating
Spring pots	± 5V	10mA
Strain gauge amplifiers	$+5$V and ± 12V	500mA
Pulse width recorder	$+18$V	50mA

As the current requirements for the $+18$V rail was relatively low compared to that required by the ± 5V and ± 12V rails together, it was decided to effectively split the power supply into two by utilising two transformers. In so doing the power rating of the transformer supplying the $+18$V rail was kept as low as possible. Power supply design is well known, and the basic procedure that was followed here can be found in Horowitz and Hill [1989].

Table A.3: Transformer design.

Step	12V rail transformer	18V rail transformer
Required output voltage (V_{req})	12V	18V
Dropout voltage ($V_{dropout}$)	3V[a]	5V[b]
5% ripple voltage (V_{ripple})[c]	0.8V	1.2V
Diode forward voltage ripple (V_F)[d]	1.1V	1.1V
Transformer peak voltage[e]	18V	26.4V
Transformer rms voltage	12.7V	18.6V

[a] The maximum dropout voltage for the KA317 when supplying at least 1.5A, as indicated in the datasheet.
[b] A dropout voltage of 5V was taken as more than sufficient for the 78XX and 79XX voltage regulators.
[c] $(V_{req} + V_{droupout}) \left(\frac{1}{1-0.05} - 1\right)$
[d] As specified in the datasheet, note that $2V_F$ must be used to account for full wave rectification.
[e] $V_{req} + V_{droupout} + V_{ripple} + 2V_F$

Table A.4: Output capacitor design.

Step	12V rail transformer	18V rail transformer
Transformer voltage rating	$15V_{rms}$	$18V_{rms}$
Peak voltage (V_{peak})	21.2V	25.5V
Rectified voltage (V_{rec})[a]	19.0V	23.3V
Ripple voltage (V_{ripple})[b]	1.9V	1.2V
Maximum rms current[c]	670mA	89mA
Maximum peak current (I_{peak})	945mA	126mA
Output capacitance[d]	4.98mF	1.05mF

[a] $V_{peak} - 2V_F$
[b] $0.05V_{rec}$ for a 5% ripple and $0.1V_{rec}$ for a 10% ripple.
[c] $\frac{P_{rating}}{V_{rating}}$
[d] $\frac{I_{peak}T}{V_{ripple}}$ - T is equivalent to half the period of the AC signal, for 50Hz $T = 10$ms [Horowitz and Hill, 1989].

Table A.5: Data acquisition card and connector block pinouts.

Signal pinouts			Ground pinouts	
DAQ6024E pinout	**CB-68-LPR pinout**	**Signal**	**DAQ6024E pinout**	**CB-68-LPR pinout**
AI0	J(68)	sp_1	AI8	J(34)
AI1	J(33)	sp_2	AI9	J(66)
AI2	J(65)	sp_3	AI10	J(31)
AI3	J(30)	sp_4	AI11	J(63)
AI4	J(28)	SG_1	AI12	J(61)
AI5	J(60)	SG_2	AI13	J(26)
AI6	J(25)	Ch_1	AI14	J(58)
AI7	J(57)	Ch_2	AI15	J(23)

The voltage ratings of each transformer were calculated by taking into account:

- The required voltage rail.
- The *dropout* voltage needed to enure that the voltage regulators operated properly.
- A 5% ripple on the rectified voltage.
- The forward voltage drop seen across the diodes in the fullwave rectifier.

The values found for each of these steps is shown in table A.3, for both transformers. From these results a $230V_{rms}$:$15V_{rms}$ transformer was selected for the 12V rail. The secondary was required to have two secondary windings, so that both $\pm$12V rails could be realised, as shown in figure A.7. The transformer used had a power rating of 10VA, so that it could easily supply the 510mA required by the amplifier and spring pots. Similarly a $230V_{rms}$:$18V_{rms}$ transformer was selected for the 18V rail. The transformer had a power rating of 1.6VA, as it was only required to supply enough current to drive the pulse width recorder.

The required size of the power supply output capacitors were then calculated, as presented in Horowitz and Hill [1989], allowing for a 5% voltage ripple in the rectified output voltage of the 18V supply rail and 10% ripple for the $\pm$12V supply rail. It was decided to allow for a larger ripple in the latter to keep the output capacitor values a reasonable size. Furthermore, a larger voltage ripple would not be detrimental as the $15V_{rms}$ transformer used well exceeded the required $12V_{rms}$. The design steps for both transformers are given in table A.4.

A.3.4 DAQ6024E connector block

A CB-68LPR connector block was used in the interconnection box to facilitate the connection of the DAQ6024E to the spring pots, amplifiers and pulse width recorder. Table A.5 lists the connections realised between the data acquisition card, the connector block and each of the input signals. A shielded cable, SHC68-68EPM, manufactured by *National Instruments*, was used to physically connect the CB-68LPR to the DAQ6024E.

A.4 Simultaneous solution of distance equations

The final quadratic equation for a set of simultaneous distance equations in three-dimensional space was presented by Hsiao and Keyserling [1990] and Yu [1999]. Here the solutions are presented again with a step by step break down of how to obtain the solutions. This was necessary so that the same procedure could be followed in order to find a similar solution for the two-dimensional case.

A.4.1 Solution in two dimensions

From figure A.8(a) the following distance equations can be defined:

$$\tilde{L}_1^2 = (x_1 - x)^2 + (y_1 - y)^2 \tag{A.1}$$

$$\tilde{L}_2^2 = (x_2 - x)^2 + (y_2 - y)^2 \tag{A.2}$$

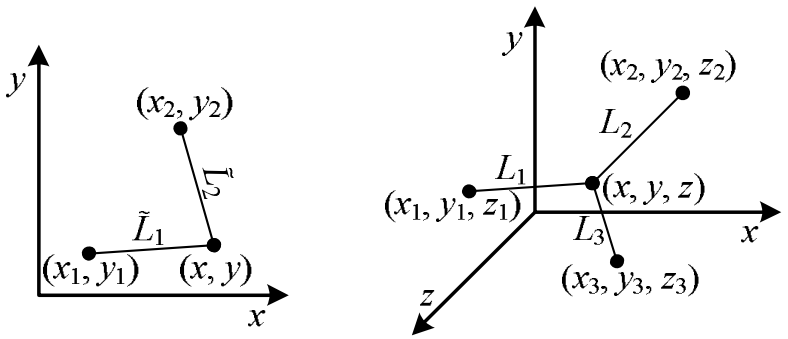

(a) Two-dimensional case. (b) Three-dimensional case.

Figure A.8: Geometric setup used to define the distance equations.

By expanding equations A.1 and A.2, and subtracting one from another, the result can be written as in equation A.3, using the definitions in equations A.4 and A.5.

$$\tilde{p} + \tilde{q} - \tilde{L}_2^2 = -2\left[(x_1 - x_2)\, x + (y_1 - y_2)\, y\right] \tag{A.3}$$

$$\tilde{p} = \tilde{L}_1^2 - \left(x_1^2 + y_1^2\right) \tag{A.4}$$

$$\tilde{q} = x_2^2 + y_2^2 \tag{A.5}$$

Equation A.3 can be solved for x as follows:

$$x = \tilde{a}y + \tilde{b} \tag{A.6}$$

where,

$$\tilde{\Delta} = 4\,(x_1 - x_2) \tag{A.7}$$

$$\tilde{a} = \frac{-4\,(y_1 - y_2)}{\tilde{\Delta}} \tag{A.8}$$

$$\tilde{b} = \frac{-2\left(\tilde{p} + \tilde{q} - \tilde{L}_2^2\right)}{\tilde{\Delta}} \tag{A.9}$$

By substituting equation A.6 back into equation A.1 and rearranging the terms yields:

$$\left(\tilde{a}^2 + 1\right) y^2 - 2\left[\tilde{a}\left(x_1 - \tilde{b}\right) + y_1\right] y + \left(x_1 - \tilde{b}\right)^2 + y_1^2 - L_1^2 = 0 \tag{A.10}$$

Equation A.10 is recognised as a quadratic equation of the form $\tilde{A}y^2 + \tilde{B}y + \tilde{C} = 0$, which has the well known solution:

$$z = \frac{-\tilde{B} \pm \sqrt{\tilde{B}^2 - 4\tilde{A}\tilde{C}}}{2\tilde{A}} \tag{A.11}$$

The terms of equation A.10 can be rewritten as in equations A.12 through A.14, using the definition of $\tilde{p}$ given in equation A.4.

$$\tilde{A} = \tilde{a}^2 + 1 \tag{A.12}$$

$$\tilde{B} = 2\tilde{a}\tilde{b} - 2\tilde{a}x_1 - 2y_1 \tag{A.13}$$

$$\tilde{C} = \tilde{b}^2 - 2x_1\tilde{b} - \tilde{p} \tag{A.14}$$

A.4.2 Solution in three-dimensions

A similar procedure is used to solve the three-dimensional distance equations shown below:

$$L_1^2 = (x_1 - x)^2 + (y_1 - y)^2 + (z_1 - z)^2 \tag{A.15}$$

$$L_2^2 = (x_2 - x)^2 + (y_2 - y)^2 + (z_2 - z)^2 \tag{A.16}$$

$$L_3^2 = (x_3 - x)^2 + (y_3 - y)^2 + (z_3 - z)^2 \tag{A.17}$$

Subtract equation A.16 from equation A.15 to yield:

$$\begin{aligned} x_1^2 - x_2^2 - 2(x_1 - x_2)x + y_1^2 - y_2^2 - 2(y_1 - y_2)y \ldots \\ + z_1^2 - z_2^2 - 2(z_1 - z_2)z = L_1^2 - L_2^2 \end{aligned} \tag{A.18}$$

where,

$$p + q - L_2^2 = -2\left[(x_1 - x_2)x + (y_1 - y_2)y + (z_1 - z_2)z\right] \tag{A.19}$$

$$p = L_1^2 - \left(x_1^2 + y_1^2 + z_1^2\right) \tag{A.20}$$

$$q = x_2^2 + y_2^2 + z_2^2 \tag{A.21}$$

Similarly, subtracting equation A.17 from equation A.15 can be written as in equation A.22, where r is defined in equation A.23.

$$p + r - L_3^2 = -2\left[(x_1 - x_3)x + (y_1 - y_3)y + (z_1 - z_3)z\right] \tag{A.22}$$

$$r = x_3^2 + y_3^2 + z_3^2 \tag{A.23}$$

Equation A.19 can then be used to solve for x.

$$x = \frac{-\frac{p+q-L_2^2}{2} - (y_1 - y_2)y - (z_1 - z_2)z}{(x_1 - x_2)} \tag{A.24}$$

By substituting equation A.24 back into equation A.22, a solution for y, can be found as shown in equations A.25 through A.28.

$$y = cz + d \tag{A.25}$$

$$\Delta = 4\left(x_1 - x_2\right)\left(y_1 - y_3\right) - 4\left(x_1 - x_3\right)\left(y_1 - y_2\right) \tag{A.26}$$

$$c = \frac{4\left(x_1 - x_3\right)\left(z_1 - z_2\right) - 4\left(x_1 - x_2\right)\left(z_1 - z_3\right)}{\Delta} \tag{A.27}$$

$$d = \frac{2\left(p + q - L_2^2\right)\left(x_1 - x_3\right) - 2\left(p + r - L_3^2\right)\left(x_1 - x_2\right)}{\Delta} \tag{A.28}$$

The solution for y can then be used in conjunction with equation A.24 to find a solution for x:

$$x = az + b \tag{A.29}$$

$$a = \frac{4\left(y_1 - y_2\right)\left(z_1 - z_3\right) - 4\left(y_1 - y_3\right)\left(z_1 - z_2\right)}{\Delta} \tag{A.30}$$

$$b = \frac{2\left(p + r - L_3^2\right)\left(y_1 - y_2\right) - 2\left(p + q - L_2^2\right)\left(y_1 - y_3\right)}{\Delta} \tag{A.31}$$

Substituting equations A.29 and A.25 into equation A.15 and rearranging the terms, yields:

$$\begin{aligned}\left(a^2 + c^2 + 1\right)z^2 - 2\left[a\left(x_1 - b\right) + c\left(y_1 - d\right) + z_1\right]z \ldots \\ + \left(x_1 - b\right)^2 + \left(y_1 - d\right)^2 + z_1^2 - L_1^2 = 0\end{aligned} \tag{A.32}$$

Once again, this is recognised as a quadratic equation of the form $Az^2 + Bz + C = 0$, with the following solution:

$$z = \frac{-B \pm \sqrt{B^2 - 4AC}}{2A} \tag{A.33}$$

The factors of equation A.32 can be rewritten as follows, using the definition of p given in equation A.20.

$$A = a^2 + c^2 + 1 \tag{A.34}$$

$$B = 2\left(ab + cd\right) - 2\left(ax_1 + cy_1\right) - 2z_1 \tag{A.35}$$

$$C = b^2 + d^2 - 2\left(x_1 b + y_1 d\right) - p \tag{A.36}$$

Appendix B

Error analysis

B.1 *Codamotion* investigation of Bi-moment chair assumptions

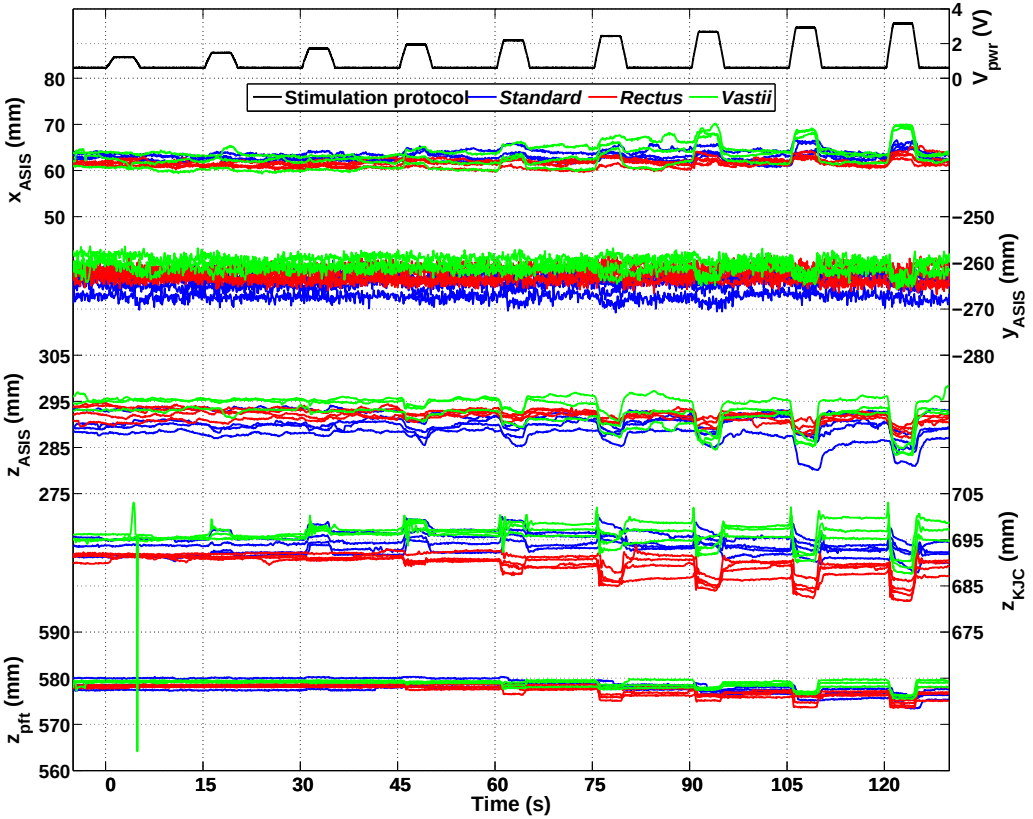

(a) Movement in the ASIS in three-dimensional space and lateral movement (along the z-axis), in the KJC and point p_{ft}.

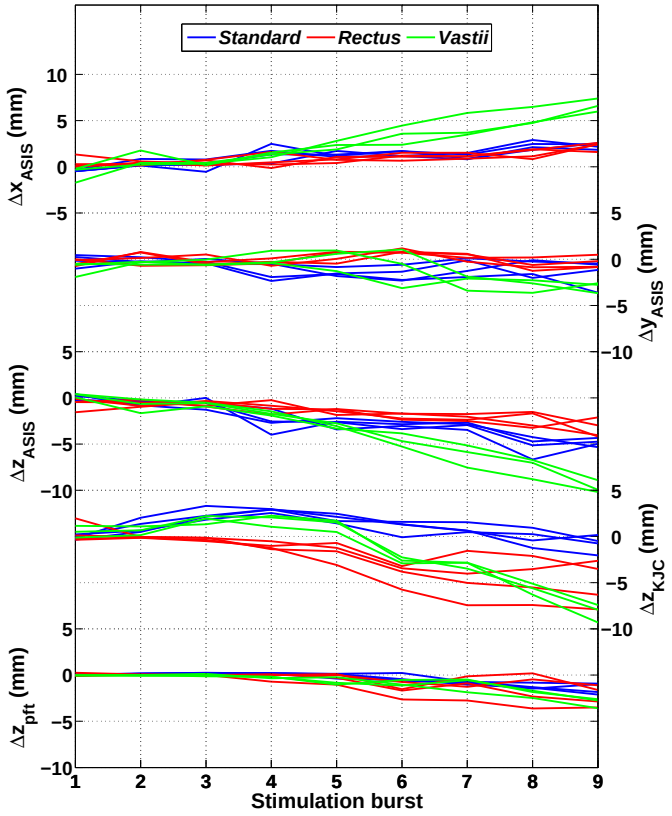

(b) Change in ASIS position in three-dimensional space and lateral change in position, in the KJC and point p_{ft}.

Figure B.1: *Codamotion* analysis system measurements of movement in the ASIS, KJC and point p_{ft}, (subject B).

Appendix C

Biphasic stimulator design and construction

C.1 Stanmore stimulator

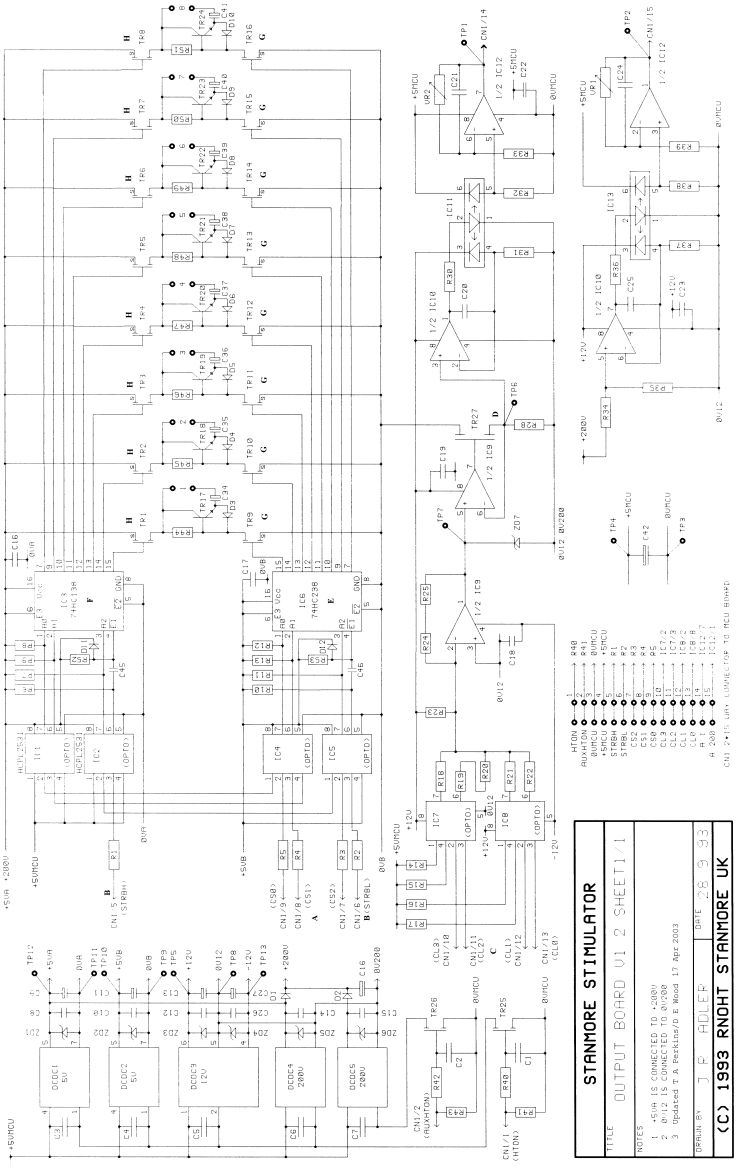

Figure C.1: Circuit schematic of the Stanmore stimulator Monophasic Output board, reproduced from Phillips et al. [2003], with permission.

C.2 Biphasic stimulator user guide

The Start menu features:

- **Run/Stop**

  Used to start and stop the stimulation. When the stimulator is inactive, the **Run** option will be displayed, and if selected, will start the stimulation (green press button - *Run/Select*). Conversely, during stimulation the **Stop** command is displayed which will stop the stimulation if selected by pressing any of the press buttons, included as a safety feature.

- **C<n>: <PW_n>μs <PW_r>%**

  Used to increase or decrease (press buttons *Up* or *Down*) the pulse width ratio setting for channel 1 (C1) and channel 2 (C2). Both the negative phase pulse width, in μs, and the pulse width ratio percentage are displayed. These settings can be adjusted when the stimulator is inactive as well as during stimulation.

- **Channel <n>: <Mode>**

  Displays the currently selected mode for the respective channel. The mode options are *Continuous stimulation*, *Recruitment curve* and *Off*. Whatever mode is displayed here, for the respective channels, is the type of stimulation that will occur when the stimulator is activated. The mode for each channel can be independently set. The *Up* and *Down* (black) press buttons can be used to scroll through the mode options. By pressing the (green) *Run/Select* button the menu display will change to that associated with the selected mode, for the channel corresponding with the position of the pointer.

- **Ch<n>: <x>mA**

  Cannot be selected by user. Realtime display of current amplitude settings for both channels. When the stimulator is inactive, the monitored values of CA_{ch1} and CA_{ch2} are displayed. During stimulation the values measured for CA_LIVE are shown.

The Continuous stimulation and Recruitment curve menus are the same for both channels. All of the parameters, except for the 'stimulation period', can be set individually for either channel. The 'stimulation period' parameter if adjusted by the user, automatically forces both channels to have the same parameter option. The (black) *Up* and *Down* press buttons can be used to scroll through the list of available parameters (if the pointer is to the left of said list), or, alternatively to scroll through the list of parameter options, for a specific parameter (pointer to the right of the parameter list). The parameter option currently displayed is the setting that will be used during stimulation.

The Continuous stimulation menu parameters:

1. **Pulsewidth (μs):**

   Pulse width setting for the positive phase of the biphasic pulse, PW_p. The negative phase pulse width is adjusted according to the PW_r setting in the Start menu.

   Parameter options: 20, 40, 60, 80, 100, 120, 140, 160, 180, 200, 225, 240, 250, 280, 300, 320, 360, 400

2. **Stimulation period (ms):**

   Determines the frequency with which stimulation pulses are generated. The stimulation period for both channels is automatically set to the same user defined value.

   Parameter options: 20, 30, 40, 50, 100, 500, 1000, 2000, 3000, 4000, 5000

The Recruitment curve (see Section 4.2.2), menu parameters:

1. **Pulsewidth (μs):**

   As in the Continuous stimulation menu.

2. **Stimulation period (ms):**

   As in the Continuous stimulation menu.

3. **No. of stimulation bursts:**

   Number of bursts of stimulation after which the channel mode is set to *Off*. The length of a stimulation burst is given by t_rampOn + t_burst + t_rampOff.

   Parameter options: 1, 2, 3, 4, 5, 6, 7, 8, 9, 10

4. **Start pulsewidth (%):**

   Percentage of the PW_p setting, specified in parameter 1, that the positive phase pulse width will be adjusted to during the first burst of stimulation. PW_n will be adjusted according to the PW_r setting in the Start menu and the adjusted positive phase pulse width.

   Parameter options: 10, 20, 30, 40, 50, 60, 70, 80, 90, 100

5. **Pulsewidth increment (%):**

   Percentage of the PW_p setting, specified in parameter 1, that the positive phase pulse width will increase by with each burst of stimulation. PW_n in each burst of stimulation, will be adjusted according to the PW_r setting in the Start menu and the positive phase pulse width used during the stimulation burst.

   Parameter options: 0, 10, 20, 30, 40, 50, 60, 70, 80, 90, 100

6. **t_burst (s):**

   The length of time defining the part of a stimulation burst during which the pulse width settings are unaltered.

   Parameter options: 1, 2, 3, 4, 5, 6, 7, 8, 9, 10

7. **t_off (s):**

   The length of time between stimulation bursts during which the stimulator is inactive.

   Parameter options: 1, 2, 3, 4, 5, 6, 7, 8, 9, 10

8. **t_rampOn (s):**

   Length of time, at the start of a stimulation burst, during which the stimulation intensity is linearly increased from zero to the maximum intensity setting for the given burst of stimulation. The stimulation intensity is increased by changing the PW_p setting. PW_n will be adjusted according to the PW_r setting in the Start menu and the current value used for PW_p.

   Parameter options: 0, 1, 2, 3

9. **t_rampOff (s):**

   Length of time, at the end of a stimulation burst, during which the stimulation intensity is linearly decreased from the maximum intensity setting for the given burst of stimulation to zero. The stimulation intensity is decreased by changing the PW_p setting. PW_n will be adjusted according to the PW_r setting in the Start menu and the current value used for PW_p.

   Parameter options: 0, 1, 2, 3

Appendix D

Blanking amplifier design and construction

D.1 Circuit description of the AD844

Text reproduced from AD [1989], with permission from Analog Devices:

> A simplified schematic is shown in Figure D.1. The AD844 differs from a conventional op amp in that the signal inputs have radically different impedance. The noninverting input (Pin 3) presents the usual high impedance. The voltage on this input is transferred to the inverting input (Pin 2) with a low offset voltage, ensured by the close matching of like polarity transistors operating under essentially identical bias conditions. Laser trimming nulls the residual offset voltage, down to a few tens of microvolts. The inverting input is the common emitter node of a complementary pair of grounded base stages and behaves as a current summing node. In an ideal current feedback op amp, the input resistance is zero. In the AD844, it is about 50Ω.
>
> A current applied to the inverting input is transferred to a complementary pair of unity-gain current mirrors that deliver the same current to an internal node (Pin 5) at which the full output voltage is generated. The unity-gain complementary voltage follower then buffers this voltage and provides the load driving power. This buffer is designed to drive low impedance loads, such as terminated cables, and can deliver ±50mA into a 50Ω load while maintaining low distortion, even when operating at supply voltages of only ±6 V. Current limiting (not shown) ensures safe operation under short-circuited conditions.
>
> It is important to understand that the low input impedance at the inverting input is locally generated and does not depend on feedback. This is very different from the virtual ground of a conventional operational amplifier used in the current summing mode, which is essentially an open circuit until the loop settles. In the AD844, transient current at the input does not cause voltage spikes at the summing node while the amplifier is settling. Furthermore, all of the transient current is delivered to the slewing (TZ) node (Pin 5) via a short signal path (the grounded base stages and the wideband current mirrors).
>
> The current available to charge the capacitance (about 4.5 pF) at the TZ node is always proportional to the input error current, and the slew rate limitations associated with the large signal response of the op amps do not occur. For this reason, the rise and fall times are almost independent of signal level. In practice, the input

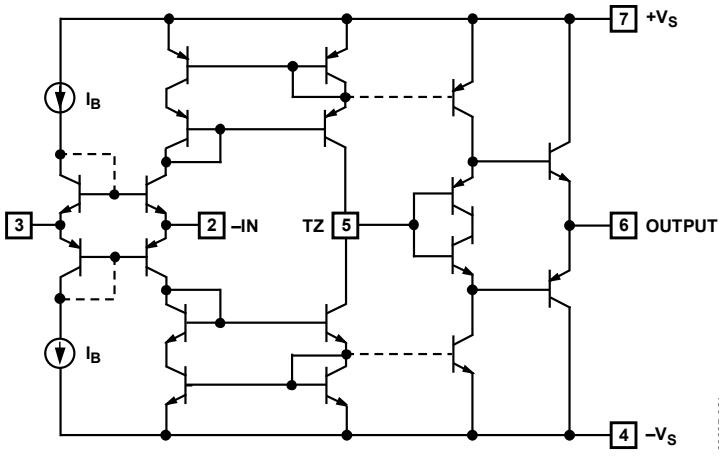

Figure D.1: Simplified schematic of the AD844, reproduced from AD [1989], with permission from Analog Devices.

current eventually causes the mirrors to saturate. When using ±15 V supplies, this occurs at about 10 mA (or ±2200 V/μs). Because signal currents are rarely this large, classical slew rate limitations are absent.
This inherent advantage is lost if the voltage follower used to buffer the output has slew rate limitations. The AD844 is designed to avoid this problem, and as a result, the output buffer exhibits a clean large signal transient response, free from anomalous effects arising from internal saturation.

D.2 Isolation amplifier design

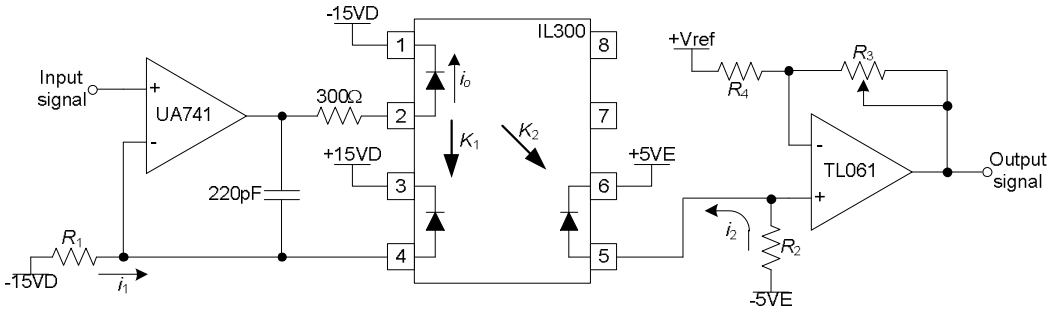

Figure D.2: Isolation amplifier circuit, after Vishay [2004], with permission from Vishay Intertechnology, Inc.

The LED currents are related through the coupler gains as in equation D.1. The typical coupler gain values are $K_1 \approx 0.007$, $K_2 \approx 0.007$ and $K_3 \approx 1$.

$$i_1 = K_1 i_o \qquad i_2 = K_2 i_o \qquad K_3 = K_2/K_1 \tag{D.1}$$

The larger the value of R_1, the smaller the value of i_1 and i_o, which means that the input op-amp is required to supply less current. For the LED, the best linearity can be obtained at drive currents between 5mA to 20mA. This lead to the choice of the UA741 as the input op-amp, as it is capable of supplying 25mA at its output pin. Current i_1 will assume its maximum value when the input signal swings all the way to the positive rail (+15VD). Under these conditions, the output current is given by equation D.2.

$$i_o = \frac{2(\text{+15VD})}{K_1 R_1} \tag{D.2}$$

By choosing $R_1 = 240\text{k}\Omega$, we obtain an output current of around 18mA, which is within the current supplying capability of the op-amp and large enough to ensure that the LED behaves linearly. Due to the difference in supply rails on either side of the isolation barrier, the signal seen at the non-inverting input of the TL061 output op-amp needed to be a third of the input signal seen at the non-inverting input of the UA741.

$$(V_{+UA741} = V_{-UA741}) \;=\; 3\,(V_{+TL061} = V_{-TL061}) \tag{D.3}$$

From equations D.1 and D.3 we can solve for R_2 as in equation D.4, which gives a value of 80kΩ (realised with a 75kΩ resistor in the circuit).

$$R_2 = \frac{R_1}{3K_3} \tag{D.4}$$

D.3 Differential gain calibration

The overall gain of the EMG amplifiers was dependent on two potentiometers, R_CC-GAIN, found at the output of the current conveyor, and R_ISO-GAIN, used to adjust the gain of the isolation amplifier.

R_CC-GAIN was realised with a 50kΩ trimmer, found on the Preamplifier board. For all three EMG amplifiers the trimmer position was set so that the current conveyor gain was at a maximum, and remained fixed at that level thereafter.

R_ISO-GAIN is accessible through the front panel of the amplifier box, thereby allowing the user to set the gain. The panel mounted potentiometer was fitted with a dial so that the position of the potentiometer's wiper could be monitored. The numbers on the dial, d_n ranged from 0 to 84.

The overall gain of each EMG amplifier was calibrated over the range of dial settings (R_ISO-GAIN adjustment) by measuring the EMG amplifier output voltages for a 100Hz, sine wave input (function generator connected through a 1000× resistive attenuator). The measured data was separated into two parts and calibrated independently. In the first part, a second order least squares fit was applied to the data for dial settings less than or equal to 20, refer to figure D.3(a). The equations for the fitted curves are shown in the figure. A first order least square fit was then applied to the rest of the data, refer to figure D.3(b). The gain in dB, for the entire dial setting range, for both the fitted curves and the measured data is shown in figure D.3(c).

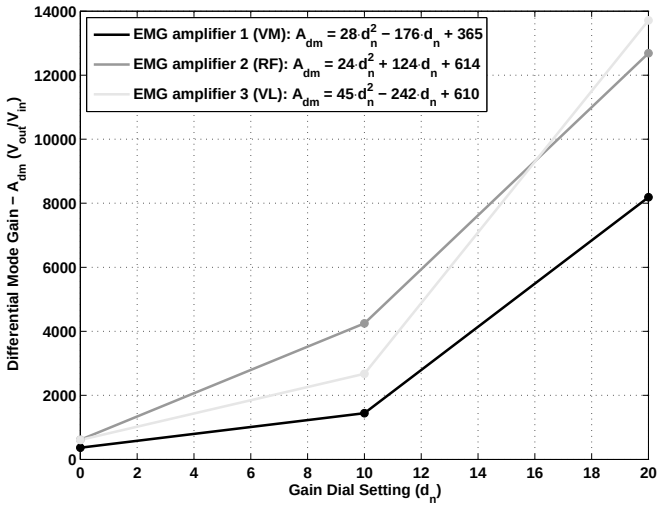

(a) Fitted curve for dial settings less than or equal to 20.

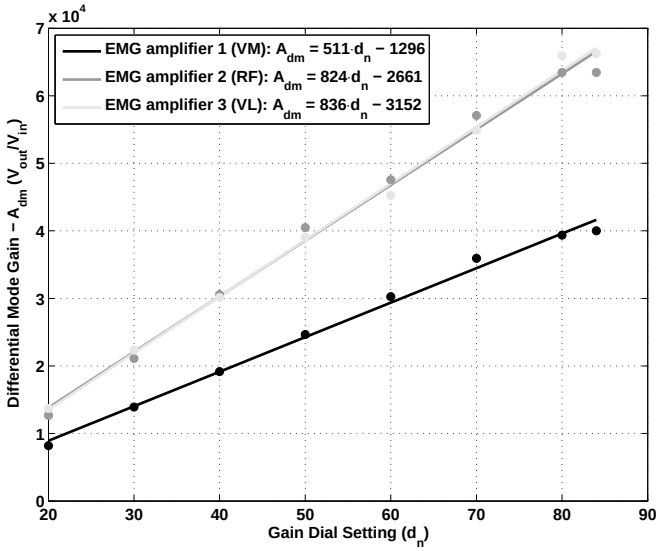

(b) Fitted curve for dial settings greater than or equal to 20.

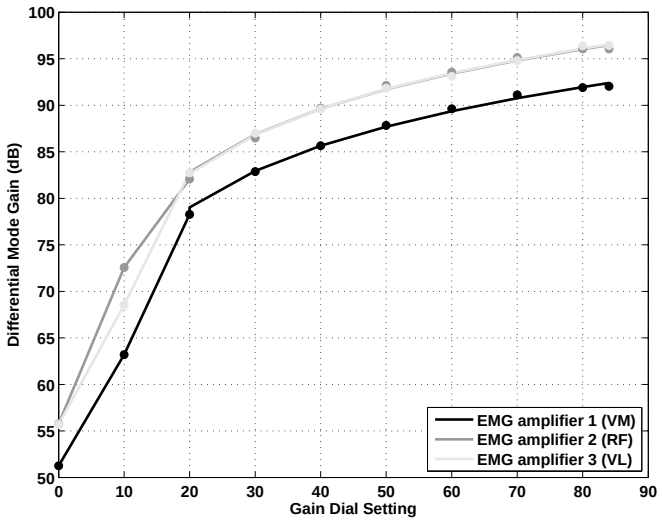

(c) Gain plot in dB using a second order fit for $d_n \leq 20$ and a first order fit for $d_n \geq 20$.

Figure D.3: Gain calibration curves for gain adjustment potentiometer (R_ISO-GAIN), for each EMG amplifier.

Appendix E

Stimulation artefact

E.1 Estimation of time constants from measured data

Perkins [2004] provides a definition for the time constant of an exponential decay as the inverse of its relative curvature, as given in equation E.1.

$$\tau = \frac{[V(2T) - V(0)]\,T}{2\,[2V(T) - V(0) - V(2T)]} \tag{E.1}$$

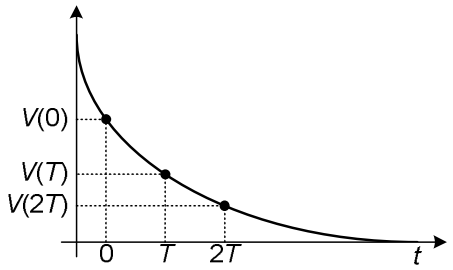

Figure E.1: Points used to calculate the time constant of an exponential waveform.

E.2 Derivation of PW_r equations, as used for the recruitment curve protocol

The gradients, m, and the intercepts, c, of the straight lines fitted to the data, shown in figure 7.16 are given in table E.1.

Even though the data measured for the different current amplitudes had a large spread, the gradients of the fitted lines, for 40μs $\leq PW_p \leq 200\mu$s were consistently around 0.2. This lead to the use of the simple approximation given in equation E.2 to estimate the required PW_r setting provided that $PW_{p\text{-}max} \leq 200\mu$s.

$$PW_r = PW_{r\text{-}min} + 0.2\,(PW_{p\text{-}max} - PW_p) \tag{E.2}$$

A similar relation was found for PW_p values in the range $240\mu\text{s} \leq PW_p \leq 400\mu$s. This was used together with equation E.2 to express the relationships between PW_r and PW_p for a $PW_{p\text{-}max}$ value greater than 240μs, as shown in equation E.3.

Table E.1: PW_r setting dependence on PW_p.

$40\mu s \leq PW_p \leq 200\mu s$		
Current	m	c
20mA	-0.19	102
21mA	-0.25	103
30mA(1)	-0.21	102
30mA(2)	-0.20	102
35mA	-0.19	101
36mA	-0.21	101
40mA(1)	-0.20	102
40mA(2)	-0.21	105
50mA	-0.22	104
Average	-0.20	102

$240\mu s \leq PW_p \leq 400\mu s$		
Current	m	c
40mA(3)	-0.03	74

$$PW_r = \begin{cases} PW_{r\text{-}240} + 0.2\,(240 - PW_p)\,; & PW_p < 240 \\ PW_{r\text{-}min} + 0.03\,(PW_{p\text{-}max} - PW_p)\,; & PW_p \geq 240 \end{cases} \tag{E.3}$$

$$PW_{r\text{-}240} = PW_{r\text{-}min} + 0.03\,(PW_{p\text{-}max} - 240)$$

For clarity, an example has been included in table E.2, in which the required PW_r settings for each of the nine stimulation bursts, of the recruitment curve protocol, was calculated using equation E.3.

Table E.2: Example PW_r calculation.

$PW_{p\text{-}max} = 400\mu s$ $PW_{r\text{-}min} = 30\%$		
Stimulation burst	PW_p **(**μ**s)**	PW_r **(%)**
1	80	66.8
3	120	58.8
3	160	50.8
4	200	42.8
5	240	34.8
6	280	33.6
7	320	32.4
8	360	31.2
9	400	30.0

E.3 Residual charge on recording electrodes

It is possible to represent both the stimulating and recording electrodes with the three-component model of figure 7.7. Using this approach, the complete *Stimulator-Body-Amplifier* system is shown in figure E.2. The blocking capacitor, C_b, and discharge resistor, R_d, of the

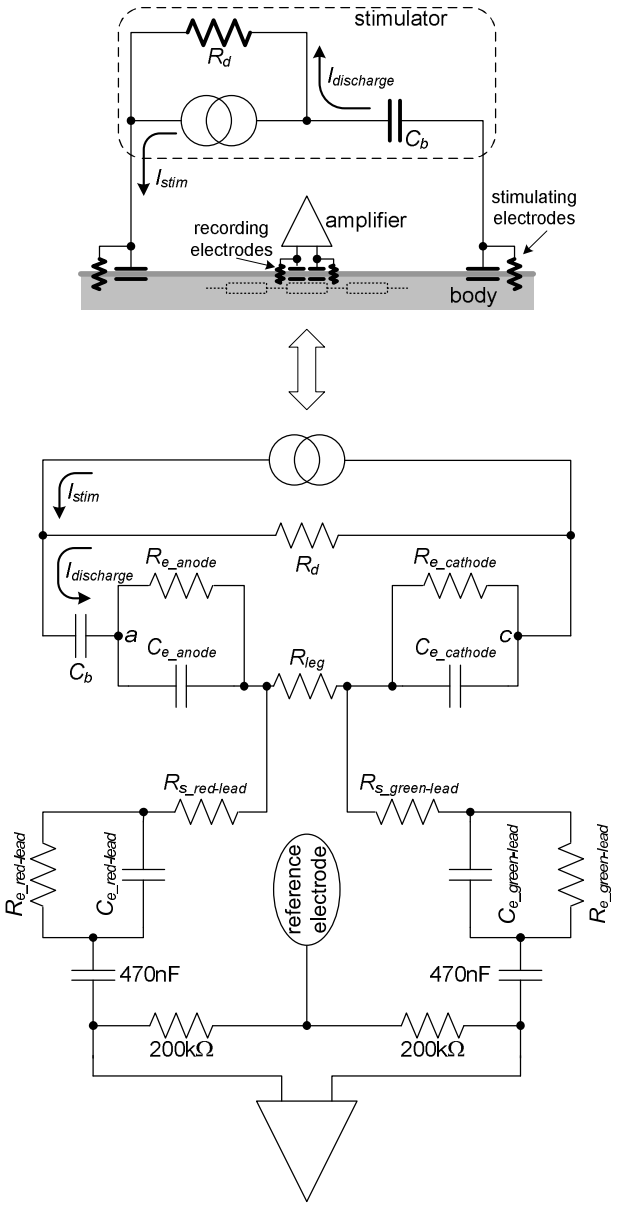

Figure E.2: Skin-electrode interface effect at the recording site.

stimulator have been explicitly shown, as well as the clamping diodes and the input filter found in the preamplifier circuit (refer to figure 6.5).

Method

A PSPICE model of figure E.2 was produced. The component values, used for the stimulating electrode model, were the same as those used in Section 7.3.1. The component values used for the recording electrodes were based on values measured by Perkins [2004] for a 3.2cm surface electrode. He presented nominal values for C_e, R_e and R_s of 21nF, 5kΩ and 870Ω, respectively. These values were adjusted by $\pm 10\%$, to ensure the same values were not used for both recording electrodes. The components used for the preamplifier input filter had nominal values and tolerances of 200kΩ $\pm$ 1%, for the resistors, and 470nF $\pm$ 10%, for the capacitors. The PSPICE circuit schematic is shown in figure E.3.

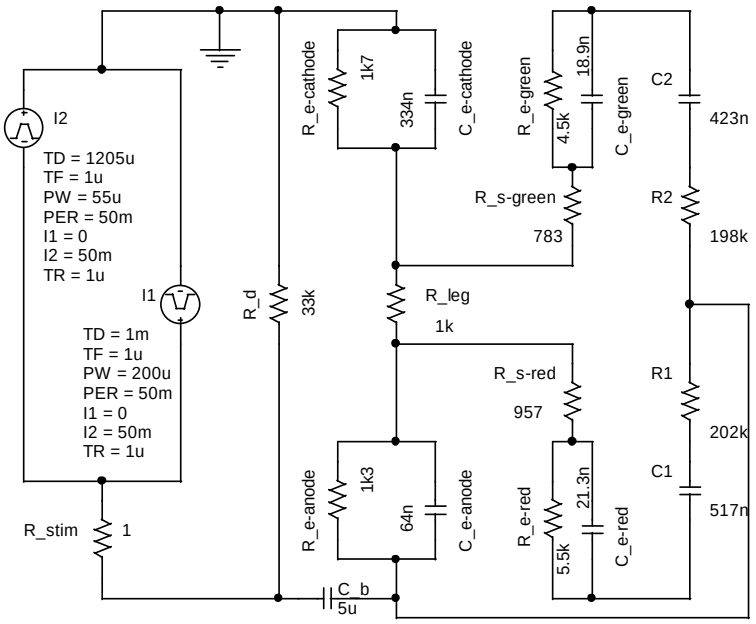

Figure E.3: PSPICE simulation of the electrode-skin interface (both stimulating and recording electrodes).

When placing the electrodes on a subject, provided that the reference electrode is placed on the knee, it would be close in proximity to the anode-first stimulating electrode. The potential of the reference electrode would therefore be close to that of the anode-first electrode. For this reason, the node to which the reference electrode is attached in figure E.2 was connected to one end of the anodal electrode in the PSPICE circuit.

Results

The voltages across the four electrodes (stimulating electrodes *anode* and *cathode*; recording electrodes *red* and *green*, as determined by the colour of the lead between the electrode and the preamplifier) and the blocking capacitor, C_b, were found immediately after a stimulation pulse. Figure E.4(a) shows how the voltages varied with PW_r setting. The residual voltage across the stimulating electrodes only, V_{res_SE}, the recording electrodes only, V_{res_RE}, and the combined residual voltage, V_{res} were calculated as in equations E.4 through E.6.

$$V_{res\_SE} = V_{anode} + V_{cathode} + V_{Cb} \tag{E.4}$$

$$V_{res\_RE} = V_{red} + V_{green} \tag{E.5}$$

$$V_{res} = V_{res\_SE} + V_{res\_RE} \tag{E.6}$$

The PW_r settings for which each of the voltages, shown in figure E.4(a), crossed the 0V line were found. Figure E.4(b) shows the discharge current waveforms, immediately after the negative phase of the stimulation pulse, for each of these PW_r settings.

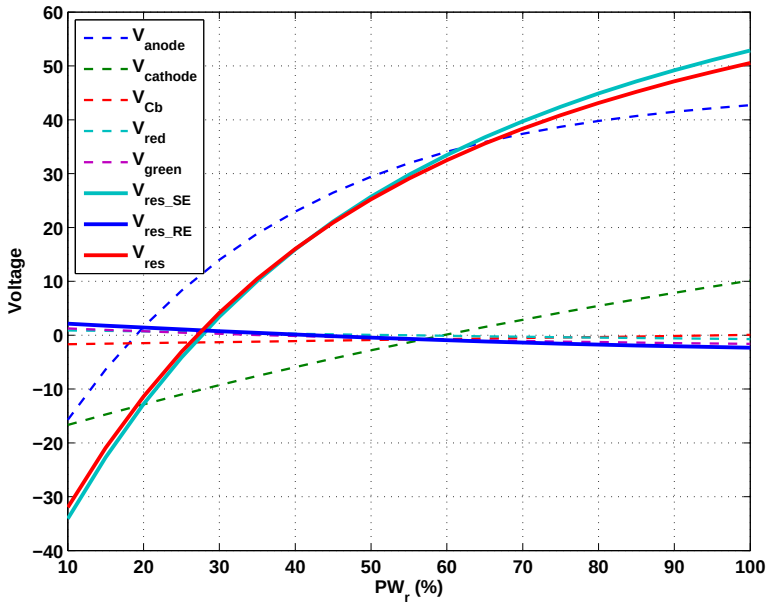

(a) Voltage across model components, immediately after a stimulation pulse, as a function of PW_r.

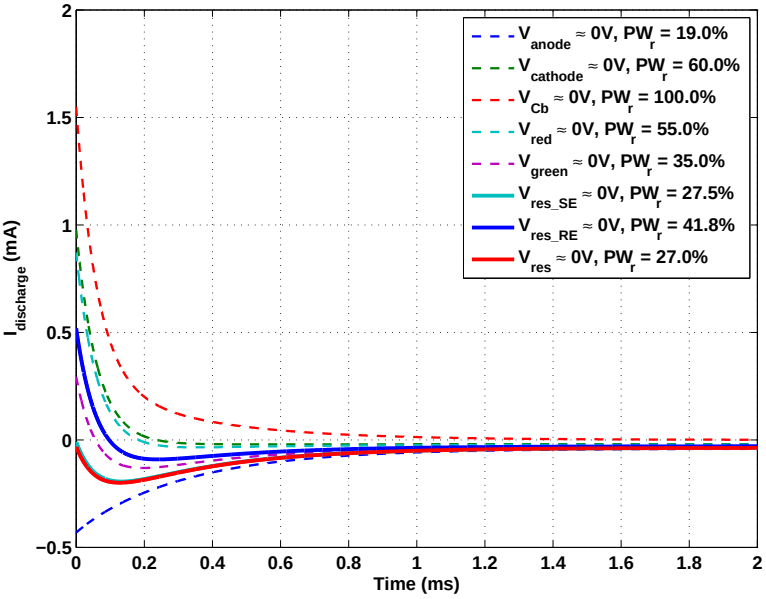

(b) Discharge current waveforms immediately after a stimulation pulse.

Figure E.4: PSPICE simulation of the residual charge present at the electrode-skin interface.

Discussion

By comparing figures 7.11 and E.4, we can see that the amplitude of the discharge current had decreased after including the recording electrodes into the simulation model. However, the shape of the current waveforms, stayed the same, even that of the wave-like response when $V_{res} = 0$V. The PW_r setting at which this happened was slightly less, 27.0% as compared with 27.5%. The current waveforms for V_{res_SE} and V_{res} virtually overlap, further indicating that any residual charge on the recording electrodes plays a very minor role in the presence of the discharge current.

Appendix F

Bi-moment chair study

F.1 Origin of the *major* positions

The SENIAM (Surface Electromyography for the Non-Invasive Assessment of Muscles) project gives guidelines for the placement of recording electrodes when measuring EMG. These guidelines served as the starting point for the protocol that was devised (by Lynsey Duffell and Di Newham, of Kings College London), concerning the placement of the stimulating electrodes for the three *major* positions. Table F.1 lists the SENIAM recommendations for the three superficial muscles of the Quadriceps.

The recommendations were modified by using 5 people, of different shape and size, placing the stimulating electrodes on their legs, and investigating these placements by palpating the muscles during voluntary contractions. This approach was used for each of the three *major* positions:

Rectus Using SENIAM's guidelines the recording electrodes are placed near the belly of RF (50% along the line between ASIS and patella). It was decided to move the stimulating electrodes further apart, towards either end of the muscle, so as to target as much of the muscle as possible. However, by looking at the anatomy of RF, if the electrodes were moved too far apart they would be placed above the tendon's present at the proximal and distal end of RF. Through experimentation with the 5 people, and palpation of RF during voluntary contractions, it was decided to place the proximal and distal electrodes at 25% and 75% along the line between ASIS and patella.

Vastii For both VM and VL, the distal stimulating electrodes are placed where the SENIAM guidelines recommend the recording electrodes should be placed. By considering the muscle anatomy and through palpation of the contracted muscles, positions were found for the proximal stimulating electrodes. The individual positions found for each person were then related to their leg circumference. The average of these values were then used in the final protocol.

Standard While working with SCI cyclists Duffell [2007] had regularly used the stimulating electrode positions of Perkins et al. [2001] to activate the Quadriceps muscles. However, the positions were randomly placed and no well-defined protocol existed. A protocol

along the same lines as that already found for the *Rectus* and *Vastii* positions, was then devised for the *Standard* position, to describe the placement of the electrodes according to where past experience indicated they should be.

Table F.1: SENIAM recommendations for recording electrode placement on the superficial muscles of Quadriceps, reproduced from Hermens et al. [1999], with permission.

Starting posture (for all muscles)	Sitting on a table with the knees in slight flexion and the upper body slightly bend backward.
Rectus femoris	
Muscle anatomy	*Origin:* Straight head from ASIS. Reflected head from groove above rim of acetabulum. *Insertion:* Proximal border of the patella and through patellar ligament.
Electrode placement	The electrodes need to be placed at 50% on the line from the ASIS to the superior part of the patella.
Vastus medialis	
Muscle anatomy	*Origin:* Distal half of the intertrochanteric line, medial lip of line aspera, proximal part of medial supracondylar line, tendons of adductor longus and adductor magnus and medial intermuscular septum. *Insertion:* Proximal border of the patella and through patellar ligament.
Electrode placement	Electrodes need to be placed at 80% on the line between the ASIS and the joint space in front of the anterior border of the medial ligament.
Vastus lateralis	
Muscle anatomy	*Origin:* Proximal parts of intertrochanteric line, anterior and inferior borders of GT, lateral lip of gluteal tuberosity, proximal half of lateral lip of linea aspera, and lateral intermuscular septum. *Insertion:* Proximal border of the patella and through patellar ligament.
Electrode placement	Electrodes need to be placed at 2/3 on the line from the ASIS to the lateral side of the patella.
Clinical test to detect EMG (for all muscles)	Extend the knee without rotating the thigh while applying pressure against the leg above the ankle in the direction of flexion.

F.2 Stanmore stimulator recruitment curve protocol settings

The settings for the Stanmore Stimulator, as described in Phillips et al. [2003], required to generate the recruitment curve stimulation protocol, are given in table F.2. For completeness, the stimulator settings used to generate a single burst of stimulation at 400μs, that was used to determine the tolerable current amplitude used in the stimulation protocol, are also provided.

Table F.2: Settings used on the Stanmore Stimulator, reproduced from [Duffell and Newham, 2008], with permission.

Set-up stimulator settings - Mode 2								
	1	2	3	4	5	6	7	8
V	1	0 or 1	0	0	0	0	0	0
W	6	4	20	20	100	0	0	1
Stimulation protocol stimulator settings - Mode 1								
	1	2	3	4	5	6	7	8
V	1	0 or 1	0	0	0	0	0	0
W	15	4	20	20	20	10	0	9

F.3 T-test analysis of the *major* position moment curves

A T-test was performed, where the null hypothesis was such that the mean moments measured with the *Rectus* and *Vastii* positions were the same as those measured with the *Standard* position. P-values were calculated for each burst of stimulation in a test (9 in total). The results are shown in table F.4. P-values less than 0.05, indicating a significant difference, have been highlighted.

For subjects A through H the maximum PW_p was set to 200μs, while for subjects I through L it was increased to 400μs (refer to table 8.3). Thus the stimulation intensity for the first 6 subjects was generally lower than that for the last 4 subjects. Consequently, instead of using the results from the entire table to find the percentage of significant differences found (as was done in Chapter 4), only the results for the ninth stimulation burst (outlined in the table), were used. The results are shown in table F.3.

Table F.3: Percentage of significant differences found.

	Standard - Rectus	***Standard - Vastii***
$\mathbf{M}_k$	70% (7/10)	70% (7/10)
$\mathbf{M}_h$	80% (8/10)	80% (8/10)

For the majority of hip and knee joint moments measured using the *Rectus* and *Vastii* positions, the difference was significant when compared with moments measured using the *Standard* position.

Table F.4: T-test results investigating the difference between mean moments measured with the three *major* positions. P-values were calculated for each stimulation burst. Highlighted p-values indicate a significant difference.

	Stimulation burst	**1**	**2**	**3**	**4**	**5**	**6**	**7**	**8**	**9**
					$\mathbf{M_k}$					
Standard - Rectus	Subject A	0.51	0.08	0.10	0.01	0.01	0.01	0.01	0.01	<0.01
	Subject B	0.31	0.79	0.97	0.10	0.03	<0.01	0.01	<0.01	0.03
	Subject E	0.35	0.08	0.04	0.10	0.02	0.28	0.16	0.17	0.08
	Subject F	0.02	<0.01	<0.01	<0.01	<0.01	<0.01	0.14	0.02	0.01
	Subject G	0.13	0.23	0.16	0.14	0.07	0.05	0.01	0.11	0.16
	Subject H	0.30	0.61	0.26	0.32	0.16	0.03	0.07	0.08	0.04
	Subject I	0.33	0.13	0.19	0.17	0.14	0.05	0.08	0.04	0.04
	Subject J	0.23	0.01	0.11	0.03	<0.01	0.26	0.01	0.01	<0.01
	Subject K	0.02	0.05	0.01	0.01	0.03	0.01	<0.01	<0.01	<0.01
	Subject L	0.18	0.07	0.11	0.08	0.08	0.06	0.06	0.08	0.07
Standard - Vastii	Subject A	0.07	0.09	0.14	0.10	0.05	0.03	0.04	0.04	0.04
	Subject B	0.77	0.34	0.10	0.70	0.37	0.33	0.04	0.06	0.07
	Subject E	0.40	0.01	0.02	<0.01	<0.01	0.01	0.01	0.02	<0.01
	Subject F	0.13	0.03	0.12	0.05	0.02	0.01	0.02	0.01	0.01
	Subject G	0.04	0.34	0.31	0.13	0.01	0.04	0.03	0.05	0.13
	Subject H	0.32	0.86	0.06	0.06	0.03	0.01	0.03	0.01	0.02
	Subject I	0.40	0.68	0.08	0.16	0.02	0.07	<0.01	0.03	0.04
	Subject J	0.07	<0.01	<0.01	<0.01	0.01	<0.01	<0.01	<0.01	<0.01
	Subject K	0.03	0.51	0.09	0.03	0.51	0.05	0.01	0.01	0.02
	Subject L	0.09	0.03	<0.01	0.13	0.46	<0.01	0.10	0.13	0.41
					$\mathbf{M_h}$					
Standard - Rectus	Subject A	0.15	0.08	0.08	<0.01	0.29	0.17	0.04	0.10	0.12
	Subject B	0.74	0.71	0.28	0.12	0.08	<0.01	0.01	0.01	0.02
	Subject E	0.94	0.92	0.23	0.16	0.05	0.04	0.02	0.02	0.03
	Subject F	0.52	0.04	<0.01	0.01	0.02	<0.01	0.02	0.03	0.04
	Subject G	0.96	0.57	0.45	<0.01	0.01	<0.01	<0.01	<0.01	<0.01
	Subject H	0.56	0.45	0.30	0.91	0.03	0.03	0.06	0.10	0.08
	Subject I	0.22	0.02	0.14	0.03	0.01	<0.01	<0.01	<0.01	<0.01
	Subject J	0.01	0.12	0.20	0.12	<0.01	<0.01	<0.01	<0.01	<0.01
	Subject K	0.98	0.09	0.07	0.07	0.58	0.08	0.03	<0.01	0.02
	Subject L	0.45	0.11	0.01	0.04	0.02	0.02	0.01	0.03	0.02
Standard - Vastii	Subject A	0.06	0.05	0.25	0.33	<0.01	0.01	<0.01	0.01	0.01
	Subject B	0.27	0.01	0.02	0.04	0.06	0.05	0.08	0.10	0.03
	Subject E	0.15	0.34	0.07	0.74	0.92	1.00	0.33	0.06	0.04
	Subject F	0.03	0.07	0.09	<0.01	0.17	0.03	0.07	0.04	0.02
	Subject G	0.07	0.03	0.34	0.12	0.10	<0.01	0.21	0.02	0.01
	Subject H	0.14	0.57	0.64	0.38	0.07	0.07	0.01	0.07	0.19
	Subject I	0.92	0.29	0.89	0.56	0.10	0.07	0.11	0.92	0.29
	Subject J	0.02	0.02	0.04	0.07	0.01	0.07	0.02	0.01	<0.01
	Subject K	0.04	0.05	0.02	0.66	0.79	0.03	0.02	<0.01	0.02
	Subject L	0.05	0.05	0.01	<0.01	<0.01	<0.01	<0.01	<0.01	0.01

F.4 M-wave scatter plots and EMG curves without crosstalk adjustments

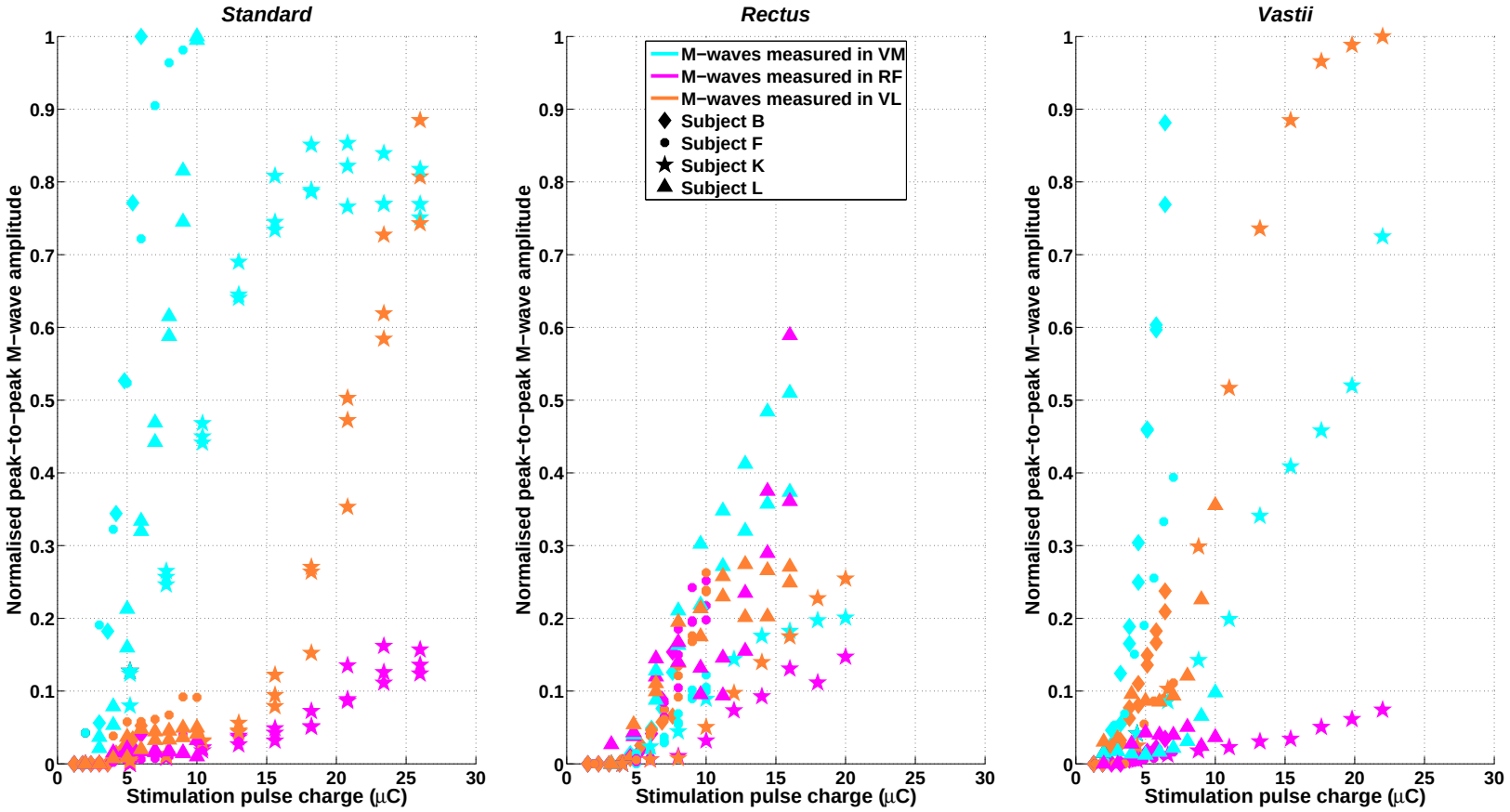

(a) (b) (c)

Figure F.1: Normalised peak-to-peak M-wave amplitudes, measured in the Quadriceps muscles, plotted against the charge delivered with each stimulation pulse, for the three *major* positions. No adjustments have been made to account for crosstalk.

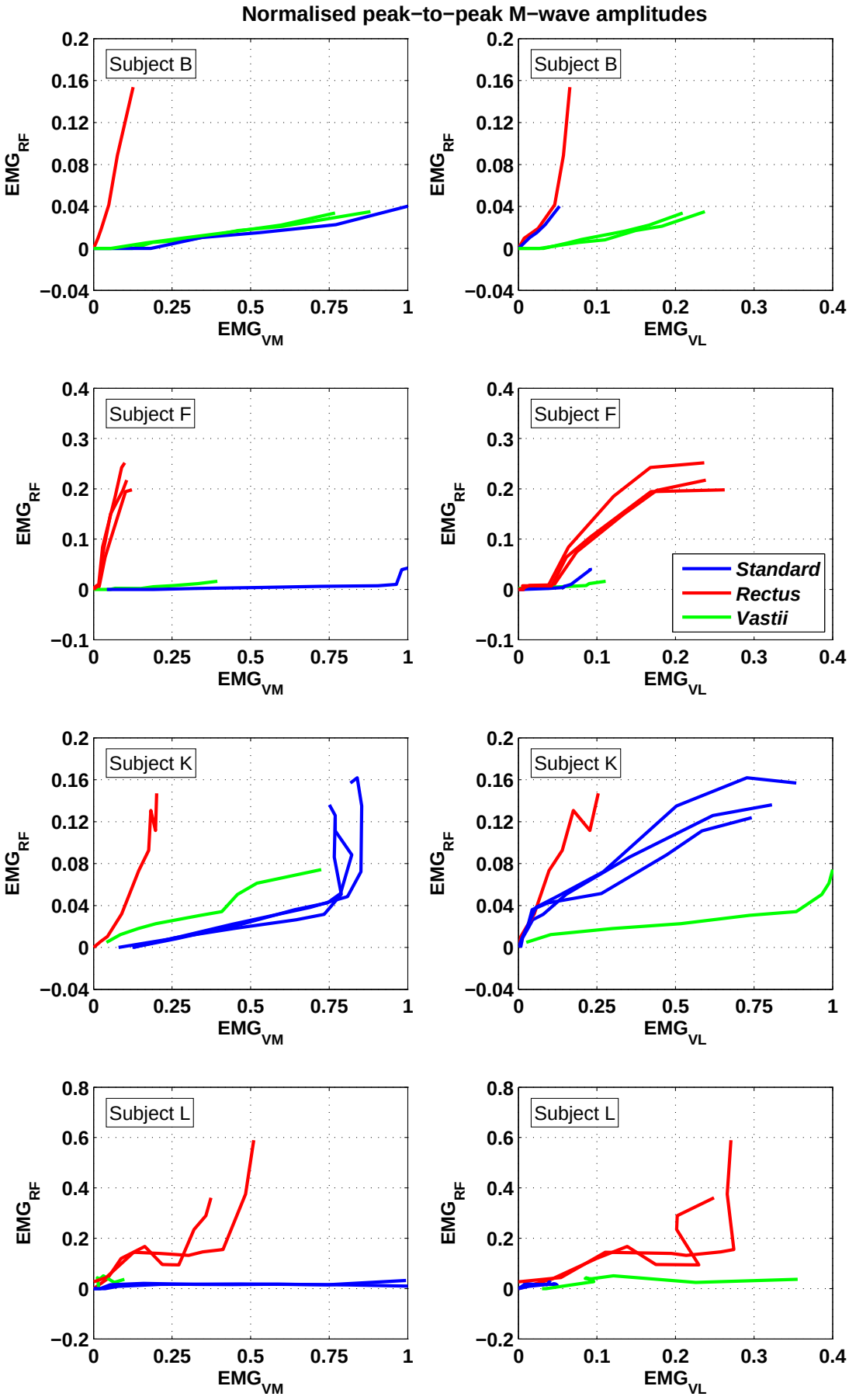

Figure F.2: EMG curves captured for all three *major* electrode positions, for each of the 4 subjects with complete data sets. No adjustments have been made to account for crosstalk.

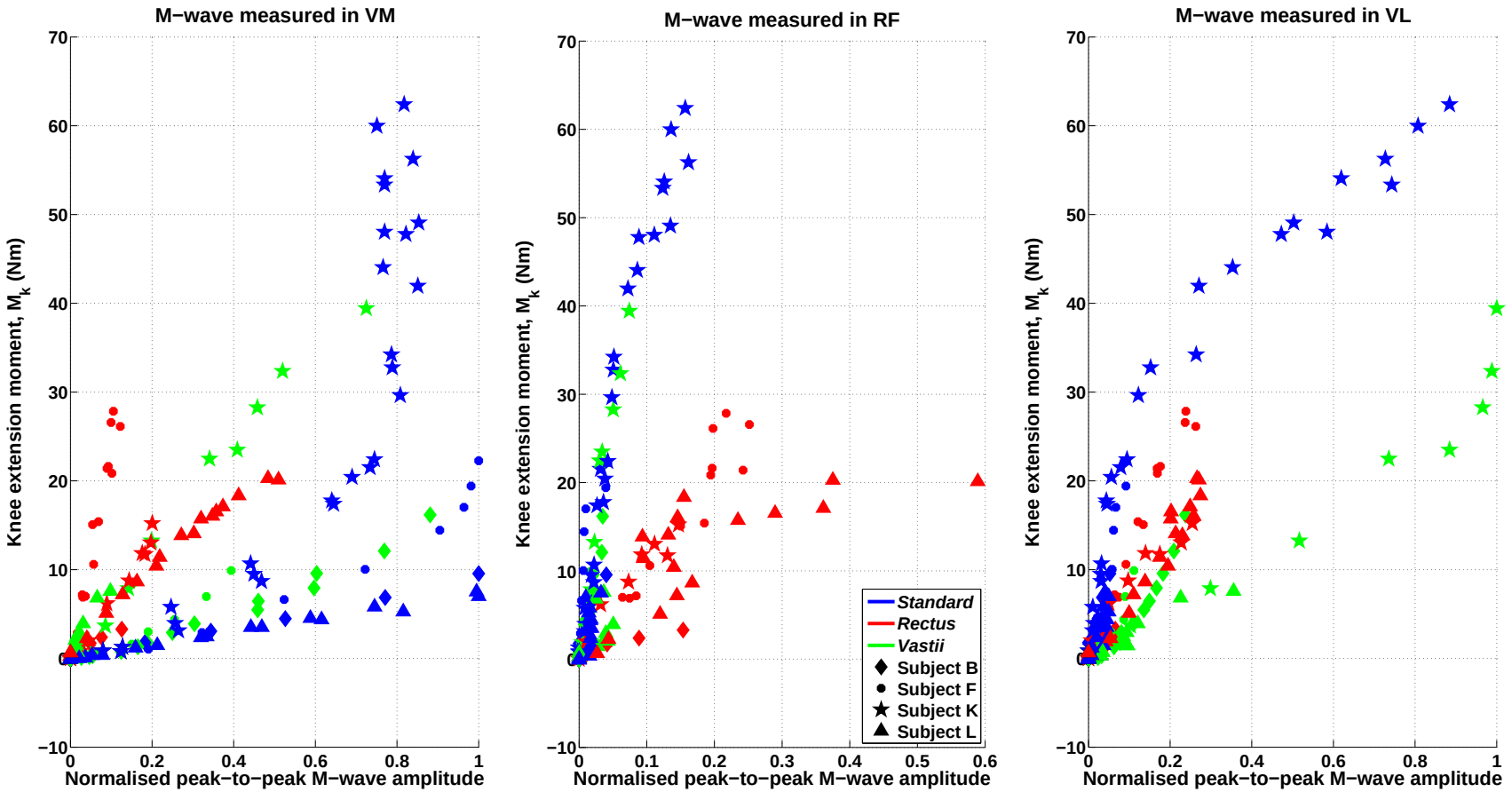

(a) (b) (c)

Figure F.3: Normalised peak-to-peak M-wave amplitudes, plotted against the knee extension moment, for the three superficial muscles of the Quadriceps. No adjustments have been made to account for crosstalk.

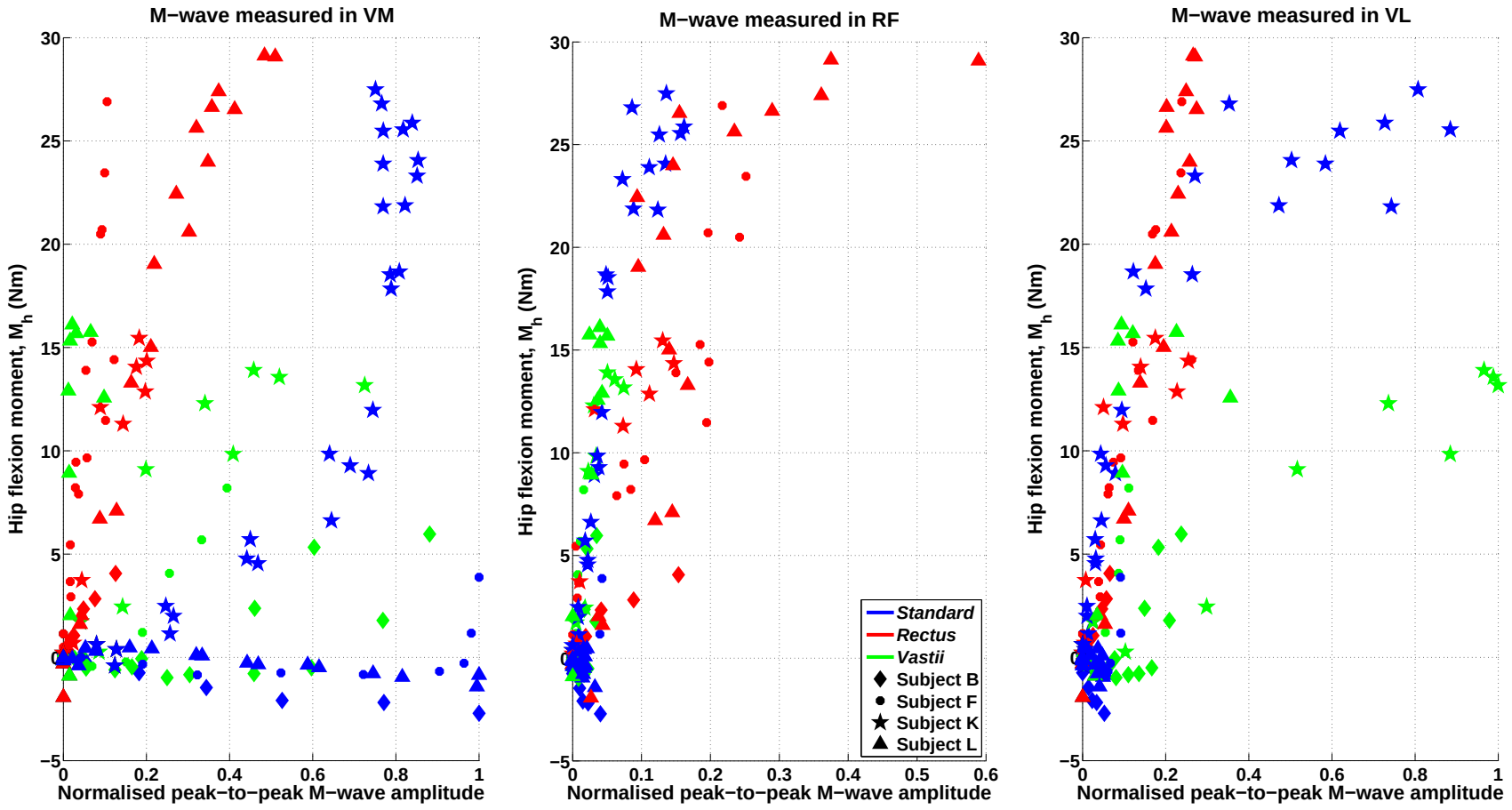

(a) (b) (c)

Figure F.4: Normalised peak-to-peak M-wave amplitudes, plotted against the hip flexion moment, for the three superficial muscles of the Quadriceps. No adjustments have been made to account for crosstalk.

References

AD. *60 MHz 2000 V / μs Monolithic Op Amp*. Analog Devices, Inc., 1989. URL http://www.analog.com/static/imported-files/data_sheets/AD844.pdf.

AD. *Low Cost Low Power Instrumentation Amplifier - AD620*. Analog Devices, Inc., 2004. URL http://www.analog.com/static/imported-files/data_sheets/AD620.pdf.

Andriacchi T.P., Andersson G.B., Fermier R.W., Stern D., and Galante J.O. "A study of lower-limb mechanics during stair-climbing." *The Journal of Bone and Joint Surgery*, 62:749–757, 1980.

Babb T.L., Mariani E., Strain G.M., Lieb J.P., Soper H.V., and Crandall P.H. "A sample and hold amplifier system for stimulus artifact suppression." *Electroencephalography and Clinical Neurophysiology*, 44(4):528–31, 1978. ISSN 0013-4694.

Barclay C.J., Constable J.K., and Gibbs C.L. "Energetics of fast- and slow-twitch muscles of the mouse." *Journal of Physiology*, 472:61–80, 1993.

Basmajian J.V. and De Luca C.J. *Muscles Alive - Their Functions Revealed by Electromyography*. Waverly Press Inc., 5th edition, 1985. ISBN O-683-00414-X.

Bell A.L., Brand R.A., and Pedersen D.R. "Prediction of hip joint centre location from external landmarks." *Human Movement Science*, 8(1):3–16, 1989. ISSN 01679457.

Bilodeau M., Cincera M., Gervais S., Arsenault A.B., Gravel D., Lepage Y., and McKinley P. "Variations in the shape of the EMG power spectrum during an increasing force level." In "Proceedings of the 15th Annual International Conference of the IEEE Engineering in Medicine and Biology Society", pages 1205–1206. IEEE, 1993. ISBN 0-7803-1377-1.

Binder-Macleod S.A. and McDermond L.R. "Changes in the force-frequency relationship of the human quadriceps femoris muscle following electrically and voluntarily induced fatigue." *Physical Therapy*, 72(2):95–104, 1992. ISSN 0031-9023.

Bobrow L.S. *Fundamentals of Electrical Engineering*. Oxford University Press, 2nd edition, 1996. ISBN 0-19-510509-5.

Bronzite M. "Simple active flters - Design procedure." *Wireless World*, pages 117–119, 1970. URL www.electronicsworld.co.uk. Publisher: SJP Business Media.

Bruun E. and Haxthausen E.U. "Current conveyor based EMG amplifier with shutdown control." *Electronics Letters*, 27(23):2172–2174, 1991.

Cash M. *Pocket Atlas of the Moving Body: For All Students of Human Biology, Medicine, Sports and Physical Therapy*. Edbury Press, 2000. Illustrations by A. Wadmore.

Chaplin E. "Functional neuromuscular stimulation for mobility in people with spinal cord injuries. The Parastep I System." *The Journal of Spinal Cord Medicine*, 19(2):99, 1996.

Charnwood Dynamics Ltd. *CODA User Guide.*, 2008.

Chesler N.C. and Durfee W.K. "Surface EMG as a fatigue indicator during FES-induced isometric muscle contractions." *Journal of Electromyography and Kinesiology*, 7(1):27–37, 1997. ISSN 1050-6411.

De Luca C.J. and Merletti R. "Surface myoelectric signal cross-talk among muscles of the leg." *Electroencephalography and Clinical Neurophysiology*, 69(6):568–75, 1988. ISSN 0013-4694.

Denny-Brown D. "Interpretation of the electromyogram." *Archives of Neurology and Psychiatry*, 61(2):99–128, 1949. ISSN 0096-6754.

Dorgan S.J. and Reilly R.B. "A model for human skin impedance during surface functional neuromuscular stimulation." *IEEE Transactions on Rehabilitation Engineering*, 7(3):341–348, 1999. ISSN 10636528.

Duffell L.D. *An investigation of functional electrical stimulation cycling for people with spinal cord injury*. Ph.D. thesis, Kings College London, 2007.

Duffell L.D., Donaldson N.d.N., and Newham D.J. "Why is the metabolic efficiency of FES cycling low?" *IEEE Transactions on Neural Systems and Rehabilitation Engineering*, 17(3):263–9, 2009. ISSN 1558-0210.

Duffell L.D., Donaldson N.d.N., Perkins T.A., Rushton D.N., Hunt K.J., Kakebeeke T.H., and Newham D.J. "Long-term intensive electrically stimulated cycling by spinal cord-injured people: Effect on muscle properties and their relation to power output." *Muscle & Nerve*, 38(4):1304–11, 2008. ISSN 0148-639X.

Duffell L.D. and Newham D.J. "Bi-moment chair - Protocol for recruitment curves." Technical report, Kings College London, 2008.

Dymond A.M. "Characteristics of the metal-tissue interface of stimulation electrodes." *IEEE Transactions on Biomedical Engineering*, BME-23(4):274–280, 1976. ISSN 0018-9294.

Farina D., Blanchietti A., Pozzo M., and Merletti R. "M-wave properties during progressive motor unit activation by transcutaneous stimulation." *Journal of Applied Physiology*, 97(2):545–55, 2004*a*. ISSN 8750-7587.

Farina D., Merletti R., Indino B., and Graven-Nielsen T. "Surface EMG crosstalk evaluated from experimental recordings and simulated signals. Reflections on crosstalk interpretation, quantification and reduction." *Methods of Information in Medicine*, 43(1):30–5, 2004*b*. ISSN 0026-1270.

Farina D., Merletti R., Indino B., Nazzaro M., and Pozzo M. "Surface EMG crosstalk between knee extensor muscles: Experimental and model results." *Muscle & Nerve*, 26(5):681–95, 2002. ISSN 0148-639X. URL http://onlinelibrary.wiley.com/doi/10.1002/mus.10256/abstract.

Glaser R.M., Figoni S.F., Hooker S.P., Rodgers M.M., Ezenwa B.N., Suryaprasad A.G., Gupta S.C., and Mathews T. "Efficiency of FNS leg cycle ergometry." In "Proceedings of the 11th Annual International Conference of the IEEE Engineering in Medicine and Biology Society", pages 961–963. Ieee, 1989.

Hakansson N.A. and Hull M.L. "Functional roles of the leg muscles when pedaling in the recumbent versus the upright position." *Journal of Biomechanical Engineering*, 127(2):301, 2005. ISSN 01480731.

Hansen E.A., Andersen J.L., Nielsen J.S., and Sjøgaard G. "Muscle fibre type, efficiency, and mechanical optima affect freely chosen pedal rate during cycling." *Acta Physiologica Scandinavica*, 176(3):185–94, 2002. ISSN 0001-6772.

Harding G.W. "A method for eliminating the stimulus artifact from digital recordings of the direct cortical response." *Computers and Biomedical Research*, 24(2):183–95, 1991. ISSN 0010-4809.

Hermens H.J., Freriks B., Merletti R., Rau G., Disselhorst-Klug C., Stegeman D.F., and Hägg G.M. "SENIAM - European recommendations for surface electromyography." 1999. URL http://www.seniam.org/.

Hodgkin A.L., Huxley A.F., and Katz B. "Measurement of current-voltage relations in the membrane of the giant axon of Loligo." *The Journal of Physiology*, 116:424–448, 1952.

Horowitz P. and Hill W. *The Art of Electronics*. Cambridge University Press; 2 edition, 1989. ISBN 0521370957.

Hsiao H. and Keyserling W.M. "A three-dimensional ultrasonic system for posture measurement." *Ergonomics*, 33(9):1089–1114, 1990.

Hunt K.J., Saunders B.A., Perret C., Berry H., Allan D., Donaldson N.d.N., and Kakebeeke T.H. "Energetics of paraplegic cycling: A new theoretical framework and efficiency characterisation for untrained subjects." *European Journal of Applied Physiology*, 101(3):277–85, 2007. ISSN 1439-6319.

Jarmey C. *The Atlas of Musculo-Skeletal Anatomy*. North Atlantic Books, 2004. ISBN 1556435290.

Johnston T.E., Barr A.E., and Lee S.C.K. "Biomechanics of submaximal recumbent cycling in adolescents with and without cerebral palsy." *Physical Therapy*, 87(5):572–85, 2007. ISSN 0031-9023.

Jones D., Round J., and de Haan A. *Skeletal Muscle from Molecules to Movement - A Textbook of Muscle Physiology for Sport, Exercise, Physiotherapy and Medicine*. Churchill Livingstone, 2004.
Figure 1.3 after Chapter 4: *Fibre types and motor units*, Figure 4.1, page 32.
Figure 4.4 after Chapter 9: *Introduction to fatigue*, Figure 9.11, page 99.

Kern H., Frey M., Holle J., Mayr W., Schwanda G., Stöhr H., and Thoma H. "Funktionelle elektrostimulation querschnittgelähmter patienten - 1 jahr praktische anwendung." *Zeitschrift für Orthopädie und ihre Grenzgebiete*, 123:1–12, 1985.

Kirkwood R.N., Culham E.G., and Costigan P. "Radiographic and non-invasive determination of the hip joint center location: Effect on hip joint moments." *Clinical Biomechanics*, 14(4):227–35, 1999. ISSN 0268-0033.

Kjær M., Perko G., Secher N.H., Boushel R., Beyer N., Pollack S., Horn A., Fernandes A., Mohr T., Lewis S.F., and Galbo H. "Cardiovascular and ventilatory responses to electrically induced cycling with complete epidural anaesthesia in humans." *Acta Physiologica Scandinavica*, 151(2):199–207, 1994.

Knaflitz M. and Merletti R. "Suppression of simulation artifacts from myoelectric-evoked potential recordings." *IEEE Transactions on Biomedical Engineering*, 35(9):758–63, 1988. ISSN 0018-9294.

Knaflitz M., Merletti R., and Catani F. "Crosstalk assessment in human thigh muscles." In W. Walinga, H. Boom, and J. de Vries, editors, "Electrophysiological Kinesiology", pages 261–264. Elsevier Science Publishers B. V. (Biomedical Division), 1988.

Koh T.J. and Grabiner M.D. "Evaluation of methods to minimize cross talk in surface electromyography." *Journal of Biomechanics*, 26 Suppl 1:151–7, 1993. ISSN 0021-9290.

Kornfield M.J., Cerra J., and Simons D.G. "Stimulus artifact reduction in nerve conduction." *Archives of Physical Medicine and Rehabilitation*, 66(4):232–5, 1985. ISSN 0003-9993.

Kralj A.R. and Bajd T. *Functional Electrical Stimulation: Standing and Walking After Spinal Cord Injury*. CRC Press, 1989. ISBN 0849345294.

Kwatny E., Thomas D.H., and Kwatny H.G. "An application of signal processing techniques to the study of myoelectric signals." *IEEE Transactions on Biomedical Engineering*, BME-17(4):303–313, 1970. ISSN 0018-9294.

McGill K.C., Cummins K.L., Dorfman L.J., Berlizot B.B., Leutkemeyer K., Nishimura D.G., and Widrow B. "On the nature and elimination of stimulus artifact in nerve signals evoked and recorded using surface electrodes." *IEEE Transactions on Biomedical Engineering*, 29(2):129–37, 1982. ISSN 0018-9294.

McLean L., Scott R.N., and Parker P.A. "Stimulus artifact reduction in evoked potential measurements." *Archives of Physical Medicine and Rehabilitation*, 77:1286–1292, 1996.

Merletti R., Knaflitz M., and De Luca C.J. "Electrically evoked myoelectric signals." *Critical Reviews in Biomedical Engineering*, 19(4):293–340, 1992. ISSN 0278-940X.

Minzly J., Mizrahi J., Hakim N., and Liberson A. "Stimulus artefact suppressor for EMG recording during FES by a constant-current stimulator." *Medical & Biological Engineering & Computing*, 31(1):72–75, 1993. ISSN 0140-0118.

Mohr T., Andersen J.L., Biering-Sørensen F., Galbo H., Bangsbo J., Wagner A., and Kjær M. "Long term adaptation to electrically induced cycle training in severe spinal cord injured individuals." *Spinal Cord*, 35(1):1–16, 1997*a*.

Mohr T., Pødenphant J., Biering-Sørensen F., Galbo H., Thamsborg G., and Kjær M. "Increased bone mineral density after prolonged electrically induced cycle training of paralyzed limbs in spinal cord injured man." *Calcified Tissue International*, 61(1):22–5, 1997*b*. ISSN 0171-967X.

Muraoka Y. "Development of an EMG recording device from stimulation electrodes for functional electrical stimulation." *Frontiers of Medical and Biological Engineering*, 11(4):323–333, 2002.

Neumann M.R. "Biopotential Electrodes." In J.D. Bronzino, editor, "The Biomedical Engineering Handbook", CRC Press LLC, 2nd edition, 2000.

NI. *DAQ 6023E/6024E/6025E User Manual*. National Instruments Corporation, 2000. URL http://digital.ni.com/manuals.nsf/websearch/0C88F40FFE7F28CD862569AE00574AC1.

NI. *NI 6023E/6024E/6025E Family Specifications*. National Instruments Corporation, 2005. URL http://www.ni.com/pdf/manuals/370719c.pdf.

Nilsson J., Ravits J., and Hallett M. "Stimulus artifact compensation using biphasic stimulation." *Muscle & Nerve*, 11(6):597–602, 1988. ISSN 0148-639X.

O'Keeffe D.T., Lyons G.M., Donnelly A.E., and Byrne C.A. "Stimulus artifact removal using a software-based two-stage peak detection algorithm." *Journal of Neuroscience Methods*, 109(2):137–45, 2001. ISSN 0165-0270.

OLIMEX. "MSP430-Hxxx-E Header board for MSP430F14x and MSP430F41x microcontrollers." 2002. URL http://www.olimex.com/dev/.

Parsa V., Parker P., and Scott R. "Convergence characteristics of two algorithms in non-linear stimulus artefact cancellation for electrically evoked potential enhancement." *Medical & Biological Engineering & Computing*, 36(2):202–214, 1998. ISSN 0140-0118.

Perkins T., Donaldson N., Fitzwater R., Phillips G., and Wood D. "Leg powered paraplegic cycling system using surface functional electrical stimulation." In "7th Vienna Internationnal Workshop on Functional Electrical Stimulation", pages 36–39. 2001.

Perkins T.A. "Impedance of common surface stimulation electrodes." In "Proceedings of the 9th Annual IFESS Conference", pages 419–421. Bournemouth, UK, 2004.

Petrofsky J.S., Heaton H., and Phillips C.A. "Outdoor bicycle for exercise in paraplegics and quadriplegics." *Journal of Biomedical Engineering*, 5(4):292–6, 1983. ISSN 0141-5425.

Petrofsky J.S. and Stacy R. "Effect of training on endurance and the cardiovascular responses of individuals with paraplegia during dynamic exercise induced by functional electrical stimulation." *European Journal of Applied Physiology*, 64:487–492, 1992.

Phillips G.F., Wood D.E., and Perkins T.A. *Stanmore Stimulator, Neuromuscular Stimulator - Clinician and User Instruction Manuals.*, 2003.

Reed A. and Low J. *Electrotherapy Explained: Principles and Practice*. Butterworth-Heinemann, 3rd edition, 2000. ISBN 0750641495.

Reichel M., Bijak M., Mayr W., Lanmüller H., Rafolt D., Sauermann S., Unger E., and Turkof E. "Biphasic stimulation: An alternative approach to minimize the stimulus artifact for diagnostic and for control applications." In "7th Vienna International Workshop on Functional Electrical Stimulation", pages 118–121. 2001.

Reiser R.F., Peterson M.L., and Broker J.P. "Understanding recumbent cycling: Instrumentation design and biomechanical analysis." *Biomedical Sciences Instrumentation*, 38:209, 2002.

Rosell J., Colominas J., Riu P., Pallas-Areny R., and Webster J.G. "Skin impedance from 1Hz to 1MHz." *IEEE Transactions on Biomedical Engineering*, 35(8):649–51, 1988. ISSN 0018-9294.

Scott R.N., McLean L., and Parker P.A. "Stimulus artefact in somatosensory evoked potential measurement." *Medical & Biological Engineering & Computing*, 35(3):211–5, 1997. ISSN 0140-0118.

Sedra A. and Smith K.C. "A second-generation current conveyor and its applications." *IEEE Transactions on Circuit Theory*, 17(1):132–134, 1970. ISSN 0018-9324.

Sedra A. and Smith K.C. *Microelectronic Circuits*. Oxford University Press, USA, 4th edition, 1998. ISBN 0-19-511690-9.

Sennels S., Biering-Sørensen F., Andersen O.T., and Hansen S.D. "Functional neuromuscular stimulation controlled by surface electromyographic signals produced by volitional activation of the same muscle: Adaptive removal of the muscle response from the recorded EMG-signal." *IEEE Transactions on Rehabilitation Engineering*, 5(2):195–206, 1997. ISSN 10636528.

Shell D. "High-accuracy bridge amplifier." *Electronics World & Wireless World*, pages 582–583, 1990. URL www.electronicsworld.co.uk. Publisher: SJP Business Media.

Smith K.C. and Sedra A. "The current conveyor - A new circuit building block." In "Proceedings of the IEEE", pages 1368–1369. 1968.

Solomonow M., Baratta R., Bernardi M., Zhou B., Lu Y., Zhu M., and Acierno S. "Surface and wire EMG crosstalk in neighbouring muscles." *Journal of Electromyography and Kinesiology*, 4(3):131–42, 1994. ISSN 1050-6411.

Spencer H.J. "An automatic, optically isolated, biphasic constant current stimulator adapter for artefact suppression." *Electroencephalography and Clinical Neurophysiology*, 51(2):215–217, 1981. ISSN 00134694.

Szecsi J., Krause P., Krafczyk S., Brandt T., and Straube A. "Functional output improvement in FES cycling by means of forced smooth pedaling." *Medicine & Science in Sports & Exercise*, 39(5):764–80, 2007. ISSN 0195-9131.

Taylor J.R. *An Introduction to Error Analysis: The Study of Uncertainties in Physical Measurements*. University Science Books, Oxford University Press, 1982. ISBN 0935702105.

Thorsen R. "An artefact suppressing fast-recovery myoelectric amplifier." *IEEE Transactions on Biomedical Engineering*, 46(6):764–6, 1999. ISSN 0018-9294.

Tortora G.J. and Derrickson B.H. *Introduction to the Human Body: The Essentials of Anatomy and Physiology*. John Wiley & Sons, 7th edition, 2006. ISBN 0471691232.

Trew M. "Musculoskeletal Basis for Movement." In M. Trew and T. Everett, editors, "Human Movement: An Introductory Text (Physiotherapy Essentials)", pages 7–40. Churchill Livingstone, 5th edition, 2005. ISBN 0443074461.

Tucker K.J., Tuncer M., and Türker K.S. "A review of the H-reflex and M-wave in the human triceps surae." *Human Movement Science*, 24(5-6):667–688, 2005. ISSN 0167-9457.

Van Soest A.J., Gföhler M., and Casius L.J.R. "Consequences of ankle joint fixation on FES cycling power output: A simulation study." *Medicine & Science in Sports & Exercise*, 37(5):797–806, 2005. ISSN 0195-9131.

Vishay. *Linear Optocoupler , High Gain Stability , Wide Bandwidth - IL300*. Vishay Intertechnology, Inc., 2004. URL http://www.vishay.com/docs/83622/il300.pdf.

Vøllestad N.K. "Measurement of human muscle fatigue." *Journal of Neuroscience Methods*, 74(2):219–227, 1997. ISSN 01650270.

Walker D.D. and Kimura J. "A fast-recovery electrode amplifier for electrophysiology." *Electroencephalography and Cinical Neurophysiology*, 45(6):789–92, 1978. ISSN 0013-4694.

Webster J.G., Clark Jr. J.W., Neuman M.R., Olson W.H., Peura R.A., Primiano Jr. F.P., Siedband M.P., and Wheeler L.A. *Medical Instrumentation: Application and Design*. John Wiley & Sons, Inc., 4th edition, 2009. ISBN 0471676004.
Figure 4.9 after Figure 5.23(a), page 232.

Winter D.A. *Biomechanics and Motor Control of Human Movement*. Wiley, 3rd edition, 2005. ISBN 047144989X.

Yu C.H. *New method for restoring standing to paraplegics: Control of leg muscle stimulation by the handle support reactions*. Ph.D. thesis, University College London, 1999.

Zhang Q., Hayashibe M., Fraisse P., and Guiraud D. "FES-induced torque prediction with evoked EMG sensing for muscle fatigue tracking." *IEEE/ASME Transactions on Mechatronics*, 16(5):816–826, 2011. ISSN 1083-4435.